Doxorubicin-Induced Cardiotoxicity: Investigating Metabolic Dysfunction and the Implication of Iron in Chronic DOX-Induced Cardiotoxicity In Vivo

Sterk, Pippa

Awarding institution:
King's College London

Doxorubicin-Induced Cardiotoxicity:

Investigating Metabolic Dysfunction and the Implication of Iron in Chronic DOX-Induced Cardiotoxicity *In Vivo*

A thesis submitted by

Melissa Gargaro

For the degree of

Doctor of Philosophy

University of London

2024

School of Biomedical Engineering and Imaging Sciences

King's College London

DECLARATION

I, Melissa Gargaro confirm that the PhD thesis entitled "Doxorubicin-Induced Cardiotoxicity: Investigating Metabolic Dysfunction and the Implication of Iron in Chronic DOX-Induced Cardiotoxicity In Vivo" is no more than 100,000 words in length including quotes and exclusive of tables, figures, appendices, bibliography, and references. No part of this thesis has been submitted in support of any other application for a degree or qualification of King's College London, or any other university or institute of learning. I confirm that this work is my own. Where information has been derived from other sources it has been indicated.

COVID-19 IMPACT STATEMENT

Lab closures due to COVID-19 significantly disrupted my PhD project as my research is entirely lab-based. Access to labs was limited between March 2020 and August 2020, as well as from November 2020 to March 2021, due to closures, efforts to protect my household from COVID-19, and lab booking backlogs. The interruption resulted in a loss of over six months of crucial lab time. During the early stages of my work this was particularly impactful; My PhD program started in Sept 2019 and there were limited options for off-site analytical work beyond thesis writing and literature review. Therefore, although this period was utilized, it did not substantially advance my project timeline.

My research relied heavily on developing longitudinal in vivo models and studies, each taking 2-5 months to complete. The time lost forced the need to conduct the final two longitudinal in vivo studies back-to-back, preventing the analysis of previous results before initiating the next. Hence, decisions on Doxorubicin dosage for the final study had to rely solely on functional data. Because of this, I proceeded with a final dose that was too low to invoke the pathology that we were intending to see, which meant that we weren't able to test our hypotheses as we would otherwise have done.

Furthermore, delayed refurbishments at the London Metallomics Facility due to the pandemic resulted in extensive closures and back log, impeding access to necessary resources required for ICP-MS based measurements of cardiac iron. Due to closures and inaccessibility between Oct 2022-Aug 2023, critical iron measurements from the final in vivo studies were only obtainable during the last two months of funding This restricted timeframe prevented further experiments, essential for refining the iron measurement protocol and identifying potential outliers, such as intended mass balance studies.

In summary, the COVID-19 disruptions had a profound impact on my research, leading to delays in data collection, analysis, and refinement. The sequential execution of studies, limited access to facilities, and constrained timeframes have posed significant challenges, necessitating adaptive strategies and compromises in research methodologies.

ABSTRACT

Doxorubicin (DOX) is a widely used chemotherapeutic drug, but its utility is compromised by cardiotoxicity, which can be debilitating and potentially lethal. Current diagnostic methods assessing structural and contractile dysfunction are often unable to detect its onset before irreversible damage has occurred. The relative importance of the various mechanisms underlying DOX-induced cardiotoxicity remain unclear, but iron overload and oxidative stress are known to play an important role. Cancer patients with pre-existing cardiac iron overload due to blood transfusion or genetic disorders are known to be at elevated risk.

The aim of this thesis was to examine the relationship between cardiac iron overload and metabolic dysfunction in a clinically relevant *in vivo* preclinical model of chronic DOX-induced cardiotoxicity.

An ICP-MS based protocol was optimised for the measurement of total and mitochondrial cardiac iron; cardiac function was monitored by echocardiography and metabolic profiling was performed by high field NMR. Two clinically relevant rat models were developed and characterised, 1) cardiac iron overload using iron dextran to emulate the elevated levels of iron observed in cancer patients undergoing DOX treatment, and 2) a clinically relevant model of chronic DOX-induced cardiotoxicity. These models were used to test whether pre-existing iron overload exacerbates chronic DOX-induced cardiotoxicity, and to investigate the potential cardioprotective efficacy of pre-treatment with the iron chelator deferiprone.

A dose-dependent reduction in LVEF and alterations in cardiac metabolism six weeks after the end of DOX treatment was observed. Total cellular cardiac iron did not show significant elevation with the administration of clinically equivalent DOX doses (2 mg/kg/wk and 3 mg/kg/wk for four weeks). These results suggest that total cardiac iron is not perturbed long term in chronic DOX-induced cardiotoxicity, however the importance of labile iron versus bound may be more significant.

It was found that iron loading did not exacerbate cardiac dysfunction or alter cardiac metabolism within the timeframe of our study and at the dosage used. However, iron loading did induce a non-significant reduction in LVEF compared to DOX treatment alone. This difference may become more pronounced over time due to the progressive nature of chronic DOX-induced cardiotoxicity, potentially impacting life expectancy beyond the 6-week

observation period. Deferiprone did mitigate the decline in LVEF by normalizing it to levels observed in animals treated with DOX alone. Though LVEF remained significantly reduced compared to control and baseline levels, pre-treatment of deferiprone may hold clinical significance in the longer term as chronic DOX-induced cardiotoxicity progresses.

Lastly, preliminary investigations on DOX lipotoxicity revealed that DOX treatment invoked systemic changes in lipid metabolism (measured by elevated serum lipid levels and altered liver metabolism), suggesting additional mechanisms may potentiate anthracycline-induced cardiotoxicity. This suggests the possibility of testing the cardioprotective potential of statins on the development of DOX-induced cardiotoxicity using our *in vivo* models.

ACKNOWLEDGEMENTS

Firstly, I extend my sincere gratitude to my supervisors Dr Richard Southworth and Dr Thomas Eykyn. Rick, your patience, guidance, and unwavering encouragement throughout my PhD journey have been truly invaluable. Tom, I am grateful for your willingness to always explain complex and intricate concepts, as well as your constructive criticism which has been indispensable. Without their combined dedication I could not have got here.

Thank you to the rest of the department, students, post docs and academics, for their support and guidance. Particular thanks to Dr Fred Baark for essentially teaching me everything I know about *in vivo* work, and to Dr Yu Jin Chung for being a fount of knowledge and always finding time to help and advise.

Special thanks to Alina, Marguerita and Faysal. We all started our PhD's together and we have been in it together ever since. We've supported and motivated each other through tough times with words of encouragement and laughter, and I am eternally grateful for the friendship we formed.

To my wonderful friends Sharb, Kelly, Cat, Issy, Bo, Louise, Johanna and Annabel. Your messages of encouragement whilst I was MIA were little nuggets of motivation and I love you all dearly. To Temi, who was always on the other end of the line to give me a pep talk when I thought I had nothing left to give, thank you.

Thank you to my Brother Michael who is always in my corner, to my Grandma who has always supported me (yes this is my last degree!), and to my Grandad and Abuelito who always encouraged me to keep studying.

A special thank you to Matt. You have been there through all the tears, lifted me up when I was at my lowest, and kept me going when finishing seemed like an impossible task. Without you I doubt I would have got to the end.

Finally, I want to dedicate this thesis to my Parents. Thank you for the endless support throughout my long and seemingly never-ending university degrees. To my Dad, thank you for always believing in me, especially in moments when I didn't believe in myself, and to my Mum whose constant love has given me strength when I needed it most. I couldn't have done it without you both, thank you.

TABLE OF CONTENTS

LIST OF FIGURES

LIST OF TABLES

LIST OF ABBREVIATIONS

•OH	Hydroxyl Radical
ABCB8	ATP-binding cassette (ABC) transporter (Mitochondrial iron exporter)
ADP	Adenosine Diphosphate
ATP	Adenosine Triphosphate
CACT	Carnitine:acylcarnitine translocase
CD36	Cluster of differentiation 36 (Fatty acid transporter)
$CDCl_3$	Deuterated Chloroform
CoA	Coenzyme A
CPS	Counts Per Second
CPT I	Carnitine Palmitoyl Transferase I
CPT II	Carnitine Palmitoyl Transferase II
D_2O	Deuterated Water
DIC	DOX-Induced Cardiotoxicity
DMT-1	Divalent Metal Transporter-1
DOX	Doxorubicin
ECG	Electrocardiography
EDTA	Ethylenediaminetetraacetic Acid
ETC	Electron Transport Chain
$FABP_{pm}$	Plasma Membrane Fatty Acid binding protein
FAD	Flavin Adenine Dinucleotide
$FADH_2$	Flavin Adenine Dinucleotide + 2 Hydrogen
FATP	Fatty Acid Transport Protein
Fe/S clusters	Iron/Sulfur Clusters
Fe^{2+}	Ferrous Iron
Fe^{3+}	Ferric Iron
FS	Fractional Shortening

GAPDH	Glyceraldehyde-3-Phosphate Dehydrogenase
GLUT1	Glucose Transporter 1
GLUT4	Glucose Transporter 4
H_2O_2	Hydrogen Peroxide
HK	Hexokinase
I.P.	Intraperitoneal
I.V.	Intravenous
ICP-MS	Inductively Coupled Plasma-Mass Spectrometry
IRE	Iron-Responsive Element
IRP	Iron Regulatory Protein
kDa	Molecular Mass
LAMP 1	Lysosome-Associated Membrane Protein 1
LDH	Lactate dehydrogenase
LIP	Labile Iron Pool
LTCC	L-Type Calcium Channels
LVEF	Left Ventricular Ejection Fraction
MtF	Mitochondrial Ferritin
NAD+	Nicotinamide Adenine Dinucleotide
NADH	Nicotinamide Adenine Dinucleotide + Hydrogen
NMR	Nuclear Magnetic Resonance
NTBI	Non-Transferrin-Bound Iron
O2•-	Superoxide
PDH	Pyruvate Dehydrogenase
PFK	Phosphofructokinase
PK	Pyruvate Kinase
Q	Ubiquinone
QH_2	Ubiquinol

ROS	Reactive Oxygen Species
SDH	Succinate Dehydrogenase
TCA	Tricarboxylic acid
TfR1	Transferrin Receptor 1
TMS	Tetramethylsilane
TOP2	Topoisomerase II
TSP	Trimethylsilyl Propionate
VDAC	Voltage-Dependent Anion Channel
ΔΨm	Mitochondrial membrane potential

INTRODUCTION

The global cancer epidemic is constantly increasing due to population growth and ageing [1] [2]. Cancer research UK reported 18 million new cases of cancer worldwide in 2020 and this is projected to increase to 28 million new cases each year by 2040 [1]. However, advancements in treatment and early diagnosis have led to a dramatic increase in cancer survival; The 10-year survival rate has doubled in England and Wales in the last 40 years [3] and in the US is estimated to be 67% and 75% in adult and paediatric cancer patients, respectively [4]. With such improvement in long term cancer survival, the care paradigm is shifting from survival to survivorship.

Increasingly attention is being directed towards long-term adverse effects of cancer treatment itself, with particular emphasis on the cardiotoxicity of anthracycline agents used in chemotherapy. Doxorubicin (DOX) is an anthracycline class medication and is the most widely prescribed on the market for both adult and paediatric patients. DOX is extensively used as the first line of defence for the treatment of a variety of different cancers, predominantly solid tumours and hematologic malignancies, and cancers of the breast, bladder, and other metastatic cancers (Jain, 2000; Santos and Goldenberg, 2018) (Xu, Persson and Richardson, 2005) [7] [8]. However, its utility is compromised by life-threatening cardiotoxicity that can develop up to 10 years after treatment (Sandra M. Swain, Whaley and Ewer, 2003a)].

Improved cancer survival rates have exposed the development of cardiac morbidities in cancer survivors treated with DOX, including cardiomyopathy, left ventricular dysfunction and congestive heart failure (Sandra M. Swain, Whaley and Ewer, 2003a).The impact is greatest in paediatric cancer survivors who face living with life-long cardiac complications; approximately 60% of paediatric cancer patients are treated with an anthracycline and 10% develop symptomatic cardiomyopathy within 15 years [10][11]. Current diagnostic methods assess structural and contractile dysfunction but cannot detect chronic cardiotoxicity before irreversible damage has occurred. The mechanisms underlying DOX-induced cardiotoxicity (DIC) remain unclear. While anthracycline cardiotoxicity has a complex multifactorial pathology incorporating Topoisomerase IIα inhibition, inflammation, microvascular injury, and senescence, anthracycline-induced iron overload is a long-established contributary factor [9] [10] [11]. As described in this thesis, there is extensive experimental and clinical evidence

that iron overload exacerbates DOX-related cardiotoxicity, and iron chelation offers protection, both of which implicate iron as a key mediator of the pathology.

The overarching focus of this thesis is to examine the inter-relationship between cardiac iron overload and metabolic dysfunction/remodelling in a clinically relevant *in vivo* model of chronic DIC. To determine whether cardiac iron overload exacerbates DIC leading to metabolic perturbations and impaired cardiac function, and to investigate whether the clinically approved iron chelator Deferiprone can remove cardiac iron to ameliorate DIC.

This introductory chapter begins by outlining normal cardiac metabolism and iron homeostasis. Then describes the proposed mechanisms responsible for DIC, including the evidence supporting the role of iron in its development. Lastly, explores the potential for iron chelation as a cardioprotective strategy.

1.1 Cardiac Metabolism

Cardiac energy metabolism consists of a network of multiple interacting pathways necessary for the tight coupling of adenosine triphosphate (ATP) production and myocardial contraction (Figure 1). The majority of the cardiac ATP pool is derived from oxidative phosphorylation (~70%-90%), the remainder comes from glycolysis (~10%-30%) and the tricarboxylic acid (TCA) cycle [12]. Mitochondria coordinate energy transduction under normoxic conditions, is responsible for more than 95% of cardiac-generated ATP [13]. ATP synthesis consists of three main steps: 1) Substrate delivery to the TCA cycle, 2) The TCA cycle generating the reducing equivalents, (NADH and $FADH_2$), required to drive oxidative phosphorylation, and 3) Oxidative phosphorylation; production of ATP via the oxidation of the reducing equivalents within the electron transport chain (ETC) [14].

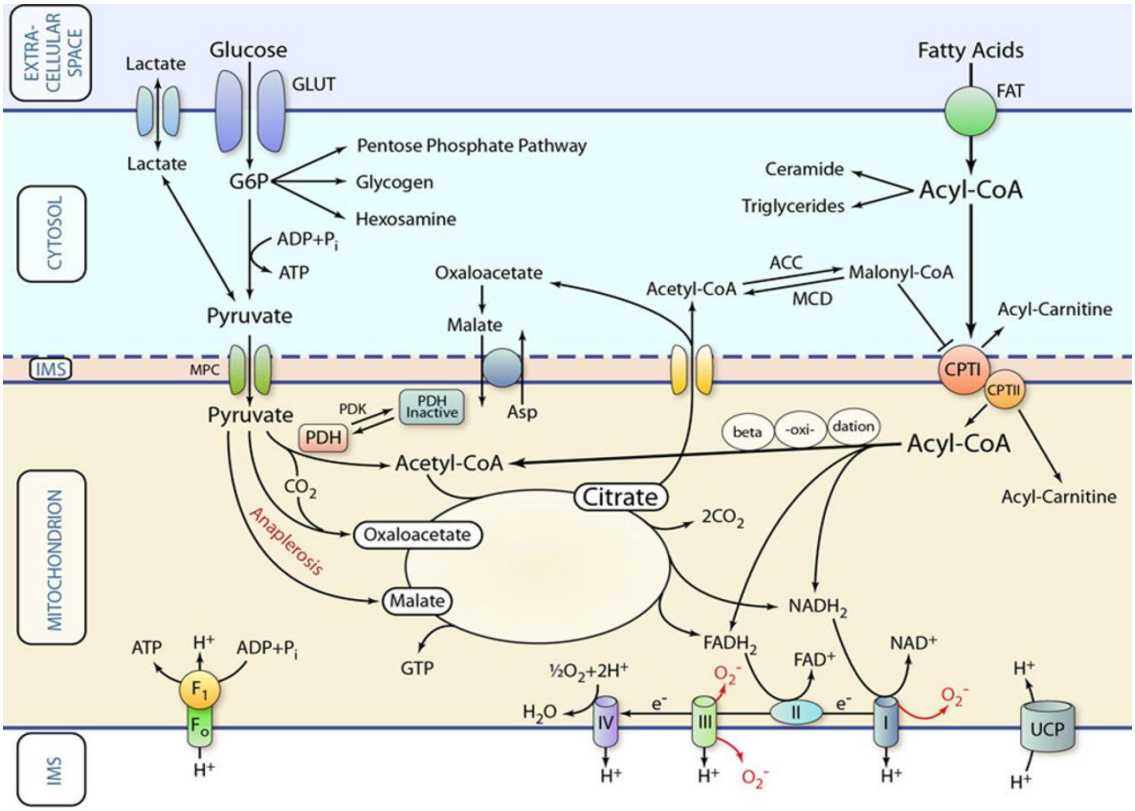

Figure 1: Schematic of cardiac metabolism pathways. Substrates are transported into the cytosol and are metabolized through several pathways. Metabolic intermediates, such as pyruvate and acyl-CoA, are transported into the mitochondria by specific transport systems for oxidation. Substrates are then oxidized or carboxylated and fed into the TCA cycle for the generation of NADH2 and FADH reducing equivalents, which are then used by the ETC for the production of ATP. ACC; acetyl-CoA carboxylase, CoA ; coenzyme A ,CPT; carnitine palmitoyltransferase, FAT; fatty acid transporter, G6P; glucose 6-phosphate, GLUT; glucose transporter, IMS; mitochondrial intermembrane space, MCD; malonyl-CoA decarboxylase, MPC; mitochondrial pyruvate carrier, PDH; pyruvate dehydrogenase, and PDK; pyruvate dehydrogenase kinase.[12]

The constant supply of substrates through the metabolic network is required for ATP production. The heart can utilize a variety of energy substrates, including carbohydrates, lipids, amino acids, glucose, and ketone bodies [15].

The major pathways of substrate breakdown, β-oxidation for fatty acid breakdown and glycolysis for glucose breakdown, are described here.

1.1.1 β-Oxidation of Fatty Acids

The heart relies on fatty acids as its primary substrate, accounting for approximately 70% of ATP generation. The oxidation of fatty acids can be described via three main steps: uptake into the cytosol, transport across the mitochondrial membrane and oxidation within the mitochondria (Figure 2).

Fatty acids are negatively charged, their entry into the cytosol is via fatty acid transport proteins (CD36 and FATP) located on the plasma membrane. This process is facilitated by the plasma membrane fatty acid binding protein $FABP_{pm}$ [16]. Once inside the cytosol, free fatty acids

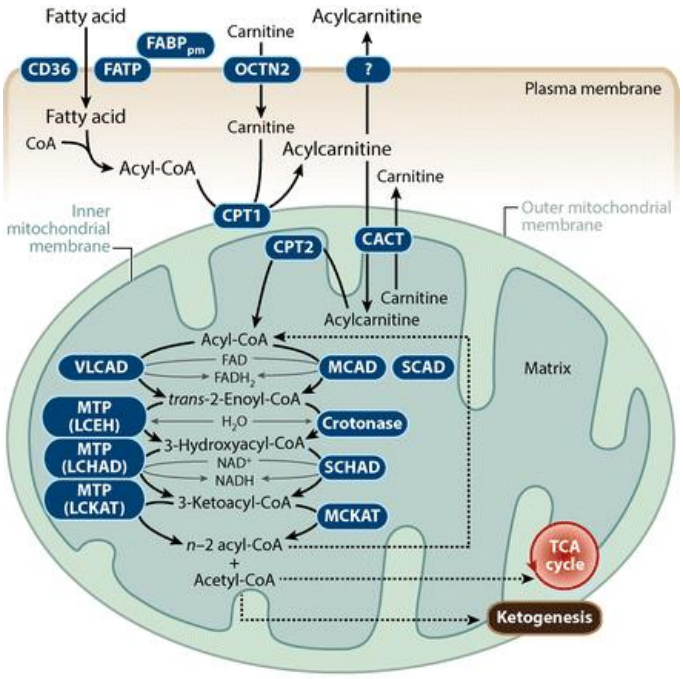

Figure 2: A schematic representation of β-oxidation of fatty acids. Fatty acids are broken down into acetyl-CoA molecules through a series of enzymatic reactions. This process generates acetyl-CoA, NADH, and $FADH_2$, which can enter the TCA cycle and ETC for ATP production. CACT; carnitine acylcarnitine translocase, CPT1/2; carnitine palmitoyltransferases 1 and 2; FABPpm; plasma membrane fatty acid binding protein; FATP; fattyacid transport protein; LCEH; long-chain enoyl-CoA hydratase; LCHAD; long-chain (S)-3-hydroxyacylCoA dehydrogenase; LCKAT; long-chain 3-ketoacyl-CoA thiolase; MCAD; medium-chain acyl-CoAdehydrogenase; MCKAT; medium-chain 3-ketoacyl-CoA thiolase; MTP; mitochondrial trifunctionalprotein; SCAD; short-chain acyl-CoA dehydrogenase; SCHAD; short-chain (S)-3-hydroxyacyl-CoAdehydrogenase; VLCAD; very long chain acyl-CoA dehydrogenase. [17]

undergo activation by the addition of Coenzyme A (CoA) to form fatty acyl-CoA, facilitated by acyl-CoA synthase.

As the mitochondrial membrane is impermeable to acyl-CoAs, the carnitine shuttle is required for transportation of fatty acyl-CoA into the mitochondria[17]. The system requires carnitine palmitoyl transferase I (CPT I), carnitine acylcarnitine translocase (CACT), and carnitine palmitoyl transferase II (CPT II).[18]. CPT I is located on the outer mitochondrial membrane and converts cytosolic fatty acyl-CoA to long-chain fatty acylcarnitine. CACT facilitates the transport of long-chain acylcarnitine into the mitochondrial matrix in exchange for carnitine. CPT II converts the long-chain fatty acylcarnitine back into fatty acyl-CoA [12].

Once inside the mitochondria, acyl-CoA molecules are degraded via β-oxidation in a cyclic process by four main enzymes: acyl-CoA dehydrogenase, enoyl-CoA hydratase, hydroxyacyl-CoA dehydrogenase, and ketoacyl-CoA thiolase [19][20]. Acetyl-CoA is generated through the release of two carboxy-terminal carbon atoms from acyl-CoA, thus the acyl-CoA generated is two carbons shorter after each cycle [20]. The acetyl-CoA generated is used to fuel the TCA cycle. The β-Oxidation of fatty acids also generates the reducing equivalents NADH and $FADH_{2,}$ which are vital for ATP production through the ETC [17] [19].

1.1.2 Glycolysis

Glycolysis is the metabolic pathway which converts glucose into pyruvate, NADH, and ATP (Figure 3) [21]. Glucose oxidation contributes only a small component of the total ATP pool in comparison to the contribution of fatty acid oxidation [13]. Glycolysis consists of a series of enzymatic reactions. There are three enzymes that are critical in governing this process [22]; hexokinase (HK), phosphofructokinase (PFK) isoforms PFK1 and PFK2, and pyruvate kinase (PK). Glucose is transported into the cytosol via glucose transporters GLUT1 or GLUT4 [21]. Intracellular glucose is converted to fructose 1,6-bisphosphate through consecutive reactions catalysed by HK and PFK, utilising two molecules of ATP in the process. Fructose 1,6-bisphosphate enters the energy pay off phase where PK facilitates its conversion into pyruvate. This yields 2 NADH molecules and 4 ATP molecules, a net gain of 2 NADH molecules and 2 ATP molecules from the glycolytic pathway per glucose molecule [21]. Pyruvate is reduced to lactate by lactate dehydrogenase (LDH) during anaerobic conditions or utilized to form alanine [21]. Under aerobic conditions, pyruvate is transported into the mitochondrial matrix where it

undergoes oxidation to acetyl-CoA by pyruvate dehydrogenase (PDH) for utilization in the TCA cycle[23].

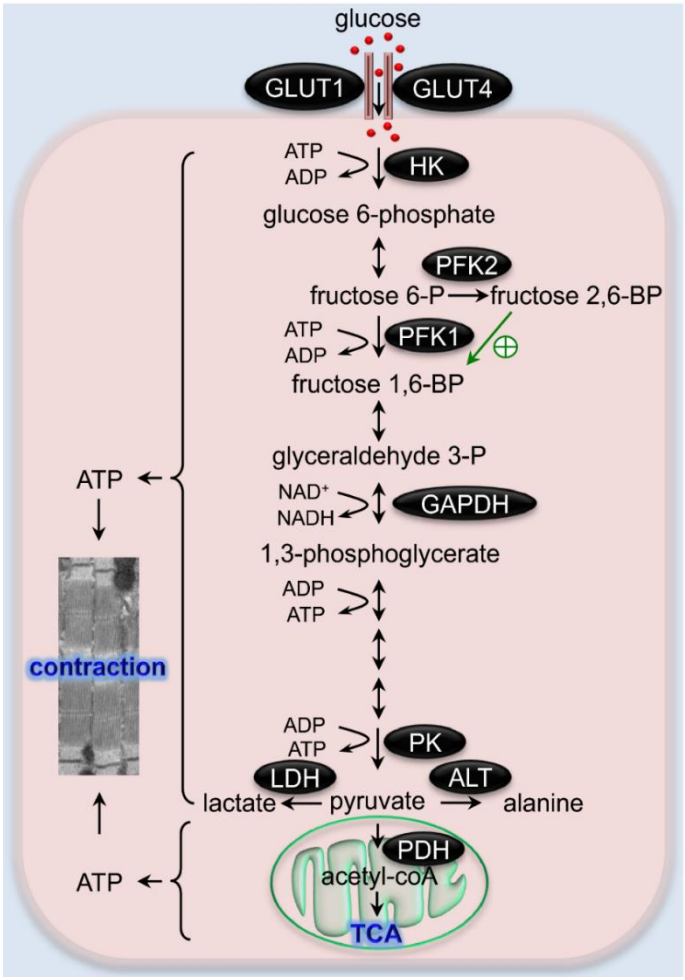

Figure 3: Schematic of the glycolytic pathway. The glycolytic pathway converts glucose into pyruvate through a series of enzymatic reactions, generating ATP and NADH in the cytoplasm of cells. GLUT; Glucose transporter, HK; Hexokinase, PFK; Phosphofructokinase, LDH; Lactate dehydrogenase, PK; Pyruvate kinase, PDH; Pyruvate dehydrogenase; ALT; alanine transaminase [553]

1.1.3 Tricarboxylic Acid Cycle

The TCA cycle occurs in the mitochondrial matrix. Acetyl-CoA produced by glycolysis and β-Oxidation enters the TCA cycle generating reducing equivalents NADH and $FADH_2$ and one molecule of ATP (Figure 4) [12]. The two-carbon acetyl group from acetyl-CoA is transferred to the four-carbon oxaloacetate to form citrate, a six-carbon compound [24]. Through a series of enzyme-catalysed transformations, the citrate is gradually converted back into oxaloacetate, losing two carboxyl groups as CO_2 in the process [14].The majority of electrons made available by the oxidative steps of the TCA cycle are transferred to NAD+, resulting in the formation of NADH. For each acetyl group that enters the TCA cycle, three molecules of NADH are

produced [12]. The oxidation of succinate into fumarate forms $FADH_2$, as two electrons are transferred from succinate to FAD, a process facilitated by SDH [12]. The NADH and $FADH_2$ generated by the TCA cycle is used in the oxidative phosphorylation pathway for ATP synthesis [14].

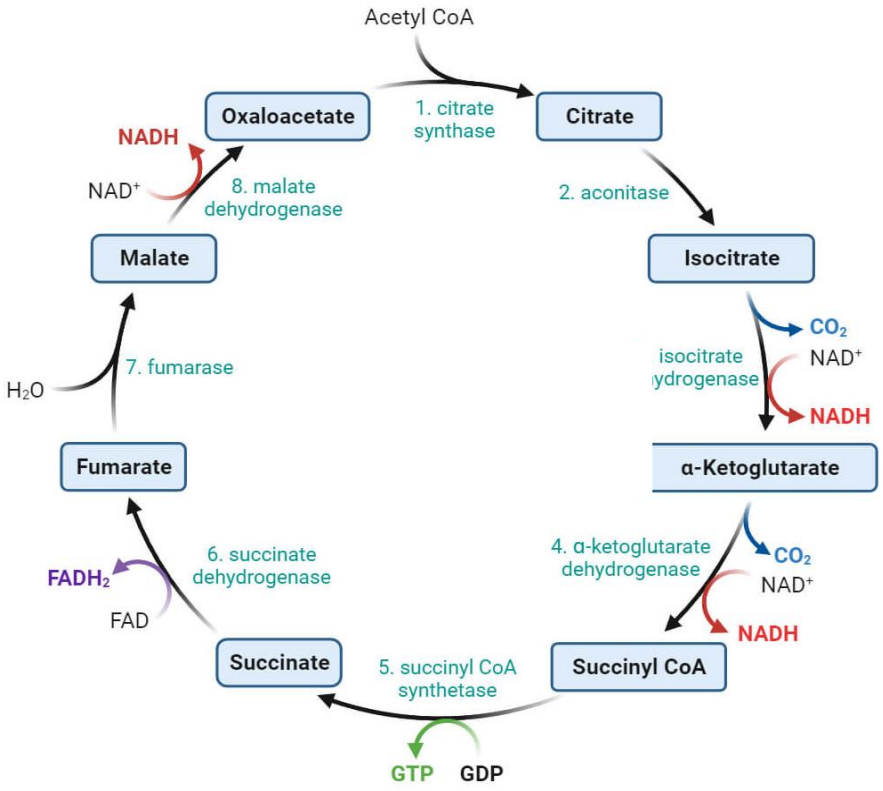

Figure 4: Schematic of the TCA cycle. The TCA cycle involves a series of enzyme-catalysed reactions that oxidize acetyl-CoA to produce ATP, as well as reducing equivalents such as NADH and $FADH_2$ [554]

1.1.4 Oxidative Phosphorylation and the Electron Transport Chain

The reducing equivalents, NADH and $FADH_2$ produced during glycolysis, fatty acid oxidation, and the TCA cycle, participate in oxidative phosphorylation by donating electrons into the electron transport chain (ETC) (Figure 5). The ETC is comprised of a series of five protein complexes located in the inner mitochondrial membrane. Electrons from NADH and $FADH_2$ are shuttled through the ETC in a series of redox reactions[25][26][27]. NADH and $FADH_2$ donate electrons to the ETC via Complexes I and II, respectively. These electrons are donated to ubiquinone (Q) which is subsequently reduced to ubiquinol (QH_2). QH_2 transfers the electrons from Complex I and II to Complex III, recycling itself in the process. Cytochrome c

then transfers electrons from Complex III to Complex IV, the final protein complex in the chain, where oxygen acts as the final electron acceptor and is reduced to water.

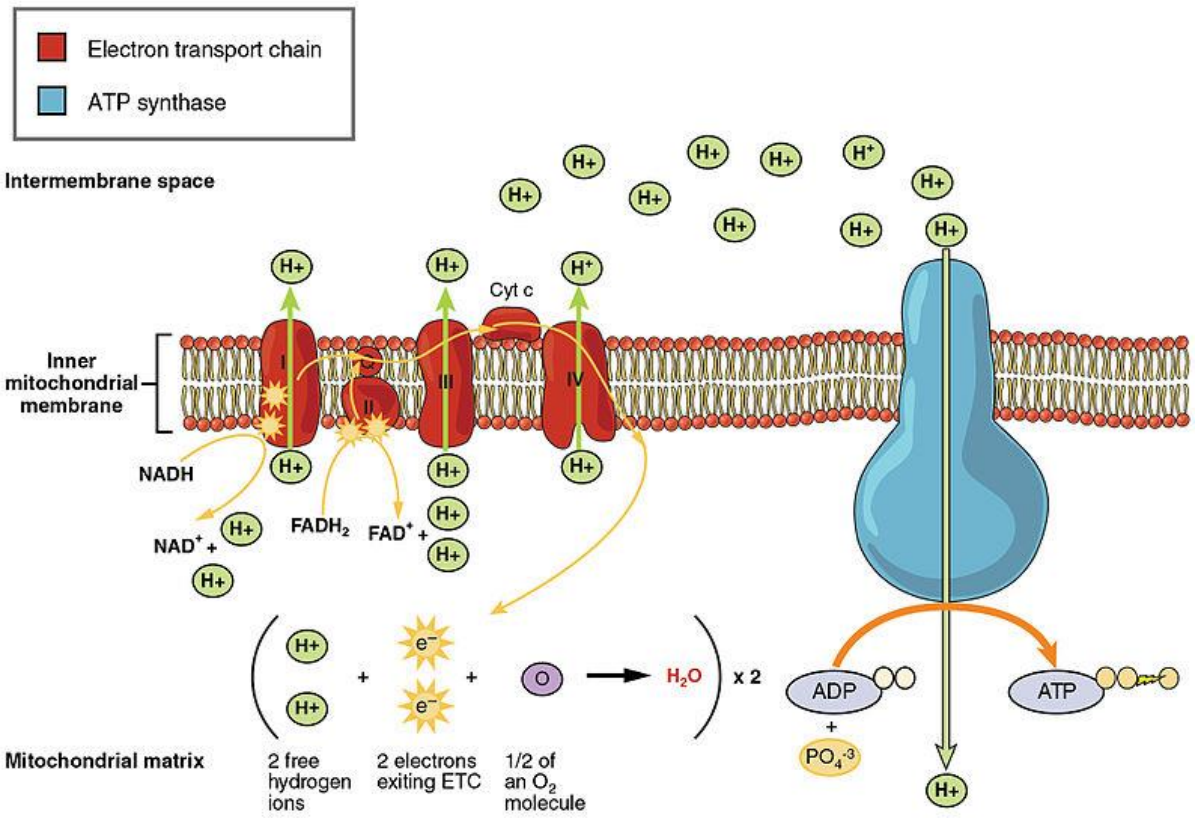

Figure 5: Schematic of Oxidative phosphorylation and the ETC. (Gopalan & Kirk, 2022)

As the electrons are transferred though the protein complexes, carriers undergo reduction upon receiving electrons and oxidation when passing them to the next carrier, releasing energy at each reaction[28]. At Complex I, III and IV, this energy is used to transport protons out of the mitochondrial matrix and across the inner mitochondrial membrane. The accumulation of protons in the inner membrane space creates a proton gradient across the inner mitochondrial membrane relative to the matrix, termed the mitochondrial membrane potential ($\Delta\Psi m$) [27]. This gradient generated by the ETC provides the energy that drives ATP synthesis. Complex V, also known as ATP synthase, allows the proton motive force to be discharged [14]. ATP synthase governs the movement of protons back into the mitochondrial matrix. The resulting energy from this proton flux is used to generate ATP by the phosphorylation of ADP. .

1.2 Iron Homeostasis

Iron (Fe) is an essential trace element, involved in numerous essential biochemical processes, including energy metabolism, DNA synthesis/repair, oxygen transport and cellular respiration [29]. It is vital for many biological functions, and its dysregulation can cause a range of deleterious effects and pathophysiological conditions [30]. An excess of iron disrupts redox homeostasis and induces the formation of destructive reactive oxygen species (ROS) through Fenton chemistry [31], [32]. Iron readily cycles between its reduced ferrous (Fe^{2+}) and oxidised ferric (Fe^{3+}) forms which can disrupt cellular redox equilibrium [33]. This results in oxidative stress ultimately leading to peroxidative damage to vital cell structures, tissue injury and disease [34].

The limited solubility of oxidised Fe^{3+} means its bioavailability is poor [35]. Consequently, to meet cellular demands, while minimising potential iron-induced injury, sophisticated regulatory mechanisms have evolved to ensure both cellular and systemic iron concentrations are conserved within an optimal physiological range [36]. Such mechanisms are dependent on specialised proteins governing the uptake, transport, and storage of iron; transferrin, transferrin receptors, iron regulatory proteins (IRPs), hepcidin, ferroportin and ferritin are all fundamental to this [37], [32]. This section describes the mechanisms by which iron homeostasis is maintained.

1.2.1 Principles of Iron Homeostasis

The amount of iron in a healthy individual is maintained within a range of 4-5g by tightly regulated absorption, transport, storage and recycling [38]. The vast majority (~2.3g) is distributed in the haemoglobin of red blood cells and developing erythroid cells (the erythron), a key and fundamental role in oxygen transport [39]. Substantial amounts of iron exist in macrophages and in muscle myoglobin, <0.6g and ~0.3g respectively [40], [41]. Other tissues have lower quantities of iron and ~1g of excess body iron is stored in the liver. At steady state, ~3g of total body iron exists complexed to transferrin in plasma [33]. The remainder is found intracellularly within peripheral tissue, complexed to protein chaperones (e.g. ferritin) or present in functional groups. The rest is referred to as the cellular labile iron pool (LIP) [42].

1.2.1.1 The Labile Iron Pool

The cellular labile iron pool, LIP, is a pool of Fe^{2+} and Fe^{3+} chelatable and redox-active iron. It is primarily located in the cytosol and represents only a minor fraction (<5%) of total cellular iron (50 –100µM)[43]. Predominantly made up of Ferrous iron (Fe^{2+}) this free intracellular non-protein bound iron can function as a catalyst in the generation of oxygen free radicals via Fenton-type reactions. The size of the LIP is restricted to prevent excessive ROS generation through Fenton-type reactions(Kakhlon and Z. Ioav Cabantchik, 2002). Intracellular iron levels are tightly maintained by regulating ferritin, the iron sequestering protein, and the Transferrin receptor (TfR1), the major iron uptake protein [45]. Iron regulatory proteins (IRPs) are key regulators of cardiac iron homeostasis which maintain the cytosolic LIP low by regulating intracellular levels of ferritin and TfR1 [46][47][48]. DOX-induced dysregulation of iron storage and sequestration processes lead to an expansion of the LIP and expose cells to oxidative damage and ultimately myocardial injury [43] [49].

1.2.2 Iron Absorption

Iron excretion from the body is not actively regulated, Iron is lost either through bleeding or the process of skin and mucosal sloughing [50]. Iron homeostasis is maintained by tight regulation of dietary iron absorption and iron recycling (Figure 6). The transferrin iron pool fraction is primarily recycled through the degradation of senescent red blood cells by tissue macrophages [51]. Heme oxygenase 1(HO-1) facilitates the degradation of heme during erythophagocytosis [51]. Fe^{2+} is released into plasma for re-utilization following its release from macrophages via the trans-membrane iron exporter protein ferroportin [51].

The remaining fraction of the transferrin iron pool (~10%) is provided by newly absorbed dietary iron and replenishes non-specific iron loss [52]. This process occurs in the duodenum at the intestinal lumen. Here, non-heme Fe^{3+} is reduced to Fe^{2+} by the ferric reductase duodenal cytochrome b (Dcytb) [53]. The divalent metal transporter-1 (DMT-1) facilitates the transportation of Fe^{2+} across the apical membrane of enterocytes [54]. Fe^{2+} is released from the basolateral membrane into the bloodstream via the Fe^{2+} transporter ferroportin. The ferroportin-mediated export of Fe^{2+} is coupled to its re-oxidation to Fe^{3+} [50], as depicted in (Figure 6).

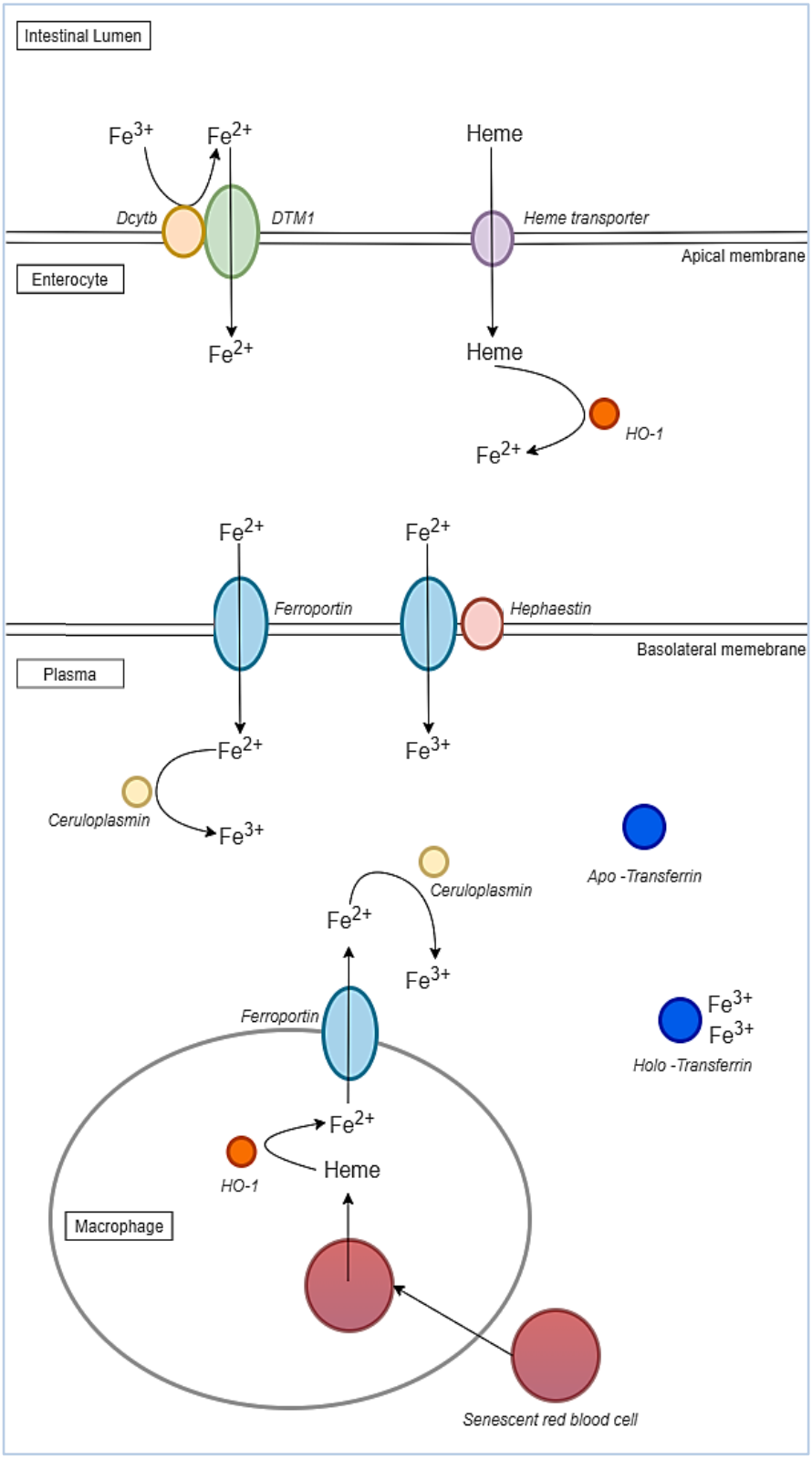

Figure 6: Iron absorption and recycling schematic. The transferrin iron pool is recycled through macrophage-mediated degradation of senescent red blood cells facilitated by HO-1, this process releases Fe2+ into the plasma via ferroportin for re-utilization. Additionally, newly absorbed dietary iron from the duodenum is released into the bloodstream for reuse via ferroportin, facilitated by Dcytb and DMT-1. HO-1; Heme oxygenase 1, Dcytb; duodenal cytochrome b, DMT-1; divalent metal transporter-1. [Figure made in app.diagrams.net]

This re-oxidation is catalysed by the membrane-associated ferroxidase hephaestin through direct interaction with ferroportin [55]. Re-oxidation can also occur via plasma soluble ceruloplasmin, a hephaestin homologue [56]. Fe^{3+} is immediately scavenged by transferrin for transport to tissues. Transferrin maintains Fe^{3+} in a redox-inert state, it can bind up to two atoms of Fe^{3+} with high affinity. In normal circumstances, ~30% of circulating transferrin iron binding sites are occupied [57]. The remainder of circulating transferrin provides significant buffering capacity against the accumulation of toxic non-transferrin bound and redox-active Iron. Iron loading disorders frequently manifest when the transferrin pool becomes saturated and the non-transferrin bound iron concentration significantly increases.

1.2.3 Systemic Iron Homeostasis

Hepcidin is a peptide hormone produced within the hepatocytes of the liver. Hepcidin is the primary regulator governing the entry of iron into the blood stream, central to systemic iron homeostasis [58] [59]. The expression of hepcidin modulates in response to variation in body iron demand through communications with the liver. The hepcidin peptide is cleaved from the hepcidin precursor pre-pro-peptide and released into the blood stream for distribution to its target site [50], [59], [60].

When the body is high in iron, hepcidin is upregulated and its concentration amplified in the blood stream. Under these conditions, duodenal iron uptake is prevented, iron is retained in tissue, its supply to the plasma is reduced and iron recycling from senescent red blood cells is prevented [50]. When iron is depleted, hepcidin synthesis decreases triggering iron redistribution from intracellular iron stores to target cells and increased intestinal iron absorption [52].

Hepcidin acts as negative regulator of iron uptake by binding to ferroportin on target cells, primarily the intestinal duodenum and macrophages. [59]. The ferroportin-hepcidin complex degrades via proteasomal processing [61]. Ferroportin loss from the cell surface results in low transferrin saturation in response to the decrease in iron entry into the plasma. Consequently, less iron is delivered to target cells and developing erythroblasts. The binding of hepcidin occludes iron efflux, impeding the capacity of iron to be released into the bloodstream [62].

Hepcidin synthesis is complex and is regulated at the transcriptional level. Hemochromatotic proteins located on the plasma membrane of hepatocytes are key in the positive regulation of hepcidin. Key proteins involved include transferrin receptor 2 (TfR2), hemochromatosis

protein (HFE) and hemojuvulin (HJV), bone morphogenic protein (BMP) 6, BMP receptors, and transferrin [58], [63]. These key proteins regulate hepcidin levels via tight coordination signalling of the BMP-HJV-SMAD regulatory pathway [50], [64]. Erythroferrone (ERFE) an erythroid protein is involved in the regulation of iron metabolism functions through its negative regulation of hepcidin. An increase in ERFE suppresses hepcidin synthesis through the inhibition of its expression. ERFE binds to BMPs, resulting in the inhibition of the BMP pathway governing hepcidin expression [64], [65]. The suppression of hepcidin by ERFE decreases the inhibitory effect of hepcidin which increases the iron transport capacity of ferroportin, enhancing iron bioavailability.

2.1.1 Cardiomyocyte Iron Homeostasis

To maintain cellular iron homeostasis in the cardiovascular system, multiple proteins participate in iron uptake, storage, regulation, and export (Figure 7).

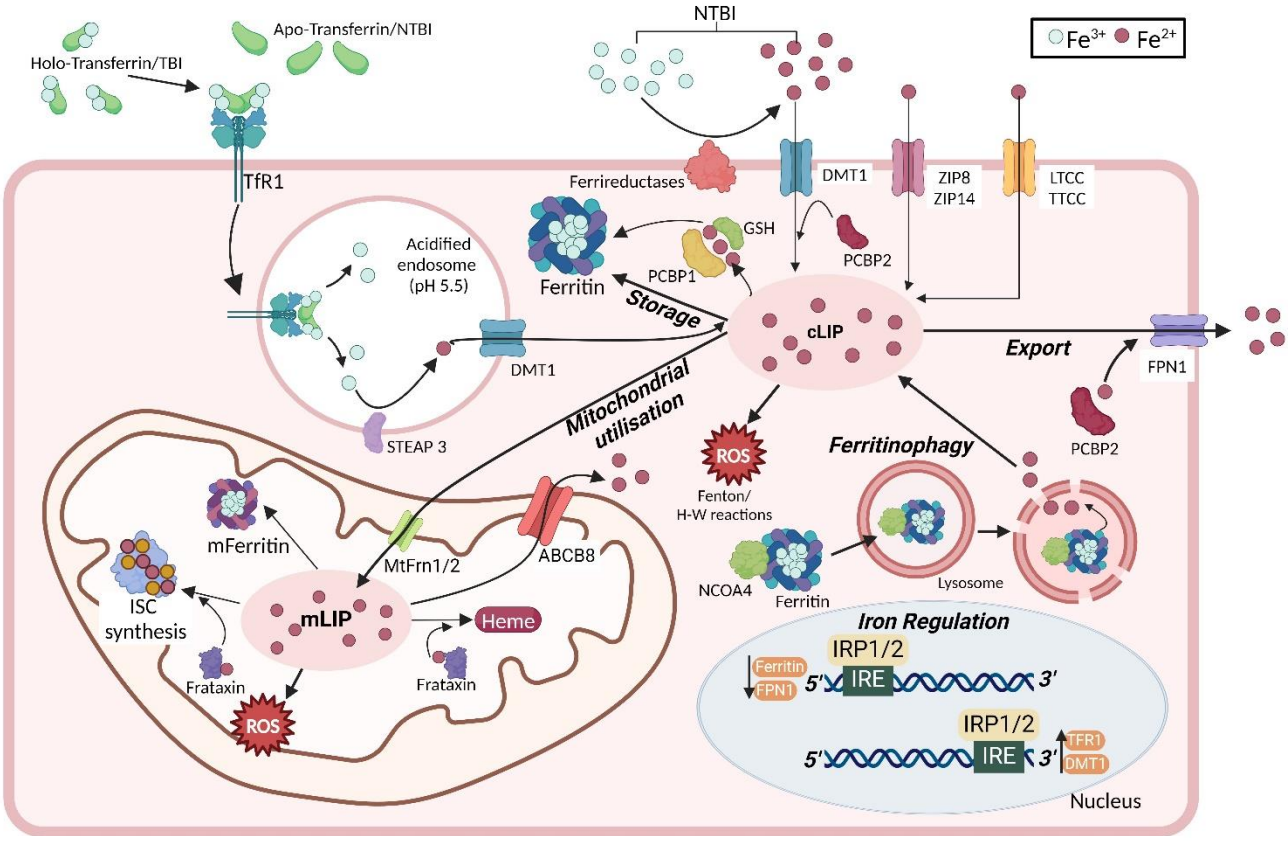

Figure 7: Cardiomyocyte iron homeostasis. Transferrin bound iron binds to TfR1 on the cell surface plasma membrane and the complex is internalised through endocytosis. The endosome undergoes acidification which mediates the dissociation of Fe^{3+} from transferrin, Fe^{3+} is then reduced into Fe^{2+} by STEAP3 and released into the cytoplasm via DMT-1. Non-transferrin bound iron can enter the cell via DMT1, as well as zinc and calcium transporters. In the cytoplasm, Fe is rapidly sequestered into ferritin where Fe^{2+} is oxidised into Fe^{3+} for storage, to minimise ROS production. PCBP1 is the primary iron chaperone, responsible for binding Fe^{2+} in the cytosolic labile iron pool (LIP) and delivering them safely to various iron-dependent enzymes and to ferritin. The IRE/IRP system regulates iron homeostasis; IRPs bind to IREs found in the untranslated regions of mRNAs, and encode key iron-related proteins such as TfR1, ferritin, DMT1, and iron exporter ferroportin (FPN1). PCBP2 acts as an iron chaperone but is particularly involved in regulating iron import and export by interacting with DMT1 and FPN1. Ferritinophagy, regulated by NCOA4, is the process where ferritin is selectively degraded in lysosomes to release stored iron, crucial for maintaining cellular iron homeostasis. Mitoferrin 1 and 2 facilitate the transport of iron across the inner mitochondrial membrane into the matrix, where the majority of intracellular iron is used by the mitochondria for the synthesis of heme and iron-sulphur clusters. The mitochondrial protein Frataxin has been shown to play a role in both heme and iron-sulphur cluster synthesis, as well as iron storage; Frataxin binds Fe^{2+} and contributes to its controlled oxidation to Fe^{3+} and/or to incorporate it into Fe-containing proteins. TTCC; T-type calcium channels, LTCC; L-type calcium channels, ZIP8; Zinc transporter 8, ZIP14; Zinc transporter 14, FPN1; Ferroportin 1, TfR1; Transferrin receptor 1, STEAP3; Six-transmembrane epithelial antigen of prostate 3 (metalloreductase), DMT1; Divalent metal transporter 1, FPN; Ferroportin, MtFrn1/2; Mitoferrin transporter 1/2, ISC; Iron-sulphur cluster, ABCB8; Mitochondrial export protein, IRP1 and IRP2; Iron regulatory proteins 1 and 2, IREs; Iron responsive elements, NTBI; Non-transferrin bound iron, TBI; Transferrin bound iron, cLIP; cytosolic labile iron pool, mLIP; mitochondrial labile iron pool, PCBP1 and PCBP2; Poly C-binding proteins 1 and 2, GSH; Glutathione, NCOA4; nuclear receptor co-activator 4. [Figure made in BioRender]

Iron is delivered and acquired by cells through an endocytic mechanism, referred to as the transferrin cycle. Iron loaded transferrin binds to transferrin receptor 1 (TfR1) on the cell surface plasma membrane [66]. This complex is internalised through clathrin-mediated endocytosis. The endosome undergoes acidification to pH 5.5, initiating dissociation of Fe^{3+} from transferrin. The ferrireductase STEAP3 reduces released Fe^{3+} into Fe^{2+} [67]. DMT-1 exports Fe^{2+} across the endosomal membrane into the cytosol or directly to the mitochondria. The affinity of transferrin to TfR1 is reduced by ~500 fold following the release of iron, and the transferrin-TfR1 complex dissociates [33] [68]. Free transferrin secretes into the bloodstream for Fe^{3+} recapture and the cycle re-commences. The utilisation of intracellular iron depends on the metabolic requirements of the cell, but. the majority of intracellular iron is used by the mitochondria for the synthesis of heme and iron-sulphur clusters [50].

Due to the risk of ROS generation from Fenton-chemistry associated with excess intracellular labile iron [69], Fe is rapidly sequestered into the primary intracellular iron storage protein ferritin, [70]. Ferritin is a large spherical cytosolic protein which oxidises Fe^{2+} into Fe^{3+} for safe storage, whilst retaining it bioavailable for cellular metabolism [71]. It is composed of 24 heavy (H) and light (L) subunits that assemble into a shell-like structure. The incorporation of iron into the cavity of this structure is facilitated by the ferroxidase activity of H–ferritin [72]. Ferritin has a high iron storage capacity; each ferritin molecule can store up to 4500 iron atoms. Its expression increases in response to a rise in intracellular iron concentration [73].

Ferritin is secreted from cells into the blood stream in small amounts. Under steady-state conditions, the level of ferritin present in blood serum strongly correlates with the concentration of intracellular iron. This association makes serum ferritin a convenient indicator of iron stores, which is used clinically as an accurate and readily measurable estimate of total body iron stores [74].

Poly C-binding proteins 1 and 2 (PCBP1 and PCBP2), with the assistance of GSH, are critical cytosolic iron chaperones that ensure that iron is efficiently utilized and safely stored, preventing iron toxicity and supporting essential cellular processes [75] [76] . PCBP1 is the primary iron chaperone, binding Fe^{2+} in the cytosolic LIP and delivering it to various iron-dependent enzymes and ferritin for safe storage. This process is crucial for the proper functioning of iron-dependent enzymes, such as those involved in hypoxia responses and DNA synthesis, and for preventing oxidative damage caused by labile iron [77] . A key aspect of PCBP1's function is its interaction with glutathione (GSH), a small molecule that plays a crucial

role in iron coordination. GSH forms complexes with Fe^{2+}, which are then bound by PCBP1. This interaction enables the safe transport of iron within the cytosol, as GSH helps stabilize the iron, preventing it from catalyzing the formation of ROS. The GSH-iron complex is the primary species coordinated by PCBP1, ensuring that iron is delivered precisely where needed without causing cellular damage. PCBP2, although closely related to PCBP1, has more specialized roles. It acts as an iron chaperone with a particular focus on regulating iron import and export by interacting with key iron transporters like divalent metal transporter 1 (DMT1) and ferroportin. This interaction facilitates the efficient uptake of dietary iron and its controlled release into the bloodstream, playing a crucial role in systemic iron balance. Additionally, PCBP2 can bind and capture iron released during heme degradation, contributing to iron recycling and homeostasis.

Ferritinophagy plays a critical role in maintaining iron homeostasis within cells by regulating the release of iron from ferritin [78] . This process involves the selective degradation of ferritin within lysosomes, thereby liberating iron into the cytosolic LIP to meet the cell's metabolic demands. The degradation of ferritin in lysosomes is mediated by the nuclear receptor co-activator 4 (NCOA4). NCOA4 serves as an autophagy receptor that specifically binds to ferritin heavy-chains of ferritin and targets it for autophagic degradation [78] . This regulation is not unidirectional, whereby intracellular iron levels govern the ferritinophagy flux [78] . When iron is abundant, a large E3 ubiquitin ligase HERC2 binds to NCOA4, which targets NCOA4 for proteasomal degradation. This prevents ferritinophagy, allowing ferritin to accumulate and store excess labile iron safely. Conversely, under conditions of iron deficiency or increased iron demand, NCOA4 is not ubiquitinated by HERC2 so is able to bind to ferritin, facilitating its autophagic degradation to release iron. This dynamic regulation ensures that cells can mobilize stored iron when needed while avoiding iron toxicity by storing excess iron safely.

The iron-responsive element (IRE)/iron regulatory protein (IRP) system (IRE/IRP) is a regulatory mechanism that controls cellular iron homeostasis [33]. IRPs are proteins that bind to specific RNA structures called IREs found in the untranslated regions of mRNAs and encode key iron-related proteins such as TfR1, ferritin, ferroportin and DMT1 [37]. When cellular iron levels are low, IRP bind to IREs promoting iron uptake and preventing iron storage. IRP bound to ferritin mRNA blocks its translation, ferritin production is consequently suppressed when iron storage is not required, such as when cellular iron concentrations are low [79]. To prevent TfR1 nucleolytic degradation, IRPs bind to the multiple IREs present on the 3’UTR region of

TfR1 mRNA [79]. This results in an upregulation of TfR1 expression on the cell membrane which enables cellular iron intake to be maximised. When cellular iron is abundant, IRPs do not bind to IREs of the key iron-related proteins. The lack of IRE/IRP interactions permits the translation of ferritin mRNA to occur. The TfR1 mRNA is now exposed to nucleolytic degradation during low cellular iron concentrations [50] inhibiting iron uptake. In addition to the mRNAs that encode the key iron related proteins, the mRNA of DMT1 and FPN1 also contain IREs [80]. The range of IRE-containing -mRNAs all contribute towards the appropriate physiological response required to conserve intracellular iron concentrations within a non-pathological range.

2.1.1.1 Iron in the Mitochondria

Mitochondria are essential to the metabolism of transition metals such as iron [81]. The mitochondrion is the site where iron is transformed into its biologically active form, via the heme and iron–sulphur cluster (Fe/S) biosynthetic pathways [82]. Fe/S clusters serve as co-factors of proteins necessary for electron-transfer, metabolism, and regulation of gene expression [82]. To meet mitochondrial iron requirements, iron transport mechanisms exist for the transportations of iron across the mitochondrial membrane [83][84]. Mitochondrial iron concentration is tightly regulated as iron is a powerful inducer of ROS generation. As mitochondria are the site of electron transport and oxidative phosphorylation, the simultaneous presence of iron and oxygen could result in iron-dependent oxidative stress leading to mitochondrial damage. Mitochondrial iron is therefore maintained in a safe, bio-available form to prevent oxidative damage [85]. Although the mechanisms by which it does this while retaining the iron as bioavailable are not currently well understood.

2.1.1.1.1 Mitochondrial Iron Import

Despite the requirement for the tight regulation of mitochondrial iron, how iron is transported from the transferrin-endosomal lumen to the mitochondrial matrix, particularly across the outer mitochondrial membrane (OMM), remains elusive. To date, there are multiple mechanisms proposed that describe iron transport into the mitochondria, which include direct trafficking of extracellular iron to the mitochondria and/or intracellular uptake from the cytosolic LIP. It is likely that cells have the capacity to employ multiple mechanisms to maintain mitochondrial iron homeostasis.

The “kiss and run” model, describes the direct delivery of transferrin-bound iron from the endosome to the mitochondria [86]. This occurs through formation of transient contacts of holo-transferrin-containing endosomes with the OMM, followed by iron transfer into the mitochondrial matrix [86]. The direct transfer of iron to the mitochondria prevents its entry into the redox-active cytosolic LIP [44]. This mechanism has been demonstrated in erythrocytes but has yet to be described in other cell types [87].

Mitoferrin facilitates and regulates the transport of Fe^{2+} across the inner mitochondrial membrane (IMM) into the matrix. There are two main isoforms of mitoferrin, mitoferrin 1 (MtFrn1) and mitoferrin 2 (MtFrn2) [76] . MtFrn1 is predominantly expressed in developing erythroid cells, where mitochondrial iron import is critical to support haemoglobin production. MtFrn2 has a broader expression profile across various different tissues, contributing to general mitochondrial iron import [88].

The mitochondrial calcium uniporter (MCU) may also contribute to IMM iron transport. Multiple studies suggest that blocking MCU-mediated calcium entry inhibits mitochondrial iron uptake[88][89].

2.1.1.1.2 Mitochondrial Iron Export

ATP-binding cassette (ABC) transporter ABCB8 is a mitochondrial inner membrane protein involved in mitochondrial iron export. Genetic deletion of ABCB8 in mouse hearts resulted in mitochondrial iron accumulation and cardiomyopathy. Down-regulation of ABCB8 *in vitro* resulted in decreased iron export from isolated mitochondria, and its overexpression had the opposite effect[90][91].

2.1.1.1.3 Mitochondrial Iron Metabolism

The chemical form of iron, once transported into the mitochondria, remains unclear. Studies have indicated the existence of a LIP located in the matrix of the mitochondria. This mitochondrial LIP is referred to as “chelatable” iron. It is potentially redox-active and is expected to be present in very low levels (Petrat, Weisheit, et al., 2002) [94]. It is well known that mitochondria are a major source of ROS and labile iron and increases in this redox-active mitochondrial LIP is thought to contribute to a variety of human diseases [83]. To maintain mitochondrial LIP at low levels, the rate of iron influx is tightly coordinated with its

incorporation into three major pathways [95]. Mitochondrial iron can either be used for Fe/S cluster synthesis, heme synthesis or stored in mitochondrial ferritin (MtF).

2.1.1.1.3.1 Iron Storage in the Mitochondria

Mitochondrial ferritin (MtFrn) is an iron storage protein specifically localised inside the mitochondrial matrix. Its primary role appears to be the regulation of the redox-active mitochondrial LIP. MtFRN binds to free mitochondrial iron, forming an iron-MtF complex that is not easily accessible to Fenton reactions [96]. Sequestering iron in this manner contributes to the prevention of iron-induced ROS generation, limiting iron-dependent oxidative damage to the mitochondria. This has also been supported by the elevated expression of MtF in cells exhibiting high metabolic activity and oxygen consumption, such as in the heart[97] [98].

The mitochondrial protein Frataxin has been proposed to function as a metallochaperone and iron storage protein within mitochondria, with studies showing evidence of its ability to bind divalent metal ions using a group of exposed acidic [99] . These residues form on acidic ridge on the protein, allowing weak and non-specific electrostatic bonding of iron and other divalent metals, which can then be incorporated into Fe-containing proteins[100].

2.1.1.1.3.2 Fe/S Cluster Biosynthesis

Iron/Sulphur (Fe/S) clusters are inorganic compounds that serve as co-factors in proteins playing important roles in a variety of metabolic pathways[101].

Fe/S clusters are necessary for the function of metabolic enzymes of the TCA cycle, including aconitase and succinate dehydrogenase. The iron atoms of Fe/S clusters are either Fe^{2+} or Fe^{3+}. The ability to cycle between these two redox states permits Fe/S clusters to regulate electron transfer within the respiratory complexes of the ETC [102]. The biosynthesis of Fe/S clusters is complex involving three key steps; 1) the assembly of the Fe/S cluster on a scaffold protein, 2) the chaperone mediated release of the Fe/S cluster to target apo-proteins, and 3) cytosolic Fe/S cluster Assembly [84][103].

Frataxin is involved in the synthesis of Fe/S clusters, crucial cofactors for many mitochondrial enzymes, by interacting with key proteins in the biosynthesis machinery such as IscU, Nfs1, and Isd11 [104] [99] . Initially, frataxin was thought to act as an iron donor for the assembly of these clusters on IscU, the scaffold protein where Fe/S clusters are first formed [77] .

However, more recent research suggests that frataxin may also function as an allosteric regulator rather than an iron donor [105]. It appears to modulate the activity of Nfs1, a desulfurase enzyme, thereby influencing the production of Fe/S clusters in response to iron levels.

2.1.1.1.3.3 Heme Biosynthesis

The synthesis of heme is exclusive to the mitochondria and occurs in all cells, especially erythroid cells and hepatocytes [83]. Heme is an important prosthetic group of numerous metalloproteins required for essential cellular processes, including oxygen transport and storage, electron transfer, metabolism, signal transduction, ligand binding, and regulation of gene expression [106].

Frataxin plays a role in the biosynthesis of heme by physically interacting with ferrochelatase, the enzyme responsible for catalyzing the incorporation of the iron atom into protoporphyrin IX, which is the final step in heme synthesis [99] . Although the exact mechanism of how iron is provided to ferrochelatase remains unknown, *in vitro* studies have demonstrated a physical interaction between frataxin and ferrochelatase with a 1 to 2 stoichiometry, which is consistent with the dimeric nature of ferrochelatase [107] .

2.2 Iron-overload

2.2.1 Systemic Iron Overload

Typically, iron overload happens when the liver's capacity for iron handling is exceeded, resulting in excess iron levels in the blood. Under normal conditions, the blood transferrin pool is approximately 30% saturated. In cases of iron overload, transferrin becomes fully saturated, resulting in increased labile ferrous iron in the plasma (termed non-transferrin-bound iron (NTBI)), which is a potentially redox active and toxic phenomenon[108]. Under conditions of iron overload, L-type calcium channels (LTCC) and divalent metal transporters facilitate NTBI uptake into cardiac cells due to the shared affinity between Fe^{2+} and calcium, resulting in cardiac iron overload[109][108]. A portion of ferrous cytosolic iron is transported into cardiac mitochondria through the activity of the iron transporter protein mitoferrin-2 (Mfrn2) and the mitochondrial calcium uniporter (mCU).

2.2.2 Cardiac Iron Overload

The pathophysiology of iron overload in the heart is primarily caused by reactive oxidative stress. Cardiac iron toxicity occurs when there is an excessive expansion of the cytoplasmic and mitochondrial labile iron pool. This free iron reacts with superoxide (O2•-) and hydrogen peroxide (H_2O_2) via the Haber-Weiss and Fenton-type reactions, culminating in the production of highly reactive free radicals (•OH) (See 2.5.2.1.1). This free radical production leads to an increase in the levels of reactive oxygen species (ROS). Free radical byproducts also have the capability to initiate secondary oxidation reactions within the mitochondria and, to a certain extent, within the cytosol[110][111]. The ETC provides the O2•- and H_2O_2 that labile iron interacts with, making mitochondria particularly susceptible to damage from iron-catalysed oxidants[112]. This cascade leads to damage of cellular components, lipid peroxidation and ultimately cardiac functional impairment and heart failure.

2.2.3 Clinical Hallmarks of Cardiac Iron Overload

Iron overload has the potential to induce both systolic and diastolic dysfunctions, contingent upon the severity of the iron overload and the disease stage. The pathological staging of iron overload is influenced by the underlying mechanism triggering the iron accumulation and the duration of iron exposure[113]. During the early stages, patients are often asymptomatic, with low levels of iron overload. In the chronic phase of iron overload, as iron overload increases in severity, diastolic dysfunction typically precedes systolic dysfunction.

Initial diagnostic assessments for iron overload typically involve blood tests to screen for serum ferritin levels and transferrin saturation, which serve as a measure of iron overload status. Serum ferritin is measured to determine the body's iron stores, while transferrin saturation measures the percentage of iron-binding sites in the blood that are occupied by iron. According to clinical guidelines, iron overload is characterized by a patient having a plasma transferrin saturation of >55% and a serum ferritin level of >200 ng/ml in women or >300 ng/ml in men[114]. Serum ferritin has been demonstrated to be closely correlated with liver iron content and increases linearly with the number of blood transfusions, and iron overload symptoms typically appear in patients with serum ferritin levels above 1000 ng/ml.[115][116][117]. However, it exhibits a poor correlation with cardiac iron overload, where high myocardial iron deposition may occur even in the presence of low serum ferritin levels [118]. Additionally,

serum ferritin is an acute-phase protein, meaning it can also rise in response to various other conditions, including inflammation, infection, and liver disease [119].

T2* Cardiac magnetic resonance (CMR) imaging, allows quantitative assessment of cardiac iron load during its reversible phase and provides a highly representative measurement of global cardiac iron levels. A T2* relaxation time value of 20 ms is recognized as the threshold for cardiac iron overload. Patients with >20 ms relaxation time are deemed low risk for developing congestive heart failure and are characterized by an absent or benign iron load with normal cardiac function. Patients with a T2* relaxation time of 10 to 20 ms and <10 ms are categorized as having an intermediate and severe risk of developing congestive heart failure, respectively, with the latter being indicative of severe iron overload. Additionally, T2* relaxation values show a strong inverse correlation with LVEF, however no relationship is observed between T2* values and serum ferritin or liver iron[117] [120][121]. In a study of 652 patients with thalassemia major, a condition known for iron overload complications, the risk of developing congestive heart failure within one year was 47% for those with a T2* value of <6 ms, 21% for T2* values between 6 and 10 ms, and only 0.2% for those with a T2* value >10 ms [122]. Iron overload-induced cardiomyopathy is clinically diagnosed when characteristic functional changes coexist with systemic iron overload parameters (serum ferritin >300 ng/mL, transferrin saturation >55%) and a cardiac T2* value of less than 20 ms. Clinical cardiac iron data for DOX-treated patients is unavailable, as clinical guidelines do not require the monitoring of cardiac iron levels during or prior to DOX treatment.

Direct cardiac iron measurements are only attainable from post-mortem examinations in patients with end-stage pathologies, as performing cardiac biopsies is considered unsafe. Cardiac iron levels were examined in 10 hearts obtained from transfusion-dependent patients. The hearts were acquired from individuals who experienced heart failure leading to death (n=6) or underwent cardiac transplantation for end-stage heart failure (n=4) [123] [121]. Measurements of total cardiac iron were conducted using inductively coupled plasma atomic emission spectroscopy (ICP-AES). In these 10 patients, total cardiac iron content was 5980 ± 2420 ugFe/g dry tissue, ranging from 3190 to 9500 ugFe/g dry tissue. This represents a significant 17-fold increase in cardiac iron compared to the normal ranges previously reported, where the typical cardiac iron concentration is measured at 340 ugFe/g dry tissue, with a range of 290–470 ugFe/g dry tissue.

2.3 Anthracyclines

Doxorubicin (DOX), a cytotoxic anthracycline antibiotic widely used in cancer chemotherapy [124], was first isolated in the 1960s from the bacterium Streptomyces peucetius var. caesius [125], [126]. DOX is used extensively as the first line of defence in the treatment of cancer in both adult and paediatric patients and remains the most widely prescribed and effective cytotoxic chemotherapeutic drug on the market, sold under the brand name Adriamycin® and Rubex®. DOX is used for the treatment of a variety of different cancers, predominantly solid tumours, and hematologic malignancies, including Hodgkin's/non-Hodgkin's lymphoma, acute lymphoblastic and myeloblastic leukaemia and cancers of the breast, bladder, stomach, liver, and ovary(Jain, 2000; Santos and Goldenberg, 2018) (Xu, Persson and Richardson, 2005). DOX is often used in combination with other antitumour medication, or alongside surgery and radiation, and is administered either via intravenous injection or as a continuous infusion through a central catheter line [127][128]. The general chemical structure of anthracycline compounds, including DOX, consists of a tetracycline moeity of four cyclohexane chains with adjacent quinones on the ring structure and a conjugated amino sugar residue (Figure 9).

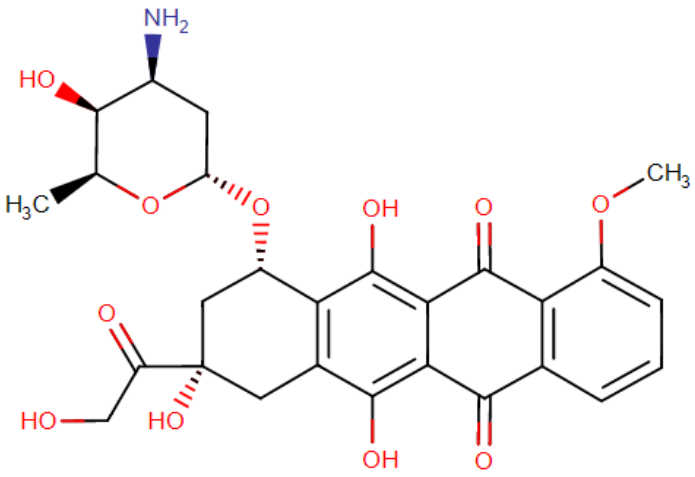

Figure 8: Structure of Doxorubicin [556]

2.3.1 Mechanisms of DOX Cytotoxicity

DOX, and its major metabolite doxorubicinol, bind to plasma proteins and enter cells via passive diffusion [69]. Two main theories exist that describe the mechanisms by which DOX exerts its anti-cancer activity: 1) Through its intercalation into DNA [69] [129], and 2) its inhibitory effect of topoisomerase II (TOP2) in fast-proliferating cancer cells [130] [131] [132].

2.3.1.1 Intercalation of DOX into DNA

DOX is thought to intercalate between nucleotide base pairs in the DNA helix [69] to prevent nucleotide replication, damage DNA and inhibit protein synthesis. DOX enters the cell and forms a complex with the proteasome of the cytoplasm [129] which is then transported into the nucleus via nuclear pores, allowing it to concentrate at 50-fold higher concentrations compared to the cytoplasm. Once in the nucleus DOX dissociates from the proteasome to bind to DNA, which it has a higher affinity for [129][133][134].

2.3.1.2 The Inhibitory Effect of TOP2 in Fast-Proliferating Cancer Cells

DOX is thought to primarily exert its cytotoxic effect through the inhibition topoisomerase II (TOP2) [128].TOP2 is an enzyme involved in the replication of the DNA, by regulating temporary double-stranded breaks during the normal cell cycle [130] [131]. Anthracyclines inhibit TOP2 enzymes by forming a complex with DNA, preventing the resealing of DNA breaks. A TOP2-DOX-DNA ternary complex is formed following the intercalation of DOX between the nucleotide base pairs of the DNA helix [135]. This stable complex impedes the re-ligation of the double-stranded DNA break, halting the process of replication [136]. There are two TOP2 iso-enzymes, TOP2α and TOP2β. TOP2α is a key mediator in DNA replication and believed to be central to DOX anti-cancer activity. [137]. When the TOP2- DOX-DNA ternary complex involves TOP2α, it arrests the cell cycle in G1/G2 [138]. The accumulation of stabilized DNA cleavage complexes disrupts DNA replication and transcription processes, leading to the apoptosis of malignant cells [138]. Using a well characterized mouse model of lymphoma, TOP2α expression levels have been shown to be a major determinant in the cytotoxicity of DOX; the suppression of TOP2α produces resistance to DOX *in vitro* and *in vivo* [139]. DOX -induced inhibition of TOP2α are selectively more toxic towards cancer cells compared to healthy cells because of their higher rate of multiplication.

2.4 Doxorubicin-Induced Cardiotoxicity

The clinical efficacy of DOX treatment of cancer is hindered by the cumulative dose-related cardiotoxicity associated with its use. This is becoming an increasingly important problem as cancer survival rates increase, leaving cancer survivors at increased risk of cardiomyopathy, left ventricular dysfunction and congestive heart failure [9]. Here, I have provided a clinical overview of DOX-induced cardiotoxicity, addressing its prevalence, the risk factors contributing to its development, and its clinical classification. I also review the limitations associated with the current strategies of diagnosis, treatment, and prevention of DOX-induced cardiotoxicity.

2.4.1 Incidence and Risk Factors

The development of heart failure as a complication of DOX treatment was recognised soon after its widespread clinical introduction. DOX-induced cardiotoxicity (DIC) was first identified by Von Hoff *et al*. in a large, retrospective study of ~4000 patients [140]. Of these patients, 2.2% developed clinical signs and symptoms of congestive heart failure. It was acknowledged that the true incidence of DOX-induced congestive heart failure was expected to be much higher than this as the study was based on clinician-identified symptoms, omitting subclinical left ventricular dysfunction. The Von Hoff *et al.* study was significant in demonstrating that the development of DOX -induced heart failure is determined by cumulative dose; a sharp increase in the incidence of heart failure observed in patients receiving a cumulative dose of 550mg/m^2 of DOX.

Since that initial retrospective study conducted by Von Hoff *et al.,* cumulative dose has remained a key clinical determinant in the development of DOX -induced cardiotoxicity. This was supported by an important retrospective analysis of three trials of DOX treatment conducted by Swain *et al.* [9]. In a group of 630 patients with either breast cancer or small cell lung carcinoma. The study confirmed cumulative dose-dependence of DOX cardiotoxicity, 32 of the 630 patients had evidence of congestive heart failure or a significant decline in LVEF (Figure 10).

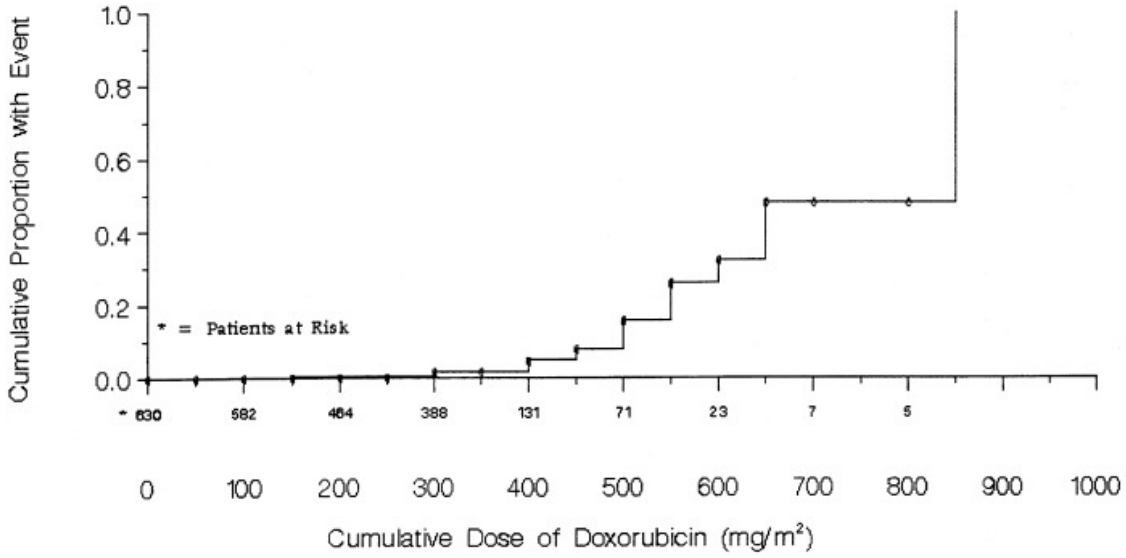

Figure 9: Dose Related Risk of a Doxorubicin-Induced cardiac event in 630 patients (based on data from the retrospective analysis of three trials of doxorubicin treatment of breast cancer or small cell lung cancer (Multicenter trials 088001, 088006 and 088002)). A Cardiac event was defined as a decline in absolute value ≥ 20% in LVEF from baseline, a decline in absolute value ≥10% in LVEF from baseline and to below the institution's lower limit of normal, a post baseline decline in absolute value ≥ 5% in LVEF below the institution's lower limit of normal, or the occurrence of congestive heart failure during the study.

Their findings also identified that individual susceptibility could result in the development of anthracycline-induced cardiotoxicity at cumulative doses below the clinically recommended limit and previously considered low risk (cardiac events were observed at a cumulative dose as low as 150 mg/m^2). The incidence of DOX-induced cardiotoxicity, based an increased detection of heart failure and left ventricular dysfunction, were also found to be higher than previously predicted (Table 1) [141].

Table 1: The incidence of Doxorubicin-induced heart failure at 450 mg/m^2, 550 mg/m^2 and 700 mg/m^2 DOX cumulative dose. [9]

Incidence of DOX-induced heart failure	**Doxorubicin cumulative dose (mg/m^2)**		
	400	550	700
Previous	3%	7%	18%
Revised, 2003	5%	16%	26%

Age is also a significant risk factor associated with the development of DOX -induced cardiotoxicity; the incidence of anthracycline cardiotoxicity increased steadily with age within the Von Hoff *et al.* study. Similarly, within the retrospective analysis by Swain *et al.*, as the

cumulative dose of doxorubicin increased to 400 mg/m^2, the risk of congestive heart failure in patients over 65 years old was seen to be two-fold greater than that observed in younger patients [9]. The incidence of DOX -induced cardiotoxicity has also been shown to be increased in patients with pre-existing cardiac pathologies (e.g. hypertension, LV hypertrophy and coronary artery disease), cardiac risk factors (e.g. hypertension, diabetes, obesity, and hyperthyroidism) or prior radiation exposure [142].

2.4.2 Classification

DIC is classified into three types according to its clinical manifestation: 1) Acute, 2) early-onset chronic progressive cardiotoxicity, and 3) late-onset chronic progressive cardiotoxicity.

Acute cardiotoxicity occurs within 2–3 days of DOX treatment and manifests in approximately 11% of patients[143] [125] [9]. It is characterized by vasodilatation, hypotension and cardiac dysrhythmias that result in a depression of myocardial contractility, which is often reversible within 1 week following the end of treatment [144].

Early-onset chronic cardiotoxicity can be progressive and is ultimately related to the development of a chronic dilated cardiomyopathy. It is characterized by systolic or diastolic ventricular dysfunction and the progressive reduction of left ventricular ejection fraction[145]. Early-onset cardiotoxicity manifests up to 1 year after the end of treatment and occurs in 5–35% of DOX -treated patients[145] [146].

Late-onset chronic progressive cardiotoxicity manifests after a much longer latency period, ranging from 1 year up to 10-15 years after the end of DOX treatment [147] [148]. During the latency period, the patient is asymptomatic, exhibiting normal cardiac function. Following this, chronic dilated cardiomyopathy develops and/or decreased left ventricular function [148]. This can lead to the development of congestive heart failure [147] [149].

Long term anthracycline-induced cardiotoxicity is increasingly clinically relevant due to the increased rate of cancer survival. The late-onset chronic form of DIC is particularly relevant in adult survivors of paediatric cancers; cardiac disease is the leading non-malignant cause of death in long-term survivors of childhood cancer. The impact is greatest in this subset of cancer survivors as they face living with the life-long cardiac complications associated with DOX treatment; approximately 60% of paediatric cancer patients are treated with an anthracycline and within 15 years ~10% develop symptomatic cardiomyopathy and 65% exhibit

echocardiographic evidence of left ventricular contractile abnormalities [10], [11]. The Childhood Cancer Survivor Study, consisting of 14,358 5-year cancer survivors diagnosed under the age of 21, was important in highlighting the substantial long term risk of cardiovascular disease associated with anthracycline treatment [150]. This study showed that the use of an anthracycline at a cumulative dose of ≥250 mg/m^2 was associated with a 2-5 fold higher risk of developing congestive heart failure, pericardial disease, and valvular abnormalities compared to patients who did not receive anthracyclines as part of their cancer treatment [150]. A retrospective analysis in 2006 by Oeffinger *et al*. revealed that among 10,397 survivors of childhood cancer, there was 15 fold higher rate of heart failure, a 10 fold higher rate of other cardiovascular diseases, and a nine-fold higher rate of stroke 30 years after diagnosis compared with results of siblings [141].

2.4.3 Diagnosis

The clinical diagnosis of DIC is primarily based on the evaluation of cardiac functional status and morphological examination [151] [152]. Medical intervention is often ineffective at the point at which such changes are identified [151] [152]. The diagnosis of DIC is primarily based on changes in left ventricular (LV) systolic function. A fall or change in left ventricular ejection fraction (LVEF) is interpreted as an early indication of cardiotoxicity [153]. Variation in LVEF is principally identified by echocardiography, tissue doppler echocardiography, cardiac MRI, and multi-gated radionuclide angiography (MUGA) [152] [154] [155] [156][157] [158] [70] [159]. The thresholds for LVEF as an indicator of DIC is identified clinically as a loss of LVEF of >10% from baseline to a value below 50% [153]. The identification of DIC in this manner is limited by considerable intra-observer and inter-observer variability and discrepancy among the imaging modalities themselves. A fall in LVEF is detectable via current clinical imaging modalities after considerable cardiac damage or dysfunction has occurred and compensatory mechanisms are exhausted. The detection of cardiac dysfunction by LVEF probes mechanical and structural cardiac function, but changes in these parameters are often irreversible by the time of detection [154]. LVEF may appear normal despite the presence of myocardial injury as the heart can undergo ventricular remodelling in response to a cardiac injury to maintain adequate cardiac output [160]. Endomyocardial biopsy and serum biochemical indicators are often evaluated in conjunction to aid diagnosis [161][162] [163] [164], [165] [166][167][168][169]. These tests are not specific for the diagnosis of DOX-induced cardiotoxicity, and we and others are developing imaging tools which can detect cardiotoxicity

sooner by the molecular imaging of biochemical injury to the heart before it manifests as contractile dysfunction.

2.4.4 Management

2.4.4.1 Treatment Strategies

At present, there is no specific evidence-based treatment for established DIC. The loss of contractile function often manifests at a point in which medical intervention is no longer effective and the contractile and structural changes that underlie this dysfunction are irreversible. As a result, clinicians aim to prevent existing cardiomyopathy from worsening and to alleviate symptoms to improve the functional status of the patient [170][171]. Treatment options are non–specific and primarily include: β-blockers, diuretics, antioxidants, and angiotensin converting enzyme inhibiters (ACEI). There is no specific treatment for the total recovery of DOX-induced myocardial injury, and the only viable option for patients with end stage heart failure is cardiac transplantation [172].

2.4.4.2 Preventative Strategies

Limiting cumulative dose is the main method utilised for the prevention of DIC. Maximum cumulative dose of 550 mg/m^2 DOX is currently recommended and should only be exceeded with close cardiac monitoring [172] [173] [174]. Prolonged continuous delivery of DOX (6-96 h), compared to the administration of DOX as a bolus, has been employed to reduce the risk of DIC [175] [176]. An analysis by Shapira *et al*. investigated the cardioprotective effect of a prolonged infusion of DOX (over 6 hours) compared with the standard mode of administration (rapid infusion over 15 -20 mins) in 62 cancer patients [176]. DOX was associated with significantly lower cardiotoxicity with prolonged infusion than when administered by standard rapid infusion, suggesting that DOX cardiotoxicity may be worse with high peak blood concentrations rather than exposure time; The mean decline in LVEF after a cumulative DOX dose of 300 mg/m^2 was 17% in the rapid infusion group, and 6% in the prolonged infusion group. However, the cardioprotective effect of the continuous infusion of DOX has not been seen in paediatric cancer patients[177] [178]. The prolonged infusion of DOX over 48 hours for childhood leukaemia failed to find any cardioprotective advantage over bolus infusion; both administration strategies were associated with progressive subclinical cardiotoxicity [178].

Dexrazoxane is an iron chelator and is the only clinically approved pharmaceutical agent for the prevention of DIC. Dexrazoxane has been shown to minimise LVEF fall and to reduce the production of oxygen free radicals, lipid peroxidation products and myocardial apoptosis [177] [179] [180]. However, the exact mechanism by which Dexrazoxane reduces the cardiotoxic effects of DOX remain controversial. While dexrazoxane was originally thought to act as an iron chelator (as discussed in Section 1.12), recent evidence suggests and alternate mechanism based on the inhibition of cardiac topoisomerase IIβ [177] [179] [180] [181][182].

2.5 Mechanisms of Doxorubicin-Induced Cardiotoxicity

The exact mechanism of DIC is believed to be a multifactorial process. The dysregulation of essential processes, such as calcium homeostasis, topoisomerase action, sarcomere structure, gene expression, and apoptosis, have all been reported to contribute to the development of DIC [183][184][145][185][186][187]. The relative weight of each individual mechanism in the development of DIC is unknown and is likely to involve a combination of multiple mechanisms.

The most heavily supported mechanism used to explain the complex pathophysiology of DIC is through the generation of ROS [125] [188] [94][185][189] [190][191][192][193]. Evidence suggests that DOX catalyses the formation of intracellular oxygen radicals through the interaction with the mitochondrial respiratory chain and other cytochrome-containing enzymes. The role of iron in DIC has also been reported extensively with evidence suggesting the interaction of DOX with iron is a key pathway through which ROS is formed[194] [183] (Xu, Persson and Richardson, 2005) [188]

2.5.1 Mitochondrial Dependent ROS Generation

The best described mechanism that links DOX to lipid peroxidation of the cell membrane and myocardium injury is induction of free radical production [125][170][185][195][196][197]. Oxidative stress in cardiomyocytes is induced by the reductive activation of a DOX quinone moiety (ring C of the DOX tetracyclic), that occurs in a sequence of reactions is known as “redox cycling” (Figure 11) [198][145][185][199][186].

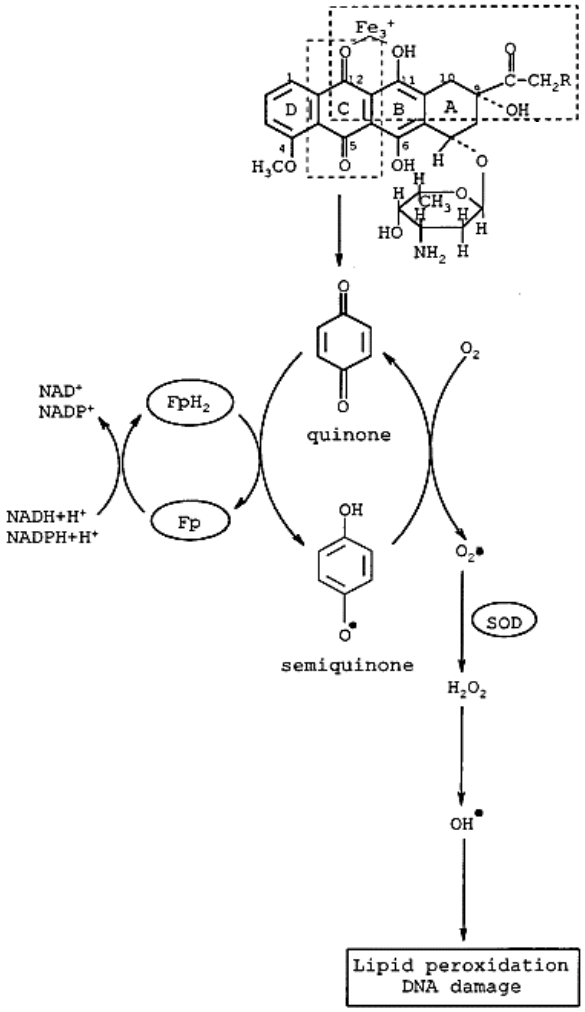

Figure 10: Formation of oxygen free radicals by DOX. Redox cycling of the quinone moiety (ring C) of the DOX molecule. [229]

This process leads to an increased production of ROS, with the formation of superoxide and hydroxyl radicals. Redox cycling of DOX begins at complex 1 of the ETC. Here, NADH or NADPH reduces ring C resulting in the formation of a semiquinone free radical [200][201]. This reduction is reversible and is catalysed by electron transfer flavoproteins located on the matrix face of the inner mitochondrial membrane[202] [200]. The unpaired electron of the semiquinone free radical is donated to oxygen, resulting in the formation of a superoxide radical ($O^{2\,\bullet-}$), leading to the generation of ROS, including hydroxyl radicals ($OH^{\bullet}$) and hydrogen peroxide (H_2O_2)[203][204]. The dismutation of superoxide ($O^{2\,\bullet-}$) to hydrogen peroxide (H_2O_2) is thought to be catalysed by superoxide dismutase or may occur spontaneously[202] [200]. OH• is highly reactive and can directly damage DNA, leading to

lipid peroxidation. The generation of OH• from H_2O_2 is believed to be dependent on the catalytic role of trace elements, especially iron (See 2.5.2.1.3).

The mitochondria are the most extensively injured organelles associated with DIC [184][186] with evidence suggesting that DOX preferentially accumulates in the mitochondria of cardiomyocytes [205] [206] [207], likely due to DOX binding with high affinity to cardiolipin within the mitochondrial membrane [205] [206] [207][206]. Cardiolipin, which constitutes ~20% of the total lipid composition of the inner mitochondrial membrane, is required for the proper functioning of the ETC proteins, such as cytochrome C oxidase and NADPH cytochrome[208]. It is suggested that the binding of DOX with high affinity to cardiolipin disrupts the cardiolipin-protein interface that stabilizes the ETC chain [209]. This disruption leads to electron leakage from the ETC, resulting in the partial reduction of oxygen to form superoxide, thus increasing superoxide formation and oxidative stress [210]. The generation of ROS, particularly superoxide, can lead to further mitochondrial damage, including changes in membrane potential and permeability. The resulting mitochondrial dysfunction impairs normal efflux mechanisms, causing DOX to be retained in the mitochondria, further exacerbating the cycle of oxidative damage and mitochondrial retention of DOX [211]. Supportive of this, DOX, a cationic drug, has been shown to be retained in the inner membrane of the mitochondria by forming a complex with anionic cardiolipin(E. Goormaghtigh et al., 1990). Goormaghtigh *et al.* has shown that mitochondrial enzymatic complex I–III are inhibited following disruption of the cardiolipin-protein interface by DOX, leading to an increase in superoxide formation [212][213][206] [214].

The heart is particularly rich in mitochondria with ~50% of cardiomyocyte mass and has been shown to be both a source and target of ROS [146] [204]**.** Mitochondria produce >95% of the ATP used in the heart, thus mitochondrial disruption can result in extensive cardiac injury [215][12]. An increase in ROS was observed in the mitochondria of isolated rat cardiomyocytes following a 20 min exposure to DOX at concentration of 40-160 µM [216]. Cardiac tissue is also particularly vulnerable to oxidative stress because of the high turnover of oxygen and its relatively low antioxidant capacity [217]. Increased ROS generation within the mitochondria contributes to the pathological oxidation of proteins and signalling molecules, disrupting mitochondrial function [218][219]. The brain however, despite also being mitochondria rich does not exhibit the same mitochondrial disruption as the heart because the blood brain barrier prevents the entry of anthracyclines [220].

The reduction of mitochondrial function caused by DOX has been shown to alter cardiac energetic metabolism [184][145][160]. This is evidenced by a decline in ATP production, which likely contributes to the abnormal contraction and relaxation often seen in heart failure [221][222].

2.5.2 Iron-Dependent Mechanisms of Doxorubicin-Induced Cardiotoxicity

There is significant evidence supportive of the role of iron overload in DOX cardiotoxicity despite controversy of its relative importance [47][48]. Many studies demonstrate the role of iron as an amplifier of toxic free radical generation (initiated by the redox cycling of DOX), other evidence suggest its role in DIC is not solely restricted to oxidative stress [43][49] [47][48]. DOX has been shown to exert control over different aspects of iron homeostasis, which in turn are hypothesised to contribute to the progression of cardiac dysfunction (Figure 12) [43] [49].

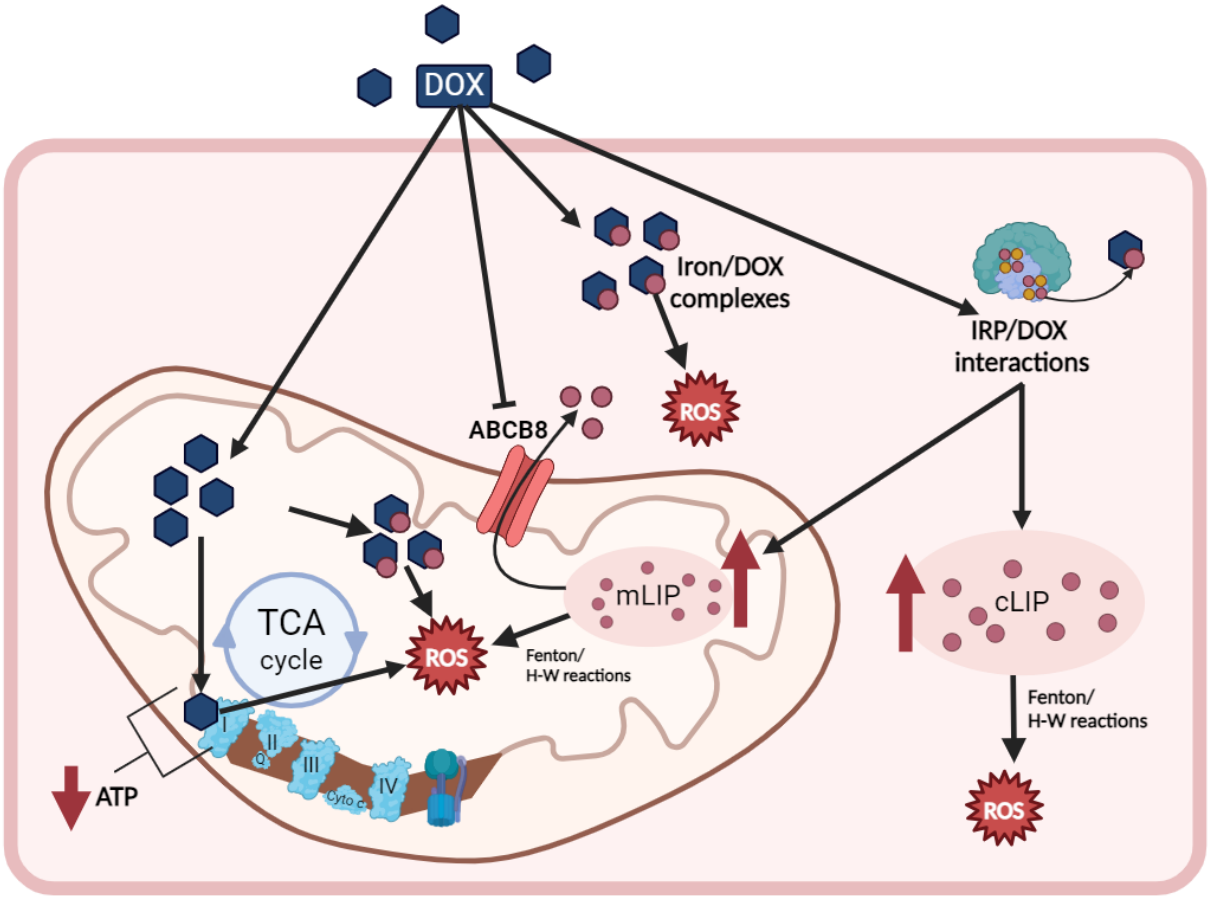

Figure 11: Iron mediated molecular mechanisms of doxorubicin-induced cardiotoxicity. Iron is proposed to exacerbate DOX-induced cardiotoxicity through several mechanisms, including interactions with IRP's, that can increase both mitochondrial and cytosolic LIP's, and through the formation of redox-active iron-DOX complexes. These mechanisms collectively contribute to increased ROS production, leading to increased oxidative stress, mitochondrial dysfunction, and ultimately resulting in cardiac damage. IRP; iron regulatory proteins, cLIP; cytosolic labile iron pool, mLIP; mitochondrial labile iron pool; ABCB8; ATP-binding cassette (ABC) transporter 8. [Figure made in BioRender]

2.5.2.1 Iron-Dependent ROS Generation

There are two main pathways proposed by which iron promotes ROS formation in DOX-exposed cells, these involve: 1) Fenton and Haber-Weiss reactions. and 2) The formation of iron-DOX complexes

2.5.2.1.1 Fenton and Haber-Weiss Reactions

Iron may likely promote and exacerbate the production of ROS in DOX exposed cells through the Fenton and Haber-Weiss reactions [200] [223][224][225]. The redox cycling of DOX results in the generation of H_2O_2 and $O_2^{\bullet-}$. Superoxide dismutase (SOD) facilitates the dismutation of superoxide $O2^{\bullet-}$ and H_2O_2 is normally neutralised by catalase/glutathione peroxidase into water and oxygen. However, in the presence of iron, H_2O_2 and $O_2^{\bullet-}$ can generate highly toxic $^{\bullet}OH$ via the Haber-Weiss reaction (Equation 1) in a two-step process [202] [226]. Firstly, ferric iron (Fe^{3+}) is reduced to ferrous iron (Fe^{2+}) by $O_2^{\bullet-}$(Equation 2). The Fe^{2+} then reacts with H_2O_2 as part of the Fenton reaction, resulting in the formation of highly toxic $^{\bullet}OH$ (Equation 3). [227] [225] [228].

Equation 1

$$O_2^{\bullet-} + H_2O_2 \rightarrow O_2 + OH^- + {}^{\bullet}OH$$

Equation 2

$$O_2^{\bullet-} + Fe^{3+} \rightarrow O_2 + Fe^{2+}$$

Equation 3

$$H_2O_2 + Fe^{2+} \rightarrow OH^- + {}^{\bullet}OH + Fe^{3+}$$

2.5.2.1.2 Iron-Doxorubicin Complexes

DOX also engages in direct interactions with iron, resulting in the formation of DOX-iron complexes. This interaction induces a cycling of iron between Fe^{2+} and Fe^{3+}, leading to the generation of toxic hydroxyl radicals OH• (Figure 13, a). Iron-DOX complexes can form OH• in both the presence and absence of a reducing system (Figure 13, b). NADH cytochrome P450 reductase, along with the thiol groups of cysteine or glutathione, act as reducing systems, facilitating the reduction of DOX-Fe^{3+} complexes to DOX-Fe^{2+} [229][230]. The DOX-Fe^{2+} complex can react with oxygen to form $O_2^{\bullet-}$, which then undergoes dismutation to form H_2O_2.

The generated H_2O_2 can then participate in the Haber-Weiss reaction, ultimately leading to the generation of OH•. The DOX-Fe^{2+} complex can also react with H_2O_2 directly to yield $OH^{\bullet}$. The DOX-Fe^{3+} complex can also undergo iron reduction in the absence of a reducing system, facilitated by oxidation of the DOX molecule [224] This process leads to the formation of a DOX free radical-Fe^{2+} complex (DOX$^{\bullet}$ -Fe^{2+}). This complex can also react with O_2 and H_2O_2 to generate $O_2^{\bullet-}$ and $OH^{\bullet}$, respectively. The oxidation of DOX continues until the fully oxidized version is attained.

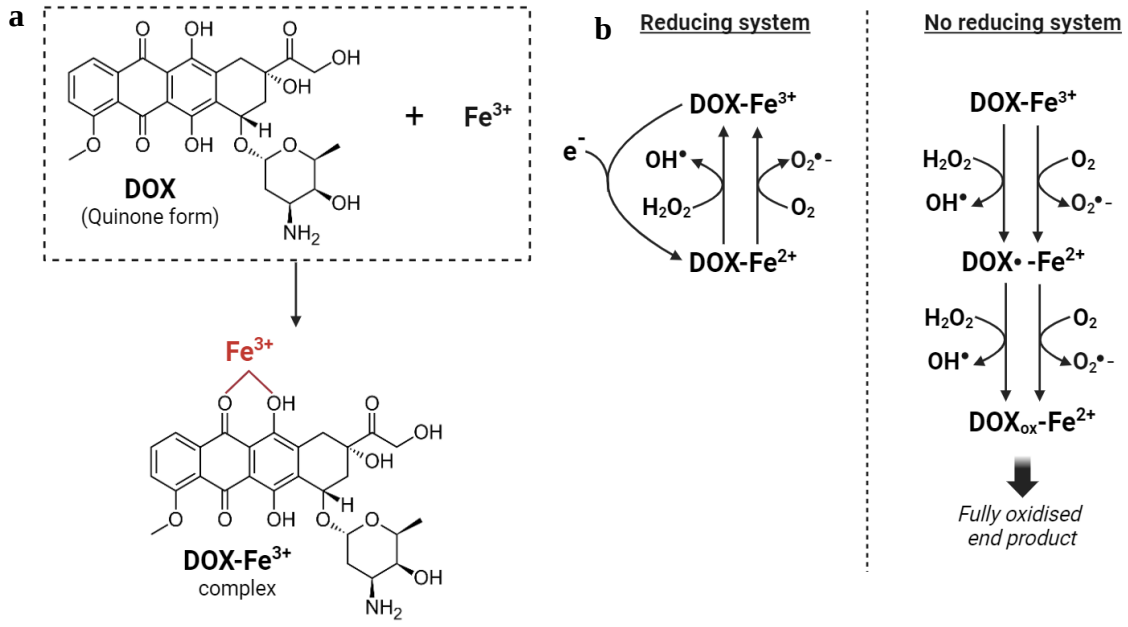

Figure 12: DOX-iron complexes a Formation of DOX-Fe^{3+} **b** ROS production generated by DOX-iron complexes, in the presence and absence of a reducing system. [Figure made in BioRender]

2.5.2.1.3 Iron-mediated Doxorubicin Redox Cycling

Elevated levels of labile iron also contribute to the generation of ROS induced by DOX by facilitating the re-oxidation of DOX to its quinone form (Figure 14) [231]. This process aids in sustaining the redox cycle of DOX.

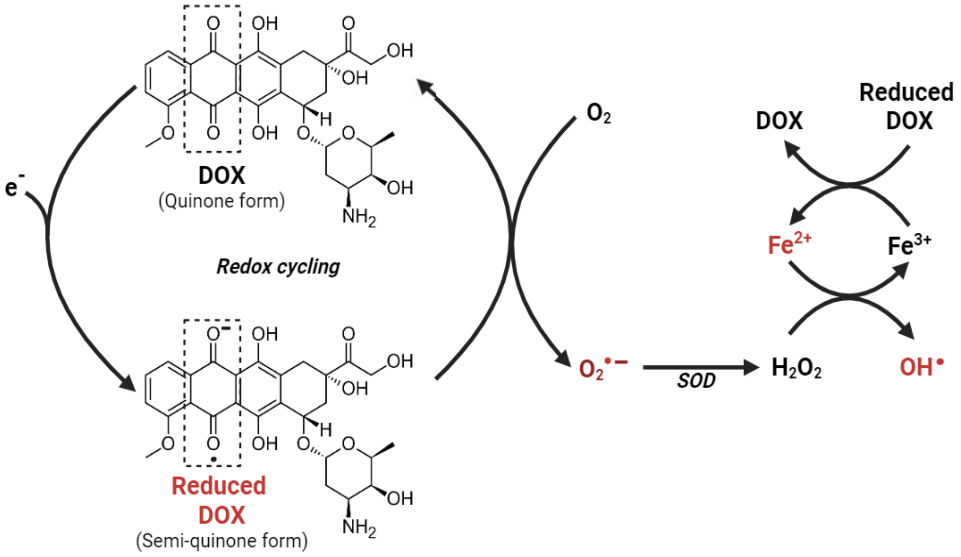

Figure 13: Iron exacerbated DOX redox cycling. Labile Fe^{3+} can re-oxidise DOX to its quinone form contributing to the continued redox cycle of DOX. SOD; Superoxide dismutase. [Figure made in BioRender]

2.5.2.2 Dysregulation of Iron Regulatory Proteins

DOX interaction with iron regulatory proteins IRP1 and IRP2, leading to labile iron accumulation within cardiomyocytes, is a key factor linking iron to DIC[232][233][194][234].

To maintain low levels of labile iron, IRPs tightly control intracellular iron homeostasis by regulating iron acquisition, transport, and storage through influencing the expression of key iron uptake and storage proteins at a translational level [49]. IRPs modulate the expression of the transferrin receptor (TfR1) which governs the entry of transferrin into cells, and the iron storage protein ferritin[194].

When labile iron levels are elevated, iron homeostasis is restored through the action of IRPs on ferritin and TfR1 (Figure 15, a). The binding capacity of IRP-1 to the iron regulatory elements (IRE) in mRNA is modulated by the presence or absence of an iron-sulphur [4Fe-4S] cluster within the protein. Under conditions of iron overload, IRP-1 contains a [4Fe–4S] cluster and cannot bind to the IRE in the mRNA of ferritin, and IRP-2 is degraded. The lack of IRP binding to IREs allows for the translation of mRNAs containing an IRE in the 5' UTR (Ferritin)

and nucleolytic degradation of mRNAs containing IREs in the 3' UTR (TfR1). Absence of IRE/IRP interaction allows translation of ferritin mRNA, facilitating increased storage and detoxification of labile iron, and rendering TfR1 mRNA susceptible to nucleolytic degradation, impeding iron uptake.

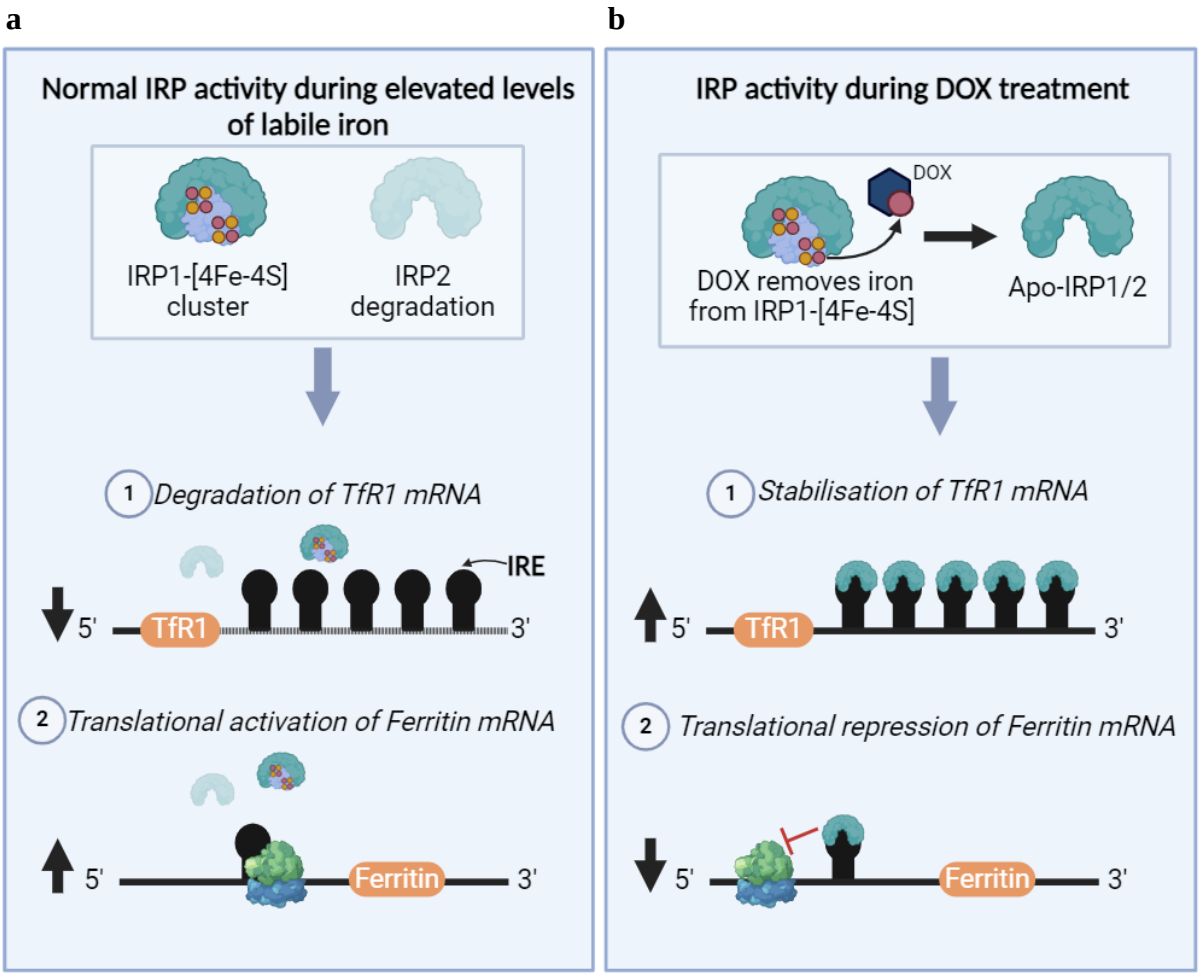

Figure 14: Regulation of Ferritin and Transferrin Receptor 1 by Iron Regulatory Proteins in the Presence and Absence of DOX. a When labile iron levels are elevated, IRP-2 is degraded, and IRP-1 contains a [4Fe–4S] cluster, preventing IRP binding to IRE of mRNA. This lack of IRP/IRE interaction leads to the degradation TfR1 mRNA and promotes Ferritin translation. Consequently, labile iron storage increases and iron uptake decreases, restoring homeostasis. **b** DOX deactivates IRPs by stripping iron from their iron-sulfur cluster, which stabilizesTfR1 mRNA and represses ferritin mRNA translation. This results in elevated TfR1 expression and decreased ferritin levels, leading to elevated cardiac iron levels. IRP1 and IRP2; Iron regulatory proteins 1 and 2, IREs; Iron responsive elements, TfR1; Transferrin receptor 1. [Figure made in BioRender]

DOX can inactivate IRPs, leading to decreased ferritin levels and the increased expression of TfR1 to elevate cardiac iron levels (Figure 15, b) [232][233][194]. The DOX metabolite doxorubicinol directly interacts with the [4Fe-4S] cluster in IRP1, converting [4Fe-4S]-IRP1 into apo-IRP1[194], and releasing iron. Apo-IRP1 and IRP2 can both bind to the IRE present

in the mRNA of ferritin and TfR1. IRP binding to ferritin mRNA obstructs its translation, suppressing the synthesis of ferritin. IRPs bind to the multiple IREs located on the 3' region, preventing TfR1 nucleolytic degradation which in turn increases iron accumulation within cardiac cells.

2.5.2.3 Mitochondrial Iron

Attention has been given to mechanisms involved in the regulation of mitochondrial iron in DIC, given the role of mitochondria in cellular iron homeostasis and as producer and target of ROS.

Ardehali *et al.* demonstrated that DIC develops through preferential accumulation of iron in the mitochondria, leading to increased mitochondrial iron and cellular ROS levels in isolated cardiomyocytes treated with DOX [205]. They also demonstrated that overexpressing mitochondrial iron exporter ABCB8 in transgenic mice reduces the DOX-induced increase in mitochondrial labile iron, providing protection against DIC. Additionally, Menon *et al* demonstrated that ABCB8 also mediates DOX efflux and that that ABCB8 expression is regulated by iron status[90].

Furthermore, ex-planted hearts from DOX-induced cardiomyopathy patients displayed significantly higher mitochondrial iron levels compared to hearts from other cardiomyopathy patients and those with normal cardiac function [205]. Although limitations exist due to unknown treatment details, potential damage during isolation and storage, the results support the concept that DIC correlates with increased mitochondrial iron.

2.6 Iron Overload in Cancer Patients: A Potential Modulator of DOX-Induced Cardiotoxicity

Examining the impact of cardiac iron in DIC holds clinical significance due to the wide variability of body iron levels observed among both adult and paediatric patients undergoing chemotherapy. Patients may experience considerable iron overload both during and as a consequence of chemotherapy, particularly in conditions such as leukaemia and lymphoma, where bone marrow stem cells are liable to damage [235] [193]. Chemotherapy exerts suppressive effects on the hematopoietic activity of bone marrow, impairing the production of red blood cells and resulting in chemotherapy-induced anaemia[236][237]. When bone marrow

transplant is required, the existing bone marrow can sustain damage due to the high doses of chemotherapy typically administered prior to the transplant, resulting in a reduced ability to produce red blood cells[238]. In this context, blood transfusions represent a vital clinical intervention to replenish red blood cell count in cancer patients[239][240][241]. Some cancer patients are transfused with multiple units of iron-containing packed red blood cells following chemotherapy and bone marrow transplantation; normal body iron stores are 3-4g and a typical blood transfusion contains 400–500 mg of iron [120] [115]. There is no mechanism for removal of the iron meaning that patients receiving regular transfusions develop iron overload, even with as few as 10 transfusions. The transfusion requirements vary among patients, with some needing only one or two transfusions, while others may require weekly transfusions[242]. In a study of 2,719 patients with diverse solid tumours undergoing chemotherapy in 28 UK centres, 33% required at least one blood transfusion, and 16% needed multiple transfusions[243]. This highlights the significant variations in transfusion needs within the patient group. Furthermore, several studies focusing on leukaemia patients suggested that chemotherapy-induced iron overload can be long-lasting. Among long-term survivors, 14-20% exhibit moderate to severe levels of clinically significant iron overload[244][245][246].

There is wide variation in body iron levels observed in patients even before initiating cancer chemotherapy. These variations can also stem from blood transfusions, as well as other factors such as iron supplementation, nutritional status, and genetic disorders. Hereditary hemochromatosis is the most common genetic disorder associated with iron overload, characterized by unregulated intestinal iron absorption, leading to the accumulation of excess iron in the heart, liver, and pancreas [247][248][249]. Hereditary hemochromatosis develops due to mutations in the iron regulatory HFE gene, and individuals with heterozygous mutations of this gene, specifically ($C282Y^{+/-}$) and ($H63D^{+/-}$), experience subclinical and asymptomatic iron overload. These mutations are found in 8% and 20% of individuals of Northern European descent in the American population, respectively[250][251].

Transgenic mouse models of hereditary hemochromatosis have shown the association between iron overload and DIC, and that iron overload increases the susceptibility of DOX-dependent cardiac damage. Miranda *et al.*, demonstrated that HFE-deficient mice had increased susceptibility to DIC compared to wildtype animals [252]. In the study, 8 week old wild-type, Hfe-/+, and Hfe-/- female mice were injected intraperitoneally with saline or 5 mg/kg of DOX (for a total cumulative dose of 30 mg/kg). Compared to wild type and Hfe-/+ mice, Hfe-/-mice

treated with DOX exhibited decreased body weight, enhanced alterations in iron metabolism, cardiac iron deposits, mitochondrial damage, and increased mortality. These changes were more prominent in Hfe-/- mice compared with wild-type mice, whereas Hfe-/+ mice showed intermediate modifications.

This observation highlights the potential importance of identifying patients with genetic iron-associated susceptibility (particularly those with the asymptomatic heterozygote HFE gene) who may be at elevated risk of cardiotoxicity before they embark upon their chemotherapy with a view to closer monitoring and/or personalised therapeutic/cardioprotective regimes [240][362].

2.6.1 Pre-existing Cardiac Iron Overload and DOX Cardiotoxicity

As discussed in Section 2.5, DOX can lead to iron accumulation in the heart by increasing the redox active labile iron pool through interactions with IRP's and by downregulating ABCB8[205]. These two effects act synergistically to generate hydroxyl radicals (OH•) in the heart via Fenton chemistry (Xu, Persson and Richardson, 2005), leading to oxidative stress. It is therefore likely that individuals undergoing cancer therapy with pre-existing elevated levels of iron and expanded labile iron pools, may be at greater risk of DIC.

The range of factors contributing to iron overload in cancer patients, inherited or acquired, highlights the complexity of managing iron levels within this patient population. Pre-existing iron overload could serve as an explanation for the notable variability in individual susceptibility to DIC. The differences in body iron levels among patients, evident even before the initiation of cancer chemotherapy, could be leveraged to optimize cardioprotective treatment strategies. This information could aid in determining the most suitable timing for administering these treatments, titrating personalised doses, or starting cardioprotective strategies sooner. As it stands, the only clinically approved iron chelator, dexrazoxane, is recommended exclusively for adults aged >25 who have received a cumulative 300 mg/m^2 dose of DOX, and still require additional anthracycline treatment[253]. There is a rationale to consider the use of iron chelators even before the administration of DOX, particularly in patients with elevated iron levels. It would seem intuitive that patient cardiac iron levels should be normalised prior to embarking on anthracycline chemotherapy whenever possible to avoid the exacerbation of cardiotoxicity.

2.7 Iron Chelation

In the management of chronic iron overload conditions, such as β-thalassemia major, extensive research has been undertaken to determine the cardioprotective properties of iron chelators. β-thalassemia major is a life-threatening genetic condition in which the β-globin chain constituent of haemoglobin is either severely reduced or absent[254]. Erythropoiesis is rendered ineffective, due to profound anaemia and an excess of α-globin chains, and life-long blood transfusions are required from the age of 1-2 years in these individuals[255][256].

A typical blood transfusion transfers 400-500mg of iron. For a typical 4-6 transfusion events per year, but up to 12 in severe cases[257], iron accumulations of 1,600–6,000 mg per year can occur. This is significantly higher than the 400–700 mg absorbed per year with a normal diet. This level of iron accumulation necessitates life-long iron chelation therapy to prevent iron-induced free radical production and damage to the heart, endocrine organs, and liver[258]. Current treatment of β-thalassemia major is based on chelation therapy. There are three clinically approved iron chelators: Deferoxamine, Deferasirox, and Deferiprone. Heart failure due to excess cardiac iron deposition though remains the leading cause of morbidity and mortality in β-thalassemia major patients[259].

Studies investigating the therapeutic effect of iron chelators on cardiac dysfunction are predominantly centred on β-thalassemia major patients. Other iron overload conditions, such as hereditary hemochromatosis and sickle cell anaemia, also exhibit cardiac dysfunction and have been shown to benefit from iron chelation therapy[260][261]. However, the evidence base is lower in these conditions and therefore the clinically approved iron chelators are discussed here in the context of β-thalassemia major.

2.7.1 Iron Chelator Chemistry

Iron chelators coordinate with iron ions and reduce their reactivity, making them chemically inert. Iron has a coordination number of six and iron chelators are classified according to the number of coordination sites they form with the central iron atom[262][263]. Hexadentate chelators; each molecule coordinates with one ferric iron, forming a 1:1 Fe^{3+}-chelator complex. Tridentate chelators; two molecules coordinate with each ferric iron, forming a 1:2 Fe^{3+}-chelator complex. Bidentate chelator; three molecules coordinate each ferric iron, forming a

1:3 Fe^{3+}-chelator complex. These complexes are water soluble, permitting entry into the bloodstream and elimination via urine/faeces[264].

2.7.2 Iron Chelation Principles

The clinical efficacy of iron chelators depends on a variety of chemical and biomedical characteristics. A chelating agent must be able to reach its target site at sufficient concentration to be able to exert its pharmacological effect. Orally administered iron chelators must be efficiently absorbed from the gastrointestinal tract and be able to permeate biological membranes[265]. The absorption, bioavailability, and penetrating ability of an iron chelator to cross biological membranes is governed by three fundamental factors: 1) lipophilicity, 2) molecular weight, and 3) molecular charge/ionisation state [266].

The lipophilicity of an oral iron chelator determines the extent of its absorption; lipid solubility is beneficial in facilitating movement across into the GI tract. Drugs with molecular weights of <200 are able to cross membranes via passive diffusion, whereas those with molecular weights >500 are largely impermeable and thus poorly absorbed by oral administration[267][268]. Bidentate and tridentate iron chelators with lower molecular weights possess higher oral absorption efficiencies then hexadentate chelators (molecular weight ~500-900)[266]. The molecular charge impacts membrane permeability, uncharged molecules can cross cell membranes at a faster rate than their charged counterparts[269].

Metal selectivity and iron-chelator structure are key factors associated with toxicity and clinical utility. Iron chelators should have a higher selectivity for iron ions over other metal ions; it is important to preferentially bind to the target metal ion (Fe^{3+}) to avoid the chelation of other biologically important trace metals such as calcium. Prolonged chelation of other physiologically important metals could lead to their deficiency[266]. The stability of iron-chelator complexes needs to be greater than those formed by iron and endogenous ligands[264]. Iron should be appropriately coordinated so that its surface is entirely masked to limit toxicity, rendering the iron-chelator complex kinetically inert[266]. Insufficiently coordinated iron-chelator structures leave the iron atoms exposed to oxygen and hydrogen peroxide, resulting in the production of free radicals. Hexadentate chelators typically mask the entire surface of the bound iron. At biological pH, bidentate and tridentate chelators can also completely coordinate the iron atom by forming appropriate iron-chelator complex ratios[266]. The selectivity of an iron chelator for Fe^{3+} over Fe^{2+} is also considered desirable for the prevention redox cycling.

2.7.3 Clinical Available Iron Chelators for the Treatment B-Thalassemia Major

There are three iron chelators currently used in clinical practice for the management of iron overload conditions: Deferoxamine, Deferasirox, and Deferiprone[264].

Deferoxamine is a hexadentate chelator; each Deferoxamine molecule coordinates with one ferric iron, forming a 1:1 Fe^{3+}-chelator complex. Deferasirox is tridentate; two Deferasirox molecules coordinate each ferric iron, forming a 1:2 Fe^{3+}-chelator complex. Deferiprone is a bidentate chelator; three Deferiprone molecules coordinate each ferric iron, forming a 1:3 Fe^{3+}-chelator complex. These complexes are water soluble, permitting entry into the bloodstream and elimination via urine/faeces. The stereochemical structures of these three iron chelators are depicted in Figure 16 and a summary of their key properties in Table 2.

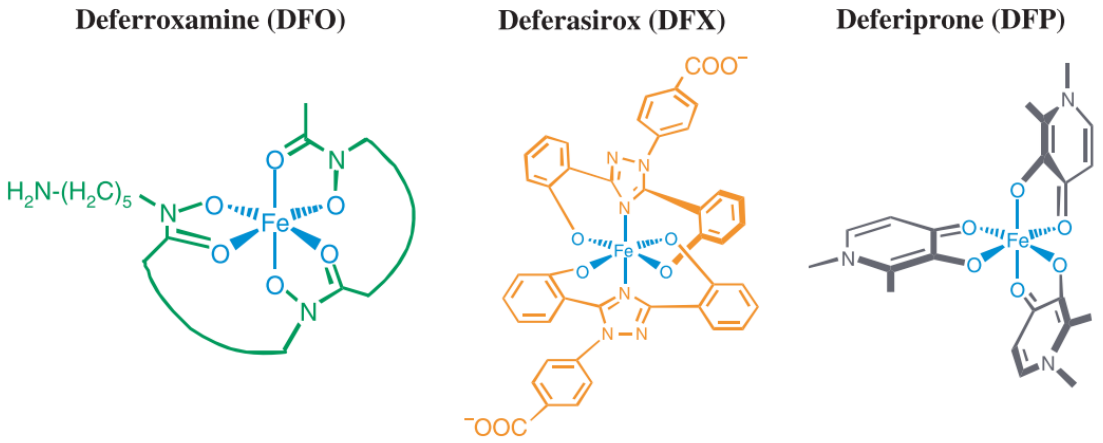

Figure 15: The stereochemical structures of Deferoxamine, Deferasirox, and Deferiprone. Deferoxamine is a hexadentate chelator (chelating ratio 1 : 1), Deferasirox is tridentate (chelating ratio 1 : 2), and Deferiprone is a bidentate (chelating ratio 1 : 3). [262]

2.7.3.1 Deferoxamine

Deferoxamine is a hexadentate siderophore extracted from *Streptomyces pilosus* and was the first drug to be clinically approved for the treatment of iron overload conditions, including β-thalassemia major[266]. Deferoxamine is a highly hydrophilic molecule with a large molecular weight, making it less able to pass through cellular membranes. It primarily chelates extracellular iron in the bloodstream and promotes iron elimination through the urine[270] [271]. Deferoxamine also utilises a facilitated transport system to enter the liver and can form complexes with hepatocellular iron too, making it an effective liver iron chelator[272]. Its inability to permeate cells helps reduce the potential of iron redistribution. Despite its wide

commercial availability, the clinical efficacy of deferoxamine is limited due to its route of administration and rapid renal clearance (plasma half-life 5-10 mins)[273]. Deferoxamine is ineffective administered orally due to its high molecular weight and so is administered parenterally via intravenous or subcutaneous infusions. Its short half-life requires that the patient must either undergo a 24-hour intravenous infusion or frequent subcutaneous infusions (8-12 hours, 5-7 nights/week) via a mobile pump[266]. This often results in poor patient compliance, which is a considerable limitation of constant infusion therapy. The lack of permeability also limits its ability to effectively chelate and remove excess cardiac iron, an important consideration in β-thalassemia major treatment.

2.7.3.2 Deferiprone

Deferiprone is a synthetic bidentate hydroxypyridonone iron chelator, developed in 1981 by Hider *et al*[274]. It was the first available orally active iron chelator and was granted FDA approval as a second line treatment for transfusion-induced β-thalassemia in 2011 [275]. Deferiprone has a 2-3 hour half-life and is orally administered three times a day for a total daily dose of 75mg/kg body weight[276][277].

Clinically significant is its ability to cross cellular membranes in both its unbound and complexed form. Deferiprone is able to 1) penetrate cells due to its low molecular weight and lipophilicity, 2) form a neutral 1:3 Fe^{3+}-chelator complex intracellularly, and due to its zero net charge, can 3) efflux the cell in its complexed form[264][278]. Deferiprone is thus able to chelate labile iron in the blood and remove iron from iron loaded cells, including

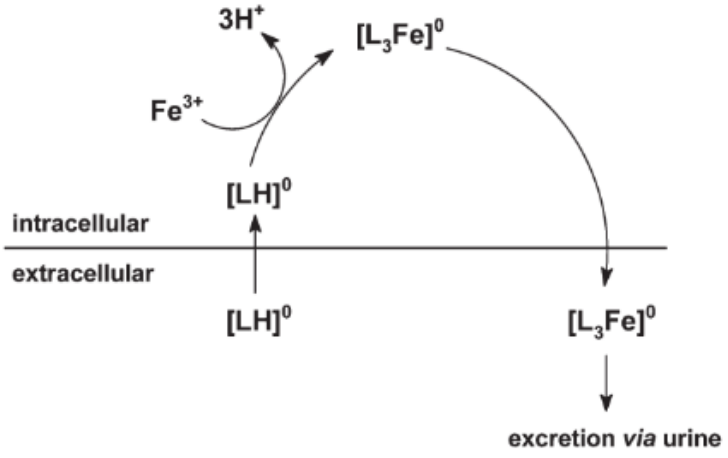

Figure 16: The non facilitated diffusion and efflux of deferiprone through a cardiomyocyte membrane. [557]

cardiomyocytes (Figure 17)[279][280]. Controlled trials have shown that used as a monotherapy or in combination with deferoxamine, significant reductions in cardiac iron and improvement in left ventricular ejection fraction is seen in β-thalassemia patients[279][281][282][283].

Deferiprone undergoes extensive metabolism in the liver. The 3-hydroxyl functionality is essential for scavenging iron, however it is also a target for glucuronidation; >85% of the administered deferiprone dose is recovered in the urine as the non-chelating O-glucuronide. Deferiprone is thus only effective at a relatively high dose (75mg/kg/day). The most common adverse reactions associated with deferiprone are gastrointestinal symptoms, however low incidence of agranulocytosis has also been reported(Hider and Hoffbrand, 2018a[285].

2.7.3.3 Deferasirox

Deferasirox was the second oral iron chelator to obtain clinical approval from the FDA. It is highly lipophilic and can readily penetrate cell membranes; it is 4-5 times more effective in excreting chelatable hepatocellular iron hypertransfused in rats compared to deferoxamine[286]. A single daily oral dose of deferasirox is absorbed rapidly and has a long half-life of 12 to 16 hours after administration which is maintained within a therapeutic range over 24 hours[264]. Deferasirox is a tridentate iron chelator which forms a 1:2 Fe^{3+}-chelator complex. This iron complex has a net charge of 3^- and large molecular weight of over 800[266], therefore deferasirox-iron complexes that form intracellularly likely remain trapped. Deferasirox is highly selective for Fe^{3+} therefore it can stabilise intracellular Fe^{3+} and inhibit its potential to redox cycle.

Table 2: Summary table of the key properties of Deferiprone, Deferasirox, and Deferoxamine. Repurposed table from Hoffbrand *et al* and Kwiatkowski *et al* [270] [271].

Property	Deferiprone	Deferasirox	Deferoxamine
Molecular weight (g/mol)	139	373	560
Chelator: iron ratio in complex	3:1 (bidentate)	2:1 (tridentate)	1:1 (hexadentate)
Lipid solubility	Medium	High	Low
Route of administration	Oral	Oral	Subcutaneous or intravenous
Iron excretion	Urinary	Faecal	Urinary and faecal
Half-life	2-3 hr	12–16 hr	20 min
Dosage (mg/kg/day)	75 cumulative dose (administered 3 times a day)	20–40	40
License	For treatment of iron overload in Thalassemia major when deferoxamine is contraindicated or inadequate	U.S.: For treatment of Thalassemia major (age, ≥2 yr). Europe: for treatment of Thalassemia (age, ≥6 yr, when deferoxamine is contraindicated or inadequate)	For treatment of chronic iron overload resulting from transfusion-dependent patients with anaemia
Cost for patient (63-kg body weight)	£5,519 (7 days/wk;75 mg/kg)	£23,179 (7 days/wk;30 mg/kg)	£5,584 (5 days/wk; 90 mg/kg)
Cardiac iron	Most effective of the three chelators; improvement in T2*-weighted MRI with monotherapy	Improvement in T2*-weighted MRI with monotherapy or in combination with deferoxamine	Improvement in T2*-weighted MRI, but adherence problems, not effective in all patients; continuous IV administration ameliorates cardiac dysfunction; effective in combination with deferiprone and deferasirox
Principal side effects	Gastrointestinal symptoms, neutropenia, agranulocytosis, arthralgia, elevated liver enzyme levels, zinc deficiency in patients with diabetes	Gastrointestinal symptoms, rashes, adverse renal effects	Reactions at infusion site, auditory and retinal toxic effects, allergy, bone abnormalities, yersinia infection

2.7.4 Iron Chelation to Ameliorate Doxorubicin-Induced Cardiotoxicity

Iron chelation therapy is fundamental in the treatment of chronic iron overload in β-thalassemia patients[264]. Repeated blood transfusions lead to cardiac complications that often manifest due to excess cardiac iron deposition[264]. Cardiomyopathy being the principal cause of death in these patients[287]. There are three clinically approved iron chelators available for the treatment of β-thalassemia (and other iron-loaded conditions), the parenteral iron chelator deferoxamine and the oral iron chelators deferiprone and deferasirox[264]. They all ameliorate the adverse effects of chronic iron overload and substantially improve cardiovascular morbidity and mortality. Due to the success of iron chelation therapy in the treatment β-thalassemia, extensive research has been conducted to determine the cardio-protective effect of iron chelators in the context of DOX-induced cardiotoxicity[205][288][289].

It has been suggested that iron chelation can also be utilised during anthracycline treatment to 1) displace iron from iron-DOX complexes, or 2) to prevent cardiac iron loading by chelating labile or loosely bound cellular iron in the heart. In doing so, inhibiting site-specific iron-catalysed ROS damage to cardiomyocytes and thus cardiac injury. This hypothesis has been reinforced by the protective efficacy of the iron chelator dexrazoxane, the only cardioprotective agent clinically approved for use in conjunction with DOX treatment [290]. While Dexrazoxane has successfully been used to ameliorate DOX-induced cardiotoxicity, it does not entirely eliminate the risk [179] [291].

The pharmacokinetic properties of iron chelators are critical for effective therapy (Hider and Hoffbrand, 2018a. Based on this, Deferiprone is proposed here as a more effective iron chelator option for the prevention of DOX-induced cardiotoxicity.

2.7.4.1 Dexrazoxane

Dexrazoxane is the only FDA-approved cardioprotective drug on the market. To reduce the incidence and severity of cardiomyopathy in women with metastatic breast cancer who have received a cumulative DOX dose of 300mg/m^2[180]. Dexrazoxane is given as a fifteen-minute IV infusion into a central venous line, it is administered thirty minutes prior to DOX treatment to ensure dexrazoxane is bio-available during the DOX infusion[292].

2.7.4.1.1 Evidence As a Cardio Protectant in Doxorubicin Therapy

Numerous clinical trials have consistently demonstrated the cardioprotective effect of dexrazoxane in DOX treated patients. The Speyer et al. study and the randomised, double-blind studies conducted by Swain *et al.* were key in demonstrating the cardioprotective effect of dexrazoxane [179] [291]. In these studies, patients with advanced metastatic breast cancer received either DOX + placebo (n=285) or DOX + Dexrazoxane (n=249). There was a significant difference found in cardiac events between the dexrazoxane treated patients (14%) and the placebo patient group (31%).

2.7.4.1.2 The Clinical Adoption of Dexrazoxane is Limited

Despite the evidence supporting the cardioprotective effects of dexrazoxane, its clinical adoption has been limited. This reflects concerns of interference with the anti-tumour efficacy of DOX and of second primary malignancies/second malignant neoplasms (SMNs). The FDA approved indication of dexrazoxane is only approved for women with metastatic breast cancer with cumulative DOX dose $\geq 300 mg/m^2$, which excludes significant patient populations at risk from cardiotoxicity [290], perhaps most notably paediatric patients who would benefit most from intervention.

A key study from which these concerns originated was conducted by Tebbi *et al.* This analysis showed an increased incidence of second malignant neoplasms in paediatric patients when treated with dexrazoxane during chemotherapy treatment[293]. When considered in the context of the greater body of evidence [179] [291], there is no further supporting studies that have corroborated this finding. The treatment protocol of this trial included the administration of etoposide as part of the chemotherapy treatment plan, and subsequent studies which have included etoposide have resulted in non-significant increases in second malignant neoplasms. The inclusion of etoposide within the Tebbi *et al.* study could be a likely explanation for their anomalous finding. Analysis from the Childrens Oncology's Group trials provide further evidence that dexrazoxane exposure is not associated with an increased risk of SMNs or altered cancer response[294]; 5- and 10-year survival figures did not differ between the dexrazoxane and control/placebo groups and the use of dexrazoxane was not associated with an increased hazard of relapse.

The Cochrane Group meta-analysis, the latest update which includes 13 eligible randomised controlled trials (five paediatric and eight adult), showed the efficacy of dexrazoxane [295].

Dexrazoxane was evidenced to prevent cardiotoxicity in adults treated with anthracyclines and specifically clinical heart failure and subclinical myocardial dysfunction in children. No negative effect on overall survival, progression-free survival, and tumour response rates was identified in adults; and no negative effect on tumour response rate and overall mortality was found in children.

Following the evidence reflecting current clinical and scientific knowledge supporting both 1) the use of dexrazoxane as cardio protectant during chemotherapy treatment and 2) negating the perceived association with the SMNs and interference with cancer response, the Committee for Medicinal Products for Human Use (CHMP) re-evaluated its contraindication. It was concluded that the contraindication for children receiving a cumulative dose of more than 300 mg/m^2 of DOX be revoked[296]. The European Commission issued an EU-wide decision to implement the CHMP recommendations and the contraindication for dexrazoxane was removed from the European labelling. The field of oncology has accepted the potential cardioprotective benefits of dexrazoxane by including it in clinical practice guidelines. However, ingrained and historical perceptions of risk associated with its clinical use persist and its clinical adoption remains poor.

2.7.4.1.2.1 The Cardioprotective Efficacy of Dexrazoxane

Dexrazoxane a neutral prodrug analogue of EDTA has cardioprotective effects attributed to its active metal ion-binding hydrolysis product ADR-925[297]. It is a cell permeating-prodrug that diffuses readily into cardiomyocytes that then undergoes a stepwise hydrolysis via one-ring open intermediates into its final ring-opened form (ADR-925) (Figure 18) [202] [298].

This ADR-925 product has strong binding affinity to Fe^{3+} and therefore rapidly displaces Fe^{3+} iron from the iron-DOX complex [202]. ADR-925 can also bind labile redox-active intracellular iron. inhibiting the iron-based conversion of O_2^- and H_2O_2 into the more potent hydroxyl radicals reducing oxidative damage to cardiac tissue[299]. This is consistent with the hypothesis of cardiotoxicity arising due to the iron-dependent oxidative stress fuelled by the "redox cycling" of DOX.

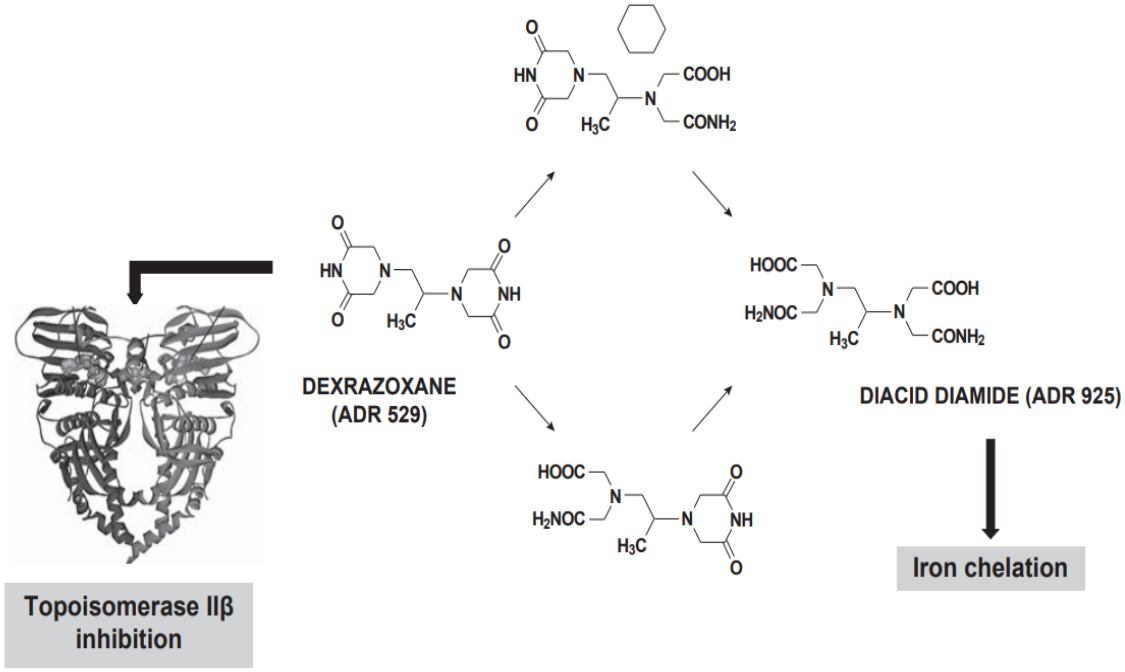

Figure 17: The hydrolytic metabolism of Dexrazoxane into its metal ion-chelating form. Dexrazoxane enters the cell where it metabolises first into its one-ring open intermediates and then into its fully ring open form (ADR 925). [297]

Evidence also suggests that the cardioprotective efficacy of dexrazoxane may not be explicable through iron chelation alone, but also, at least in part, by inhibiting topoisomerase IIβ[299]. Topoisomerase exists in two isoforms: 1) Topoisomerase IIα, primarily expressed in tumour cells and non-malignant proliferating cells and 2) Topoisomerase IIβ, primarily expressed in cardiomyocytes and other non-proliferating cells.

Topoisomerase IIα is a key mediator in DNA replication and understood to be central to DOX anti-cancer activity; DOX exerts its anti-tumour activity by antagonizing topoisomerase IIα complex formation during DNA cleavage, impeding DNA resealing[300]. In the presence of DOX, a topoisomerase IIα-DOX-DNA complex is formed. This stable complex impedes the re-ligation of the double-stranded DNA break and arrests the cell cycle in G1/G2 halting the process of DNA replication and leading to the apoptosis of malignant cells. The DOX-induced inhibition of topoisomerase IIα is more toxic towards cancer cells where cell replication is more prolific.

The cardiomyocyte-expressed IIβ-isoform is also similarly inhibited by DOX. The cardioprotective efficacy of Dexrazoxane can be explained by its inhibitory effect on the formation of the topoisomerase IIβ-DOX-DNA complex. Dexrazoxane is a catalytic inhibitor

of topoisomerase IIβ, forcing topoisomerase IIβ to form a closed-clamp configuration by competing for its ATP-binding site[301]. This inhibits the formation of the topoisomerase IIβ-DOX-DNA complex, preventing DNA damage downstream. There is evidence that dexrazoxane is also responsible for the degradation of topoisomerase IIβ, which is protective against DOX-induced DNA damage. This theory, evidenced by numerous *in vivo* studies[302][303][304] [299]. Zhang *et al*. showed that the deletion of topoisomerase IIβ in mice prevented the development of both DOX-induced double strand breaks and progression to heart failure[305]. Iron chelation alone is therefore unlikely to be the sole mechanism by which dexrazoxane offers cardio protection. This does not, however, mean that iron chelation has no utility in cardioprotection against anthracyclines.

2.7.4.2 Deferiprone

2.7.4.2.1 Evidence As a Cardio Protectant in Doxorubicin Therapy

The cardioprotective effect of deferiprone against DIC has been demonstrated by two *in vitro* studies and an *in vivo* study. Deferiprone was examined by Barnabe *et al*. for its ability to protect neonatal rat cardiac myocytes from DOX-induced damage[306]. Ventricular myocytes were isolated from Sprague Dawley rats, and DOX lactate dehydrogenase (LDH), a commonly used measure of DOX-induced damage in cardiomyocytes. The cumulative LDH released was increased in the DOX-only treated cardiomyocytes compared to those also treated with deferiprone. It was also shown that the Fe^{3+} was displaced from its DOX complex by deferiprone. Repeat spectral scans taken at 2 minute intervals showed that deferiprone rapidly displaced Fe^{3+} from its complex with DOX, resulting in a spectrum equivalent to that of uncomplexed DOX.

The displacement of iron Fe^{3+} from its DOX complex in cardiomyocytes, and deferiprone's ability at reducing DOX-induced LDH release, provides a mechanistic basis by which deferiprone could be used against DOX cardiotoxicity, and in the prevention of site-specific ROS formation.

A second *in vitro* study by Xu *et al*., that investigated the cardioprotective effectiveness of deferiprone in spontaneously-beating isolated rat atria was confirmed in work by Barnabe *et al* [306]. Prior to a 1 hour acute co-incubation with DOX, isolated atria were pretreated with deferiprone for 10 min. Contractility was assessed at 10 min intervals during the co-incubation

period. Deferiprone was shown to preserve contractility that was reduced in the atria treated with DOX alone. Mitochondrial cristae disruption and swelling was also evident in the DOX alone group. This study indicates that deferiprone offers mitochondrial function and integrity protection in the presence of DOX.

An *in vivo* study conducted by Ammat *et al*., investigated the effects of deferiprone against DIC in rats[307]. DOX (15 mg/kg) was injected intraperitoneally as a single dose into adult male Sprague-Dawley rats, and then DFP (10 mg/kg) was administered orally for 10 days. For the DOX only group, cardiotoxicity was evidenced by significant abnormalities in ECG parameters compared to the control group; increased heart rate (41%), elevation of ST segment (96%), prolongation of QTc interval (36%), and increase in T wave amplitude (57%) compared to the control group. In contrast, the deferiprone with DOX group did not differ significantly to the control group. The administration of deferiprone with DOX significantly attenuated the ECG parameters compared to the DOX only group; decreased heart rate (22%), ST segment elevation (28%), QTc interval prolongation (21%), and T wave amplitude (27%).

The administration of deferiprone similarly significantly attenuated the biochemical changes seen in the DOX only group. Compared to the control group, cardiotoxicity of DOX alone was confirmed biochemically by significant elevation in serum creatine kinase-MB (140%) and lactate dehydrogenase activities (66%), myocardial malondialdehyde (59%) and reduced glutathione (46%) contents. Whereas, for the deferiprone with DOX group, serum CK-MB (63%) and LDH activities (62%), myocardial MDA (22%) and GSH contents (28%) all significantly decreased compared to the DOX only group. These results evidence the potential of deferiprone as a cardioprotective agent against acute DOX-induced cardiotoxicity.

2.7.4.2.2 Deferiprone Controversy Limited Adoption

Despite evidence supporting the cardioprotective effects of deferiprone in DOX therapy, its clinical translation has been controversially thwarted by a study published by Popelova *et al*, in 2008 [308]. A key aim of this study was to assess whether deferiprone co-treatment could overcome or significantly reduce chronic anthracycline cardiotoxicity in an *in vivo* rabbit model (daunorubicin i.v., 3mg/kg/week for 10 weeks). Deferiprone was administered orally (10 or 50 mg/kg), 45 minutes prior to each daunorubicin injection. The study concluded that the oral treatment of deferiprone does not protect against chronic anthracycline cardiotoxicity,

as it failed to protect against daunorubicin-induced mortality, oxidative stress, left ventricular cardiac dysfunction, morphological cardiac damage, and heart failure.

However, when considering the pharmacodynamics of both daunorubicin and deferiprone, it is unsurprising that that no beneficial effect was observed in this study. Deferiprone has a relatively short biological half-life of ~2 hours versus the 13-hour cardiac half-life of daunorubicin[309]. Furthermore, the daunorubicin metabolite, daunorubicinol, has a half-life of 38.5 hours[309]. The deferiprone dose was administered 45 minutes before each dose of daunorubicin thus it is unlikely that there would be sufficient deferiprone in the myocardium during the anthracycline insult. The lack of cardio-protection observed is therefore not unexpected.

The findings published can be attributed to inappropriate experimental design. The assessment of the cardioprotective effects of deferiprone against chronic anthracycline cardiotoxicity cannot be concluded from this study. Unfortunately, being the first *in vivo* study investigating deferiprone as a cardio-protectant against anthracycline treatment it has adversely influenced clinical interest since.

2.7.5 Mechanistic Benefits of Deferiprone Versus Dexrazoxane

Iron selectivity is an important factor. Dexrazoxane is a cell-permeating prodrug and does not itself chelate iron; it is hydrolysed to its open ring form ADR-925, an EDTA analogue, that then binds to iron[297]. Dexrazoxane's metabolite ADR-925 is not selective for iron, it also binds $Ca^{2+}$and Mg^{2+}, a potential limiting factor to cardioprotective effectiveness[310]. Deferiprone is not a prodrug and is able to chelate iron directly; it is a small, neutrally charged cell permeable molecule that can penetrate cardiac cells due to its low molecular weight and lipophilicity (Hider and Hoffbrand, 2018a. Deferiprone has both a higher affinity for iron (Ka 10^{37} vs 10^{21}) and a lower affinity for calcium (Ka 10^{3} vs 10^{11}) compared to dexrazoxane, and therefore is not impacted by the same potential binding competition.

A clinically significant property of deferiprone is its ability to cross cellular membranes in both its unbound and complexed form. Deferiprone is able to penetrate cardiac cells, form a neutral 1:3 Fe^{3+}-chelator complex intracellularly, and due to its zero net charge, can efflux the cell in its complexed form (Hider and Hoffbrand, 2018a. Accordingly, deferiprone is capable of removing iron from iron loaded cardiomyocytes (Hider and Hoffbrand, 2018a [311][312]. Dexrazoxane's metabolite ADR-925 can chelate iron intracellularly, however the ADR-

925:iron complex is negatively charged and hydrophilic, limiting the capability of diffusion of the complexed iron out of cells and its removal from tissue. The chelation of iron intracellularly without removal does not eliminate the risk of site-specific ROS production[313][314]. Iron chelation alone is unlikely to be the sole mechanism by which dexrazoxane offers cardio protection based on its pharmacodynamic limitations[315][304][303].

Dexrazoxane has demonstrated to offer some protection against DOX-induced cardiotoxicity, however it does not entirely eliminate the risk. Compared to dexrazoxane, deferiprone has several advantageous pharmacokinetic properties critical for effective therapy and is proposed here as a more effective iron chelator option for the prevention DOX-induced cardiotoxicity.

2.8 Summary and Project Aims

DOX is a highly effective chemotherapeutic drug; however its utility is compromised by life-threatening cardiotoxicity that can manifest years after treatment. Current diagnostic methods assess structural and contractile dysfunction but cannot detect cardiotoxicity before irreversible damage has occurred. This is a clinical problem that is set to intensify as improved cancer survival rates increase exposing more cancer survivors to an increased risk of developing anthracycline-induced cardiac morbidities.

The mechanisms underlying DIC remain unclear and is associated with the limited treatment options available. There is evidence that iron overload exacerbates DOX-related cardiotoxicity, and iron chelation offers some protection, implicating iron as a mediator of the pathology. The overarching aim is to examine the inter-relationship between cardiac iron overload and metabolic dysfunction and remodelling in the pathophysiology of chronic DOX-induced cardiotoxicity.

Cardiac metabolites were measured by high resolution solution state Nuclear Magnetic Resonance (NMR) of extracted tissue. The relationship between cardiac iron and DIC has been studied before in proof-of-concept studies *in vivo*. To our knowledge, an NMR based metabolomic characterisation of the correlation of intracellular iron changes in the heart with metabolism and cardiac function in response to DOX in a clinically relevant model of chronic DIC is a largely unexplored area.

In this study we hypothesise that cardiac iron overload exacerbates chronic DIC leading to metabolic perturbations that contribute to impaired cardiac function. We also hypothesise that

iron chelation with deferiprone ameliorates the effects of chronic cardiotoxicity due to its favourable pharmacokinetic dynamics.

To test these hypothesises I intend to develop and optimise an ICP-MS based iron quantification protocol for the measurement of total and mitochondrial cardiac iron. Following this, I aim to develop and characterise two clinically relevant rat models; 1) one of cardiac iron overload that emulates the iron levels observed in cancer patients undergoing DOX treatment, and 2) a clinically relevant model that effectively replicates the pathology of chronic DOX-induced cardiotoxicity. These models serve to test whether clinically relevant pre-existing iron overload exacerbates chronic DOX-induced cardiotoxicity and test the cardioprotective potential of iron chelation therapy using deferiprone.

This research is intended to contribute to advancing the proof-of-concept studies that explored the connection between iron and DIC using clinically irrelevant *in vivo* models. By developing clinically relevant models, this work aims to characterise the cardiac metabolic profile and intracellular levels of cardiac iron in chronic DOX-induced cardiotoxicity. By interpreting the role of iron in this condition and exploring potential treatments targeting iron metabolism, this work is proposed to emphasise the relevance and potential efficacy of iron-based therapies in clinical practice.

MATERIALS AND METHODS

3.1 Materials

3.1.1 Animal Experiments

The animal experiments were carried out in accordance with the United Kingdom Home Office Guide on the Operation of Animal (Scientific Procedures) Act of 1986. The procedures were approved under the Project License number PP8261525 (Professor Rene Botnar, King's College London) and were carried out at the Biological Services Unit and the Biomedical Engineering and Imaging Sciences department, St Thomas Hospital, King's College London. The Male Wistar rats (7-9 weeks old, 200-300g) were obtained from either Envigo or Charles River, UK. The animals were housed under standard laboratory conditions with food and water available *ad libitum*.

3.1.2 Chemicals

All reagents were purchased from Sigma Aldrich or Fisher Scientific unless otherwise stated. Purified, trace-metal free water (MilliQ – resistivity ≥18.2 MΩ cm) was obtained from a Millipore Elix 3 system (Merck Millipore) and was used for all solution preparations. Iron ferrocene enriched diet (0.2% ferrocene) and control base diet was purchased from Rettenmaier UK Ltd. Iron dextran solution was purchased from Merck Life Science UK Ltd. The iron chelator Deferiprone was kindly supplied by Professor Robert Hider, King's College London, UK. Doxorubicin Hydrochloride (15007-50 mg-CAY) was purchased from Cambridge Bioscience, UK. ICP-MS iron analysis reagents were trace metal grade and purchased from Fisher Scientific UK Ltd.

3.1.3 Statistical Analysis

Unsupervised principal component analysis (PCA) was used to analyse the distribution of the metabolomic data derived from the control and ferrocene groups. If separation between the groups was observed, supervised partial least squares discriminant analysis (PLS-DA) was performed to better discriminate between the groups and to maximize separation associated with class membership. Unpaired Student's t-tests, one-way or two-way ANOVA with Tukey's HSD adjustment method for multiple comparisons were used and performed as indicated in each figure legend. Significance was assumed at $P < 0.01$. PCA and PLS-DA analysis was

performed in MatLab, all other statistical analysis was performed in Prism 10 (GraphPad, La Jolla, CA, US).

3.2 *In Vivo* Procedures

3.2.1 Aseptic Technique

All *in vivo* procedures were conducted using a sterile, aseptic technique. During procedures, sterile gowns and gloves were worn and all tools were autoclaved prior to use and all substances administered to animals were sterile and filtered.

3.2.2 Tail Vein Cannulation for Blood Withdrawal and Intravenous Injection

Rats were initially anaesthetised with 4% isoflurane mixed with 0.8 L/min 100% O_2 in an induction chamber, then transferred to a heating pad where anaesthesia was maintained using a nose cone at 1% isoflurane at a flow rate of 0.5 L/min. Their tails were then gently warmed using a UV heat lamp (Charles River, UK) to promote vasodilation. A 27G needle, connected to a syringe by fine tubing, was inserted into one of the lateral tail veins and blood slowly withdrawn. For IV injections, the appearance of blood in the tubing was used to confirm patency of cannulation and the solution then injected slowly as a bolus.

3.2.3 Intraperitoneal Injections

Rats were placed gently within the corner of a folded towel and scuffed from the outside of the towel so that heads were covered. The rats were restrained within a towel to minimise stress during the procedure. The restrained rats were turned over, exposing the abdomen. A 21-25G needle was injected into the IP space of the lower right or left quadrant of the abdomen, and the solution then injected slowly as a bolus.

3.2.4 Oral Gavage

Rats were scruffed by gently and firmly grasping the nap of the neck between the thumb and forefinger. The animals then lifted by the scruff and held in an upright position so that they could not use their legs for leverage or have free movement of their heads. A curved stainless-steel syringe was inserted to the right or the left of the inner jaw midline and discharged swiftly with care. The animals were monitored after oral gavage to ensure there were no signs of aspiration and that breathing was within normal limits.

3.2.5 Measurement of Regional Cardiac Contractility by Echocardiography

Echocardiography is used extensively in clinical and pre-clinical evaluation of cardiovascular function and disease progression. It is a non-invasive medical imaging technique that uses ultrasound waves to construct images of the heart's chambers, valves, and blood flow patterns. It was used to confirm and characterise the development of DOX-induced cardiotoxicity (DIC) in the *in vivo* models.

3.2.5.1 Principles of Echocardiography

Echocardiography operates on the principles of ultrasound physics, to provide precise and detailed images of the heart and cardiovascular system. Echocardiography employs high-frequency sound waves, typically in the range of 1-20 MHz, generated by a piezoelectric crystal within a transducer (probe). For cardiac echocardiography, the transducer is placed onto the chest of the animal and high-frequency ultrasound waves emitted into the heart and tissue beneath. The Ultrasound waves can propagate through tissue, and the speed of travel is determined by the tissue's density and elasticity. When ultrasound waves encounter boundaries between tissues with different densities, some of the waves are reflected back toward the transducer. This reflection occurs due to an acoustic impedance mismatch between the tissues. The greater the difference in tissue density, the stronger the reflection. A piezoelectric crystal within the transducer serves as a receiver that detects the returning echoes, converting them into electrical signals. The total time it takes for the ultrasound waves to 1) travel from the transducer to a tissue boundary and 2) to be returned as an echo, is used to calculate the distance to the cardiac structure. These measurements and changes in amplitude and pitch of sound, allow the depth and position of structures to be determined. The echo signal data is processed to create two-dimensional reconstructions of the heart; echo intensity is translated into shades of grey, with denser tissues appearing brighter.

3.2.5.2 Echocardiography Protocol

Rats were initially anaesthetised (4% isoflurane mixed with 0.8 L/min 100% O_2) in an induction chamber. After loss of the righting reflex, each rat was transferred to a heating pad where anaesthesia was maintained using a nose cone at 2% isoflurane at flow rate of 0.5 L/min. The core temperature was monitored using a rectal probe and maintained at 37°C. Fur was then

removed from the chest and abdomen region using a trimmer. Any remaining hair was removed using hair removal cream (Veet).

3.2.5.3 Image Acquisition

Echocardiography was performed using a Vevo 770 High Resolution Imaging System (VisualSonics, Toronto, Canada) with a RMV-710B transducer probe at 25 MHz (VisualSonics RMV-710B). Ultrasound gel was applied to the shaved area and the ultrasound probe was positioned using a specifically designed clamp-stand. B-mode (brightness mode) was used to obtain a high resolution two-dimensional, left ventricular cross section of the heart, in long axis view (Figure 19, a). The B-mode image was utilised to locate the papillary muscle and M-mode (motion mode) imaging was then employed at this position (Figure 19, b).

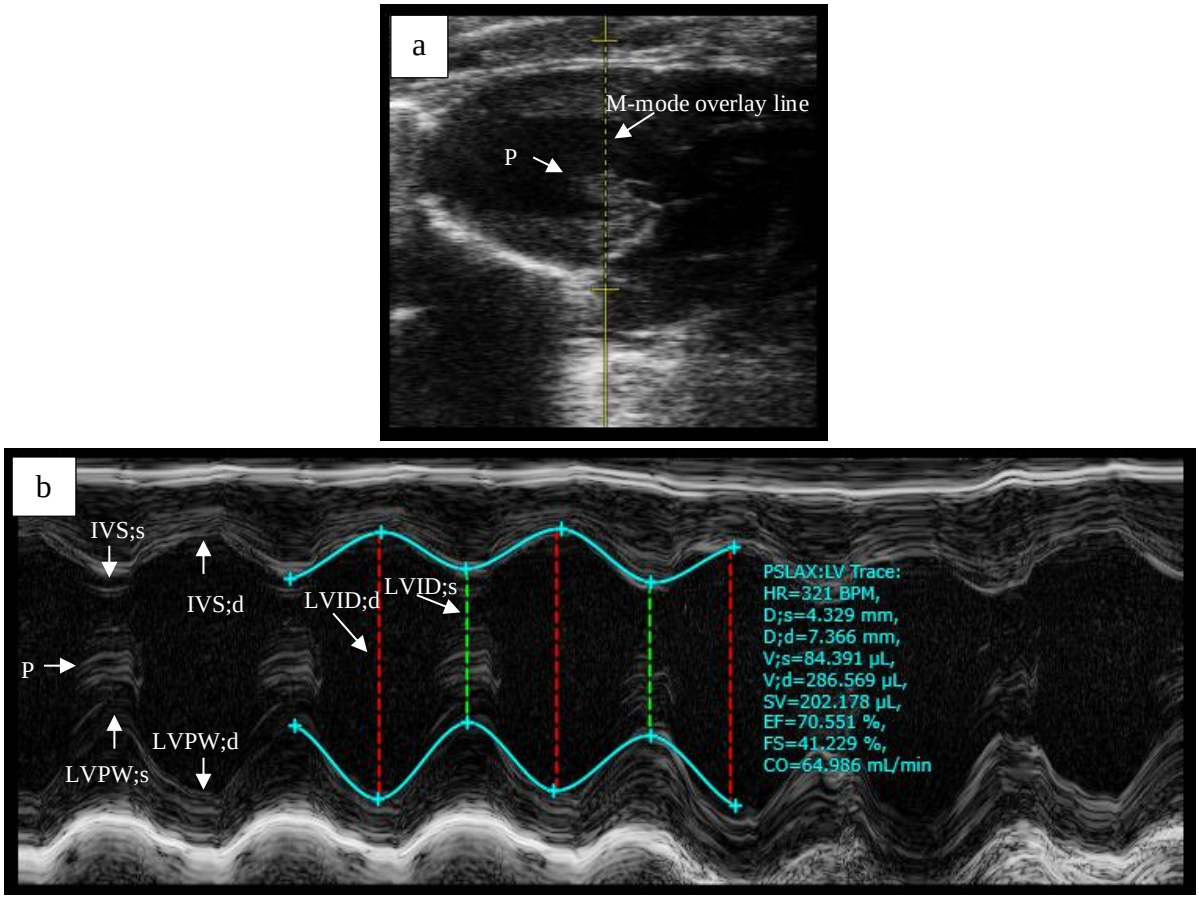

Figure 18: (a) B-mode image of the left ventricle (LV) with a long-axis view at the papillary muscle (PM). (b) M-mode image of the (LV) displays dimensions of the ventricular walls, LV cavity, and cardiac function measurements. The M-mode image shows the left ventricle posterior wall (LVPW) throughout diastole and systole. The echogenic peaks visible along the posterior wall represent the papillary muscle entering the field of view during systole. Left ventricle posterior wall at diastole (LVPW;d), left ventricle posterior wall at systole (LVPW;s), interventricular septum at diastole (IVS;d), interventricular septum at systole (IVS;s), left ventricular internal diameter in diastole (LVID;d) and left ventricular internal diameter in systole (LVID;s).

3.2.5.4 Echocardiographic Analysis

The left ventricular ejection fraction (LVEF) is a measure of the heart's pumping efficiency and represents the percentage volume of blood ejected from the left ventricle with each contraction. LVEF is a fundamental clinical tool for the diagnosis and prognosis of cardiac disease, including heart failure. LVEF was obtained during all *in vivo* studies to monitor cardiac function in response to DOX. LVEF is determined using Equation 4.

Equation 4: Left Ventricular Ejection Fraction (%)

$$LVEF\ (\%) = \left[\frac{(EDV\ -\ ESV)}{EDV}\right] x\ 100$$

The difference between End-Diastolic Volume (EDV) and End-Systolic Volume (ESV) represents the volume of blood that is ejected with each heartbeat, (stroke volume). Dividing this difference by EDV and multiplying by 100 gives LVEF as a percentage.

Echocardiography images were analysed using the Vevo 770 software programme (VisualSonics). The M-mode image of the left ventricle was used to determine the ventricular wall dimensions, the left ventricular internal diameter in diastole (LVID;d) and left ventricular internal diameter in systole (LVID;s).

EDV and the ESV were obtained using M-Mode images; a line was traced along the interventricular septum and the left ventricular posterior wall, the EDV and ESV were calculated using the distances between these two lines during diastole and systole (Figure 19). Reduced LVEF is an indicator of increasing cardiac dysfunction and a common clinical predictor and diagnostic of heart failure and cardiomyopathy. Normal LVEF for rats is in the range of 60% to 85%.

Fractional Shortening (FS) is a cardiac parameter that measures the percentage of shortening of the left ventricle during contraction (systole). It is a valuable indicator of ventricular contractility and function and is often used alongside LVEF to comprehensively evaluate heart health. The calculation of FS involves two key measurements: 1) End-Diastolic Diameter (EDD), the diameter of the left ventricle at the end of diastole, and 2) End-Systolic Diameter (ESD), the diameter of the left ventricle at the end of systole.

The difference between EDD and ESD represents the shortening of the left ventricle during systole, and this difference when divided by EDD and multiplied by 100 gives FS as a percentage (Equation 5).

Equation 5: Fractional Shortening (%)

$$FS\ (\%) = \left[\frac{(EDD\ -\ ESD)}{EDD}\right] x\ 100$$

Cardiac Output (CO) is a fundamental physiological parameter used to evaluate cardiac performance and overall cardiac function that provides insight into the heart's capability to meet the body's metabolic demands. CO represents the volume of blood ejected by the heart into the systemic circulation per minute. The calculation involves two key measurements: 1) Stroke volume and 2) heart rate (bpm). CO was obtained during all *in vivo* studies to monitor cardiac function (Equation 6).

Equation 6: Cardiac Output (mL/min)

$$CO\ (mL/min)) =\ Stroke\ Volume\ x\ Heart\ Rate\ x\ 1000$$

3.2.6 Serum Collection

Blood was collected as described in 3.2.2 and transferred into sterile Eppendorf tubes and left to clot for about 30 minutes to 1 hour at room temperature. The samples then centrifuged at 1500 xg for 10-15 minutes. After centrifugation, the serum separated from the clot and red blood cells to the top of the tube and was pipetted into fresh Eppendorf tubes. Serum was stored at -80°C until use.

3.2.7 Harvesting Tissue

3.2.7.1 Harvesting Cardiac Tissue

Rats were initially anaesthetised with 4% isoflurane mixed with 0.8 L/min 100% O_2 in an induction chamber and then transferred to a heating pad. Anaesthesia was maintained using a nose cone at 4% isoflurane at flow rate of 0.5 L/min. The lack of pedal response confirmed depth of anaesthesia. Incisions were made along the abdomen and rib cage to gain access to the chest cavity. Once exposed, ice-cold saline was injected into the apex of the heart to perfuse

the cardiac tissue with saline to reduce contamination with red blood cells. The heart was rapidly excised via direct severing of the aorta and removal of excess connective tissue to ensure excisation of relevant cardiac tissue. The excised hearts were immediately snap frozen in liquid nitrogen to avoid thawing and prevent metabolic degradation. A pestle and mortar pre-cooled using dry ice was used to ground the heart samples into a fine powder under liquid nitrogen. The powdered cardiac samples were stored at -80°C until use.

3.2.7.2 Harvesting Liver Tissue

Liver samples were collected immediately after the hearts were excised and harvested (3.2.7.1). The livers were removed and immediately snap frozen in liquid nitrogen to avoid thawing and prevent metabolic degradation. A pestle and mortar were pre-cooled using dry ice and the liver samples then ground into a fine powder under liquid nitrogen. The powdered liver samples were stored at -80°C until use.

3.3 Mitochondrial Isolation

3.3.1 Mitochondrial Isolation Buffer Composition

The mitochondrial isolation buffer consisted of the following reagents: 250 mM sucrose, 2 mM EDTA, 100 mM Tris-HCl (pH 7.4)) and purified trace-metal free water (MilliQ – resistivity ≥18.2 MΩ cm) obtained from a Millipore Elix 3 system (Merck Millipore). A 1ml glass Dounce homogenizer, with a loose-fitting pestle, was purchased from Generon (1984-10002). The mitochondrial isolation buffer was made up fresh on the day, pH adjusted to 7.8 and kept on ice throughout the isolation procedure.

3.3.2 Isolating Mitochondria by Differential Centrifugation

A two-step differential centrifugation method was used to isolate mitochondria; a low-speed centrifugation was used to remove cell/tissue debris and nuclei from whole cardiac tissue, followed by a high-speed centrifugation to concentrate mitochondria and separate them from other organelles. The mitochondrial isolation procedure was always performed over ice.

Hearts were harvested as described in 3.2.7.1. For each sample, 50 mg of cardiac tissue was transferred into a pre-prepared 1.5 mL Eppendorf vial containing 1mL of isolation buffer (3.3.1). The solution then transferred to a glass Dounce homogeniser, and the sample

homogenised until smooth using 10 strokes of a loose-fitting pestle. The homogenate was then transferred to a 1.5 mL Eppendorf vial. To ensure full transfer of tissue, 250 uL of isolation buffer was added to the glass Dounce homogeniser.

The sample was then centrifuged at low speed (600 xg for 10 mins, 4°C). The resulting pellet (containing cellular debris and nuclei) was discarded, and the supernatant was split; each portion transferred to a 1.5mL Eppendorf vial and both centrifuged at high speed (11000 xg for 10 mins, 4°C). The supernatant (consisting mainly of cytosol and lysosome) was discarded, and the two resultant mitochondrially enriched pellets were washed. One pellet was used for ICP-MS analysis, and the other for a BCA assay to determine the protein concentration in the sample. The iron concentration of the mitochondria in the pellet allocated for ICP-MS analysis (μg of Fe/mg of protein) was calculated using the protein content calculated in the pellet assigned for the BCA assay.

3.4 Measurement of Organelle Contamination in Isolated Mitochondria by Western Blot

The western blot technique detects proteins of interest in a sample by separating target proteins by molecular mass (kDa) using gel electrophoresis. The protein is then transferred onto a polyvinylidene fluoride (PVDF) membrane using an electrical current. The target protein on the membrane is probed using a primary antibody that specifically recognises the target protein and binds to it. A secondary antibody is then used to bind to the primary antibody. The secondary antibody can be visualised using a chemiluminescence detection reagent, allowing the indirect detection of the target protein.

3.4.1 Sub-cellular Marker Selection

To assess organelle contamination and mitochondrial enrichment, a western blot analysis was performed on mitochondria isolated from cardiac tissue using a Trans-Blot Turbo Transfer System (Bio-Rad Laboratories, Inc.). The isolated mitochondrial samples were probed for the subcellular markers; Voltage-dependent anion channel (VDAC), Succinate dehydrogenase (SDH), Glyceraldehyde-3-phosphate dehydrogenase (GAPDH), and Lysosome-associated membrane protein 1 (LAMP 1), see Table 3.

VDAC is a pore-forming protein that is expressed and located at the outer mitochondrial membrane. It allows the diffusion of metabolites between the cytosol and the mitochondrion, functioning as a gatekeeper for the entry and exit of mitochondrial metabolites[316][317] [318]. SDHA is a subunit of succinate dehydrogenase (SDH, also known as Complex II), it is a key component of the TCA cycle and the ETC. The SDH complex is located on the inner mitochondrial membrane and SDHA converts succinate to fumarate within the TCA cycle [319]. GAPDH is a key component of glycolysis where it catalyses the phosphorylation of glyceraldehyde-3-phosphate [320]in the cytosol. LAMP1 is lysosomal transmembrane proteins located on the lysosomal inner leaflet whereby its carboxy terminus and is involved in regulating lysosomal motility [321].

Table 3: List of antibodies used to assess organelle contamination in and mitochondrial enrichment isolated mitochondria.

Subcellular marker		Primary Antibodies	Secondary antibodies
VDAC	Outer mitochondrial membrane protein	VDAC Recombinant Rabbit Monoclonal 1:2000 dilution (Thermo Fisher Scientific)	Goat Anti-Rabbit IgG H&L (HRP) preadsorbed 1:40,000 dilution (Abcam Ltd)
SDHA	Inner mitochondrial membrane protein	Mouse monoclonal to SDHA 1:1000 dilution (2E3GC12FB2AE2, Abcam Ltd)	Goat Anti-Mouse IgG H&L (HRP) 1:20,000 dilution (Abcam Ltd)
GAPDH	Cytosolic protein	Rabbit monoclonal to GAPDH 1:10,000 dilution (EPR16891, Abcam Ltd)	Goat Anti-Rabbit IgG H&L (HRP) preadsorbed 1:40,000 dilution (Abcam Ltd)
LAMP 1	Lysosomal protein	Rabbit polyclonal to LAMP1 1:1000 dilution (Abcam Ltd)	Goat Anti-Rabbit IgG H&L (HRP) preadsorbed 1:40,000 dilution (Abcam Ltd)

3.4.2 Western Blot Buffer Compositions

The pH of all buffers, Table 4, was measured at room temperature using a PP-15, Sartorius Professional Meter. Water for all buffers was obtained from a Millipore Elix 3 system (Merck Millipore– resistivity ≥18.2 MΩ cm).

Table 4: Western blot buffer compositions.

Western blot buffers	**Reagents**
Lysis buffer: Radioimmunoprecipitation assay buffer (RIPA buffer)	150 mM NaCl 1.0% NP-40 or 0.1% Triton X-100 0.5% sodium deoxycholate 0.1% SDS (sodium dodecyl sulphate) 50 mM Tris-HCl, pH 7-8 1 mM sodium orthovanadate 1 mM NaF Protease inhibitors
Loading buffer	4% Sodium dodecyl sulphate (SDS) 10% 2-mercaptoethanol 20% glycerol 0.004% bromophenol blue 0.125 M Tris-HCL
Running buffer	25 mM Tris base 190 mM glycine 0.1% SDS
Transfer buffer	25 mM Tris base 190 mM glycine 20% methanol
TBS-T	20 mM Tris, pH 7.5 150 mM NaCl 0.1% Tween 20

3.4.3 Western Blot Protocol

3.4.3.1 Sample Preparation for Protein Extraction

Ice-cold lysis buffer was added to all sample types at ~1 mL per 100 mg or ~100 µL of sample. The samples were maintained on constant agitation at 4°C and sonicated in an ice bath to

complete lysis and reduce sample viscosity, then centrifuged in a pre-cooled centrifuge at 16,000 xg for 20 minutes at 4°C. The supernatants (consisting of the extracted protein) were collected into fresh Eppendorf vials over ice, and 25µLeach lysate was removed to perform a BCA protein assay (3.5). The amount of protein to be loaded into the gel for separation was determined using the BCA assay (~20–30 µg), to this, an equal volume of loading buffer was added. Each sample was then boiled at ~100°C for 10 min.

3.4.3.2 Gel Electrophoresis

The sample proteins were then separated using gel electrophoresis. Samples were separated by hand-cast Tris-Glycine SDS-PAGE gels (12.5%), with a 4% stacking gel. SDS-PAGE (sodium dodecyl sulphate–polyacrylamide gel electrophoresis) was used for the electrophoretic separation of proteins by molecular mass. SDS masks the proteins intrinsic charge. The use of SDS as a buffer and the use of SDS in the gel removes the influence of protein charge, ensuring that proteins are separated by mass difference.

The protein was electrophoresed through the stacking gel at 90 V for ~20 minutes, and the voltage was increased to 120 V for ~ 60 minutes to run through the resolving gel. After SDS-PAGE, western blotting was conducted to detect the subcellular proteins of interest using the antibodies listed in Table 3.

3.4.3.3 Transfer

Electroblotting was used to move the proteins from the gel onto a or polyvinylidene difluoride (PVDF) membrane, accessible for antibody detection. The membrane was first soaked in methanol and rinsed in transfer buffer and the gel was equilibrated in transfer buffer for ~5 minutes. The transfer stack then prepared and assembled within a semi-dry electroblotting transfer cell (Bio-Rad), and transfer performed for 30 minutes at 100 V.

3.4.3.4 Blocking

After transfer, the non-specific binding sites on the membrane were blocked by incubating the membrane in freshly prepared 3% non-fat milk powder in TBS-T buffer for 1 hour on a shaking platform at room temperature. Protein blocking prevented interactions between the membrane and the antibody, leaving the target protein as the only available binding site.

3.4.3.5 Incubation and Chemiluminescent Detection

Each primary antibody was diluted in TBS-T and 3% non-fat milk powder. The membranes were incubated overnight (4°C with gentle agitation) in their respective target protein specific antibody solution, see Table 3. The blot was then rinsed with three times with TBS-T to wash away unbound probe and incubated once more with the relevant secondary antibody solution for 1 hour at room temperature (dilution in TBS-T and 3% non-fat milk powder). Again, the membranes were rinsed three times with TBS-T. Each blot was developed using Enhanced Chemiluminescence reagent (ECL) and exposed to HyperFilm in a darkroom.

3.5 BCA Assay

The bicinchoninic acid assay (BCA) determines the total concentration of protein in a solution (µg/mL). It was used to determine the mitochondrial protein concentrations following isolation of mitochondria from the *in vivo* preparations. The total protein concentration of a sample is determined by a proportional colour change. The amount of protein present in a sample solution is quantified by using a colorimetric technique; the absorption spectra is measured and compared to standard solutions of known protein concentration.

BCA working reagents contain bicinchoninic acid and copper(II) sulphate pentahydrate. The BCA assay consists of two reactions: 1) The Cu^{2+} ions of the copper(II) sulphate are reduced to Cu^{1+} by protein peptide bonds in the sample solution, whereby the extent of reduction is proportional to protein concentration, 2) a purple-coloured complex forms when bicinchoninic acid chelates with Cu^{1+}. This complex absorbs light at a wavelength of 562 nm. The amount of protein present can be quantified by measuring the absorption spectra, comparing it with that of BCA standards of known concentration.

3.5.1 BCA Assay Protocol

The BCA standards are prepared within a working range of 0–2000 µg/mL containing known protein concentrations. The working reagent prepared by mixing 50 parts of BCA Reagent A with 1 part of BCA Reagent B. Each standard and sample (25 µL of each) was pipetted into a microplate well in duplicate. The working reagent was added to each well (200 µL) and the microplate mixed on a plate shaker for 30 seconds then incubated at 37°C for 30 minutes. Incubation at 37°C was conducted for the peptide bonds to contribute to the formation of the reaction complex at higher temperatures to increase the assay sensitivity. The microplate then

cooled to room temperature and the absorbance measured at 562 nm on a plate reader. Protein concentration in each sample solution was determined from the BCA standard curve (0–2000 µg/mL). A blank correction was also conducted to account for background signal.

3.6 Measuring Iron by ICP-MS

A fundamental aspect of this research involved examining the influence of DOX treatment on the redistribution of cellular iron, particularly between total intracellular iron and mitochondrial cardiac iron levels.

Inductively coupled plasma-mass spectrometry (ICP-MS) is an analytical technique that measures elements at trace levels in biological samples. It is considered the gold standard for the measurement of iron due to its detection sensitivity (ppt). ICP-MS uses high ionization energy to produce elemental ions; the singly charged ions (corresponding to the analyte of interest) are separated and quantified based on their specific mass to charge ratio using a mass spectrometer. ICP-MS was used to obtain absolute quantification of total iron and mitochondrial iron in cardiac tissue, expressed as µg of iron/g of tissue and µg of iron/mg of protein, respectively. Chapter 4 outlines the ICP-MS-based method development undertaken for quantifying cardiac iron.

The ICP-MS measurements were performed on a NexION 350 ICP-MS Spectrometer (PerkinElmer, Inc) in collaboration with the London Metallomics Facility (LMF), King's College London, and the Natural History Museum. The iron concentration was based on the measurement of ^{56}Fe as the most abundant iron isotope. Contamination from airborne particles and environmental iron was mitigated by use of the ICP-MS dedicated clean room facility at the LMF when possible. All sample preparation was conducted within a fume hood.

3.6.1 ICP-MS Fundamentals

ICP-MS uses an argon plasma to transform samples into singly charged ions with different m/z (mass-charge) ratios. The target elements then measured according to their m/z using a mass spectrometer (Figure 20)[322][323][324][325].

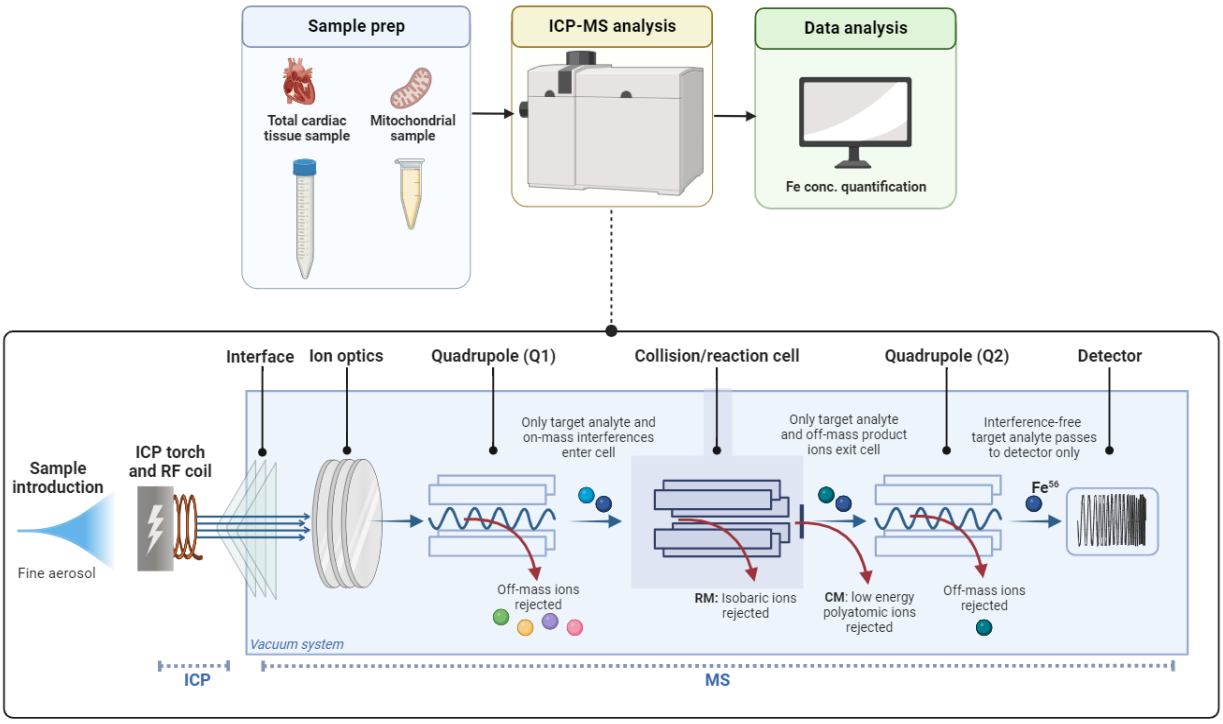

Figure 19: ICP-MS analysis workflow. RM: Reaction mode, and CM: Collision mode. [Figure made in BioRender]

Samples are nebulised and introduced into an argon plasma as a fine aerosol. The ICP torch and RF coil generate the argon plasma. The high-temperature plasma dries the aerosol droplets, dissociates the molecules, and removes an electron from the components, resulting in the formation of singly charged ions. The interface extracts the ion source (at atmospheric pressure) into the vacuum system of the mass spectrometer. The interface region is situated between a series of conical disks that facilitate a stepwise reduction in pressure. Ion optics focus and direct the ion beam into the first quadrupole mass filter that sets voltages and radio frequencies to separate ions based on their m/z. Only ions with the m/z of the target analyte remain stable within the rods and pass through, whereas ions with different m/z are unstable and are ejected. Ions with the single m/z exit the first quadrupole and enter the collision/reaction cell that resolves the target analyte from other interfering ions of the same m/z. Only target analyte ions, and off-mass ions produced in the collision/reaction cell, emerge, and pass into

the second quadrupole. The second quadrupole mass filter rejects the off-mass product ions and interference-free target analyte ions exit and strike an electron multiplier. The impact of the ions on the first dynode of the electron multiplier releases a cascade of electrons, which are subsequently amplified until they become a measurable pulse, quantified by the detector in units of 'counts per second' (CPS). The concentration of the target isotope within a sample determined by comparing its signal intensity to that of an external calibration curve. The calibration curve is established by analysing a set of liquid calibration standards generated for the element of interest. A basic overview of the main ICP-MS components is outlined in Table 5.

Table 5: Components of the ICP-MS instrument[326][327] [325]**.**

Component	Constituents/Purpose
Sample introduction system	Composed of a nebulizer and spray chamber. Forms a fine aerosol mist, composed of consistently uniform droplets, from the liquid sample.
ICP torch and RF coil	Generate the argon plasma (the ICP). The plasma converts the elements in the sample aerosol into a singly charged ion source for the ICP-MS.
Interface	Extracts the ion source (at atmospheric pressure) into the vacuum system of the mass spectrometer. The interface region is situated between a series of conical disks (cones) that allow a stepwise reduction in pressure.
Vacuum system	Removes as many gas molecules as possible to prevent obstruction of the singly charged ion beam. Provides high vacuum for ion optics, the quadrupole, and detector
Ion optics	A series of lenses separates positively charged ions from background signal (neutral species and photons) and focusing the ion beam through the first quadrupole.
Collision/reaction cell	Used to remove interferences (that can degrade detection limits) from the positively charged ion stream before it reaches the second quadrupole mass spectrometer. A collision/reaction cell consists of a multipole ion guide enclosed in a cell that can be pressurized with a gas.
Quadrupole mass spectrometer/filter (Q1 and Q2)	A mass filter that sort ions by their mass-to-charge ratio (m/z). The quadrupole uses specific voltages and radio frequencies so that only ions of a spingle m/z remain stable within the rods and reach the detector. A quadrupole mass filter consists of four rods arranged in perpendicular pairs.
Detector	The ion beam strikes the first dynode of the detector (an electron multiplier). The dynode releases an electron every time an ion strikes it and starts an amplification process. The detector receives and amplifies an ion signal that is proportional to concentration, as determined through calibration standards. This amplification cascade generates a measurable signal, recorded as counts per second (CPS).

3.7 Profiling Metabolism using ^{1}H-NMR

Metabolomics is defined as the large-scale study of metabolites and their response to genetic and pathophysiological stimuli within biological systems. Metabolites, which are small molecules ranging in size from approximately 5 to 1500 Daltons, encompass both the substrates and the end products of various metabolic and biochemical processes[328]. Metabolites encompass a broad spectrum of compounds, including sugars, amino acids, lipids, and other small molecules. Metabolomics aims to identify, quantify, and profile the dynamic changes in metabolite levels in response to external stimuli (such as drug treatment). The interpretation of metabolite profiles obtained from biological samples provide opportunity to investigate how metabolic processes are perturbed during pathology. Metabolomics is a powerful tool as it is representative of the molecular phenotype; the concentration of metabolites directly reflects the underlying biochemical activity and state of cells and tissues [329].

Metabolites can serve as biochemical markers that respond to the damage inflicted by DOX in cardiac tissue. Alterations in specific metabolites can help reveal which metabolic pathways are disrupted in response to DOX and provide insight into the complex interplay between DOX and the metabolic processes that contribute to the cardiotoxicity it induces.

Here, ^{1}H-NMR is employed to assess the metabolic phenotype of cardiac tissue in response to DOX treatment enabling a metabolomic profile of cardiac tissue to be established. Analysis of the cardiac metabolite profile, through the identification of key metabolic fluxes, metabolomics can provide insights into the biochemical pathways and mechanisms underlying DIC [330].

The metabolic profile of serum was also obtained using ^{1}H-NMR. Serum metabolomics captures systemic alterations by identifying shifts in metabolite profiles that extend beyond the heart that are representative of the overall metabolic health of the organism. Profiling serum provides a comprehensive view of systemic metabolic changes associated with DIC.

DOX is not only toxic to the heart; its toxicity is known to extend to the liver. The inter-relation between hepatotoxicity and cardiotoxicity is currently unclear, but it was decided appropriate to include liver tissues in our analysis for completeness.

3.7.1 Principles of NMR

Nuclear magnetic resonance (NMR) spectroscopy is a powerful and well-established technique for identifying and quantifying metabolites and lipid molecules in complex biological samples, such as tissue extracts and serum[331][332][328]. NMR utilises an intrinsic property of nuclei called "spin" that is subjected to an external magnetic field and electromagnetic radiation[333]. "Spin" can be defined as the nucleus of an atom rotating on its axis, resulting in the generation of a magnetic moment[334]. Only certain nuclei possess spin; atoms with an odd mass number such as ^{1}H and ^{13}C are spin I = ½ nuclei[335] [336].

^{1}H NMR is extensively utilized in metabolomics because the proton nucleus is the most sensitive and abundant NMR-active nucleus in biological compounds[337][335][331]. When a sample is placed within a strong magnetic field, lower-energy proton nuclei align parallel to the magnetic field, while the higher-energy nuclei align antiparallel to it. The population of these two states is not equal (according to the Boltzmann distribution) and therefore the sample possesses a net magnetic moment. If electromagnetic radiation is applied at the correct frequency (the Larmor precession rate for that nucleus), in the form of radiofrequency pulses, then the magnetization will be excited by tilting it away from the z-axis of the static magnetic field B_0. After excitation, the proton nuclei precess in the magnetic field to induce a current in the receiver coil. The resulting signal, known as the Free Induction Decay (FID), is detected by the radiofrequency coil. Fourier transformation converts the time-domain FID signals (signal intensity versus time) into a frequency-domain spectrum of peaks (signal intensity versus frequency).

The phenomenon of chemical shift allows the distinction of proton nuclei that resonate at different frequencies. In a molecule, the magnetic field that a proton nucleus experiences is influenced by its unique chemical environment (specifically, the motion of its surrounding electrons) and the degree to which a nucleus is shielded from the static magnetic field by the surrounding electron density in its molecular orbital influencing the magnetic environment experienced by the nucleus[331]. Therefore, proton nuclei in different chemical environments or different molecules 'feel' the applied magnetic field differently, thus causing them to resonate at distinct frequencies. This property is the basis for the diagnostic power of ^{1}H NMR, allowing to distinguish between proton environments within different molecules.

The chemical shift along the x-axis of a spectrum is quoted in parts per million (ppm) relative to the reference frequency of the spectrometer. Each type of proton nucleus within a metabolite has a distinct chemical shift as well as possible coupling patterns, and therefore metabolites can be identified based on their positions along the chemical shift axis relative to a reference compound. A further advantage of NMR is that the area underneath a peak is proportional to the concentration of the protons which in turn is proportional to metabolite concentration. Metabolite concentration can be quantified by comparing the integral of a metabolite peak to that of a reference peak of known concentration.

A simplified diagram of an NMR spectrometer is depicted in **Figure 21**. At the centre of the NMR spectrometer is a superconducting magnet submerged in liquid helium in order to maintain it at 4 K[338]. The liquid helium jacket is prevented from evaporating by surrounding it in a liquid nitrogen jacket under vacuum. The NMR probe contains the radiofrequency coil and sits in the centre of the superconducting magnet within its bore. The NMR tube is then inserted into the probe on a cushion of air. The superconducting magnet creates a large static magnetic field that causes the proton nuclei to align, which are then excited by the pulses generated by the radiofrequency coil. The radiofrequency coil also collects the Free Induction

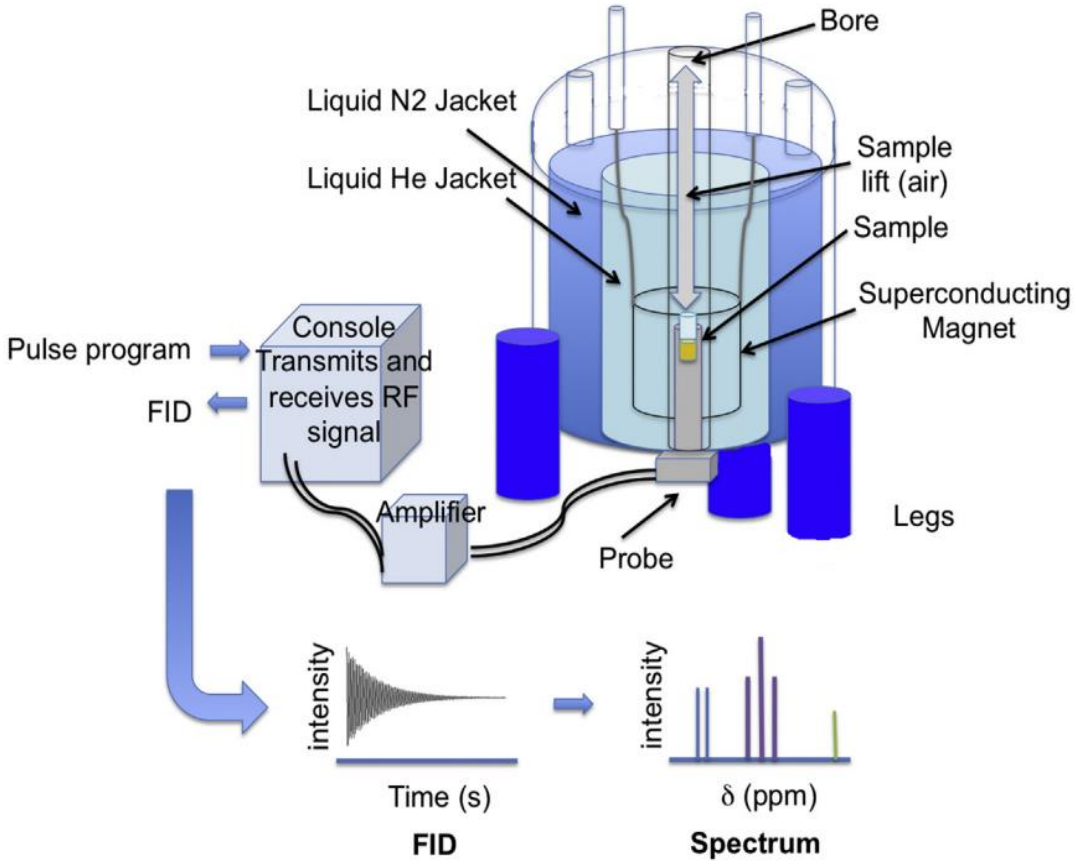

Figure 20: Summary diagram of an NMR spectrometer [338].

Decay (FID). Pulse programs are created using the computer and sent to the console, from which the radiofrequency pulse is transmitted, and signal received. The FIDs are Fourier transformed to produce ^{1}H NMR spectra of signal intensity versus chemical shift (ppm).

3.7.2 ^{1}H-NMR Cardiac Tissue Sample Preparation

NMR based metabolomic analysis requires proteins to be removed (or reduced in concentration)[339]. Proteins are large molecules that can produces broad and intense NMR signals. Protein NMR spectra are inherently more complex than those of metabolites, with numerous overlapping peaks. In high concentrations, protein signals can overlap the signals of smaller target metabolites, making it difficult to detect, assign and quantify their signals[340]. Proteins can also undergo chemical exchange processes; protons within a protein molecule can undergo chemical exchange with a solvent molecule or other protons. This chemical exchange process can lead to line broadening[341]. Broadened signals reduce spectral resolution by obscuring the fine details of metabolite peaks, in turn hindering peak assignments and the determination of chemical shifts.

To address these challenges, proteins in tissue samples are removed or reduced before conducting NMR analysis. This was achieved using the chloroform-methanol-water protein precipitation method, which is a widely used sample preparation technique in metabolomics to extract and separate metabolites in biological samples[331]. Water, methanol, and chloroform are used in the process to separate the sample into three distinct layers: 1) an upper aqueous phase (contains hydrophilic metabolites such as amino acids and sugars), 2) a middle protein layer, and 3) a lower organic phase (contains lipophilic components like lipids and fatty acids.). The aqueous and organic lipophilic layers undergo dehydration and reconstitution prior to ^{1}H NMR analysis. Dual-phase extraction facilitates the isolation and analysis of aqueous and lipid metabolites. An overview of the NMR tissue sample preparation process is depicted in Figure 22.

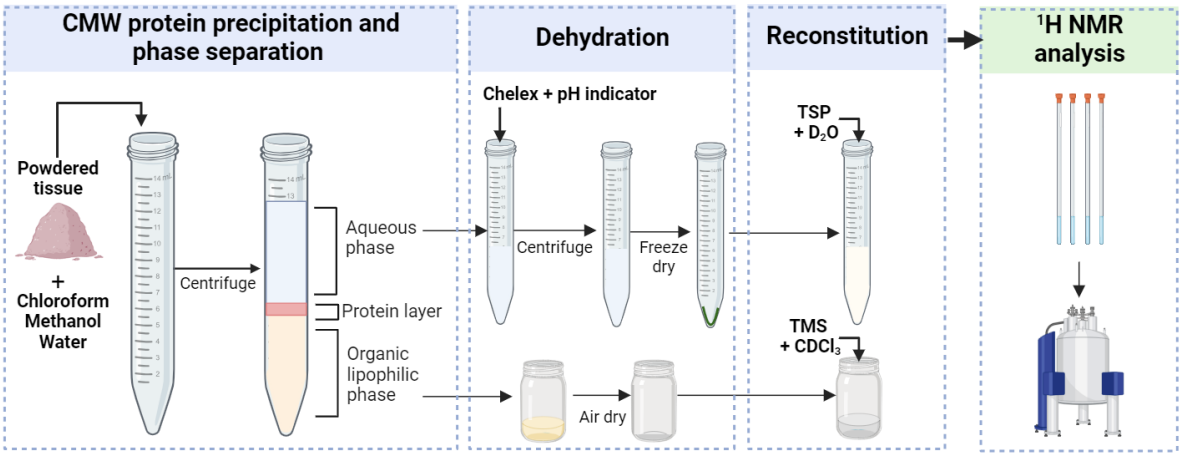

Figure 21: 1H-NMR tissue sample preparation schematic. NMR compatible solvents: D_2O; Deuterated water and $CDCl_3$; Deuterated chloroform. Internal standard: TSP; Trimethylsilyl propionate and TMS; Tetramethylsilane. CMW; Chloroform-methanol-water [Figure made in BioRender]

3.7.2.1 Dual-Phase Protein Precipitation and Phase Separation

The dual-phase method includes the following steps: Sample homogenisation, methanol extraction, chloroform and water extraction, phase separation, and aqueous and lipophilic layer collection[340].

The tissue sample is ground into a fine powder to break down cell structures and release metabolites. Methanol is added to the homogenized sample and plays a multifaceted role in the separation and extraction of aqueous metabolites[342]. Methanol is a polar solvent and miscible with water; it forms a homogeneous mixture with the water-soluble metabolites of the sample. This helps separate the aqueous metabolites in the samples (such as sugars, amino acids, organic acids, and other hydrophilic compounds) from lipids and nonpolar compounds. Methanol also serves to denature proteins present in the sample and facilitates their precipitation out of solution, separating them from the rest of the sample. Methanol denaturation deactivates enzymes present in the sample which might otherwise degrade metabolites or facilitate chemical reactions and impact on the composition of metabolites. This ensures that no undesired changes occur prior to analysis and so an accurate representation of the metabolites present at the time of sample collection is obtained.

Chloroform and water are then added to the methanol-sample mixture. The primary role of chloroform is to extract lipids and nonpolar compounds from the biological sample[342]. Chloroform an organic solvent immiscible with water is an effective solvent for dissolving hydrophobic lipids in biological material due to its similar nonpolar nature. Chloroform

separates the nonpolar lipids in the sample from the polar water-soluble metabolites, creating a two-phase separation system: the upper aqueous phase and the lower organic phase. Chloroform is heavier than water and methanol and forms a layer at the bottom of the falcon tube. The chloroform also serves as a continuation of the protein denaturation process initiated by methanol. In the presence of chloroform, proteins continue to undergo structural changes and unfolding, resulting in decreased solubility and their subsequent precipitation out of solution. This aids the removal of interfering proteins from the sample. The addition of water is also important in the dual-phase method. Water is immiscible with chloroform and is the primary solvent for aqueous metabolites. Water assists in phase separation, forming a layer between the upper aqueous (methanol) phase and the lower organic (chloroform) phase.

The mixture is then centrifuged separating it into three distinct layers: The top aqueous layer, a middle interphase layer, and the bottom organic layer. The aqueous layer is carefully collected and consists mainly of polar, water-soluble metabolites. The metabolites identified within this aqueous layer are integral to various fundamental metabolic pathways and cellular processes, including glycolysis, the TCA cycle, amino acid metabolism, nucleotide synthesis, and energy metabolism[343]. Coenzymes and cofactors can also be found within this layer. These metabolites provide a snapshot of the dynamic metabolic landscape in the sampled tissue, providing insight into the physiological activities and underlying biological state of the animal under investigation[342][343]. The middle interphase layer mainly consists of precipitated protein and is not collected. The bottom organic layer is primarily composed of chloroform and lipids. The lipids within this layer include various classes such as: Triglycerides, phospholipids, cholesterol and cholesterol esters, fatty acids, and sphingolipids[332]. These lipids contribute to various metabolic cycles and lipid-related processes, including lipid metabolism, energy storage, and membrane structure, fatty acid oxidation, cholesterol biosynthesis, and sphingolipid metabolism[342]. The composition of the organic layer offers insights into the status of lipid metabolism within the sampled tissue, and sheds light on the implication of lipids on cardiac function.

Chelex was added to each aqueous sample and centrifuged once more. Chelex chelates and remove metal ions from solution; it is a resin-based material that contains ligands that can interact, immobilize, and remove metal ions[342]. Removal of metal ions from our samples is important as they can cause signal interference and unwanted spectral artifacts, leading to paramagnetic effects and broadened spectral lines.

3.7.2.2 Dehydration

Dehydration is important for three key reasons: 1) Preservation of metabolites, 2) sample concentration, and 3) removal of the ^{1}H signal from chloroform and water that would otherwise dominate the spectrum.

3.7.2.2.1 Drying the Aqueous Metabolite Layer

Freeze-drying is a dehydration process commonly used in the preparation of the aqueous layer for NMR-based metabolomic analysis. Freeze-drying, a gentle and non-destructive method, removes water from a sample so that the metabolites remain unaltered and preserved in their native state. Water as a polar solvent can produce broad and intense signals in NMR spectra, removal of water is important as its signal interference can overshadow metabolite signal. The removal of water concentrates the metabolites within the sample, leading to improved detection sensitivity and spectral quality; concentrated samples produce stronger NMR signals. Drying the aqueous layer allows for re-dissolving the metabolites in the appropriate NMR-compatible solvent. NMR requires samples to be dissolved in non-protonated solvents to provide a strong NMR signal and, unlike water, do not interfere with the metabolite signal.

3.7.2.2.2 Drying the Organic Lipophilic Layer

The organic lipophilic layer was dried by evaporation to remove the chloroform solvent and concentrate the lipids. The non-polar chloroform solvent was removed as it can produce an intense signal in the NMR spectrum which can overshadow the lipid signal and interfere with detection. Drying the organic lipophilic layer allows for re-dissolving the lipid metabolites in an appropriate NMR-compatible solvent. NMR requires samples to be dissolved in non-protonated solvents as they do not interfere with the lipid signal.

3.7.2.3 Reconstitution

3.7.2.3.1 Reconstituting the Aqueous Metabolite Layer

The dried aqueous samples were reconstituted in deuterated water (D_2O), a chemically inert solvent commonly used in NMR analysis of aqueous samples[342]. D_2O is a variant of water where the hydrogen atoms (^{1}H) are substituted with deuterium atoms (^{2}H). Deuterium an isotope of hydrogen and its atoms consists of one proton and one neutron, this additional

neutron makes deuterium twice as heavy as regular hydrogen. D_2O is chemically stable and non-reactive, ensuring the chemical integrity of the samples is maintained during analysis. D_2O is also important in the suppression of residual water peaks. Removing the dominant water peaks means the signals from the metabolites of interest can be detected. D_2O serves as lock solvent by providing a stable reference signal (lock frequency) based on its deuterium nuclei. D_2O results in a unique NMR signal when placed in the magnetic field, and this signal is used as a reference. The reference signal remains stable as deuterium nuclei are less sensitive to magnetic field variations compared to the hydrogen nuclei found in H_2O. A stable reference signal enables the NMR spectrometer to correct for fluctuations in the magnetic field. This ensures that NMR spectra are acquired under constant conditions.

For our aqueous samples, Trimethylsilyl propionate (TSP) was used for both chemical shift calibration and as an internal standard for the quantification of metabolites. TSP is used as it is soluble in aqueous solutions. A known quantity of TSP is dissolved in the D_2O solvent and added to each dried aqueous sample during reconstitution. TSP generates a sharp and well-defined NMR peak at a specific chemical shift in the spectrum, which was calibrated to 0 ppm on the NMR scale and used as a reference. Calibrating the NMR spectrum with TSP means the chemical shifts of the metabolites of interest can be accurately measured. TSP was used as an internal quantification standard; a known quantity of TSP was added to each sample and the integral of the TSP peak corresponds to a known concentration of TSP. The concentration of metabolites of interest determined by comparing the metabolite integral to that of the TSP. This comparison allows for the quantification of specific metabolite concentration based on the ratio of integrated areas, the known TSP concentration, and the number of protons contributing to each peak. The estimates of absolute metabolite concentration directly compared between different samples and the metabolite concentrations further scaled to the unit weight of wet tissue used for the extraction.

3.7.2.3.2 Reconstituting the Organic Lipophilic Layer

The dried organic lipophilic samples were reconstituted in deuterated chloroform ($CDCl_3$). Deuterated chloroform contains deuterium (^2H) atoms instead of regular hydrogen (^1H) atoms. The absence of NMR-active hydrogens ensures that the NMR signals are not related to the solvent. Like deuterated water, deuterated chloroform also serves as an internal lock and enables the NMR spectrometer to correct for fluctuations in the magnetic field[342].

Tetramethylsilane (TMS) is highly soluble in nonpolar organic solvents like chloroform and was used for both chemical shift calibration and as an internal standard for the quantification of lipids. A known quantity of TMS is dissolved in the $CDCl_3$ solvent and added to each dried organic lipophilic sample during reconstitution. The TMS generates a single sharp and NMR peak at 0 ppm on the NMR scale and was used as a chemical shift reference. The lipid peaks were measured relative to the TMS reference peak, allowing precise determination of the chemical shifts of the various lipid peaks in the sample. TMS was also used as an internal quantification standard; a known quantity of TMS was added to each sample and the integral of the TMS peak corresponds to a known concentration of TMS. Estimates of the absolute concentration of lipid metabolites was calculated in the same way as described for the aqueous metabolites (see 3.7.2.3.1).

3.7.3 ^{1}H-NMR Tissue Sample Preparation Protocol

Tissue was harvested as described in 3.2.7, and stored at -80°C until use. A tissue sample (100-200mg) was placed into a pre-weighed 15mL falcon tubes containing ice-cold methanol (2mL/100mg cardiac tissue). Ice-cold chloroform (1mL/100mg tissue) and water (1mL/100mg tissue) were added to the falcon tube and vortexed for 30 seconds. This step was repeated once more, and the total volume of chloroform and water added was 2mL/100mg tissue and 2mL/100mg tissue, respectively. The suspension then centrifuged for 1 hour at 3600 RPM at 4°C. After centrifugation, three layers formed: an upper aqueous methanol layer; a middle solid protein interphase layer; and a lower lipophilic organic chloroform layer.

The upper aqueous layer was transferred to a new 15mL falcon tube containing 30mg Chelex 100, vortexed for 30 seconds and then centrifuged at 3600 RPM for 5 minutes at 4°C. The supernatant then transferred to a new falcon tube containing 20µL universal indicator and vortexed for 30 seconds. Each sample was snap frozen and freeze dried. The dried samples were reconstituted in 600µL of a deuterium oxide (D_2O) solution containing TSP. The TSP present in the D_2O solution used to avoid possible chemical shift drifts due to pH effects and serves as an internal standard. The reconstituted samples were transferred to 5mm NMR tubes (Norel Inc, USA) for ^{1}H NMR analysis. The pH of the samples was corrected to ~pH 6.5 using 1M hydrochloric acid.

The lower organic lipophilic layer was transferred to glass vials, and the chloroform was left to evaporate under a fume hood. The dried samples were reconstituted in 600µL of deuterated

chloroform ($CDCl_3$) solution containing TMS and vortexed. The TMS present in the $CDCl_3$ solution used to avoid possible chemical shift drifts due to pH effects and serving as an internal standard. The reconstituted samples were transferred to 5mm NMR tubes (Norel Inc, USA) for ^1H NMR analysis.

3.7.4 ^1H-NMR Serum Sample Preparation Protocol

Serum metabolites were quantified using NMR analysis. Serum samples were collected as described in 3.2.6 and 100µl of thawed serum was vortexed with 500µl D_2O solution containing TSP. The role of D_2O and TSP in serum NMR analysis as described in 3.7.3. The samples then transferred to 5mm NMR tubes (Norel Inc, USA) for ^1H NMR analysis.

3.7.5 ^1H NMR Spectroscopy Parameters

All metabolite extraction and ^1H NMR optimisation analysis was performed on a 600-MHz Bruker spectrometer (Bruker, Germany). Spectra were acquired using a 9.3 kHz spectral width and 32 000 data points with acquisition time of 1.67 seconds, relaxation delay of 5 seconds, and 128 scans.

3.7.6 Processing ^1H NMR Spectra

Spectra were post-processed in TopSpin software version 3.6.1 (Bruker, Germany). Post-processing of ^1H NMR spectra consisted first of a Fourier transform; to transform the data from the time domain into the frequency domain, achieved using an exponential multiplication. Each spectrum was phase corrected and baseline corrected, and chemical shifts normalised by setting the internal standard (TSP or TMS) signal to 0 ppm.

3.7.7 Metabolite Identification

The metabolite peaks were integrated manually in the first spectrum., The metabolic profiles of cardiac and serum samples determined using Chenomx NMR Profiler Version 9.0 (Chenomx, Canada). Achieved by comparing chemical shifts and coupling constants with 1H NMR spectra of reference compounds acquired under the same conditions. The integral text file written for the first spectrum of each sample type used to automatically integrate the remaining spectra. Integration regions were manually adjusted where required.

3.7.7.1 Metabolic Profile in Control Aqueous Samples

Thirty-two metabolites were identified within the aqueous extracts of both cardiac and liver tissue. The representative ^{1}H NMR spectra are shown in Figure 23 and the assigned metabolites are as follows: 1) Leucine; 2) Isoleucine; 3) Valine; 4) Lactate; 5) Alanine; 6) Acetate; 7) Glutamate; 8) Succinate; 9) Glutamine; 10) Aspartame; 11) Creatine; 12) Acetyl carnitine; 13) Choline; 14) Phosphocholine; 15) Carnitine; 16) Taurine; 17) Glycine; 18) Creatine; 19) Phosphocreatine; 20) Myoinositol; 21) a-glucose; 22) Fumarate; 23) Histidine; 24) Tyrosine; 25) Phenylalanine; 26) ATP + ADP; 27) Formate; 28) ATP; 29) AMP; 30) Niacinamide; 31) NADP; 32) NAD. Table 6 shows the ^{1}H NMR chemical shift values used for the quantification of metabolite concentration.

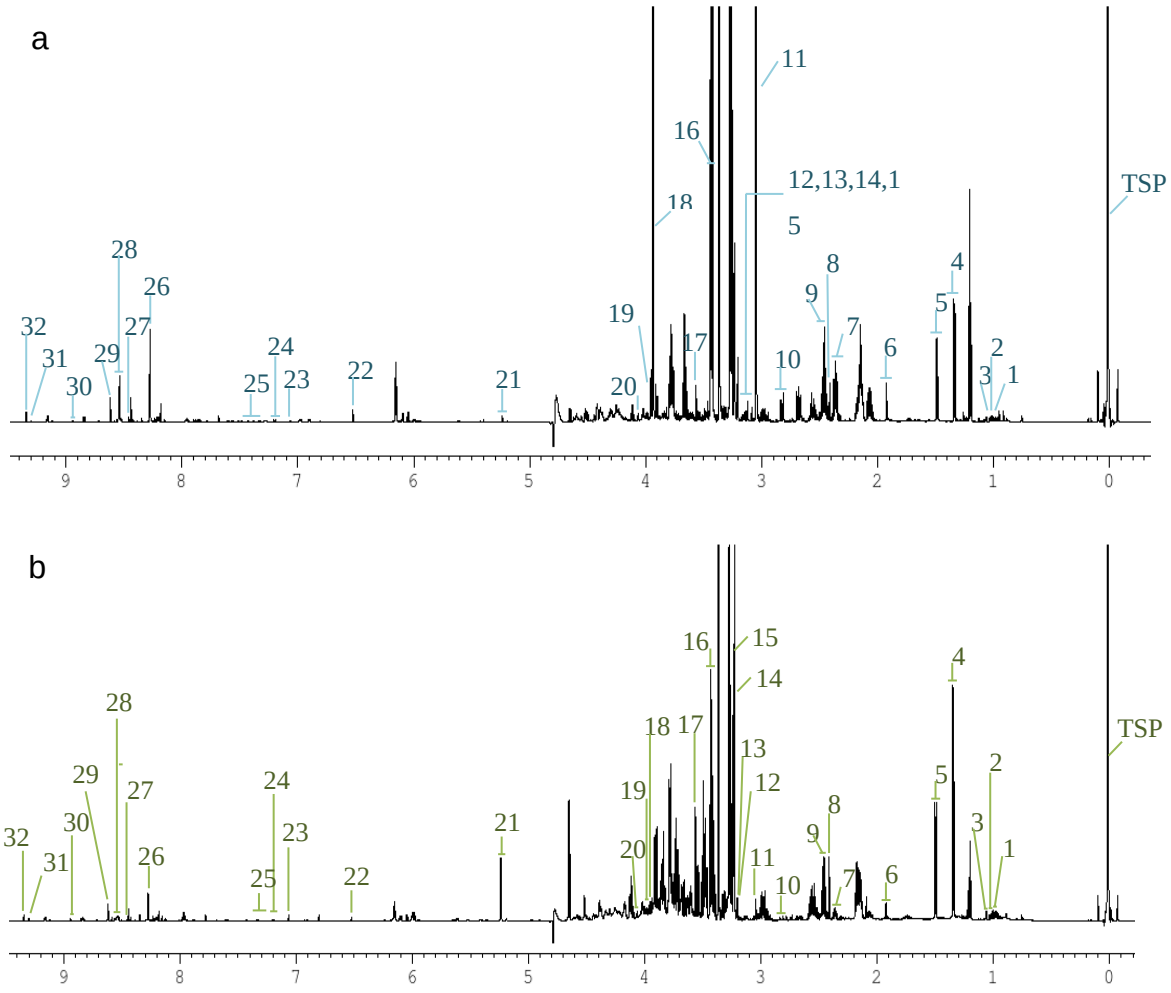

Figure 22: Typical 600 MHz ^{1}H NMR spectra of the aqueous extracts. **a** Cardiac samples, and **b** Liver samples. Metabolites were respectively listed in Table 6, along with their chemical shifts.

Table 6: List of ^{1}H NMR chemical shift values (ppm) for metabolites identified in aqueous samples of cardiac tissue and liver tissue.

Entry	Metabolite	Chemical shift (ppm)
Reference	TSP	0
1	Leucine	0.9649
2	Isoleucine	1.0133
3	Valine	1.0448
4	Lactate	1.3327
5	Alanine	1.4796
6	Acetate	1.9217
7	Glutamate	2.3562
8	Succinate	2.4055
9	Glutamine	2.462
10	Asp	2.8139
11	Creatine	3.0427
12	Acetyl carnitine	3.1976
13	Choline	3.2065
14	Phosphocholine	3.2242
15	Carnitine	3.2318
16	Taurine	3.4258
17	Glycine	3.5613
18	Creatine	3.9331
19	Phosphocreatine	3.9532
20	Myoinositol	4.0638
21	a-glucose	5.2372
22	Fumarate	6.5226
23	Histidine	7.0616
24	Tyrosine	7.1973
25	Phenylalanine	7.3858
26	ATP + ADP	8.2753
27	Formate	8.46
28	ATP	8.5392
29	AMP	8.6184
30	Niacinamide	8.9409
31	NADP	9.2964
32	NAD	9.3413

3.7.7.2 Metabolic Profile in Control Organic Lipophilic Samples

Twenty-one metabolites were identified within the lipophilic extracts of both cardiac and liver tissue. The representative ^{1}H NMR spectra are shown in Figure 24 and the assigned metabolites are as follows: 1) Cholesterol 18-CH3; 2) Lipids CH3; 3) Cholesterol 21-CH3; 4) Ω3 CH3; 5) Free cholesterol 19-CH3; 6) Lipids (CH2)n; 7) Lipids CH2CH2CO; 8) Lipids CH2CH=C; 9) Lipids CH2CO; 10) Lipids =CHCH2CH=; 11) Phosphatidylethanolamine N(CH3)3; 12 Phosphatidylcholine N(CH3)3; 13) Phosphatidylcholine N-CH2; 14) Glycerophospholipid backbone 3-CH2; 15) Glycerol backbone 1,3-CH2; 16) Glycerol backbone 1,3-CH2; 17) Phosphatidylcholine PO-CH2; 18) Phosphatidylcholine PO-CH2; 19) 0 Glycerophospholipid backbone 2-CH; 20) Lipid CH=CH; 21) Sphingomyelin. Table 7 shows the ^{1}H NMR chemical shift values used for the quantification of metabolite concentration.

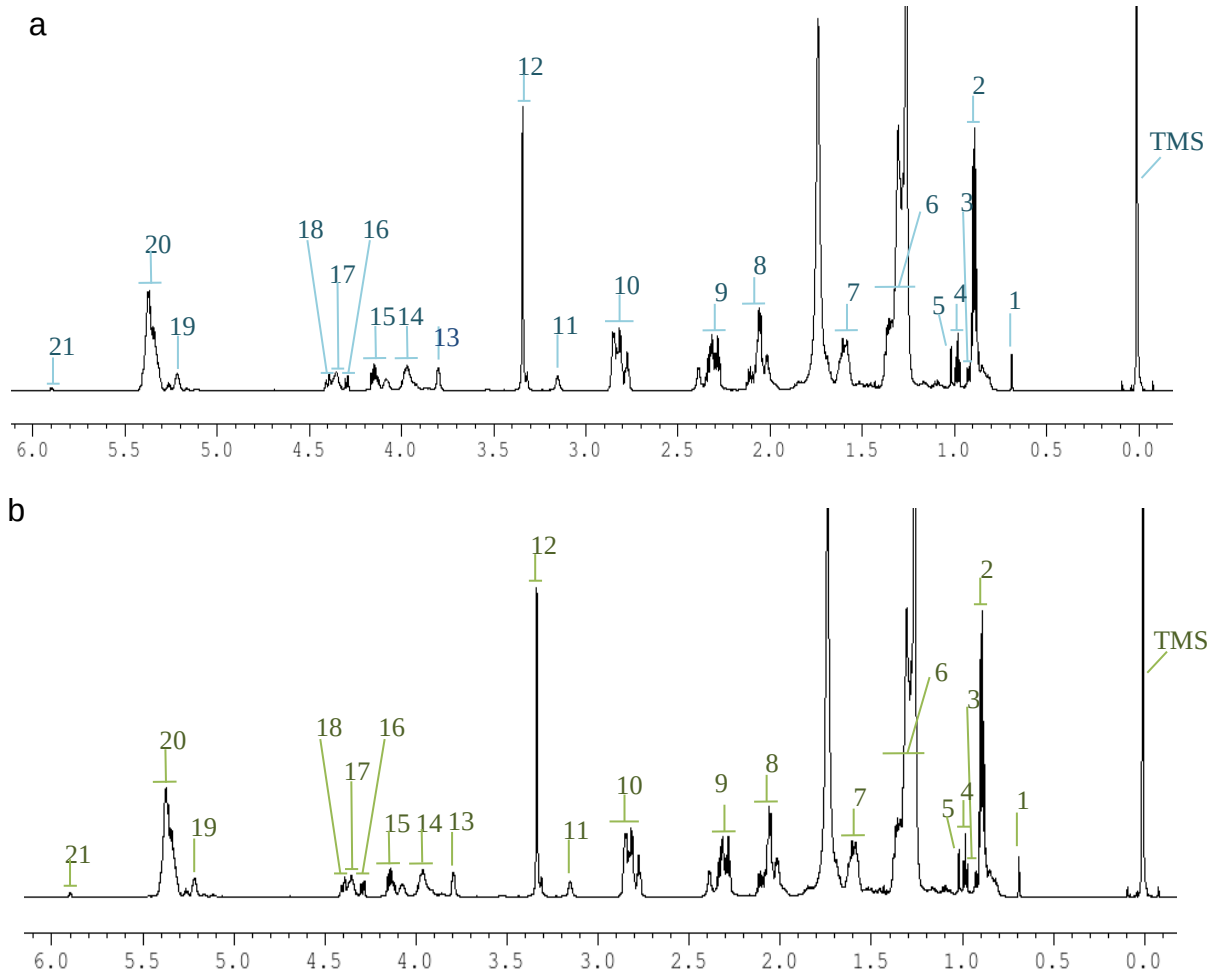

Figure 23: Typical 600 MHz ^{1}H NMR spectra of the lipophilic extracts. a Cardiac samples, and **b** Liver samples. Metabolites were respectively listed in Table 7, along with their chemical shifts.

Table 7: List of ^{1}H NMR chemical shift values (ppm) for metabolites identified in the lipophilic extracts of cardiac and liver tissue.

Entry	Metabolite	Chemical shift (ppm)
Reference	TMS	0
1	Cholesterol 18-CH3	0.6769
2	Lipids CH3	0.8778
3	Cholesterol 21-CH3	0.9153
4	Ω3 CH3	0.9736
5	Free cholesterol 19-CH3	1.0084
6	Lipids (CH2)n	1.271
7	Lipids CH2CH2CO	1.5878
8	Lipids CH2CH=C	2.0799
9	Lipids CH2CO	2.2932
10	Lipids =CHCH2CH=	2.8083
11	Phosphatidylethanolamine N(CH3)3	3.1551
12	Phosphatidylcholine N(CH3)3	3.3302
13	Phosphatidylcholine N-CH2	3.7779
14	Glycerophospholipid backbone 3-CH2	3.9533
15	Glycerol backbone 1,3-CH2	4.1325
16	Glycerol backbone 1,3-CH2	4.2885
17	Phosphatidylcholine PO-CH2	4.3337
18	Phosphatidylcholine PO-CH2	4.3902
19	0 Glycerophospholipid backbone 2-CH	5.2118
20	Lipid CH=CH	5.3625
21	Sphingomyelin	5.8988

3.7.7.3 Metabolic Profile in Control Serum Samples

Twenty-two metabolites were identified within the ^{1}H NMR spectra of serum samples. A representative spectrum is shown in Figure 25.The assigned metabolites are as follows: 1) Fatty acid residues (ω-CH3); 2) Leucine; 3) Isoleucine; 4) Valine; 5) 3-hydroxybutyrate; 6) Lactate; 7) Alanine; 8) Fatty acid residues (COCH2-CH2); 9) Acetate; 10) Glutamate; 11) Pyruvate; 12) Glutamine; 13) Citrate; 14) Creatine; 15) Glycine; 16) a-glucose; 17) Fatty acid residues (−CH=CH-); 18) Tyrosine; 19) Histidine; 20) Phenylalanine; 21) Tryptophan; 22) Formate. Table 8 shows the ^{1}H NMR chemical shift values used for the quantification of metabolite concentration.

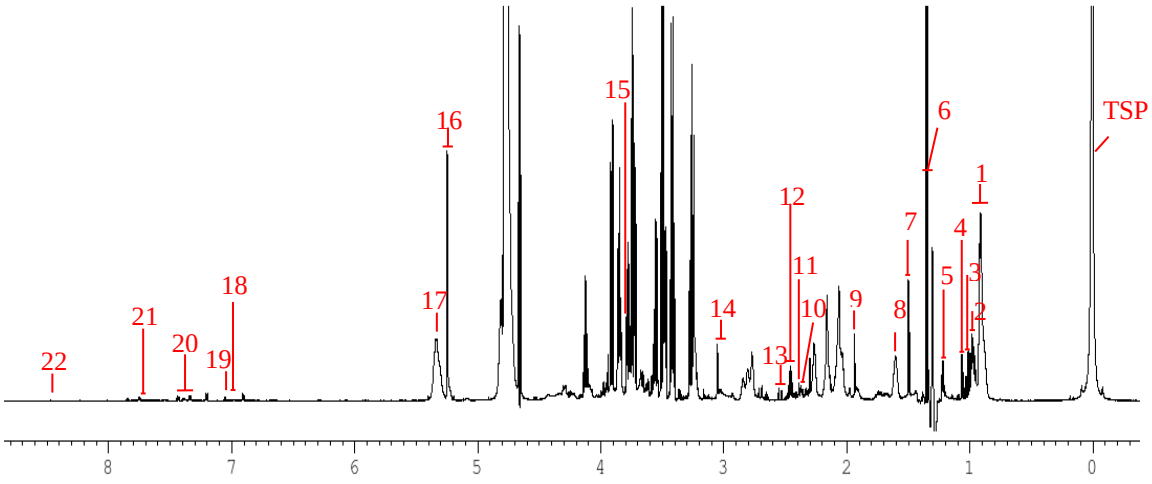

Figure 24: Typical 600 MHz 1 H NMR spectra of serum samples. Metabolites were respectively listed in Table 8, along with their chemical shifts.

Table 8: List of ^{1}H NMR chemical shift values (ppm) for metabolites identified in serum samples.

Entry	Metabolite	Chemical shift (ppm)
Reference	TSP	0
1	Fatty acid residues (ω-CH3)	0.881
2	Leucine	0.9706
3	Isoleucine	1.0251
4	Valine	1.0471
5	3-hydroxybutyrate	1.2045
6	Lactate	1.3315
7	Alanine	1.4853
8	Fatty acid residues (COCH2-CH2)	1.5893
9	Acetate	1.9217
10	Glutamate	2.3502
11	Pyruvate	2.3775
12	Glutamine	2.4651
13	Citrate	2.5346
14	Creatine	3.0427
15	Glycine	3.5574
16	a-glucose	5.2365
17	Fatty acid residues (−CH=CH-)	5.3304
18	Tyrosine	6.9038
19	Histidine	7.0465
20	Phenylalanine	7.3914
21	Tryptophan	7.5518
22	Formate	8.4647

3.7.8 Metabolite Quantification

Normalisation is used to make all spectra comparable to each other, it is required to reduce sample variability that can arise due to differences in sample concentrations. Metabolite integrals were normalised relative to an internal standard. TSP was used as the internal quantification standard for the aqueous extracts of cardiac and liver samples. TMS was used as the internal quantification standard for the lipophilic extracts cardiac and liver samples, and serum samples. The concentration of the internal standard is known and has a well-defined NMR peak that doesn't overlap with other metabolite peaks.

The concentration of metabolites within the cardiac and liver aqueous samples was calculated by incorporating the metabolite integral and the TSP integral into Equation 7. This was done with respect to the initial wet tissue mass used for the metabolite extraction process.

Equation 7: Quantifying metabolite concentration in aqueous tissue extracts

$$\boldsymbol{Metabolite\ concentration} = \frac{\boldsymbol{TSP} \times \boldsymbol{I_{Metabolite}} \times \boldsymbol{P_{TSP}}}{\boldsymbol{P_{Metabolite}} \times \boldsymbol{M_{Sample}} \times \boldsymbol{I_{TSP}}}$$

Where,

$TSP = Concentration\ of\ TSP\ in\ sample\ (mol)$

$I_{Metabolite} = Integral\ of\ metabolite\ peak\ relative\ to\ TSP\ integral$

$P_{TSP} = Number\ of\ protons\ that\ give\ rise\ to\ the\ TSP\ peak$

$P_{Metabolite} = Number\ of\ protons\ that\ give\ rise\ to\ the\ metabolite\ peak$

$M_{Sample} = Initial\ mass\ of\ tissue\ sample\ used\ for\ NMR\ analysis\ (g)$

$I_{TSP} = Integral\ of\ TSP\ peak$

The concentration of metabolites within the cardiac and liver lipid samples was calculated by incorporating the metabolite integral and the TMS integral into Equation 8. This was done with respect to the initial wet tissue mass used for the metabolite extraction process.

Equation 8: Quantifying metabolite concentration in lipophilic tissue extracts

$$\boldsymbol{Metabolite\ concentration} = \frac{\boldsymbol{TMS} \times \boldsymbol{I_{Metabolite}}}{\boldsymbol{M_{Sample}} \times \boldsymbol{I_{TMS}}}$$

Where,

$TMS = Concentration\ of\ TMS\ in\ sample\ (mol)$

$I_{Metabolite} = Integral\ of\ metabolite\ peak\ relative\ to\ TMS\ integral$

$M_{Sample} = Initial\ mass\ of\ tissue\ sample\ used\ for\ NMR\ analysis\ (g)$

$I_{TMS} = Integral\ of\ TMS\ peak$

The concentration of metabolites within the serum samples was calculated by incorporating the metabolite integral and the TMS integral into Equation 9. This was done in respect to the volume of serum from which the NMR data was acquired.

Equation 9: Quantifying metabolite concentration in serum samples

$$\boldsymbol{Metabolite\ concentration} = \left(\frac{\boldsymbol{TMS} \times \boldsymbol{I_{Metabolite}} \times \boldsymbol{P_{TMS}}}{\boldsymbol{P_{Metabolite}} \times \boldsymbol{I_{TSP}}}\right) / \boldsymbol{V_{Sample}}$$

Where,

$TMS = Concentration\ of\ TMS\ in\ sample\ (mol)$

$I_{Metabolite} = Integral\ of\ metabolite\ peak\ relative\ to\ TMS\ integral$

$P_{TMS} = Number\ of\ protons\ that\ give\ rise\ to\ the\ TMS\ peak$

$P_{Metabolite} = Number\ of\ protons\ that\ give\ rise\ to\ the\ metabolite\ peak$

$V_{Sample} = Volume\ of\ serum\ used\ for\ NMR\ analysis\ (L)$

$I_{TMS} = Integral\ of\ TMS\ peak$

3.7.9 Metabolic Pathways

The cardiac and liver tissue metabolites identified by ^{1}H NMR were categorized into specific metabolic pathways (Table 9): fatty acid oxidation, glycolysis, the TCA cycle, energy transfer/utilization, amino acid metabolism, and lipid metabolism. Figure 26 provides a visual representation of each metabolite's role in cardiac metabolic processes, serving as a reference for contextualizing changes in metabolites during *in vivo* investigations. While the fundamental metabolic processes in the heart are preserved in the liver, there are several key differentiators, such as glycogenolysis, gluconeogenesis, and liver metabolism, illustrated in Figure 27.

Table 9: Cardiac and Liver metabolites categorised into metabolic pathways.

Metabolic process	Metabolite
Fatty acid oxidation	Acetyl carnitine
	Carnitine
Glycolysis	a-glucose
	Lactate
TCA cycle	Succinate
	Fumarate
	Isoleucine
	Leucine
	Glycine
	Taurine
	Glutamine
	Glutamate
	Alanine
	Valine
	Phenylalanine
	Aspartate
Energetics (transfer and utilization)	ATP
	AMP
	NAD
	NADP
	Creatine
	Phosphocreatine
	Niacinamide
	Tyrosine
	Acetate
Lipid metabolism	Choline
	Phosphocholine
	Lipids (CH2)n
	Lipid CH=CH
	Cholesterol 18-CH3
	Glycerol backbone 1,3-CH2
	Phosphatidylcholine N(CH3)3
	Phosphatidylethanolamine N(CH3)3
	Sphingomyelin
Other	Histidine
	Formate
	Myo inositol

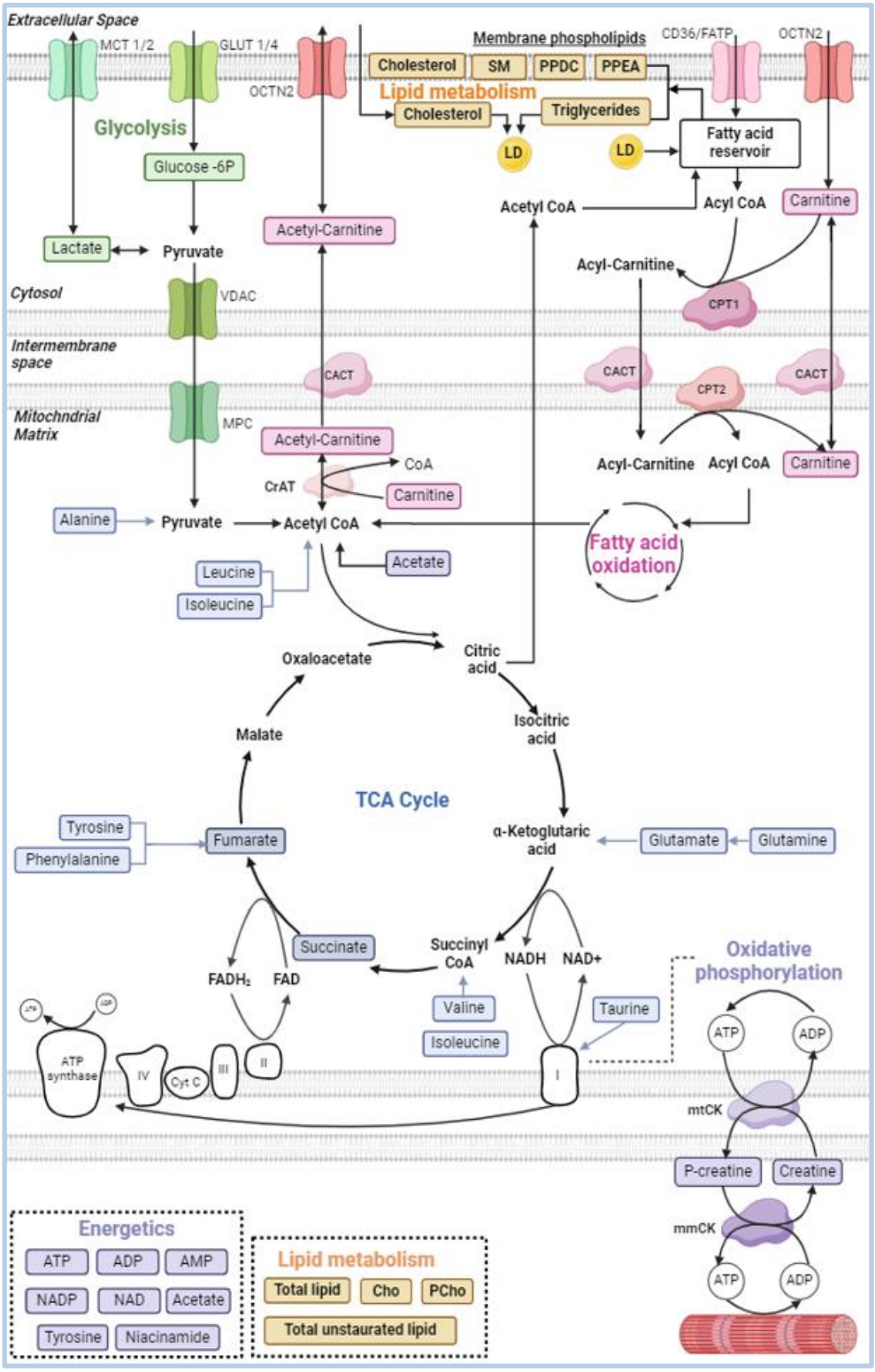

Figure 25: Schematic of cardiac metabolites and their associated metabolic pathways in the heart. CPT1; Carnitine palmitoyltransferase I, CPT2; Carnitine palmitoyltransferase II, CACT; carnitine/acylcarnitine translocase transporter, LD; Lipid droplet, MPC; Mitochondrial pyruvate carrier, VDAC; Voltage-dependent anion channel, MCT 1/2; Monocarboxylate transporters, GLUT 1/4; Glucose transporters, OCTN2; Organic cation transporter novel family member 2, CD36/FATP; Fatty acid transporters, CrAT; Carnitine acetyltransferase, CoA; Coenzyme A, Cho; Choline, PCho; Phosphocholine, P-creatine: Phosphocreatine, mmCK; Myofibrillar creatine kinase, mTCK; Mitochondrial creatine kinase, SM; Sphingomyelin, PPDC; Phosphatidylcholine, PPEA; Phosphatidylethanolamine. [Figure made in BioRender]

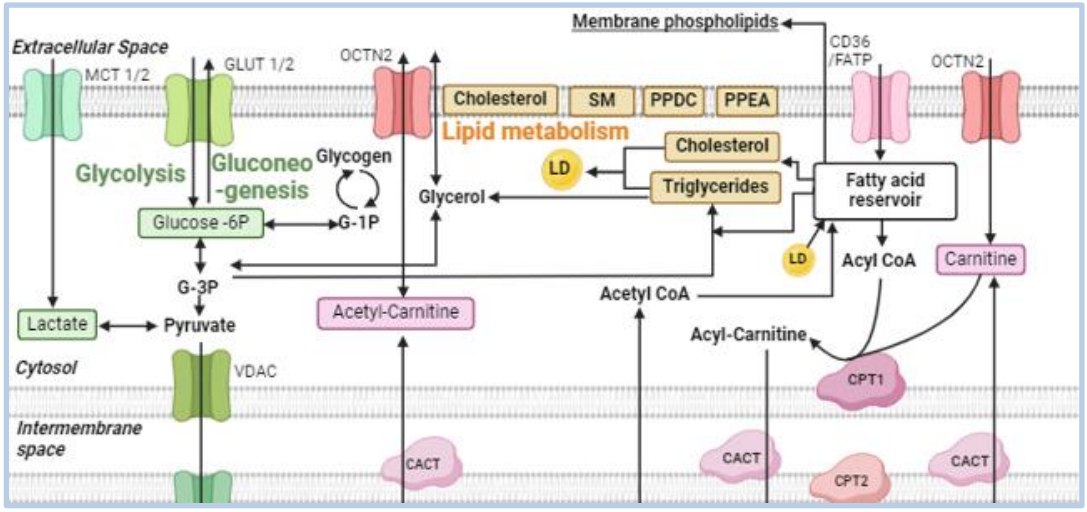

Figure 26: Schematic of liver metabolites and their associated metabolic pathways. CPT1; Carnitine palmitoyltransferase I, CPT2; Carnitine palmitoyltransferase II, CACT; carnitine/acylcarnitine translocase transporter, LD; Lipid droplet, SM; Sphingomyelin, PPDC; Phosphatidylcholine, PPEA; Phosphatidylethanolamine, VDAC; Voltage-dependent anion channel, MCT 1/2; Monocarboxylate transporters, GLUT 1/4; Glucose transporters, OCTN2; Organic cation transporter novel family member 2, CD36/FATP; Fatty acid transporters. [Figure made in BioRender]

ICP-MS BASED QUANTIFICATION OF TOTAL AND MITOCHONDRIAL CARDIAC IRON

4.1 Introduction

The central aim is to determine whether alterations in cardiac iron underpins the metabolic perturbation caused by DOX cardiotoxicity and to examine how DOX treatment influences the redistribution of cellular iron. This required the development of a reliable and accurate method for quantifying total cardiac intracellular iron and mitochondrial iron levels.

A variety of methods are available to characterise iron concentrations in biological samples: Inductively coupled plasma-mass spectrometry (ICP-MS), ICP-atomic emission spectroscopy (ICP-AES), graphite furnace-atomic absorption spectroscopy (GF-AAS), flame atomic absorption spectroscopy (FAAS), or colorimetric methods[344] [322].

ICP-MS uses high ionization energy, plasma, to produce elemental ions; the singly charged ions are separated and quantified based on their specific mass to charge ratio using a mass spectrometer[325].

ICP-AES systems excite atoms to emit analytically useful radiation using high temperature plasma (1000 °C)[345]. Processed samples aspirated into the plasma flame and element specific light is emitted and analysed by a multi-element detector.

GF-AAS and FAAS are based on the principle that atoms of an element absorb light at a specific wavelength[346]. The sample is atomized, the light of the specific wavelength is absorbed by the atom resulting in transition from ground to an excited state; with analyte concentrations calculated using the amount of energy absorbed[347].

In a colorimetric assay, iron is first released from a sample using an acidic buffer and reduced, the iron then reacts with a chromogen resulting in a colorimetric product that is proportional to the iron present in the sample[348][349].

ICP-MS is an analytical technique used to measure elements at trace levels in biological samples, it is considered the gold standard for the measurement of iron due to its detection sensitivity (ppt-ppb). ICP-AES, GF-AAS and AAS achieve a much lower detection threshold (ppb) compared to ICP-MS[350][351][322]. The concentration of iron measured by a

colorimetric method is an indirect method, and typically underestimates due to incomplete liberation and reduction[352]. ICP-MS can detect multiple elements for simultaneous interrogation. In consideration of these factors, ICP-MS was chosen as our analytical tool for the measurement of iron for this project. Refer to 3.6.1 for an overview of ICP-MS fundamentals.

4.2 Aims

The aim of this chapter is to develop and optimise an ICP-MS based iron quantification protocol for the measurement of total cardiac iron in both whole cardiac tissue samples and mitochondrial isolations. These methods are required to characterise cardiac iron in our *in vivo* investigations.

Sample preparation and instrument configuration are integral for the accurate and sensitive quantification of iron via ICP-MS, which were core considerations during the method development and optimisation procedures.

4.3 Strategies for Mitigating Interference in ICP-MS

Spectral interference develops when the m/z ratio of non-target analyte ions overlap with that of the target analyte[353]. Non-spectral interference refers to matrix effects or instrument drift[354] [322]. Matrix effects occur when there is a change in instrument sensitivity to the target analyte element due to the presence of contaminants. This results in the signal of the target analyte being either enhanced or suppressed due to the properties or constituents of the sample matrix. Instrumental drift refers to the progressive signal suppression that occurs during ICP-MS. Dissolved solids can deposit in and occlude the nebulizer or the interface cones, resulting in a reduction of ion transmission into the mass spectrometer. Over time, the degree of occlusion increases, leading to a downward drift in signal [355]. Interferences can be an important limiting factor in ICP-MS. This chapter considers the strategies that were employed to mitigate and correct for them. The cleanliness of the laboratory environment in which samples are prepared is also an important consideration to avoid potential contamination of samples.

4.3.1 Spectral Interferences

Spectral interferences are categorised as either isobaric or polyatomic, and result when ionic species have an overlapping m/z with the target analyte[353]. Isobaric interferences refer to different elements whose naturally occurring isotopes share a common mass as the target analyte. Polyatomic interferences occur when two or more isotopes from different elements either combine with each other or the ICP to form ions of the same m/z as the target analyte[353]. Polyatomic interferences are a particularly important consideration when measuring ^{56}Fe. Argon (^{40}Ar) from the ICP and oxygen (^{16}O) from the sample matrix combine to form $^{56}ArO^{+}$[325]. Non-removal of $^{56}ArO^{+}$ interference would result in an inaccurate measurement of ^{56}Fe. Opting for an alternate iron isotope would be inappropriate as ^{56}Fe is the most abundant isotope of iron and would lead to inferior detection limits.

To mitigate for spectral interference, the collision/reaction cell was operated in collision mode to improve the removal of spectral interferences, leading to reduced background, lower detection limits and better accuracy of analytes. In collision mode, inert gas (He) and a kinetic energy discrimination (KED) is used to remove interferences [356]. The collision/reaction cell is pressurized with He so that ions passing through the cell collide with He atoms[325] and lose kinetic energy with each collision. The polyatomic ions (the interferents) collide more frequently with He compared to the target analyte due to their larger ionic cross section [325] and leave the collision/reaction cell with a lower residual energy. They can then be filtered out using a positive bias voltage “step”, which discriminates higher-energy ions form low ones[325] [322] [327]. Collision mode requires that only ions with a narrow energy spread enter the cell[325]; the NexION 350 ICP-MS Spectrometer used for all ICP-MS analysis is a triple quadrupole ICP-MS, with an additional quadrupole mass filter between the ion lens and the Collision/reaction cell [356] [357]. The ion beam is filtered before reaching the collision/reaction cell so that only a single mass enters at any given time.

Collision (KED) mode can resolve interferences from polyatomic ions, though it is not as effective at removing isobaric interferences as the difference in collisional cross-section between this type of interferent and the target analyte are minor[327]. Therefore, the reaction mode was used to account for isobaric interferences.

In reaction cell mode, the cell is pressurised with a reactive gas (NH_3) [327]. The gas reacts exothermally with interferents to become a new neutral species within a few collisions [358],

which are immediately expelled from the cell as they are no longer stable in the reactive gas due to their lack of charge[327]. Analyte ions react endothermally and pass through the gas and exit the cell. The reactive gas can form new reaction products within the cell [358]. However, the additional quadrupole (Q1) before the collision/reaction cell limits entry to ions of a single mass (the target analyte and on-mass interferences), removing the possibility of overlapping product formation[325].

4.3.2 Non-Spectral Interference

Non-spectral interference refers to matrix effects or instrument drift. Matrix effects are either enhancement or suppression of the signal of the target analyte due to properties or components of the sample matrix[322]. Dissolved solids can lead to plasma loading effects that lower the ionisation efficiency of the ICP[353], reducing sensitivity. Deposit buildup in the autosampler probe, nebulizer or spray chamber can lead to progressive signal suppression and instrument drift[354][322]. Compensatory techniques for non-spectral interference include sample dilution, use of an internal standard, and matrix-matched calibration standards.

4.3.2.1 Dilution

Samples were diluted using HNO_3 and H_2O during preparation to reduce the intensity of the matrix effects and reduce potential instrumental drift from deposit buildup.

4.3.2.2 Internal Standardisation (Ga)

An internal standard corrects for changes in instrument operating conditions ('signal drift') and sample-specific matrix effects[322]. ^{71}Ga was selected as the internal standard due to its similar mass and ionisation potential to iron but does not itself spectrally interfere with ^{56}Fe.

The same amount of ^{71}Ga was added to each sample, and the signal of the target analyte was divided by that of the internal standard. The concentration of ^{71}Ga was maintained the same in all sample types involved in the analytical process (i.e. procedural samples, non-procedural samples and calibrants) to correct for matrix effects and signal fluctuations.

4.3.2.3 Matrix Matched Calibration Standards

The signal measured by the ICP-MS (in CPS) was converted to a concentration value. Standards with known concentrations of iron were used to construct a calibration curve. The calibration standards were matrix-matched to the samples by making up the calibration standards using volumes of HNO_3 and H_2O consistent with that added to the samples as part of their preparation (during digestion and dilution steps).

4.3.3 Sample Contamination

Controlling environmental contamination during sample preparation is crucial for data quality, accuracy, and robustness. For sample preparation including tissue harvesting, mitochondrial isolation, sample digestion and dilution, blank and calibration solution preparation, iron is commonly present. The following precautions were taken to avoid external iron contamination during sample preparation.

Freshly extracted cardiac tissue can be contaminated with red blood cells which can dramatically affect the accuracy of tissue iron measurements. To mitigate for this, the heart was perfused with PBS/saline via the apex of the heart prior to excision.

Labware and reagents are one of the largest sources of contamination; pipette tips, sample tubes, de-ionised water supply and reagents such as nitric acid and hydrochloric acid are common sources of contamination[359]. To mitigate this, trace metal grade ultrapure water with a resistivity of 18.2 MΩ cm was used. Nitric acid and hydrochloric acid used during sample preparation were also of trace metal grade (Fisher Chemical's TraceMetal®). Surface contamination of sample tubes (Falcon tubes and Eppendorf vials) was mitigated by soaking them in dilute (0.5% (v/v)) nitric acid prior to rinsing in trace metal grade ultrapure water. Pipette tips were pre-cleaned by pipetting dilute nitric acid and dispensing to waste before use.

To mitigate contamination from dust and airborne particles, the ICP-MS dedicated clean room facility at the London Metallomics Facility (LMF) was used when possible. Sample preparation was conducted within a fume hood. The order in which samples are run on the ICP-MS is important. Quality control samples (non-procedural blanks) were periodically analyzed along with the test samples to monitor for the presence and degree of contamination. Procedural

samples were analyzed prior to the test sample to avoid autosampler-induced cross contamination between samples, also known as sample-to-sample memory effects[360][360].

4.4 ICP-MS Based Quantification of Total Cardiac Iron

The ICP-MS-based quantification of total iron in cardiac tissue required preparation of procedural (test samples, procedural CRM, and procedural blanks) and non-procedural samples (Non-procedural CRM, non-procedural blank, and calibrants) followed by ICP-analysis (Figure 28). The purpose of each sample type required for ICP-MS analysis is outlined in Table 10.

Table 10: Overview of each sample type required for ICP-MS analysis.

Procedural samples	
Test samples	Cardiac tissue samples from which iron concentration is determined.
Procedural CRM	Used to determine the accuracy of the iron concentration quantification; the iron concentration of the procedural CRM sample is known (255µg of Fe / g of dry pig kidney tissue). Can b be used for blank correction
Procedural blanks	Used to determine iron levels in the solvents/acids used during sample preparation and for blank correction during the iron quantification. Contains the same volumes of H_2O_2, HNO_3, H_2O and Ga that were added to the cardiac and CRM samples, but no biological material.
Non-procedural samples	
Non-procedural blank	To determine the limit of detection for the quantification of iron.
Non-procedural CRM	Informs how accurately the system can measure iron.
Calibrants	Converts iron signal intensities measured by the ICP-MS detector (in CPS) to an iron concentration value; calibration standards contain known concentrations of iron and are used to construct a calibration curve.
Internal standard	
Ga	To correct for changes in instrument operating conditions (‘signal drift’) and sample-specific matrix effects, which may enhance or suppress the analyte signal. The same Ga concentration was added to all sample types involved in the analytical process for effective correction of matrix effects and fluctuations of signals.

The preparation of procedural samples comprises three main steps (Figure 28):

1) *Drying of cardiac tissue***:** Total cardiac iron is quantified using dry weight measurements (µg of iron per g of tissue), which is less variable than using wet weight. A variety of factors, including harvesting technique and condensation when transferring wet tissue to falcon tubes can impact measured weight. It is therefore important that the tissue samples are completely dry.

2) *Thermal acid digestion*: Digestion of cardiac tissue to a liquid state is essential to generate reliable quantitative ICP-MS data. The quantification of total cardiac iron requires the test samples to be completely dissolved for accurate analysis; undissolved analytes are not accurately measured. Digestion of cardiac tissue was carried out using conc. acids (HNO_3 and H_2O_2) at 70°C. The H_2O_2 was added as it breaks down organic matter efficiently.

3) *Dilution:* As discussed in 4.3.2.1, diluting the samples is key to reducing the intensity of the matrix effects and instrumental drift.

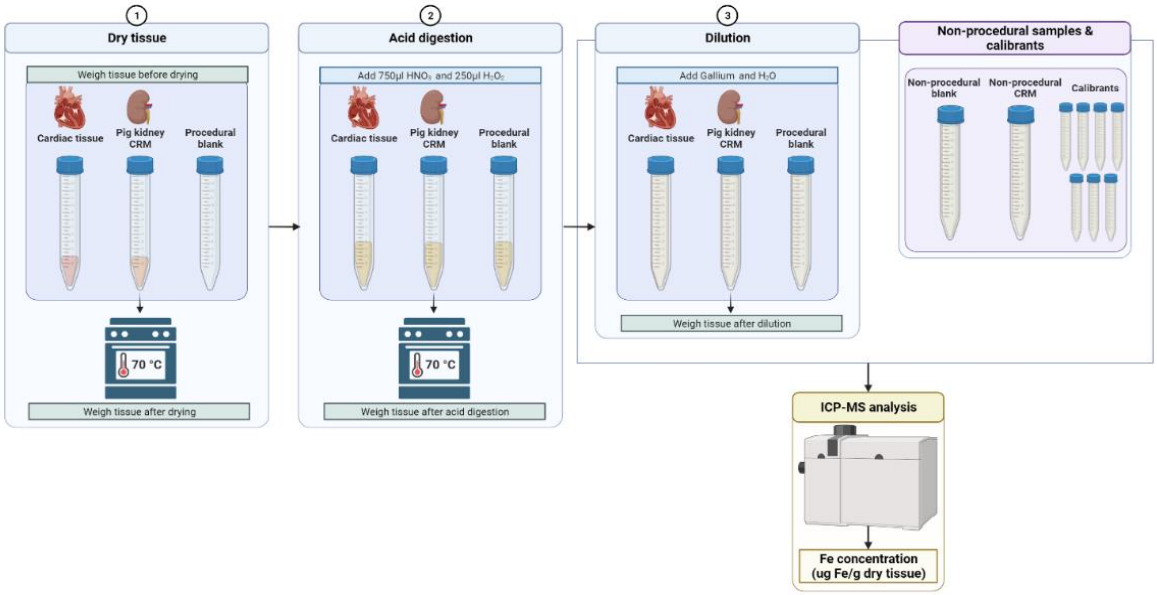

Figure 27: Workflow required for the ICP-MS based quantification of total cardiac iron. [Figure made in BioRender]

4.4.1 Sample Preparation for ICP-MS Analysis of Total Cardiac Iron

4.4.1.1 Materials and Reagents

Ultra-high-purity grade acids were used to prepare and process samples; Optima grade concentrated H_2O_2 (30–32% w/w; Sigma Aldrich), and Optima grade concentrated HNO_3 (67–69% w/w; Fisher Scientific).

Purified, trace-metal free water (MilliQ – resistivity ≥18.2 MΩ cm) was obtained from a Millipore Elix 3 system (Merck Millipore) and was used for all solution preparations.

The calibration standards for iron were made using multi elemental standard solutions purchased from Sigma Aldrich (TraCERT ICP-MS multi-element standard solution VI (100 ppm)); all standard solutions were prepared fresh daily before the ICP-MS analysis. The ^{71}Ga internal standard was purchased from Leeman Labs (100 ppm). Trace metals in powdered pig kidney (ERM-BB186) was used as the procedural CRM, and High Purity Standards Trace Metal Drinking Water (CRM HPS TMDW) was used as the non-procedural CRM.

All ICP-MS measurements were performed on a NexION 350 ICP-MS Spectrometer (PerkinElmer, Inc). The following gases were used for the collision/reaction cell in ICP-MS: Helium gas (>99.999% purity) and pre-purified grade Argon (>99.999% purity).

4.4.1.2 Procedural Sample Preparation

Drying: The harvested hearts as described in 3.2.7 were stored at -80°C until use. Cardiac tissue, 150 mg, was transferred to pre-weighed 15 mL acid-cleaned trace metal grade HDPP centrifuge tubes (Elkay Labs). To prevent contamination, and to allow moisture to escape, the tubes were capped but left unscrewed. All samples were then placed to dry overnight (or until completely dry) in an oven at 70 °C. Then removed from the oven and left to cool at room temperature and weighed using a 0.01 mg sensitivity balance to obtain the sample dry weight.

Thermal acid digestion: Each sample underwent thermal acid digestion. First, 0.25 mL of Optima grade concentrated H_2O_2 (30–32% w/w; Sigma Aldrich) was added to each sample. To allow the initial reaction to settle, the samples were left to stand at room temperature for 30 minutes. Then, 0.75 mL Optima grade concentrated HNO_3 (67–69% w/w; Fisher Scientific) was added to each sample and left for another 30 minutes. During the two 30-minute standby periods, caps were placed on the tubes to protect the samples from contamination but left

unscrewed to allow escape of CO_2. Once initial reactions had subsided, the tubes were tightly capped and placed in an oven at 70 °C to digest overnight.

Dilution: The digested samples were removed from the oven and left to cool at room temperature. The samples then weighed using a 0.01 mg sensitivity balance to obtain the weight of the digested material. Each sample was diluted to a total volume of 15mL using trace metal grade ultrapure water and Gallium (^{71}Ga) as an internal standard (Leeman Labs Ltd). The diluted samples then capped, and the combined weight of the sample digest and the diluent recorded using a 0.01 mg sensitivity balance. A representative dilution is described in Equation 10.

Equation 10: Representative ICP-MS sample dilution

$$\text{Ga to add } (0.15\text{mL}) = \frac{\text{Total vol. of sample } (15\text{mL}) \times 50 \text{ ppb (Conc. Ga required)}}{5\text{ppm Ga (Ga stock conc.)}}$$

$$\text{Water to add}(13.85\text{mL}) = \text{Total vol. of sample}(15\text{mL}) - \text{Ga}(0.15\text{mL}) - \text{Vol. of acids added during digestion}(1\text{mL})$$

The identical procedure was followed for powdered pig kidney (BB186), which served as the procedural control reference material (CRM). The same process was also conducted for a procedural blank.

4.4.1.3 Non-procedural Sample Preparation

4.4.1.3.1 Nitric Acid Stock

A nitric acid stock solution was prepared to match the concentration of nitric acid in the test samples (as described in Equation 11), to ensure it was matrix matched. This solution was utilized to prepare the non-procedural blank and calibrants, maintaining a consistent matrix with the test samples.

Equation 11: Representative Nitric stock solution calculation

$$\text{Conc. nitric in test samples } (20 \text{ fold dilution}) = \frac{15 \text{ ml (total vol. sample)}}{0.75 \text{ ml(vol. Nitic used for digestion)}}$$

$$\text{Nitric acid to add } (2.5\text{mL}) = \frac{50\text{mL (Total vol. of stock)}}{20 \text{ (dilution factor in conc. nitric in test samples)}}$$

$$\text{Water to add } (47.5\text{mL}) = 50\text{mL} - 2.5\text{mL nitric acid}$$

4.4.1.3.2 Non-procedural Blank

The non-procedural blank was prepared using the nitric stock solution, to maintain the same matrix as the test samples. The volume of internal standard (Ga) added to the non-procedural blank was calculated to be the same concentration as in the test samples (Equation 12). This blank was used to calculate the limit of detection.

Equation 12: Representative non-procedural blank sample calculation

$$\text{Ga to add (0.5ml)} = \frac{\text{50mL (vol. of blank wanted)} \times \text{50ppb (conc. in all other samples)}}{\text{5ppm Ga (Ga stock conc.)}}$$

$$\text{Nitric acid stock to add (49.5mL)} = \text{50mL-0.5mL of Ga}$$

4.4.1.3.3 Calibrants

Calibration solutions were prepared volumetrically using three stock solutions derived from a ICP-MS multi-element standard solution (TraCERT, Sigma Aldrich) (Equation 13). They were prepared with the nitric stock solution to maintain a consistent matrix with the procedural samples. The volume of internal standard (^{71}Ga) added to each calibrant was calculated to match the concentration found in the test samples (Equation 14). The iron concentration range of the calibrants covered the range of the test samples (0.1–1000 µg Fe/L was sufficient)Table 11.

Equation 13: Representative calculation for calibrant stock solutions

$$\text{Stock solution A (10mg/L Fe)} = \text{0.5mL (multi-element standard solution)} + \text{4.5mL (Nitric acid stock)}$$

$$\text{Stock solution B (1mg/L Fe)} = \text{0.25mL of (stock solution A)} + \text{2.25mL (Nitric acid stock)}$$

$$\text{Stock solution C (0.01mg/L Fe)} = \text{0.025mL of (stock solution B)} + \text{2.475mL (Nitric acid stock)}$$

Equation 14: Representative calculation: Determining the Required Volume of Internal Standard (Ga) required for calibrants preparation.

$$\text{Ga to add (0.15mL)} = \frac{\text{50 ppb (Conc. Ga required)} \times \text{15 ml (vol. calibrants)}}{\text{5ppm Ga (Ga stock conc.)}}$$

Table 11: Representative calculation of calibration solutions

Standard	Fe conc. (µg/L)	Stock in 15mL (mL)	Ga (mL)	Nitric (mL)
1	0.1	0.15 of stock solution C	0.15	14.7
2	1	1.5 of stock solution C	0.15	13.35
3	10	0.15 of stock solution B	0.15	14.7
4	50	0.75 of stock solution B	0.15	14.1
5	100	0.15 of stock solution A	0.15	14.7
6	500	0.75 of stock solution A	0.15	14.1
7	1000	1.5 of stock solution A	0.15	13.35

4.4.1.3.4 Non-procedural CRM (TMDW)

The non-procedural CRM was prepared using Trace Metal Drinking Water (TMDW), which has a known iron concentration. It incorporated the nitric stock solution with concentrated nitric acid to ensure its matrix was consistent with that of the test samples. Since the TMDW stock solution was prepared in 2% nitric acid, additional concentrated nitric acid was required to increase the acid matrix concentration for a uniform match. The volume of internal standard (^{71}Ga) added to the non-procedural CRM was calculated to align with the concentration found in the test samples.

4.4.2 ICP-MS Analysis

All ICP-MS measurements were performed on a NexION 350 ICP-MS Spectrometer (PerkinElmer, Inc) under Helium gas during collision mode and Argon gas during reaction mode. Prior to running the samples, the instrument was tuned to make the necessary adjustments according to manufacturer's instructions. The instrument was calibrated at the beginning of the analysis. A calibration curve (0.1–1000 µg Fe/L) was obtained using calibration solutions with matrix-matched acid reagents. The method was validated by determining linear calibration range, system stability, limit of detection, limit of quantitation (LOQ), and accuracy. The non-procedural CRM (TMDW) was used to evaluate the accuracy of the calibration.

4.4.3 Quantification of Total Cardiac Iron (ug of Fe/g of dry cardiac tissue)

ICP-MS provides numerical data, expressing iron signal intensities in counts per second (CPS). Firstly, the limit of detection was quantified using the standards and non-procedural blank to identify samples below the limit of detection that cannot be quantified. The limit of detection is defined as the lowest concentration that can be distinguished from the non-procedural blank[361]. Iron concentration in each sample then determined comparing the CPS measured for iron against those in the calibration curve, constructed using the calibration solutions. The signal intensities of each sample then matched with the calibration curve to determine the concentration of iron in micrograms per litre (µg /L). The concentration of iron per gram of dry tissue (µg /g) for each sample was calculated using Equation 15. The concentration of iron in the procedural CRM evaluated to assess the accuracy of iron quantification. The iron concentration in the procedural CRM sample was determined to be 255 µg of Fe/g of dry tissue, and a deviation of 10% was considered acceptable. The percentage deviation of iron concentration could be used to correct the iron concentration values of the test samples. Procedural blanks were analysed to determine the presence of iron in the solvents and acids, as well as to gauge contamination levels during sample preparation.

Equation 15: Calculating total cardiac iron concentration (ug/g)

$$\text{Total cardiac iron (ug/g)} = \frac{(\text{Fe}_\text{L}/1000/\text{Density}) \times \text{Digest} \times \text{DF}}{\text{M}_\text{Dry}}$$

Where,

Fe_L = Iron concentration (ug/L)

Density = Density of sample (g/mL)

DF = Dilution factor

Digest = Mass of acid and tissue sample after acid digestion (g)

M_Dry = Mass of tissue sample after drying (g)

4.4.4 Optimisation of the Sample Preparation Protocol

The process of drying cardiac tissue is a crucial step in the sample preparation process because the quantification of total cardiac iron is based on the mass of dry cardiac tissue. A study established the correct initial mass of 'wet' cardiac tissue necessary to yield suitable dry mass values for robust and reproducible quantification of total cardiac iron. The aim to assess whether variations in the starting mass of cardiac 'wet' tissue result in variability in ICP-MS iron concentration measurements.

Control hearts were excised as described in 3.2.7, ground into a fine powder under liquid nitrogen, and stored at -80°C until required. Four 'wet' masses were evaluated from each cardiac sample: 50mg, 100mg, 150mg, and 200mg (Table 12). ICP-MS sample preparation and analysis were conducted on each of these samples, following the procedures outlined in 4.4.1.

Table 12: Assessment of starting cardiac tissue mass.

Cardiac sample	Starting 'wet' mass (mg)			
1	50	100	150	200
2	50	100	150	200
3	50	100	150	200
4	50	100	150	200
5	50	100	150	200
6	50	100	150	200

ICP-MS analysis was conducted to measure the iron concentration in each 'wet' mass group (Figure 29). A one-way ANOVA was performed to assess the impact of the initial 'wet' mass on the measured iron concentration. The analysis indicated a statistically significant difference in iron concentration among at least two groups ($p < 0.05$). Subsequent Tukey's Test for multiple comparisons demonstrated that the mean iron concentration in the 50mg 'wet' mass group was significantly different from all other groups ($p < 0.05$). However, there was no statistically significant difference among the 100mg, 150mg, and 200mg 'wet' mass groups.

Simple linear regression was used to assess if the resultant dry mass values (obtained after drying the 'wet' mass samples as part of the ICP-MS preparation process) had a significant impact on the measured iron concentration by ICP-MS (Figure 30). The overall regression was statistically significant ($R^2 = 0.4729$, $F(1, 22) = 19.74$, $p < 0.05$), whereby the slope is significantly non-zero ((95% Confidence Interval: -2.648 to -0.9625, P-value: <0.05) (Figure 30, c). This indicates a significant influence of dry mass values on iron concentration. However, it was evident that the 50mg 'wet' mass group was responsible for this systematic offset, as demonstrated in Figure 29 and in Figure 30, b. When the linear regression analysis excluded the 50mg 'wet' mass group, the slope became insignificantly non-zero (95% Confidence Interval: -1.625 to 0.6630, P-value: 0.386).

Errors in weighing are amplified in smaller mass samples. The 50mg 'wet' mass group was the smallest mass category, leading to correspondingly smaller dry masses. Any error in measuring this small mass is consequently magnified, likely accounting for its offset. Thus, it can be inferred that the initial 'wet' mass significantly impacts total cardiac iron measurements. Samples derived from 'wet' tissue masses below 100mg are prone to inaccuracies. Consequently, all ICP-MS analyses utilized a starting 'wet' mass of >100mg to determine total cardiac iron.

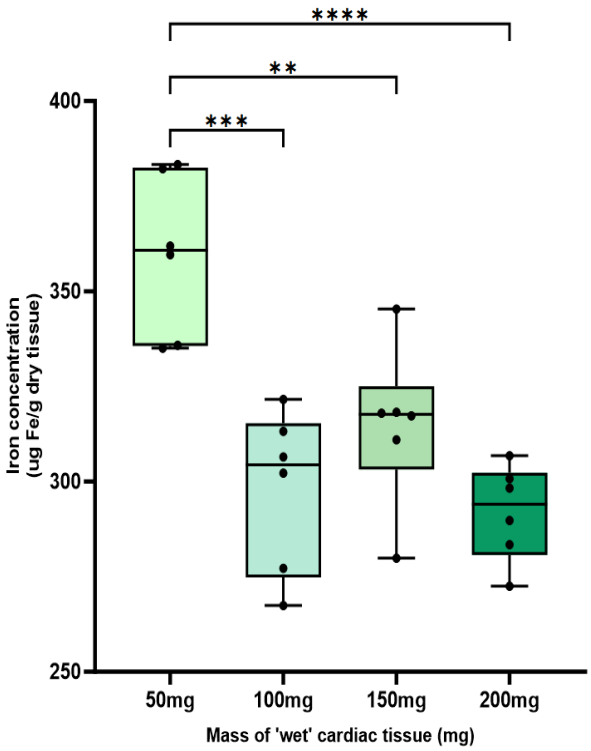

Figure 28: Evaluating variability in ICP-MS iron concentration measurements, dependent on starting cardiac 'wet' tissue mass. Statistical analysis was conducted using a one-way ANOVA ($p < 0.05$).

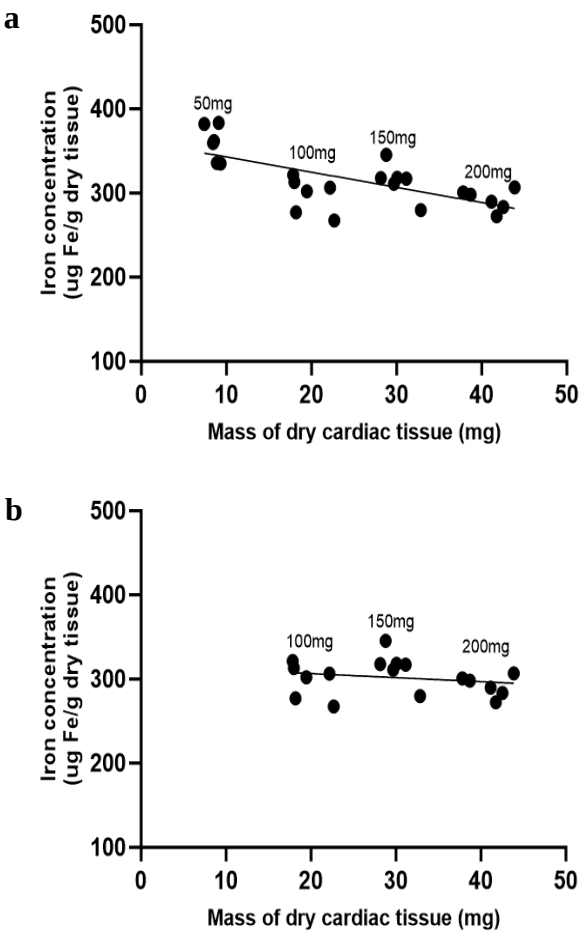

Figure 29:Concentration of iron in various masses of dry cardiac tissue (mg). a A simple linear regression analysis of all starting 'wet' mass groups tested (95% CI: -2.648 to -0.9625, P-value: <0.05). **b** Linear regression analysis excluding the 50mg 'wet' weight mass group (95% CI: -1.625 to 0.6630, P-value: 0.386). Annotation of clusters refer to the starting 'wet' cardiac mass they correspond to.

4.4.5 Evaluating Total Cardiac Iron Variability in Control Rats

Biological repeat studies were conducted to assess the variability of total cardiac iron in control heart samples. The first study was performed on a group of age-matched control animals (n=6). A second more comprehensive retrospective biological repeat study was carried out comprising a larger sample size of 43 control rats. These rats were compiled from *in vivo* studies conducted as part of this PhD research. Hearts were excised from the control animals and processed following the previously described method (3.2.7). ICP-MS sample preparation and analysis was performed on each of these samples as described in 4.4.1. The limit of detection was calculated as 0.05 ppb. The variability in total cardiac iron concentration in the higher-powered biological repeat study was

determined (Figure 31); Iron ± SD: 270.9 ± 46.87 ug Fe/g dry tissue, Range: 144.7, 195.6 to 340.3 ug Fe/g dry tissue. These total cardiac iron values are consistent with those reported in the literature[362][363]. These values can serve as a 'Reference Interval,' establishing a benchmark for control concentrations of total cardiac iron. Therefore, they can be used to evaluate the development of the iron overload models by contextualizing the iron overload they induce.

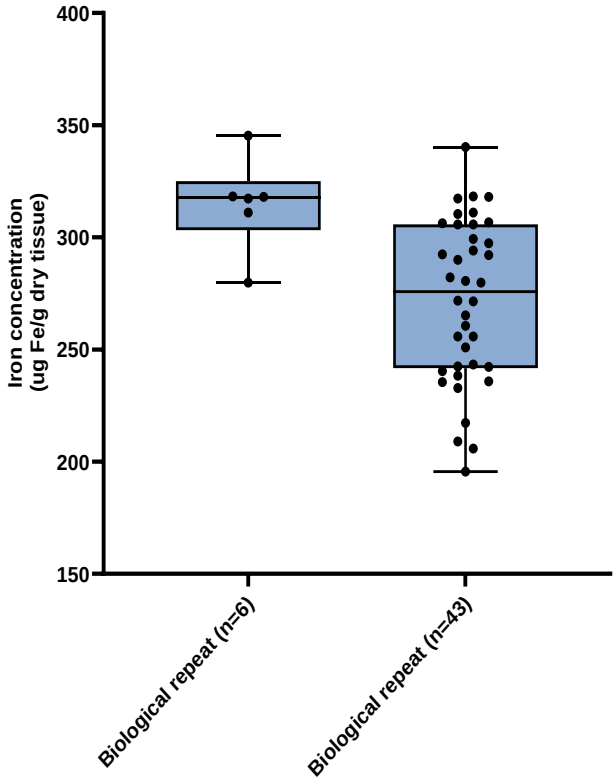

Figure 30: A biological repeat study (n=6 and n=43) to evaluate the variability of total cardiac iron in control cardiac tissue.

4.5 Mitochondrial Isolation for Iron Analysis Using ICP-MS

ICP-MS was used to obtain absolute quantification of mitochondrial iron in rodent cardiac tissue (expressed as µg of iron per g of protein). Intact mitochondria were first isolated from cardiac tissue using the differential centrifugation method.

Differential centrifugation is a widely used technique based on 1) homogenisation of the cardiac sample followed by 2) sequential centrifugation of tissue homogenates at increasing speed. Differential centrifugation results in the separation of organelles according to their size and sedimentation velocity. This method was selected as it is inexpensive and relatively fast. Isolated mitochondria have even been shown to be pure enough for respirometry assays[364].

A two-step centrifugation method was chosen to minimise the possibility of environmental iron contamination by isolating mitochondria using the fewest possible steps while ensuring an adequate level of enrichment.

A key consideration in the choice of method, was the potential for isolated mitochondria to become contaminated with other cellular components. An evaluation of the isolation protocol was conducted assessing the purity of the isolated mitochondria. A western blot analysis was performed to gauge the quality of fractionation. The presence of cytosolic and lysosomal contamination was examined using specific proteins: GAPDH (cytosol) and LAMP1 (lysosome). The mitochondrial enrichment of the isolated fractions was assessed employing mitochondrial-specific proteins: VDAC (outer mitochondrial membrane) and SDHA (mitochondrial intermembrane space) (See 3.4).

Quantifying mitochondrial iron concentration is challenging. Weighing the mitochondrial pellet is prone to measurement inaccuracies due to its small mass. This section describes the considerations in developing the most appropriate approach.

4.5.1 Isolating Mitochondria via Differential Centrifugation

4.5.1.1 Materials and Reagents

Purified, trace-metal free water (MilliQ – resistivity ≥18.2 MΩ cm) was obtained from a Millipore Elix 3 system (Merck Millipore). The isolation buffer reagents (250 mM sucrose, 2 mM EDTA, 100 mM Tris-HCl (pH 7.4)) were purchased from Sigma Aldrich; the isolation buffer was made fresh on the day, pH adjusted to 7.8, and kept on ice throughout the isolation procedure. A 1ml glass Dounce homogenizer, with a loose-fitting pestle, was purchased from Generon (1984-10002).

4.5.1.2 Methodology

A two-step differential centrifugation method was used to isolate mitochondria; a low-speed centrifugation was used to remove cell/tissue debris and nuclei from whole cardiac tissue, followed by a high-speed centrifugation to concentrate mitochondria and separate them from other organelles. The mitochondrial isolation procedure was always performed over ice.

Hearts were harvested as described in 3.2.7. For each sample, 50 mg of cardiac tissue was transferred into a pre-prepared 1.5 mL Eppendorf containing 1mL of isolation buffer (3.3.1).

The solution then transferred to a glass Dounce homogeniser, and the sample homogenised until smooth using 10 strokes of a loose-fitting pestle. The homogenate was then transferred to a 1.5 mL Eppendorf vial. To ensure full transfer of tissue, 250 uL of isolation buffer was added to the glass Dounce homogeniser.

The sample was then centrifuged at low speed (600 xg for 10 mins, 4°C). The resulting pellet (containing cellular debris and nuclei) was discarded, and the supernatant was split; each portion transferred to a 1.5mL Eppendorf vial and both centrifuged at high speed (11000 xg for 10 mins, 4°C). The supernatant (consisting mainly of cytosol and lysosome) was discarded, and the two resultant mitochondrially enriched pellets were washed. One pellet was used for ICP-MS analysis, and the other for a BCA assay to determine the protein concentration in the sample. The iron concentration of the mitochondria in the pellet allocated for ICP-MS analysis (μg of Fe/mg of protein) was calculated using the protein content calculated in the pellet assigned for the BCA assay.

4.5.1.2.1 Methodology Considerations

Mitochondrial iron concentration couldn't be calculated using dry weight; drying and weighing the mitochondrial pellet would be inappropriate due to the heightened risk of measurement inaccuracies associated with its small mass. Therefore, quantifying mitochondrial iron concentration by protein content is a more suitable option.

Two approaches were considered to determine protein content in the mitochondrial pellet: 1) Splitting the mitochondrial pellet, and 2) splitting the supernatant after the first centrifugation and pelleting down two mitochondrial fractions. In both approaches, the iron concentration of the mitochondria in one portion is determined using the protein concentration calculated in the other portion.

Method 1 was rejected due to several limiting factors. Firstly, resuspension of the mitochondrial pellet is necessary to divide it. The portion of the resuspended pellet allocated for ICP-MS analysis would contribute to matrix mis-match effects. It would be challenging to match the resuspended mitochondrial sample matrix with the other ICP-MS samples (procedural blanks and non-procedural samples).

In Method 2, no resuspension is necessary, the isolated mitochondrial pellet designated for ICP-MS analysis can be directly subjected to the thermal digestion step in the ICP-MS sample

preparation process. Achieving accurate splitting is challenging due to the lack of complete homogeneity in the resuspension of the mitochondrial pellet. Splitting at the supernatant stage can be accomplished reliably and accurately since it is completely homogeneous. Moreover, this approach carries a reduced risk of introducing iron contamination to the ICP-MS allocated sample compared to the potential contamination risks associated with the resuspension process.

Considering these factors, method 2 was selected to produce two mitochondrial pellets. One of them was designated for ICP-MS analysis, and the other was allocated for a BCA assay (Figure 32).

4.5.2 Determining the Optimal ICP-MS:BCA Supernatant Volume Ratio for Quantifying Mitochondrial Iron using ICP-MS

As described in 4.5.1.2.1, two mitochondrial pellets are derived from splitting the supernatant after the first centrifugation step of the mitochondrial isolation protocol (Figure 32). It is preferable to allocate the majority of this supernatant to the generation of the mitochondrial pellet allocated for ICP-MS analysis.

However, to ensure that the mitochondrial pellet allocated for protein analysis allowed sufficient protein to be measured by the BSA assay. The highest ICP-MS:BCA volume ratio of the supernatant that could be used was derived from BCA assay analysis of varying volumes of supernatant.

The following percentages of the total supernatant volume were centrifuged to generate mitochondrial pellets: 50%, 40%, 30%, 20%, and 10%. The protein concentration of each pellet was measured, which resulted in 140.91, 123.59, 124.82, 129.56, and 22.73 ug of protein/ml of resuspended mitochondrial pellet, respectively. Deriving a mitochondrial pellet from a 10% volume of the supernatant was rejected due to its lower protein concentration compared to the other percentage volumes. For the 50%, 40%, 30%, and 20% supernatant volumes tested, little variation in the protein concentration in the resulting mitochondrial pellets was measured. Therefore, obtaining a mitochondrial pellet from a 20% volume of the supernatant was chosen as optimal, representing the lowest volume of supernatant from which the measured protein concentration did not diminish.

This for the analyses, an ICP-MS:BCA supernatant volume ratio of 4:1 was used to derive the two mitochondrial pellets.

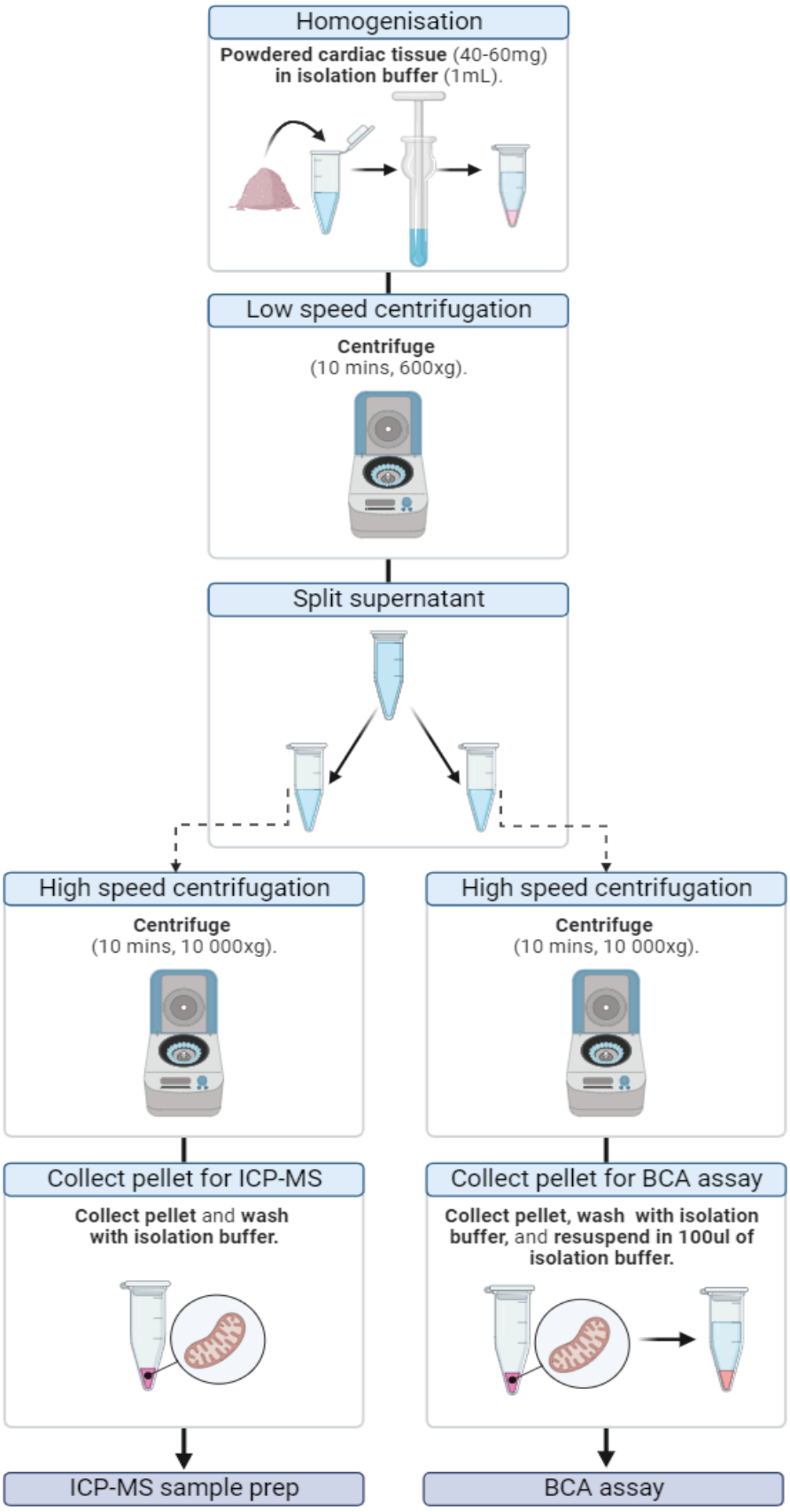

Figure 31: Mitochondrial isolation protocol schematic. [Figure made in BioRender]

4.5.3 Optimization of the Mitochondrial Isolation Method: the Preservation of Mitochondrial Integrity

One of the significant concerns associated with the differential centrifugation technique is the potential damage to the integrity of mitochondria during the homogenization step of the isolation process. The impact of different stroke numbers of the Dounce homogenizer during the homogenization step of the isolation procedure was evaluated for its effect on mitochondrial integrity. The purity of the mitochondrial isolation was also assessed. Four stroke number groups were tested: 10, 20, 30, and 40. Western blot analysis of the isolated mitochondria obtained from each stroke test group was performed using a Trans-Blot Turbo Transfer System (Bio-Rad Laboratories, Inc.). The integrity of the isolated mitochondria was evaluated by examining specific organelle contamination in the final mitochondrial pellet (Pellet $2_{ICP\text{-}MS}$, D) (Figure 33). Organelle-specific proteins VDAC (outer mitochondrial membrane) and GAPDH (cytosol) were used to assess contamination in the mitochondrial fractions.

For context, other fractions generated during the mitochondrial isolation process were also investigated by western blot: The whole tissue sample (A), the pellet produced after the first centrifugation (Pellet 1, B), and the supernatant collected after the second centrifugation (Supernatant $2_{ICP\text{-}MS}$, C).

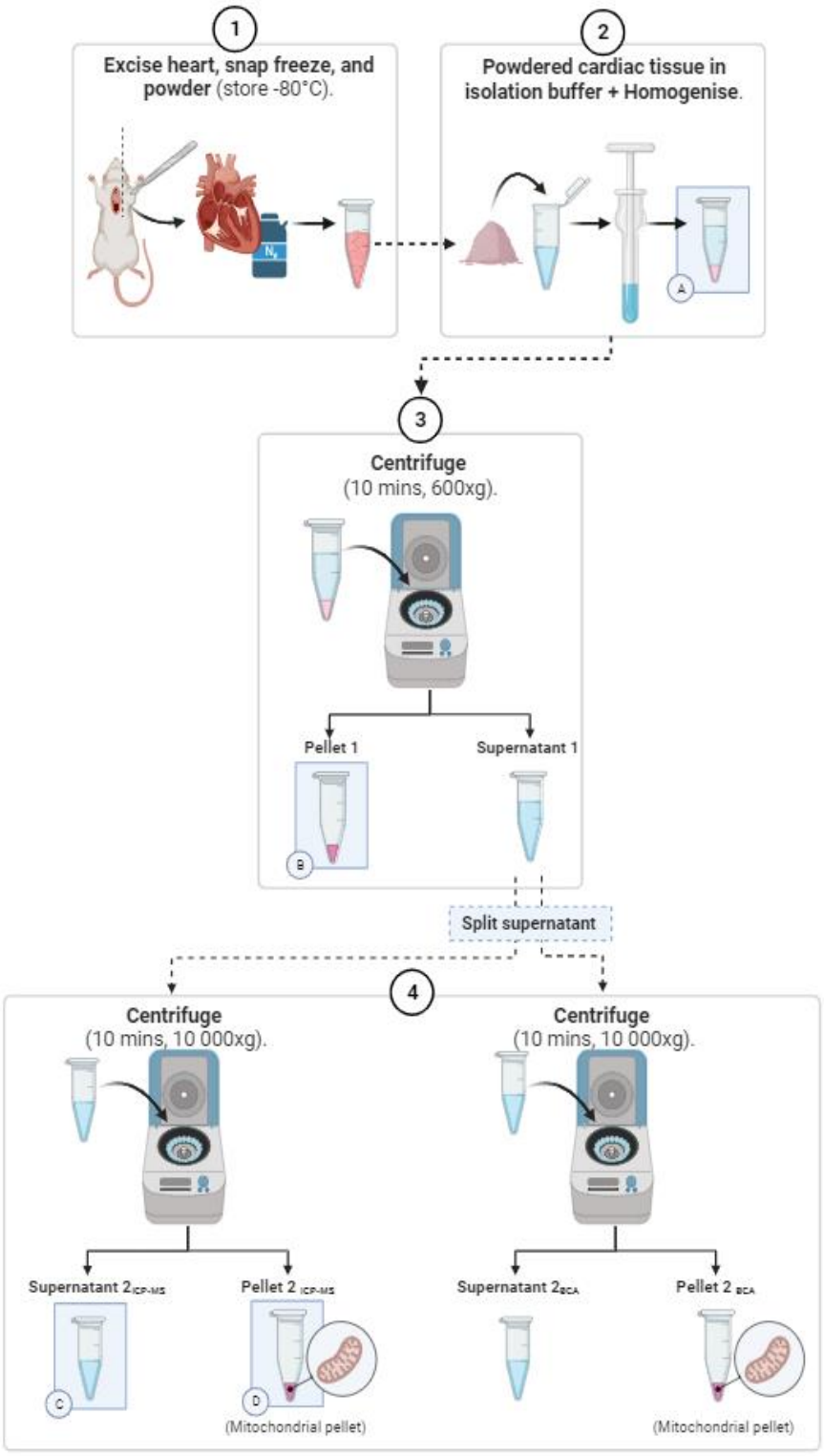

Figure 32: Mitochondrial isolation protocol schematic reference for optimisation studies. The labelled fractions in blue boxes were collected for mitochondrial isolation optimisation assessments: A) Whole tissue B) Pellet 1 (Cell debris and nuclei) C) Supernatant $2_{ICP\text{-}MS}$ (Plasma membrane, lysosomes, microsomes and cytosol) D) Pellet $2_{ICP\text{-}MS}$ (Crude mitochondrial fraction). [Figure made in BioRender]

The expression of both mitochondrial and cytosolic proteins in the fractions collected during the isolation procedure are presented in Figure 34.

In the 10, 20, and 30 stroke groups both mitochondrial and cytosolic proteins were present in the whole tissue group. This was expected as cardiac cells undergo lysis during the western blot analysis, exposing mitochondrial and cytosolic proteins for detection. Mitochondrial proteins were detected in Pellet 1 due to their size and density. The homogenization step mechanically disrupts the cardiac cells, and this cell lysis causes mitochondria, along with other cellular debris, to concentrate and form Pellet 1. The inference being that the cytosolic proteins concentrate in the initial supernatant after the first centrifugation step, which is then collected and spun down during the second centrifugation. Therefore, these cytosolic proteins are not expressed in Pellet 1. Supernatant $2_{ICP\text{-}MS}$ shows expression of both mitochondrial and cytosolic proteins, whereas there is only mitochondrial protein expression in pellet $2_{ICP\text{-}MS}$. Pellet $2_{ICP\text{-}MS}$ also displays greater mitochondrial expression compared to supernatant $2_{ICP\text{-}MS}$.

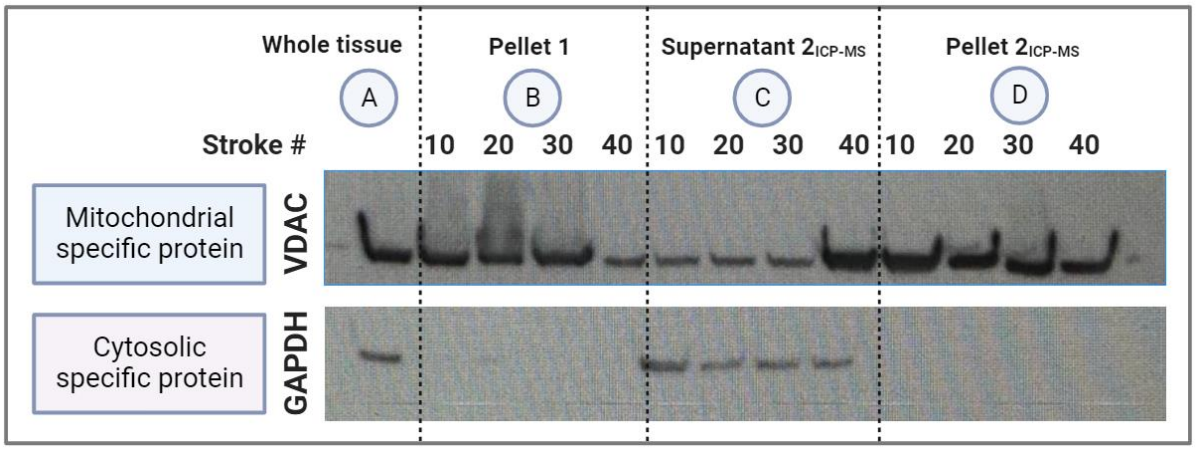

Figure 33: Mitochondrial integrity evaluation based on number of Dounce homogeniser strokes (10, 20, 30, 40) during the isolation. A western blot a\n analysis of mitochondrial and cytosolic contamination was conducted to assess mitochondrial integrity. The following organelle specific proteins were used: VDAC (outer mitochondrial membrane protein) and GAPDH (cytosol protein). A) Whole tissue B) Pellet 1 (Cell debris and nuclei) C) Supernatant $2_{ICP\text{-}MS}$ (Plasma membrane, lysosomes, microsomes and cytosol) D) Pellet 2 $_{ICP\text{-}MS}$ (Mitochondrial fraction).

In the 40-stroke group the mitochondrial protein expression is greater in supernatant $2_{ICP\text{-}MS}$ and decreased in pellet $2_{ICP\text{-}MS}$ compared to the other stroke groups, suggesting that the 40-stroke homogenization was detrimental to mitochondrial integrity. We therefore concluded the 10-stroke group with two-step differential centrifugation was the most effective means of isolating intact mitochondrial from cardiac tissue in the future experiments.

4.5.4 Evaluating Isolated Mitochondrial Quality through Organelle-Specific Protein Analysis

Western blot analysis was performed on mitochondria isolated from cardiac tissue (n=5) using a Trans-Blot Turbo Transfer System (Bio-Rad Laboratories, Inc.). To assess organelle contamination and mitochondrial enrichment, the isolated mitochondrial samples were probed for the following protein expression: VDAC (outer mitochondrial membrane protein), SDHA (mitochondrial intermembrane space protein), GAPDH (cytosolic protein), and LAMP 1 (lysosomal protein). To provide context for evaluating mitochondrial enrichment and organelle contamination in the isolated mitochondrial pellet (pellet $2_{ICP\text{-}MS}$, D), other fractions generated during the mitochondrial isolation process were also subjected to western blot analysis. These included the whole tissue sample (A), the pellet produced after the first centrifugation (Pellet 1, B), and the supernatant collected after the second centrifugation (Supernatant $2_{ICP\text{-}MS}$, C) (Figure 35).

In the whole tissue group, the expression of all probed proteins was detected. This was expected because the western blot analysis involved lysing the cardiac cells, exposing all cellular proteins for detection. Both mitochondrial-specific proteins (VDAC and SDHA) were expressed in Pellet 1. The presence of these proteins in Pellet 1 can be attributed to the lysis of cardiac cells caused by EDTA within the isolation buffer. Consequently, some mitochondria and lysosomes (as they are relatively large organelles), along with other cellular debris, concentrated to form the initial pellet. The cytosolic proteins are presumed to concentrate in the initial supernatant obtained after the first centrifugation. This first supernatant is further processed (spun down) during the second centrifugation step, leading to the absence of cytosolic protein expression in Pellet 1. Supernatant $2_{ICP\text{-}MS}$ exhibits expression of both lysosomal and cytosolic proteins, with negligible mitochondrial protein expression. In pellet $2_{ICP\text{-}MS}$, both mitochondrial proteins are expressed, and notably, their expression is enriched compared to that observed in supernatant $2_{ICP\text{-}MS}$. Compared to supernatant $2_{ICP\text{-}MS}$, there is reduced lysosomal contamination in pellet $2_{ICP\text{-}MS}$ and a negligible cytosolic protein expression.

The mitochondrial isolation method evaluated here yields a crude mitochondrial fraction (pellet $2_{ICP\text{-}MS}$). While it is possible to introduce additional centrifugation steps to isolate a purer mitochondrial fraction, each added step raises the risk of iron contamination. The two-step mitochondrial centrifugation isolation method produces a pellet that is mitochondrially

enriched, with reduced levels of cytosolic and lysosomal organelle contamination. Therefore, this method was deemed appropriate for the mitochondrial isolations.

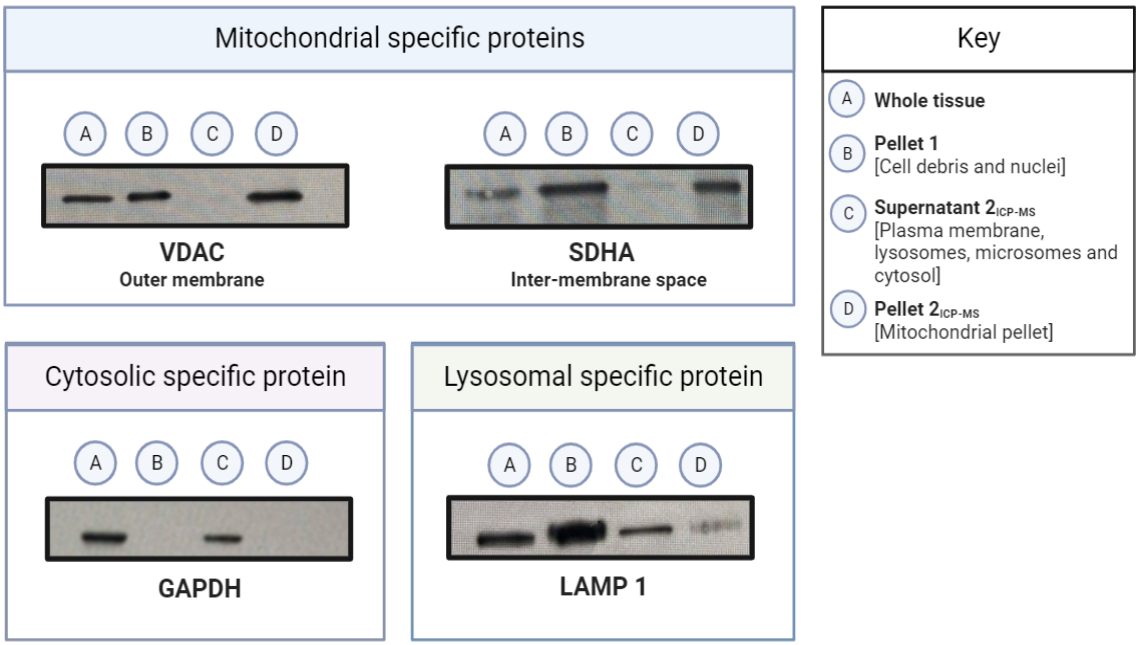

Figure 34: Representative images of western blots assessing the quality of mitochondrial isolations. Isolated mitochondria are assessed for organelle contamination and mitochondrial enrichment.

4.6 ICP-MS Based Quantification of Mitochondrial Iron

The ICP-MS-based quantification of total mitochondrial iron in cardiac tissue required the preparation of procedural (test samples and procedural blanks) and non-procedural samples (Non-procedural CRM, non-procedural blank, and calibrants) (Figure 36). The purpose of each sample type required for ICP-MS analysis was outlined in (Table 10).

The preparation of procedural samples is comprised of two steps: 1) Thermal acid digestion and 2) Dilution. The quantification of mitochondrial iron is calculated using mg of protein, thus, the drying step in the total cardiac iron workflow is unnecessary here. The digestion of isolated mitochondria carried out using conc. acid (HNO_3) at 50°C.

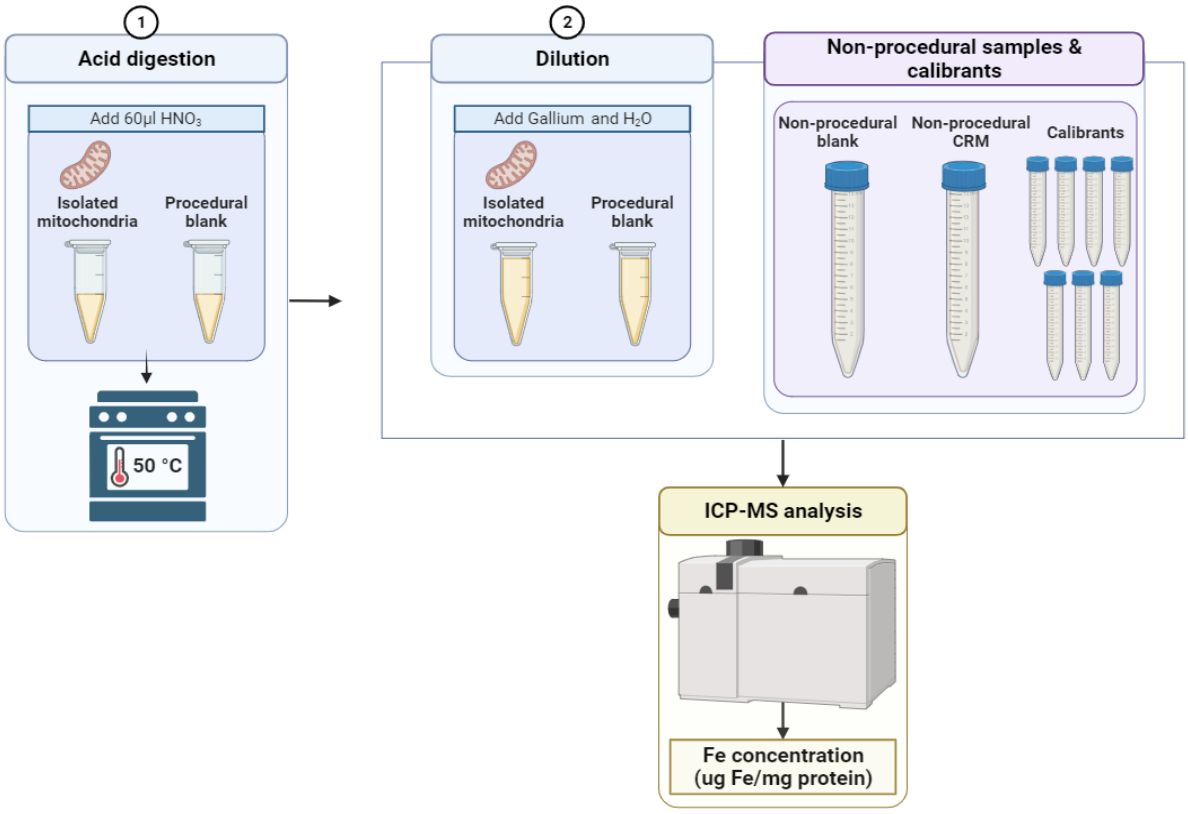

Figure 35: Workflow required for the ICP-MS based quantification of mitochondrial cardiac iron. CRM; Control reference material. [Figure made in BioRender]

4.6.1 Sample Preparation for ICP-MS Analysis of Mitochondrial Iron

4.6.1.1 Materials and Reagents

For the preparation and processing of samples ultra-high-purity grade acids were used; Optima grade HNO_3 (67–69% w/w; Fisher Scientific). Purified, trace-metal free water MilliQ – resistivity ≥18.2 MΩ cm obtained from a Millipore Elix 3 system (Merck Millipore) was used for all solution preparations. The calibration standards for iron made using multi elemental standard solution purchased from Sigma Aldrich (TraCERT ICP-MS multi-element standard solution VI (100 ppm)); all standard solutions were prepared fresh daily before the ICP-MS analysis. The Ga internal standard was purchased from Leeman Labs (100 ppm). High Purity Standards Trace Metal Drinking Water (CRM HPS TMDW) used as the non-procedural CRM. All ICP-MS measurements were performed on a NexION 350 ICP-MS Spectrometer (PerkinElmer, Inc). The following gases were used for the collision/reaction cell in ICP-MS: Helium gas (>99.999% purity) and pre-purified grade Argon (>99.999% purity) Procedural sample preparation

Thermal acid digestion: Each sample underwent thermal acid digestion. For this, 60µL of Optima grade concentrated HNO_3 (67–69% w/w; Fisher Scientific) was added to each sample. To allow the initial reaction to settle, the samples were left to stand at room temperature for 30 minutes. During the 30-minute standby period, the Eppendorfs were left uncapped to allow CO_2 to escape. Whilst the samples were uncapped, they were placed within a larger plastic box to protect the samples from contamination. Once the initial reactions had subsided, the tubes were then capped and placed in an oven at 50 °C to digest overnight.

Dilution: The digested samples were removed from the oven and allowed to cool at room temperature. Using trace metal grade ultrapure water and Gallium (^{71}Ga) as an internal standard (diluted from a 100-ppm stock solution, Leeman Labs Ltd), each sample was diluted to a total volume of 1.2µL. A representative dilution is described in Equation 16.

Equation 16: Representative ICP-MS sample dilution

$$\text{Ga to add } (1.2\mu L) = \frac{\text{Total vol. of sample } (1.2\mu L) \times 50 \text{ ppb (Conc. Ga required)}}{5\text{ppm Ga (Ga stock conc.)}}$$

$$\text{Water to add}(1128\mu L) = \text{Total vol. of sample}(1.2\mu L) - \text{Ga}(12\mu L) - \text{Vol. of acids added during digestion}(60\mu L)$$

The exact same procedure was carried out for the procedural blanks.

4.6.1.2 Non-procedural Sample Preparation

All non-procedural sample preparation was conducted as described for in the total tissue analysis (4.4.1.3).

4.6.2 ICP-MS Analysis

ICP-MS analysis was performed as described for in the total tissue analysis in (4.4.2).

4.6.3 Quantification of mitochondrial iron (ug of Fe/mg of protein)

ICP-MS provides numerical data, expressing iron signal intensities in counts per second (CPS). Iron concentration in each sample was determined by comparing the measured CPS for iron against those on the calibration curve, constructed using calibration solutions. The sample signal intensities then matched with the calibration curve to ascertain iron concentration in micrograms per Liter (ug/L). Iron concentration per microgram of protein (ug/mg) for each sample was calculated using Equation 17. The sample protein concentration determined through a BCA assay. Procedural blanks analysed to assess iron presence in solvents and acids and to gauge contamination levels during sample preparation. These blanks also served for iron quantification correction purposes.

Equation 17: Calculating mitochondrial iron concentration (ug/mg)

$$\text{Mitochondrial iron (ug/mg)} = \frac{Fe_L}{(P/DF)} \times 1000$$

Where,

Fe_L = Iron concentration (ug/L)

P = protein concentration (ug/L)

DF = Dilution factor

4.6.4 Evaluating Total Mitochondrial Cardiac Iron Variability in Control Rats

To evaluate the variability of total mitochondrial cardiac iron in control heart samples a biological repeat study was conducted. An initial study involving age-matched control animals (n=6) was performed. Subsequently, a more comprehensive retrospective biological repeat study was undertaken, comprising a larger sample size (n=48). These rats were compiled from *in vivo* studies conducted as part of this PhD research. The control hearts were excised as described previously (3.2.7), ground into a fine powder under liquid nitrogen, and stored at -80°C until required. The mitochondrial isolation and the ICP-MS sample preparation and

analysis was performed as described in 4.5. The variability of mitochondrial iron concentration was assessed in control animals (Figure 37).

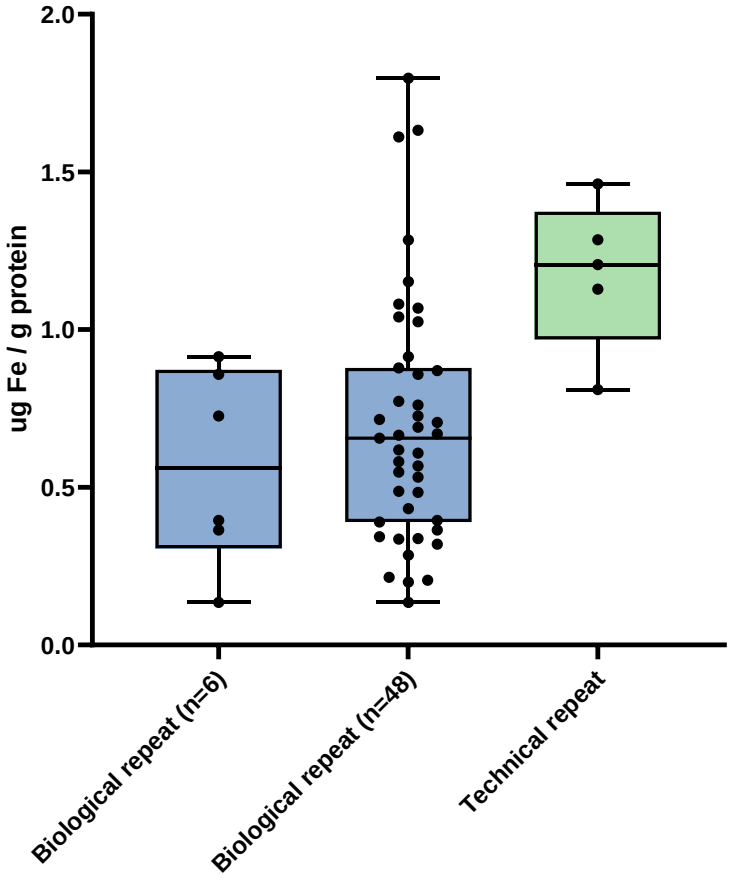

Figure 36: ICP-MS-based quantification of mitochondrial iron (ug Fe/g protein). A biological repeat study (n=6 and n=43) and a technical repeat (n=6).

For the higher-powered biological repeat study, the recorded iron measurements were as follows: Iron ± SD: 0.7 ± 0.4 ug Fe/mg protein, with a range from 0.1 to 1.8 ug Fe/mg protein. The mitochondrial iron values measured by ICP-MS can be utilized as a 'Reference Interval' for mitochondrial iron concentration in control rats. To our knowledge, the method developed for quantifying mitochondrial iron, combining the optimized mitochondrial isolation method with ICP-MS-based analysis, is not described elsewhere in the literature.

A technical repeat study was conducted assessing the variability of the mitochondrial isolation protocol. A control heart was excised, and five mitochondrial pellets were isolated from the cardiac sample, processed, and analysed identically to those in the biological repeat study. The variability of mitochondrial iron concentration was determined in the mitochondrial samples (Figure 37); Coefficient of variation: 20.4%. The variation in mitochondrial iron concentration

of this technical repeat analysis (0.18097 to 1.463 ug Fe/mg protein) falls within the mitochondrial iron ‘Reference interval’, and therefore considered acceptable.

4.7 Discussion

A robust and reproducible method for the quantification of total and mitochondrial cardiac iron is fundamental to characterise the interrelationship between cardiac iron and metabolic dysfunction in DOX-induced cardiotoxicity. This chapter described the development of sample preparation protocols for the quantification of total iron concentration in cardiac tissue and mitochondrial samples. The following summarises the conclusions and implications of this chapter:

4.7.1 ICP-MS Limitation Mitigation Strategies

The limitations of ICP-MS and strategies to mitigate these limitations were considered. ICP-MS is highly sensitive but can be limited by interferences, categorized as spectral or non-spectral[365]. Spectral interferences arise from overlapping m/z ratios of non-target analyte ions with the target analyte. Non-spectral interferences include matrix effects and instrument drift[322]. Matrix effects are changes in instrument sensitivity caused by sample matrix constituents. Instrument drift, progressive signal reduction during ICP-MS runs due to deposit buildup[355].

The following strategies enhanced the accuracy and reliability of ICP-MS analysis, in the context of trace-level iron measurements and potential contamination challenges.

4.7.1.1 Spectral Interferences

Spectral interferences were mitigated using the collision/reaction cell in collision mode. This involved the introduction of an inert gas (He) and kinetic energy discrimination (KED). The collision cell causes collisions between ions, leading to energy loss. Only ions with higher energy, such as the target analyte, pass through[325]. The cell can also operate in reaction mode using a reactive gas (NH_3) to eliminate isobaric interferences.

4.7.1.2 Non-Spectral Interferences

Samples are diluted with HNO_3 and H_2O during preparation to reduce matrix effects and minimize instrumental drift. Gallium (^{71}Ga) has similar properties to iron and used as an internal standard. Ga concentrations are kept consistent across samples to correct for matrix effects and signal fluctuations. Calibration standards with known iron concentrations are matrix-matched to the samples by using similar volumes of HNO_3 and H_2O during sample preparation.

4.7.1.3 Sample Contamination Mitigation

During cardiac tissue harvest, perfusion with PBS/saline is performed to minimize contamination by red blood cells. Trace metal grade ultrapure water, nitric acid, and hydrochloric acid used to avoid contamination from labware and reagents. Pipette tips and sample tubes pre-cleaned to minimize contamination risks. An ICP-MS dedicated clean room facility is utilized, when possible, to reduce contamination from dust and airborne particles. All sample preparation is conducted within a fume hood. Quality control samples are periodically analysed alongside test samples to monitor contamination, and procedural samples are run before test samples to prevent autosampler-induced cross-contamination.

4.7.2 Optimization of the Sample Preparation Protocol for ICP-MS Iron Analysis of Cardiac Tissue

The cardiac tissue drying process plays a crucial role in the quantification of total cardiac iron, a central parameter for iron concentration assessment. The aim to determine the appropriate starting mass of 'wet' cardiac tissue that would ensure accurate and reproducible quantification of total cardiac iron using ICP-MS analysis.

The influence of varying starting 'wet' cardiac tissue masses (ranging from 50mg to 200mg) on the quantification of iron concentration by ICP-MS was systematically evaluated. Statistical analysis using one-way ANOVA revealed a significant difference in iron concentration between at least two groups ($p < 0.05$) and Tukey's Test showed significant differences between the 50mg 'wet' mass group and all other groups. No significant difference was found in iron concentration between the 100mg, 150mg, and 200mg ‘wet’ mass groups. Simple linear regression assessed if the dry mass values (obtained after drying the "wet" mass samples) significantly affected the iron concentration measured by ICP-MS. The regression showed that

dry mass values do significantly influence iron concentration. However, the 50mg "wet" mass group was responsible for this systematic offset. When this group was excluded from the analysis, the slope became insignificantly non-zero, indicating that the other "wet" mass groups did not show a significant influence.

Errors in weighing are known to be more pronounced in smaller mass samples and weighing errors are markedly propagated in samples of smaller masses. This was the case for the 50mg "wet" mass group and explains the systematic offset observed. It was concluded that starting 'wet' mass is a critical factor in measuring total cardiac iron and that error propagation was more pronounced in smaller mass samples, notably within the 50mg group.

For all ICP-MS analyses, a starting "wet" mass of greater than 100mg was used.

4.7.3 Variability in Cardiac Iron Concentration Measurements by ICP-MS

A biological repeat study assessed the variability of total cardiac iron in control heart samples (n=43). ICP-MS analysis was performed. The results yielded a mean iron concentration of 272 ± SD 36.42 µg Fe/g dry tissue, with a range of 195.5 µg Fe/g dry tissue to 340.2 µg Fe/g dry tissue. These values align with literature[362][363], confirming the reliability of the approach and establishing a reference interval for normative cardiac iron content in control settings. The reference interval functions as a benchmark for contextualizing variations in iron concentrations in future *in vivo* studies, especially of iron overload models.

4.7.4 Isolation of Mitochondria for ICP-MS Iron Analysis

The objective to establish an accurate and reproducible method for determining mitochondrial iron levels by ICP-MS, while addressing challenges related to isolation purity, mitochondrial integrity, and potential contamination.

The isolation of intact mitochondria for ICP-MS analysis was achieved using a two-step differential centrifugation method. To ensure the purity of isolated mitochondria and to assess potential cellular contamination, a Western blot analysis was conducted. Specific organelle proteins (GAPDH for cytosol, LAMP1 for lysosome, VDAC and SDHA for mitochondria) were used to probe for contamination and mitochondrial enrichment. The successful isolation of mitochondria was achieved. Differential centrifugation yielded mitochondrially enriched

pellets with minimal cytosolic and lysosomal contamination, suitable for future mitochondrial isolations.

The impact of the number of strokes during the homogenization step on mitochondrial integrity was evaluated. Western blot analysis was used to assess the expression of mitochondrial and cytosolic proteins. Through testing different stroke numbers during homogenization (10, 20, 30, and 40), a 10-stroke homogenization procedure was identified as optimal for maintaining mitochondrial integrity, evidenced by the expression of mitochondrial protein and negligible cytosolic protein expression.

Unlike total cardiac iron, which is calculated based on dry tissue weight, mitochondrial iron concentration is calculated based on protein content. To counter the challenges associated with measuring small mass samples, a shift from traditional dry mass-based calculations to a protein content-centric approach was used, enhancing the accuracy and reliability of mitochondrial iron quantification. Two approaches to determine protein content in the mitochondrial pellet were considered: splitting the final mitochondrial pellet and splitting the supernatant after the first centrifugation. The latter method was preferred for its practicality and reduced risk of contamination.

The optimal ratio of ICP-MS supernatant to BCA supernatant volume was determined to ensure sufficient protein in the final pellet for analysis while also minimizing the risk of iron contamination. The optimal ICP-MS:BCA supernatant volume ratio was determined as 4:1.

The analysis of our optimised mitochondrial isolation protocol produces mitochondrial isolations with sufficient purity and mitochondrial integrity. This method was used for all mitochondrial isolations in this thesis.

4.7.5 Variability in Mitochondrial Iron Concentration Measurements by ICP-MS

A biological repeat study was undertaken to assess the natural variation in mitochondrial iron levels in control cardiac samples. The mitochondrial isolation and subsequent ICP-MS analysis were carried out as detailed in sections 4.5 and 4.6. The investigation revealed that the mitochondrial iron concentration in control cardiac tissue had a mean of 0.6967 ± 0.3908 µg Fe/mg protein, with a range spanning from 0.1352 µg Fe/mg protein to 1.797 µg Fe/mg protein. These measurements establish a 'Reference Interval' for mitochondrial iron concentration in control animals. The mitochondrial reference interval, as for the total cardiac iron reference

interval, acts as a benchmark for interpreting fluctuations in mitochondrial iron concentrations in future *in vivo* studies, particularly in the development of iron overload models. This contextual information is essential for comprehending the cardiac iron overload induced by these models.

A technical repeat study was conducted to evaluate the variability of the mitochondrial isolation protocol. The investigation revealed a range of variability in mitochondrial iron concentration of 0.6526 µg Fe/mg protein. This range, spanning from 0.18097 µg Fe/mg protein to 1.463 µg Fe/mg protein, falls within the established 'Reference Interval' for mitochondrial iron concentration, indicating that the technical repeat analysis results are deemed acceptable.

4.7.6 Summary

In summary, this chapter optimized the precision of ICP-MS for cardiac iron analysis with strategies implemented addressing spectral and non-spectral interferences, reduce contamination risks, and enhance sample preparation protocols.

Spectral interferences were mitigated through collision/reaction cell usage. Non-spectral interferences countered via dilution, internal standardization with gallium, and matrix-matched calibration standards. Minimizing contamination risks involved careful tissue harvesting, employing high-purity reagents, and use of clean room facilities.

The research underscored the importance of the initial 'wet' tissue mass, highlighting that smaller masses (particularly the 50mg 'wet' group) are prone to weighing errors, impacting iron measurements. Consequently, a 'wet' mass of >100mg was recommended as a minimum for future ICP-MS analyses.

Mitochondrial iron quantification was optimized using a two-step differential centrifugation approach and a 10-stroke homogenization process. Reference intervals for cardiac and mitochondrial iron concentrations in control samples were established, offering essential benchmarks for characterising cardiac iron overload in the development of the *in vivo* cardiac iron overload models.

DEVELOPING AND VALIDATING AN *IN VIVO* MODEL OF CARDIAC IRON OVERLOAD

5.1 Introduction

This chapter outlines the development of a cardiac iron overload model in rats. The establishment of this model is essential to facilitate the investigation into the relationship between elevated cardiac iron and the exacerbation of DOX-induced cardiotoxicity (DIC). This model is intended to replicate the elevated iron levels observed in patients undergoing DOX treatment as part of their cancer therapy.

5.1.1 The Rationale for Developing a Clinically Relevant *in vivo* Model of Cardiac Iron Overload

The aim is to create an iron overload model that mimics the pre-existing iron overload observed in patients undergoing chemotherapy treatment, caused by blood transfusions, as well as other contributors like nutritional status and genetic disorders such as hemochromatosis[123]. We hypothesize that these patients are particularly vulnerable to developing DIC. I have established baseline levels of cardiac iron in rats, including total cardiac iron (272 ± SD 36.42 µg Fe/g dry tissue) and total mitochondrial iron (0.6967 ± SD 0.3908 ug Fe/mg protein) (Chapter 4). These total cardiac iron levels align with those reported *in vivo* and in patients, providing confidence in the accuracy of our measurements [366][367]. The clinical relevance of cardiac iron overload was interpreted using post-mortem data from transfusion-dependent patients with end-stage heart failure, providing valuable upper limit values for comparison [123] [121] . I aimed to induce cardiac iron overload with total cardiac iron levels significantly above our established baselines, without causing significant signs of cardiac dysfunction associated with heart failure. This approach is intended to replicate the condition observed in patients with subclinical iron overload at the time of DOX treatment, where severe cardiac dysfunction is not evident.

I also aimed to increase cardiac mitochondrial iron levels, as previous studies have demonstrated an increase in the transport of iron into cardiac mitochondria under conditions of systemic iron overload [109] [108]. Furthermore, reducing mitochondrial iron levels has been proven effective in reversing DOX-induced cardiomyopathy: Overexpressing ABCB8, a protein responsible for mitochondrial iron export, can ameliorate DIC *in vitro* and in mice[205].

To the best of our knowledge, values for mitochondrial iron concentration measured during *in vivo* investigations into cardiac iron overload have not been reported in the literature. Our understanding is primarily inferred from mitochondrial structural and functional parameters. Mitochondrial dysfunction observed in iron-overloaded rats include increased mitochondrial ROS production, mitochondrial depolarization, swelling, and an imbalance in the expression of proteins involved in oxidative phosphorylation, compared to non-iron-loaded rats[113] [113] [368].

Another essential criterion for our iron overload model is its ability to induce a prolonged iron overload, aiming to mitigate the toxic effects of the iron-delivering vehicle itself. Each iron supplement has specific pharmacokinetics and pharmacodynamics that could impact the animal's response. This has the potential to result in misinterpretations of the functional and metabolic parameters that I planned to measure. To ensure that any parameters measured during the upcoming coadministration study with DOX and iron chelation are not confounded by the effects of the iron overload compound itself, I planned to integrate a washout period into my model. The rationale is to enable us to ensure as far as possible that any observed functional and metabolic changes are due to iron overload itself, rather than that of the delivery compound, which may have different intracellular biodistribution, reactivities etc.

5.1.2 Modelling Cardiac Iron Overload *in vivo*: A Review

Animal models for studying iron overload and chelation therapy have been developed since the early twentieth century for preclinical research, primarily in mice, rats, and gerbils[369][370]. There is considerable variability among the developed models, which include both exogenous and transgenic methods for inducing iron overload. This variability includes factors such as dosage, routes of administration, and duration and frequency of treatment. Additionally, the evaluation of the iron overload itself varies; There is no standardized investigation to determine the impact of the iron overload on cardiac iron levels and cardiac function.

I conducted a review of the current landscape of cardiac iron overload models to inform the most appropriate approach for inducing cardiac iron overload for our experiments, in accordance with the selection criteria detailed in 5.1.1. Here, I reviewed the various protocols used to induce cardiac iron overload, focusing on those implemented in rats and those that evaluated cardiac iron parameters, specifically. I have chosen to focus on rat models to

maintain compatibility across our historical research, and because rat hearts are significantly larger than mice, provide us with sufficient tissue to allow us to conduct all assays in the same animal for cross-correlation of biomarkers etc. I limited our review to research papers in which iron overload was induced through either enteral or parenteral routes. Genetically modified animals to induce iron overload were to be too expensive and can be difficult to interpret due to compensatory genetic changes which are hard to characterise.

5.1.2.1 The Current Landscape of *in vivo* Models of Cardiac Iron Overload in Rats

In my initial evaluation of iron overload models, I observed that the induction of iron overload *in vivo* has traditionally centred on investigating pathologically elevated iron levels in the liver, and that cardiac iron levels were often not recorded [371][372][370]. Among the models that directly investigated cardiac iron levels, the majority were developed to investigate conditions such as hemochromatosis and thalassemia resulting from regular blood transfusions. Furthermore, models have predominantly shifted towards utilizing mice due to cost and convenience.

The *in vivo* models identified through our search criteria used protocols involving an iron-rich diet and I.P. injections of iron dextran to induce cardiac iron overload (Table 13). Direct comparison of recorded iron levels between publications is often challenging because of the diversity of measurement techniques used. Where possible, iron levels have been converted to ug Fe/g of dry tissue to align with the units used in our iron measurements, and measurements were converted to fold changes compared to their respective controls, to allow comparison between studies to be made.

Table 13: Currently available *in vivo* models for studying cardiac iron overload in rats. I.P. ; Intraperitoneal, NTBI; Non-transferrin bound iron, ROS; Reactive oxygen species, MDA; Malondialdehyde, LVEDP; Left ventricular end-diastolic pressure, LVSP; Left ventricular systolic pressure, LVESP ; Left ventricular end-systolic pressure, LVFS; Left ventricular fractional shortening, LVEF; Left ventricular ejection fraction, Pmax; Maximum pressure, CK-MB; Creatine kinase-myoglobin binding, TBARS; Thiobarbituric acid reactive substances, NR; Not reported, FC; Fold change. Cardiac iron overload values presented as Control vs iron overloaded groups (mean± SD). *P<0.05.

Iron administered	Mode of iron administration	Strain, sex, age dose, and duration of iron administration	Results (compared to controls)					
				Cardiac iron conc.	Cardiac function	Cardiac mitochondrial iron	Cardiac mitochondrial function	Other iron overload parameters
Ferrocene	Dietary	**a) Wistar (M, 180–200 g):** Fed with chow diet containing ferrocene (0.2% w/w, 2000 ppm) for 4-5months[372].	↑	Colorimetric assay ~8.0 vs ~43.0* (μM Fe/mg protein). FC=~5.3	↓ LV systolic function, ↓ LVESP, ↓ LVFS, ↓ Pmax, ↓ stroke volume, ↓ cardiac output, ↑ cardiac MDA	NR	↑ ROS, ↑ depolarization, ↑ swelling	↑ plasma NTBI
		b) Wistar (M 180–200 g): Fed with chow diet containing ferrocene (0.2% w/w, 2000 ppm) for 4-5months[373].	↑	Colorimetric assay 8.04±0.47 vs 42.00±7.91* (μM Fe/mg protein). FC=~5.2	↓ LV systolic function, ↓ LVEF, ↑ cardiac MDA	NR	NR	↑ plasma NTBI
Carbonyl iron	Dietary	**c) Sprague-Dawley (M, 6 weeks):** Fed with 10,000 ppm carbonyl iron diet for 10 weeks[374].	↑	Atomic absorption 48.33 ± 7.88 vs 59.00 ± 4.56 (ug Fe/g). FC=~1.2	↔Loss of myofilaments	NR	NR	↔Prussian blue staining
		d) Sprague-Dawley (M, 50g): Fed with 20,000 ppm carbonyl iron diet for 4-6 months [366].	↑	Atomic absorption 320± 7 vs 550± 210 (ug Fe/g dry tissue). FC=~1.7	NR	NR	NR	NR

Iron Dextran	Parenteral (I.P injection)	**e) Wistar (M, 8 months old):** I.P. injections of iron dextran at 100 mg/kg/day, 5 days/week for 4 weeks[367].	↑	Atomic absorption ~200 vs ~575* (ug Fe/g dry tissue). FC=~2.8	↑LVEDP, ↔LVSP, ↔Heart rate, ↓contractile force, ↑CK-MB levels, ↑TBARS	NR	NR	↑Serum iron, ↔transferrin, ↑transferrin saturation,↑ Prussian blue staining, ↑Plasma TBARS

Of these models, incorporating ferrocene into the diet to induce iron overload appears to be the most appropriate approach based on our selection criteria. All the studies reported increases in cardiac iron, however none measured mitochondrial iron levels specifically. Study a, which utilized dietary ferrocene to induce iron overload, was the only study to assess mitochondrial functional parameters. The altered mitochondrial function reported in the study suggests that the model likely induces mitochondrial iron overload, but no definitive conclusions could be drawn regarding the iron levels in the mitochondria in the other studies. As detailed in 5.1.1, the requirement to elevate cardiac iron levels, both globally and within the mitochondria of cardiac tissue is important, as both aspects are integral to the pathology observed in cardiac iron overload. Secondly, despite the evident cardiac damage observed after 5 months of ferrocene in the diet, as indicated by cardiac functional parameters, this model serves as a valuable initial framework. By employing a longitudinal dose titration, I aim to determine the timeline of cardiac iron overload leading to the development of cardiac dysfunction. Furthermore, the ferrocene protocol has been replicated (Study a and b), demonstrating reproducibility, albeit within the same group. Aside from the lack of mitochondrial iron data, inducing cardiac iron overload via carbonyl iron wasn't considered a suitable method for our study. The 10,000 ppm dose in Study c showed a non-significant increase in cardiac iron, while the 20,000 ppm dose of carbonyl iron in Study d did result in a significant elevation. However, the reproducibility of the iron levels in these studies raises concerns. There is significant variability in control cardiac iron levels between the two studies, even though both employed atomic absorption for measuring cardiac iron in animals that were roughly age/weight matched at the time of sacrifice. Furthermore, the control iron levels recorded in Study c are not consistent with other control iron measurements reported in literature.

5.2 Aims

The overarching aim is to establish a clinically relevant model of cardiac iron overload emulating the iron levels observed in cancer patients undergoing DOX treatment. ICP-MS was used to quantify the total cardiac iron and mitochondrial cardiac iron levels that result from the iron overload protocol. The impact of iron overload on cardiac function and metabolism was also be assessed. These are important parameters for future studies, where we intend to integrate the iron overload protocol with DOX treatment. Understanding the metabolic profile of the heart during iron overload is essential for identifying metabolic signatures associated with this pathological state. Information needed to provide crucial insight into the physiological and biochemical changes occurring during iron overload and its interplay with DOX treatment.

5.3 Model 1: Ferrocene Iron Overload Model

5.3.1 Introduction

Ferrocene ($Fe(C_5H_5)_2$), is an organometallic compound consisting of two cyclopentadienyl rings bound to a central iron atom. Our research employs a ferrocene-enriched diet to induce iron overload, guided by the studies conducted by Wongjaikam et al [373] [112]. Their study achieved elevated total cardiac tissue and mitochondrial iron, aligning well with our selection criteria. I used their same dosage, 10 times that of the standard rat diet, typically 200ppm of iron[375], over 5 months. My experimental design incorporates a time-dependent dose titration, where a cohort of animals are culled at monthly intervals throughout the protocol for assessment of tissue iron loading and metabolomic consequence. The rationale is to help determine the point at which iron overload occurs and the interval to measurable cardiac functional change. The original protocol was modified to incorporate a 2-week washout period. During this period, animals were transition from a ferrocene-rich diet to a standard diet for two weeks prior to sacrifice. This to confirm that the iron which has been delivered is loaded into the myocardium, and not transiently accumulated.

5.3.2 Methods

For additional details about the methods described below, please refer to Chapter 3.

5.3.2.1 Animal Preparation

All animal experiments conformed with our institutional animal care guidelines and the United Kingdom Home Office Guide on the Operation of Animal (Scientific Procedures) Act of 1986. Eighty adult male Wistar rats (7-9 weeks old, 200-300g) were purchased from Charles River Laboratories. Animals were housed in groups of four under controlled conditions: at 23 ± 2°C with 12 h light/dark cycles. Animals were acclimated for 7 days before the start of the study and had access to water and food *ad libitum* for the duration of the study.

5.3.2.2 High Iron Diet Preparation

A chow diet containing 0.2% of ferrocene ($C_{10}H_{10}Fe$; Sigma-Aldrich) (w/w) was purchased and prepared by Rettenmair UK Ltd. One kilogram of chow diet was mixed with 2 grams of ferrocene, followed by the addition of 1.2 litres of deionized water. The mixture then moulded and baked at 80°C for 24 hours in a hot air oven.

5.3.2.3 Experimental Protocol

Adult male Wistar rats (200-300g) were divided into 5 cohorts, each of which were further split into those receiving a high iron diet (0.2% ferrocene w/w) (n=8) and those receiving a regular diet (n=8). The animals within cohorts 1, 2, 3, 4 and 5 received their assigned diets for 1, 2, 3, 4 and 5 months, respectively. All animals received a regular diet for the two-week washout period prior to culling. This two-week period washout period was implemented to understand the sustained impact of the iron overload beyond the initial exposure. Body weight and cardiac function were measured at baseline and every two weeks during the course of the study. At the end of the study, the rats were sacrificed, and the hearts were excised for metabolic analysis and iron quantification measurements. A schematic timeline representative of this study is presented in Figure 38.

I opted for the use of monthly cohorts to determine when iron overload is achieved, with the intention of refining the protocol to shorten its duration in future experiments.

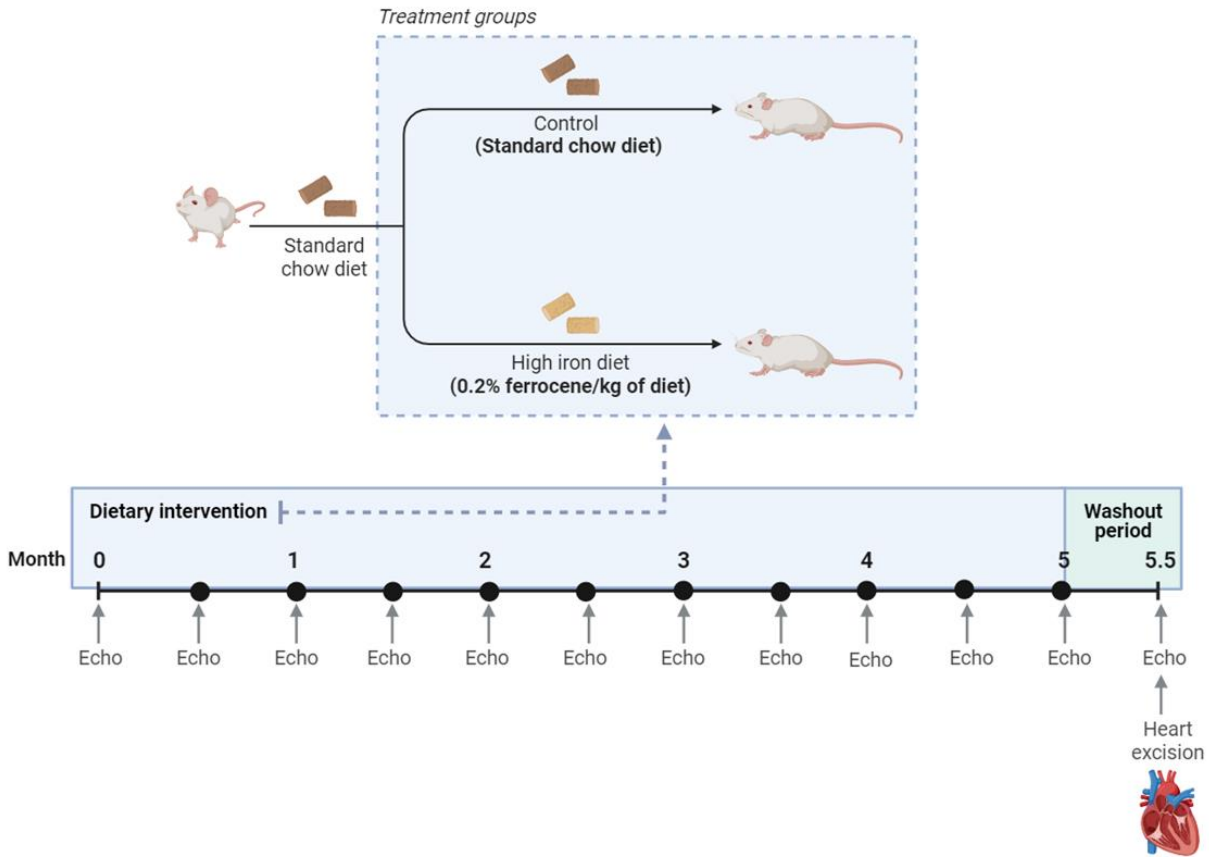

Figure 37: Study schematic: Inducing cardiac iron overload through dietary intervention with the use of ferrocene. The timeline depicted here presents the protocol followed by cohort 5. This is representative of the protocol carried out in cohorts 1 to 4, with the sole variation being the timelines unique to each cohort (1 to 4 months, respectively). [Figure made in BioRender]

5.3.2.4 Echocardiographic Measurements

Cardiac function was assessed by echocardiography. Rats were anaesthetised (4% isoflurane mixed with 0.8 L/min 100% O_2) in an induction chamber and then transferred to a heating pad where anaesthesia was maintained using a nose cone at 2% isoflurane at a flow rate of 0.5 L/min. Fur was shaved and depilated from the chest and abdomen region and echocardiography performed using a Vevo 770 High Resolution Imaging System (VisualSonics, Toronto, Canada) with a RMV-710B transducer probe at 25 MHz (VisualSonics RMV-710B). The M-mode image of the left ventricle was used to determine multiple cardiac function parameters: left ventricular ejection fraction (LVEF), Fractional Shortening (FS), Cardiac Output (CO), Diastolic volume (DV) and Systolic volume (SV). All parameters were indexed to body weight.

5.3.2.5 Sample Collection

Hearts were harvested as described in (3.2.7). In brief, rats were anesthetized (4% isoflurane mixed with 0.8 L/min 100% O2) in an induction chamber and then transferred to a heating pad,

where anaesthesia was maintained using a nose cone at 4% isoflurane at flow rate of 0.5 L/min. Following a negative pedal response, incisions were made along the abdomen and rib cage to access the chest cavity. Ice-cold saline was injected into the heart apex to perfuse the cardiac tissue and minimize red blood cell contamination. Hearts were rapidly excised by directly severing the aorta and immediately snap-frozen in liquid nitrogen to prevent metabolite degradation. Each heart was individually ground with a pre-cooled pestle and mortar under liquid nitrogen. The resulting powdered cardiac samples were stored at -80°C for subsequent analysis.

5.3.2.6 NMR Measurements for metabolomics

Cardiac tissue metabolites (100-200mg) were extracted using chloroform, methanol, and water in a 1:1:1 ratio (2mL/100mg tissue, respectively). Suspensions were centrifuged (1 hour at 3600 RPM at 4°C), resulting in the formation of three layers: 1) an upper aqueous methanol layer, 2) middle solid protein interphase layer and, 3) a lower lipophilic organic chloroform layer. The upper aqueous layer was transferred to a new 15mL falcon tube containing 30mg Chelex 100 and centrifuged once more (3600 RPM for 5 minutes at 4°C). The supernatant was transferred to a new falcon tube and 20µL universal indicator was added to it. Each sample was then snap frozen and freeze dried, and reconstituted in 600µL of a deuterium oxide (D_2O) solution containing TSP. The samples were corrected to ~pH 6.5 and transferred to 5mm NMR tubes (Norel Inc, USA) for ^{1}H NMR analysis.

^{1}H spectroscopy was performed on a 700-MHz NMR spectrometer (Bruker, Germany). Aqueous cardiac samples were analysed using a Nuclear Overhauser Effect Spectroscopy (NOESY) pulse sequence. Spectra were acquired using the following parameters: spectrometer frequency; 700.19 MHz, spectral width; 20.5 ppm/14367.8 Hz, acquisition time; 2.28 seconds, relaxation delay; 4 seconds, and number of scans; 68 scans.

All ^{1}H NMR spectra were post-processed in TopSpin software version 3.6.1 (Bruker, Germany). Metabolite peaks were manually integrated, and metabolic profiles determined using Chenomx NMR Profiler Version 9.0 (Chenomx, Canada). Cardiac metabolite concentrations were determined by reference to the TSP peak and normalizing the metabolite peak integrals to the initial wet tissue mass used for the metabolite extraction (See 3.7.8).

5.3.2.7 Measuring Cardiac Iron by ICPMS

5.3.2.7.1 Sample Preparation for Total Cellular Cardiac Iron Measurements

Cardiac tissue (150 mg) was transferred to pre-weighed 15 mL centrifuge tubes (Elkay labs) and placed in an oven at 70 ℃ to dry overnight (or until completely dry). The dried samples were weighed to obtain the sample dry weight. Each sample then underwent thermal acid digestion: 0.25 mL of Optima grade concentrated H_2O_2 (30–32% w/w; Sigma Aldrich) and 0.75 mL Optima grade concentrated HNO3 (67–69% w/w; Fisher Scientific) was added to each sample and placed in an oven at 70 ℃ to digest overnight. The digested samples were weighed to obtain the weight of the digested material. Each sample was diluted to a total volume of 15mL using trace metal grade ultrapure water and Gallium (Ga) as an internal standard (Leeman Labs Ltd). The combined weight of the sample digest and the diluent was recorded. ICP-MS total iron quantification in cardiac tissue also involves preparation of procedural (CRM and blanks) and non-procedural samples (Non-procedural CRM, non-procedural blank, and calibrants). Refer to 3.4. for detailed information on these sample types and their preparation.

5.3.2.7.2 Sample Preparation for Total Mitochondrial Iron Measurements

A two-step differential centrifugation method was used to isolate mitochondria from cardiac tissue. A 50 mg sample of cardiac tissue was homogenised in 1mL of isolation buffer (250 mM sucrose, 2 mM EDTA, 100 mM Tris-HCl (pH 7.4)) until smooth using a glass Dounce homogeniser and 10 strokes of a loose-fitting pestle. An additional 250 µL of isolation buffer was used to ensure full transfer of the homogenate into a 1.5 mL Eppendorf vial. The homogenate then centrifuged at low speed (600 xg for 10 mins, 4℃). The supernatant was collected, divided into two Eppendorf vials and centrifuged at high speed (11000 xg for 10 mins, 4℃). The two resultant mitochondrially enriched pellets were washed. One pellet was used for ICP-MS analysis, the other for a BCA assay used to determine protein concentration. Total mitochondrial iron concentration (µg of Fe/mg of protein) calculated using the protein content calculated in the pellet assigned for the BCA assay.

The ICPMS allocated mitochondrial pellets underwent thermal acid digestion: 60µL of Optima grade concentrated HNO_3 (67–69% w/w; Fisher Scientific) was added to each sample and placed in an oven at 50 ℃ to digest overnight. The digested samples were diluted to a total

volume of 1.2µL using trace metal grade ultrapure water and Gallium (Ga) (Leeman Labs Ltd). ICP-MS total iron quantification in isolated mitochondria also involved preparation of procedural blanks and non-procedural samples (Non-procedural CRM, non-procedural blank, and calibrants). Refer to 3.6 for detailed information on these sample types and their preparation.

5.3.2.7.3 ICPMS Operation

All ICP-MS measurements were performed on a NexION 350 ICP-MS Spectrometer (PerkinElmer, Inc). Total cardiac iron measurements are expressed as µg of iron per mg of cardiac tissue. Total mitochondrial cardiac iron measurements are expressed as µg of iron per mg of protein.

5.3.2.8 Statistical Analysis

Unsupervised principal component analysis (PCA) was used to analyse the distribution of the metabolomic data derived from the control and ferrocene groups. If separation between the groups was observed, then supervised partial least squares discriminant analysis (PLS-DA) performed to better discriminate between the groups and to maximize separation associated with class membership. Unpaired Student's t-tests, one-way or two-way ANOVA with Tukey's HSD adjustment method for multiple comparisons were used and performed as indicated in the figure legends. Significance was assumed at $P < 0.05$. Only significances from multiple comparisons are displayed in the figures and not the ANOVA interactions. The longitudinal data is presented as mean ± SD in the graphs, while the endpoint data is presented using a box plot**.** PCA and PLS-DA analysis was performed in MatLab, all other statistical analysis was performed in Prism 10 (GraphPad, La Jolla, CA, US).

5.3.3 Results

The results presented here are exclusively from the five-month treatment cohort. It is within this group that any significant changes would be most prominent.

5.3.3.1 The Effect of Dietary Ferrocene on Body Weight

Rats receiving the ferrocene enriched diet gained weight more slowly than rats in the control group (Figure 39, a), the difference becoming significant from week 10 ($p<0.05$). Following the two-week washout period, during which both groups were fed the same standard diet, there was no statistically significant difference in the average body weight between the two groups (Figure 39, b). This reduced body weight gain during the ferrocene diet administration period followed by its return suggest an intermediary effect that only occurs during ferrocene treatment, possibly due to suppression of appetite by the iron-loaded diet.

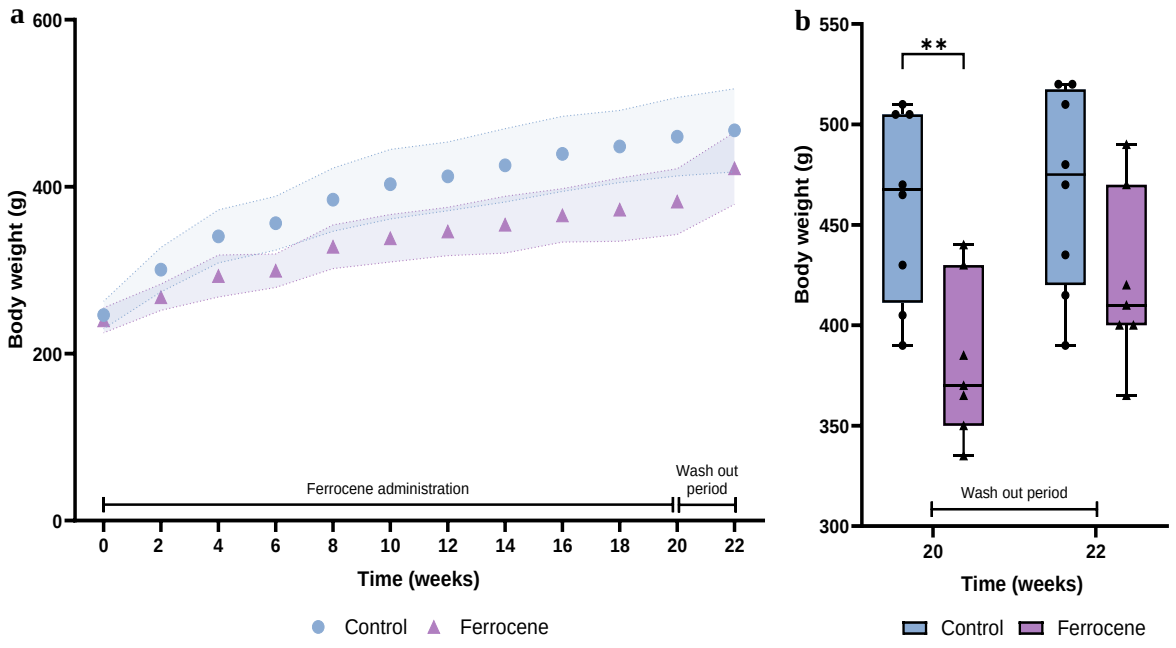

Figure 38: Average rat body weight measurements in the ferrocene treated group and the control group. a Average rat body weight gain per week throughout the 22-week study (mean±SD). **b** Average rat body weight at the end of the study. Statistical comparison by two-way ANOVA with Tukey's HSD correction method for multiple comparisons. **P<0.01.

5.3.3.2 The Effect of Dietary Ferrocene on Cardiac Contractile Function

Cardiac functional parameters were assessed by conducting echocardiography imaging every two weeks throughout the study period (Figure 40 and Figure 41). There were no significant functional differences observed between the ferrocene-treated and control rats.

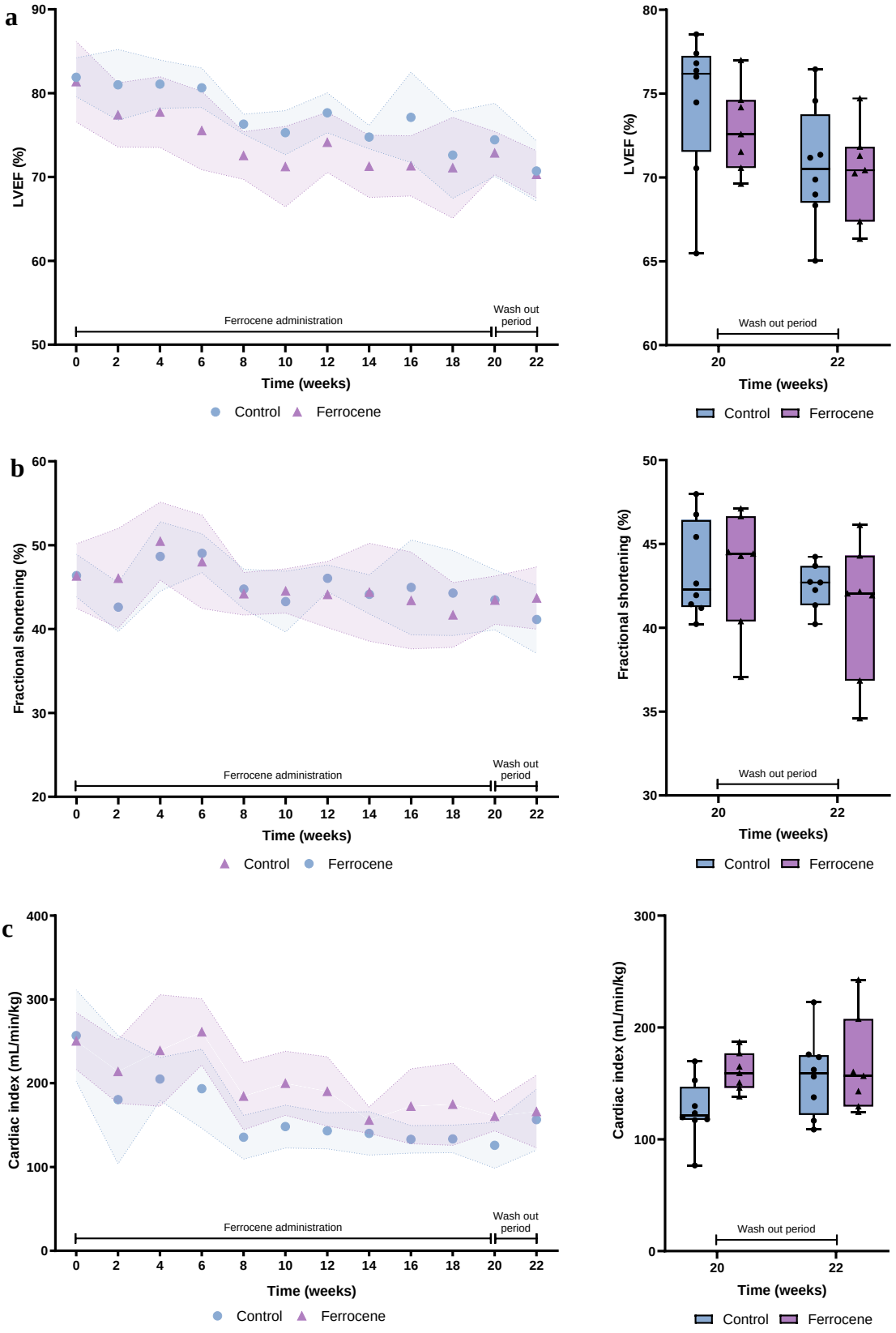

Figure 39: Cardiac functional parameters obtained by echocardiography. a Left ventricular ejection fraction (LVEF) **b** Fractional shortening **c** Cardiac index**.** Statistical comparison by one-way ANOVA with Tukey's HSD correction method for multiple comparisons. The longitudinal data is presented as mean ± SD in the graphs (left), while the endpoint data is shown using a box plot (right).

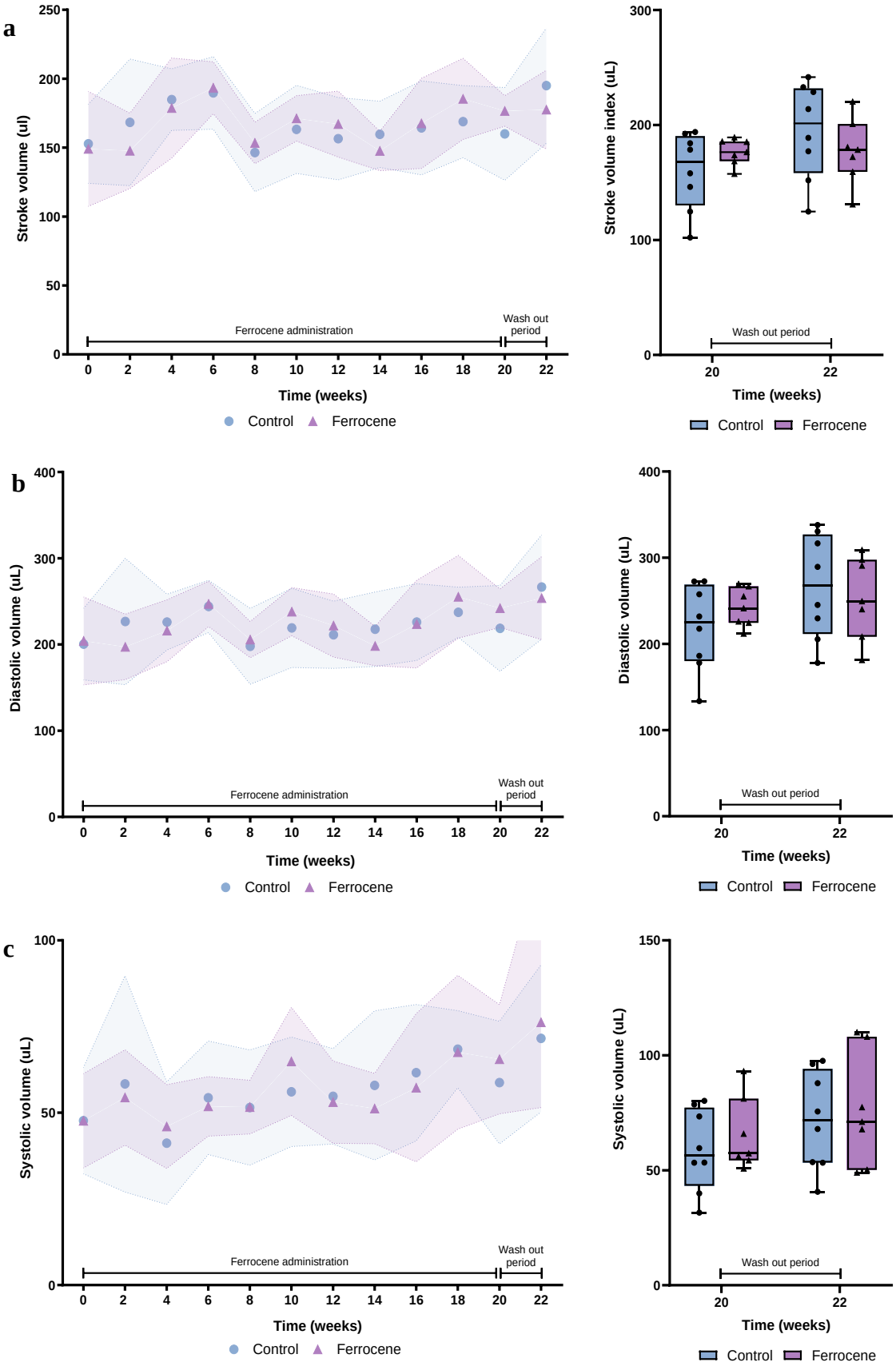

Figure 40: Cardiac functional parameters obtained by echocardiography. a Stroke volume index **b** Diastolic volume index **c** Systolic volume index. Statistical comparison by one-way ANOVA with Tukey's HSD correction method for multiple comparisons. The longitudinal data is presented as mean ± SD in the graphs (left), while the endpoint data is shown using a box plot (right).

5.3.3.3 The Effect of Dietary Ferrocene on Cardiac Iron Levels

The ferrocene-enriched diet led to a significant increase in both the total cardiac iron concentration and the total mitochondrial iron content when compared to the control group, exhibiting increases of ~1.5-fold and ~2-fold, respectively (Figure 42). However, the average increase in total cardiac iron observed in this study was significantly lower than the 5.3-fold increase reported in the reference study that employed the same protocol. The prior studies utilizing this protocol did not assess total iron content within the mitochondria, meaning that no comparison can be drawn in this regard.

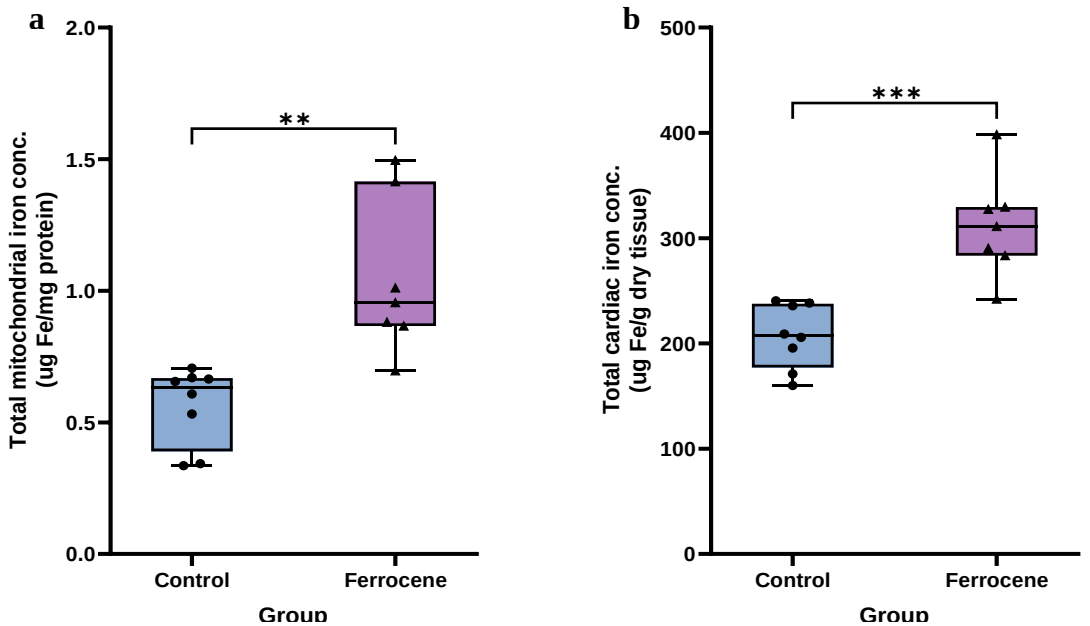

Figure 41: Total cardiac iron levels as assessed by ICPMS (^{56}Fe). a Ferrocene increased total cellular cardiac iron ~1.5-fold compared to the control (311.79±44.95 SD and 206.99±28.63 SD, respectively).Total cardiac iron concentration**,** expressed as µg of iron per g of cardiac tissue. **b** Ferrocene increased total mitochondrial cardiac iron ~2-fold compared to the control (1.04±0.27 SD and 0.54±0.13 SD, respectively).Total mitochondrial iron concentration, expressed as µg of iron per mg of protein. Statistical comparison by T-test. **P<0.01, ***P<0.001.

5.3.3.4 The Effect of Dietary Ferrocene on Cardiac Metabolism

Unsupervised Principal Component Analysis (PCA) revealed no separation between the cardiac metabolite profiles of the ferrocene group and the control, Figure 44. The fold change of aqueous cardiac metabolites is depicted in Figure 43. For mean metabolite concentrations, refer to Appendix (Table 15)

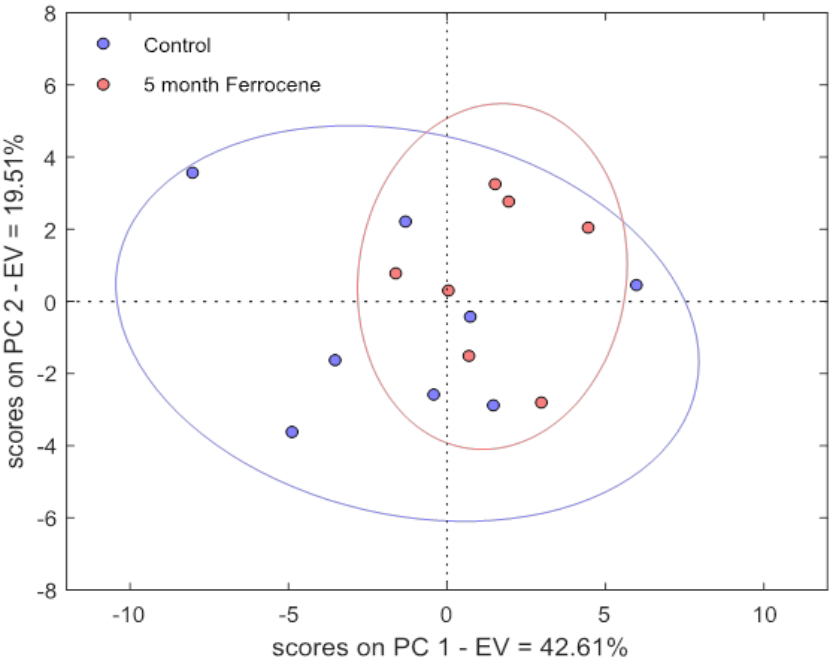

Figure 43: Principal Component Analysis (PCA) score plot from the aqueous cardiac metabolites of the ferrocene and control groups. In the 2D PCA score plot, control animals on the standard chow diet are denoted by the blue dots, while animals on the ferrocene-enriched diet are represented by the red dots. PC1 accounted for 42.61% of the total variance, and PC2 accounted for 19.51% of the total variance.

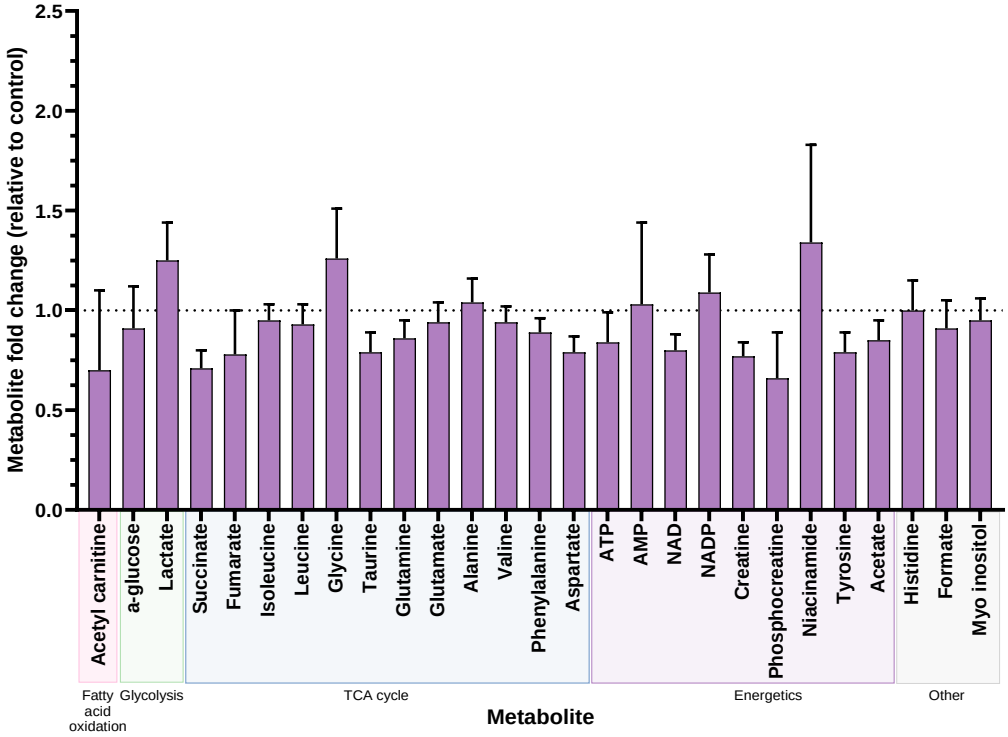

Figure 42: The fold change of aqueous cardiac metabolites in the ferrocene diet group relative to the control group. The fold change in metabolite concentration is represented as the mean ± SEM. Statistical comparison by T-test. *P<0.01.

5.3.4 Discussion

A 5-month dietary ferrocene approach was implemented to induce cardiac iron overload, referencing the protocol published by Wongjaikam *et al*. A two-week washout period to observe the sustained effects of a ferrocene-rich diet was included, a component not part of the study regimen in the reference protocol. Our findings regarding cardiac function did not align with the results reported in the reference papers. While the reference paper documented a decrease in left ventricular systolic function, FS, cardiac output, and LVEF, I found no significant change in any cardiac function parameter at the end of the 5-month ferrocene-rich diet treatment.

The cardiac loading achieved in our study did not align with that reported in the reference papers. I found that 5 months of dietary ferrocene loading, followed by a two-week washout period, resulted in a 1.5-fold increase in total cardiac iron compared to the control, against the 5-fold increase reported in the reference papers. A mild increase in total cardiac mitochondrial iron levels was observed resulting from the ferrocene-rich diet. This elevation did not demonstrate a statistically significant difference from the control reference range measurements I established prior (4.7.5). Thus, it does not meet a crucial requirement outlined for our iron overload model.

Previous studies have demonstrated an increase in the transport of iron into cardiac mitochondria under conditions of systemic iron overload [109] [108]. Therefore, this aspect was considered an important requirement in terms of the clinical relevance of our model. The relatively mild increase in cardiac iron measured after two weeks may indicate that iron is being washed out. Unfortunately, a timepoint at the end of the ferrocene dietary loading period was not included to determine this.

The metabolic profile of the heart using ^{1}H NMR was examined, an aspect not investigated in our referenced papers. The findings showed no significant differences between the metabolic profiles of the ferrocene-fed rats and the control group, consistent with the lack of changes in contractile function observed in these animals.

In the ferrocene-treated group, we observed a reduction in weight compared to the control group, which has also previously been reported in rats by Nielson *et al.* [376] This weight loss was reversed upon cessation of the ferrocene treatment, with weights returning to control levels. Gastrointestinal side-effects are the most commonly reported adverse effects associated

with oral iron treatment [377], and it's been reported that excess unabsorbed iron travels through the colon and engages in the Fenton and Haber-Weiss reactions, which can have detrimental effects on the intestinal structure [378] . Therefore, the weight loss during treatment is likely attributable to gastrointestinal disturbances caused by ferrocene ingestion, which could have led to irritation and inflammation of the GI tract. This irritation could impair normal digestive processes, reduce nutrient absorption, and result in symptoms such as nausea, ultimately reducing food intake and contributing to the observed weight loss [379] . Once the ferrocene treatment ended, the gastrointestinal tract likely recovered, restoring normal digestive function and nutrient absorption, which allowed the animals to regain the lost weight and return to control levels.

5.3.4.1 Conclusions

The requirement to elevate cardiac iron levels, both globally and within the mitochondria of cardiac tissue is important, as both aspects are integral to the pathology observed in cardiac iron overload, section 1.1.3. Dietary loading using ferrocene did not meet the pre-outlined requirements for our cardiac iron overload model.

Although total cardiac iron exhibited a mild elevation, the change in mitochondrial cardiac iron following ferrocene dietary loading was statistically insignificant when compared to our reference control measurements. A key criterion for our iron overload model is its ability to induce a prolonged iron overload, allowing the assessment of functional and metabolic changes independently of the iron compound's properties. In the context of relatively mild increase in cardiac iron, we cannot conclusively determine whether the induced increase in total cardiac iron levels is sustained after rats are switched from the ferrocene-rich diet to a standard diet. Consequently, this method of cardiac iron loading was not be carried forward for use in our co-administration studies with DOX and iron chelation.

5.4 Model 2: Iron Dextran Iron Overload Model

5.4.1 Introduction

After evaluating the ferrocene dietary approach for inducing iron overload, I revisited the initial pool of iron overload models (Table 13). Guided by the selection criteria, I concluded that

investigating iron dextran for cardiac iron overload would be a suitable subsequent alternative approach.

Avila *et al*.'s protocol, utilizing intraperitoneal injections of iron dextran at a dose of 100 mg/kg/day for 5 days a week over a 4-week period, served as our reference for inducing chronic iron overload[367]. This reference study further investigated the effects of a subsequent 9-week period, during which rats were subjected to either treadmill training or maintained under standard living conditions. Their primary aim was to assess whether moderate-intensity aerobic training could mitigate cardiac damage associated with experimental iron overload in rats. Their protocol efficiently elevated serum iron levels, mirroring the elevated levels observed in iron-overloaded patients[380] [249]. [381]Elevated serum iron is associated with recurrent blood transfusions and various types of cancers[382][383]. Transferrin saturation surpassed the commonly used diagnostic limit of 20–50% for iron overload[384][385]. Hence, this model can be deemed to simulate a clinically relevant iron overload state in rats that is also observed in cancer patients and those with transfusional iron overload.

The iron dextran-based model induced a significant ~2.8-fold increase in total cardiac iron levels. The control cardiac iron levels demonstrated comparability with literature reports and our measurements (Chapter 4), enhancing confidence in the reliability of the model. The widespread use of iron-dextran based protocols for inducing iron overload in mice enhances our confidence in its clinical relevance and reproducibility [386][387][388][389][390][391][392][393]. Furthermore, the iron dextran treatment spanned 4 weeks and was discontinued during the aerobic exercise phase. This phase, in effect, constituted a washout period. Cardiac iron levels were measured 9 weeks after the cessation of dextran treatment, revealing sustained elevation in cardiac iron levels during this extended period. Although the study by Avila *et al*., did not record the impact of iron dextran on cardiac mitochondrial iron levels, studies in mice have demonstrated that iron dextran can lead to mitochondrial DNA damage and dysfunction in mitochondrial respiration chain synthesis[394][395]. Changes in these parameters may indicate an increase in mitochondrial iron levels in response to iron dextran; mitochondrial dysfunction is expected to manifest due to increased oxidative stress induced by elevated labile iron levels within the mitochondria under conditions of iron overload.

Given the factors discussed here, the iron dextran-based iron overload protocol described by Avila *et al*, aligns with the requirements set for the iron overload model. Furthermore, inducing

iron overload through an I.P. route, as opposed to oral administration in the diet, provides the advantage of enabling more controlled dosing and bypassing intestinal processes that regulate iron absorption during overload conditions[396][397]. This protocol also offers the benefit of inducing cardiac iron overload in a significantly shorter timeframe compared to the ferrocene approach (4 weeks vs. 5 months, respectively).

5.4.1.1 Enhancements to Study Design

Building on experience from the ferrocene study, the original study design was refined by obtaining cardiac iron measurements and metabolic profiles at both the initiation and conclusion of the washout period, as well as at intervals within it. The iron dextran-based cardiac loading protocol outlined by Avila *et al*. was modified to incorporate a 4-week washout period, during which groups of animals were sacrificed at the end of dextran treatment, two weeks post-treatment, and four weeks post-treatment.

5.4.2 Methods

The animal preparation, echocardiographic measurements, sample collection, NMR measurements, and cardiac iron measurement were carried out as described in Chapter 3.

5.4.2.1 Experimental Protocol

The experimental procedure is summarised in the timeline schematic, Figure 45.

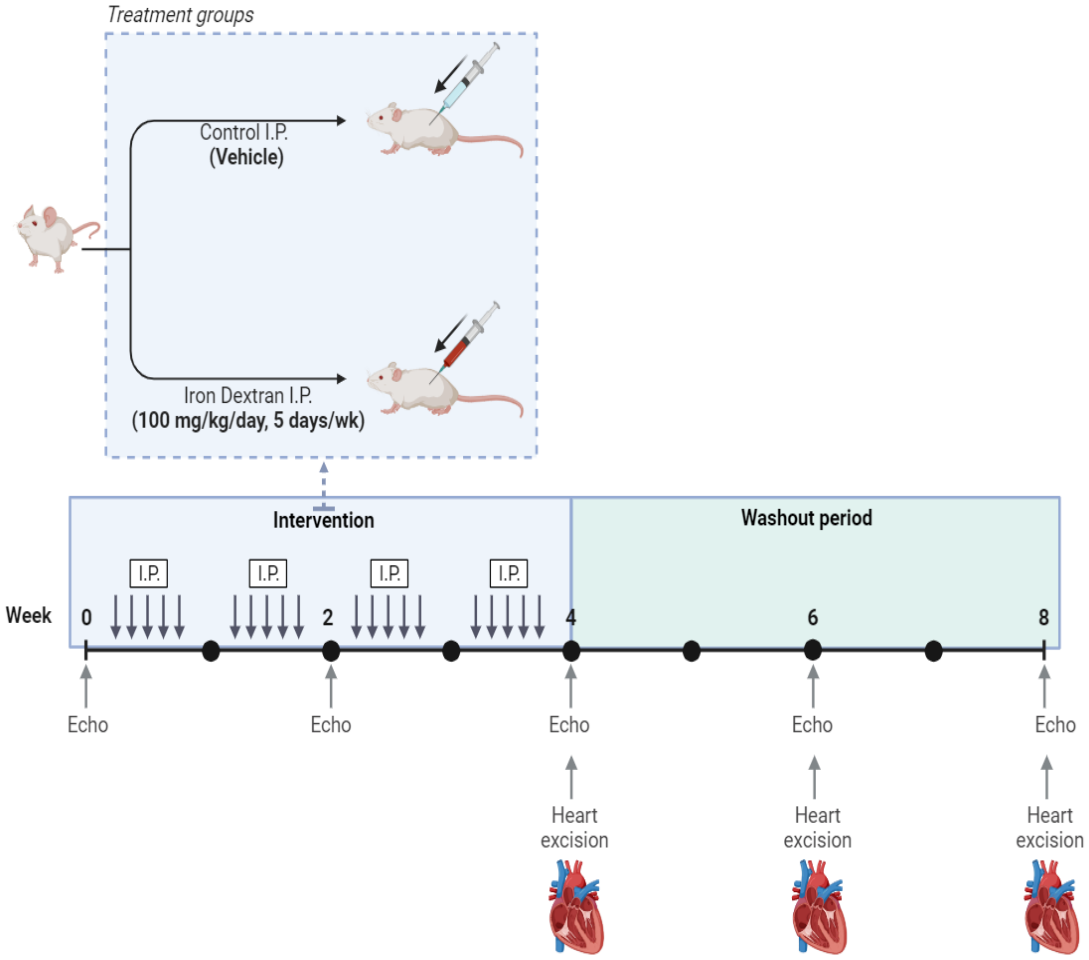

Figure 44: Study schematic: Inducing cardiac iron overload by iron dextran interperitoneally. Animals were subjected to iron overload by iron dextran or injected with saline for 4 weeks (I.P. injections at 100 mg/kg/day, 5 days/week, respectively), followed by a 4-week washout period. [Figure made in BioRender]

Adult male Wistar rats (200-300g) were divided into 4 groups (n=8): a vehicle control group and three groups subjected to iron overload. The iron overload groups received daily I.P. injections of iron dextran (100 mg/kg/day, 5 days/week) for 4 weeks. The first iron overload group was referred to as the 0-week washout (0 wk w/o), culled at the end of the treatment period. The two 2-week washout group (2 wk w/o) and 4-week washout (4 wk w/o) group were culled two weeks and four weeks after the final iron dextran dose, respectively. These groups were sacrificed at the three separate timepoints throughout the 4-week washout period to gain insight into the sustained and/or evolving effects of the iron overload beyond the initial

exposure. At the culmination of each group's designated endpoint, the rats were sacrificed, and their hearts excised for subsequent metabolic analysis and assessment of cardiac iron levels.

Body weight was measured each week during the 4-week treatment period and every two weeks during the washout period. Cardiac function was measured at two-week intervals throughout the study.

5.4.2.2 Statistical Analysis

Unsupervised principal component analysis (PCA) analysed the distribution of the metabolomic data derived from the control and Dextran groups. If separation between the groups was observed, supervised partial least squares discriminant analysis (PLS-DA) was performed to better discriminate between the groups and to maximize separation associated with class membership. A one-way or two-way ANOVA with Tukey's HSD adjustment method for multiple comparisons was used and performed as indicated in the figure legends. Significance was assumed at $P < 0.05$. Only significances from multiple comparisons are displayed in the figures and not the ANOVA interactions. The longitudinal data is presented as mean ± SD in the graphs, while the endpoint data is presented using a box plot. PCA and PLS-DA analysis was performed in MatLab, all other statistical analysis was performed in Prism 10 (GraphPad, La Jolla, CA, US).

5.4.3 Results

5.4.3.1 Body Weight

Rats receiving iron dextran gained weight more slowly than rats in the control group. Average body weights of the two groups are shown in Figure 46. The average body weight gain in rats treated with iron dextran became significantly different from that of the control group from the end of week 1. This difference persisted throughout the duration of iron dextran administration and throughout the subsequent four-week washout period.

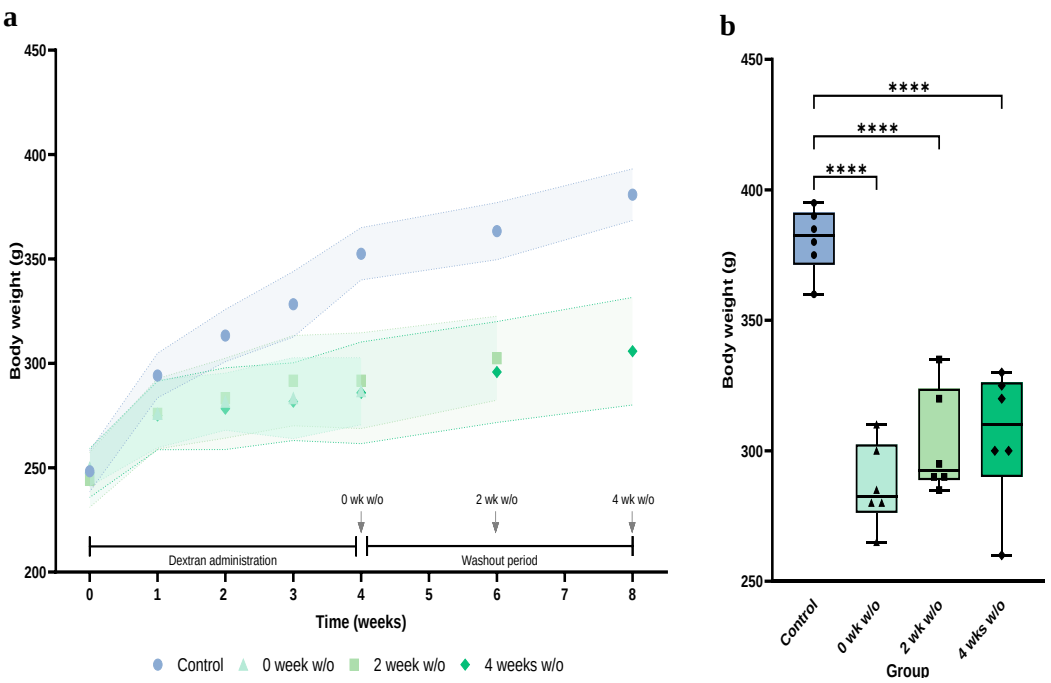

Figure 45: Average rat body weight measurements in the iron dextran groups and the control group. a Average rat body weight gain per week throughout the 8-week study (mean±SD). **b** The average rat body weight at the end of the iron dextran treatment period, as well as two weeks and four weeks thereafter. Statistical comparison by one-way ANOVA with Tukey's HSD correction method for multiple comparisons. ****P<0.0001.

5.4.3.2 Cardiac Function in Response to Iron Dextran Treatment

Upon completing the 4-week iron dextran treatment, a statistically significant increase in cardiac index was observed compared to the control group (Figure 47 and Figure 48). However, this lost statistical significance during the subsequent washout period. Iron dextran treatment also led to a significant decrease in stroke volume 4 weeks post-treatment.

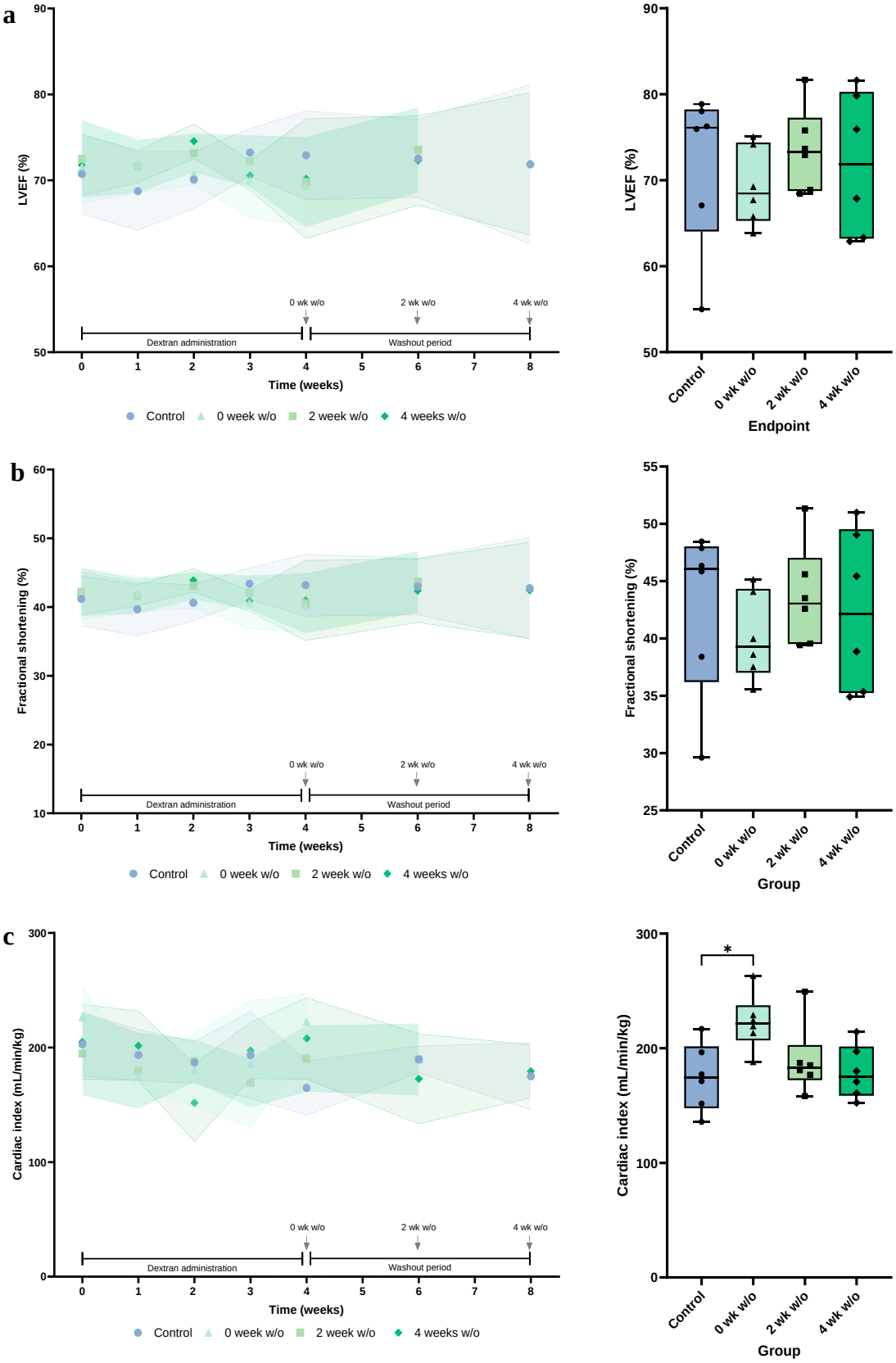

Figure 46: Cardiac functional parameters obtained by echocardiography. a Left ventricular ejection fraction (LVEF) **b** Fractional shortening **c** Cardiac index**.** Statistical comparison by one-way ANOVA with Tukey's HSD correction method for multiple comparisons. The longitudinal data is presented as mean ± SD in the graphs (left), while the endpoint data is shown using a box plot (right).

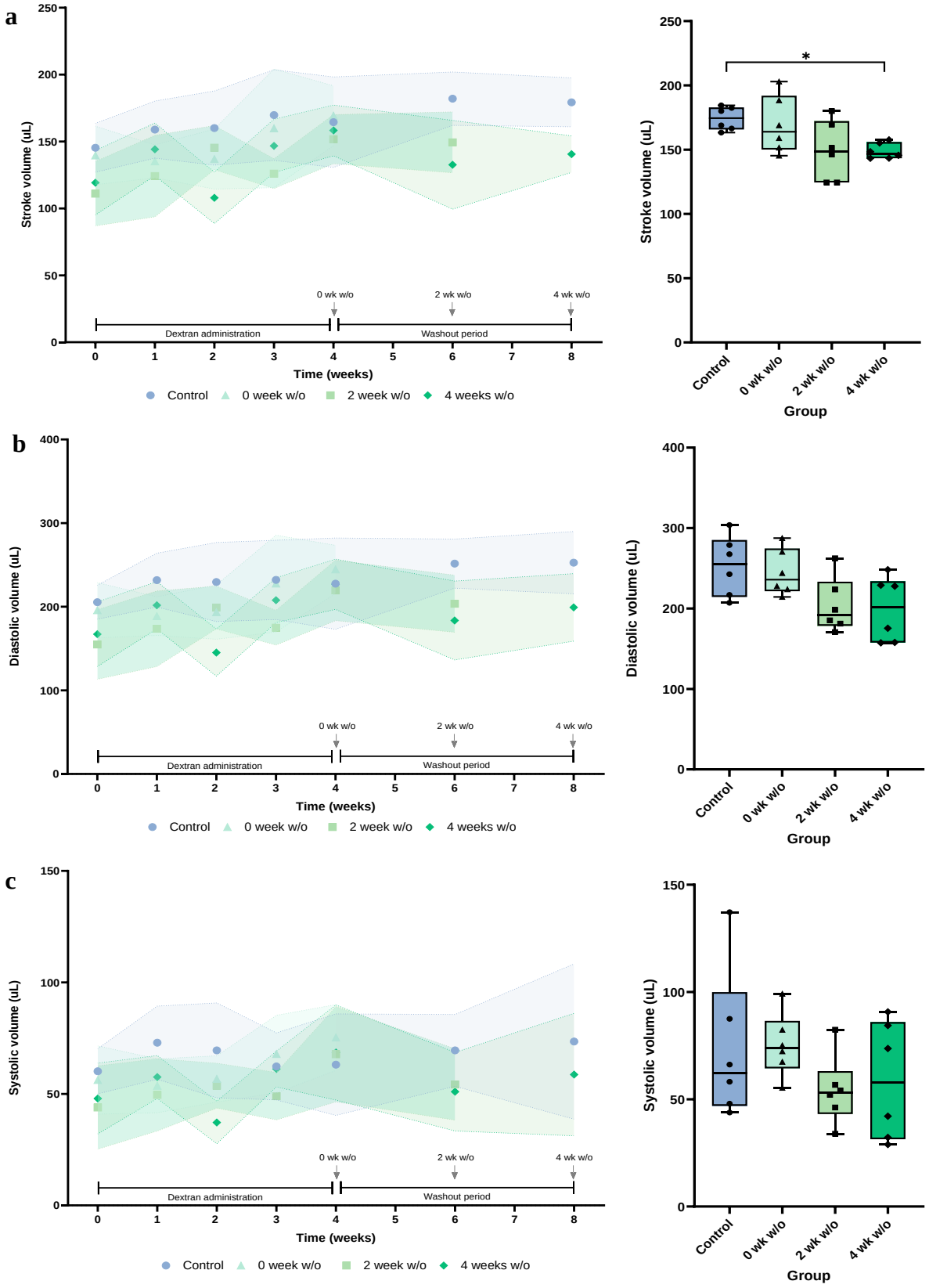

Figure 47: Cardiac functional parameters obtained by echocardiography. a Left ventricular ejection fraction (LVEF) **b** Fractional shortening **c** Cardiac index**.** Statistical comparison by one-way ANOVA with Tukey's HSD correction method for multiple comparisons. The longitudinal data is presented as mean ± SD in the graphs (left), while the endpoint data is shown using a box plot (right).

5.4.3.3 Cardiac Iron in Response to Iron Dextran Treatment

Iron dextran treatment led to significant increase in both the total cardiac iron concentration and the total mitochondrial iron content compared to the control group, exhibiting increases of ~2.9-fold and ~3.5-fold, respectively (Figure 49). The total cardiac iron measurements aligned with the reference study that employed the same iron overload protocol, resulting in a 2.8-fold increase in total cardiac iron. In the reference study, cardiac iron measurements were conducted following a 9-week washout period, suggesting that cardiac iron overload is likely to persist for at least as long as that period. The reference study did not evaluate the total iron content within the mitochondria, therefore no comparisons can be made in this regard.

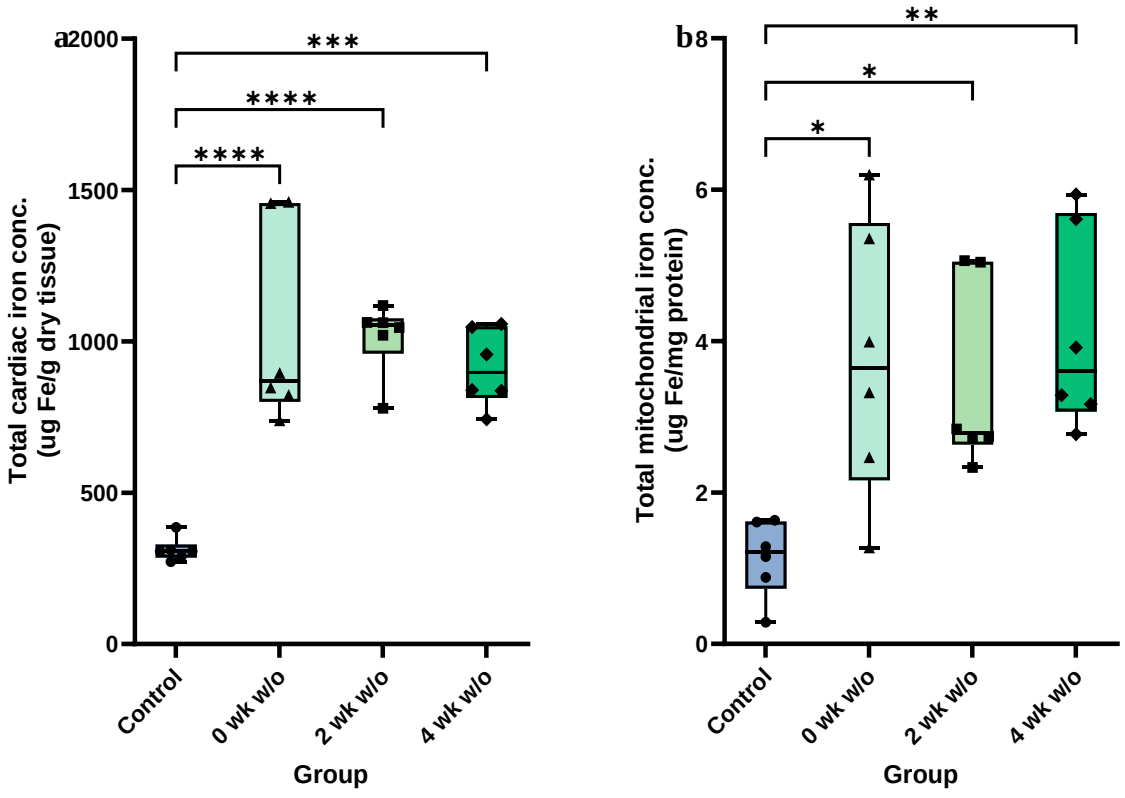

Figure 48: Total cardiac iron levels as assessed by ICPMS (56Fe). a Iron dextran increased total cellular cardiac iron 2.9-fold compared to the control (913.22±116.26 SD and 311.69±35.55 SD, respectively).Total cardiac iron concentration, expressed as µg of iron per g of cardiac tissue. **b** Iron dextran increased total mitochondrial cardiac iron ~3.5-fold compared to the control (4.11±1.22 SD and 1.14±1.22 SD, respectively).Total mitochondrial iron concentration, expressed as µg of iron per mg of protein. Statistical comparison by one-way ANOVA with Tukey's HSD correction method for multiple comparisons. *P<0.05, **P<0.01, ***P<0.001, and ****P<0.0001.

5.4.3.4 Cardiac Metabolism in Response to Iron Dextran Treatment

No significant differences in the overall cardiac metabolic profiles of the control and dextran groups were found. PCA analysis (Figure 50) failed to demonstrate clear separation between the groups. This was supported by fold change analysis (Figure 51), showing few and transient changes: a decrease in lactate at the end of iron dextran treatment, a decrease in aspartate until the second week of the washout period, and a decrease in taurine by the end of the washout period.

For mean metabolite concentrations, refer to Appendix (Table 16).

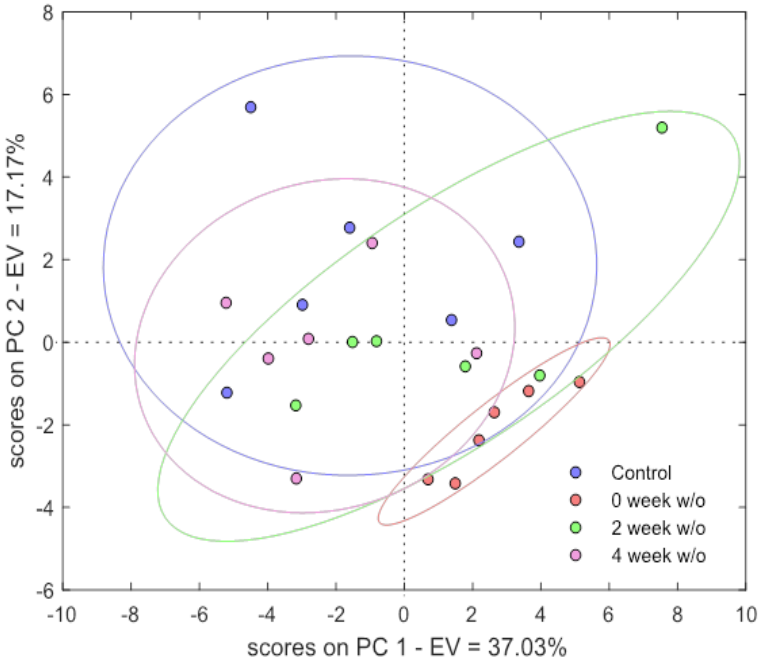

Figure 49: Principal Component Analysis (PCA) score plot from the aqueous cardiac metabolites of the iron dextran groups and control groups. In the 2D PCA score plot, control animals are denoted by the blue dots, while animals in the 0- week, 2-week, and 4- week groups are represented by the red, green, and pink dots, respectively. PC1 accounted for 37.03% of the total variance, and PC2 accounted for 17.17% of the total variance.

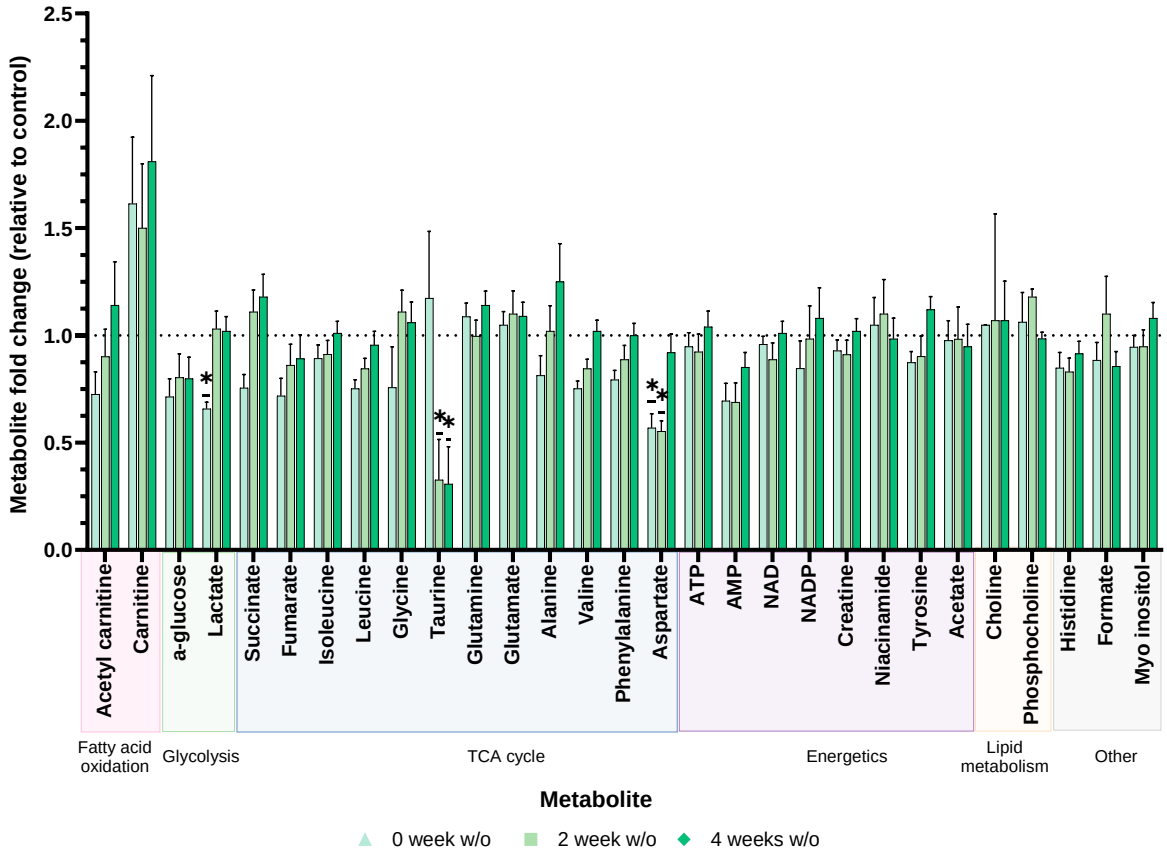

Figure 50: The fold change of aqueous cardiac metabolites at 0-weeks, 2-weeks, and 4-weeks after the end of iron dextran administration, relative to the control group. The fold change in metabolite concentration is represented as the mean ± SEM. Statistical comparison by one-way ANOVA with Tukey's HSD correction method for multiple comparisons. *P<0.01.

5.5 Discussion

A 4-week iron dextran I.P. approach to induce cardiac iron overload was implemented, referencing the protocol published by Avila *et al*[367]. A four-week washout period was included to observe the sustained effects of iron dextran, a component that was not part of the study regimen in the reference protocol.

The cardiac loading achieved in our study aligned with that reported in the reference paper. It was found that 4 weeks of iron dextran treatment followed by a 4-week washout period, resulted in a 2.9-fold increase in total cardiac iron compared to the control. This increase is comparable to the 2.8-fold reported in the reference paper. The fold increase reported in the reference paper was measured 9 weeks after the termination of iron dextran treatment. This suggests that the iron overload induced in our study is likely to be sustained for a similar time period after the end of iron dextran administration. As previously discussed, earlier studies demonstrated increased cardiac mitochondrial iron during systemic iron overload, making it

an important requirement for the clinical relevance of our model [109] [108]. In the present study, a ~3.5-fold increase in total cardiac mitochondrial iron levels was observed following the iron dextran treatment. This elevation was found to be statistically significant compared to our previously established reference control ranges (Chapter 4). This observation therefore fulfils a critical requirement outlined for our iron overload model. The reference study did not evaluate the total iron content within the mitochondria, therefore no comparisons can be made in this regard.

Cardiac index is perturbed at the end of the iron dextran treatment period but normalises during the washout. Stroke volume, however, progressively decreases after the end of iron dextran treatment, but left ventricular function is not perturbed enough to cause a measurable effect on LVEF, a key parameter used for the diagnosis of cardiotoxicity. This suggests that while changes in stroke volume occur, it does not have a substantial impact on overall cardiac function.

Iron dextran treatment did not significantly alter the metabolic profile of the heart. A few notable changes in specific metabolic concentrations were observed, which were transient; a decrease in lactate at the end of iron dextran treatment, a decline in aspartate until the second week of the washout period, and a reduction in taurine by the end of the washout period. The changes in lactate and aspartate normalize back to control levels by the end of the washout period, suggesting that their alteration is likely associated with the iron dextran treatment. Taurine is the only altered metabolite that remains perturbed by the end of the washout period. It plays roles in cardiac metabolism, including ion regulation, cellular signalling, and membrane stabilization. Metabolism is a complex network of interconnected pathways, and alterations in a single metabolite may not necessarily reflect a meaningful physiological change unless they are part of a larger metabolic shift or are accompanied by changes in other metabolites. As cardiac function has not changed and other metabolites remain at control levels, a change in a single metabolite such as taurine may be interpreted as a minor perturbation rather than a significant alteration in cardiac metabolism. Therefore, we conclude that these changes are relatively minor as they do not significantly impact the cardiac metabolic profile, as indicated by PCA analysis.

We observed that rats administered iron dextran via I.P. experienced a notable decrease in body weight compared to the control group. This weight loss can be attributed to several interrelated factors stemming from iron overload. Excess iron can accumulate in organs such

as the liver, heart, and pancreas, impairing their function. Impaired function of these key metabolic organs can disrupt nutrient metabolism and absorption, increases energy expenditure, and further contributes to weight loss, as seen in hemochromatosis patients [398] . In the Liver, excessive iron deposition can disrupt carbohydrate, fat, and protein metabolism, reducing overall energy availability, meaning the body may have to draw on stored energy reserves, such as muscle tissue. Excess iron also catalyzes the production of ROS, which damage cellular structures, leading to apoptosis, fibrosis, and systemic inflammation. This inflammation affects the body's ability to maintain homeostasis and can result in a chronic catabolic state, where muscle proteins are again degraded for energy due to the compromised nutrient metabolism, potentially leading to the weight loss we have observed [399] .

5.5.1 Conclusions

The iron dextran-based iron overload model presented in this study successfully elevated both global cardiac iron and mitochondrial iron levels, without permanently perturbing metabolism or overall cardiac dysfunction. This elevation was sustained over a 4-week period.

I therefore propose that this rat model is used to represent iron-overloaded patients at increased susceptibility to the cardiotoxic effects of DOX treatment. It was demonstrated that iron dextran had no sustained effects on cardiac function and metabolism that would significantly impact future studies, particularly those involving DOX.

To our knowledge, this is the first time the iron dextran iron overload model has been characterized in this manner, despite its widespread use in literature across rat, mice, and gerbil models.

5.6 A Comparative Analysis on Inducing Cardiac Iron Overload: Ferrocene and Iron Dextran Approaches

Iron dextran and ferrocene significantly elevated total cardiac iron levels compared to their respective controls. However, only the iron dextran study induced a significant increase compared to the reference range values established in Chapter 4 (Figure 52, a and b). The increase in total cardiac iron levels induced by 4 weeks of iron dextran treatment (100 mg/kg/day, 5 days/week) was significantly greater compared to that induced by 5 months of dietary ferrocene.

For clinical context, it is worth noting that total cardiac iron levels are consistent with normal Human cardiac iron levels (340 mg Fe/g dry tissue; range 290–470 mg Fe/g dry tissue) and are considerably lower than that reported in transfusion-dependent patients following either death or transplantation for end-stage heart failure (5980 ± 2420 mg Fe/g dry tissue) [123] [121].

For mitochondrial cardiac iron, a two-way ANOVA with Tukey's correction for multiple comparisons revealed that iron levels exhibited a significant elevation only in response to iron dextran treatment, compared to the respective study control and the reference range values. However, the increase in mitochondrial iron levels induced by dietary ferrocene did not reach significance compared to either control parameter. Neither strategy was found to result in significant cardiac function and metabolism alterations after their respective washout periods.

Throughout the study I characterized the sustained effects of iron dextran. The cardiac iron levels remained at the same elevation throughout the washout period and cardiac metabolism was not significantly perturbed. Only the iron dextran model met the key requirements outlined in terms of clinical relevance (5.1.1); Iron dextran induced increases in both global and mitochondrial cardiac iron compared to control values, and this effect was sustained after treatment.

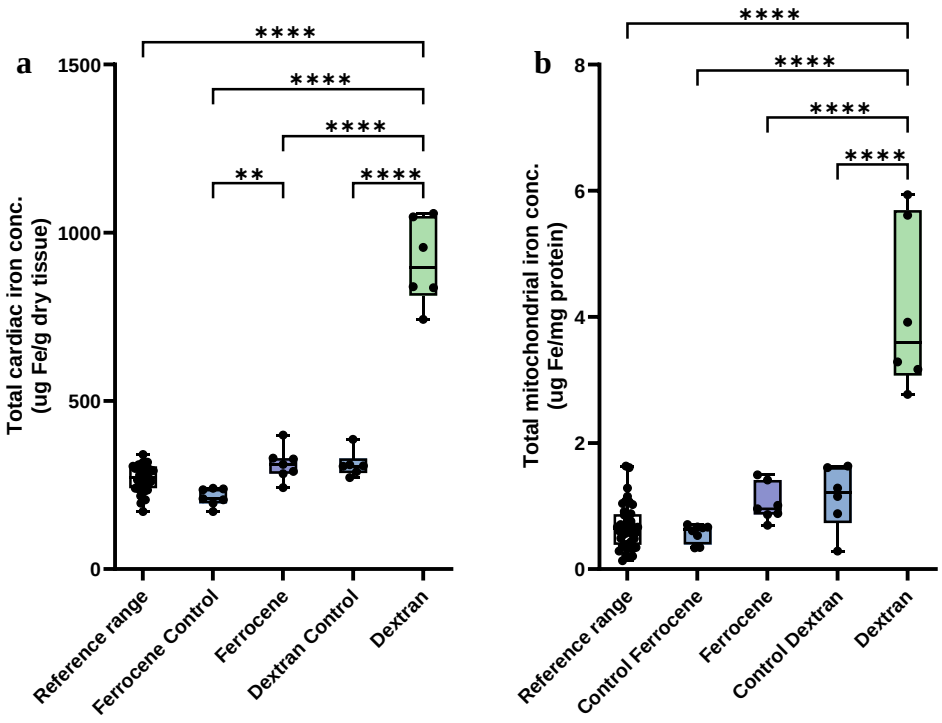

Figure 51: Comparative Evaluation of Cardiac Iron Overload Induced by Ferrocene and Iron Dextran Models. Total cardiac iron levels assessed by ICP-MS Analysis (56Fe). **a** Comparison of total cardiac iron levels induced by iron dextran and ferrocene models, along with respective controls, in reference to a previously established range derived from data on control cardiac tissue. Total cardiac iron concentration, expressed as µg of iron per g of cardiac tissue. **b** Comparison of total mitochondrial cardiac iron levels induced by iron dextran and ferrocene models, along with respective controls, in reference to a previously established range derived from data on control cardiac tissue. Total mitochondrial iron concentration, expressed as µg of iron per mg of protein. Statistical comparison by one-way ANOVA with Tukey's HSD correction method for multiple comparisons. *P<0.05, **P<0.01, ***P<0.001, and ****P<0.0001.

5.7 Summary

The aim of this chapter was to establish a rat model of cardiac iron overload for sub-clinically elevated iron levels as observed in a subset of cancer patients undergoing chemotherapy treatment. To permit the study of the inter-relationship between cardiac iron overload and DIC in evaluating the potential of iron chelation as a cardioprotective strategy.

The first direct quantification of mitochondrial cardiac iron during dietary iron overload was provided, which has only previously been inferred from indirect parameters [112][400][374][366][367]. To our knowledge, these studies are the first to evaluate cardiac iron overload models in terms of cardiac function, metabolism, and iron levels. Incorporating a washout period to distinguish the direct effect of iron overload from the residual presence of the iron delivery vehicle.

Ferrocene induced a milder elevation in both global and mitochondrial cardiac iron levels compared to iron dextran and required a five-fold longer dietary loading regimen. It was important to note that ferrocene was unable to load iron into the mitochondria, which likely impacts its ability to mimic the clinical situation.

The iron dextran-based iron overload model was employed in future coadministration studies with DOX and iron chelation. This model successfully elevated both global cardiac iron and mitochondrial iron levels. The model represents a subclinical representation of patients at increased susceptibility to the cardiotoxic effects of DOX treatment, as neither the cardiac function nor the metabolism was significantly perturbed. I characterized the iron dextran model in terms of its sustained effects and observed that iron levels remain constant during a 4-week washout period.

DEVELOPING AND VALIDATING AN *IN VIVO* MODEL OF CHRONIC DOX-INDUCED CARDIOTOXICITY

6.1 Introduction

This chapter outlines the development of a chronic model of DOX-induced cardiotoxicity (DIC) in rats. The model serves a dual purpose: to characterize the long-term chronic effects of DOX on cardiac function, iron levels and metabolism, and to determine the potential of therapeutic iron chelation as a cardioprotective strategy against anthracycline cardiotoxicity.

6.1.1 Clinical Features and Symptoms of DOX-Induced Cardiotoxicity

DIC causes a progressive, dose-dependent decline in both left ventricular systolic and diastolic function. Cardiomyopathy induced by DOX is characterized by the dilation of all heart chambers and severe left ventricular systolic dysfunction, ultimately leading to congestive heart failure[401]. The widely recognized diagnosis of cardiotoxicity is based on an absolute decrease in LVEF as an early sign of possible cardiotoxicity. The thresholds for a clinically significant drop in LVEF for the diagnosis of DIC varies depending on different authors and guidelines[402][403][404][153]:[405]. The European Society of Cardiology (ESC) specify a drop in LVEF of $\geq$ 10% from baseline to a value below the lower limit of normality as clinically significant[406]. Left ventricular fractional shortening (FS) can be also used as supplementary marker with clinical evidence of decrease in long-term survivors of DIC.[407][408].

The relationship between DIC and cumulative dose is widely documented[409][149]. However, the true incidence of DOX cardiotoxicity remains controversial due to differences in how it is measured. In a seminal retrospective study, Swain *et al*., demonstrated that heart failure occurred in 5% of patients with a cumulative dose of 400 mg/m^2, 16% at 500 mg/m^2, 26% at 550 mg/m^2, and 48% at 700 mg/m^2 [4]. Following these findings, the FDA recommended that the lifetime cumulative dosage of DOX should be limited to 450–550 mg/m^2[410], due to the increased risk of developing irreversible congestive cardiac failure, despite DOX doses as low as 250 mg/m2 being demonstrated to have cardiotoxic effects[411][412][413].

DIC is clinically classified according to time of onset[414][145]. Acute DIC occurs during or immediately after DOX treatment, while “early-onset DIC” occurs within a year post-

treatment. The chronic form, which we seek to model, is characterized by cardiac dysfunction that manifests >1 year post treatment. The interval preceding the onset of cardiac dysfunction is termed the latency period, during which the patient remains asymptomatic and exhibits normal cardiac function. The latency period can be considerably longer in paediatric patients[415][187][147]. A study conducted by Pein *et al*., involving 299 paediatric patients the risk of cardiac failure or severe abnormalities persisted even 15 years after the end of treatment, with reported cases up to 25 years later[416].

6.1.2 Rat Models of DOX-Induced Cardiotoxicity: An Evaluation of Clinical Relevance

DIC has been modelled in a variety of animals. Marala *et al*. was the first to model DIC using rabbits in 1967[417], with later studies conducted in larger laboratory animals such as pigs, monkeys, and dogs[418]. The transition to smaller animal models was driven by cost factors such as drug quantity needed, prolonged periods for the onset of cardiotoxic effects, and increased experimental costs associated with larger animals[419]. As a result, the current preference for modelling DIC is in rats and mice, given their ability to expedite the study of DOX effects within a shorter duration and with a larger sample size.

Mettler *et al*. were the first to assess the feasibility of using rats as a model for DIC[420]. Male Fischer rats received weekly doses of 1-2 mg/kg DOX for 10-14 weeks. Three to 23 weeks after the end of DOX treatment, cardiomyopathy developed in 36% and 92% of rats in the 1 and 2 mg/kg DOX groups, respectively, with 40-70% exhibiting signs of congestive heart failure. Since then, rat models have been widely employed for investigating the cardiotoxicity associated with DOX (and other anthracyclines), and the therapeutic approaches to mitigate its development.

Rat models of DIC can be broadly classified into acute and chronic models. In acute models, animals are typically administered either a relatively large dose of DOX (~10–30 mg/kg) via a single injection or smaller doses (>2 mg/kg) over a short period, typically spanning days to less than two weeks[419]. The administration of DOX is generally followed by immediate endpoints, typically within two weeks from the initiation of DOX treatment. Chronic models use similar cumulative doses as those in acute models but are administered serially (usually 1–5 mg/kg/week) over an extended time period[421]. The term "chronic models" does not

imply they are specifically designed to model chronic DIC. The designation refers to the dosage regime of serial dosing over a longer time compared to acute models.

Historically, models of DIC involving serial administrations have been categorized as chronic. I propose further subcategorizations, short-term chronic models and long-term chronic models based on the duration between the end of DOX treatment and sacrifice. Short-term chronic models refer to models that finish either immediately or within a few weeks after the end of DOX treatment. During this timeframe, any cardiac parameters measured reflect the acute effects of serial DOX treatment, valuable for understanding the early and immediate impact of DOX on the heart. Long-term chronic models assigned to studies that extend for several weeks or months following the last DOX dose. This facilitates the evaluation of the evolving, long-term and sustained impact of DOX on the heart, which is relevant to our research as we explore the role of iron in the subset of patients who develop cardiotoxicity several years after the end of DOX treatment, chronic DIC. It is also relevant to future ambitions in the molecular imaging of cardiotoxicity, for the detection of evolving cardiotoxicity during the clinically silent latent period.

Rat models of cardiotoxicity vary significantly with respect to cumulative dose, dosage protocol, time of sacrifice following DOX treatment, and clinical relevance, as depicted in Table 14. The serial dosing regimen in chronic models can be considered more clinically relevant than the bolus injections employed in acute models. Hayward *et al*., compared a single injection of 10 mg/kg DOX with serial administration of the same cumulative dose (2 mg/kg/week for 5 weeks)[421]. Serial administration manifested more clinical signs of DIC, as evaluated through echocardiography. Mortality rates were significantly reduced in the serial administration group; survival was 20 % after 28 days in the single bolus group, whereas 20% survival was 107 days in the serial administration group. As both groups received the same cumulative dose (10 mg/kg), the higher mortality rates observed in the acute group could be attributed to the substantial peak in DOX blood concentration induced by the single bolus injection. Clinically, DOX chemotherapy patients typically undergo up to six cycles of slow intravenous infusions to reach a total cumulative dose[422]. Patients would never receive their total cumulative dose in a single administration. A single bolus injection would likely invoke injury mechanisms that are not clinically relevant, contributing to the higher mortality rates observed in the study and in acute models in general. Serial administration is more closely aligned with the dosage regimen observed in clinical settings.

The administration of DOX in *in vivo* rat studies varies, involving either I.P. or I.V. injections. In clinical practice, DOX is typically administered to patients through repeat I.V. injections or continuous I.V. infusions [423]. Thus, I.P. injections lack clinical significance and I.V. injections through the tail vein better replicate actual treatment approaches. Administration of DOX by I.P. injection has been demonstrated to induce peritoneal inflammation, pain and eventual peritoneal fibrosis with bowel obstructions[424]. Such abdominal perturbations can lead to alterations in food intake and other confounding effects, invoked by the mode of DOX administration rather than DOX itself[425]. As such, they are less clinically relevant and include confounders which make data interpretation difficult.

Most patients undergoing DOX treatment do not exceed the recommended cumulative dose limit of 550 mg/m^2[426]. For comparability with *in vivo* cumulative dose values, this upper limit can be converted into mg/kg using the following calculation.

Using the average mass and height of a UK man (85.1 kg, 175.5 cm)[427], resulting in a body surface area of 2.03 m^2, a patient receiving the upper limit dose of 550 mg/m^2 would receive a total of 1116.5 mg of DOX, equivalent to a cumulative dose of 13.1 mg/kg. It is evident that most animal models of DOX-cardiotoxicity employ doses of DOX exceeding the clinically relevant recommended limit for patients, as denoted in Table 14. There are few 'long-term chronic' models of DIC that incorporate a clinically relevant cumulative dose as part of their treatment regimen.

The generalised classifications of 'acute' and 'chronic' for inducing DIC in rats fails to capture the considerable variation in dosage and dosing regimens found in the literature and illustrated in Table 14. Measurements of total cellular and mitochondrial cardiac iron during DOX treatment remain largely unexplored in rat models of DIC, an aspect we aim to investigate.

Table 14: Modelling of DOX-Induced cardiomyopathy in rats. Table modified from Podyacheva *et al*.,[419] incorporating additional studies and introducing 'Time of sacrifice after last DOX dose' and 'Iron measurement' columns, along with corrections for the route of administration. Values marked with an asterisk (*) correspond to cumulative dose values that exceed the upper recommended clinical cumulative DOX dose limit, calculated based on the height and weight of the average UK man.Number of doses (d).Studies ordered chronologically.

Reference	Sex, strain, age/ bodyweight	Dose of DOX			Route of administration	Time of sacrifice after last DOX dose	Cardiac iron investigations
		Dose per injection	Cumulative dose	Dosage regime			
Mettler, *et al.*, (1977).[420]	Male Fischer, 6wks.	1mg/kg	75mg/kg*	Weekly/10wks	I.V.	End of life (3-23wks)	-
		2mg/kg	120-156mg/kg*	Weekly/14wks			
Lanza *et al.*, (1989).[428]	Female, 150g.	3mg/kg	9mg/kg	3d; Every 3 days/9 days	I.V.	8.5wks	-
Villani *et al.*, (1991).[429]	Female CD, 120–130g.	3mg/kg	12mg/kg	4d; Once wk/4wks	I.V.	5wks	-
Sacco *et al,*. (2001).[430]	Male Sprague–Dawley, 27–29 old.	1.5 mg/kg	7.5 mg/kg	5d; Once wk/5wks	I.V.	4wks	-
Sayed-Ahmed *et al,*. (2001).[431]	Male Sprague–Dawley, 200–250g.	5 mg/kg	5 mg/kg	Single dose	I.V.	24hrs	-
			10 mg/kg	2d;Every other day			
			15 mg/kg*	3d;Every other day			
			20 mg/kg*	4d;Every other day			
Panjrath *et al,*. (2007).[374]	Male Sprague–Dawley, 16wks.	6 mg/kg	6 mg/kg	Single dose	I.P.	2wks	✓
Hayward *et al,*. (2007).[421]	Male Sprague–Dawley, 250–300g.	10m/kg	10mg/kg	Single dose	I.P.	16wks	-
		1m/kg		10d; Daily/10days		14wks	
		2m/kg		5d; Weekly/5wks		10wks	
Rahimi Balaei *et al.*, (2010).[432]	Male Wistar 200–230g.	1.25 mg/kg	20 mg/kg*	16d; 4x wk/4wks	I.P.	4wks	-
Anmar *et al,*. (2011).[307]	Male	15mg/kg	15mg/kg*	Single dose	I.P.	4wks	-
Hydock *et al.*, (2012).[433]	Female Sprague-Dawley, 200g.	1 mg/kg	15 mg/kg*	15d; Daily/15days	I.P.	8wks	-
		2.5 mg/kg	15 mg/kg*	6d; Once wk/6wks		4wks	
Ivanová *et al.*, (2012).[414]	Male Wistar, 230–260g.	2.15 mg/kg	15 mg/kg*	7d; Every 3 days/3wks	I.P.	4wks	-
						8wks	

Todorova *et al.*, (2012).[434]	Female Sprague-Dawley	12 mg/kg	12 mg/kg	Single dose	I.P.	48 hours	-
Hole *et al*,. (2013).[435]	Male Wistar, 200±2g.	2 mg/kg	15 mg/kg*	5d; Daily/5days	I.P.	9 days 9wks	-
Merlet *et al*,. (2013). [436]	Male Sprague–Dawley, 225–250g.	2.5 mg/kg	15 mg/kg*	6d; Every 2-3 days/2wks	I.P.	3wks 8wks	-
Toblli *et al*,. (2014). [437]	Male wistar, 19wks.	3, 4, or 5 mg/kg	18, 24, 30mg/kg, resp.*	6d; Weekly/6wks	I.P.	2wks	n/a
Lončar-Turukalo *et al*,. (2015).[438]	Male wistar, 300±10g.	2.5 mg/kg	17.5 mg/kg*	7d; Every 2 days /2wks	I.P.	10wks	-
Qian-Yun Niu *et al*,. (2016).[439]	Male Sprague–Dawley, 180–220g.	Consecutive: 1, 1, 2, 2, 3, 3, 4, and 4mg/kg	20 mg/kg*	8d; Every 2 days/15 days	I.P.	48 hours	-
Razmaraii *et al*,. (2016).[440]	Male Wistar, 180–220g.	2 mg/kg	12 mg/kg	6d; Every 2 days /12 days	I.P.	24 hours	-
O'Connell *et al*,. (2017).[441]	Male Wistar, ~250g.	2.5 mg/kg	15 mg/kg*	6d; Every 2-3days/2wks	I.P.	Immediate	-
		2 mg/kg	18 mg/kg*	9d; Weekly/9wks			
Ahmad *et al*,. (2017).[442]	Male Albino Wistar, 150–180g.	2.5 mg/kg	15 mg/kg*	6d; Every 2-3 days /2wks	I.P.	24 hours	-
Cappetta *et al*,. (2017).[443]	Female Fischer, 3 months.	2.5 mg/kg	15 mg/kg*	6d; Every 2 days /2wks	I.P.	4wks	-
Kang *et al*,. (2017).[444]	Male wistar, 250.4±4.3g.	2.5 mg/kg	10 mg/kg	4d; Weekly/4wks	I.P.	1wk	-
		3 mg/kg	12 mg/kg				
		3.5 mg/kg	14 mg/kg*				
		4 mg/kg	16mg/kg*				
Medeiros-Lima *et al*,. (2019).[445]	Male, 220–250g.	2.5 mg/kg	15 mg/kg*	6d; Every 2-3days/2wks	I.P.	Immediate	-
Aygun *et al*,. (2019).[446]	Male Wistar, 225–280g.	6 mg/kg	18 mg/kg*	3d; Daily/3 days	I.P.	24 hours	-
Barış *et al*,. (2019).[447]	Male Sprague–Dawley, 300–400g.	8.3 mg/kg	25 mg/kg*	3d; Daily/3 days	I.P.	24 hours	-
Aykan *et al*,. (2019).[448]	Male Wistar, 200–300g.	1.25 mg/kg	20 mg/kg*	16d; Every 4days/4wks	I.P.	4wks	-
Chakouri *et al.*, (2020). [449]	Male wistar, 96.4±1.9 g.	1.5 mg/kg	7.5 mg/kg	6d; Weekly/5wks	I.V.	16wks	-
		2 mg/kg	10 mg/kg				
		2.5 mg/kg	12.5mg/kg				
Timm *et al.*, (2020). [425]	Male wistar, 238 ± 36g.	2 mg/kg	12 mg/kg	5d; Weekly/6wks	I.V.	Immediate	-

		3 mg/kg	15 mg/kg*	5d; Weekly/5wks			
Adıyaman *et al.*, (2022).[450]	Male Sprague–Dawley, 300–400g.	10 mg/kg	10 mg/kg	Single dose	I.P.	1wk	-
Chen *et al.*, (2023).[451]	Male, adult.	2.5 mg/kg	20 mg/kg*	8d; twice weekly/4wks	I.P.	4wks	-

6.2 Aims

Our aim was to develop a model that replicates the pathology of chronic DIC. The study evaluated three cumulative DOX doses (8 mg/kg, 12 mg/kg, and 16 mg/kg) administered via I.V. tail vein injection over a 4-week period, followed by a 6-week latency period during which no drug was administered. This study served a dual purpose: To characterize cardiac function, metabolism, and iron levels in chronic DIC, and to develop a model suitable for our coadministration study involving iron overload and iron chelation treatment. The study was designed to ensure that the treatment regimen closely resembled clinical DOX treatment in patients. The clinical relevance of key treatment parameters were carefully considered, specifically focusing on cumulative dose, dosage protocol, and administration route.

6.2.1 Experimental Design Rationale

The frequency of dosing varies among patients depending on the required chemotherapy cycles, which can be adjusted during treatment. As cumulative dose is a consistent guideline adhered to during DOX treatment, I focused on ensuring the clinical relevance of the chosen DOX dose groups in terms of cumulative dose.

As outlined in section 6.1.2, the maximum recommended cumulative dose limit is 550 mg/m^2, equivalent to a cumulative dose of 13.1 mg/kg. The recommended starting dose for DOX treatment typically commences at 60 mg/m^2 [426][452]. For a standard regimen of 6 cycles[422], the resulting lower end cumulative dose is 360 mg/m^2, equivalent to 8.5 mg/kg. Considering these clinically relevant dose ranges, I chose 8 mg/kg dose as the lower limit and 12 mg/kg dose as the upper limit for our study. Both doses represent a clinically relevant cumulative dose. I also included a high cumulative dose group of 16 mg/kg, despite exceeding the recommended clinical dose limit. This decision was based on evidence indicating that

similar cumulative doses have been associated with the development of cardiac injury characteristic of DIC in rats within 6-10 weeks of DOX treatment[421] [453]. Examining a range of DOX doses was considered important for establishing a model of DIC, enabling the identification of the minimum dose at which observable effects occur. The selected doses were selected with the aim of establishing a dose-response relationship and to identify thresholds where adverse metabolic effects and cardiac iron changes became more pronounced.

6.3 Methods

The methodology for the following parameters were conducted as previously described in Chapter 3: Echocardiography, cardiac tissue collection, NMR sample preparation and acquisition parameters (relevant to cardiac tissue and aqueous metabolites), and ICPMS-based cardiac iron measurements.

6.3.1 Animal Preparation

All animal experiments conformed with our institutional animal care guidelines and the United Kingdom Home Office Guide on the Operation of Animal (Scientific Procedures) Act of 1986. Eighty adult male Wistar rats (7-9 weeks old, 200-300g) were purchased from Charles River Laboratories. Animals were housed in groups of four under controlled conditions: at 23 ± 2°C with 12 h light/dark cycles. Animals were acclimated for 7 days before the start of the study and had access to water and food *ad libitum* for the duration of the study.

6.3.2 Experimental Protocol

Adult male Wistar rats (200-300g) were divided into 4 experimental groups (n=12, respectively): a control group and three DOX groups. Within the DOX groups, rats were administered four intravenous (IV) injections over a 4-week period with doses of 2 mg/kg, 3 mg/kg, or 4 mg/kg of DOX dissolved in sterile saline. This regimen resulted in total cumulative DOX doses of 8 mg/kg, 12 mg/kg, and 16 mg/kg, respectively. The control group received equivalent volumes of sterile saline, following the same injection schedule as the DOX groups. Following the 4-week treatment period, the animals were subjected to a 6-week period without any interventions. This 6-week interval is referred to as the latency period, serving as representative of the duration during in which patients typically remain asymptomatic before the onset of clinically diagnosable DIC. Body weight was measured weekly throughout the entire study and cardiac function was measured bi-weekly. At the end of the study, rats were

sacrificed, and the hearts excised for metabolic analysis and iron quantification measurements. A schematic timeline of this study is presented in Figure 53.

6.3.3 Intravenous Injection of DOX

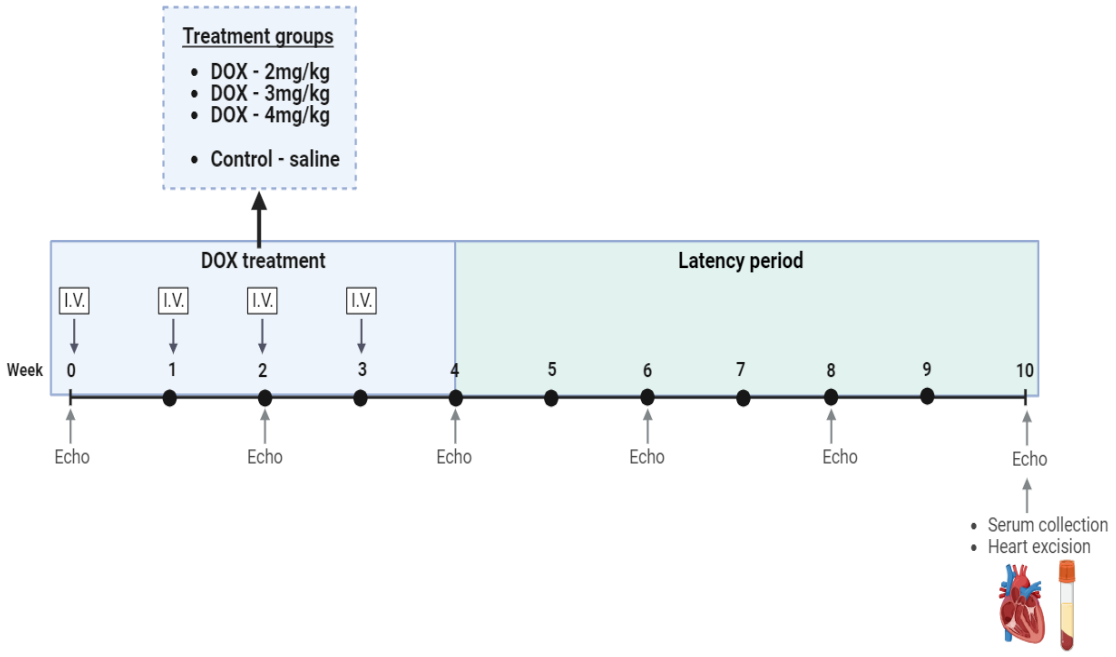

Figure 52: Study schematic: Inducing chronic DOX induced cardiotoxicity. The timeline depicted here presents the protocol followed by all treatment groups. I.V. injection of DOX or saline solution was administered once a week for 4 weeks, followed by a 6-week latency period. Cardiac function was assessed throughout the study using echocardiography. [Figure made in BioRender]

DOX (Cambridge Bioscience, UK) was dissolved in a sterile saline solution to a total injection volume of 400µl. Control rats were administered an equivalent volume of sterile saline solution.

Rats were anaesthetised (4% isoflurane mixed with 0.8 L/min 100% O2) in an induction chamber and transferred to a heating pad where anaesthesia was then maintained using a nose cone at 1% isoflurane at flow rate of 0.5 L/min. The tail of the rat was gently heated using a UV heat lamp (Charles River, UK) to promote vasodilation. A 27G needle, connected to a syringe by fine tubing, was inserted into one of the lateral tail veins. The appearance of blood in the tubing was used to confirm patency of cannulation and the DOX solution was then injected slowly as a bolus.

6.3.4 Echocardiographic Measurements

Cardiac function was assessed by echocardiography (3.2.5.2). Rats were anaesthetised (4% isoflurane mixed with 0.8 L/min 100% O_2) in an induction chamber and then transferred to a heating pad where anaesthesia was maintained using a nose cone at 2% isoflurane at flow rate of 0.5 L/min. Fur was then removed from the chest and abdomen region and echocardiography was performed using a Vevo 770 High Resolution Imaging System (VisualSonics, Toronto, Canada) with a RMV-710B transducer probe at 25 MHz (VisualSonics RMV-710B). The M-mode image of the left ventricle was used to determine multiple cardiac function parameters: left ventricular ejection fraction (LVEF), Fractional Shortening (FS), Cardiac Output (CO), Diastolic volume (DV) and Systolic volume (SV). All parameters were indexed to body weight.

6.3.5 Serum Collection

Rats were anesthetized (4% isoflurane mixed with 0.8 L/min 100% O_2) in an induction chamber and then transferred to a heating pad, where a nose cone was used to maintain anaesthesia at 4% isoflurane at flow rate of 0.5 L/min. A 27G needle, connected to syringe by fine tubing, was inserted into one of the lateral tail veins and blood slowly withdrawn and then transferred into sterile Eppendorf tubes. Blood was left to clot for ~30 minutes to 1 hour at room temperature. Each sample was centrifuged at 1500 xg for 10-15 minutes. After centrifugation, the serum separated to the top of the tube and was pipetted into Eppendorf vials. Serum was stored at -80°C until use.

6.3.6 NMR Measurements in Serum

6.3.6.1 Sample Preparation

Serum samples were collected as described in section 6.3.5 and 100µl of thawed serum was vortexed with 500µl D_2O solution containing Tetramethylsilane (TMS). The role of D_2O and TMS in serum NMR analysis is as described in 3.7.1. The samples were then transferred to 5mm NMR tubes (Norel Inc, USA) for ^{1}H NMR analysis.

6.3.6.2 Acquisition Parameters and Analysis

^{1}H NMR spectroscopy was performed on a 600-MHz Bruker spectrometer (Bruker, Germany). Serum samples were analysed using a Carr–Purcell–Meiboom–Gill (CPMG) pulse sequence.

Spectra were acquired using the following parameters: spectrometer frequency; 700.20 MHz, spectral width; 20.1 ppm/14097.7 Hz, acquisition time; 2.32 seconds, relaxation delay; 4 seconds, and number of scans; 64 scans, temperature; 298K.

All ^{1}H NMR spectra were post-processed in TopSpin software version 3.6.1 (Bruker, Germany). Metabolite peaks were manually integrated, and metabolic profiles were determined using Chenomx NMR Profiler Version 9.0 (Chenomx, Canada). Serum metabolite concentrations were calculated by referencing the metabolite integral and the TMS integral with respect to the volume of serum used in the NMR sample preparation (See 3.7.4).

6.3.7 Statistical Analysis

Unsupervised principal component analysis (PCA) was used to analyse the distribution of the metabolomic data derived from the control and ferrocene groups. If separation between the groups was observed, supervised partial least squares discriminant analysis (PLS-DA) was performed to better discriminate between the groups and to maximize separation associated with class membership. Unpaired Student's t-tests, one-way or two-way ANOVA with Tukey's HSD adjustment method for multiple comparisons were used and performed as indicated in each figure legend. Significance was assumed at $P < 0.05$. PCA and PLS-DA analysis was performed in MatLab, all other statistical analysis was performed in Prism 10 (GraphPad, La Jolla, CA, US).

6.4 Results

6.4.1 Body and Heart Weight

The general effects of DOX were assessed by monitoring body weight gain throughout the study (Figure 54). Rats subjected to DOX treatment exhibited a slower rate of weight gain compared to the control group. Over the 10-week study period, the average weight gain was 54%, 46%, and 15% in the control, 2 mg/kg, and 3 mg/kg groups, respectively. The 4 mg/kg dose group exhibited weight loss, with a 3.25% reduction from baseline measurements. The average body weights of the DOX groups diverged from the control and each other in a statistically significant, dose-dependent manner over the course of the study. Body weight was significantly lower than the control across all DOX groups starting from the second week of treatment. The 3mg/kg and 4mg/kg DOX groups became significantly different from the 2mg/kg DOX group starting from week 3 of the DOX treatment period, and the 4mg/kg group became significantly different from the 3mg/kg group 5 weeks after the end of DOX treatment. It was evident that the 4mg/kg DOX dose had particularly adverse effects on the animals in terms of body weight. Three weeks after the conclusion of the DOX treatment, animals in the 4mg/kg group began to experience weight loss, while the other groups continued to exhibit weight gain.

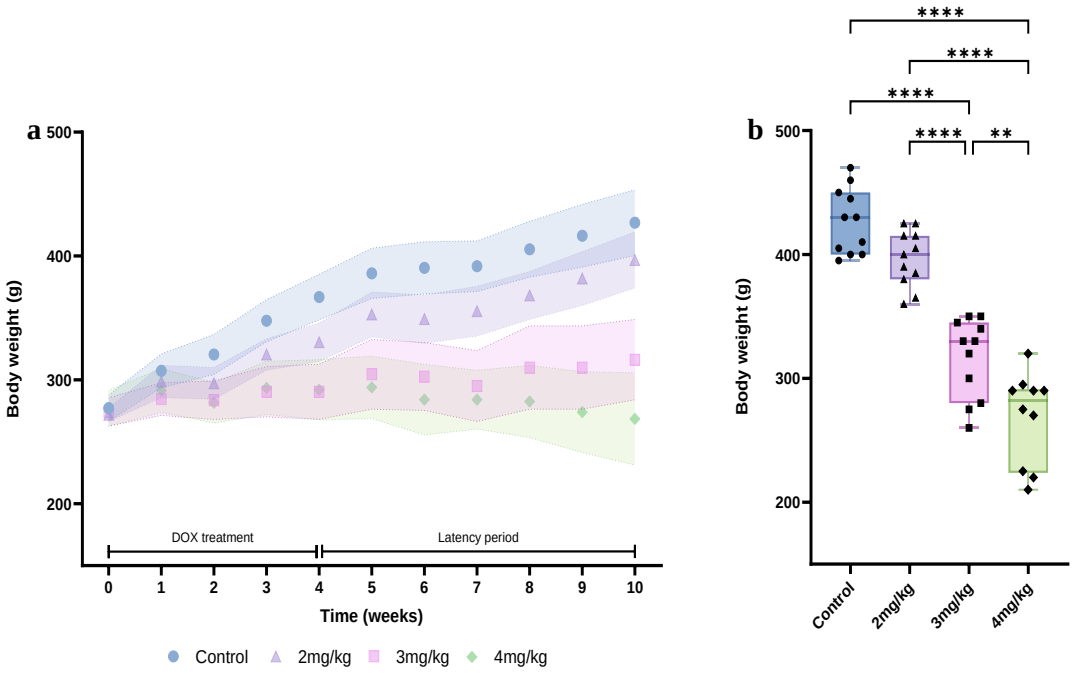

Figure 53: Average rat body weight measurements in the DOX treated groups and the control group. a Average rat body weight gain per week throughout the 10-week study (mean±SD). **b** Average rat body weight at the end of the study. Statistical comparison by one-way ANOVA with Tukey's HSD correction method for multiple comparisons. **P<0.01 and ****P<0.0001.

The divergence in average body weight from that of the control persisted across all DOX groups throughout the study, apart from in the 2mg/kg group. In the final week, the average body weight of the 2mg/kg DOX dose group became statistically insignificantly different from that of the control.

Similarly, the average heart weights in the DOX groups were all significantly lower than the control group, following a dose-dependent pattern, with the 4 mg/kg group exhibiting the lowest average heart weight (Figure 55,a).

The heart weights in the DOX groups at 3 mg/kg and 4 mg/kg were both significantly lower than those in the 2 mg/kg group, but the difference between the 3 mg/kg and 4 mg/kg groups did not reach significance.

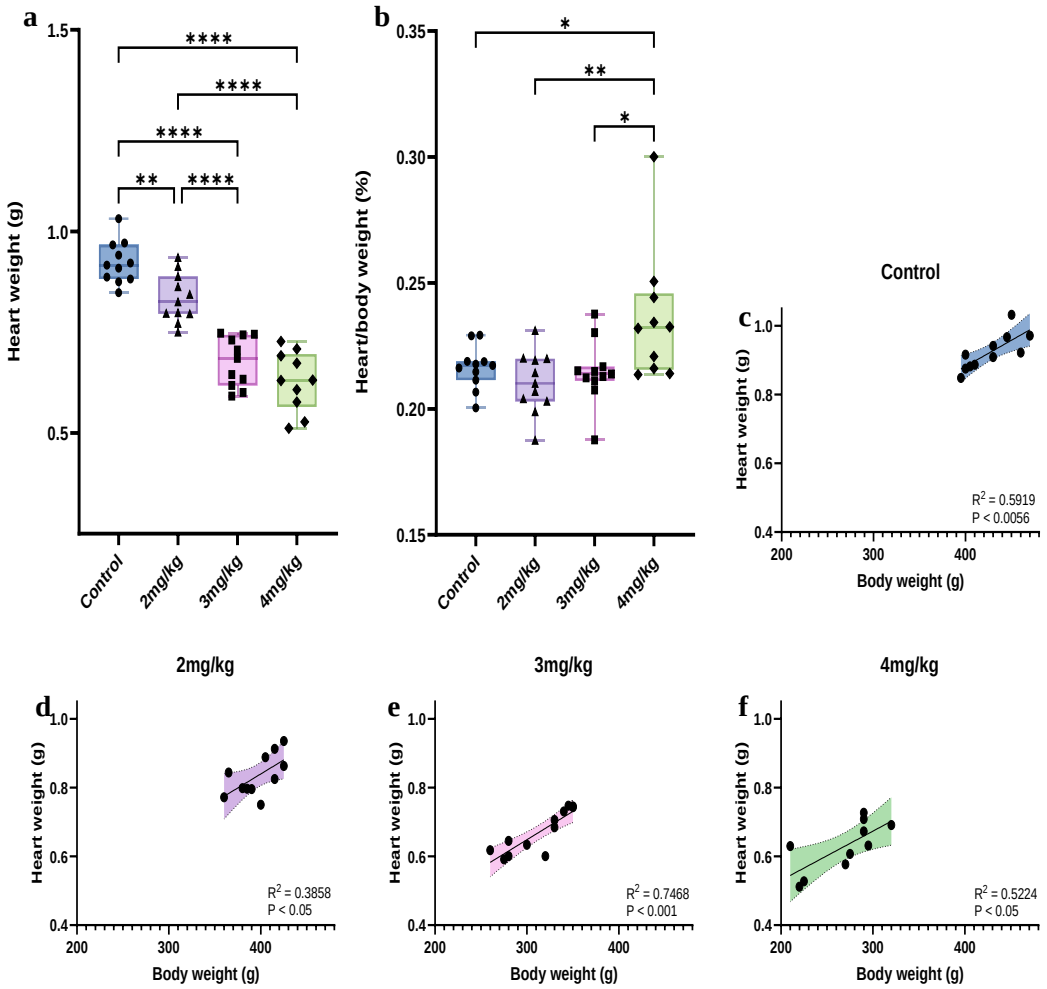

Figure 54: Average end-point rat heart weight measurements in the DOX treated groups and the control group. a Average rat heart weight. **b** Average rat heart:body weight ratio. Statistical comparison by one-way ANOVA with Tukey's HSD correction method for multiple comparisons (mean±SD). *P<0.05 , **P<0.01 and ****P<0.0001. **c, d, e**, **f** Heart weight plotted against body weight. Simple linear regression analysis.

Linear regression analysis demonstrated a positive correlation between heart weight and body weight across all groups. The heart-to-body weight ratio in the 4 mg/kg DOX group was significantly higher however than that of the control group and all other DOX groups. An elevated heart-to-body weight ratio is indicative of cardiac hypertrophy, suggesting a distinctive impact of the 4 mg/kg DOX dosage on cardiac morphology relative to the other groups[454].

6.4.2 Cardiac Function

Cardiac function parameters were assessed by conducting echocardiographic imaging every two weeks (Figure 56 and Figure 57). The impact of DOX on cardiac function was characterized by a reduction in LVEF, fractional shortening, stroke volume, and heart rate (Appendix: Figure 90) compared to the control, with the severity of the reduction correlating with increasing dose. Conversely, systolic volume exhibited a dose-dependent increase compared to the control.

Over the duration of the study, a 3% reduction was observed in LVEF in the control group, from an initial value of 77.26 ± 4.1% at baseline to 74.49 ± 25.96%. DOX treatment resulted in more substantial reductions in LVEF: 78.08 ± 4.49% to 68.13 ± 5.19% (2 mg/kg), 78.00 ± 2.98% to 62.91 ± 3.69% (3 mg/kg), and 75.27 ± 3.46% to 51.17 ± 5.18% (4 mg/kg), equivalent to drops of 12%, 20%, and 32%, respectively. Similar trends were observed in stroke volume and fractional shortening. Fractional shortening measurements decreased 6%, 14%, 27%, and 42%, for the control, 2 mg/kg, 3 mg/kg, and 4 mg/kg groups, respectively. After six-weeks, a dose-dependent reduction in LVEF in all DOX groups was seen compared to the control. Notably, the 4 mg/kg DOX dose induced the largest reduction. Fractional shortening and stroke volume endpoint measurements displayed the same pattern.

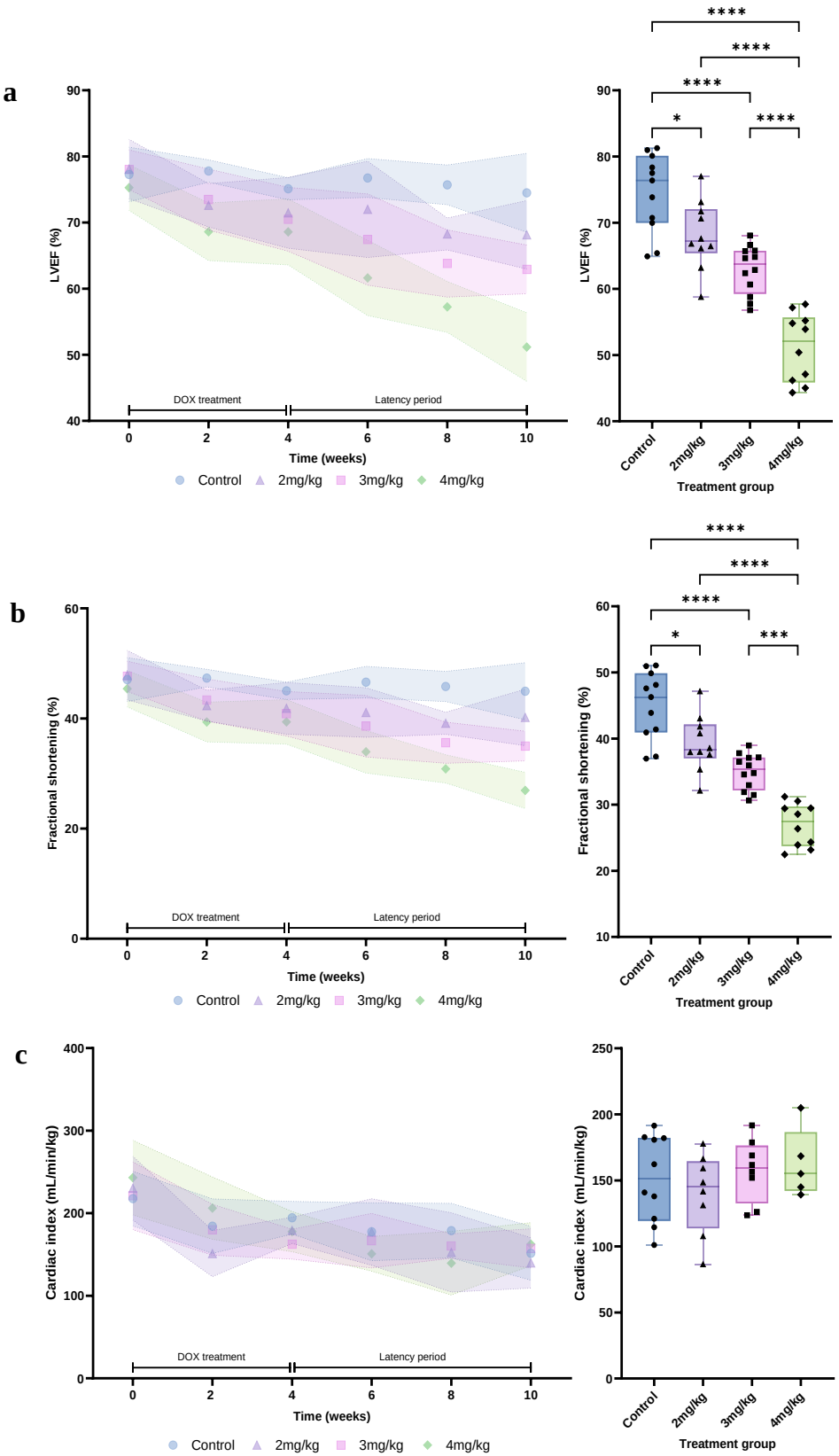

Figure 55: Cardiac functional parameters obtained by echocardiography. a Left ventricular ejection fraction (LVEF) **b** Fractional shortening **c** Cardiac index**.** Statistical comparison by one-way ANOVA with Tukey's HSD correction method for multiple comparisons. The longitudinal data is presented as mean ± SD in the graphs (left), while the endpoint data is shown using a box plot (right).

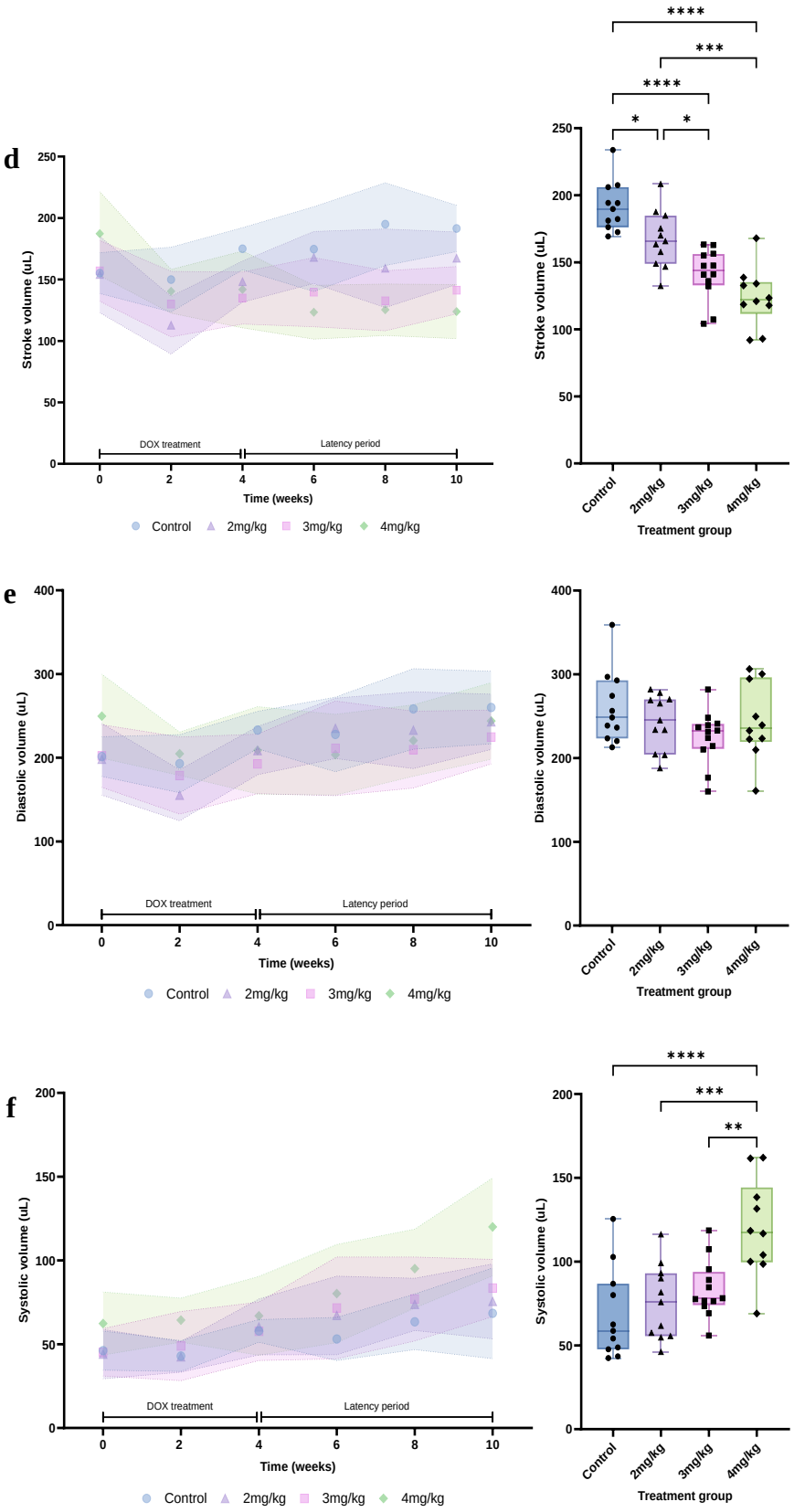

Figure 56: Cardiac functional parameters obtained by echocardiography. a Stroke volume index **b** Diastolic volume index **c** Systolic volume index. Statistical comparison by one-way ANOVA with Tukey's HSD correction method for multiple comparisons. The longitudinal data is presented as mean ± SD in the graphs (left), while the endpoint data is shown using a box plot (right).

In all DOX groups, endpoint systolic volume measurements were dose-dependently elevated compared to the control. This increase was statistically significant in the 4 mg/kg group. Measurements of systolic volume in the 4 mg/kg group steadily diverged from the control throughout the duration of the study, and the rate of increase away from the control group accelerated towards the end of the latency period. No statistically significant differences were observed in diastolic volume, cardiac output and stroke volume among the groups.

6.4.3 Cardiac Iron

A dose-dependent increase in total cardiac iron was observed across all DOX dose groups, compared to the control (Figure 58, a). However, only the 4 mg/kg dose induced a statistically significant elevation in total cardiac iron, which was also significantly higher than the levels observed in the other DOX groups. DOX treatment did not alter mitochondrial cardiac iron (Figure 58, b).

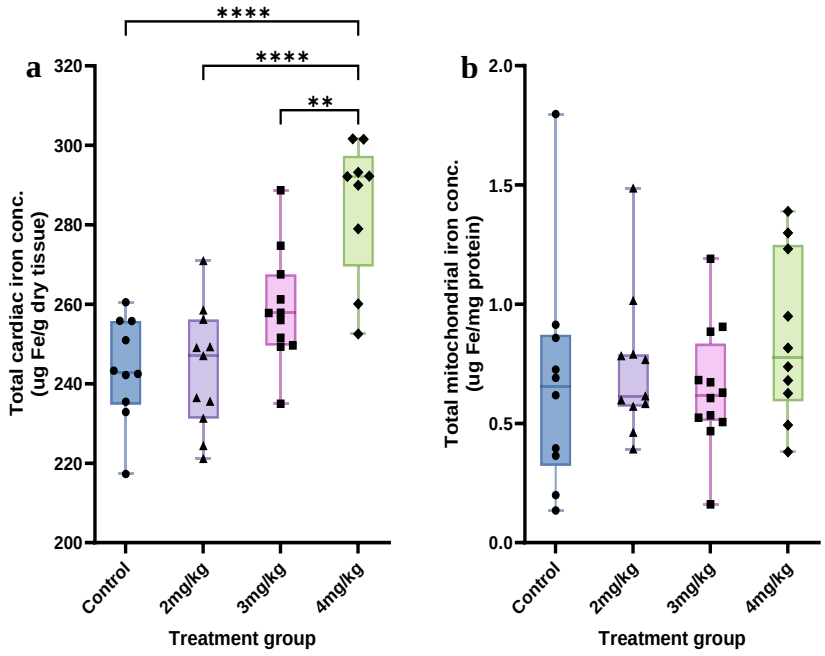

Figure 57: Total cardiac iron levels as assessed by ICPMS (^{56}Fe). a Total cardiac iron concentration**,** expressed as µg of iron per g of cardiac tissue. **b** Total mitochondrial iron concentration, expressed as µg of iron per mg of protein. Statistical comparison by one-way ANOVA with Tukey's HSD correction method for multiple comparisons, mean±SD. **P<0.01,

A potential outlier is noted in the control group. As this study marks the first instance of measuring mitochondrial iron by ICPMS, no literature benchmark values exist for comparison, leaving us unable to conclusively differentiate between elevated mitochondrial iron levels and

potential outliers. However, removing this data point did not affect the statistical significance of the DOX groups compared to the control.

6.4.4 Metabolism

6.4.4.1 Cardiac Metabolism

The PCA score plot revealed a mild dose-dependent separation between the metabolic profiles of the DOX groups and the control, the overlap with the control decreasing with increasing DOX dose (Figure 59, a). Given this observation, a PLS-DA analysis was conducted to enhance discrimination between the groups and maximize separation associated with class membership. The PLS-DA score plot illustrated a clear dose-dependent change in cardiac metabolism induced by DOX (Figure 59, b).

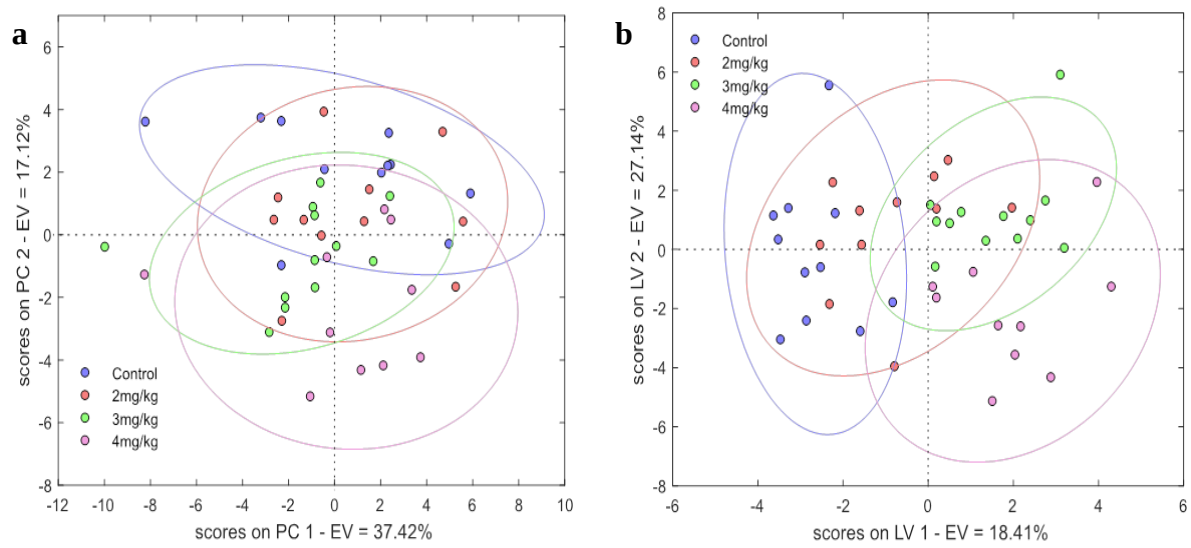

Figure 58: Principal Component Analysis (PCA) and Partial least squares-discriminant analysis (PLS-DA) score plots from the aqueous cardiac metabolites of the DOX and control groups. a PCA score plot: PC1 accounted for 37.42% of the total variance, and PC2 accounted for 17.12% of the total variance. **b** PLS-DA score plot: LV1 accounted for 18.41% of the total variance, and LV2 accounted for 27.14% of the total variance. Control animals are denoted by the blue dots, while animals in the 2mg/kg, 3mg/kg, and 4mg/kg groups are represented by the red, green, and pink dots, respectively.

The fold change analysis (Figure 60) indicates that the separation from the control group could be driven by altered metabolites across multiple metabolic pathways. Some key alterations detected in the 4mg/kg group include an elevation in lactate levels, a reduction in carnitine, and a decrease in phosphocreatine, suggesting a potential shift towards greater reliance on glycolytic metabolism. For mean metabolite concentrations, refer to Appendix (Table 15).

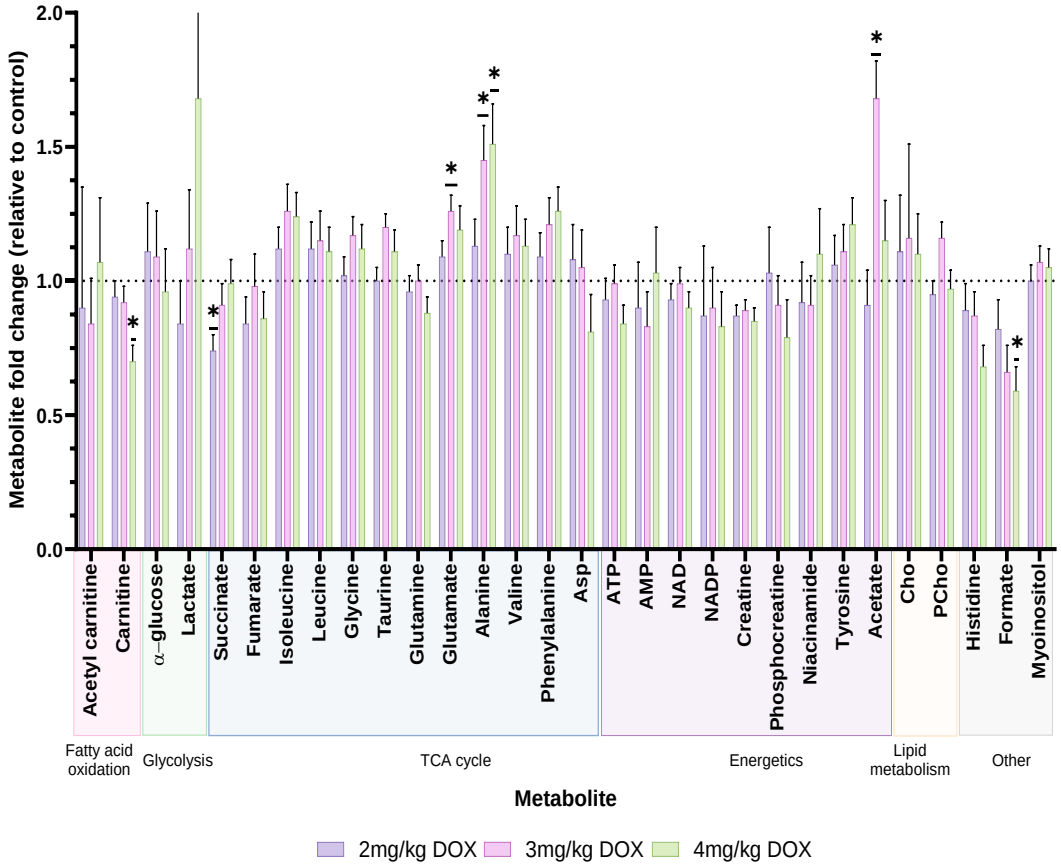

Figure 59: The fold change of aqueous cardiac metabolites in the DOX groups relative to the control group. The fold change in metabolite concentration is represented as the mean ± SEM. Statistical comparison by one-way ANOVA with Tukey's HSD correction method for multiple comparisons.

6.4.4.2 Serum Metabolites

The PCA and PLS-DA score plot showed that the DOX groups differed dose-dependently from the control, with elevated variability observed in the 3mg/kg DOX group and nearly complete separation from the control in the 4mg/kg group (Figure 61).

The fold change analysis (Figure 62) indicates that the respective degree of separation of the DOX groups from the control is driven by changes across multiple metabolic pathways, including glycolysis, the TCA cycle, energetics, lipid metabolism, and ketogenesis. The most substantial metabolic change was the increase in fatty acid residues, which were approximately 7-fold higher in the 3mg/kg and 4mg/kg groups compared to the control. TCA cycle amino acids experienced disruptions: glycine, glutamine, and phenylalanine decreased in the 3mg/kg and 4mg/kg groups, whereas isoleucine, leucine, and glutamate increased in the 4mg/kg group.

Additionally, a decrease in the energetic metabolite tyrosine was noted in both the 3mg/kg and 4mg/kg groups, alongside a reduction in glucose observed solely in the 4mg/kg group.

For mean metabolite concentrations, refer to Appendix (Table 18).

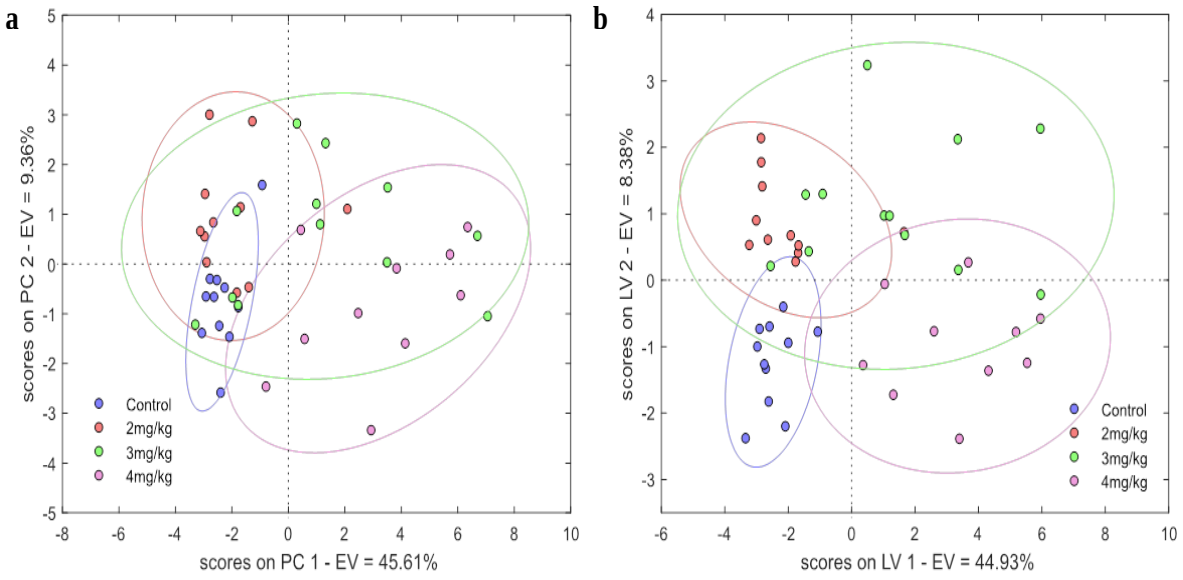

Figure 60: Principal Component Analysis (PCA) and Partial least squares-discriminant analysis (PLS-DA) score plots from the serum metabolites of the DOX and control groups. a PCA score plot: PC1 accounted for 45.61% of the total variance, and PC2 accounted for 9.36% of the total variance. **b** PLS-DA score plot: LV1 accounted for 44.93% of the total variance, and LV2 accounted for 8.38% of the total variance. Control animals are denoted by the blue dots, while animals in the 2mg/kg, 3mg/kg, and 4mg/kg groups are represented by the red, green, and pink dots, respectively.

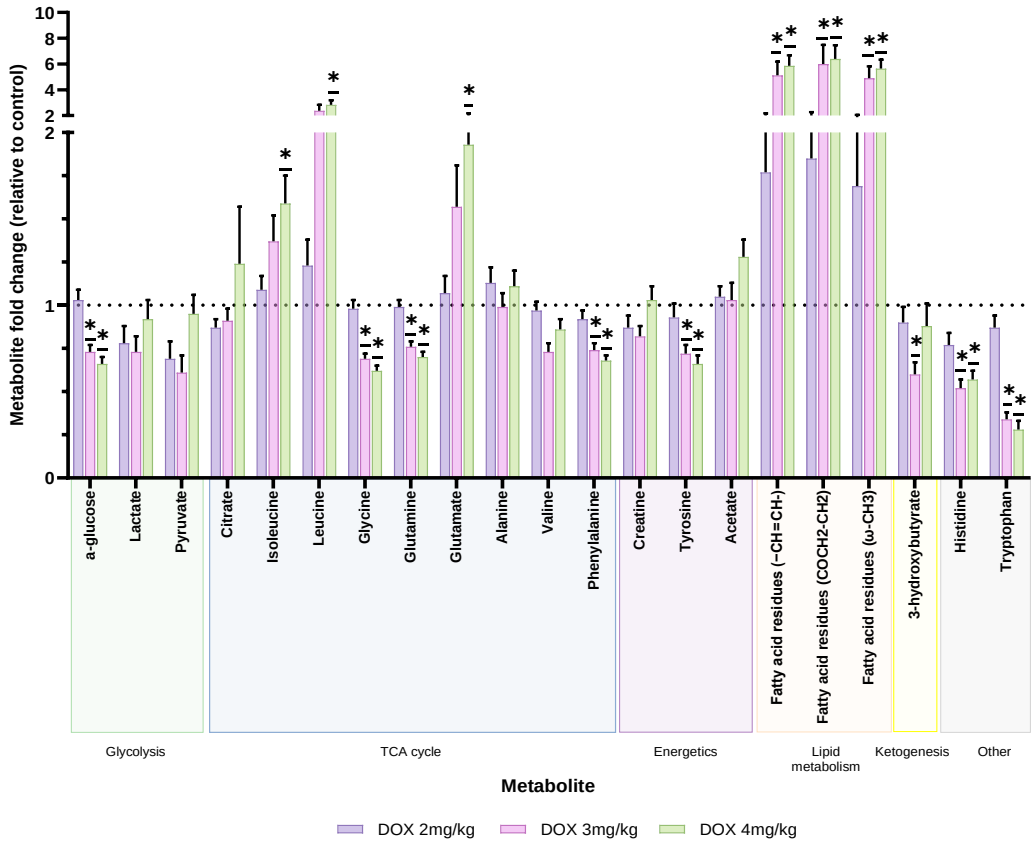

Figure 61: The fold change of serum metabolites in the DOX groups relative to the control group
The fold change in metabolite concentration is represented as the mean ± SEM. Statistical comparison by one-way ANOVA with Tukey's HSD correction method for multiple comparisons. *P<0.01.

6.5 Discussion

In the model, male Wistar rats received treatment with repeated administrations of either sterile saline or DOX at doses of 2 mg/kg (cumulative dose 8 mg/kg), 3 mg/kg (cumulative dose 12 mg/kg), or 4 mg/kg (cumulative dose 16 mg/kg) over a 4-week period. The effects of DOX were evaluated by continuous monitoring of body weight and echocardiography to assess cardiac function. Cardiac metabolism and iron levels were analysed several weeks after the end of treatment. The DOX treatment protocol was informed by clinical practice and literature pertaining to rat models of delayed DIC. The objective was to induce chronic DIC in rats within a condensed timeframe, resembling the presentation observed in humans several years after the end of treatment.

6.5.1 Dose-Dependent Reduction in Weight Gain Induced by DOX

DOX toxicity was evidenced as a decline in body weight gain compared to saline-treated controls, with significance observed in all groups starting from the second week of DOX treatment. Through the study, the 2 mg/kg, 3 mg/kg, and 4 mg/kg groups experienced average body weight changes of 46%, 15%, and -3.25%, respectively, while the saline-treated control group showed an average body weight gain of 54%.

The variation in average body weight gain among the DOX groups occurred in a dose-dependent manner, with the 4 mg/kg group being the most affected, evidenced by weight loss starting from the third week of the latency period. Weight loss attributed to DOX treatment in rats is widely reported in the literature (Table 14). The weight loss was initially attributed to a probable reduction in food intake caused by DOX-induced loss of appetite. However, Desai *et al.*, demonstrated that the average daily food intake in DOX-treated mice, subjected to a similar cumulative dose and treatment regimen as utilized in our study, was not significantly different compared to saline-treated mice[455]. Chemotherapy-induced gastrointestinal (GI) damage is commonly reported among cancer patients, where gastrointestinal toxicity is responsible for dose reductions, treatment delays, and discontinuation of cancer treatment. DOX-induced GI toxicity has also been observed, with vacuolation of GI epithelial cells[456]. The detrimental impact of DOX on the GI epithelial lining likely contributes to malabsorption, resulting in the significant reduction in body weight gain observed.

6.5.2 Elevated Heart-to-Body Weight Ratio in the 4 mg/kg DOX Group

Cardiac hypertrophy is widely a described manifestation of DIC, characterized by elongation of cardiac myocytes, causing left ventricular dilation, and left ventricular wall thickening[457][458][459][460][403]. Elevated heart: body weight ratio is an indicator of cardiac hypertrophy[454][457]. In rats, heart weight closely correlates with body weight, as evidenced by linear regression analysis that revealed a positive correlation across all the groups. The heart's growth relative to total body growth remains relatively constant under diverse dietary conditions[454]. The significant increase in heart: body weight ratio observed in the 4 mg/kg group compared to both the control group and all other DOX-treated groups is an indicator of cardiac hypertrophy[454][457].

The presence of cardiac hypertrophy in the 4 mg/kg group is substantiated by the large 32% reduction in LVEF. The characteristic thickening of the left ventricular walls in cardiac

hypertrophy leads to elevated blood pressure, that progressively impedes the heart's efficiency in pumping blood could be contributing to the reduction in LVEF observed[461].

6.5.3 Dose-Dependent Cardiac Dysfunction Induced by DOX

DIC is characterized clinically and *in vivo* as a progressive, dose-dependent decline in left ventricular function[462][463]. LVEF is a key parameter used to determine left ventricular dysfunction, a reduction in LVEF is an established clinical hallmark in the diagnostic criteria of DIC[464][403][465]. Left ventricular FS is also commonly used in conjunction with LVEF to evaluate left ventricular systolic dysfunction[421][466][467][462].

In the study, DOX induced a progressive reduction in left ventricular function, evidenced by a significant dose-dependent reduction in LVEF and FS in every DOX group. DOX treatment also led to elevated systolic volume, indicative of compromised systolic cardiac performance and left ventricular function. DIC can result in elevated systolic volume through several pathways. DOX-induced cardiac cell damage can lead to a decrease in contractility and inefficient cardiac emptying, prompting a decrease in cardiac emptying [468]. Altered myocardial remodelling due to DOX can disrupt normal heart structure and function, impairing contractility [184].

The 4mg/kg group also had indications of heart failure; exhibiting a statistically significant increase in systolic volume with a decrease in heart rate. A decreased heart rate, commonly reported during DOX treatment *in vivo*, is a possible compensatory mechanism to maintain cardiac output when contractility is compromised[425][469][470]. Changes in systolic volume and heart rate did not reach statistical significance in the 2mg/kg group and 3mg/kg groups, however subclinical changes of the same pattern can be seen. In line with clinical findings, the degree of DIC in our study exhibited dose-dependent patterns, reflected by the escalating dysfunction severity across the DOX dose groups.

Cardiac dysfunction evolved progressively throughout the study, changes in cardiac parameters became more pronounced in all groups over time. Similar to the pattern seen in chronic DIC[187][147], serial cardiac echocardiography measurements revealed subclinical dysfunction in LVEF and FS in all groups, evolving into significant dysfunction over time. The subclinical phase characteristic of chronic DIC is referred to as the latency period, during which cardiac dysfunction is not significantly different to the control (outlined in 6.1.1)[147]. Changes in cardiac parameters did not revert to control levels after the end of DOX treatment,

indicating that the damage incurred was non-acute. Acute DIC typically returns to control levels after treatment cessation, whereas the model exhibited a progressive and evolving dysfunction[403][187][147].

Considering these factors, we can infer that our model effectively induces cardiotoxicity, and resembles the clinical presentation of chronic DIC.

6.5.4 Metabolic Changes Induced by DOX-cardiotoxicity

1H NMR analysis was conducted on cardiac tissue to assess the impact of DOX treatment on cardiac metabolism. The objective to evaluate the biochemical effects induced by DOX to characterise our experimental model. Six weeks after the end of DOX treatment, metabolomic analysis demonstrated a dose-dependent change in the cardiac metabolic profiles, reflecting a difference in cardiac dysfunction severities between the models. The cardiac metabolic profile of the 4 mg/kg group exhibited the largest alteration, while there was minimal difference between the 2 mg/kg group and the control.

It was hypothesized that DOX treatment would induce a switch from oxidative to glycolytic metabolism. In a healthy heart, the primary source of cardiac ATP is mitochondrial oxidative phosphorylation, with glycolysis contributing a minor proportion 5%.[471]. The majority of mitochondrial ATP production, 40-60%, is derived from fatty acid oxidation, with the remainder attributed to the oxidation of pyruvate, ketone bodies, and amino acids[472]. In a failing heart, an energy demand-supply imbalance arises, primarily attributable to compromised fatty acid oxidation[472]. This prompts a shift to glycolysis for ATP production, whereby glycolysis converts glucose to pyruvate, generating a small amount of ATP and NADH. However, instead of proceeding into the TCA cycle, pyruvate undergoes lactic acid fermentation, regenerating the NAD+ necessary for sustaining glycolysis. This energy imbalance, leading to a shift towards glycolysis over fatty acid oxidation, may result from impaired mitochondrial respiratory capacity, changes in energy substrate levels, and reduced cardiac efficiency[473]. In the context of DOX treatment, its expected that the central element in this metabolic shift is the impairment of mitochondrial capacity, supported by substantial evidence detailing DOX-induced mitochondrial injury (as outlined in Section 2.5.2.3). Mitochondria are susceptible to oxidative stress induced by DOX-generated ROS. ROS generation results in increased mitochondrial depolarization, permeability, swelling, and direct damage to mitochondrial DNA[474][475][208][476][233]. DOX has also been shown to

preferentially accumulate in mitochondria *in vitro*, where it undergoes redox cycling, further contributing to oxidative damage[205]. Additionally, DOX can directly inhibit mitochondrial function through its interaction with Complex I of the respiratory chain[233]. In situations of compromised mitochondrial function, glycolysis emerges as a prominent pathway for ATP generation over fatty acid oxidation, providing a temporary solution to meet energy demands in the cytoplasm without requiring intact mitochondrial function.

The PCA/PLS-DA analysis showed that the metabolic cardiac profile of the 4mg/kg group was altered the most, accompanied by evidence indicative of a shift to glycolytic metabolism. Lactate is a byproduct of glycolytic metabolism, where pyruvate is converted to lactate through lactic acid fermentation, facilitated by the cytosolic enzyme lactate dehydrogenase[477]. This conversion aids the regeneration of NAD+, enabling the continuation of glycolysis for ATP production[478]. Lactate increased in the 4mg/kg groups compared to control tissue[479]. Elevated lactate levels indicate increased dependence on glycolytic metabolism for ATP generation, indicative of mitochondrial energetic compromise. Mitochondrial dysfunction likely underlies the cardiac contractile dysfunction observed in the study. This association is well-documented in the literature[480][481][476][233].

A decrease in carnitine concentration was observed in the 4mg/kg DOX group, a marker of cardiac dysfunction. Carnitine plays a critical role in the energy metabolism of tissues, particularly those relying heavily on fatty acid oxidation, such as cardiac muscles[482]. Carnitine facilitates fatty acid metabolism by aiding the transport of acyl groups into the mitochondria, for fatty acid oxidation[483]. Clinical evidence suggests that carnitine level is a significant factor in cardiovascular disorders[484]. Cardiac carnitine levels are halved in heart failure patients and carnitine deficiency observed in cardiomyopathy improves after replacement[473][485]. This has also been demonstrated clinically in the context of DIC[486][484][487][488].

Carnitine is primarily obtained through exogenous dietary sources[482]. Given evidence that DOX causes gastrointestinal damage, also indicated by reduced body weight gain in our study, it is likely that gastrointestinal effects contribute to malabsorption leading to decreased carnitine levels[489] A small amount of carnitine is synthesized endogenously, primarily by the liver. The documented DOX-induced liver damage is an additional compounding factor that contributing to the reduction of carnitine levels.

In the study, DOX treatment did not alter ATP concentration, consistent with the literature. ATP content is generally maintained until the development of end-stage heart failure[472] as glycolysis has upregulated to compensate for mitochondrial dysfunction, during the early stages of heart failure, ATP levels remain relatively stable, while phosphocreatine levels decline[490]. This dynamic may be evident in the 4 mg/kg DOX group, where stable ATP levels are observed alongside a dip in phosphocreatine. The 4mg/kg model therefore appears representative of early heart failure caused by anthracycline cardiotoxicity. The functional deficit caused by mitochondrial insufficiency, is mitigated by compensatory upregulation in glycolysis to maintain ATP production despite lower levels of cardiac phosphocreatine.

6.5.5 Elevated Fatty-Acid Metabolites in Serum as Indicators of DOX-Induced Lipotoxicity

Anthracyclines are administered systemically, and while this project focuses on the heart, the cardiac dysfunction observed may not necessarily be cardiac in origin and it is possible the alterations in systemic metabolism which might influence cardiac response to the anthracyclines.[491]. 1H NMR analysis was performed on serum samples to assess the systemic metabolic changes in response to DOX treatment. As with cardiac metabolism, the metabolic profile of serum metabolites were similarly altered dose-dependently. The cardiac metabolic profile of the 4 mg/kg group exhibited the largest alteration.

A significant observation made during serum collection was the milky-white appearance of certain samples (Figure 63). Serum samples are normally clear, and the presence of milky-white serum indicates lipemia. Dyslipidaemia refers to the imbalance of lipids, such as cholesterol, low-density lipoprotein, (LDL), high-density lipoprotein (HDL) and triglycerides. Dyslipidemic serum is characterized by elevated levels of one or more fatty substances above the normal range[492][493]. Clinically, elevated levels of fatty substances in the blood serve as a significant risk factor for cardiovascular diseases[494][495]. Dyslipidemic serum was evident in all groups in a dose-dependent manner, with the highest incidence observed in the 4mg/kg group. This visual observation correlates with the significant elevation in fatty acid metabolites measured

Figure 62: Milky-white serum in select DOX-treated animals, suggesting elevated levels of fatty substances.

in the serum. Levels of fatty acid residues exhibited dose-dependent change in all groups, with the largest change observed in the 3mg/kg and 4mg/kg groups. Approximately 7-fold higher concentrations of fatty acid residues were measured in the 3mg/kg and 4mg/kg groups compared to the control. These alterations in fatty acid residues represented the most substantial metabolite changes observed in the serum metabolomic profile. The 1H NMR analysis identified two lipid classes: Fatty acid residue (COCH2-CH2) and Fatty acid residue (ω-CH3) both constituent parts of the fatty acyl chain representing total fatty acids, and fatty acid residue (−CH=CH-), a constituent specific to unsaturated fatty acids within the fatty acyl chain[496]. The measurement of the total fatty acid lipid class is valuable given that fatty acids constitute ~60% of the total serum lipid. Approximately 25%, 20%, 14%, and 1% of fatty acids are contained in triglycerides, phospholipids, cholesterol esters, and albumin, respectively[497]. The measurement of total fatty acids in serum can serve as proxy for total serum lipid content. The substantial increase in fatty acids observed indicates that DOX has a profound effect on lipid metabolism.

These findings raise the question as to what extent do the observed increase in serum lipids (and impaired lipid metabolism, generally) contribute to the mechanism of DIC. Hepatotoxicity is a well-documented side effect of DOX treatment, [498][499]. Cytochrome P450 and carbonyl reductases mediate the hepatic metabolism of DOX, leading to the generation of ROS and oxidative stress[500][501]. Oxidative stress is associated with inflammation, mitochondrial dysfunction, and eventual hepatocyte death[502]. The liver, as the primary regulator of lipid metabolism, governs lipid uptake, formation, and export to the circulation[503]. Liver dysfunction can result in changes to circulating lipid levels, likely contributing to the dyslipidaemia observed in our study[504]. This is consistent with observations in the literature, where DOX treatment has been shown to elevate total fatty acids, total cholesterol, triglyceride, and LDL cholesterol levels in a rodent model[505]. Furthermore, DOX-induced dyslipidaemia is clinically characterized by a distinct lipid profile, featuring significantly elevated total cholesterol, triglyceride, LDL's, and decreased HDL levels[506]. Lipids also play important regulatory roles in cardiac function, serving as major structural components of biological membranes, contributing to cell transport, signalling, and as an energy substrate for fatty acid oxidation[507]. The dysregulation of lipid metabolism, involving alterations in lipid class and lipid accumulation, can therefore result in cardiac lipotoxicity[508]. Although the authors did not establish this causative link, this relationship has been recently demonstrated in the literature, where protection against DIC was achieved

through lipid-lowering activity using statins. Statins are a primary intervention for preventing cardiovascular disease, by reducing hepatic cholesterol synthesis and aiding the liver in the removal of existing LDL cholesterol from the bloodstream[509][503][510]. In a retrospective study involving 666 women, statin exposure was associated with a decreased risk of heart failure hospitalizations within a five-year period following anthracycline chemotherapy treatment for early breast cancer[511]. In another meta-analysis encompassing two randomized controlled trials (117 patients) and four observational cohort studies (813 patients), substantiated the association between statin use and a reduced risk of cardiotoxicity following anthracycline treatment[512]. The incidence of cardiotoxicity was significantly reduced in cancer survivors that underwent statin therapy during their cancer treatment, with a higher likelihood of maintaining LVEF.

Based on recent findings highlighting the potential role of statins in mitigating chronic DIC, coupled with the observed increase in serum fatty acids in this study, I aimed to further investigate the metabolic profile of the liver in both aqueous and lipophilic phases using 1H NMR as part of the coadministration study. Recognizing the central role of liver function in lipid metabolism, I investigated the metabolic effects of DOX treatment on the liver to correlate changes observed in the metabolic profile of the liver with observed alterations in the heart. To provide insight into the role of lipotoxicity in association with DIC. Considering the profound impact of DOX on serum lipid levels in our study, I intended to analyse the lipophilic phase of the cardiac metabolic profile using 1H NMR in the coadministration study. This analysis aimed to explore whether serum dyslipidaemia correlated with specific lipotoxic effects in the heart, particularly in regard to lipophilic cardiac metabolites.

6.5.5.1 Other Metabolite Changes in the Serum

Significant metabolite alterations were also detected in the serum in addition to the perturbation of fatty acids. A decrease in glucose levels were observed in the 3mg/kg and 4mg/kg groups. As discussed in Section 6.5.4, it is likely that DOX induces a shift to glycolytic respiration. The increased glucose utilisation in the heart can cause hypoglycaemia in the serum[513].

A substantial increase in select TCA metabolites was observed. High elevations were measured in isoleucine, leucine, and glutamate in the 4mg/kg group. Literature indicates that elevated levels of branched-chain amino acids (BCAAs), such as leucine and isoleucine, are predictors

of cardiovascular disease[514]. The increased concentrations of leucine and isoleucine in the serum, found in the study, correlate with the observed cardiac dysfunction.

6.5.6 Elevation of Total Cardiac Iron Levels in the 4mg/kg group only, with No Change in Mitochondrial Cardiac Iron Levels

Total cardiac iron and mitochondrial iron levels in each experimental group were quantified using ICP-MS. Compared to the control group and all other DOX groups, the 4 mg/kg dose group alone resulted in a statistically significant increase in total cardiac iron. There was no significant difference in total mitochondrial cardiac iron found amongst the groups.

6.5.6.1 Total Mitochondrial Iron

Multiple studies have proposed that accumulation of iron within mitochondria is fundamental to the development of DOX cardiotoxicity [234][205]. This accumulation linked to the interaction between DOX and ABCB8 protein found in the inner mitochondrial membrane[91]. The interaction between DOX and ABCB8 was first demonstrated *in vitro* using neonatal rat cardiomyocytes. DOX exposure resulted in a dose-dependent increase in both DOX and iron within the mitochondria, accompanied by a significant decrease in ABCB8 levels [205]. The role of ABCB8 was further explored *in vivo*, where transgenic ABCB8 knockout mice exhibited significantly elevated mitochondrial iron levels compared to wild-type mice and showed decreased LVEF. These studies indicated that mitochondrial iron increases during DOX treatment. However, no significant alteration in mitochondrial iron was observed six weeks post-treatment, suggesting that changes in total cardiac mitochondrial iron either do not occur following DOX treatment, or may only occur during DOX treatment and are not sustained over time in the absence of DOX.

This contrasts to that reported *in vivo;* 4 weeks after the end of DOX treatment, Yoshihiko *et al.* reported a significant increase in mitochondrial cardiac iron levels [205]. However, it's important to note that DOX was administered at a non-clinically relevant dose of 6 mg/kg every 3rd day for a total cumulative dose of 24 mg/kg, significantly exceeding the recommended lifetime dose limit. This was accompanied by a 20% drop in LVEF, indicative of significant cardiac dysfunction. The use of clinically or near clinically relevant doses in the DOX model, may explain the less extreme degrees of mitochondrial iron that were observed.

Mitochondrial iron levels have been compared using explanted hearts from patients requiring heart transplants due to DOX-cardiotoxicity, as well as hearts from those with non-DOX-related cardiomyopathy and individuals with normal cardiac function [205]. Mitochondrial iron levels were significantly elevated (~30% increase) in the ex-planted hearts of patients with DOX-induced cardiomyopathy. The elevated mitochondrial iron observed *in vivo* by Yoshihiko *et al.* may be associated with mitochondrial dysfunction linked to late-stage heart failure, rather than sustained elevation of mitochondrial iron levels initiated during DOX treatment.

6.5.6.1.1 Mitochondrial Iron Measurement Considerations

Potential outliers were observed, particularly in the control group, which may suggest that the ICPMS-based iron measurement method may lack the necessary sensitivity for accurately detecting mitochondrial iron changes in relation to DOX treatment. The measurement of mitochondrial iron by ICPMS performed here is the first of its kind and was developed as part of this work, and therefore we do not have literature benchmark values for comparison. The procedural and non-procedural blanks do not inform us of individual outliers, rather they are used to check for overall contamination, making it challenging to definitively differentiate between elevated mitochondrial iron levels and potential outliers. Additionally, the mitochondrial data exhibited inherent noise, further limiting our ability to detect subtle increases in mitochondrial iron levels, and highlights the need to evaluate the sensitivity threshold of ICP-MS for detecting mitochondrial iron. To improve the reliability of our mitochondrial iron measurements, especially when changes are slight, additional repeats and mass balance studies are required.

Furthermore, since measuring total mitochondrial iron content (both bound and labile) using ICP-MS doesn't show significant changes following DOX treatment, it could be more insightful to focus on the distribution, misdistribution, and trafficking of labile iron specifically. Utilizing highly sensitive mitochondrial labile iron sensors could provide a clearer understanding of these dynamics, and the ongoing development of turn-on fluorescent probes with high selectivity for labile Fe^{2+} presents a promising avenue for further investigation [44]. Initial experiments employing green fluorescent protein (GFP) in isolated neonatal rat cardiomyocytes have demonstrated the capability to detect free mitochondrial iron via quantitative laser scanning microscopy in the context of DOX treatment [205]. Utilizing such techniques could provide the sensitivity needed to more accurately characterize changes in

mitochondrial labile iron and to determine the specific proportions of different iron species within the labile iron pool. This approach could offer deeper insights into the dynamics of mitochondrial iron metabolism during DOX treatment, and its potential role in the development of DOX-induced cardiotoxicity. Established iron sensors like Calcein acetoxymethyl ester and Phen Green SK diacetate are widely used for detecting the labile iron pool and could be viable options for future research [515] [516] . While the use of mitochondrial labile iron sensors was beyond the scope of this thesis due to financial and time constraints, we intend to explore this avenue in the future to advance the specificity and sensitivity of our mitochondrial iron measurements.

6.5.6.2 Total Cardiac Iron

Six-weeks after the end of DOX treatment significant elevation in total cardiac iron was only observed in the 4mg/kg group. This may correspond with Miranda *et al.'s* findings, where mice showed no change in total cardiac iron levels three-weeks after DOX treatment compared to controls, while hearts from non-survivors were significantly iron loaded [252]. The total cardiac iron levels in the 4mg/kg group may indicate cardiac iron profiles similar to the non-survivors of this study, given that the animals in the 4mg/kg group exhibited severely compromised health with indications of heart failure. The observed increase in total cardiac iron in the 4mg/kg group may be associated with being in a state characteristic of heart failure and extensive cardiac dysfunction [234], resulting in impaired iron handling and dysregulated iron levels, rather than a persistent elevation of total cardiac iron originating from DOX-induced disruption to iron homeostasis.

We did not see significant cardiac iron elevation in the 2mg/kg and 3mg/kg group. This could suggest that the DOX-induced elevation in total cardiac iron may only be limited to the DOX treatment period or that total iron is not important in the development of DIC as hypothesised. However, even though total iron levels did not change, labile iron levels still could be, which we are unable to measure using our ICP-MS based technique.

6.5.6.3 Bound vs Labile iron

I have demonstrated that DOX treatment with clinically relevant doses does not alter total cardiac iron levels in DIC. Either total cardiac iron levels remain unaffected by DOX treatment, or total cardiac iron levels are perturbed only during DOX treatment and then normalize.

However, the proportion of labile to bound iron may differ despite unchanged total cardiac iron levels. Labile iron is characterized as a cell-chelatable pool consisting of both ionic forms of iron, Fe^{2+} and Fe^{3+}, with the potential to partake in redox-cycling reactions [44]. Labile iron levels are hypothesized to change because of DOX treatment, however under normal conditions it represents only 5% of total cell iron, equivalent to ~50–100 μM [44]. Therefore, changes in the labile iron pool may not be detected through our total cardiac iron measurements. The labile iron pool, along with various iron species within it, might undergo fluctuations and play a crucial role in the development of DIC.

6.5.7 The Timeframe in Which DOX-Induced Cardiotoxicity Develops is Likely Dose-Dependent

The 4mg/kg group exhibits later-stage DIC. It is likely that the 2mg/kg and 3mg/kg groups will eventually develop a similar level of cardiotoxicity over time. Hayward *et al*. demonstrated that with five weekly injections of 2mg/kg doxorubicin, fractional shortening decreased by 42% at week 13, and 90% of the group experienced mortality after 14 weeks[421]. Since the dosage regimen and cumulative dose were comparable, it suggests that with an extended latency period, we would likely have observed similar results in our study for the 2mg/kg and 3mg/kg groups. As such, it seems that the 4mg/kg group represents late-stage cardiotoxicity by the end of the six-week washout period, while the 2mg/kg group is more indicative of early-stage DIC.

6.6 Summary

The aim of this study was to develop and characterise a clinically relevant model of chronic DIC. The study was designed to closely mimic DOX treatment regimens used in patients undergoing DOX chemotherapy. I incorporated clinically relevant cumulative dose groups (8 mg/kg, 12 mg/kg, and 16 mg/kg) and included a latency period to assess the progression of cardiotoxicity over time.

DIC was evident in all groups based on changes in functional parameters, evidenced by dose-dependent altered cardiac metabolism and left ventricular functional decline. Cardiac dysfunction evolved progressively throughout the study, with changes in cardiac parameters becoming more pronounced in all groups over time, comparable to what occurs in the development of chronic DIC. Cardiac metabolism, serum metabolites and iron levels were

characterized in each of our DOX groups. All these parameters were perturbed in a dose-dependent manner, with the 4mg/kg group showing signs of late-stage heart failure, including evidence of a shift to glycolytic metabolism and possible cardiac hypertrophy.

Six-weeks after the end of DOX treatment, total cardiac iron measurements were only elevated in the 4mg/kg group, although at this point we have not established cause and effect. In the literature, elevated total cardiac iron has only been observed *in vivo* in non-surviving DOX-treated mice or in animals that have developed chronic DIC with severe cardiac dysfunction, induced through clinically irrelevant doses. This may explain the elevated total cardiac iron in the 4mg/kg group, as these animals' exhibited symptoms of heart failure.

To our knowledge, our study is the first attempt to directly quantify the accumulation of mitochondrial iron in a clinically relevant DOX cardiotoxicity model. However, we were unable to detect a significant difference in total mitochondrial cardiac iron following DOX treatment. It's important to note that the inherent noise associated with low protein concentrations in small sample volumes makes identifying subtle changes in mitochondrial iron challenging.

In the experimental model, I measured cardiac iron at the end of the latency period. It would have been interesting to longitudinally follow cardiac iron accumulation during the latency period to establish whether iron continued to accumulate after the DOX insult to achieve the levels that they did, or whether iron was progressively washing out from the myocardium during the latency period. Unfortunately, time and financial constraints were such that we were unable to investigate these ideas further.

A significant incidental finding in the metabolic profiling of serum was the notable increase in fatty acids in all groups, suggesting that DOX has a profound impact on lipid metabolism. This is particularly interesting in the context of recent studies who have reported the cardioprotective capacity of statin treatment, without yet having proposed a mechanism.

COADMINISTRATION STUDY: EXPLORING THE IMPACT OF PRE-EXISTING IRON OVERLOAD ON DOXORUBICIN-INDUCED CARDIOTOXICITY AND THE POTENTIAL AMELIORATIVE ROLE OF IRON CHELATION THERAPY

7.1 Introduction

This chapter uses our clinically relevant *in vivo* models, the iron overload model and chronic DOX-induced cardiotoxicity (DIC) model, to address two research questions. First, whether pre-existing iron overload exacerbates chronic DIC. We hypothesize that individuals with pre-existing iron overload are at a higher risk of developing DIC, and that iron overload may impact the severity of cardiotoxicity experienced. Second, to investigate the cardioprotective potential of iron chelation prior to DOX treatment in animals with elevated levels of cardiac iron. For this, I investigated repurposing of the clinically approved iron chelator deferiprone as a preventive cardio protectant against DIC. The cardioprotective effects of iron chelators are typically evaluated when administered during DOX treatment. However, in the context of patients with subclinical cardiac iron overload, investigating the use of iron chelators as a preventive intervention prior to DOX treatment is clinically justified and potentially crucial.

Cardiotoxicity was primarily determined by assessing cardiac functional parameters via echocardiography throughout the study. ^{1}H NMR spectroscopy was used to characterize the chronic effects of DOX on the metabolic profile of the heart, and in combination with each intervention. ICPMS was used to quantify the effects of each respective intervention on total cardiac and mitochondrial iron, and whether elevated iron correlates with cardiac dysfunction.

Building upon the incidental finding of lipemic serum in DOX-treated animals in the previous chapter, the metabolic profile of the liver in both the aqueous and lipophilic phases were investigated using 1H NMR as part of the coadministration study. The liver is the primary regulator of lipid metabolism, governing lipid uptake, formation, and export to the circulation[503]. Given its central role in lipid metabolism, we hypothesized that liver dysfunction is likely responsible for the alterations in circulating lipid levels and the dyslipidaemia observed [504]. This investigation was intended to allow us to correlate changes

observed in the metabolic profile of the liver with observed alterations in the heart, both functionally and metabolically, providing insights into the role of lipotoxicity in association with DIC. Considering the profound impact of DOX on serum lipid levels found in our study, I also analysed the lipophilic phase of the cardiac metabolic profile. This analysis aiming to explore whether serum dyslipidaemia correlates with specific lipotoxic effects in the heart, particularly related to lipophilic cardiac metabolites.

7.1.1 Iron Chelation: The Rationale for Selecting Deferiprone in Our Study

For an in-depth evaluation of the clinical history of iron chelators, specifically deferiprone, in the context of DIC and its comparison with dexrazoxane, refer to Chapter 1, Section2.7.

7.1.1.1 Why could deferiprone be a more effective cardio protectant than Dexrazoxane?

Dexrazoxane has demonstrated efficacy in mitigating DIC, however it does have some limitations in this clinical application.

Dexrazoxane is a cell-permeating prodrug that does not directly chelate iron (Hider and Hoffbrand, 2018a. Instead, it undergoes hydrolysis to its open ring form, ADR-925, that then binds to iron. As an analogue of EDTA, ADR-925 is not selective for iron and exhibits a high affinity for Ca^{2+}, which could potentially limit its cardioprotective efficacy[310]. The affinity for Ca^{2+} has the potential to adversely affect mitochondrial function and raises concerns regarding dosage. Considering the relative intracellular concentrations of Ca and Fe, it is possible that Ca could outcompete Fe to reduce its bioavailability inside the cell, which would impact its therapeutic effectiveness.

Deferiprone is not a prodrug and, unlike dexrazoxane, can directly chelate iron[264][278]. Deferiprone is a small, neutrally charged, cell-permeable molecule, that can penetrate cardiac cells owing to its low molecular weight and lipophilicity. deferiprone has a significantly higher affinity for iron (Ka 1037 vs 1021) and lower affinity for calcium (Ka 103 vs 1011) compared to dexrazoxane, thereby avoiding potential binding competition concerns.

A significant advantage of deferiprone is its ability to cross cellular membranes in both its unbound and iron-complexed forms[284]. As such, it can enter cells, bind iron, and then remove it. In contrast, while ADR-925, can chelate intracellular iron the resultant ADR-925-

iron complex is negatively charged and hydrophilic and can therefore not remove iron from cells and tissues. Chelating iron intracellularly without subsequent removal does not eliminate the risk of localised ROS production. Dexrazoxane-iron complexes have been shown experimentally to be still capable of oxidatively cleaving DNA. As a further potential complication, Dexrazoxane has been proposed to act via more than one mechanism in part been linked to its interaction with topoisomerase IIβ (See 2.7).

The potential role of iron in DOX cardiotoxicity was therefore something of a shifting landscape. Dexrazoxane was originally thought to act primarily as an iron chelator. The literature investigating other iron chelators is also unclear – the use of inappropriate iron chelators which either cannot enter the cell or chelate intracellular iron but cannot then remove it have erroneously cast doubt on the pathophysiological importance of iron.

While deferiprone should in theory be the best suited iron chelator for removing cardiac iron a high-profile study failed to see any cardioprotective effect with it [308]. However, we believe this study to be flawed because deferiprone was administered before they administered the anthracycline daunorubicin. Since the half-life of daunorubicin is 13 hours, but the half-life of deferiprone is ~2 hours, most of the deferiprone could have washed out of from the heart during the time when daunorubicin concentrations were still high[309]. Potentially significantly underestimating the cardioprotective potential of deferiprone.

7.2 Aims

In this study, our primary objectives were firstly, to investigate whether pre-existing iron overload exacerbates chronic DIC, and secondly, to explore the cardioprotective potential of iron chelation preceding DOX treatment in animals with elevated levels of cardiac iron. Additionally, considering the lipemic serum observed in our previous DOX study, to assess the effects of DOX on lipid metabolism.

These objectives were addressed through the utilization of our clinically relevant chronic DIC and iron overload model. Involving the characterization of cardiac function, cardiac iron levels, and metabolism in cardiac, liver, and serum samples.

7.3 Methods

7.3.1 Animal Preparation

All animal experiments conformed with our institutional animal care guidelines and the United Kingdom Home Office Guide on the Operation of Animal (Scientific Procedures) Act of 1986. Eighty adult male Wistar rats (7-9 weeks old, 200-300g) were purchased from Charles River Laboratories. Animals were housed in groups of four under controlled conditions: at 23 ± 2°C with 12 h light/dark cycles. Animals were acclimated for 7 days before the start of the study and had access to water and food *ad libitum* for the duration of the study.

7.3.2 Experimental Rationale (and a note of mitigation)

In previous chapters I established the dose titrations required to invoke both sub-acute DOX cardiotoxicity and cardiac iron overload. At the time of this work, which was in the final 9 months of my Ph.D., I had completed the prior longitudinal studies and metabolomics analyses, but the London Metallomics Facility had closed for refurbishment, and it was not possible to analyse our samples for their iron content. Because of the long time frame of several months required for these experimental studies, and the time remaining on the project, we were forced to decide upon the final protocol with the information that we had at the time, but before all the analyses were complete. The primary endpoints that I had at that time were largely functional, but we were concerned that using our highest dose of 4mg/kg DOX and exacerbating the injury with iron preloading would result in such an extreme cardiotoxicity that our animals could die during the protocol. Based on our functional data, it seemed reasonable that proceeding with a dose of 2mg/kg DOX would provide sufficient "ceiling" such that the expected exacerbation of cardiotoxicity would be non-lethal over the time-course of our experiments. It is unfortunate that this dosage did not result in significant elevation in cardiac iron, but this only became apparent when I finally able to perform the ICPMS iron analyses after this study was well underway and we were already committed to the protocol.

7.3.3 Experimental Protocol

Adult male Wistar rats (200-300g) were divided into 6 experimental groups (n=12, respectively). A schematic timeline of this study is presented in Figure 64.

The investigations utilised three coadministration study groups: 1) the DOX group, 2) the DOX+Fe group, and 3) the DOX+Fe+DFP group. The DOX group was subjected to DOX

treatment only, following the protocol developed in Chapter 6. A 2mg/kg dose of DOX was administered I.V once a week for four weeks. The DOX+Fe group involved treating iron loaded animals with DOX. The animals were iron overloaded using the method developed in Chapter 5, in which iron dextran was administered via I.P. (100mg/kg/day, 5 days/week) for a four-week period.

The DOX+Fe+DFP group consisted of iron loaded animals which underwent a 4-week iron chelation therapy using deferiprone (DFP) prior to DOX treatment. A clinically relevant does of deferiprone was administered via oral gavage at a dosage of 50mg/kg/day, five days a week.

Iron chelation control groups were also included to assess the efficacy of deferiprone in chelating cardiac iron in the absence of DOX. Iron overload was examined independently and in conjunction with iron chelation treatment, referred to as the Fe group and Fe+DFP group, respectively. A control group was administered saline equivalents of each intervention. A 6-week latency period followed the DOX treatment period in all groups in order to assess the chronic effects of each intervention.

The iron overload, DOX treatment, and iron chelation therapy were consistent across all relevant groups, in terms of both dosage and treatment regimen. As depicted in the study schematic, each intervention was time-matched across all groups for comparability. Body weight was measured every two weeks throughout the study, and cardiac function was measured at the start and end of the iron dextran and deferiprone treatment periods and every 2 weeks thereafter. At the end of the study period, hearts were harvested for metabolic analysis and iron quantification. Liver and serum samples were also collected for metabolic analysis.

7.3.4 Deferiprone Treatment by Oral Gavage

Each dose of deferiprone was prepared by dissolving 50 mg/kg of deferiprone in sterile saline solution to a total injection volume of 3.125ml/kg. Control rats were administered an equivalent volume of sterile saline solution. Each rat was scuffed by gently and firmly grasping the nap of the neck between the thumb and forefinger. The animal was lifted by the scruff and held in an upright position, restricting the use of its legs for leverage, and limiting free movement of its head. A curved stainless-steel syringe was inserted to the right or the left of the inner jaw midline and rapidly emptied with care. The animal was monitored after oral gavage to ensure there were no signs of aspiration and that breathing was within normal limits.

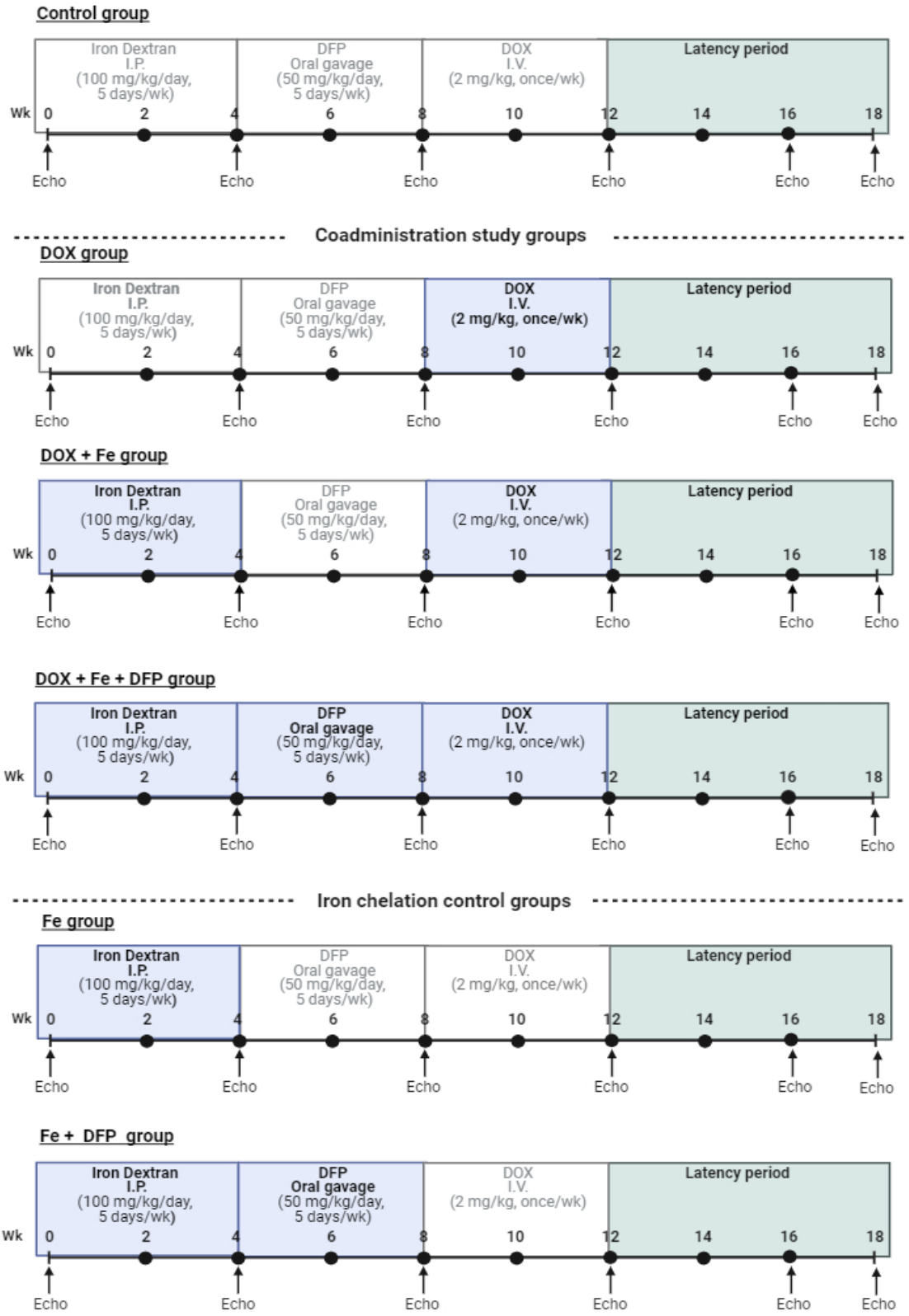

Figure 63: Coadministration study schematic. The timeline presents the respective protocols followed by each study group. Continuous assessment of cardiac function was conducted via echocardiography throughout the study period as indicated. At the end of the study, the heart and liver were harvested for metabolic analysis, accompanied by serum collection. Deferiprone; DFP, Fe; Iron loading via iron Dextran. [Figure made in BioRender]

7.3.5 Liver Harvesting

Rats were initially anaesthetised (4% isoflurane mixed with 0.8 L/min 100% O2) in an induction chamber and transferred to a heating pad, where anaesthesia was maintained using a nose cone at 4% isoflurane at flow rate of 0.5 L/min. The lack of pedal response was used to confirm depth of anaesthesia. Hearts were collected as described in Section 3.2.7. The liver samples were collected immediately after the hearts were excised. The livers were removed and immediately snap frozen in liquid nitrogen to avoid thawing and prevent metabolic degradation. A pestle and mortar were pre-cooled using dry ice and the liver samples then ground into a fine powder under liquid nitrogen which was stored at -80°C until use.

7.3.6 NMR Tissue Measurements

7.3.6.1 Sample Preparation

7.3.6.1.1 Aqueous Metabolites in The Liver

Liver tissue aqueous metabolites (100-200mg) were extracted using chloroform, methanol, and water in a 1:1:1 ratio (2mL/100mg tissue, respectively). The extraction and sample preparation were performed exactly as described for cardiac aqueous metabolites in Section 3.7.2. The samples then transferred to 5mm NMR tubes (Norel Inc, USA) for ^{1}H NMR analysis.

7.3.6.1.2 Lipophilic Metabolites in Cardiac and Liver Tissue

During the NMR sample preparation for both cardiac and liver tissues respectively, the lipophilic layer was collected in the phase separation step of the chloroform-methanol-water protein precipitation procedure, as described in Section 3.7.2. After centrifuging the respective CMW-tissue suspensions, three layers form: the upper aqueous phase, a middle layer with precipitated protein, and the lower lipophilic organic layer. Both the upper layer (containing aqueous metabolites) and the lower lipophilic layer (containing lipophilic components of interest, including various lipid species) were collected. For each sample, the lower lipophilic organic chloroform layer was transferred to glass vials, and the chloroform left to evaporate under a fume hood. The evaporated samples were reconstituted in 600µL of deuterated chloroform (CDCl3) solution containing TMS (60uL) and then vortexed. The TMS present in the CDCl3 solution used to avoid possible chemical shift drifts due to pH effects serving as an

internal standard. The reconstituted samples were transferred to 5mm NMR tubes (Norel Inc, USA) for 1H NMR analysis.

7.3.6.2 Acquisition Parameters and Analysis

1H NMR spectroscopy was performed on a 700-MHz Bruker spectrometer (Bruker, Germany). Aqueous cardiac and liver samples were analysed using a Nuclear Overhauser Effect Spectroscopy (NOESY) pulse sequence. Spectra were acquired using the following parameters: spectrometer frequency; 700.19 MHz, spectral width; 20.5 ppm/14367.8 Hz, acquisition time; 2.28 seconds, relaxation delay; 4 seconds, and number of scans; 68 scans, temperature; 298K.

Lipophilic cardiac and liver samples were analysed using a K zg pulse sequence. Spectra were acquired using the following parameters: spectrometer frequency; 700.20 MHz, spectral width; 16.1 ppm/11261.2 Hz, 64 scans, acquisition time; 2.91 seconds, relaxation delay; 4 seconds, temperature; 300K.

Serum samples were analysed using a Carr–Purcell–Meiboom–Gill (CPMG) pulse sequence. Spectra were acquired using the following parameters: spectrometer frequency; 700.20 MHz, spectral width; 20.1 ppm/14097.7 Hz, 64 scans, acquisition time; 2.32 seconds, relaxation delay; 4 seconds, temperature; 298K.

All ^{1}H NMR spectra were post-processed in TopSpin software version 3.6.1 (Bruker, Germany). Metabolite peaks were manually integrated, and metabolic profiles determined using Chenomx NMR Profiler Version 9.0 (Chenomx, Canada). Aqueous metabolite concentrations were determined by referencing the TSP peak and normalizing the metabolite peak integrals to the initial wet tissue mass used for the metabolite extraction (See 3.7.7.1). Lipophilic metabolite concentrations were determined by referencing the TMS peak and normalizing the metabolite peak integrals to the initial wet tissue mass used for the metabolite extraction (See 3.7.7.2). Serum metabolite concentrations were calculated by referencing the metabolite integral and the TMS integral with respect to the volume of serum used in the NMR sample preparation.

7.3.7 Previously Described Methodology

The methodology for the following parameters were conducted as previously described in Chapter 3: DOX administration, Iron dextran administration, echocardiography, cardiac tissue collection, serum collection, NMR sample preparation and acquisition parameters (relevant to cardiac tissue and aqueous metabolites, and serum), and ICPMS-based cardiac iron measurements.

7.3.8 Statistical Analysis

Unsupervised principal component analysis (PCA) was used to analyse the distribution of the metabolomic data derived from the control and test groups. If separation between the groups was observed, the supervised partial least squares discriminant analysis (PLS-DA) was performed to better discriminate between the groups and to maximize separation associated with class membership. Unpaired Student's t-tests, one-way or two-way ANOVA with Tukey's HSD adjustment method for multiple comparisons were used as required and performed as indicated in the figure legends. Significance was assumed at $P < 0.05$, or as stated in the figure legends. PCA and PLS-DA analysis was performed in MatLab, all other statistical analysis was performed in Prism 10 (GraphPad, La Jolla, CA, US).

7.4 Results

7.4.1 Body And Heart Weight

I first assessed the general effects of each intervention by monitoring body weight gain throughout the study (Figure 65).

At the end of the study, DOX caused a decrease in average body weight in DOX treated animals (from 454.2g ± 40.0g SD in the control to 351.0g ± 31.6g SD). This was not exacerbated by co-administration with Fe (to 302.0g ± 29.9g SD), and deferiprone treatment did not mitigate this effect (to 310.0g ± 33.8g SD).

The control group exhibited an average weight gain of 54%. Treatment with DOX slowed this rate, with an average weight gain of 23%, significantly lower than the control. This was exacerbated by co-administration with Fe (average weight gain of 12%), and deferiprone treatment did not mitigate this effect (average weight gain of 8.2%). Body weight in iron-loaded animals remained consistent throughout the study, indicating that the reduced weight gain is attributed to the iron loading intervention.

Iron loading alone had a similar effect and also led to significantly lower average body weight compared to the control (372.9.0g ± 34.1g SD, average weight gain of 32%), which again was not mitigated by deferiprone treatment (370.4.0g ± 33.9g SD, average weight gain of 33%).

DOX caused a decrease in gross heart weight, from 0.90g ± 0.09g SD in the control to 0.83g ± 0.08g SD (Figure 66 ,a). This was exacerbated by co-administration with Fe (to 0.70g ± 0.06g SD), deferiprone treatment did not mitigate this effect. Iron loading alone had a similar effect (from 0.90g ± 0.09g SD in the control to 0.81g ± 0.08g SD), which again was not mitigated by deferiprone treatment. However, when heart weight was expressed as a ratio of bodyweight (Figure 66 ,b), DOX and iron were both found to have induced a significant elevation in heart weight (from 0.20% to 0.23%), which deferiprone treatment did not affect. Iron loading alone caused a significant increase in heart weight/bodyweight ratio (from 0.20% to 0.22%), which deferiprone did normalise (0.21%).

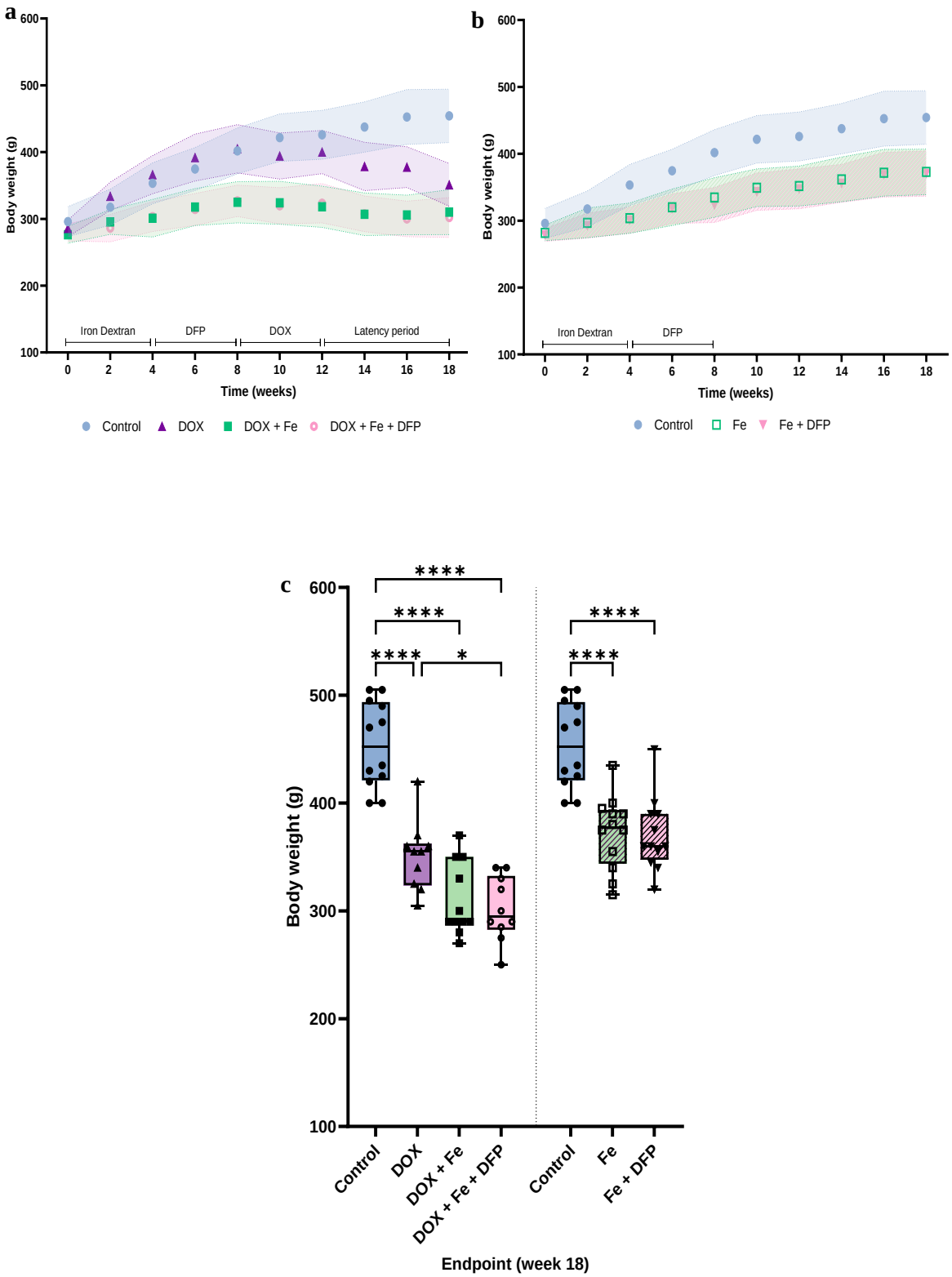

Figure 64: Average body weight measurements. a Average body weight gain per week throughout the 10-week study for study groups (mean±SD). **b** Average body weight gain per week throughout the 10-week study for control groups (mean±SD). **c** Average body weight at the end of the study. Statistical comparison by one-way ANOVA with Tukey's HSD correction method for multiple comparisons. *P<0.05, **P<0.01, ***P<0.001 and ****P<0.0001.

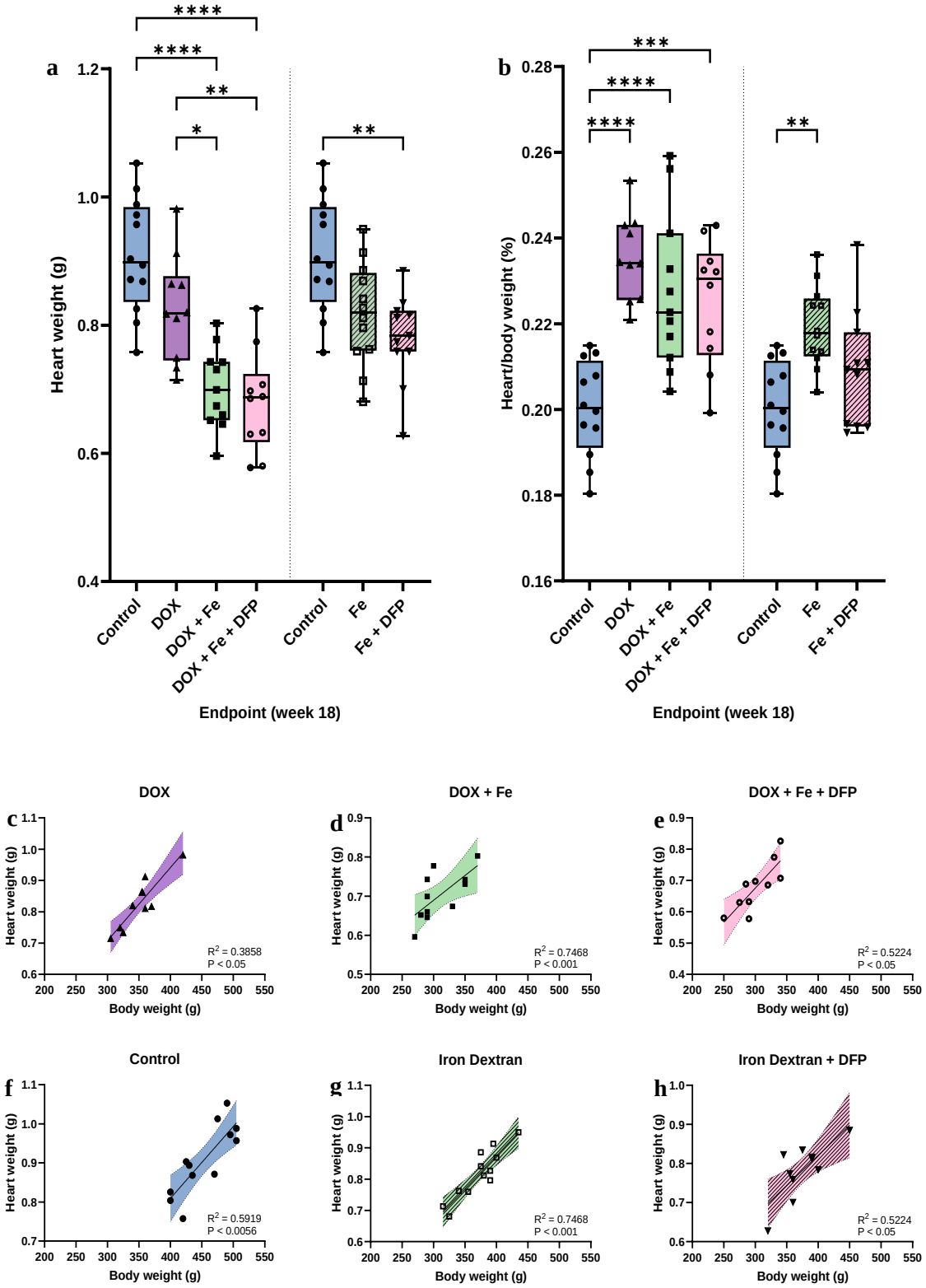

Figure 65: Average end-point heart weight measurements. a Average heart weight. **b** Average heart:body weight ratio. Statistical comparison by one-way ANOVA with Tukey's HSD correction method for multiple comparisons (mean±SD). *P<0.05 , **P<0.01 and ****P<0.0001. **c, d, e**, **f**, **h** Heart weight plotted against body weight in the respective groups. Simple linear regression analysis.

7.4.2 Cardiac Function

I evaluated cardiac function using echocardiography throughout the study (Figure 67 and Figure 68).

LVEF and FS significantly decreased in all DOX-treated animals, with the reduction intensifying during the six-week latency period following DOX treatment.

At the end of the latency period, LVEF dropped by 8% in the control group, decreasing from 74.18 ± 2.8% at baseline to 68.57 ± 4.47%. The LVEF in the DOX group was significantly reduced compared to the control, with DOX treatment resulting in 23% reduction in LVEF from baseline (73.28 ± 4.51% to 56.99 ± 5.04%). DOX treatment also significantly reduced FS and stroke volume compared to control.

Iron loading did not significantly exacerbate the reduction in LVEF compared to the control, which also dropped by 28% from baseline (73.95 ± 2.79% to 52.03 ± 3.89%), although the degree of contractile dysfunction appeared more consistent. Additionally, iron loading did not exacerbate the reductions in fractional shortening (FS) or stroke volume.

Deferiprone pre-treatment in iron-loaded rats treated with DOX did not alleviate the reduction in LVEF compared to the control and baseline (73.82 ± 2.3% to 58.05 ± 6.34%; 20% drop). There was also no significant ameliorative effect on reduced FS and stroke volume. However, deferiprone pre-treatment did significantly improve LVEF in DOX-treated iron-loaded rats, normalizing LVEF to the level induced by DOX treatment alone.

Iron loading, with or without deferiprone, only resulted in a reduction in stroke volume, driven by non-significant alterations in systolic and diastolic volumes.

Heart rate remained unchanged across all groups (Appendix:Figure 91).

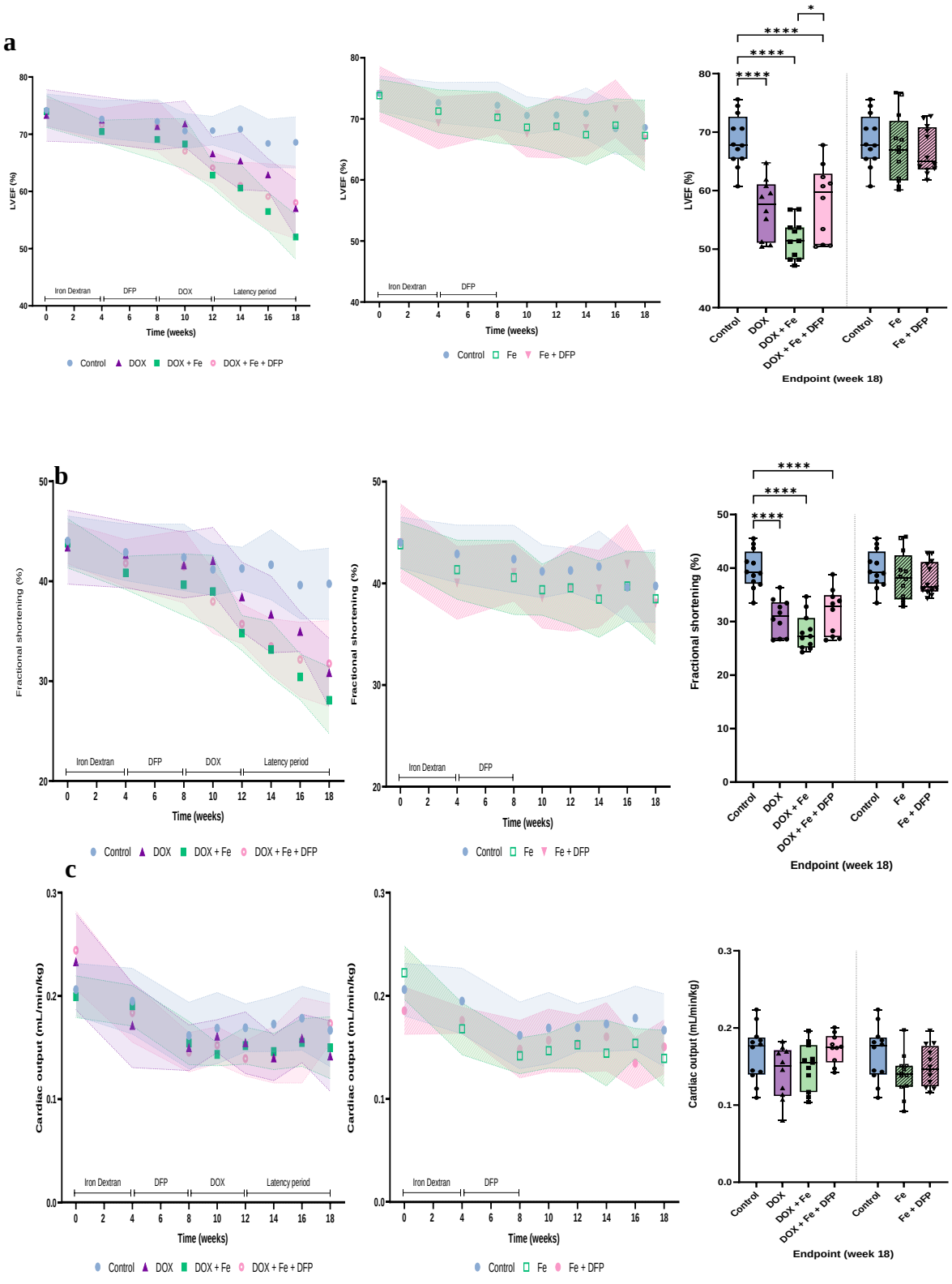

Figure 66: Cardiac functional parameters obtained by echocardiography.a Left ventricular ejection fraction (LVEF) **b** Fractional shortening **c** Cardiac index Statistical comparison by one-way ANOVA with Tukey's HSD correction method for multiple comparisons; **P<0.05, **P<0.01, ***P<0.001 and ****P<0.0001. The longitudinal data is presented as mean ± SD in the graphs (left), while the endpoint data is shown using a box plot (right).

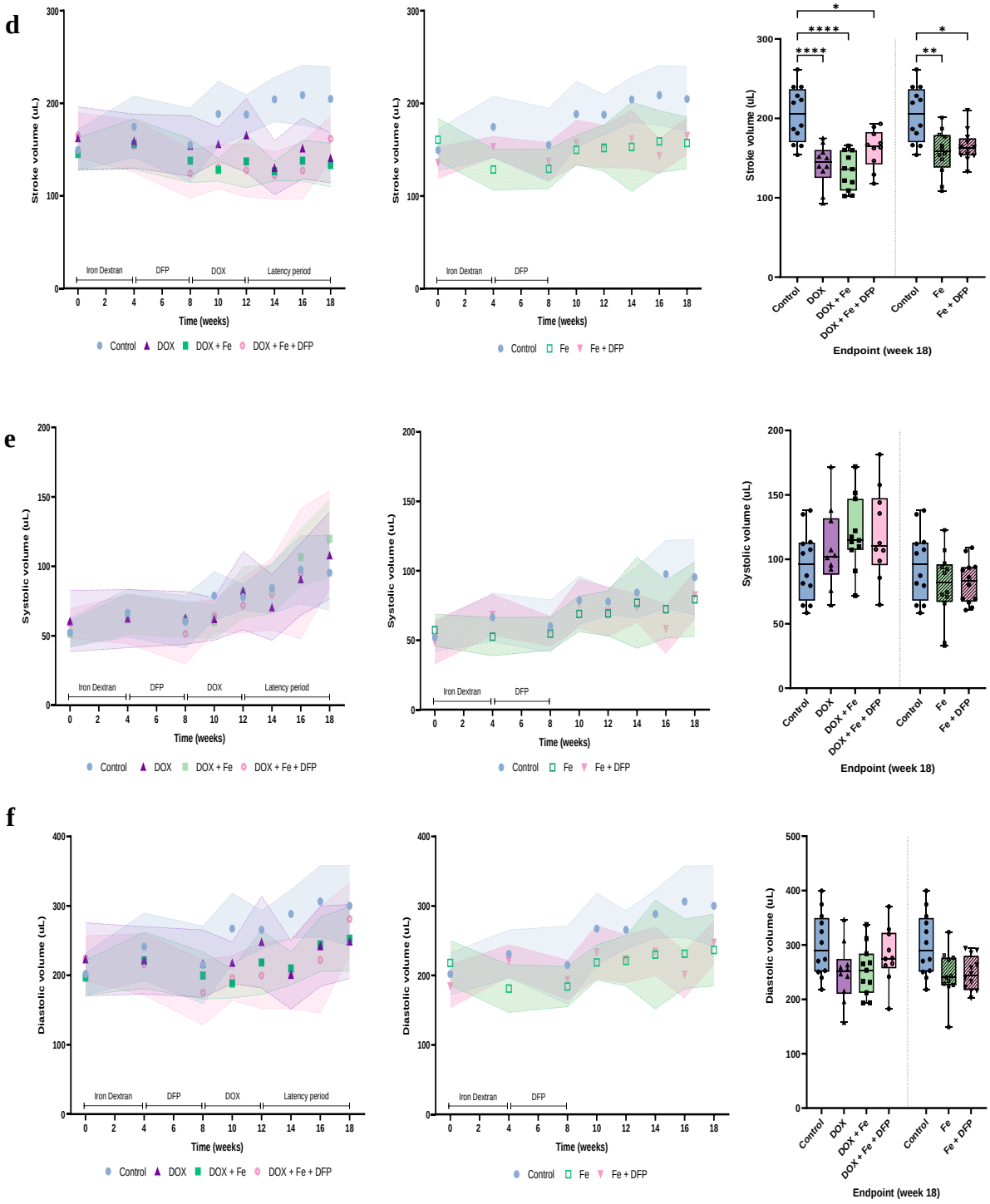

Figure 67: Cardiac functional parameters obtained by echocardiography (cont.). d Stroke volume index **e** Systolic volume index **f** Diastolic volume index. Statistical comparison by one-way ANOVA with Tukey's HSD correction method for multiple comparisons; **P<0.05, **P<0.01, ***P<0.001 and ****P<0.0001. The longitudinal data is presented as mean ± SD in the graphs (left), while the endpoint data is shown using a box plot (right).

7.4.3 Cardiac Iron

Because the London Metallomics Facility laboratories were closed for refurbishment, I had to transfer the analysis to the laboratories of their collaborators at the Natural History Museum. Unfortunately, due to a communication error following an unsuccessful analytical run, the ICP-MS facility inadvertently discarded our total cardiac iron samples in the following groups prior to analysis, and the samples were irretrievably lost: DOX+FE, DOX+FE+DFP, and the FE+DFP group. Regrettably, our analyses are limited to assessing the impact of the interventions on cardiac iron within the the limited number of samples that remained.

Of these samples, there was no change in total cellular and mitochondrial cardiac iron levels six-weeks after the end of DOX treatment (Figure 69, a and b). Iron loading did not impact total mitochondrial iron in DOX-treated animal groups compared to the control. However, deferiprone pre-treatment appeared to increase mitochondrial iron in iron-loaded animals receiving DOX. This increase may be due to variability in the data, possibly influenced by outliers from contamination.

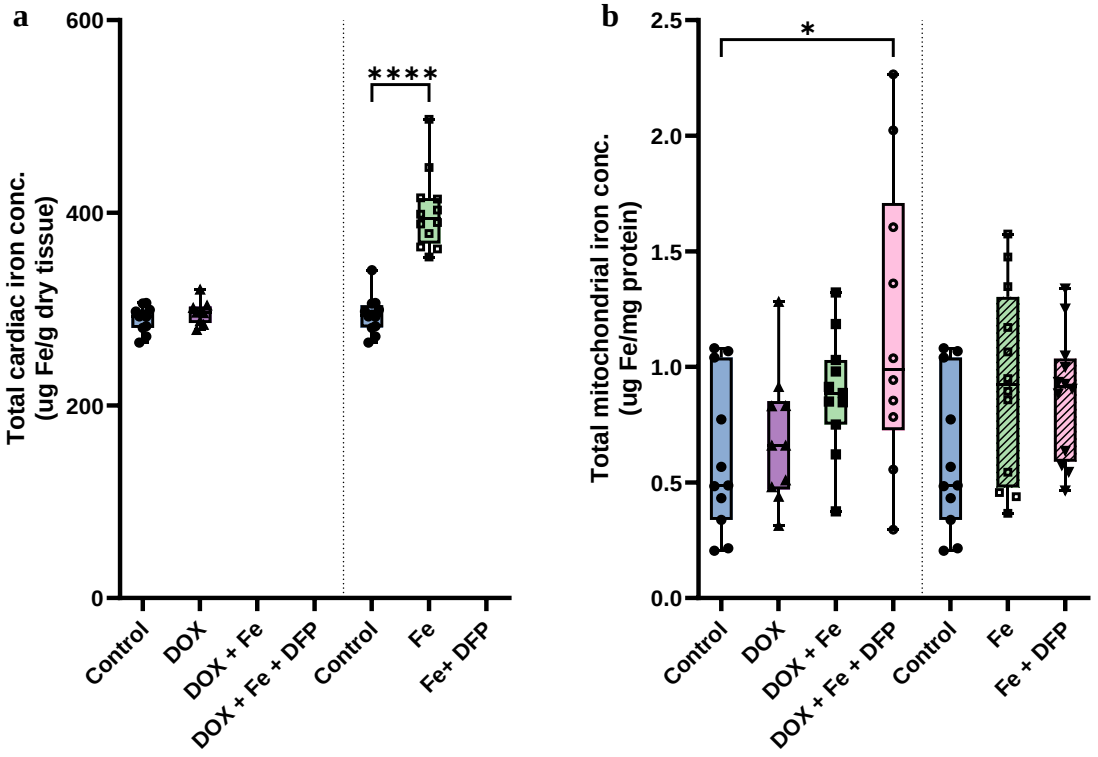

Figure 68: Total cardiac iron levels as assessed by ICPMS (^{56}Fe). a Total cardiac iron concentration, expressed as µg of iron per g of cardiac tissue. **b** Total mitochondrial iron concentration, expressed as µg of iron per mg of protein. Statistical comparison by one-way ANOVA with Tukey's HSD correction method for multiple comparisons, mean±SD. *P<0.05, ****P<0.0001.

Total cardiac iron was elevated in the iron loaded group (401 ug Fe/g dry tissue ±39 SD) compared to the control group (293 ug Fe/g dry tissue ±19 SD). However, there was no statistically significant difference in total mitochondrial iron between the iron-loaded rats and the control group. Deferiprone administration also was found to have no effect.

7.4.4 Metabolism

Refer to Chapter3, Section3.7.7 for the list of ^{1}H NMR chemical shift values (ppm) for metabolites in cardiac tissue, liver tissue, and serum samples, along with representative ^{1}H NMR spectra.

7.4.4.1 Cardiac Metabolism

Unsupervised Principal Component Analysis (PCA) of cardiac tissue revealed no separation between any group in both the aqueous and lipophilic cardiac metabolite profiles (Figure 70,Figure 72, and Figure 74, Figure 76, respectively). Figure 71 and Figure 73 depict the fold change of aqueous cardiac metabolites relative to the control group. Figure 75 and Figure 77 depict the fold change of lipophilic metabolites relative to the control group. For mean metabolite concentrations, refer to Appendix Table 15 and Table 20.

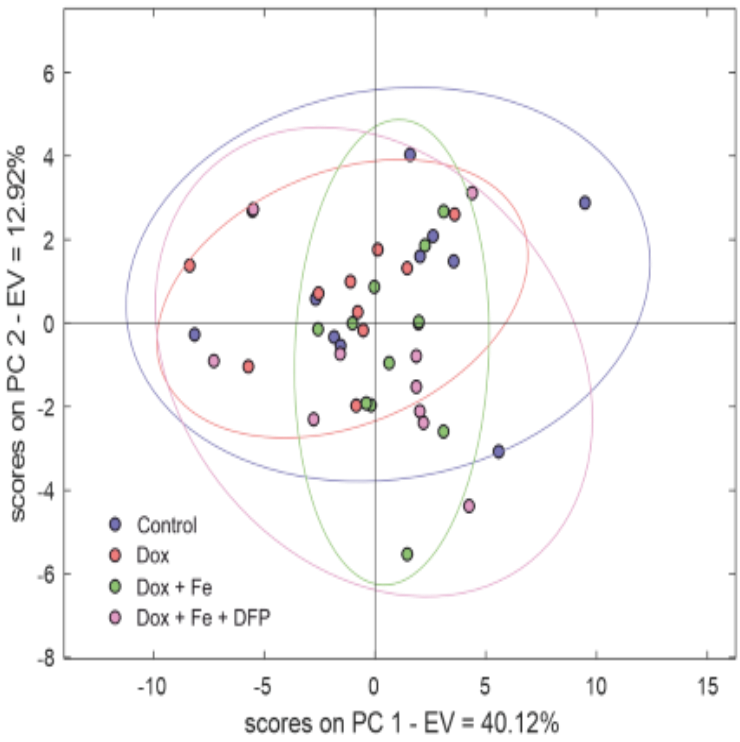

Figure 69: Principal Component Analysis (PCA) score plots from the aqueous cardiac metabolites of the coadministration groups and control groups. PCA score plot: PC1 accounted for 40.12% of the total variance, and PC2 accounted for 12.92% of the total variance. Control animals are denoted by the blue dots, while animals in the DOX, DOX+FE, and DOX+FE+DFP groups are represented by the orange, green, and pink, respectively.

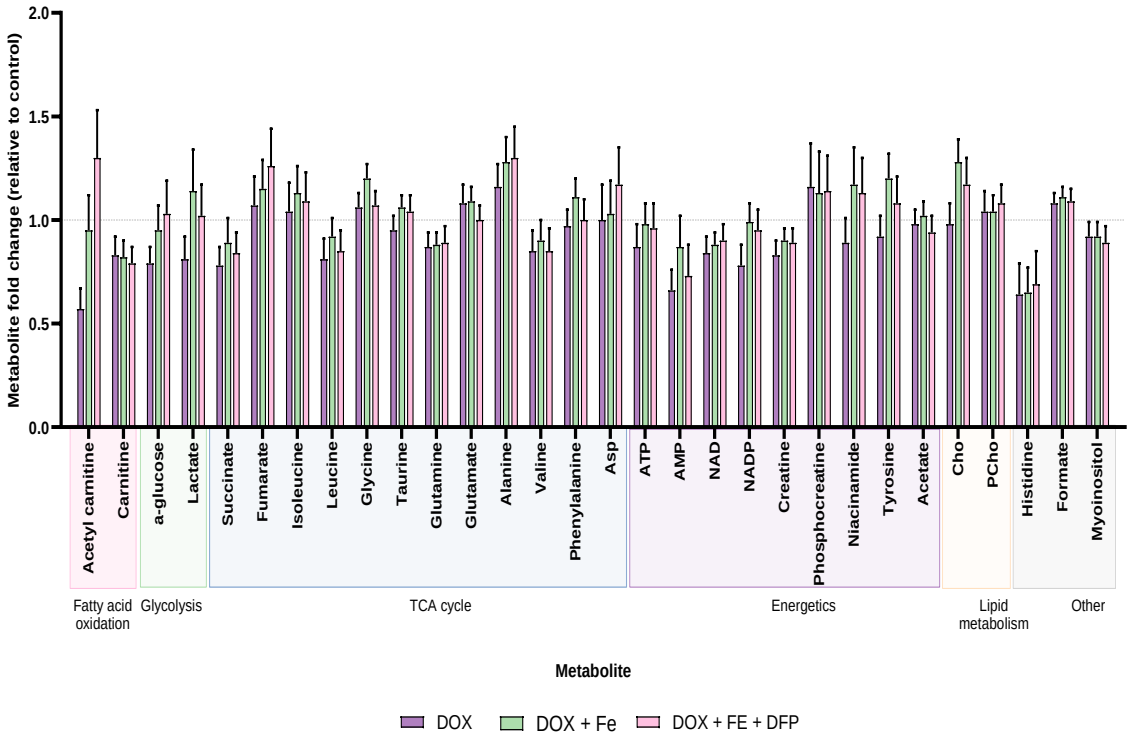

Figure 70: The fold change of aqueous cardiac metabolites relative to the control group. Fold change of the coadministration groups relative to the control. The fold change in metabolite concentration is represented as the mean ± SEM. Statistical comparison by one-way ANOVA with Tukey's HSD correction method for multiple comparisons. *P<0.05.

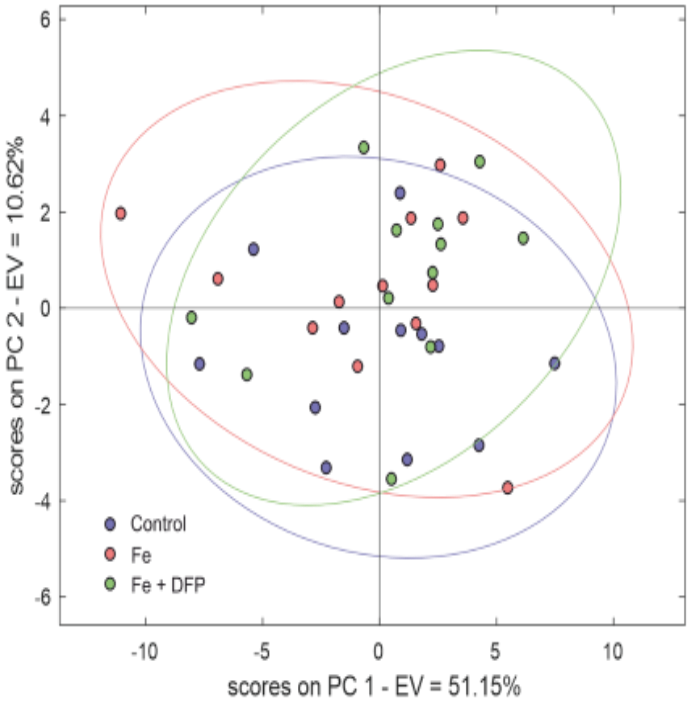

Figure 71: Principal Component Analysis (PCA) score plots from the aqueous cardiac metabolites of the iron chelation control groups. PCA score plot: PC1 accounted for 51.15% of the total variance, and PC2 accounted for 10.62% of the total variance. Control animals are denoted by the blue dots, while animals in the FE and FE+DFP groups are represented by the orange and green, respectively.

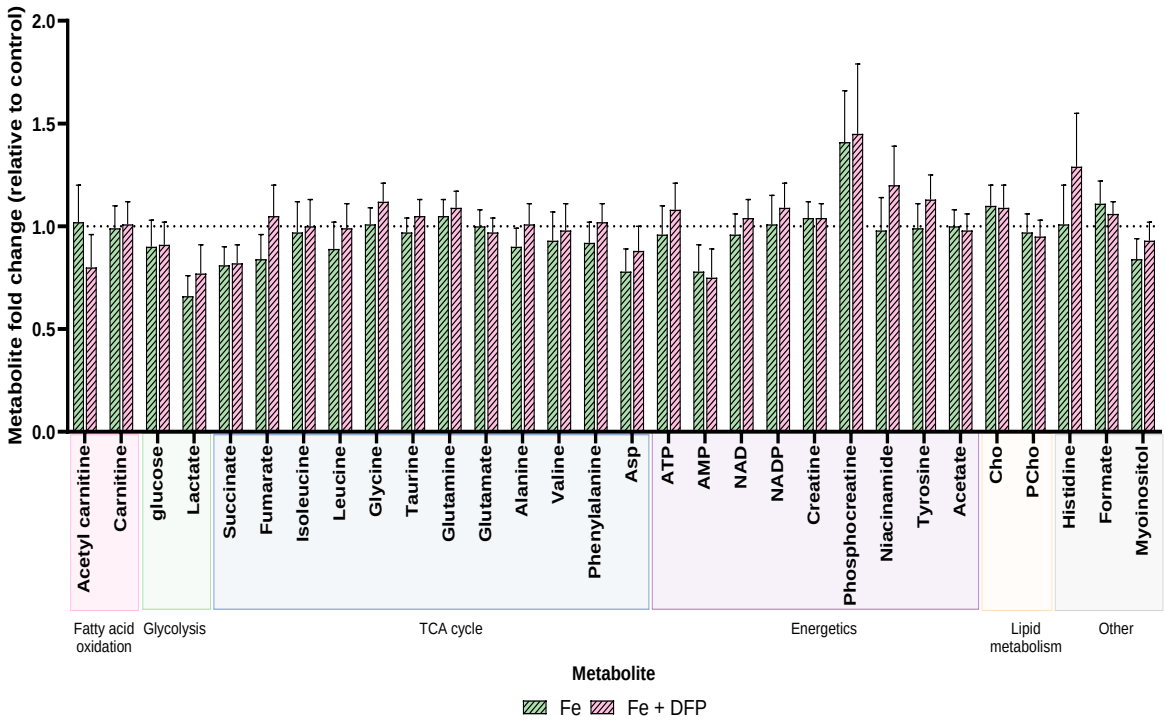

Figure 72: The fold change of aqueous cardiac metabolites relative to the control group. Fold change of the iron chelation control groups relative to the control. The fold change in metabolite concentration is represented as the mean ± SEM. Statistical comparison by one-way ANOVA with Tukey's HSD correction method for multiple comparisons. *P<0.05.

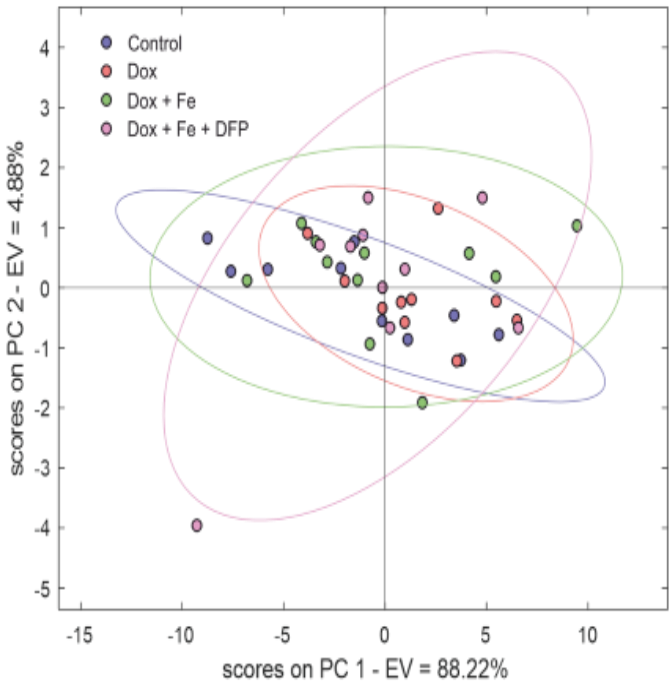

Figure 73: Principal Component Analysis (PCA) score plots from the lipophilic cardiac metabolites of the coadministration groups and control groups. PCA score plot: PC1 accounted for 88.22% of the total variance, and PC2 accounted for 4.88% of the total variance. Control animals are denoted by the blue dots, while animals in the DOX, DOX+FE, and DOX+FE+DFP groups are represented by the orange, green, and pink, respectively.

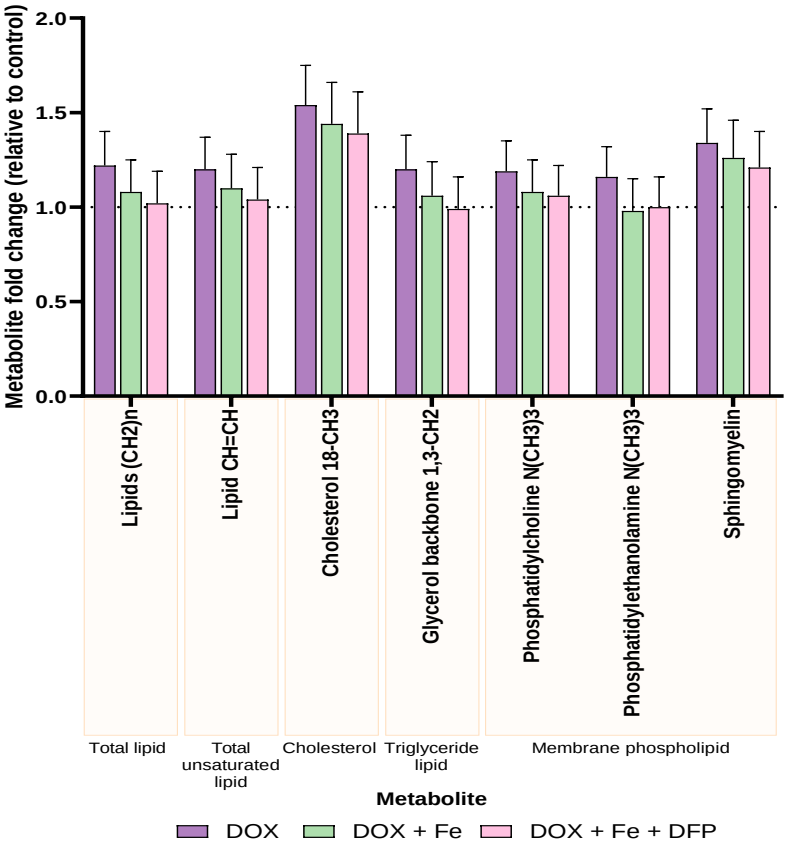

Figure 74: The fold change of lipophilic cardiac metabolites relative to the control group. Fold change of the coadministration groups relative to the control. The fold change in metabolite concentration is represented as the mean ± SEM. Statistical comparison by one-way ANOVA with Tukey's HSD correction method for multiple comparisons. *P<0.05.

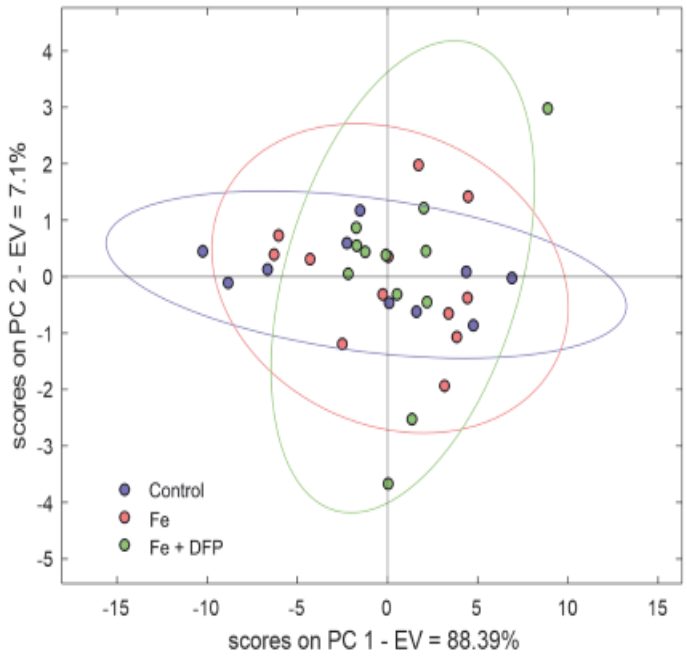

Figure 75: Principal Component Analysis (PCA) score plots from the lipophilic cardiac metabolites of the iron chelation control groups. PCA score plot: PC1 accounted for 88.39% of the total variance, and PC2 accounted for 7.1% of the total variance. Control animals are denoted by the blue dots, while animals in the FE and FE+DFP groups are represented by the orange and green,

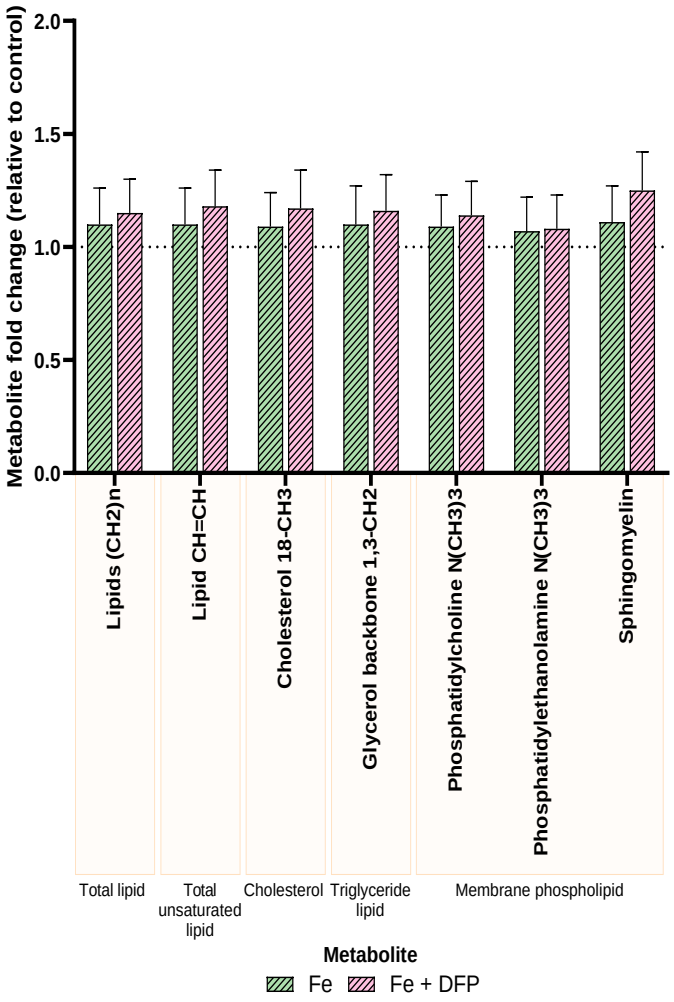

Figure 76: The fold change of lipophilic cardiac metabolites relative to the control group. a Fold change of the iron chelation control groups relative to the control. The fold change in metabolite concentration is represented as the mean ± SEM. Statistical comparison by one-way ANOVA with Tukey's HSD correction method for multiple comparisons. *P<0.05.

7.4.4.2 Liver Metabolism

7.4.4.2.1 Aqueous Metabolites in The Liver

PCA and PLS-DA analysis (Figure 78) revealed separation between the aqueous metabolic profile of the DOX groups and the control. Iron loading did not exacerbate the altered metabolic profile, and deferiprone pre-treatment in iron-loaded rats had no impact on this alteration either.

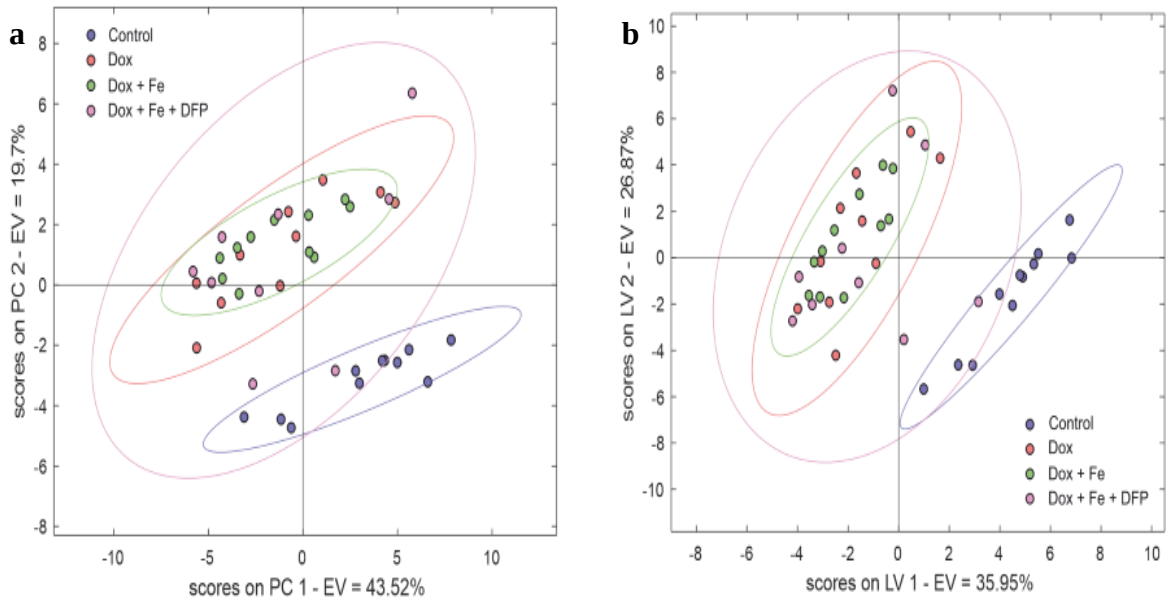

Figure 77: Principal Component Analysis (PCA) and Partial least squares-discriminant analysis (PLS-DA) score plots from the aqueous liver metabolites of the coadministration and control groups. a PCA score plot: PC1 accounted for 43.52% of the total variance, and PC2 accounted for 19.7% of the total variance. **b** PLS-DA score plot: LV1 accounted for 35.95% of the total variance, and LV2 accounted for 26.87% of the total variance. Control animals are denoted by the blue dots, while animals in the DOX, DOX+FE, and DOX+FE+DFP groups are represented by the orange, green, and pink, respectively.

The fold change analysis revealed that the altered metabolites driving the change in metabolic profiles among all DOX-treated animals were nearly identical in terms of both the affected metabolites and the intensity of these changes (Figure 79). Neither iron loading nor deferiprone pre-treatment were seen to have any effect on the liver's aqueous metabolic profile. Key alterations indicative of possible liver dysfunction and perturbed energy metabolism across all DOX-treated animals include the elevation of phosphocholine, and reduced levels of NAD, NADP, phosphocreatine, and niacinamide.

PCA and PLS-DA analysis (Figure 80) also revealed separation between the metabolic profiles of the Iron loaded animals and the control, and deferiprone had no impact on this alteration. This was further substantiated by the Fold change analysis (Figure 81). For mean metabolite concentrations, refer to Appendix (Table 21).

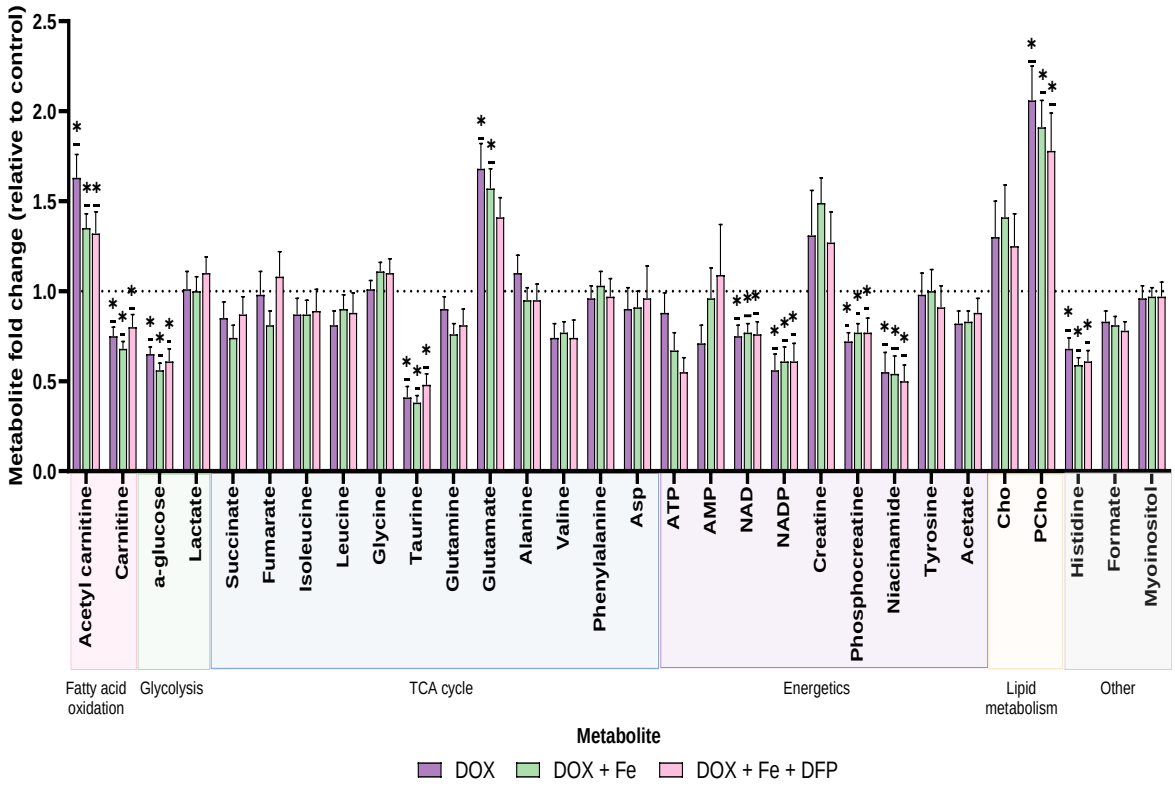

Figure 78: The fold change of aqueous liver metabolites relative to the control group. Fold change of the coadministration groups relative to the control. The fold change in metabolite concentration is represented as the mean ± SEM. Statistical comparison by one-way ANOVA with Tukey's HSD correction method for multiple comparisons. *P<0.01.

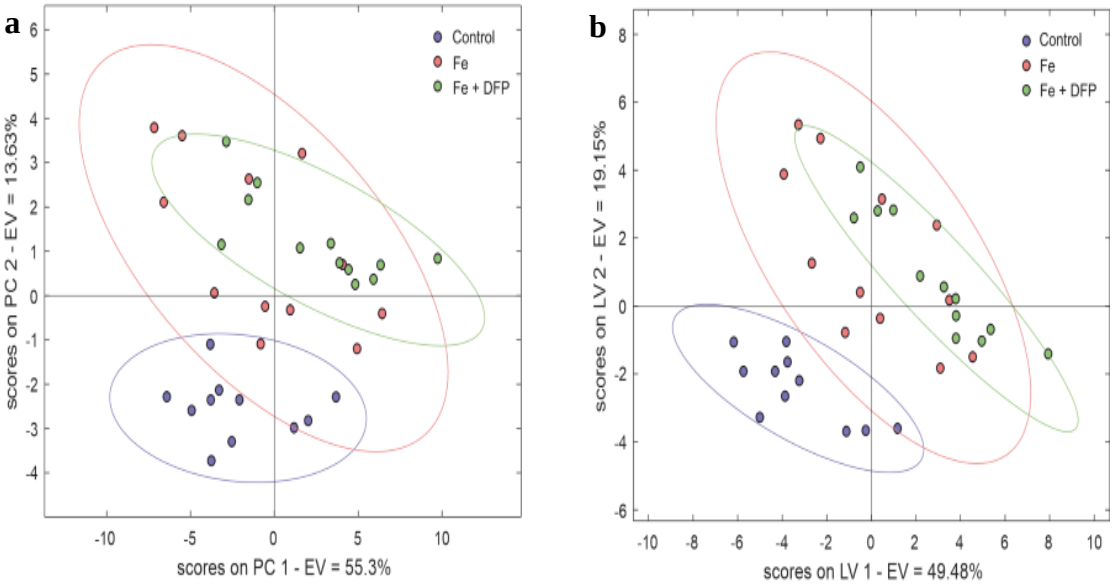

Figure 79: Principal Component Analysis (PCA) and Partial least squares-discriminant analysis (PLS-DA) score plots from the aqueous liver metabolites of the iron chelation control groups. a PCA score plot: PC1 accounted for 55.3% of the total variance, and PC2 accounted for 13.63% of the total variance. **b** PLS-DA score plot: LV1 accounted for 49.48% of the total variance, and LV2 accounted for 19.15% of the total variance. Control animals are denoted by the blue dots, while animals in the FE and FE+DFP groups are represented by the orange and green, respectively.

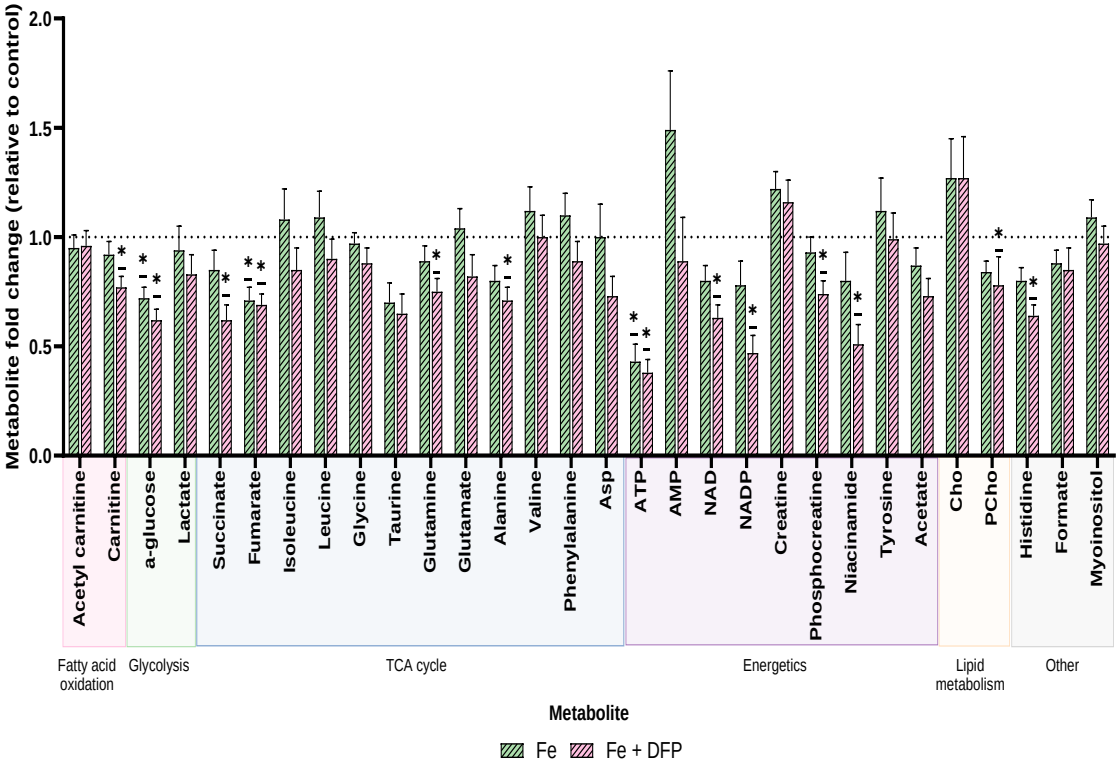

Figure 80: The fold change of aqueous liver metabolites relative to the control group. a Fold change of the iron chelation control groups relative to the control. The fold change in metabolite concentration is represented as the mean ± SEM. Statistical comparison by one-way ANOVA with Tukey's HSD correction method for multiple comparisons. *P<0.01.

7.4.4.2.2 Lipophilic Metabolites in The Liver

PCA and PLS-DA analysis (Figure 82) revealed separation between the lipophilic metabolic profile of the DOX group and the control. Iron loading was not found to exacerbate the altered metabolic profile, and nor did deferiprone pre-treatment in the iron-loaded rats. The fold change analysis (Figure 83) revealed alteration of total lipid and the phospholipids phosphatidylcholine (PC) and phosphatidylethanolamine (PE), that could be indicative of liver dysfunction.

PCA and PLS-DA analysis (Figure 84) revealed no separation between the metabolic profiles of the Iron loaded animals and the control, and deferiprone had no impact on this alteration. This was further substantiated by the Fold change analysis (Figure 85).

For mean metabolite concentrations, refer to Appendix (Table 22).

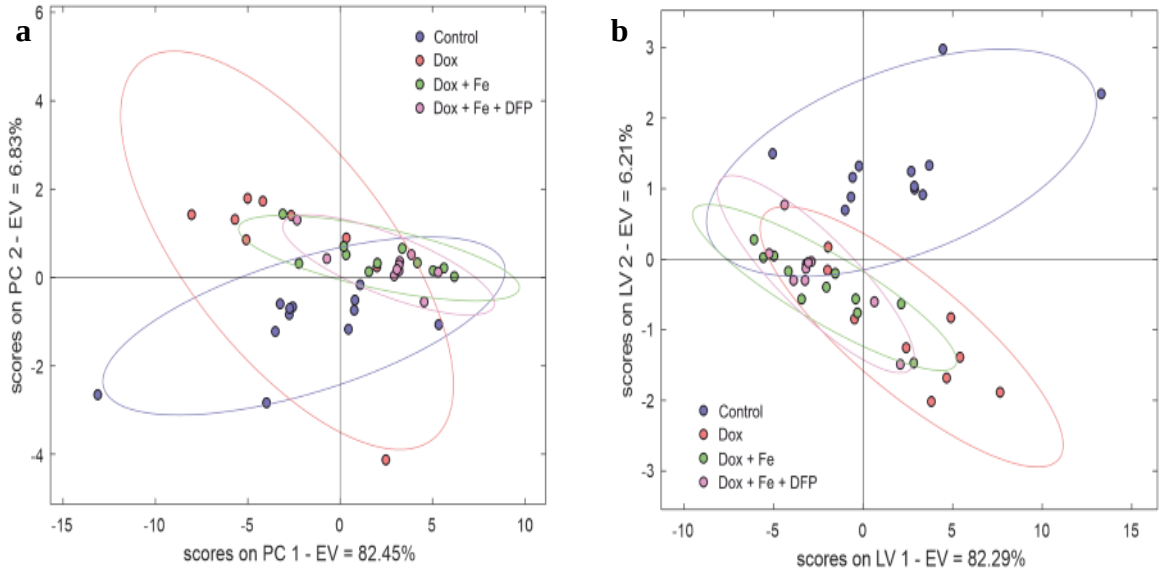

Figure 81: Principal Component Analysis (PCA) and Partial least squares-discriminant analysis (PLS-DA) score plots from the lipophilic liver metabolites of the coadministration and control groups. a PCA score plot: PC1 accounted for 82.45% of the total variance, and PC2 accounted for 6.83% of the total variance. **b** PLS-DA score plot: LV1 accounted for 82.29% of the total variance, and LV2 accounted for 6.21% of the total variance. Control animals are denoted by the blue dots, while animals in the DOX, DOX+FE, and DOX+FE+DFP groups are represented by the orange, green, and pink, respectively.

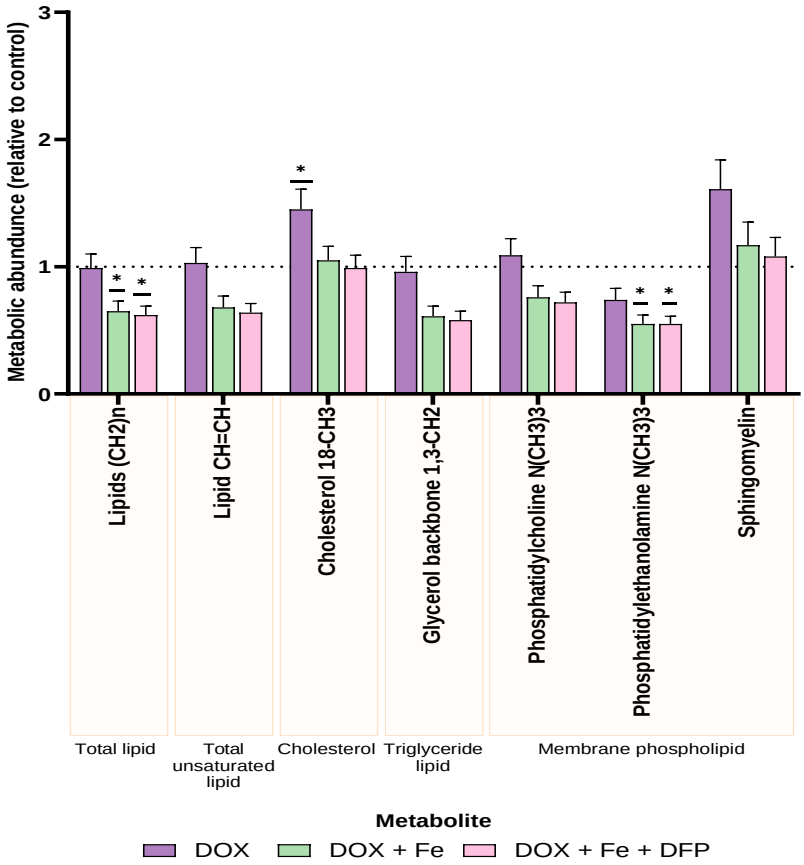

Figure 82: The fold change of lipophilic liver metabolites relative to the control group. Fold change of the coadministration groups relative to the control. The fold change in metabolite concentration is represented as the mean ± SEM. Statistical comparison by one-way ANOVA with Tukey's HSD correction method for multiple comparisons. *P<0.01.

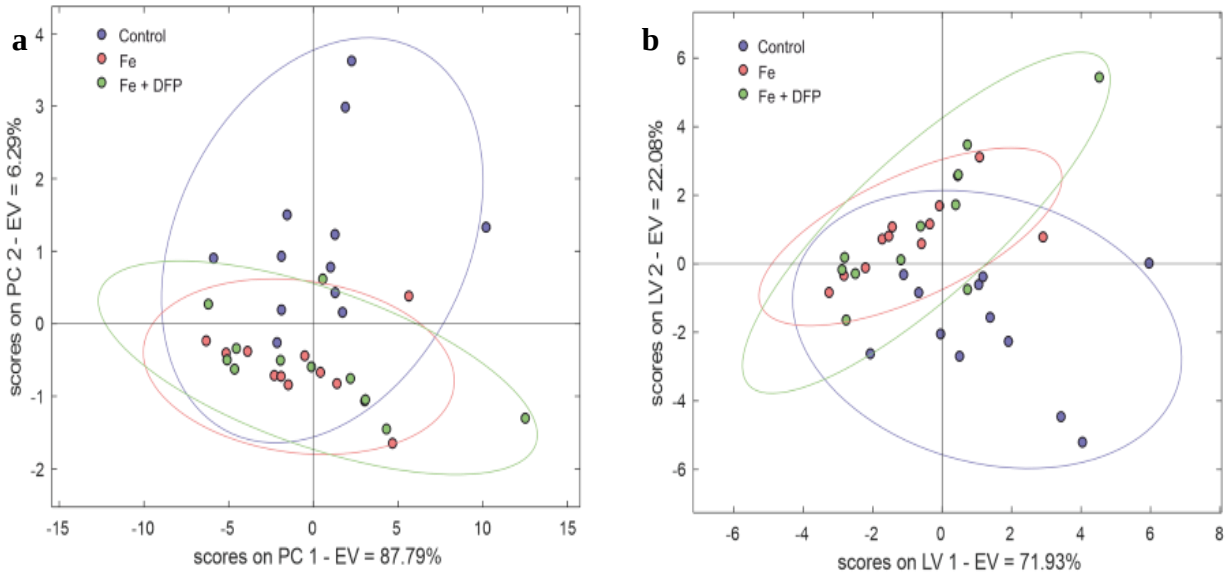

Figure 83: Principal Component Analysis (PCA) and Partial least squares-discriminant analysis (PLS-DA) score plots from the lipophilic liver metabolites of the iron chelation control groups. a PCA score plot: PC1 accounted for 87.79% of the total variance, and PC2 accounted for 6.29% of the total variance. **b** PLS-DA score plot: LV1 accounted for 71.93% of the total variance, and LV2 accounted for 22.08% of the total variance. Control animals are denoted by the blue dots, while animals in the FE and FE+DFP groups are represented by the orange and green, respectively.

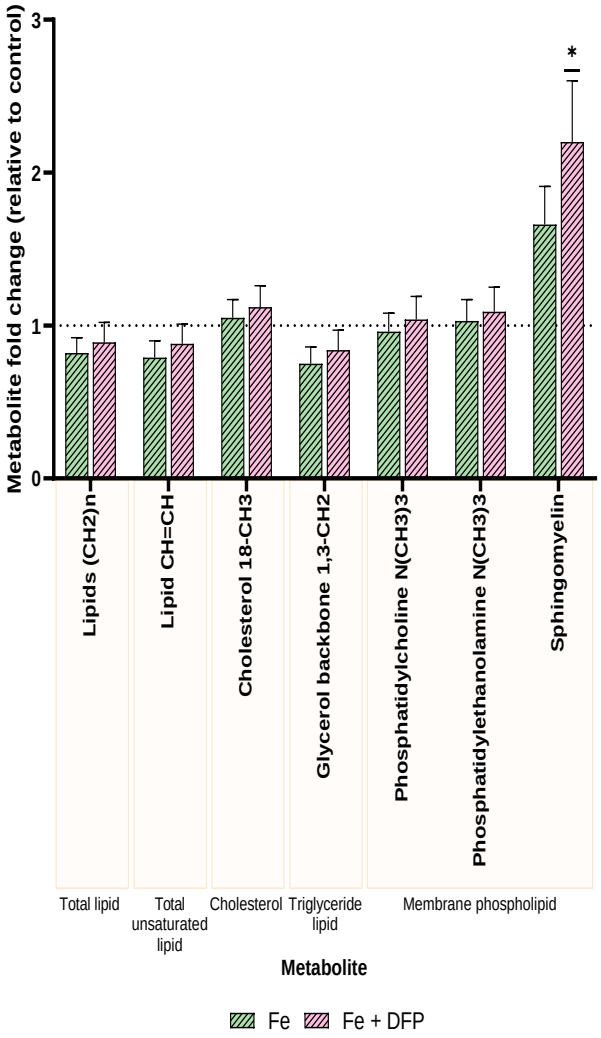

Figure 84: The fold change of lipophilic liver metabolites relative to the control group. Fold change of the iron chelation control groups relative to the control. The fold change in metabolite concentration is represented as the mean ± SEM. Statistical comparison by one-way ANOVA with Tukey's HSD correction method for multiple comparisons. *P<0.01.

7.4.4.3 Serum Metabolism

PCA and PLS-DA analysis (Figure 86) revealed complete separation between the metabolic profile of serum in the DOX group and the control group. Again, iron loading and deferiprone pre-treatment in iron-loaded rats was not found to exacerbate the altered metabolic profiles.

The fold change (Figure 87) analysis revealed that 17 out of the 22 measurable metabolites were significantly altered equally in all the DOX treated groups. The largest metabolic change occurred in fatty acid residues, in which there was a significant 4-fold increase in all DOX treated animal groups, a key indication of altered lipid metabolism.

Other metabolic changes that were consistent across all DOX treated groups included: a decrease in glycolysis metabolites (glucose and pyruvate), a change in TCA cycle metabolites (decreased glycine, glutamate, alanine, valine, and phenylalanine, and increased leucine and glutamate), decrease in energetic metabolites (creatine, tyrosine, and acetate), and increase in fatty acids and ketogenesis metabolite 3-hydroxybutyrate.

PCA and PLS-DA analysis (Figure 88) revealed separation between the metabolic profiles of the Iron loaded animal groups and the control, and that deferiprone had no impact on this alteration. The fold change analysis (Figure 89) indicated that the separation is likely driven by changes in the following metabolites: a decrease in pyruvate, TCA cycle metabolite alanine, and fatty acids.

For mean metabolite concentrations, refer to Appendix (Table 23).

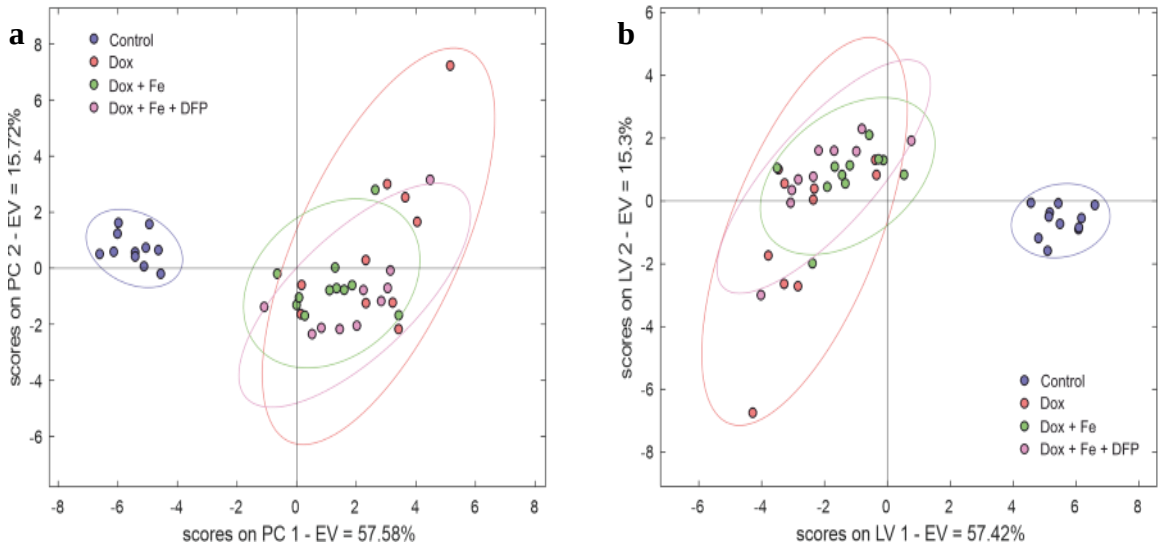

Figure 85: Principal Component Analysis (PCA) and Partial least squares-discriminant analysis (PLS-DA) score plots from serum metabolites of the coadministration and control groups. a PCA score plot: PC1 accounted for 57.58% of the total variance, and PC2 accounted for 15.72% of the total variance. **b** PLS-DA score plot: LV1 accounted for 57.42% of the total variance, and LV2 accounted for 15.3% of the total variance. Control animals are denoted by the blue dots while animals in the DOX, DOX+FE, and DOX+FE+DFP groups are represented by the orange green, and pink, respectively.

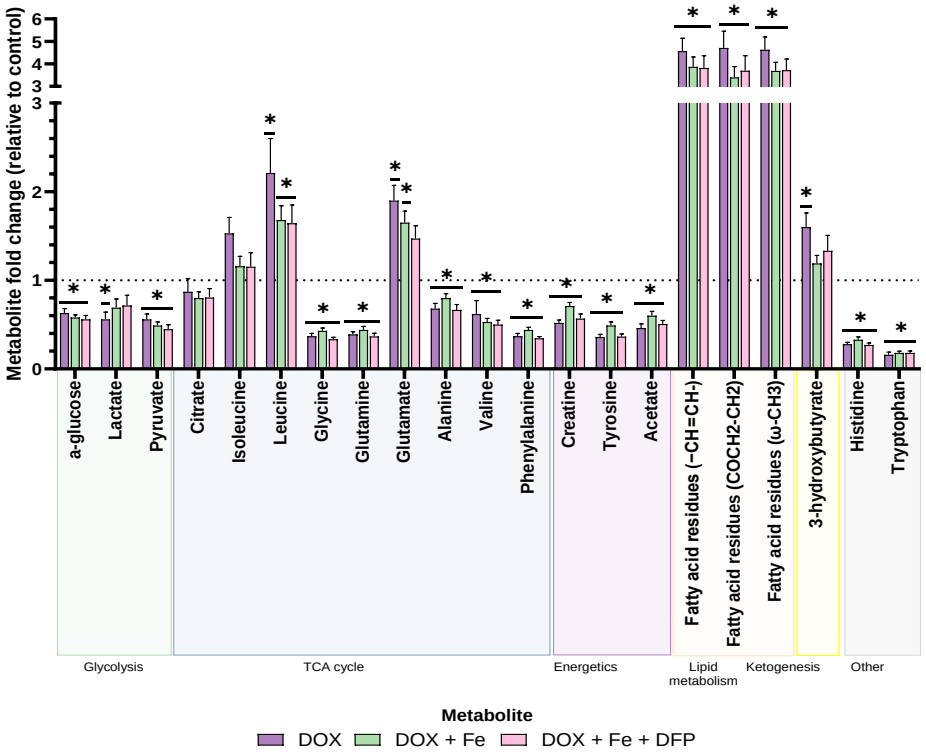

Figure 86: The fold change of serum metabolites relative to the control group. Fold change of the coadministration groups relative to the control. The fold change in metabolite concentration is represented as the mean ± SEM. Fatty acid residue (COCH2-CH2) and Fatty acid residue (ω-CH3) are both constituent parts of the fatty acyl chain representing total fatty acids, and Fatty acid residue (−CH=CH-), a constituent specific to unsaturated fatty acids within the fatty acyl chain. Statistical comparison by one-way ANOVA with Tukey's HSD correction method for multiple comparisons. *P<0.01.

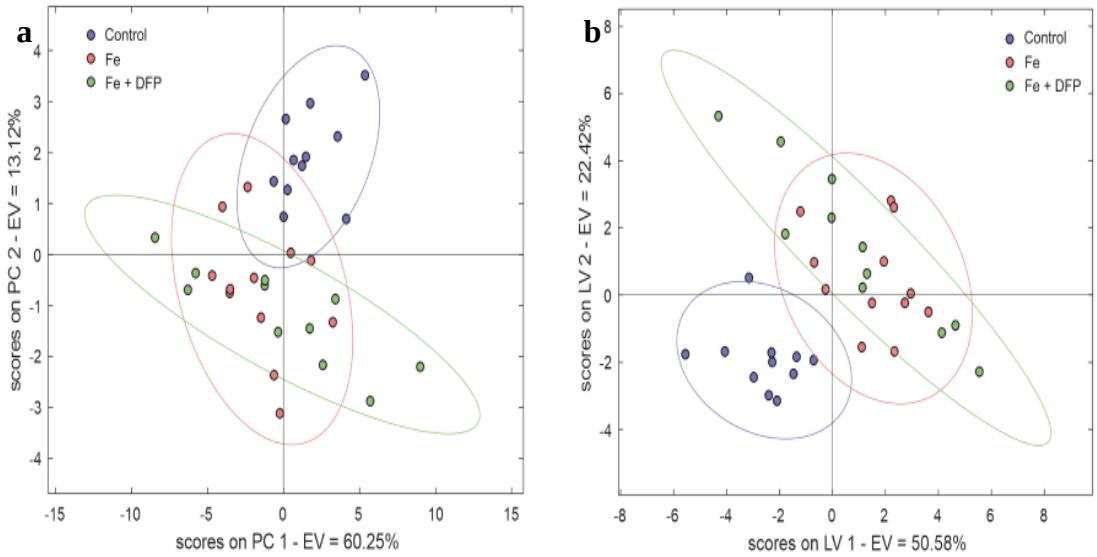

Figure 87: Principal Component Analysis (PCA) and Partial least squares-discriminant analysis (PLS-DA) score plots from serum metabolites of the iron chelation control groups. a PCA score plot: PC1 accounted for 60.25% of the total variance, and PC2 accounted for 13.12% of the total variance. **b** PLS-DA score plot: LV1 accounted for 50.58% of the total variance, and LV2 accounted for 22.42% of the total variance. Control animals are denoted by the blue dots, while animals in the FE and FE+DFP groups are represented by the orange and green, respectively.

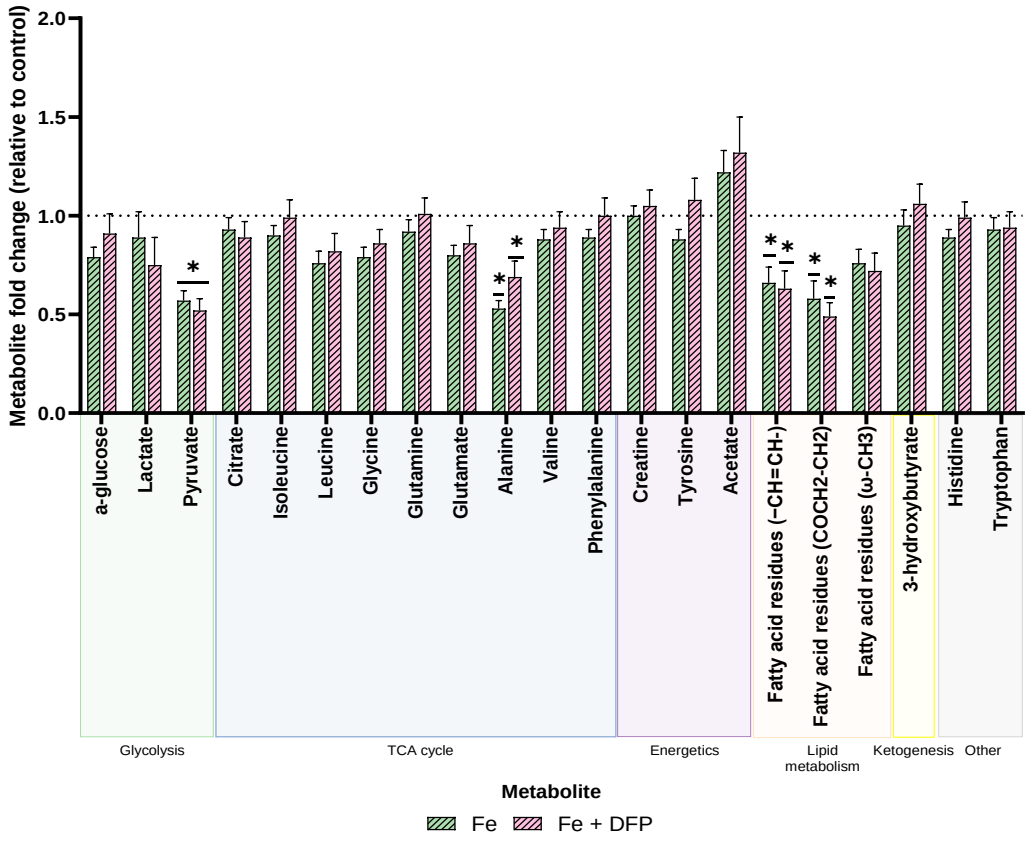

Figure 88: The fold change of serum metabolites relative to the control group. a Fold change of the iron chelation control groups relative to the control. The fold change in metabolite concentration is represented as the mean ± SEM. Fatty acid residue (COCH2-CH2) and Fatty acid residue (ω-CH3) are both constituent parts of the fatty acyl chain representing total fatty acids, and Fatty acid residue (−CH=CH-), a constituent specific to unsaturated fatty acids within the fatty acyl chain. Statistical comparison by one-way ANOVA with Tukey's HSD correction method for multiple comparisons. *P<0.01.

7.5 Discussion

This chapter investigated whether pre-existing iron overload exacerbates chronic DIC, and if iron chelation could be used as a potential cardio-protectant against anthracycline cardiotoxicity. The dosages and regimes used were as clinically relevant as possible. This is crucial as the relative importance of the potential mechanisms underpinning anthracycline cardiotoxicity are likely to be concentration and time dependent. To our understanding, this work is the first to use clinically relevant models to explore the relationship between cardiac iron and chronic DIC.

7.5.1 The Impact of Cardiac Iron Loading on Doxorubicin-Induced Cardiotoxicity

7.5.1.1 Cardiac Function and Physical Measurements

7.5.1.1.1 Cardiac Function

DOX treatment resulted in a progressive reduction in left ventricular function evidenced by the reduction in LVEF, key clinical parameters for the diagnosis of DIC[403]. The thresholds for LVEF as an indicator of DIC is identified clinically as a loss of LVEF of >10% from baseline to a value below 50 %. In this context, chronic DIC developed as a result of our DOX treatment regime but did not hit the threshold for clinical cardiotoxicity as none of the DOX treated animals exhibited an LVEF of below 50%. Therefore, the DIC achieved can be considered sub-acute.

DOX treatment also resulted in reduced FS and stroke volume, suggesting an impaired capacity of the heart to pump blood efficiently[517] [468] [414]. The reduction of LVEF, FS, and stroke volume that resulted from DOX treatment in iron loaded animals was not significantly different to the reduction induced by DOX treatment in non-iron loaded animals. Thus, we found no evidence supporting the hypothesis that iron loading exacerbates the development of chronic DIC within the timeframe of our study and the dosage used, in terms of both the degree of cardiac dysfunction and in the timing of onset. However, further verification is required to conclusively determine this, as I couldn't definitively establish whether cardiac iron was elevated in the animals treated with DOX, given that those specific samples were lost.

As per our hypothesis, the study used clinically relevant *in vivo* models of chronic DIC and iron loading to explore the impact of subclinical levels of cardiac iron overload (as observed in

a specific subset of cancer patients) on the progression of chronic DIC. The disparity between our findings and that of previous literature reports is likely attributed to the clinical relevance of the doses employed. Miranda *et al.*, reported a 30% decreased survival rate in Hfe+/- mice after a 6-week DOX treatment protocol[252]. However, their study administered a 30mg/kg cumulative DOX dose, more than twice the recommended clinical cumulative dose limit of 13.1 mg/kg. Similarly, Ardehali *et al.* reported that DIC is exacerbated by mitochondrial iron accumulation, demonstrated through ABCB8 overexpression both *in vitro* and in transgenic mice[205]. Their *in vivo* study demonstrated that elevated cardiac iron exacerbated chronic DIC a month after the end of DOX treatment. However, the use of clinically irrelevant cumulative DOX dosage regime of 30mg/kg over 10 days limits the clinical relevance of their findings. Ardehali's initial work serves as useful proof of concept, the translation into clinically relevant *in vivo* models is the next step. This study serves as a preliminarily investigation into that translation.

I found no evidence that cardiac iron loading, to the extent achieved in the protocol, significantly exacerbated the degree of DIC that developed six-weeks after DOX treatment. However, a non-significant but pronounced reduction in LVEF was observed after DOX treatment in iron-loaded animals compared to DOX treatment alone. Given that chronic DIC is characterized by progressive reduction in LVEF, this subtle difference between the groups could become more pronounced over time. This suggests that elevated levels of cardiac iron may well still exacerbate the degree of cardiac dysfunction, but that the 6-week latency period (the time post DOX treatment) might be too short to capture its development. A longer latency period is necessary to explore this further, as well as to assess the potential effects of iron loading on DOX-induced mortality.

Under clinically relevant conditions, our data suggest that the effect of elevated cardiac iron on the development of chronic DIC was less pronounced than previously anticipated by initial proof of concept studies.

7.5.1.1.2 Body and Heart Weight

DOX treatment led to decreased weight gain in rats compared to control rats. The average body weight of the DOX group was significantly lower than the control from the second week of the latency period (378±36g vs 437±37g; $p<0.01$). Assessment of whether iron loading exacerbates the effect of DOX on weight gain is challenging as iron dextran also negatively effects the rate

of weight gain independently of DOX; iron-loaded animals start DOX treatment at a lower weight than non-iron-loaded animals receiving DOX. Gastrointestinal symptoms, including nausea and abdominal pain, are listed side effects of iron infusions, and are therefore a likely cause of the reduced weight gain observed during the iron loading treatment period[518] [519].

Elevated heart: body weight ratios are used as an indicator of cardiac hypertrophy[520],[454] [457] [458] [459] [460] [403]. DOX treatment alone and in iron-loaded animals resulted in an equal and significant elevation in heart-to-body weight ratio compared to the control group, indicating that iron loading does not impact the heart:body weight ratio.

7.5.1.2 Cardiac Metabolism

Cardiac metabolism was unaltered following 2mg/kg DOX treatment alone and 2mg/kg DOX treatment in iron loaded animals. The modest change in the cardiac metabolic profile observed in Chapter 5 following the same DOX dose was not recapitulated here. The lack of change observed in the cardiac metabolic profile six-weeks after the end of DOX treatment, despite cardiac dysfunction, does not necessarily imply that metabolism is not associated with the cardiac dysfunction. The activity of metabolic reactions depends on the rate of the reaction through an enzyme. In the steady-state metabolomics approach, concentrations are exclusively measured, not the rates of enzymatic reactions. We lack information about the specific activity levels of each enzyme, which could be altered in cardiac dysfunction. Therefore, it is possible that metabolite levels can remain unchanged during cardiac dysfunction, while metabolite fluxes might be affected.

It is also important to recognise that metabolomics is a hypothesis generating tool. While it can identify changes in individual metabolites and overall metabolic profiles (as determined by PCA analysis), identifying the exact cause of these changes is challenging. Metabolomics captures an interconnected network, making it difficult to determine which flux led to alterations in a particular metabolite.

The lack of change observed in the cardiac metabolic profile six-weeks after the end of DOX treatment may also be influenced by threshold effects. Alterations in cardiac metabolism appear to occur only above a specific threshold of cardiac dysfunction. This is supported by data in our DOX study (Chapter 6), profound metabolic alterations in cardiac tissue were only observed in the higher DOX dose groups (3mg/kg and 4mg/kg), and these alterations

corresponded with severity of cardiac dysfunction in a dose dependent manner. Unfortunately, our cautious decision to administer a low cumulative DOX dose in this study, driven by concerns about the potential severity of the synergistic effect of DOX and Fe (which did not materialise), proved to be overly conservative. As a result, both the DOX treatment alone and the DOX treatment in iron-loaded animals failed to surpass the clinical cardiotoxicity threshold, and the observed cardiotoxicity is categorized as sub-acute. This cautious approach may account for the absence of significant alterations in cardiac metabolism.

7.5.1.3 Cardiac Iron

7.5.1.3.1 Total Iron

It is not possible to present a complete set of total cardiac iron measurements from the DOX+FE, DOX+FE+DFP, and FE+DFP groups. The experiments were performed as planned and tissue samples collected. However, the majority of the tissue samples obtained were inadvertently discarded by our collaborator. After a failed overnight run all the samples were discarded en masse. Regrettably, this means that I could only assess the effect of the iron loading intervention within the context of the model itself rather than in relation to DOX, as originally intended.

The average total cardiac iron levels were 1.7-fold higher in the iron loaded group compared to the control by the end of the study period. This was significantly less than the 2.9-fold increase that I had previously measured following the 4-week washout period (See Chapter 5). It is also substantially lower than the 2.8-fold increase reported after a 9-week washout period by Avila *et al.*, using the same iron overload protocol.[367].

This discrepancy may arise from the prolonged interval between the end of iron loading and the culling of the animals, a timeframe not characterised in my previous work. By the end of this study, the iron-loaded group had effectively undergone a 14-week washout period, which included of a 4-week deferiprone treatment phase, a 4-week DOX treatment phase, and a subsequent 6-week washout period, before the measurement of cardiac iron. The reduced elevation in total cardiac iron might stem from washout occurring over this 14-week period, but additional research is needed to definitively confirm this by analyzing the potential washout during this period.

7.5.1.3.2 Total Mitochondrial Iron

Total mitochondrial iron levels were found to be unaltered in the iron loaded animals treated with DOX. Total mitochondrial iron levels measured in the FE group were also found to be unaltered, despite the ~3.5-fold increase measured after a 4-week washout period as described in Chapter 5. As discussed in relation to total cardiac iron, the absence of elevation in total mitochondrial iron could be a result of washout during the final weeks of the study.

7.5.2 The Cardio-Protective Potential of Deferiprone Pre-Treatment Against Doxorubicin-Induced Cardiotoxicity in Iron Loaded Animals

7.5.2.1 Cardiac function and physical measurements

7.5.2.1.1 Cardiac Function

Although as discussed, the injury model developed was perhaps milder than intended, and the iron overload achieved was relatively slight, I did find some evidence that Deferiprone pre-treatment ameliorates left ventricular dysfunction caused by DOX treatment in iron-loaded animals.

The reduction in LVEF induced by DOX on its own was not significantly different to the reduction induced by DOX treatment in the iron loaded animals pre-treated with deferiprone. This suggests that deferiprone pre-treatment in patients with pre-existing iron overload could potentially offer cardioprotection by normalizing LVEF to levels observed in DOX-treated patients with normal cardiac iron levels. However, deferiprone pre-treatment still resulted in animals with significantly reduced LVEF within the time frame of our study, limiting its clinical utility.

As DIC is characterized by progressive reduction in LVEF, the slightly ameliorated reduction in LVEF observed from deferiprone pre-treatment in this study could though become more clinically important over time. A longer latency period than the 6-weeks of this study is required to investigate whether deferiprone pre-treatment could have meaningful clinical implications for life expectancy in patients with elevated iron levels before undergoing anthracycline chemotherapy treatment.

Due to time constraints and licensing limitations, it was not possible to investigate the cardioprotective potential of deferiprone when co-administered with doxorubicin. This is our ambition in future work, and now that our models are in place we are well positioned to perform this study.

Iron loading, both alone (FE group) and in combination with Deferiprone (FE+DFP), was investigated to examine contributory effects on the observed cardiac dysfunction. The interventions resulted in a reduction in stroke volume of the same degree. However, the decrease in ventricular volumes driving this change were not substantial enough to impact LVEF and FS. The DOX treatment was concluded to be the primary driver of the observed cardiac dysfunction, and iron loading or deferiprone treatment had minimal contributory effects.

7.5.2.1.2 Body and Heart Weight

Deferiprone pre-treatment did not affect body weight in iron loaded animals treated with DOX. Deferiprone pre-treatment also did not affect body weight in iron loaded animals not treated with DOX (DOX+FE group vs FE group). This suggests that gastrointestinal symptoms resulting from both iron loading and DOX, which can result in to decreased appetite and reduced food intake, are driving the patterns of weight gain in iron-loaded animals. Deferiprone is used to chelate iron; therefore, it is not surprising that it does not have an ameliorative effect on body weight caused by gastrointestinal factors. In line with this, Deferiprone pre-treatment also did not affect heart-to-body weight ratio in iron loaded animals treated with DOX.

7.5.2.2 Cardiac Metabolism

Despite the significant cardiac dysfunction, cardiac metabolism was also unaltered following DOX treatment in iron loaded animals with and without deferiprone pre-treatment. As discussed in 7.5.1.2, it is possible that metabolite levels can remain unchanged during cardiac dysfunction, while metabolite fluxes may be affected.

7.5.2.3 Cardiac Iron

7.5.2.3.1 Total Iron

As explained previously, all total cardiac iron measurements from the DOX+FE, DOX+FE+DFP, and FE+DFP groups were discarded by our collaborator. The insight we would have been able to gain into the efficacy of iron chelation with DFP is therefore lost.

As assessed through our previous work and the reference study, cardiac iron would likely have been elevated during the period in which the iron loaded animals were treated with Deferiprone and DOX. Thus crucially, excess cardiac iron would have been available for deferiprone to chelate prior to DOX treatment.

7.5.2.3.2 Total Mitochondrial Iron

Deferiprone pre-treatment elevated mitochondrial iron levels in iron loaded animals treated with DOX, compared to those that did not receive deferiprone pre-treatment. However, the measurements of mitochondrial cardiac iron obtained were inherently noisy, particularly in the DOX+FE+DFP group. There is a possibility that the elevation observed may well be an artefact of the noise. The cardioprotective effect deferiprone demonstrates in β-thalassemia patients with iron induce cardiotoxicity further supports that this elevation could be an artifact[278].

More biological repeats and mass balance studies are to be conducted to increase the robustness of our mitochondrial iron measurements, to better distinguish between elevated mitochondrial iron levels and potential outliers that could be driving significance, such as in the DOX+FE+DFP group.

7.5.3 The Effects of DOX on Serum Lipids and the Liver

Building on the discovery of lipemic serum in DOX-treated animals from the previous chapter, preliminary investigations into the metabolic effects of DOX treatment on the liver[503] were undertaken. Recognizing the liver's central role in lipid metabolism, our aim was to explore whether liver dysfunction correlates with alterations in circulating lipid levels and the observed dyslipidaemia observed in DOX treated animals.

7.5.3.1 Serum Lipids

This study validated the earlier finding that DOX treatment results in a substantial increase in total fatty acids in the serum (approximately 4/5-fold) six weeks after the completion of DOX treatment (DOX-induced dyslipidaemia). This aligns with recent literature findings. Retrospective studies have shown that chemotherapy, including anthracycline-based treatment, alters serum lipid profiles in breast cancer patients [521][522].

Lu *et al*. collected lipid profiles from 1740 breast cancer patients before and after chemotherapy, revealing increases in triglycerides (TG), total cholesterol (TC), and low-density lipoprotein cholesterol (LDL-C)[521]. He *et al.* conducted a second retrospective study involving 1934 breast cancer patients, where lipid profiles were elevated in the same manner[522]. These retrospective studies though only offer insight into acute changes that occur shortly after or during DOX treatment.

As there are few studies that have evaluated the long-term effect of anthracycline treatment on the serum lipid profile, it is unclear how long elevated lipid levels persist. The most relevant study was conducted by Arpino *et al.*, in breast cancer patients receiving adjuvant therapy, including anthracyclines[523]. Two years after cancer treatment, TG, TC, and LDL-C were still elevated, indicating that anthracyclines may have lasting effect on lipid metabolism.

Our study indicates that DOX treatment in isolation, and not just in combination therapy, leads to prolonged elevation in serum lipid levels. Although we could not differentiate between the different lipid classes, total fatty acid is a valuable measurement of total serum lipid, given that fatty acids constitute the majority of the total serum lipid[497]. In this context, our study provides evidence that DOX directly contributes to the observed increase in lipids in the serum of anthracycline treated cancer patients, which persist after the end of DOX treatment. These findings suggests that lipid therapy should be considered in the management of cancer patients in mitigating the risk of developing cardiovascular disease.

Statins are extensively used in clinical practice for preventing cardiovascular disease, due to their anti-inflammatory, anti-oxidative, and cholesterol-lowering effects[524]. They are also the first-line treatment for lipid disorders, able to reduce LDL-C levels by up to 60%[524]. Given the elevated lipid levels observed in our study and documented in the literature, it is plausible that statins could offer a means to mitigate the risk of cardiotoxicity in cancer patients undergoing anthracycline treatment.

Recent meta-analysis studies have investigated the use of statins as cardioprotective agents in cancer patients treated with anthracyclines which have indicated an association between statin use and decreased risk of cardiotoxicity after anthracycline exposure[512]. Data on the efficacy of statins in prevention of anthracycline-induced cardiotoxicity is based mostly on retrospective and observational studies which lack hard clinical endpoints. The varying statin doses from these studies further hinder the establishment of a specific regimen for statin use as a cardioprotective measure. However, the first large- randomized and highly anticipated Phase 2 STOP-CA (Statins to Prevent the Cardiotoxicity from Anthracyclines) trial readout in August 2023, have more robustly confirmed the cardioprotective effect of statins for certain cancers. The STOP-CA trial demonstrated that atorvastatin use during anthracycline treatment is associated with a decreased incidence of clinically significant LVEF reduction.

For patients with lymphoma receiving anthracycline-based chemotherapy (≥250mg/m2 cumulative dose)[525], the STOP-CA study showed that for individuals taking atorvastatin there was a lower incidence of a LVEF decline of ≥10% at a 12-month follow-up (9%) compared to the placebo group (22%). This, contrary to the previous PREVENT (Preventing Anthracycline Cardiotoxicity with Statins) trial[526], which suggested no prevention of LVEF decline in breast cancer patients that received low cumulative dose anthracycline treatment (~240 mg/m2 on average). The STOP-CA study indicated that certain lymphoma patients requiring higher cumulative anthracycline doses may warrant statin treatment as a cardioprotective agent.

The exact mechanism by which DOX causes an increase in serum lipids is unclear, however it is thought that a DOX-induced imbalance between lipid uptake and utilization in fatty acid oxidation may contribute, leading to an accumulation of lipids in the heart and enhanced oxidative stress[522][527][528].

Renu *et al.* investigated how DOX affects lipid metabolism through gene expression studies and found that attenuated Peroxisome proliferator-activated receptor α (PPARα) in the heart was central to this[529]. PPARα is a key transcription factor that governs regulation of various genes associated with lipid metabolism, including fatty acid transportation, lipolysis, lipid metabolism, and fatty acid oxidation. Renu *et al.* demonstrated that DOX induces a reduction in the protein expression of PPARα, causing dysregulation of lipid metabolism and fatty acid oxidation in cardiac tissue during DOX treatment. DOX treatment additionally downregulated Apolipoprotein B (APOB), a reverse TG transporter crucial for regulating excessive fatty acid

import into the heart. This dysregulation resulting in TG accumulation in the heart during DOX treatment. The TG accumulation has the potential to induce cardiac lipotoxicity through increased synthesis of toxic lipid intermediates within the heart, contributing to contractile and mitochondrial dysfunction[530]. Previous studies on isolated rat hearts have outlined the detrimental effects of elevated levels of free fatty acids on cardiac contractility[531]. Our results did not show any changes in the lipid profile of cardiac tissue, implying that any disturbance are likely limited to the DOX treatment period and does not persist 6-weeks after the end of DOX treatment. This aligns with the understanding that dysregulation of these transcription factors only occurs in the presence of DOX. This would explain why statins have demonstrated cardioprotective effects when administered during DOX treatment.

7.5.3.2 Liver Metabolism

After administration, DOX is cleared from the circulation and accumulates in the liver[532]. It is hypothesized that the metabolism of DOX in the liver generates ROS through redox cycling of the DOX semiquinone[533]. This process induces oxidative stress, lipid peroxidation, mitochondrial damage, and subsequent hepatic injury.[502][534][502]. Elevation of serum lipids could therefore also be related to the action of DOX on the liver, which regulates lipid metabolism and cholesterol homeostasis, lipid uptake, formation, and export to the circulation [522][503] [504].

Supporting this, I observed that DOX treatment significantly altered the aqueous and lipophilic metabolic profile of liver tissue compared to that of control animals. I observed an elevation in phosphocholine, a key component of phospholipids important for cell structure and function, indicating a potential change in phospholipid metabolism. Elevated phosphocholine levels can reflect changes in membrane integrity associated with liver cell damage or impaired liver function. Liver injury can disrupt cellular metabolism, impacting the synthesis and turnover of phospholipids like phosphocholine. Therefore, elevated levels of phosphocholine in the liver can be a marker of liver damage or dysfunction[535]. I also observed decreased levels of plasma membrane phospholipids phosphatidylcholine (PC) and phosphatidylethanolamine (PE), which are integral for maintaining structural integrity of cell membranes. Numerous *in vivo* and clinical studies have shown that changes in their concentrations, particularly in the PC/PE ratio, serve as determinants of liver health. Altered PC/PE ratios have been linked to the development of NAFLD and liver failure [536][537][538][535]. Reduced hepatic PC/PE levels can also disrupt various aspects of lipid metabolism, including lipid synthesis, secretion,

storage, and signalling, contributing to the development of dyslipidaemia, a known risk factor for cardiovascular diseases and heart failure[539][540][541]. This highlights the interconnectedness of liver function with systemic biology and cardiac function. The changes in phosphocholine, PC, and PE metabolite concentrations observed in our study are indicative of sustained DOX-induced liver injury, which likely contributes to the cardiac dysfunction observed with DOX treatment.

Disruption to hepatic energy metabolism and redox balance are indicated by the reduced levels of NAD, NADP, phosphocreatine, and niacinamide observed. NAD and NADP are essential coenzymes involved in various metabolic pathways, including glycolysis, the TCA cycle, and oxidative phosphorylation. A decrease in these metabolites, as well as the NAD precursor niacinamide, likely affects energy production. The decline in phosphocreatine, a key component of the ATP-creatine phosphate system, may reflect compromised cellular energy buffering capacity. The changes in these energetic-associated metabolites reflect a broader disturbance in glycolysis and fatty acid oxidation, as indicated by the altered levels of glucose, carnitine, and acetyl carnitine also observed.

The altered metabolic profile in DOX treated animals provides evidence supportive of liver damage, contributing to the observed increase in serum lipids. These metabolic alterations offer insight into the impact of DOX on liver function. This preliminary investigation study, requires further liver function tests to confirm the metabolic observations seen here and to fully assess the extent of liver injury resulting from DOX treatment

7.5.3.3 Impact of Cardiac Iron Loading and Iron Chelation on the Metabolic Profiles of the Liver and Serum

The cardiac iron loading and iron chelation interventions had no impact on the altered metabolic profile of the liver following DOX treatment, nor the altered metabolic profile of the serum. This suggests that iron does not play a significant role in the disrupted lipid profile in the serum and the persistent liver dysfunction after DOX treatment. The mechanism behind DIC is multifactorial, and while iron overload and dyslipidaemia caused by probable liver injury are potential contributory factors, they appear to be independent of each other.

7.6 Summary

A key aim of this study was to investigate the impact of clinically relevant pre-existing iron overload on the development of chronic DIC, which was investigated through assessments of cardiac function and cardiac metabolism. Contrary to our initial hypothesis and previous literature reports, I found that iron loading did not exacerbate cardiac dysfunction or alter cardiac metabolism. Therefore, it could not be concluded that iron exacerbates chronic DIC within the timeframe of our study and at the dosage used. However, I did observe a non-significant but more pronounced reduction in LVEF resulting in DOX treatment in iron-loaded animals compared to DOX treatment alone. Given the progressive nature of chronic DIC, this subtle difference between the groups may become more pronounced over time, indicating that iron overloading may adversely affect life expectancy beyond the 6-week observation period in our study. A longer latency period is necessary to explore this further, and to evaluate the potential effects of iron loading on DOX-induced mortality. Our findings suggest that the exacerbating effect of elevated cardiac iron on the development of chronic DIC may be less significant than previously anticipated by the initial proof of concept studies, but the doses used were perhaps milder than ideal for testing this hypothesis more robustly. The disparity between our findings and that of previous literature reports is likely due to their use of cumulative DOX dosage regimes that are not clinically relevant.

The second key aim of this study was to examine the potential cardioprotective effects of administering iron chelation prior to DOX treatment in animals with elevated cardiac iron levels. Deferiprone had no effect on cardiac metabolism but did mitigate the decline in LVEF by normalizing it to levels observed in animals treated with DOX alone. However, its clinical utility is limited, as LVEF remained significantly reduced compared to control and baseline levels. Nonetheless, considering the progressive nature of DIC characterized by a continual decline in LVEF, the modest improvement in LVEF reduction resulting from deferiprone pre-treatment could be clinically significant in the long-term, potentially extending life expectancy. A longer latency period is necessary to explore this further, and to evaluate the clinical relevance of deferiprone pre-treatment on DOX-induced mortality.

Expanding on the findings of lipemic serum in DOX-treated animals from the preceding chapter, preliminary investigations into the metabolic impact of DOX treatment on the liver were conducted. We hypothesised that the lipemic serum observed in our DOX study could be linked to altered liver metabolism, and potentially correlate with lipotoxicity in the heart. DOX

treatment altered the metabolic profile of the liver, which persisted six weeks after the end of treatment. This suggests that liver damage incurred during DOX treatment has long lasting effects, and likely contributes to the sustained elevation of fatty acids observed in the serum of DOX treated animals. In the liver, altered levels of phosphocholine, phosphatidylcholine (PC) and phosphatidylethanolamine (PE) were measured, which are common markers of liver dysfunction. Further investigations into liver function during and after DOX treatment is required to substantiate this. Despite the altered liver metabolism, DOX did not alter the metabolic profile of cardiac lipids in our study. Previous studies have demonstrated that DOX likely contributes to lipotoxicity in the heart by downregulating gene expression of receptors associated with lipid metabolism, including PPARα and APOB. The dysregulation of these transcription factors is anticipated to occur in the presence of DOX, thus alterations to the metabolic profile of cardiac lipids are likely limited to the DOX treatment period. This could contextualise our results as cardiac lipids were measured six weeks after DOX treatment.

To conclude, our principal findings show that increased cardiac iron, representative of cancer patients with pre-existing subclinical cardiac iron overload, does not significantly exacerbate the development of chronic DIC. Deferiprone pre-treatment normalized the decline in LVEF induced by DOX treatment in iron loaded animals to levels observed in animals treated with DOX alone, suggesting potential long-term cardioprotective benefits.

Several avenues can be explored to build upon this work and substantiate our findings. Firstly, the subtle cardiac function changes suggest that pre-existing iron overload could potentially have an adverse effect on survival, while iron chelation may extend survival. Further investigation is warranted to assess the impact of these interventions on mortality rates. Secondly, preliminary investigations into the impact of DOX on the liver revealed that liver metabolism was altered six weeks after DOX treatment, likely contributing to the elevated levels of fatty acids in the serum. Evaluating liver function during and after DOX treatment could be utilised to contextualise these findings. Lastly, the cardiac lipid profile was unaltered, suggesting that a dysregulation of cardiac lipids may be transient and confined to the DOX treatment period. Investigating the impact of DOX on cardiac metabolism during DOX treatment is important for comparing with the long-term effects observed in this study and establishing a timeline of significant perturbations.

SUMMARY AND FUTURE WORK

8.1 Summary of Major Findings

The aim of this thesis was to examine the inter-relationship between cardiac iron overload and metabolic dysfunction and remodelling in chronic Doxorubicin-induced cardiotoxicity (DIC). Using new clinically relevant models of cardiotoxicity which I developed and characterised, we investigated whether pre-existing iron overload exacerbates chronic DIC, and whether iron chelator deferiprone had potential as a cardioprotective intervention.

The thesis consists of four main chapters:

Chapter 3 described the development of an ICP-MS method to quantify total cardiac iron concentration in both whole cardiac tissue samples and mitochondrial isolations.

Chapter 4 described the development of a clinically relevant model of cardiac iron overload to emulate the iron levels observed in a subset of cancer patients undergoing DOX treatment.

Chapter 5 developed and characterised a clinically relevant model of chronic DIC.

Chapter 6 utilised the clinically relevant *in vivo* models to investigate whether pre-existing iron overload exacerbated chronic DIC and investigated the cardioprotective potential of iron chelation preceding DOX treatment in animals with elevated levels of cardiac iron.

8.1.1 ICP-MS-based Quantification of Total and Mitochondrial Cardiac Iron

Chapter 3 detailed the development of ICP-MS based iron quantification protocol for the measurement of total and mitochondrial cardiac iron. Strategies to address spectral and non-spectral interferences associated with ICP-MS based elemental quantification were implemented. Spectral interferences were mitigated through collision/reaction cell usage, and non-spectral interferences were countered via dilution, internal standardization with gallium, and matrix-matched calibration standards. Elemental contamination, a significant issue in ICP-MS trace level analysis, was minimised by careful tissue harvesting and use of high-purity reagents and clean room facilities for sample preparation.

8.1.1.1 Quantifying Total Cardiac Iron

The ICP-MS-based quantification of iron was calculated per gram of dry cardiac tissue. For accurate quantification of total cardiac iron, the iron concentration of varying tissue masses (ranging from 50mg to 200mg) was systematically assessed. The importance of the initial 'wet' tissue mass was highlighted through use of simple linear regression, noting that that smaller masses (particularly the 50mg 'wet' group) impacted the iron measurements through weighing errors. Consequently, a minimum 'wet' mass of >100mg was recommended for future ICP-MS analyses.

A repeat biological study assessed the variability of total cardiac iron in control heart samples (n=6). Through ICP-MS analysis, the mean total cardiac iron concentration was determined to be 315 ± 20.97 µg iron/g dry tissue, which aligns with literature [362] [363] and affirmed the reliability of the approach. A valuable reference interval for normative cardiac iron content in control settings was established for the development of the iron overload models, and as a benchmark for contextualizing variations in iron concentrations in future *in vivo* studies.

8.1.1.2 Quantifying Total Mitochondrial Cardiac Iron

The development of a reliable method for accurately assessing mitochondrial iron levels using ICP-MS, addressed challenges related to isolation purity, mitochondrial integrity, and contamination. Intact mitochondria were successfully isolated for analysis through a two-step centrifugation method. Western blot analysis demonstrated minimal contamination from cytosolic and lysosomal proteins was achieved. Through systematic experimentation with homogenization stroke numbers, an optimal 10-stroke procedure that maintained mitochondrial integrity during the isolation procedure was identified and validated by appropriate partitioning of marker proteins into cell fractions using Western Blotting.

To enhance the accuracy and reliability of mitochondrial iron quantification. A protein content-centric approach for measuring mitochondrial iron concentration using the BCA assay was adopted to counter the challenges associated with measuring small mass samples. Methods for determining protein content in the mitochondrial pellet were explored and it was concluded that the preferred option involved splitting the supernatant after the first centrifugation of the mitochondrial isolation process. This resulted in two pellets, one for ICP-MS analysis and one for the BCA assay. The optimal ratio of ICP-MS supernatant to BCA supernatant volume

determined to be 4:1. This ratio representing the maximum volume of supernatant allocated to produce the ICP-MS destined pellet while ensuring sufficient protein content in the pellet required for BCA analysis. This optimized mitochondrial isolation protocol yielded isolations with satisfactory purity and integrity, providing a reliable foundation for subsequent analyses.

A biological repeat study evaluated the variation in mitochondrial iron levels in control cardiac samples, which establishing reference intervals for mitochondrial iron concentrations in control samples (0.6967 ± 0.3908 µg Fe/mg protein). These values were also utilised as benchmarks for characterising mitochondrial cardiac iron in the development of our *in vivo* cardiac iron overload model.

8.1.2 Developing and Validating an *In Vivo* Model of Cardiac Iron Overload

Chapter 4 established a rat model of cardiac iron overload to simulate the iron overload observed in patients undergoing chemotherapy treatment receiving multiple blood transfusions. An essential criterion for the iron overload model was the ability to induce a prolonged intracellular iron overload to mitigate the toxic effects of the iron-delivery vehicle itself.

Two iron overload models were compared: 1) dietary ferrocene and 2) iron dextran administered by I.P. injection. To our knowledge, these studies are the first to evaluate cardiac iron overload models in terms of cardiac function, metabolism, and iron levels, incorporating a washout period to distinguish the direct effect of iron overload from the residual presence of the iron-overload compound.

Ferrocene invoked a mild elevation (1.5-fold increase) in total cardiac iron compared to the 5-fold increase reported in literature and was not found to be statistically significant compared to reference control measurements. As the elevation in iron was mild, it wasn't possible to definitively dismiss the possibility of normalization of iron levels following the discontinuation of the ferrocene diet. This method of cardiac iron loading was therefore rejected.

Incorporating our insight from the ferrocene study into our evaluation of iron dextran, I refined our protocol to extend the washout period to four weeks. Additionally, iron and metabolism at the start of the washout period was also measured. This approach enabled us to evaluate the dynamics of these parameters throughout the washout period, determining whether they undergo changes or remain stable. Iron dextran successfully elevated both total cardiac iron and mitochondrial iron levels (2.9-fold and 3.5-fold increase, respectively), which was

sustained throughout the washout period. Cardiac function and metabolism were mildly perturbed at the end of iron dextran treatment but returned to control levels at the end of the 4-week washout period. We suggest that this model represents the population of cancer patients with subclinical iron overload who may be more susceptible to the cardiotoxic effects of DOX treatment.

8.1.3 Developing and Validating an *In Vivo* Model of Chronic Doxorubicin-Induced Cardiotoxicity

Chapter 5 developed and characterised a clinically relevant model of chronic DIC. The study designed to closely mimic DOX treatment regimens for patients undergoing DOX chemotherapy. The study incorporated clinically relevant cumulative dose groups (2mg/kg/wk group, totalling 8 mg/kg, and a 3mg/kg/wk group, totalling 12 mg/kg) and one high dose group (4mg/kg/wk group, totalling 16 mg/kg) and included a latency period to assess the chronic effects of DOX. As far as we are aware, this is the first study to measure both total cellular and mitochondrial cardiac iron in an *in vivo* model of chronic DIC using clinically relevant anthracycline doses.

DOX induced progressive reduction in left ventricular function in a dose-dependent manner. Cardiac iron levels and the metabolic profiles of both cardiac tissue and serum were also altered dose-dependently.

The 4mg/kg DOX dose group showed signs of heart failure, marked by a substantial decline in LVEF, evidence of cardiac hypertrophy, and a shift towards glycolytic metabolism. In literature, total cellular and total mitochondrial cardiac iron levels have only been shown to be elevated when clinically irrelevant DOX doses have been used *in vivo* or in patients with DOX-induced heart failure[205][252]. This may explain why the 4mg/kg DOX dose was the only dose to invoke a significant elevation in total cellular and total mitochondrial cardiac iron levels 6 weeks after the end of treatment.

We did not see significant cardiac iron elevation after treatment with 2 mg/kg and 3 mg/kg DOX doses. This could suggest that the DOX-induced elevation in total cardiac iron may only be limited to the DOX treatment period or that total iron is not as important in the development of DIC as hypothesised (and as indicated by proof-of-concept studies[205][252]). We intend to investigate this further by measuring how cardiac iron levels change in the post-DOX

treatment period; this involved sacrificing a cohort at the conclusion of DOX treatment as well as after the 6-week latency period.

Crucially, the proportion of labile to bound iron may differ despite unchanged total cardiac iron levels, which we are unable to measure using our ICP-MS based technique. The labile iron pool, along with various iron species within it, might undergo fluctuations and play a crucial role in the development of DIC. We intend to investigate this further as outlined in 8.2 Future Work.

A significant incidental finding in the metabolic profiling of serum was the notable increase in fatty acids in all groups, suggesting that DOX has a profound impact on systemic lipid metabolism. This correlation between serum dyslipidaemia and heart lipotoxicity during DOX treatment was explored in Chapter 6. The 2mg/kg group was selected for the coadministration study as it exhibited milder cardiac dysfunction, with the intent of mitigating mortality risk in iron-loaded animals.

In summary, this work has successfully established a chronic DIC model through clinically relevant cumulative DOX doses, demonstrating dose-dependent cardiotoxicity development. This developed model serves as a clinically relevant platform to facilitate the future development of therapies for DOX-cardiotoxicity and mechanistic investigations.

8.1.4 Coadministration Study: Exploring the Impact of Pre-Existing Iron Overload on DOX-Induced Cardiotoxicity and the Potential Ameliorative Role of Iron Chelation Therapy

Chapter 6 investigated the impact of pre-existing iron overload on the development of chronic DIC. All DOX treated groups exhibited a reduction in LVEF, however, iron loading was not found to significantly exacerbate cardiac dysfunction or alter cardiac metabolism following the 6-week latency period. Therefore, it could not be concluded that iron exacerbates chronic DIC within the timeframe of the study.

The cardioprotective potential of using iron chelation therapy prior to DOX treatment in iron loaded animals was investigated. Deferiprone pre-treatment was found to have no effect on cardiac metabolism but did mitigate the decline in LVEF by normalizing it to levels observed in animals treated with DOX alone. However, it’s clinical utility is limited as LVEF remained significantly reduced compared to the control and baseline levels.

Considering the progressive nature of DIC characterized by a continual decline in LVEF, the subtle cardiac function changes suggest that pre-existing iron overload could potentially have an adverse effect on survival. Iron chelation may be clinically useful in the long-term. Further investigation is warranted to assess the impact of these interventions on mortality.

Preliminary investigations were conducted into the effects of DOX on liver metabolism, hypothesizing that the lipemic serum observed in the Chapter 5 DOX study could be linked to altered liver metabolism, and potentially correlate with lipotoxicity in the heart. Liver metabolism was found to be altered in all groups, suggesting that liver damage incurred during DOX treatment has long lasting effects, potentially contributing to the elevated levels of fatty acids found in the serum. Further investigation into liver function during and after DOX treatment is required to substantiate this hypothesis. The cardiac lipid profile was unaltered after the 6-week latency period, suggesting that a dysregulation of cardiac lipids may be transient and possibly confined to the DOX treatment period.

8.2 Future Work

This work represents initial investigations into the cardiotoxic effects of DOX in clinically relevant models, progressing the wide range of proof-of-concept studies that exist in literature. This initial work suggests additional experimental avenues to enhance our understanding of the development of chronic DIC involving the role of iron, as well as other factors such as lipotoxicity and liver injury.

8.2.1 Exploring the Impact of Iron Loading and Deferiprone Treatment on the Progression of Doxorubicin-Induced Cardiotoxicity Beyond Six Weeks

8.2.1.1 Extended Latency Period

In Chapter 6, the effects of cardiac iron overload or deferiprone pre-treatment on cardiac function were not found to be significant. It is evident that the interventions did not enhance nor prevent the development of DIC. Although not found to be significant within the study constraints, trends suggest that elevated iron levels might have a detrimental impact on the survival timelines of DOX-treated animals. Much of the data in the literature to date has been derived from acute models with supraphysiological doses of anthracyclines. The changes that have been reported are more robust than seen in our milder and arguably more clinically

relevant treatment protocols, but more work is required to better understand whether the mechanisms reported in these extreme models are relevant to the clinical situation. To explore these trends further, an extended latency period study would be valuable to definitively assess the effects of our interventions. This would establish whether the intervention groups exhibit significant differences in cardiac function past 6-weeks and whether such differences impact upon mortality timelines. A decrease in overall survival after DOX treatment associated with subclinical cardiac iron overload, representative of many patients undergoing cancer treatment, would be clinically significant. This finding justifies further investigations into screening for elevated cardiac iron levels. Similarly, if iron chelation by deferiprone were found to extend survival, it could be considered as a relatively simple addition to the DOX treatment regimen, or in combination with Dexrazoxane.

8.2.1.2 Characterize Total and Labile Cardiac Iron During Doxorubicin Treatment, As Well As After

In our experimental models, total cardiac iron levels were only observed to significantly change in higher dose DOX regimes, despite there being evidence of contractile dysfunction at lower doses. Either total cardiac iron levels do not change as significantly as others have suggested with more extreme models, or cardiac iron levels are elevated in acute cardiotoxicity but normalize during the latency period, or that total cardiac iron levels do not change significantly, but cardiac iron repartitions to the labile iron pool do exacerbate injury.

A simple experiment could be designed to investigate longitudinal changes in cardiac iron during and after anthracycline treatment, but they were too time consuming and expensive to investigate in this project. Labile iron levels are hypothesized to change because of DOX treatment, however under normal conditions it represents only 5% of total cell iron, equivalent to ~50–100 μM[44]. Changes in the labile iron pool may not be detected through our total cardiac iron measurements, but there is ongoing development in turn-on fluorescent probes with high selectivity for labile Fe^{2+} [44]. Initial experiments involving the use of green fluorescent protein (GFP) in isolated neonatal rat cardiomyocytes have been conducted to detect free mitochondrial iron through quantitative laser scanning microscopy in the context of DOX[205]. Characterizing labile iron in this manner could be used to investigate whether acute changes occur during DOX treatment and whether such alterations persist after the end of DOX treatment. Understanding how the levels and proportions of different iron species within the labile iron pool change would provide greater insight into the dynamics of iron metabolism

during DOX treatment, and its potential role in the development of DOX-induced cardiotoxicity. A radiolabeled 11C deferiprone PET probe has recently been developed which provides the possibility of non-invasively imaging the labile iron pool [542], and we are developing a similar approach in our department to investigate this possibility

8.2.1.3 Investigating the Impact of Deferiprone During Doxorubicin Treatment and its Utility in Examining Iron Speciation in The Labile Iron Pool

I provide evidence suggesting the potential cardioprotective effects of deferiprone in iron-loaded animals. The next step would be to explore whether iron chelation during DOX treatment provides cardioprotective benefits using our models. Implementing deferiprone chelation therapy during DOX treatment could offer mechanistic insights into the significance of different iron species within the labile iron pool in relation to the development of chronic DIC. Deferiprone forms complexes with Fe^{3+} and thus the removal of labile Fe^{3+} is likely to be cardioprotective by preventing the formation of DOX-Fe^{3+} complexes[264][278]. Deferiprone exclusively interacts with the Fe^{3+} component of the labile iron pool and does not interact with labile Fe^{2+}. However, the Fe^{2+} portion of the labile iron pool is arguably more cardiotoxic, inherently more reactive and constitutes the majority of the labile iron pool [543]. In the context of our work thus far, the observed mild cardioprotective effect of deferiprone as a pre-treatment in iron loaded animals suggests that chelating Fe^{3+} might offer some degree of cardio protection in iron-loaded animals, but in this study we did not address the potential of deferiprone cardioprotection during the index DOX injury itself. Funding is currently being sought to pursue this approach.

8.2.1.4 Investigate How Cardiac Lipid Metabolism is Perturbed during Doxorubicin Treatment and Correlate this to Long Term Metabolic Profiles

In our studies, cardiac lipid profiles were unchanged as a result of DOX treatment, despite altered liver metabolism and lipemic serum being evident. The role of lipotoxicity in the pathology of DOX cardiotoxicity is currently unknown, however some studies suggest that DOX influences the expression of genes associated with lipid metabolism in the heart[530][529][531]. This suggests that the impact of DOX on cardiac lipotoxicity could happen during the DOX treatment phase, when DOX is present to influence the expression of such genes. To investigate this further, and to supplement the longitudinal characterisation of

cardiac lipid metabolism, the *in vivo* models could be utilized to characterize the cardiac lipid profile during DOX treatment too.

8.2.1.5 Further Investigations into the Role of the Liver and Lipotoxicity in the Development of Doxorubicin-Induced Cardiotoxicity

A further important line of enquiry is the assessment of whether liver function correlates with the perturbed liver metabolism observed as a result of DOX treatment in our study. Examining the liver's metabolic profile during DOX treatment and post-treatment could offer insights into whether the metabolic changes observed six weeks after DOX treatment in our study were present during the treatment phase and persisted or progressively evolved after the initial insult. Understanding the temporal dynamics of metabolic alterations in the liver could offer understanding into critical periods of impact during DOX treatment and the duration of metabolic disturbances, potentially defining specific stages that could serve as therapeutic windows for targeted interventions.

In relation to this and the lipemic serum observed, we aim to investigate the cardioprotective effects of statins on the development of DIC using our *in vivo* models, building upon previous work in the field [511][512]. We plan to incorporate statin use alongside the DOX treatment period, and possibly explore a combination therapy with deferiprone. The relationship between cardiac steatosis, iron overload and anthracycline redox cycling is an interesting future opportunity for research in the context of statin therapy.

8.2.2 Further Mitochondrial Iron Measurement Validation

The ICPMS-based method for measuring mitochondrial iron was less sensitive and resulted in larger variation in measurements than the total cardiac iron measurements. As this method was developed in-house, we do not have literature benchmarks for comparison, and we cannot definitively determine potential outliers. Increasing the number of biological repeats would enhance understanding of normal ranges, enabling improved differentiation of outliers. Contamination is a major concern with ICPMS measurements and could be a factor influencing the variation. Our procedural and non-procedural samples give an indication of overall contamination rather than within individual samples. Conducting a mass balance experiment would provide a more accurate assessment of contamination levels and identify the specific step in the sample preparation process where contamination may occur.

8.2.3 Investigations into Liposomal DOX Formulations and Chronic DOX-Induced Cardiotoxicity

Liposomal DOX, also referred to as Doxil or Caelyx, was the first FDA-approved nanoparticle-based antitumor drug [544], and has been used in treating various tumors, offering several key benefits, including to significantly reduce the risk of cardiotoxicity compared to conventional DOX formulations [544]. Liposomal DOX has been shown to reduce the risk of cardiotoxicity by altering tissue distribution and slowing drug release, whereby the liposomes are designed to minimize direct contact of DOX with vasculature, which is hypothesized to lower myocardial drug concentrations[545] [546]. Liposomes also serve to modify the pharmacological and pharmacokinetic properties of conventional DOX, enhancing drug delivery to tumors while reducing toxicity [547]. This has been supported by several clinical trials, and notably demonstrated via a systematic review and meta-analysis of 55 randomized controlled trials by Smith *et al*, which showed that liposomal formulations of DOX resulted in a 22% lower risk of clinical cardiotoxicity compared to conventional DOX formulations [547] . However, we opted to use conventional DOX in our studies as the clinical application of liposomal DOX can be limited by issues such as short storage life, poor structural stability, drug leakage, and rapid clearance from the body [548] .

Despite this, recent developments have introduced PEGylated liposomal DOX (PLD), a formulation that enhances the stability and effectiveness of Doxil/Caelyx. PLD features polyethylene glycol (PEG) molecules attached to the surface of the liposomes, which significantly increases the structural stability of liposomal DOX, allowing for better control over drug release and distribution [549]. Studies have shown that PLD accumulates primarily in the liver, spleen, and tumor tissues, with a lower concentration in the heart [548] . While PLD has demonstrated reduced cardiotoxicity, the full extent of its impact on the heart remains an area of investigation, with one proposed mechanism being that the larger size of PLD liposomes prevents them from penetrating tight capillary junctions found in the heart and GI tract, thus limiting DOX distribution to the myocardium [550] [551] [552] . However, there is notable interindividual variability in response to PLD based on factors such as age and sex.

Given the benefits of liposomal DOX, further research is needed to fully understand how these formulations impact the heart and chronic DOX-induced cardiotoxicity. Although liposomal DOX shows benefits in reducing cardiotoxicity compared to conventional DOX formulations, current clinical trials and meta-analyses often lack detailed analysis of the impact of liposomal

DOX on the development chronic cardiotoxicity specifically, underscoring the need for targeted studies to explore its benefits in preventing long-term DOX-induced cardiac damage. Our models could provide valuable insights into how existing liposomal DOX formulations perform in minimizing cardiac damage associated with chronic DOX-induced cardiotoxicity

APPENDIX

9.1 Appendix: Chapter 4

9.1.1 Mean Metabolite Concentrations.

Table 15: Aqueous metabolite profile of cardiac tissue in Ferrocene study. Metabolite concentration presented as mean metabolite concentration/g of tissue ± SEM.

Metabolic process	Metabolite	Control group (conc./g tissue + SEM)	Ferrocene Cohort 5 (conc./g tissue + SEM)
Fatty acid oxidation	Acetyl carnitine	2.2E-04±1.1E-04	1.6E-04 ± 4.6E-05
Glycolysis	a-glucose	2.2E-04±1.7E-05	2.00E-04±4.20E-05
	Lactate	6.3E-04±5.7E-05	8.3E-04 ± 1.4E-04
TCA cycle	Succinate	1.8E-04±1.7E-05	1.3E-04 ± 9.8E-06
	Fumarate	1.9E-05±3.8E-06	1.5E-05 ± 2.8E-06
	Isoleucine	4.2E-05±3.0E-06	4.0E-05 ± 1.7E-06
	Leucine	7.3E-05±6.9E-06	6.9E-05 ± 3.7E-06
	Glycine	2.1E-04±2.6E-05	2.6E-04 ± 3.9E-05
	Taurine	1.1E-02±6.0E-04	8.9E-03 ± 1.0E-03
	Glutamine	3.2E-03±2.7E-04	2.7E-03 ± 1.3E-04
	Glutamate	2.5E-03±2.0E-04	2.4E-03 ± 1.7E-04
	Alanine	4.2E-04±3.2E-05	4.4E-04 ± 3.7E-05
	Valine	3.2E-05±2.3E-06	3.1E-05 ± 1.4E-06
	Phenylalanine	3.8E-05±2.9E-06	3.4E-05 ± 1.3E-06
	Aspartate	1.0E-03±8.2E-05	8.2E-04 ± 5.7E-05
Energetics (transfer and utilization)	ATP	1.6E-03±1.7E-04	1.4E-03 ± 1.9E-04
	AMP	4.6E-04±1.3E-04	4.8E-04 ± 1.4E-04
	NAD	3.2E-04±2.5E-05	2.6E-04 ± 1.6E-05
	NADP	2.1E-05±2.9E-06	2.3E-05 ± 2.6E-06
	Creatine	5.8E-03±2.8E-04	4.9E-03 ± 2.0E-04
	Phosphocreatine	1.3E-03±3.0E-04	8.3E-04 ± 2.0E-04
	Niacinamide	2.4E-05±7.0E-06	3.2E-05 ± 6.9E-06
	Tyrosine	4.4E-05±3.2E-06	3.5E-05 ± 3.5E-06
	Acetate	1.9E-04±1.6E-05	1.6E-04 ± 1.2E-05
Other	Histidine	5.8E-05±7.6E-06	5.8E-05 ± 4.3E-06
	Formate	1.0E-04±1.1E-05	9.3E-05 ± 9.7E-06
	Myo inositol	3.5E-04±2.8E-05	3.3E-04 ± 2.7E-05

Table 16: Aqueous metabolite profile of cardiac tissue in the iron dextran study. Metabolite concentration presented as mean metabolite concentration/g of tissue ± SEM.

Metabolic process	Metabolite	Control group (conc./g tissue + SEM)	Iron dextran groups (conc./g tissue + SEM)		
			0 week washout	2 week washout	4 week washout
Fatty acid oxidation	Acetyl carnitine	6.97E-05±8.68E-06	5.06E-05 ± 3.66E-06	6.29E-05 ± 4.14E-06	7.96E-05 ± 1.01E-05
	Carnitine	3.83E-04±9.66-06	5.47E-04 ± 4.34E-05	5.08E-04 ± 4.55E-05	6.15E-04 ± 8.34E-05
Glycolysis	a-glucose	1.38E-04±1.56E-05	9.84E-05 ± 2.84E-06	1.11E-04 ± 7.51E-06	1.10E-04 ± 5.66E-06
	Lactate	4.37E-04±1.59E-05	2.88E-04 ± 8.28E-06	4.50E-04 ± 3.26E-05	4.45E-04 ± 2.49E-05
TCA cycle	Succinate	6.05E-05±3.96E-06	4.57E-05 ± 2.38E-06	6.73E-05 ± 4.24E-06	7.13E-05 ± 4.23E-06
	Fumarate	1.73E-05±1.79E-06	1.24E-05 ± 6.05E-07	1.49E-05 ± 6.84E-07	1.54E-05 ± 1.07E-06
	Isoleucine	2.23E-05±9.77E-07	1.99E-05 ± 1.08E-06	2.03E-05 ± 1.12E-06	2.25E-05 ± 7.36E-07
	Leucine	3.64E-05±1.64E-06	2.74E-05 ± 8.71E-07	3.08E-05 ± 1.06E-06	3.48E-05 ± 1.72E-06
	Glycine	8.47E-05±7.64E-06	6.42E-05 ± 1.50E-05	9.42E-05 ± 8.83E-06	8.953E-04 ± 1.09E-05
	Taurine	3.77E-03±5.95E-04	4.43E-03 ± 9.43E-04	1.23E-03 ± 6.84E-04	1.16E-03 ± 6.26E-04
	Glutamine	1.28E-03±4.56E-05	1.39E-03 ± 6.22E-05	1.28E-03 ± 8.21E-05	1.46E-03 ± 6.60E-05
	Glutamate	8.56E-04±4.36E-05	8.97E-04 ± 2.82E-05	9.44E-04 ± 7.83E-05	9.37E-04 ± 2.79E-05
	Alanine	2.25E-04±2.42E-05	1.83E-04 ± 6.51E-06	2.28E-04 ± 1.04E-05	2.82E-04 ± 2.58E-05
	Valine	1.37E-05±4.85E-07	1.03E-05 ± 3.21E-07	1.16E-05 ± 4.36E-07	1.40E-05 ± 4.83E-07
	Phenylalanine	1.46E-05±7.09E-07	1.16E-05 ± 2.93E-07	1.30E-05 ± 7.29E-07	1.46E-05 ± 3.99E-07
	Aspartate	4.26E-04±2.61E-05	2.42E-04 ± 2.35E-05	2.36E-04 ± 1.52E-05	3.92E-04 ± 2.77E-05
Energetics (transfer and utilization)	ATP	7.10E-04±3.62E-05	6.73E-04 ± 3.03E-05	6.56E-04 ± 4.75E-05	7.37E-04 ± 3.53E-05
	AMP	2.27E-04±1.46E-05	1.58E-04 ± 1.55E-05	1.56E-04 ± 1.76E-05	1.93E-04 ± 9.53E-06
	NAD	1.16E-04±4.01E-06	1.11E-04 ± 2.12E-06	1.03E-04 ± 8.34E-06	1.18E-04 ± 5.03E-06
	NADP	1.01E-05±1.24E-06	8.56E-06 ± 7.56E-07	9.95E-06 ± 9.53E-07	1.09E-05 ± 5.01E-07
	Creatine	2.40E-03±1.11E-04	2.23E-03 ± 5.82E-05	2.19E-03 ± 1.25E-04	2.45E-03 ± 7.97E-05
	Niacinamide	1.44E-05±1.09E-06	1.51E-05 ± 1.46E-06	1.59E-05 ± 1.98E-06	1.42E-05 ± 8.68E-07
	Tyrosine	1.72E-05±5.96E-07	1.50E-05 ± 7.09E-07	1.55E-05 ± 1.54E-06	1.92E-05 ± 8.11E-07
	Acetate	4.02E-05±3.34E-06	3.93E-05 ± 1.76E-06	3.95E-05 ± 5.01E-06	3.81E-05 ± 2.69E-06
Lipid metabolism	Choline	1.64E-05±1.45E+04	1.72E-05 ± 1.33E-08	1.76E-05 ± 2.76E-05	1.76E-05 ± 3.06E-06
	Phosphocholine	7.14E-05±2.15E-06	7.59E-05 ± 9.61E-06	8.44E-05 ± 7.29E-05	7.04E-05 ± 6.20E-05
Other	Histidine	2.82E-05±1.05E-06	2.39E-05 ± 1.81E-06	2.34E-05 ± 1.56E-06	2.58E-05 ± 1.30E-06
	Formate	2.58E-05±1.36E-06	2.28E-05 ± 1.78E-06	2.85E-05 ± 4.26E-06	2.21E-05 ± 1.35E-06
	Myo inositol	1.76E-04±9.40E-06	1.66E-04 ± 3.41E-06	1.67E-04 ± 1.05E-05	1.91E-04 ± 7.95E-06

9.2 Appendix: Chapter 5

9.2.1 Heart Rate

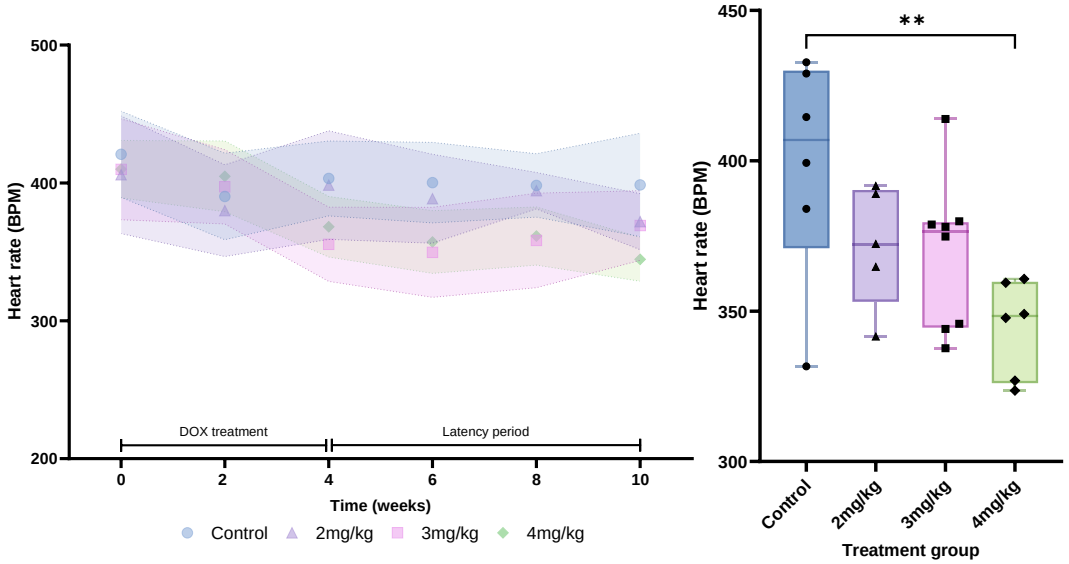

Figure 89: Heart rate parameters obtained by echocardiography. Statistical comparison by one-way ANOVA with Tukey's HSD correction method for multiple comparisons. The longitudinal data is presented as mean ± SD in the graphs (left), while the endpoint data is shown using a box plot (right).

9.2.2 Mean Metabolite Concentrations.

Table 17: Aqueous metabolite profile of cardiac tissue. Metabolite concentration presented as mean metabolite concentration/g of tissue ± SEM.

Metabolic process	Metabolite	Control group (conc./g tissue + SEM)	DOX 2mg/kg (conc./g tissue + SEM)	DOX 3mg/kg (conc./g tissue + SEM)	DOX 4mg/kg (conc./g tissue + SEM)
Fatty acid oxidation	Acetyl carnitine	1.7E-07 ± 2.5E-08	1.5E-07 ± 7.1E-08	1.4E-07 ± 1.9E-08	1.8E-07 ± 3.0E-08
	Carnitine	1.3E-06 ± 6.3E-08	1.2E-06 ± 4.1E-08	1.2E-06 ± 5.7E-08	8.9E-07 ± 6.7E-08
Glycolysis	a-glucose	5.9E-07 ± 7.5E-08	6.6E-07 ± 7.1E-08	6.4E-07 ± 5.5E-08	5.7E-07 ± 6.2E-08
	Lactate	1.5E-06 ± 2.2E-07	9.8E-07 ± 3.9E-08	1.3E-06 ± 8.9E-08	1.9E-06 ± 2.0E-07
TCA cycle	Succinate	2.7E-07 ± 1.9E-08	2.0E-07 ± 6.9E-09	2.5E-07 ± 1.0E-08	2.7E-07 ± 1.7E-08
	Fumarate	5.8E-08 ± 5.5E-09	4.9E-08 ± 3.4E-09	5.7E-08 ± 4.5E-09	5.0E-08 ± 2.9E-09
	Isoleucine	1.0E-07 ± 6.4E-09	1.2E-07 ± 5.2E-09	1.3E-07 ± 7.1E-09	1.3E-07 ± 5.8E-09
	Leucine	1.5E-07 ± 1.0E-08	1.7E-07 ± 9.4E-09	1.7E-07 ± 1.1E-08	1.7E-07 ± 7.5E-09
	Glycine	3.9E-07 ± 2.1E-08	3.9E-07 ± 1.6E-08	4.5E-07 ± 1.4E-08	4.3E-07 ± 2.4E-08
	Taurine	2.7E-05 ± 1.0E-06	2.7E-05 ± 1.0E-06	3.2E-05 ± 7.6E-07	3.0E-05 ± 1.8E-06
	Glutamine	8.5E-06 ± 4.4E-07	8.2E-06 ± 2.9E-07	8.5E-06 ± 3.1E-07	7.5E-06 ± 4.0E-07
	Glutamate	5.0E-06 ± 1.8E-07	5.5E-06 ± 2.5E-07	6.3E-06 ± 1.8E-07	5.9E-06 ± 3.9E-07
	Alanine	9.3E-07 ± 7.4E-08	1.0E-06 ± 5.0E-08	1.3E-06 ± 5.5E-08	1.4E-06 ± 8.4E-08
	Valine	6.1E-08 ± 4.3E-09	6.7E-08 ± 3.7E-09	7.1E-08 ± 4.8E-09	6.9E-08 ± 3.5E-09
	Phenylalanine	6.4E-08 ± 3.7E-09	7.1E-08 ± 4.3E-09	7.8E-08 ± 4.7E-09	8.1E-08 ± 2.9E-09
	Aspartate	2.2E-06 ± 2.0E-07	2.4E-06 ± 1.9E-07	2.3E-06 ± 2.2E-07	1.8E-06 ± 2.7E-07
Energetics (transfer and utilization)	ATP	4.1E-06 ± 2.2E-07	3.8E-06 ± 2.7E-07	4.1E-06 ± 1.6E-07	3.5E-06 ± 2.1E-07
	AMP	1.1E-06 ± 1.3E-07	9.7E-07 ± 1.4E-07	9.0E-07 ± 8.6E-08	1.1E-06 ± 1.2E-07
	NAD	7.8E-07 ± 3.3E-08	7.2E-07 ± 3.0E-08	7.7E-07 ± 3.3E-08	7.0E-07 ± 3.4E-08
	NADP	5.1E-08 ± 5.4E-09	4.4E-08 ± 1.2E-08	4.6E-08 ± 6.2E-09	4.2E-08 ± 5.2E-09
	Creatine	1.3E-05 ± 5.5E-07	1.2E-05 ± 4.2E-07	1.3E-05 ± 3.4E-07	1.2E-05 ± 5.6E-07
	Phosphocreatine	1.5E-06 ± 1.5E-07	1.6E-06 ± 2.2E-07	1.4E-06 ± 1.0E-07	1.2E-06 ± 1.8E-07
	Niacinamide	3.2E-08 ± 3.4E-09	2.9E-08 ± 3.7E-09	2.9E-08 ± 1.8E-09	3.5E-08 ± 4.0E-09
	Tyrosine	1.7E-07 ± 1.1E-08	1.8E-07 ± 1.5E-08	1.9E-07 ± 1.2E-08	2.1E-07 ± 1.2E-08
	Acetate	1.9E-07 ± 1.3E-08	1.7E-07 ± 2.1E-08	3.1E-07 ± 1.5E-08	2.2E-07 ± 2.3E-08
Lipid metabolism	Choline	3.8E-08 ± 5.6E-09	4.3E-08 ± 5.4E-09	4.4E-08 ± 1.2E-09	4.2E-08 ± 3.9E-09
	Phosphocholine	3.5E-07 ± 1.5E-08	3.3E-07 ± 7.8E-09	4.0E-07 ± 1.3E-08	3.4E-07 ± 2.1E-08
Other	Histidine	1.2E-07 ± 9.3E-09	1.1E-07 ± 8.4E-09	1.1E-08 ± 7.6E-09	8.4E-08 ± 7.0E-09
	Formate	2.2E-07 ± 2.9E-08	1.8E-07 ± 7.4E-09	1.4E-07 ± 9.8E-09	1.3E-07 ± 8.3E-09
	Myo inositol	9.5E-07 ± 4.3E-08	9.5E-07 ± 4.3E-08	1.0E-06 ± 3.2E-08	1.0E-06 ± 4.8E-08

Table 18: Metabolite profile of Serum. Metabolite concentration presented as mean metabolite concentration (M) ± SEM.

Metabolic process	Metabolite	Control group (conc. (M) + SEM)	DOX 2mg/kg (conc. (M) + SEM)	DOX 3mg/kg (conc. (M) + SEM)	DOX 4mg/kg (conc. (M) + SEM)
Glycolysis	a-glucose	4.5E-05± 1.2E-05	2.2E-05±3.3E-06	4.2E-05±8.3E-06	3.1E-05±3.5E-06
	Lactate	5.6E-05± 3.0E-06	4.9E-05±3.1E-06	1.9E-05±2.1E-06	1.6E-05±2.6E-06
	Pyruvate	1.8E-04±6.2E-06	1.7E-04±6.7E-06	1.4E-04±5.2E-06	1.2E-04±4.7E-06
TCA cycle	Citrate	1.3E-04±8.2E-06	9.8E-05±6.3E-06	6.6E-05±5.2E-06	7.3E-05±5.0E-06
	Isoleucine	1.6E-04±7.4E-06	1.5E-04±1.0E-05	1.2E-04±5.6E-06	1.1E-04±6.3E-06
	Leucine	1.1E-02±6.4E-04	2.0E-02±4.4E-03	5.8E-02±1.2E-02	6.6E-02±8.4E-03
	Glycine	8.8E-03±3.4E-04	9.1E-03±4.3E-04	6.4E-03±2.8E-04	5.8E-03±2.4E-04
	Glutamine	7.1E-04±2.0E-05	6.9E-04±3.1E-05	4.8E-04±1.9E-05	4.4E-04±1.7E-05
	Glutamate	4.3E-04±2.6E-05	3.8E-04±1.8E-05	3.6E-04±1.6E-05	4.5E-04±2.0E-05
	Alanine	8.7E-04±3.2E-05	7.6E-04±3.0E-05	7.9E-04±5.0E-05	1.1E-03±2.8E-04
	Valine	1.4E-03±3.9E-05	1.4E-03±5.1E-05	1.1E-03±3.2E-05	9.9E-04±2.9E-05
	Phenylalanine	1.3E-04±9.7E-06	9.2E-05±1.1E-05	8.2E-05±1.3E-05	1.3E-04±1.1E-05
Energetics (transfer and utilization)	Creatine	9.3E-04±3.7E-05	9.9E-04±8.2E-05	1.5E-03±2.1E-04	1.8E-03±2.1E-04
	Tyrosine	4.4E-04±1.8E-05	4.6E-04±1.8E-05	4.5E-04±3.8E-05	5.6E-04±3.5E-05
	Acetate	3.7E-03±2.1E-04	6.9E-03±1.5E-03	2.2E-02±5.4E-03	2.4E-02±3.7E-03
Lipid metabolism	Fatty acid residues (−CH = CH-)	9.7E-04±7.0E-05	1.1E-03±4.2E-05	9.6E-04±3.8E-05	1.1E-03±3.7E-05
	Fatty acid residues (COCH2-CH2)	7.5E-03±8.0E-04	5.8E-03±3.7E-04	5.5E-03±3.3E-04	6.9E-03±3.7E-04
	Fatty acid residues (ω-CH3)	4.7E-04±3.5E-05	4.2E-04±3.0E-05	2.8E-04±2.6E-05	4.1E-04±5.0E-05
Ketogenesis	3-hydroxybutyrate	2.3E-04±7.5E-06	2.2E-04±1.0E-05	1.7E-04±9.9E-06	2.0E-04±1.3E-05
Other	Histidine	2.9E-04±7.8E-06	3.1E-04±2.0E-05	3.9E-04±4.1E-05	4.5E-04±4.5E-05
	Tryptophan	9.9E-04±2.8E-05	1.2E-03±1.4E-04	2.3E-03±4.4E-04	2.8E-03±3.3E-04

9.3 Appendix: Chapter 6

9.3.1 Heart Rate

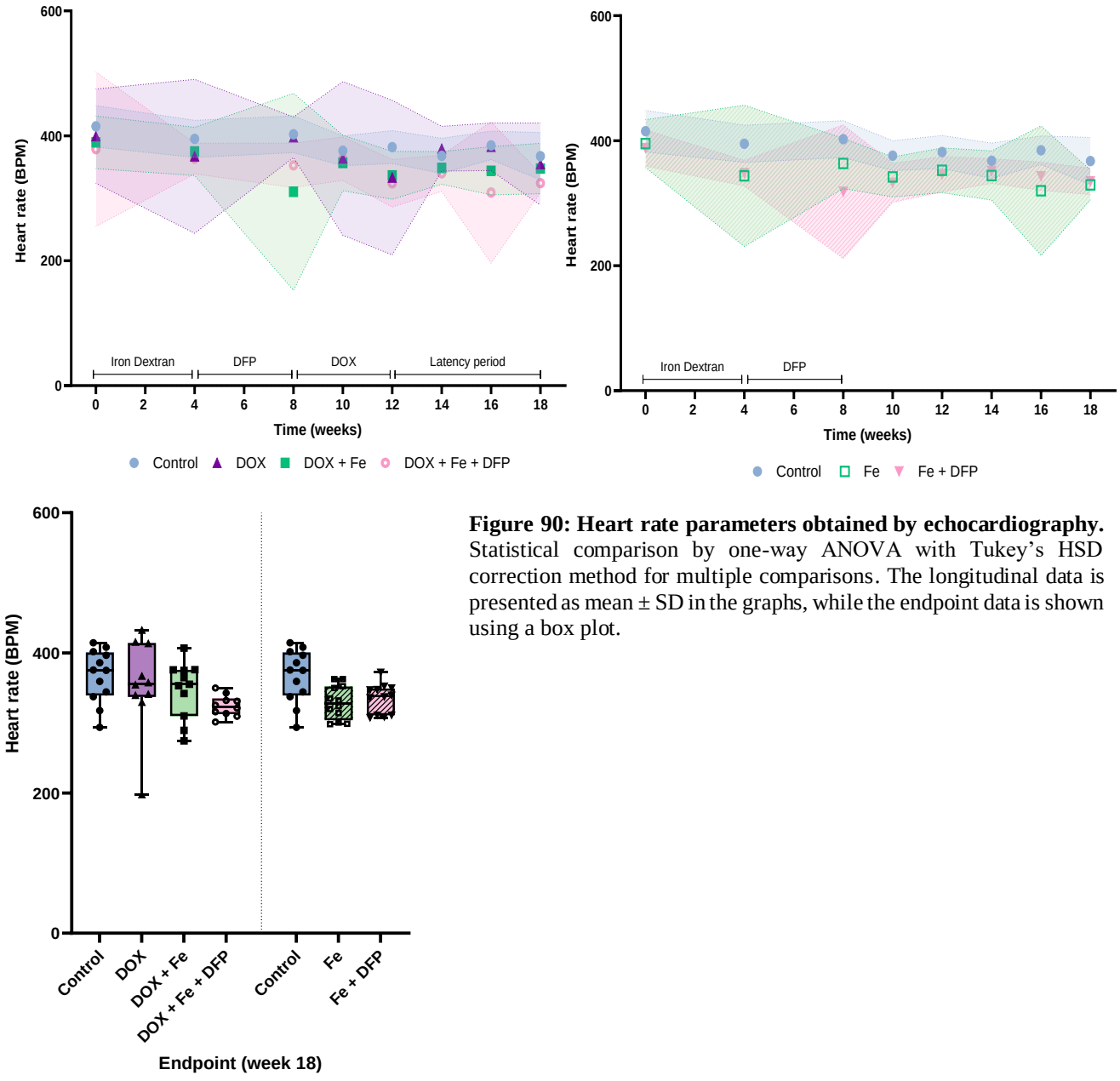

Figure 90: Heart rate parameters obtained by echocardiography. Statistical comparison by one-way ANOVA with Tukey's HSD correction method for multiple comparisons. The longitudinal data is presented as mean ± SD in the graphs, while the endpoint data is shown using a box plot.

9.3.2 Mean Metabolite Concentrations.

Table 19: Aqueous metabolite profile of cardiac tissue. Metabolite concentration presented as mean metabolite concentration/g of tissue ± SEM.

Metabolic process	Metabolite	Control (conc./g tissue + SEM)	DOX (conc./g tissue + SEM)	DOX + FE (conc./g tissue + SEM)	DOX + FE+ DFP (conc./g tissue + SEM)	FE (conc./g tissue + SEM)	FE + DFP (conc./g tissue + SEM)
Fatty acid oxidation	Acetyl carnitine	1.8E-07±2.1E-08	1.0E-07 ± 1.3E-08	1.7E-07 ± 2.5E-08	2.4E-07 ± 3.1E-08	1.9E-07 ± 2.5E-08	1.5E-07 ± 2.4E-08
	Carnitine	9.1E-07±6.7E-08	7.6E-07 ± 5.7E-08	7.5E-07 ± 4.1E-08	7.2E-07 ± 5.0E-08	9.1E-07 ± 7.5E-08	9.2E-07 ± 6.8E-08
Glycolysis	a-glucose	5.4E-07±4.3E-08	4.3E-07 ± 2.6E-08	5.1E-07 ± 5.0E-08	5.5E-07 ± 7.3E-08	4.9E-07 ± 6.1E-08	4.9E-07 ± 4.1E-08
	Lactate	2.3E-06±2.0E-07	1.9E-06 ± 2.1E-07	2.6E-06 ± 3.9E-07	2.3E-06 ± 2.7E-07	1.5E-06 ± 1.8E-07	1.8E-06 ± 2.9E-07
TCA cycle	Succinate	2.5E-07±2.0E-08	1.9E-07 ± 1.6E-08	2.2E-07 ± 2.4E-08	2.1E-07 ± 1.7E-08	2.0E-07 ± 1.5E-08	2.0E-07 ± 1.5E-08
	Fumarate	6.2E-08±6.5E-09	6.6E-08 ± 5.6E-09	7.1E-08 ± 4.5E-09	7.8E-08 ± 7.4E-09	5.2E-08 ± 5.4E-09	6.5E-08 ± 6.7E-09
	Isoleucine	1.2E-07±1.3E-08	1.2E-07 ± 1.0E-08	1.3E-07 ± 6.0E-09	1.3E-07 ± 8.6E-09	1.1E-07 ± 1.3E-08	1.2E-07 ± 8.4E-09
	Leucine	1.5E-07±1.5E-08	1.3E-07 ± 9.0E-09	1.4E-07 ± 4.5E-09	1.3E-07 ± 9.6E-09	1.4E-07 ± 1.5E-08	5E-07± 1.1E-08
	Glycine	3.6E-07±1.7E-08	3.9E-07 ± 1.6E-08	4.3E-07 ± 1.4E-08	3.9E-07 ± 2.0E-08	3.7E-07 ± 2.5E-08	4.1E-07 ± 2.5E-08
	Taurine	2.4E-05±1.3E-06	2.3E-05 ± 1.3E-06	2.6E-05 ± 7.4E-07	2.5E-05 ± 1.3E-06	2.3E-05 ± 1.3E-06	2.5E-05 ± 1.3E-06
	Glutamine	6.8E-06±3.4E-07	5.9E-06 ± 3.9E-07	6.0E-06 ± 3.2E-07	6.1E-06 ± 4.1E-07	7.2E-06 ± 4.4E-07	7.4E-06 ± 3.5E-07
	Glutamate	4.3E-06±2.1E-07	4.7E-06 ± 2.9E-07	4.7E-06 ± 2.0E-07	4.3E-06 ± 2.4E-07	4.3E-06 ± 2.7E-07	4.2E-06 ± 2.1E-07
	Alanine	1.0E-06±8.4E-08	1.2E-06 ± 6.2E-08	1.3E-06 ± 5.1E-08	1.3E-06 ± 9.9E-08	9.1E-07 ± 5.7E-08	1.0E-06 ± 5.2E-08
	Valine	6.5E-08±6.7E-09	5.5E-08 ± 3.2E-09	5.9E-08 ± 2.1E-09	5.5E-08 ± 3.8E-09	6.0E-08 ± 6.9E-09	6.4E-08 ± 5.5E-09
	Phenylalanine	6.0E-08±4.4E-09	5.8E-08 ± 2.0E-09	6.6E-08 ± 2.7E-09	6.0E-08 ± 4.4E-09	5.5E-08 ± 4.1E-09	6.1E-08 ± 3.4E-09
	Aspartate	1.7E-06±1.8E-07	1.7E-06 ± 2.2E-07	1.7E-06 ± 1.9E-07	2.0E-06 ± 2.3E-07	1.3E-06 ± 1.2E-07	1.5E-06 ± 1.4E-07
Energetics (transfer and utilization)	ATP	3.2E-06±3.0E-07	2.7E-06 ± 2.1E-07	3.1E-06 ± 1.1E-07	3.0E-06 ± 2.3E-07	3.0E-06 ± 3.2E-07	3.4E-06 ± 2.5E-07
	AMP	4.3E-07±5.2E-08	2.8E-07 ± 2.8E-08	3.7E-07 ± 4.5E-08	3.1E-07 ± 5.4E-08	3.4E-07 ± 3.6E-08	3.2E-07 ± 4.3E-08
	NAD	5.4E-07±3.4E-08	4.5E-07 ± 3.5E-08	4.7E-07 ± 1.6E-08	4.8E-07 ± 3.3E-08	5.2E-07 ± 3.9E-08	5.6E-07 ± 2.9E-08
	NADP	5.7E-08±4.3E-09	4.4E-08 ± 4.6E-09	5.6E-08 ± 3.3E-09	5.4E-08 ± 3.6E-09	5.7E-08 ± 6.6E-09	6.2E-08 ± 4.6E-09
	Creatine	1.1E-05±5.3E-07	9.1E-06 ± 6.5E-07	9.9E-06 ± 4.6E-07	9.7E-06 ± 6.2E-07	1.1E-05 ± 6.9E-07	1.1E-05 ± 5.8E-07
	Phosphocreatine	9.0E-07±1.2E-07	1.1E-06 ± 1.2E-07	1.0E-06 ± 1.1E-07	1.0E-06 ± 7.2E-08	1.3E-06 ± 1.4E-07	1.3E-06 ± 2.5E-07
	Niacinamide	6.6E-08±7.5E-09	5.8E-08 ± 3.8E-09	7.7E-08 ± 8.1E-09	7.5E-08 ± 7.6E-09	6.5E-08 ± 7.5E-09	7.9E-08 ± 8.5E-09
	Tyrosine	1.4E-07±1.3E-08	1.3E-07 ± 7.3E-09	1.7E-07 ± 5.4E-09	1.5E-07 ± 1.2E-08	1.4E-07 ± 1.2E-08	1.6E-07 ± 9.6E-09
	Acetate	3.2E-07±1.8E-08	3.1E-07 ± 1.3E-08	3.2E-07 ± 1.1E-08	3.0E-07 ± 1.8E-08	3.2E-07 ± 1.9E-08	3.1E-07 ± 1.7E-08
Lipid metabolism	Choline	4.0E-08±2.8E-09	3.9E-08 ± 3.0E-09	5.1E-08 ± 2.2E-09	4.7E-08 ± 3.7E-09	4.4E-08 ± 2.7E-09	4.3E-08 ± 3.4E-09
	Phosphocholine	2.9E-07±1.8E-08	3.0E-07 ± 2.3E-08	3.0E-07 ± 1.3E-08	3.1E-07 ± 1.6E-08	2.8E-07 ± 1.8E-08	2.8E-07 ± 1.4E-08
Other	Histidine	1.0E-07±1.7E-08	6.6E-08 ± 1.1E-08	6.6E-08 ± 4.0E-09	7.0E-08 ± 1.2E-08	1.0E-07 ± 8.3E-09	1.3E-07 ± 1.5E-08
	Formate	9.4E-08±2.7E-09	1.0E-07 ± 3.8E-09	1.0E-07 ± 3.6E-09	1.0E-07 ± 5.2E-09	1.0E-07 ± 9.7E-09	1.0E-07 ± 5.2E-09
	Myo inositol	8.3E-07±6.1E-08	7.6E-07 ± 1.8E-08	7.6E-07 ± 1.7E-08	7.4E-07 ± 3.9E-08	6.9E-07 ± 6.1E-08	7.8E-07 ± 4.3E-08

Table 20: Lipophilic metabolite profile of cardiac tissue. Metabolite concentration presented as mean metabolite concentration/g of tissue ± SEM.

Metabolic process	Metabolite	Control (conc./g tissue + SEM)	DOX (conc./g tissue + SEM)	DOX + FE (conc./g tissue + SEM)	DOX + FE+ DFP (conc./g tissue + SEM)	FE (conc./g tissue + SEM)	FE + DFP (conc./g tissue + SEM)
Lipid metabolism	**Lipids (CH2)n** (Total lipid)	1.5E-08±1.7E-09	1.7E-06±1.2E-07	1.5E-06±1.5E-07	1.5E-06±1.6E-07	1.6E-06±1.2E-07	1.6E-06±7.4E-08
	Lipid CH=CH (Total unsaturated lipid)	2.6E-08±3.1E-09	3.8E-07±2.6E-08	3.5E-07±3.6E-08	3.3E-07±3.6E-08	3.5E-07±2.5E-08	3.8E-07±1.7E-08
	Cholesterol 18-CH3 (Total cholesterol)	2.4E-07±6.4E-09	1.9E-08±1.4E-09	1.8E-08±1.8E-09	1.7E-08±1.8E-09	1.3E-08±9.4E-10	1.4E-08±1.2E-09
	Glycerol backbone 1,3-CH2 (Triglyceride lipid)	4.7E-08±6.1E-09	2.4E-08±2.5E-09	2.0E-08±2.7E-09	1.7E-08±2.8E-09	2.2E-08±2.7E-09	2.3E-08±2.7E-09
	Phosphatidylcholine N(CH3)3 (membrane phospholipid)	2.0E-08±2.4E-09	1.7E-07±1.1E-08	1.5E-07±1.7E-08	1.5E-07±1.6E-08	1.5E-07±1.0E-08	1.6E-07±9.5E-09
	Phosphatidylethanolamine N(CH3)3 (membrane phospholipid)	2.2E-07±2.8E-08	2.3E-08±1.4E-09	1.9E-08±2.3E-09	2.0E-08±2.1E-09	2.1E-08±1.5E-09	2.1E-08±1.2E-09
	Sphingomyelin (membrane phospholipid)	3.4E-09±4.0E-10	4.5E-09±3.3E-10	4.3E-09±4.6E-10	4.1E-09±4.5E-10	3.8E-09±2.9E-10	4.3E-09±3.2E-10

Table 21: Aqueous metabolite profile of liver tissue. Metabolite concentration presented as mean metabolite concentration/g of tissue ± SEM.

Metabolic process	Metabolite	Control (conc./g tissue + SEM)	DOX (conc./g tissue + SEM)	DOX + Fe (conc./g tissue + SEM)	DOX + Fe+ DFP (conc./g tissue + SEM)	Fe (conc./g tissue + SEM)	Fe + DFP (conc./g tissue + SEM)
Fatty acid oxidation	Acetyl carnitine	1.93E-07±9.35E-09	3.14E-07±1.94E-08	2.61E-07±8.54E-09	2.55E-07±1.95E-08	1.84E-07±8.72E-09	1.84E-07±1.01E-08
	Carnitine	1.46E-06±6.83E-08	1.10E-06±5.68E-08	9.97E-07±2.49E-08	1.16E-06±9.28E-08	1.34E-06±5.26E-08	1.12E-06±4.72E-08
Glycolysis	a-glucose	6.14E-06±2.98E-07	3.97E-06±1.76E-07	3.46E-06±1.86E-07	3.73E-06±3.65E-07	4.42E-06±1.92E-07	3.81E-06±2.34E-07
	Lactate	6.61E-06±4.40E-07	6.69E-06±4.48E-07	6.64E-06±3.25E-07	7.25E-06±3.93E-07	6.19E-06±5.80E-07	5.49E-06±4.57E-07
TCA cycle	Succinate	7.67E-07±5.64E-08	6.54E-07±5.35E-08	5.68E-07±3.19E-08	6.64E-07±5.62E-08	6.56E-07±5.13E-08	4.77E-07±3.97E-08
	Fumarate	5.94E-08±3.75E-09	5.82E-08±6.99E-09	4.82E-08±3.63E-09	6.39E-08±7.00E-09	4.24E-08±2.74E-09	4.10E-08±1.84E-09
	Isoleucine	3.33E-07±2.22E-08	2.88E-07±2.27E-08	2.89E-07±1.98E-08	2.96E-07±3.55E-08	3.60E-07±4.04E-08	2.82E-07±2.58E-08
	Leucine	4.92E-07±2.94E-08	3.98E-07±2.98E-08	4.41E-07±2.74E-08	4.34E-07±4.80E-08	5.35E-07±4.84E-08	4.45E-07±3.61E-08
	Glycine	1.95E-06±6.10E-08	1.97E-06±8.65E-08	2.17E-06±8.26E-08	2.15E-06±1.35E-07	1.89E-06±7.22E-08	1.73E-06±1.21E-07
	Taurine	1.36E-05±8.13E-07	5.53E-06±8.01E-07	5.22E-06±3.94E-07	6.55E-06±6.93E-07	9.58E-06±1.01E-06	8.86E-06±1.08E-06
	Glutamine	6.42E-06±3.29E-07	5.77E-06±2.95E-07	4.90E-06±2.81E-07	5.17E-06±4.88E-07	5.69E-06±3.50E-07	4.84E-06±2.79E-07
	Glutamate	1.80E-06±8.44E-08	3.02E-06±2.09E-07	2.83E-06±1.43E-07	2.54E-06±1.47E-07	1.87E-06±1.34E-07	1.47E-06±1.68E-07
	Alanine	3.71E-06±2.14E-07	4.08E-06±3.05E-07	3.54E-06±1.31E-07	3.51E-0±62.43E-07	2.96E-06±2.11E-07	2.62E-06±1.62E-07
	Valine	2.24E-07±1.31E-08	1.66E-07±1.39E-08	1.73E-07±1.04E-08	1.66E-07±2.01E-08	2.50E-07±2.06E-08	2.23E-07±1.76E-08
	Phenylalanine	1.18E-07±6.00E-09	1.13E-07±5.58E-09	1.22E-07±6.97E-09	1.15E-07±1.01E-08	1.30E-07±1.03E-08	1.05E-07±9.44E-09
	Aspartate	1.21E-06±9.43E-08	1.08E-06±1.16E-07	1.10E-06±7.20E-08	1.16E-06±2.04E-07	1.21E-06±1.61E-07	8.86E-07±9.14E-08
Energetics (transfer and utilization)	ATP	1.48E-06±6.88E-08	1.30E-06±1.47E-07	9.93E-07±1.46E-07	8.13E-07±1.12E-07	6.41E-07±1.15E-07	5.65E-07±8.98E-08
	AMP	9.78E-07±6.25E-08	6.89E-07±8.86E-08	9.36E-07±1.53E-07	1.07E-06±2.63E-07	1.45E-06±2.44E-07	8.67E-07±1.84E-07
	NAD	7.31E-07±3.44E-08	5.47E-07±3.79E-08	5.63E-07±2.83E-08	5.53E-07±4.04E-08	5.88E-07±4.32E-08	4.59E-07±4.07E-08
	NADP	2.84E-07±2.18E-08	1.60E-07±2.25E-08	1.72E-07±1.77E-08	1.72E-07±2.40E-08	2.21E-07±2.54E-08	1.33E-07±2.01E-08
	Creatine	3.57E-07±1.90E-08	4.67E-07±8.41E-08	5.31E-07±4.03E-08	4.55E-07±5.75E-08	4.36E-07±1.66E-08	4.12E-07±2.98E-08
	Phosphocreatine	7.45E-07±3.46E-08	5.34E-07±3.08E-08	5.73E-07±2.40E-08	5.74E-07±5.03E-08	6.91E-07±3.62E-08	5.52E-07±3.45E-08
	Niacinamide	1.85E-07±1.60E-08	1.02E-07±1.82E-08	9.97E-08±1.63E-08	9.31E-08±1.51E-08	1.49E-07±2.11E-08	9.44E-08±1.55E-08
	Tyrosine	2.77E-07±2.55E-08	2.72E-07±2.18E-08	2.78E-07±2.12E-08	2.51E-07±2.19E-08	3.10E-07±3.00E-08	2.74E-07±2.15E-08
	Acetate	4.41E-07±2.40E-08	3.63E-07±2.55E-08	3.67E-07±1.60E-08	3.90E-07±2.69E-08	3.86E-07±2.90E-08	3.22E-07±2.90E-08
Lipid metabolism	Choline	4.66E-08±5.52E-09	6.08E-08±5.61E-09	6.57E-08±2.57E-09	5.80E-08±5.08E-09	5.90E-08±4.21E-09	5.91E-08±5.13E-09
	Phosphocholine	2.72E-06±9.36E-08	5.59E-06±4.85E-07	5.20E-06±3.68E-07	4.83E-06±5.54E-07	2.28E-06±1.03E-07	2.13E-06±3.38E-07
Other	Histidine	5.44E-07±2.37E-08	3.71E-07±2.82E-08	3.21E-07±1.79E-08	3.31E-07±2.94E-08	4.37E-07±2.90E-08	3.50E-07±2.35E-08
	Formate	9.90E-08±3.88E-09	8.26E-08±5.28E-09	8.02E-08±3.94E-09	7.72E-08±3.96E-09	8.74E-08±4.89E-09	8.42E-08±8.98E-09
	Myo inositol	1.12E-06±4.60E-08	1.08E-06±6.12E-08	1.09E-06±4.22E-08	1.09E-06±7.23E-08	1.23E-06±7.05E-08	1.09E-06±7.89E-08

Table 22: Lipophilic metabolite profile of liver tissue. Metabolite concentration presented as mean metabolite concentration/g of tissue ± SEM.

Metabolic process	Metabolite	Control (conc./g tissue + SEM)	DOX (conc./g tissue + SEM)	DOX + Fe (conc./g tissue + SEM)	DOX + Fe+ DFP (conc./g tissue + SEM)	Fe (conc./g tissue + SEM)	Fe + DFP (conc./g tissue + SEM)
Lipid metabolism	**Lipids (CH2)n** (Total lipid)	4.05E-08±2.67E-09	3.20E-06±2.33E-07	2.09E-06±1.76E-07	2.01E-06±1.43E-07	2.64E-06±2.44E-07	2.88E-06±3.29E-07
	Lipid CH=CH (Total unsaturated lipid)	6.27E-08±5.51E-09	7.36E-07±5.46E-08	4.88E-07±4.43E-08	4.58E-07±3.44E-08	5.66E-07±5.91E-08	6.34E-07±7.45E-08
	Cholesterol 18-CH3 (Total cholesterol)	2.45E-07±5.07E-09	5.66E-08±5.10E-09	4.12E-08±3.02E-09	3.87E-08±2.67E-09	4.10E-08±3.51E-09	4.37E-08±4.65E-09
	Glycerol backbone 1,3-CH2 (Triglyceride lipid)	1.08E-07±1.05E-08	4.67E-08±7.32E-09	2.64E-08±3.29E-09	2.50E-08±3.16E-09	2.40E-08±4.13E-09	3.00E-08±4.85E-09
	Phosphatidylcholine N(CH3)3 (membrane phospholipid)	2.83E-08±2.66E-09	4.41E-07±3.84E-08	3.06E-07±2.53E-08	2.91E-07±1.76E-08	3.87E-07±3.58E-08	4.22E-07±4.83E-08
	Phosphatidylethanolamine N(CH3)3 (membrane phospholipid)	4.87E-07±4.22E-08	2.10E-08±1.82E-09	1.55E-08±1.31E-09	1.55E-08±8.52E-10	2.91E-08±2.81E-09	3.08E-08±3.63E-09
	Sphingomyelin (membrane phospholipid)	6.70E-10±6.17E-11	1.64E-0±95.45E-10	7.84E-10±1.00E-10	7.26E-10±7.90E-11	1.11E-09±1.32E-10	1.48E-09±2.32E-10

Table 23: Metabolite profile of Serum. Metabolite concentration presented as mean metabolite concentration/g of tissue ± SEM.

Metabolic process	Metabolite	Control (conc. (M) + SEM)	DOX (conc. (M) + SEM)	DOX + Fe (conc. (M) + SEM)	DOX + Fe+ DFP (conc. (M) + SEM)	Fe (conc. (M) + SEM)	Fe + DFP (conc. (M) + SEM)
Glycolysis	a-glucose	1.41E-02±3.37E-04	8.80E-03v6.89E-04	8.13E-03±4.17E-04	7.88E-07±5.78E-04	1.12E-02±6.40E-04	1.28E-02±1.38E-03
	Lactate	8.81E-03±1.13E-03	4.95E-03±2.75E-04	6.08E-03±3.25E-04	6.31E-07±6.22E-04	7.86E-03±4.97E-04	6.65E-03±9.02E-04
	Pyruvate	2.47E-04±1.63E-05	1.38E-04±1.23E-05	1.20E-04±6.12E-06	1.11E-08±9.64E-06	1.42E-04±8.47E-06	1.29E-04±1.09E-05
TCA cycle	Citrate	1.41E-03±4.93E-05	1.22E-03±2.10E-04	1.14E-03±8.43E-05	1.14E-07±1.35E-04	1.31E-03±6.73E-05	1.26E-03±1.03E-04
	Isoleucine	5.34E-04±1.90E-05	8.187E-04±8.91E-05	6.20E-04±5.24E-05	6.16E-08±8.22E-05	4.82E-04±2.30E-05	5.30E-04±4.61E-05
	Leucine	2.68E-03±1.49E-04	5.92E-03±9.86E-04	4.50E-03±3.40E-04	4.41E-07±4.88E-04	2.05E-03±1.07E-04	2.21E-03±2.11E-04
	Glycine	1.42E-03±4.98E-05	5.32E-04±3.78E-05	6.13E-04±4.01E-05	4.78E-08±2.50E-05	1.13E-03±5.93E-05	1.23E-03±9.37E-05
	Glutamine	2.89E-03±9.91E-05	1.13E-03±8.90E-05	1.26E-03±1.12E-04	1.06E-07±9.43E-05	2.64E-03±1.35E-04	2.92E-03±2.19E-04
	Glutamate	1.46E-03±6.66E-05	2.78E-03±2.07E-04	2.42E-03±1.61E-04	2.15E-07±1.87E-04	1.16E-03±5.38E-05	1.25E-03±1.24E-04
	Alanine	2.47E-03±7.25E-05	1.68E-03±1.39E-04	1.97E-03±1.09E-04	1.65E-07±1.39E-04	1.31E-03±9.19E-05	1.71E-03±2.02E-04
	Valine	4.83E-04±1.56E-05	6.00E-04±2.87E-04	2.54E-04±1.50E-05	2.42E-08±2.21E-05	4.25E-04±1.86E-05	4.55E-04±3.79E-05
	Phenylalanine	3.79E-04±1.06E-05	1.41E-04±1.07E-05	1.68E-04±1.08E-05	1.31E-08±5.84E-06	3.36E-04±1.14E-05	3.77E-04±3.20E-05
Energetics (transfer and utilization)	Creatine	1.36E-03±3.70E-05	7.08E-04±3.85E-05	9.66E-04±4.58E-05	7.72E-08±6.66E-05	1.35E-03±5.12E-05	1.42E-03±1.01E-04
	Tyrosine	3.27E-04±1.59E-05	1.18E-04±9.41E-06	1.62E-04±1.13E-05	1.20E-08±7.67E-06	2.89E-04±8.61E-06	3.52E-04±3.31E-05
	Acetate	1.03E-03±6.35E-05	4.72E-04±4.01E-05	6.21E-04±3.84E-05	5.24E-08±2.80E-05	1.26E-03±8.43E-05	1.37E-03±1.65E-04
Lipid metabolism	Fatty acid residues (–CH=CH-)	2.12E-02±1.65E-03	9.70E-02±9.46E-03	8.20E-02±6.81E-03	8.11E-06±9.52E-03	1.40E-02±1.34E-03	1.34E-02±1.51E-03
	Fatty acid residues (COCH2-CH2)	9.20E-03±8.52E-04	4.34E-02±5.50E-03	3.13E-02±3.29E-03	3.40E-06±5.25E-03	5.30E-03±6.15E-04	4.54E-03±5.45E-04
	Fatty acid residues (ω-CH3)	2.41E-02±1.58E-03	1.11E-01±1.17E-02	8.89E-02±6.96E-03	8.96E-06±1.03E-02	1.82E-02±1.33E-03	1.74E-02±1.87E-03
Ketogenesis	3-hydroxybutyrate	1.01E-03±3.53E-05	1.62E-03±1.56E-04	1.21E-03±7.98E-05	1.35E-07±1.69E-04	9.65E-04±7.25E-05	1.08E-03±8.97E-05
Other	Histidine	2.35E-04±5.71E-06	6.58E-05±5.37E-06	7.78E-05±7.12E-06	6.36E-09±4.86E-06	2.08E-04±8.77E-06	2.33E-04±1.86E-05
	Tryptophan	1.04E-04±3.83E-06	1.65E-05±3.20E-06	1.90E-05±2.04E-06	1.87E-09±2.22E-06	9.60E-05±4.50E-06	9.77E-05±8.04E-06
	Formate	3.13E-05±1.09E-05	3.29E-0±56.40E-06	3.99E-05±6.19E-06	2.63E-05±2.78E-06	6.95E-05±1.31E-05	4.99E-05±9.39E-06

REFERENCES

[1] ‘Worldwide cancer incidence statistics | Cancer Research UK’. Accessed: Apr. 23, 2019. [Online]. Available: https://www.cancerresearchuk.org/health-professional/cancer-statistics/worldwide-cancer/incidence

[2] ‘Cancer’. Accessed: Apr. 22, 2020. [Online]. Available: https://www.who.int/health-topics/cancer#tab=tab_1

[3] ‘Cancer mortality statistics | Cancer Research UK’. Accessed: Apr. 23, 2019. [Online]. Available: https://www.cancerresearchuk.org/health-professional/cancer-statistics/mortality

[4] K. D. Miller *et al.*, ‘Cancer treatment and survivorship statistics, 2016’, *CA Cancer J Clin*, vol. 66, no. 4, pp. 271–289, Jul. 2016, doi: 10.3322/caac.21349.

[5] X. Xu, H. L. Persson, and D. R. Richardson, ‘Molecular pharmacology of the interaction of anthracyclines with iron’, 2005. doi: 10.1124/mol.105.013383.

[6] D. Jain, ‘Cardiotoxicity of doxorubicin and other anthracycline derivatives’, *Journal of Nuclear Cardiology*, vol. 7, no. 1, 2000, doi: 10.1067/mnc.2000.103324.

[7] D. S. dos Santos and R. C. dos S. Goldenberg, ‘Doxorubicin-Induced Cardiotoxicity: From Mechanisms to Development of Efficient Therapy’, in *Cardiotoxicity*, 2018. doi: 10.5772/intechopen.79588.

[8] X. Xu, H. L. Persson, and D. R. Richardson, ‘Molecular Pharmacology of the Interaction of Anthracyclines with Iron’, *Mol Pharmacol*, vol. 68, no. 2, pp. 261–271, Aug. 2005, doi: 10.1124/mol.105.013383.

[9] S. M. Swain, F. S. Whaley, and M. S. Ewer, ‘Congestive heart failure in patients treated with doxorubicin’, *Cancer*, vol. 97, no. 11, pp. 2869–2879, Jun. 2003, doi: 10.1002/cncr.11407.

[10] L. C. M. Kremer, E. C. van Dalen, M. Offringa, and P. A. Voûte, ‘Frequency and risk factors of anthracycline-induced clinical heart failure in children: a systematic review.’,

Ann Oncol, vol. 13, no. 4, pp. 503–12, Apr. 2002, Accessed: Apr. 23, 2019. [Online]. Available: http://www.ncbi.nlm.nih.gov/pubmed/12056699

[11] D. L. Hershman, R. B. McBride, A. Eisenberger, W. Y. Tsai, V. R. Grann, and J. S. Jacobson, 'Doxorubicin, Cardiac Risk Factors, and Cardiac Toxicity in Elderly Patients With Diffuse B-Cell Non-Hodgkin's Lymphoma', *Journal of Clinical Oncology*, vol. 26, no. 19, pp. 3159–3165, Jul. 2008, doi: 10.1200/JCO.2007.14.1242.

[12] T. Doenst, T. Dung Nguyen, and E. Dale Abel, 'Cardiac Metabolism in Heart Failure-Implications beyond ATP production', *Circ Res*, vol. 113, no. 6, pp. 709–724, 2013, doi: 10.1161/CIRCRESAHA.113.300376.

[13] S. C. Kolwicz, S. Purohit, and R. Tian, 'Cardiac Metabolism and Its Interactions with Contraction, Growth, and Survival of the Cardiomyocte', doi: 10.1161/CIRCRESAHA.113.302095.

[14] M. Saleet Jafri, S. J. Dudycha, and B. O'rourke, 'CARDIAC ENERGY METABOLISM: Models of Cellular Respiration', 2001.

[15] S. C. Kolwicz and R. Tian, 'SPOTLIGHT REVIEW Glucose metabolism and cardiac hypertrophy', doi: 10.1093/cvr/cvr071.

[16] G. J. Van Der Vusse, M. Van Bilsen, and J. F. C. Glatz, 'Cardiac fatty acid uptake and transport in health and disease', Jan. 14, 2000, *Cardiovasc Res*. doi: 10.1016/S0008-6363(99)00263-1.

[17] S. M. Houten, S. Violante, F. V. Ventura, and R. J. A. Wanders, 'The Biochemistry and Physiology of Mitochondrial Fatty Acid β-Oxidation and Its Genetic Disorders', *Annu Rev Physiol*, vol. 78, no. 1, pp. 23–44, Feb. 2016, doi: 10.1146/annurev-physiol-021115-105045.

[18] G. D. Lopaschuk, J. R. Ussher, C. D. L. Folmes, J. S. Jaswal, and W. C. Stanley, 'Myocardial fatty acid metabolism in health and disease', 2010, *Physiol Rev*. doi: 10.1152/physrev.00015.2009.

[19] S. Michel Houten and R. J. A Wanders, 'A general introduction to the biochemistry of mitochondrial fatty acid β-oxidation', doi: 10.1007/s10545-010-9061-2.

[20] ‘Oxidation of Fatty Acids - via Beta-Oxidation | Biochemistry Notes | PharmaXChange.info’. Accessed: Jun. 15, 2020. [Online]. Available: https://pharmaxchange.info/2013/10/oxidation-of-fatty-acids/

[21] D. H. Tran and Z. V. Wang, ‘Glucose Metabolism in Cardiac Hypertrophy and Heart Failure’, *J Am Heart Assoc*, vol. 8, no. 12, Jun. 2019, doi: 10.1161/JAHA.119.012673.

[22] R. Chaudhry and M. Varacallo, *Biochemistry, Glycolysis*. StatPearls Publishing, 2018.

[23] E. , D. Abel, ‘Glucose transport in the heart’, *Frontiers in Bioscience*, vol. 9, no. 1–3, p. 201, 2004, doi: 10.2741/1216.

[24] G. Czibik, V. Steeples, A. Yavari, and H. Ashrafian, ‘Citric Acid Cycle Intermediates in Cardioprotection’, *Circ Cardiovasc Genet*, vol. 7, no. 5, pp. 711–719, Oct. 2014, doi: 10.1161/CIRCGENETICS.114.000220.

[25] H. Lodish, A. Berk, S. L. Zipursky, P. Matsudaira, D. Baltimore, and J. Darnell, ‘Electron Transport and Oxidative Phosphorylation’, 2000.

[26] M. P. Murphy, ‘How mitochondria produce reactive oxygen species’, *Biochem. J*, vol. 417, pp. 1–13, 2009, doi: 10.1042/BJ20081386.

[27] R. H. Garrett, C. M. Grisham, and M. Sabat, *Biochemistry FOURTH EDITION With molecular graphic images*. 2010.

[28] Biology of Cardiovascular and Metabolic Diseases, ‘Pyruvic Acid Derivative’, Biology of Cardiovascular and Metabolic Diseases. Accessed: Mar. 10, 2024. [Online]. Available: https://www.sciencedirect.com/topics/medicine-and-dentistry/pyruvic-acid-derivative

[29] G. J. Anderson and D. M. Frazer, ‘Current understanding of iron homeostasis’, in *American Journal of Clinical Nutrition*, Oxford University Press, Dec. 2017, pp. 1559S-1566S. doi: 10.3945/ajcn.117.155804.

[30] R. Gozzelino and P. Arosio, ‘Molecular Sciences Iron Homeostasis in Health and Disease’, 2016, doi: 10.3390/ijms17010130.

[31] W. H. Koppenol, ‘The centennial of the Fenton reaction’, *Free Radic Biol Med*, vol. 15, no. 6, pp. 645–651, Dec. 1993, doi: 10.1016/0891-5849(93)90168-T.

[32] C. Zhang, ‘Essential functions of iron-requiring proteins in DNA replication, repair and cell cycle control’, *Protein Cell*, vol. 5, no. 10, pp. 750–760, Oct. 2014, doi: 10.1007/s13238-014-0083-7.

[33] J. Wang and K. Pantopoulos, ‘Regulation of cellular iron metabolism’, *Biochem. J*, vol. 434, pp. 365–381, 2011, doi: 10.1042/BJ20101825.

[34] D. Galaris and K. Pantopoulos, ‘Oxidative Stress and Iron Homeostasis: Mechanistic and Health Aspects’, *Crit Rev Clin Lab Sci*, vol. 45, no. 1, pp. 1–23, Jan. 2008, doi: 10.1080/10408360701713104.

[35] P. Ponka, ‘Cellular iron metabolism’, 1999, *Blackwell Publishing Inc*. doi: 10.1046/j.1523-1755.1999.055suppl.69002.x.

[36] S. Lakhal-Littleton, ‘Mechanisms of cardiac iron homeostasis and their importance to heart function’, 2019, doi: 10.1016/j.freeradbiomed.2018.08.010.

[37] M. W. Hentze, M. U. Muckenthaler, B. Galy, and C. Camaschella, ‘Two to Tango: Regulation of Mammalian Iron Metabolism’, Jul. 2010. doi: 10.1016/j.cell.2010.06.028.

[38] K. Gkouvatsos, G. Papanikolaou, and K. Pantopoulos, ‘Regulation of iron transport and the role of transferrin’, Mar. 01, 2012, *Elsevier*. doi: 10.1016/j.bbagen.2011.10.013.

[39] D. L. Zhang, M. C. Ghosh, and T. A. Rouault, ‘The physiological functions of iron regulatory proteins in iron homeostasis - an update’, 2014, *Frontiers Research Foundation*. doi: 10.3389/fphar.2014.00124.

[40] E. H. J. M. Kemna, H. Tjalsma, H. L. Willems, and D. W. Swinkels, ‘Hepcidin: From discovery to differential diagnosis’, *Haematologica*, vol. 93, no. 1, pp. 90–97, Jan. 2008, doi: 10.3324/haematol.11705.

[41] N. C. Andrews, ‘Disorders of iron metabolism’, Dec. 23, 1999. doi: 10.1056/NEJM199912233412607.

[42] F. Petrat, H. de Groot, R. Sustmann, and U. Rauen, ‘The chelatable iron pool in living cells: A methodically defined quantity’, 2002. doi: 10.1515/BC.2002.051.

[43] Z. Qu, P. Li, X. Zhang, and K. Han, ‘A turn-on fluorescent chemodosimeter based on detelluration for detecting ferrous iron (Fe2+) in living cells’, *J Mater Chem B*, 2016, doi: 10.1039/c5tb02090e.

[44] O. Kakhlon and Z. I. Cabantchik, ‘The labile iron pool: Characterization, measurement, and participation in cellular processes’, *Free Radic Biol Med*, vol. 33, no. 8, pp. 1037–1046, Oct. 2002, doi: 10.1016/S0891-5849(02)01006-7.

[45] G. Cairo and A. Pietrangelo, ‘Iron regulatory proteins in pathobiology’, 2000. doi: 10.1042/0264-6021:3520241.

[46] G. Cairo and S. Recalcati, ‘Iron-regulatory proteins: molecular biology and pathophysiological implications’, 2007, doi: 10.1017/S1462399407000531.

[47] G. Cairo, S. Recalcati, A. Pietrangelo, and G. Minotti, ‘The iron regulatory proteins: Targets and modulators of free radical reactions and oxidative damage’, *Free Radic Biol Med*, 2002, doi: 10.1016/S0891-5849(02)00825-0.

[48] T. A. Rouault, ‘The role of iron regulatory proteins in mammalian iron homeostasis and disease’, 2006. doi: 10.1038/nchembio807.

[49] S. Recalcati, G. Minotti, and G. Cairo, ‘Iron regulatory proteins: From molecular mechanisms to drug development’, 2010. doi: 10.1089/ars.2009.2983.

[50] D. Galaris, A. Barbouti, and K. Pantopoulos, ‘Iron homeostasis and oxidative stress: An intimate relationship’, Dec. 01, 2019, *Elsevier B.V.* doi: 10.1016/j.bbamcr.2019.118535.

[51] T. Ganz, ‘Systemic iron homeostasis’, *Physiol Rev*, vol. 93, no. 4, pp. 1721–1741, Oct. 2013, doi: 10.1152/physrev.00008.2013.

[52] R. Daher and Z. Karim, ‘Iron metabolism: State of the art’, Sep. 01, 2017, *Elsevier Masson SAS*. doi: 10.1016/j.tracli.2017.06.015.

[53] A. T. McKie *et al.*, ‘An iron-regulated ferric reductase associated with the absorption of dietary iron’, *Science (1979)*, vol. 291, no. 5509, pp. 1755–1759, Mar. 2001, doi: 10.1126/science.1057206.

[54] Y. Nevo and N. Nelson, ‘The NRAMP family of metal-ion transporters’, Jul. 01, 2006, *Elsevier*. doi: 10.1016/j.bbamcr.2006.05.007.

[55] C. D. Vulpe *et al.*, ‘Hephaestin, a ceruloplasmin homologue implicated in intestinal iron transport, is defective in the sla mouse’, *Nat Genet*, vol. 21, no. 2, pp. 195–199, Feb. 1999, doi: 10.1038/5979.

[56] S. Cherukuri, R. Potla, J. Sarkar, S. Nurko, Z. L. Harris, and P. L. Fox, ‘Unexpected role of ceruloplasmin in intestinal iron absorption’, *Cell Metab*, vol. 2, no. 5, pp. 309–319, Nov. 2005, doi: 10.1016/j.cmet.2005.10.003.

[57] P. Brissot, M. Ropert, C. Le Lan, and O. Loréal, ‘Non-transferrin bound iron: A key role in iron overload and iron toxicity’, Mar. 01, 2012, *Elsevier*. doi: 10.1016/j.bbagen.2011.07.014.

[58] I. De Domenico, D. M. Ward, and J. Kaplan, ‘Hepcidin regulation: Ironing out the details’, Jul. 02, 2007, *American Society for Clinical Investigation*. doi: 10.1172/JCI32701.

[59] E. Nemeth *et al.*, ‘Hepcidin regulates cellular iron efflux by binding to ferroportin and inducing its internalization’, *Science (1979)*, vol. 306, no. 5704, pp. 2090–2093, Dec. 2004, doi: 10.1126/science.1104742.

[60] Z. Zhou, M. J. Xu, and B. Gao, ‘Hepatocytes: A key cell type for innate immunity’, May 01, 2016, *Chinese Soc Immunology*. doi: 10.1038/cmi.2015.97.

[61] B. Qiao *et al.*, ‘Hepcidin-induced endocytosis of ferroportin is dependent on ferroportin ubiquitination’, *Cell Metab*, vol. 15, no. 6, pp. 918–924, Jun. 2012, doi: 10.1016/j.cmet.2012.03.018.

[62] S. Aschemeyer *et al.*, ‘Structure-function analysis of ferroportin defines the binding site and an alternative mechanism of action of hepcidin’, *Blood*, vol. 131, no. 8, pp. 899–910, Feb. 2018, doi: 10.1182/blood-2017-05-786590.

[63] P. J. Schmidt, P. T. Toran, A. M. Giannetti, P. J. Bjorkman, and N. C. Andrews, 'The Transferrin Receptor Modulates Hfe-Dependent Regulation of Hepcidin Expression', *Cell Metab*, vol. 7, no. 3, pp. 205–214, Mar. 2008, doi: 10.1016/j.cmet.2007.11.016.

[64] J. Arezes *et al.*, 'Erythroferrone inhibits the induction of hepcidin by BMP6', *Blood*, vol. 132, no. 14, pp. 1473–1477, Oct. 2018, doi: 10.1182/blood-2018-06-857995.

[65] R. Coffey and T. Ganz, 'Erythroferrone: An Erythroid Regulator of Hepcidin and Iron Metabolism', 2018, doi: 10.1097/HS9.0000000000000035.

[66] P. Ponka, C. Beaumont, and D. R. Richardson, 'Function and regulation of transferrin and ferritin', 1998.

[67] R. S. Ohgami *et al.*, 'Identification of a ferrireductase required for efficient transferrin-dependent iron uptake in erythroid cells', *Nat Genet*, vol. 37, no. 11, pp. 1264–1269, Nov. 2005, doi: 10.1038/ng1658.

[68] S. P. Young, A. Bomford, and R. Williams, 'The effect of the iron saturation of transferrin on its binding and uptake by rabbit reticulocytes', *Biochemical Journal*, vol. 219, no. 2, pp. 505–510, 1984, doi: 10.1042/bj2190505.

[69] O. Tacar, P. Sriamornsak, and C. R. Dass, 'Doxorubicin: an update on anticancer molecular action, toxicity and novel drug delivery systems', *Journal of Pharmacy and Pharmacology*, vol. 65, no. 2, pp. 157–170, Feb. 2013, doi: 10.1111/j.2042-7158.2012.01567.x.

[70] I. Mitani, D. Jain, T. M. Joska, B. Burtness, and B. L. Zaret, 'Doxorubicin cardiotoxicity: Prevention of congestive heart failure with serial cardiac function monitoring with equilibrium radinuclide angiocardiography in the current era', *Journal of Nuclear Cardiology*, vol. 10, no. 2, pp. 132–139, 2003, doi: 10.1067/mnc.2003.7.

[71] H. Shi, K. Z. Bencze, T. L. Stemmler, and C. C. Philpott, 'A cytosolic iron chaperone that delivers iron to ferritin', *Science (1979)*, vol. 320, no. 5880, pp. 1207–1210, May 2008, doi: 10.1126/science.1157643.

[72] E. C. Theil, ‘Ferritin: Structure, Gene Regulation, and Cellular Function in Animals, Plants, and Microorganisms’, *Annu Rev Biochem*, vol. 56, no. 1, pp. 289–315, Jun. 1987, doi: 10.1146/annurev.bi.56.070187.001445.

[73] S. C. Andrews *et al.*, ‘Structure, function, and evolution of ferritins’, *J Inorg Biochem*, vol. 47, no. 1, pp. 161–174, Aug. 1992, doi: 10.1016/0162-0134(92)84062-R.

[74] ‘Ferritin | South Tees Hospitals NHS Foundation Trust’. Accessed: May 11, 2020. [Online]. Available: https://www.southtees.nhs.uk/services/pathology/tests/ferritin/

[75] C. C. Philpott *et al.*, ‘Iron-tracking strategies: Chaperones capture iron in the cytosolic labile iron pool’, *Front Mol Biosci*, vol. 10, Feb. 2023, doi: 10.3389/fmolb.2023.1127690.

[76] B. Galy, M. Conrad, and M. Muckenthaler, ‘Mechanisms controlling cellular and systemic iron homeostasis’, *Nat Rev Mol Cell Biol*, vol. 25, no. 2, pp. 133–155, Feb. 2024, doi: 10.1038/s41580-023-00648-1.

[77] C. C. Philpott, S. J. Patel, and O. Protchenko, ‘Management versus miscues in the cytosolic labile iron pool: The varied functions of iron chaperones’, *Biochimica et Biophysica Acta (BBA) - Molecular Cell Research*, vol. 1867, no. 11, p. 118830, Nov. 2020, doi: 10.1016/j.bbamcr.2020.118830.

[78] J. He *et al.*, ‘Ferroptosis and ferritinophagy in diabetes complications’, *Mol Metab*, vol. 60, p. 101470, Jun. 2022, doi: 10.1016/j.molmet.2022.101470.

[79] K. Pantopoulos, ‘Iron metabolism and the IRE/IRP regulatory system: An update’, 2004, *New York Academy of Sciences*. doi: 10.1196/annals.1306.001.

[80] A. J. Schwartz *et al.*, ‘Hepatic hepcidin/intestinal HIF-2α axis maintains iron absorption during iron deficiency and overload’, *Journal of Clinical Investigation*, vol. 129, no. 1, pp. 336–348, Jan. 2019, doi: 10.1172/JCI122359.

[81] F. Pierrel, P. A. Cobine, and D. R. Winge, ‘Metal Ion availability in mitochondria’, in *BioMetals*, Jun. 2007, pp. 675–682. doi: 10.1007/s10534-006-9052-9.

[82] J. Gerber and R. Lill, ‘Biogenesis of iron-sulfur proteins in eukaryotes: Components, mechanism and pathology’, *Mitochondrion*, vol. 2, no. 1–2, pp. 71–86, Nov. 2002, doi: 10.1016/S1567-7249(02)00041-7.

[83] I. Napier, P. Ponka, and D. R. Richardson, ‘Iron trafficking in the mitochondrion: novel pathways revealed by disease’, 2005, doi: 10.1182/blood-2004-10-3856.

[84] T. A. Rouault and W. H. Tong, ‘Iron-sulphur cluster biogenesis and mitochondrial iron homeostasis’, Apr. 2005. doi: 10.1038/nrm1620.

[85] R. Lill and U. Mühlenhoff, ‘Maturation of Iron-Sulfur Proteins in Eukaryotes: Mechanisms, Connected Processes, and Diseases’, *Annu Rev Biochem*, vol. 77, no. 1, pp. 669–700, Jun. 2008, doi: 10.1146/annurev.biochem.76.052705.162653.

[86] A. D. Sheftel, A. S. Zhang, C. Brown, O. S. Shirihai, and P. Ponka, ‘Direct interorganellar transfer of iron from endosome to mitochondrion’, *Blood*, vol. 110, no. 1, pp. 125–132, Jul. 2007, doi: 10.1182/blood-2007-01-068148.

[87] A. Hamdi, T. M. Roshan, T. M. Kahawita, A. B. Mason, A. D. Sheftel, and P. Ponka, ‘Erythroid cell mitochondria receive endosomal iron by a “kiss-and-run” mechanism’, *Biochim Biophys Acta Mol Cell Res*, vol. 1863, no. 12, pp. 2859–2867, Dec. 2016, doi: 10.1016/j.bbamcr.2016.09.008.

[88] J. V. Dietz, J. L. Fox, and O. Khalimonchuk, ‘Down the Iron Path: Mitochondrial Iron Homeostasis and Beyond’, *Cells*, vol. 10, no. 9, p. 2198, Aug. 2021, doi: 10.3390/cells10092198.

[89] H.-I. Hung, J. M. Schwartz, E. N. Maldonado, J. J. Lemasters, and A.-L. Nieminen, ‘Mitoferrin-2-dependent Mitochondrial Iron Uptake Sensitizes Human Head and Neck Squamous Carcinoma Cells to Photodynamic Therapy’, *Journal of Biological Chemistry*, vol. 288, no. 1, pp. 677–686, Jan. 2013, doi: 10.1074/jbc.M112.422667.

[90] A. V. Menon and J. Kim, ‘Iron Promotes Cardiac Doxorubicin Retention and Toxicity Through Downregulation of the Mitochondrial Exporter ABCB8’, *Front Pharmacol*, vol. 13, Mar. 2022, doi: 10.3389/fphar.2022.817951.

[91] Y. Ichikawa *et al.*, ‘Disruption of ATP-binding cassette B8 in mice leads to cardiomyopathy through a decrease in mitochondrial iron export’, *Proceedings of the National Academy of Sciences*, vol. 109, no. 11, pp. 4152–4157, Mar. 2012, doi: 10.1073/pnas.1119338109.

[92] F. Petrat, D. Weisheit, M. Lensen, H. De Groot, R. Sustmann, and U. Rauen, ‘Selective determination of mitochondrial chelatable iron in viable cells with a new fluorescent sensor’, *Biochemical Journal*, vol. 362, no. 1, pp. 137–147, Feb. 2002, doi: 10.1042/0264-6021:3620137.

[93] U. Rauen *et al.*, ‘Assessment of chelatable mitochondrial iron by using mitochondrion-selective fluorescent iron indicators with different iron-binding affinities’, *ChemBioChem*, vol. 8, no. 3, pp. 341–352, Feb. 2007, doi: 10.1002/cbic.200600311.

[94] U. Rauen *et al.*, ‘Assessment of chelatable mitochondrial iron by using mitochondrion-selective fluorescent iron indicators with different iron-binding affinities’, *ChemBioChem*, vol. 8, no. 3, pp. 341–352, Feb. 2007, doi: 10.1002/cbic.200600311.

[95] D. R. Richardson *et al.*, ‘Mitochondrial iron trafficking and the integration of iron metabolism between the mitochondrion and cytosol’, Jun. 15, 2010, *National Academy of Sciences*. doi: 10.1073/pnas.0912925107.

[96] S. Levi and P. Arosio, ‘Mitochondrial ferritin’, Oct. 01, 2004, *Pergamon*. doi: 10.1016/j.biocel.2003.10.020.

[97] S. Levi, M. Ripamonti, M. Dardi, A. Cozzi, and P. Santambrogio, ‘Mitochondrial Ferritin: Its Role in Physiological and Pathological Conditions’, *Cells*, vol. 10, no. 8, p. 1969, Aug. 2021, doi: 10.3390/cells10081969.

[98] S. Levi *et al.*, ‘A Human Mitochondrial Ferritin Encoded by an Intronless Gene*’, 2001, doi: 10.1074/jbc.C100141200.

[99] D. Alsina, R. Purroy, J. Ros, and J. Tamarit, ‘Iron in Friedreich Ataxia: A Central Role in the Pathophysiology or an Epiphenomenon?’, *Pharmaceuticals*, vol. 11, no. 3, p. 89, Sep. 2018, doi: 10.3390/ph11030089.

[100] A. Pastore and H. Puccio, ‘Frataxin: a protein in search for a function’, *J Neurochem*, vol. 126, no. s1, pp. 43–52, Aug. 2013, doi: 10.1111/jnc.12220.

[101] R. Lill *et al.*, ‘Mechanisms of iron-sulfur protein maturation in mitochondria, cytosol and nucleus of eukaryotes’, Jul. 2006. doi: 10.1016/j.bbamcr.2006.05.011.

[102] P. Hinchliffe and L. A. Sazanov, ‘Biochemistry: Organization of iron-sulfur clusters in respiratory complex I’, *Science (1979)*, vol. 309, no. 5735, pp. 771–774, Jul. 2005, doi: 10.1126/science.1113988.

[103] C. Wachnowsky, I. Fidai, and J. A. Cowan, ‘Iron-sulfur cluster biosynthesis and trafficking-Impact on human disease conditions HHS Public Access’, doi: 10.1039/c7mt00180k.

[104] J. V. Llorens, S. Soriano, P. Calap-Quintana, P. Gonzalez-Cabo, and M. D. Moltó, ‘The Role of Iron in Friedreich’s Ataxia: Insights From Studies in Human Tissues and Cellular and Animal Models’, *Front Neurosci*, vol. 13, Feb. 2019, doi: 10.3389/fnins.2019.00075.

[105] S. Adinolfi *et al.*, ‘Bacterial frataxin CyaY is the gatekeeper of iron-sulfur cluster formation catalyzed by IscS’, *Nat Struct Mol Biol*, vol. 16, no. 4, pp. 390–396, Apr. 2009, doi: 10.1038/nsmb.1579.

[106] T. L. Poulos, ‘Heme enzyme structure and function’, Apr. 09, 2014, *American Chemical Society*. doi: 10.1021/cr400415k.

[107] T. Yoon and J. A. Cowan, ‘Frataxin-mediated Iron Delivery to Ferrochelatase in the Final Step of Heme Biosynthesis’, *Journal of Biological Chemistry*, vol. 279, no. 25, pp. 25943–25946, Jun. 2004, doi: 10.1074/jbc.C400107200.

[108] C.-F. Cheng and W.-S. Lian, ‘Prooxidant Mechanisms in Iron Overload Cardiomyopathy’, *Biomed Res Int*, vol. 2013, pp. 1–8, 2013, doi: 10.1155/2013/740573.

[109] R. R. Crichton, R. J. Ward, and R. C. Hider, ‘The Efficacy of Iron Chelators for Removing Iron from Specific Brain Regions and the Pituitary—Ironing out the Brain’, *Pharmaceuticals*, vol. 12, no. 3, p. 138, Sep. 2019, doi: 10.3390/ph12030138.

[110] S. Wongjaikam, S. Kumfu, S. C. Chattipakorn, S. Fucharoen, and N. Chattipakorn, ‘Current and future treatment strategies for iron overload cardiomyopathy’, *Eur J Pharmacol*, vol. 765, pp. 86–93, Oct. 2015, doi: 10.1016/J.EJPHAR.2015.08.017.

[111] M. Kruszewski, ‘Labile iron pool: the main determinant of cellular response to oxidative stress’, *Mutation Research/Fundamental and Molecular Mechanisms of Mutagenesis*, vol. 531, no. 1–2, pp. 81–92, Oct. 2003, doi: 10.1016/J.MRFMMM.2003.08.004.

[112] S. Wongjaikam *et al.*, ‘Combined Iron Chelator and Antioxidant Exerted Greater Efficacy on Cardioprotection Than Monotherapy in Iron-Overloaded Rats’, *PLoS One*, vol. 11, no. 7, p. e0159414, Jul. 2016, doi: 10.1371/journal.pone.0159414.

[113] S. Kumfu *et al.*, ‘Ferroptosis inhibitor improves cardiac function more effectively than inhibitors of apoptosis and necroptosis through cardiac mitochondrial protection in rats with iron-overloaded cardiomyopathy’, *Toxicol Appl Pharmacol*, vol. 479, p. 116727, Nov. 2023, doi: 10.1016/J.TAAP.2023.116727.

[114] W. S. Aronow, ‘Management of cardiac hemochromatosis’, *Archives of Medical Science*, vol. 14, no. 3, pp. 560–568, 2018, doi: 10.5114/aoms.2017.68729.

[115] H. Saito, ‘METABOLISM OF IRON STORES.’, *Nagoya J Med Sci*, vol. 76, no. 3–4, pp. 235–254, Aug. 2014.

[116] P. Kirk *et al.*, ‘Cardiac T2* Magnetic Resonance for Prediction of Cardiac Complications in Thalassemia Major’, *Circulation*, vol. 120, no. 20, pp. 1961–1968, Nov. 2009, doi: 10.1161/CIRCULATIONAHA.109.874487.

[117] L. Anderson, ‘Cardiovascular T2-star (T2*) magnetic resonance for the early diagnosis of myocardial iron overload’, *Eur Heart J*, vol. 22, no. 23, pp. 2171–2179, Dec. 2001, doi: 10.1053/euhj.2001.2822.

[118] A. Brownell, S. Lowson, and M. Brozovic, ‘Serum ferritin concentration in sickle cell crisis.’, *J Clin Pathol*, vol. 39, no. 3, pp. 253–255, Mar. 1986, doi: 10.1136/jcp.39.3.253.

[119] T. N. Tran, S. K. Eubanks, K. J. Schaffer, C. Y. J. Zhou, and M. C. Linder, ‘Secretion of Ferritin by Rat Hepatoma Cells and Its Regulation by Inflammatory Cytokines and

Iron', *Blood*, vol. 90, no. 12, pp. 4979–4986, Dec. 1997, doi: 10.1182/blood.V90.12.4979.

[120] A. Hoffbrand, 'Diagnosing myocardial iron overload', *Eur Heart J*, vol. 22, no. 23, pp. 2140–2141, Dec. 2001, doi: 10.1053/euhj.2001.2951.

[121] J.-P. Carpenter *et al.*, 'Calibration of myocardial T2 and T1 against iron concentration', *Journal of Cardiovascular Magnetic Resonance*, vol. 16, no. 1, p. 62, Dec. 2014, doi: 10.1186/s12968-014-0062-4.

[122] J. C. Wood, 'History and Current Impact of Cardiac Magnetic Resonance Imaging on the Management of Iron Overload', *Circulation*, vol. 120, no. 20, pp. 1937–1939, Nov. 2009, doi: 10.1161/CIRCULATIONAHA.109.907196.

[123] J.-P. Carpenter *et al.*, 'On T2* Magnetic Resonance and Cardiac Iron', *Circulation*, vol. 123, no. 14, pp. 1519–1528, Apr. 2011, doi: 10.1161/CIRCULATIONAHA.110.007641.

[124] GOSH NHS Foundation Trust, 'Anthracyclines (daunorubicin, doxorubicin, idarubicin and mitoxantrone): information for families', NHS. Accessed: Mar. 03, 2024. [Online]. Available: https://www.gosh.nhs.uk/conditions-and-treatments/medicines-information/anthracyclines-daunorubicin-doxorubicin-idarubicin-and-mitoxantrone/#:~:text=idarubicin%20and%20mitoxantrone)-,Anthracyclines%20(daunorubicin%2C%20doxorubicin%2C%20idarubicin%20and%20mitoxantrone),of%20the%20possible%20side%20effects

[125] G. Takemura and H. Fujiwara, 'Doxorubicin-Induced Cardiomyopathy. From the Cardiotoxic Mechanisms to Management', *Prog Cardiovasc Dis*, vol. 49, no. 5, pp. 330–352, Mar. 2007, doi: 10.1016/j.pcad.2006.10.002.

[126] F. Arcamone, G. Franceschi, S. Penco, and A. Selva, 'Adriamycin (14-hydroxydaunomycin), a novel antitumor antibiotic', *Tetrahedron Lett*, vol. 10, no. 13, pp. 1007–1010, 1969, doi: 10.1016/S0040-4039(01)97723-8.

[127] 'Doxorubicin (Adriamycin, Rubex) Chemotherapy Drug Information'. Accessed: Nov. 28, 2020. [Online]. Available: http://chemocare.com/chemotherapy/drug-info/doxorubicin.aspx

[128] ‘Doxorubicin (Adriamycin) | Cancer drugs | Cancer Research UK’. Accessed: Nov. 28, 2020. [Online]. Available: https://www.cancerresearchuk.org/about-cancer/cancer-in-general/treatment/cancer-drugs/drugs/doxorubicin

[129] S. N. Hilmer, V. C. Cogger, M. Muller, and D. G. Le Couteur, ‘The hepatic pharmacokinetics of doxorubicin and liposomal doxorubicin’, *Drug Metabolism and Disposition*, vol. 32, no. 8, 2004, doi: 10.1124/dmd.32.8.794.

[130] J. V Mcgowan, R. Chung, A. Maulik, I. Piotrowska, & J. Malcolm Walker, and D. M. Yellon, ‘Anthracycline Chemotherapy and Cardiotoxicity’, 2017, doi: 10.1007/s10557-016-6711-0.

[131] C. Nabhan *et al.*, ‘Disease characteristics, treatment patterns, prognosis, outcomes and lymphoma-related mortality in elderly follicular lymphoma in the United States’, *Br J Haematol*, vol. 170, no. 1, pp. 85–95, Jul. 2015, doi: 10.1111/bjh.13399.

[132] G. Capranico, S. Tinelli, C. A. Austin, M. L. Fisher, and F. Zunino, ‘Different patterns of gene expression of topoisomerase II isoforms in differentiated tissues during murine development’, *Biochimica et Biophysica Acta (BBA) - Gene Structure and Expression*, vol. 1132, no. 1, pp. 43–48, Aug. 1992, doi: 10.1016/0167-4781(92)90050-A.

[133] Y. Wang, Yi Ping Wang, Y. C. Tay, and D. C. H. Harris, ‘Progressive adriamycin nephropathy in mice: Sequence of histologic and immunohistochemical events’, *Kidney Int*, vol. 58, no. 4, 2000, doi: 10.1046/j.1523-1755.2000.00342.x.

[134] M. Rook, A. T. Lely, A. B. Kramer, H. van Goor, and G. Navis, ‘Individual differences in renal ACE activity in healthy rats predict susceptibility to adriamycin-induced renal damage’, *Nephrology Dialysis Transplantation*, vol. 20, no. 1, pp. 59–64, Jan. 2005, doi: 10.1093/ndt/gfh579.

[135] S. J. Froelich-Ammon and N. Osheroff, ‘Topoisomerase poisons: Harnessing the dark side of enzyme mechanism’, 1995. doi: 10.1074/jbc.270.37.21429.

[136] J. L. Nitiss, ‘Targeting DNA topoisomerase II in cancer chemotherapy’, 2009. doi: 10.1038/nrc2607.

[137] J. C. Wang, ‘Cellular roles of DNA topoisomerases: a molecular perspective’, *Nat Rev Mol Cell Biol*, vol. 3, no. 6, pp. 430–440, Jun. 2002, doi: 10.1038/nrm831.

[138] C. Jain, H. Majumder, and S. Roychoudhury, ‘Natural Compounds as Anticancer Agents Targeting DNA Topoisomerases’, *Curr Genomics*, vol. 18, no. 1, 2016, doi: 10.2174/1389202917666160808125213.

[139] D. J. Burgess *et al.*, ‘Topoisomerase levels determine chemotherapy response in vitro and in vivo’, 2008.

[140] D. D. von Hoff *et al.*, ‘Risk factors for doxorubicin-induced congestive heart failure’, *Ann Intern Med*, vol. 91, no. 5, 1979, doi: 10.7326/0003-4819-91-5-710.

[141] K. C. Oeffinger *et al.*, ‘Chronic Health Conditions in Adult Survivors of Childhood Cancer’, *New England Journal of Medicine*, vol. 355, no. 15, pp. 1572–1582, Oct. 2006, doi: 10.1056/NEJMsa060185.

[142] M. M. Abu-Khalaf and L. Harris, ‘Anthracycline-induced cardiotoxicity: Risk assessment and management’, 2009.

[143] C. A. Geisberg and D. B. Sawyer, ‘Mechanisms of anthracycline cardiotoxicity and strategies to decrease cardiac damage’, Dec. 2010. doi: 10.1007/s11906-010-0146-y.

[144] P. K. Singal, C. M. R. Deally, and L. E. Weinberg, ‘Subcellular effects of adriamycin in the heart: A concise review’, 1987. doi: 10.1016/S0022-2828(87)80392-9.

[145] S. Raj, V. I. Franco, and S. E. Lipshultz, ‘Anthracycline-induced cardiotoxicity: A review of pathophysiology, diagnosis, and treatment’, 2014, *Current Science Inc.* doi: 10.1007/s11936-014-0315-4.

[146] M. Tokarska-Schlattner, M. Zaugg, C. Zuppinger, T. Wallimann, and U. Schlattner, ‘New insights into doxorubicin-induced cardiotoxicity: The critical role of cellular energetics’, *J Mol Cell Cardiol*, vol. 41, no. 3, pp. 389–405, Sep. 2006, doi: 10.1016/j.yjmcc.2006.06.009.

[147] A. Giantris, L. Abdurrahman, A. Hinkle, B. Asselin, and S. E. Lipshultz, ‘Anthracycline-induced cardiotoxicity in children and young adults’, *Crit Rev Oncol Hematol*, vol. 27, no. 1, pp. 53–68, 1998, doi: 10.1016/S1040-8428(97)10007-5.

[148] D. Chihara *et al.*, ‘Management strategies and outcomes for very elderly patients with diffuse large B-cell lymphoma’, *Cancer*, vol. 122, no. 20, pp. 3145–3151, Oct. 2016, doi: 10.1002/cncr.30173.

[149] E. A. Lefrak, J. Piťha, S. Rosenheim, and J. A. Gottlieb, ‘A clinicopathologic analysis of adriamycin cardiotoxicity’, *Cancer*, vol. 32, no. 2, 1973, doi: 10.1002/1097-0142(197308)32:2<302::AID-CNCR2820320205>3.0.CO;2-2.

[150] D. A. Mulrooney *et al.*, ‘Cardiac outcomes in a cohort of adult survivors of childhood and adolescent cancer: Retrospective analysis of the childhood cancer survivor study cohort’, *BMJ (Online)*, vol. 339, no. 7736, 2009, doi: 10.1136/bmj.b4606.

[151] K. Chatterjee, J. Zhang, N. Honbo, and J. S. Karliner, ‘Doxorubicin Cardiomyopathy’, *Cardiology*, vol. 115, pp. 155–162, 2010, doi: 10.1159/000265166.

[152] F. Cai *et al.*, ‘Anthracycline-induced cardiotoxicity in the chemotherapy treatment of breast cancer: Preventive strategies and treatment’, 2019. doi: 10.3892/mco.2019.1854.

[153] A. Seidman *et al.*, ‘Cardiac Dysfunction in the Trastuzumab Clinical Trials Experience’, *Journal of Clinical Oncology*, vol. 20, no. 5, pp. 1215–1221, Mar. 2002, doi: 10.1200/jco.2002.20.5.1215.

[154] I. E. Perez, S. Taveras Alam, G. A. Hernandez, and R. Sancassani, ‘Cancer Therapy-Related Cardiac Dysfunction: An Overview for the Clinician’, 2019. doi: 10.1177/1179546819866445.

[155] R. M. Lang *et al.*, ‘Recommendations for cardiac chamber quantification by echocardiography in adults: An update from the American society of echocardiography and the European association of cardiovascular imaging’, *Eur Heart J Cardiovasc Imaging*, vol. 16, no. 3, 2015, doi: 10.1093/ehjci/jev014.

[156] S. Tassan-Mangina *et al.*, ‘Tissue Doppler imaging and conventional echocardiography after anthracycline treatment in adults: Early and late alterations of left ventricular function during a prospective study’, *European Journal of Echocardiography*, vol. 7, no. 2, 2006, doi: 10.1016/j.euje.2005.04.009.

[157] L. A. Smith *et al.*, 'Cardiotoxicity of anthracycline agents for the treatment of cancer: Systematic review and meta-analysis of randomised controlled trials', *BMC Cancer*, vol. 10, 2010, doi: 10.1186/1471-2407-10-337.

[158] S. Grover *et al.*, 'Left and right ventricular effects of anthracycline and trastuzumab chemotherapy: A prospective study using novel cardiac imaging and biochemical markers', *Int J Cardiol*, vol. 168, no. 6, 2013, doi: 10.1016/j.ijcard.2013.07.246.

[159] D. Skovgaard, P. Hasbak, and A. Kjaer, 'BNP predicts chemotherapy-related cardiotoxicity and death: Comparison with gated equilibrium radionuclide ventriculography', *PLoS One*, vol. 9, no. 5, 2014, doi: 10.1371/journal.pone.0096736.

[160] P. S. Azevedo, B. F. Polegato, M. F. Minicucci, S. A. R. Paiva, and L. A. M. Zornoff, 'Cardiac Remodeling: Concepts, Clinical Impact, Pathophysiological Mechanisms and Pharmacologic Treatment', Jan. 01, 2016, *Arquivos Brasileiros de Cardiologia*. doi: 10.5935/abc.20160005.

[161] S. Tian *et al.*, 'Serum Biomarkers for the Detection of Cardiac Toxicity after Chemotherapy and Radiation Therapy in Breast Cancer Patients', *Front Oncol*, vol. 4, p. 277, Oct. 2014, doi: 10.3389/fonc.2014.00277.

[162] E. H. Herman *et al.*, 'Correlation between serum levels of cardiac troponin-T and the severity of the chronic cardiomyopathy induced by doxorubicin', *Journal of Clinical Oncology*, vol. 17, no. 7, 1999, doi: 10.1200/jco.1999.17.7.2237.

[163] S. E. Lipshultz *et al.*, 'Predictive value of cardiac troponin T in pediatric patients at risk for myocardial injury', *Circulation*, vol. 96, no. 8, 1997, doi: 10.1161/01.CIR.96.8.2641.

[164] S. H. Armenian *et al.*, 'Screening for Cardiac Dysfunction in Anthracycline-Exposed Childhood Cancer Survivors', *Clinical Cancer Research*, vol. 20, no. 24, pp. 6314–6323, Dec. 2014, doi: 10.1158/1078-0432.CCR-13-3490.

[165] M. Feola *et al.*, 'Cardiotoxicity after anthracycline chemotherapy in breast carcinoma: Effects on left ventricular ejection fraction, troponin I and brain natriuretic peptide', *Int J Cardiol*, vol. 148, no. 2, pp. 194–198, Apr. 2011, doi: 10.1016/j.ijcard.2009.09.564.

[166] L. Michel, T. Rassaf, and M. Totzeck, ‘Biomarkers for the detection of apparent and subclinical cancer therapy-related cardiotoxicity’, 2018. doi: 10.21037/jtd.2018.08.15.

[167] S. E. Lipshultz *et al.*, ‘Changes in Cardiac Biomarkers During Doxorubicin Treatment of Pediatric Patients With High-Risk Acute Lymphoblastic Leukemia: Associations With Long-Term Echocardiographic Outcomes’, *Journal of Clinical Oncology*, vol. 30, no. 10, pp. 1042–1049, Apr. 2012, doi: 10.1200/JCO.2010.30.3404.

[168] S. Bando *et al.*, ‘Plasma brain natriuretic peptide levels are elevated in patients with cancer’, *PLoS One*, vol. 12, no. 6, p. e0178607, Jun. 2017, doi: 10.1371/journal.pone.0178607.

[169] B. Ky *et al.*, ‘Early increases in multiple biomarkers predict subsequent cardiotoxicity in patients with breast cancer treated with doxorubicin, taxanes, and trastuzumab.’, *J Am Coll Cardiol*, vol. 63, no. 8, pp. 809–16, Mar. 2014, doi: 10.1016/j.jacc.2013.10.061.

[170] T. Simůnek, M. Stérba, O. Popelová, M. Adamcová, R. Hrdina, and V. Gersl, ‘Anthracycline-induced cardiotoxicity: overview of studies examining the roles of oxidative stress and free cellular iron.’, *Pharmacol Rep*, vol. 61, no. 1, pp. 154–71.

[171] M. A. MacKenzie, H. G. Buck, S. H. Meghani, and B. Riegel, ‘Unique correlates of heart failure and cancer caregiver satisfaction with hospice care’, *J Pain Symptom Manage*, vol. 51, no. 1, 2016, doi: 10.1016/j.jpainsymman.2015.09.001.

[172] X. Thomas, Q. H. Le, and D. Fiere, ‘Anthracycline-related toxicity requiring cardiac transplantation in long-term disease-free survivors with acute promyelocytic leukemia’, *Ann Hematol*, vol. 81, no. 9, 2002, doi: 10.1007/s00277-002-0534-8.

[173] A. De Angelis *et al.*, ‘Doxorubicin cardiotoxicity and target cells: a broader perspective’, *Cardio-Oncology*, vol. 2, no. 1, 2016, doi: 10.1186/s40959-016-0012-4.

[174] M. J. Adams and S. E. Lipshultz, ‘Pathophysiology of anthracycline- and radiation-associated cardiomyopathies: Implications for screening and prevention’, in *Pediatric Blood and Cancer*, 2005. doi: 10.1002/pbc.20352.

[175] S. S. Legha *et al.*, ‘Reduction of doxorubicin cardiotoxicity by prolonged continuous intravenous infusion’, *Ann Intern Med*, vol. 96, no. 2, 1982, doi: 10.7326/0003-4819-96-2-133.

[176] J. Shapira, M. Gotfried, M. Lishner, and M. Ravid, ‘Reduced cardiotoxicity of doxorubicin by a 6-hour infusion regimen. A prospective randomized evaluation’, *Cancer*, vol. 65, no. 4, 1990, doi: 10.1002/1097-0142(19900215)65:4<870::AID-CNCR2820650407>3.0.CO;2-D.

[177] G. A. Levitt, I. Dorup, K. Sorensen, and I. Sullivan, ‘Does anthracycline administration by infusion in children affect late cardiotoxicity?’, *Br J Haematol*, vol. 124, no. 4, 2004, doi: 10.1111/j.1365-2141.2004.04803.x.

[178] S. E. Lipshultz *et al.*, ‘Doxorubicin administration by continuous infusion is not cardioprotective: The Dana-Farber 91-01 acute lymphoblastic leukemia protocol’, *Journal of Clinical Oncology*, vol. 20, no. 6, 2002, doi: 10.1200/JCO.20.6.1677.

[179] S. M. Swain *et al.*, ‘Cardioprotection with dexrazoxane for doxorubicin-containing therapy in advanced breast cancer.’, *J Clin Oncol*, vol. 15, no. 4, pp. 1318–32, Apr. 1997, doi: 10.1200/JCO.1997.15.4.1318.

[180] L. R. Wiseman and C. M. Spencer, ‘Dexrazoxane’, *Drugs*, vol. 56, no. 3, pp. 385–403, 1998, doi: 10.2165/00003495-199856030-00009.

[181] C. Myers, ‘The role of iron in doxorubicin-induced cardiomyopathy’, 1998.

[182] K. L. Malisza and B. B. Hasinoff, ‘Production of hydroxyl radical by iron(III)-anthraquinone complexes through self-reduction and through reductive activation by the xanthine oxidase/hypoxanthine system’, *Arch Biochem Biophys*, vol. 321, no. 1, pp. 51–60, Aug. 1995, doi: 10.1006/abbi.1995.1367.

[183] G. MINOTTI, G. CAIRO, and E. MONTI, ‘Role of iron in anthracycline cardiotoxicity: new tunes for an old song?’, *The FASEB Journal*, vol. 13, no. 2, 1999, doi: 10.1096/fasebj.13.2.199.

[184] Y. Octavia, C. G. Tocchetti, K. L. Gabrielson, S. Janssens, H. J. Crijns, and A. L. Moens, ‘Doxorubicin-induced cardiomyopathy: From molecular mechanisms to therapeutic

strategies', *J Mol Cell Cardiol*, vol. 52, no. 6, pp. 1213–1225, Jun. 2012, doi: 10.1016/j.yjmcc.2012.03.006.

[185] J. Salazar-Mendiguchía, J. González-Costello, J. Roca, A. Ariza-Solé, N. Manito, and Á. Cequier, 'Anthracycline-mediated cardiomyopathy: Basic molecular knowledge for the cardiologist', 2014. doi: 10.1016/j.acmx.2013.08.006.

[186] A. Ghigo, M. Li, and E. Hirsch, 'New signal transduction paradigms in anthracycline-induced cardiotoxicity', 2016. doi: 10.1016/j.bbamcr.2016.01.021.

[187] S. Geiger, V. Lange, P. Suhl, V. Heinemann, and H. J. Stemmler, 'Anticancer therapy induced cardiotoxicity: Review of the literature', Jul. 2010. doi: 10.1097/CAD.0b013e3283394624.

[188] T. Šimůnek, M. Štěrba, O. Popelová, M. Adamcová, R. Hrdina, and V. Geršl, 'Anthracycline-induced cardiotoxicity: Overview of studies examining the roles of oxidative stress and free cellular iron', *Pharmacological Reports*, vol. 61, no. 1, pp. 154–171, Jan. 2009, doi: 10.1016/S1734-1140(09)70018-0.

[189] E. Goormaghtigh, P. Huart, M. Praet, R. Brasseur, and J. M. Ruysschaert, 'Structure of the adriamycin-cardiolipin complex. Role in mitochondrial toxicity.', *Biophys Chem*, vol. 35, no. 2–3, pp. 247–57, Apr. 1990, Accessed: Apr. 23, 2019. [Online]. Available: http://www.ncbi.nlm.nih.gov/pubmed/2204444

[190] J. M. C. Gutteridge, 'Lipid peroxidation and possible hydroxyl radical formation stimulated by the self-reduction of a doxorubicin-iron (III) complex', *Biochem Pharmacol*, 1984, doi: 10.1016/0006-2952(84)90340-X.

[191] G. Minotti, E. Salvatorelli, P. Menna, R. Ronchi, and G. Cairo, 'Doxorubicin irreversibly inactivates iron regulatory proteins 1 and 2 in cardiomyocytes: Evidence for distinct metabolic pathways and implications for iron-mediated cardiotoxicity of antitumor therapy', *Cancer Res*, 2001.

[192] J. C. Canzoneri and A. K. Oyelere, 'Interaction of anthracyclines with iron responsive element mRNAs', *Nucleic Acids Res*, 2008, doi: 10.1093/nar/gkn774.

[193] J. C. Barton and L. F. Bertoli, ‘Transfusion Iron Overload in Adults with Acute Leukemia: Manifestations and Therapy’, *Am J Med Sci*, vol. 319, no. 2, pp. 73–78, Feb. 2000, doi: 10.1016/S0002-9629(15)40691-3.

[194] E. Gammella, F. Maccarinelli, P. Buratti, S. Recalcati, and G. Cairo, ‘The role of iron in anthracycline cardiotoxicity’, *Front Pharmacol*, vol. 5, 2014, doi: 10.3389/fphar.2014.00025.

[195] M. F. Xu, P. L. Tang, Z. M. Qian, and M. Ashraf, ‘Effects by doxorubicin on the myocardium are mediated by oxygen free radicals’, *Life Sci*, 2001, doi: 10.1016/S0024-3205(00)00990-5.

[196] T. Šimůnek, M. Štěrba, O. Popelová, M. Adamcová, R. Hrdina, and V. Gerši, ‘Anthracycline-induced cardiotoxicity: Overview of studies examining the roles of oxidative stress and free cellular iron’, in *Pharmacological Reports*, 2009. doi: 10.1016/S1734-1140(09)70018-0.

[197] M. S. Horenstein, R. S. Vander Heide, and T. J. L’Ecuyer, ‘Molecular basis of anthracycline-induced cardiotoxicity and its prevention’, *Mol Genet Metab*, vol. 71, no. 1–2, pp. 436–444, 2000, doi: 10.1006/mgme.2000.3043.

[198] G. Link, R. Tirosh, A. Pinson, and C. Hershko, ‘Role of iron in the potentiation of anthracycline cardiotoxicity: identification of heart cell mitochondria as a major site of iron-anthracycline interaction.’, *J Lab Clin Med*, vol. 127, no. 3, pp. 272–8, Mar. 1996.

[199] G. Varricchi *et al.*, ‘Antineoplastic drug-induced cardiotoxicity: A redox perspective’, 2018. doi: 10.3389/fphys.2018.00167.

[200] R. Hrdina, V. Gersl, I. Klimtová, T. Simůnek, J. Machácková, and M. Adamcová, ‘Anthracycline-induced cardiotoxicity.’, 2000. doi: 10.14712/18059694.2019.117.

[201] G. Minotti, P. Menna, E. Salvatorelli, G. Cairo, and L. Gianni, ‘Anthracyclines: Molecular advances and pharmacologie developments in antitumor activity and cardiotoxicity’, 2004. doi: 10.1124/pr.56.2.6.

[202] M. Štěrba *et al.*, ‘Oxidative stress, redox signaling, and metal chelation in anthracycline cardiotoxicity and pharmacological cardioprotection’, 2013. doi: 10.1089/ars.2012.4795.

[203] F. S. Carvalho, A. Burgeiro, R. Garcia, A. J. Moreno, R. A. Carvalho, and P. J. Oliveira, ‘Doxorubicin-Induced Cardiotoxicity: From Bioenergetic Failure and Cell Death to Cardiomyopathy’, *Med Res Rev*, 2014, doi: 10.1002/med.21280.

[204] J. M. Berthiaume and K. B. Wallace, ‘Adriamycin-induced oxidative mitochondrial cardiotoxicity’, in *Cell Biology and Toxicology*, Jan. 2007, pp. 15–25. doi: 10.1007/s10565-006-0140-y.

[205] Y. Ichikawa *et al.*, ‘Cardiotoxicity of doxorubicin is mediated through mitochondrial iron accumulation’, *Journal of Clinical Investigation*, vol. 124, no. 2, pp. 617–630, Feb. 2014, doi: 10.1172/JCI72931.

[206] E. Goormaghtigh, P. Huart, M. Praet, R. Brasseur, and J. M. Ruysschaert, ‘Structure of the adriamycin-cardiolipin complex. Role in mitochondrial toxicity’, *Biophys Chem*, 1990, doi: 10.1016/0301-4622(90)80012-V.

[207] M. Tokarska-Schlattner *et al.*, ‘Acute toxicity of doxorubicin on isolated perfused heart: Response of kinases regulating energy supply’, *Am J Physiol Heart Circ Physiol*, 2005, doi: 10.1152/ajpheart.01057.2004.

[208] A. V. Kuznetsov, R. Margreiter, A. Amberger, V. Saks, and M. Grimm, ‘Changes in mitochondrial redox state, membrane potential and calcium precede mitochondrial dysfunction in doxorubicin-induced cell death’, *Biochimica et Biophysica Acta (BBA) - Molecular Cell Research*, vol. 1813, no. 6, pp. 1144–1152, Jun. 2011, doi: 10.1016/j.bbamcr.2011.03.002.

[209] E. Goormaghtigh, P. Chatelain, J. Caspers, and J. M. Ruysschaert, ‘Evidence of a complex between adriamycin derivatives and cardiolipin: Possible role in cardiotoxicity’, *Biochem Pharmacol*, vol. 29, no. 21, pp. 3003–3010, Nov. 1980, doi: 10.1016/0006-2952(80)90050-7.

[210] B. Aryal and V. A. Rao, ‘Deficiency in Cardiolipin Reduces Doxorubicin-Induced Oxidative Stress and Mitochondrial Damage in Human B-Lymphocytes’, *PLoS One*, vol. 11, no. 7, p. e0158376, Jul. 2016, doi: 10.1371/journal.pone.0158376.

[211] E. Goormaghtigh, P. Huart, M. Praet, R. Brasseur, and J.-M. Ruysschaert, ‘Structure of the adriamycin-cardiolipin complex’, *Biophys Chem*, vol. 35, no. 2–3, pp. 247–257, Apr. 1990, doi: 10.1016/0301-4622(90)80012-V.

[212] E. Goormaghtigh, P. Huart, R. Brasseur, and J. M. Ruysschaert, ‘Mechanism of inhibition of mitochondrial enzymatic complex I-III by adriamycin derivatives’, *BBA - Biomembranes*, 1986, doi: 10.1016/0005-2736(86)90406-2.

[213] E. Goormaghtigh, R. Brasseur, and J. M. Ruysschaert, ‘Adriamycin inactivates cytochrome c oxidase by exclusion of the enzyme from its cardiolipin essential environment’, *Biochem Biophys Res Commun*, 1982, doi: 10.1016/0006-291X(82)91976-3.

[214] M. Schlame, D. Rua, and M. L. Greenberg, ‘The biosynthesis and functional role of cardiolipin’, 2000. doi: 10.1016/S0163-7827(00)00005-9.

[215] B. Y. Nguyen, A. Ruiz-Velasco, T. Bui, L. Collins, X. Wang, and W. Liu, ‘Mitochondrial function in the heart: the insight into mechanisms and therapeutic potentials’, *Br J Pharmacol*, vol. 176, no. 22, pp. 4302–4318, Nov. 2019, doi: 10.1111/bph.14431.

[216] N. Sarvazyan, ‘Visualization of doxorubicin-induced oxidative stress in isolated cardiac myocytes’, *American Journal of Physiology-Heart and Circulatory Physiology*, vol. 271, no. 5, pp. H2079–H2085, Nov. 1996, doi: 10.1152/ajpheart.1996.271.5.H2079.

[217] P. Vejpongsa and E. T. H. Yeh, ‘Prevention of anthracycline-induced cardiotoxicity: Challenges and opportunities’, 2014. doi: 10.1016/j.jacc.2014.06.1167.

[218] R. S. Balaban, S. Nemoto, and T. Finkel, ‘Mitochondria, oxidants, and aging’, 2005. doi: 10.1016/j.cell.2005.02.001.

[219] Z. Cheng and M. Ristow, ‘Mitochondria and metabolic homeostasis’, Jul. 20, 2013, *Mary Ann Liebert, Inc. 140 Huguenot Street, 3rd Floor New Rochelle, NY 10801 USA* . doi: 10.1089/ars.2013.5255.

[220] H. von Holst *et al.*, ‘Uptake of Adriamycin in tumour and surrounding brain tissue in patients with malignant gliomas’, *Acta Neurochir (Wien)*, 1990, doi: 10.1007/BF01842886.

[221] J. S. Ingwall, ‘Energy metabolism in heart failure and remodelling’, 2009. doi: 10.1093/cvr/cvn301.

[222] M. B. Wolf and J. W. Baynes, ‘The anti-cancer drug, doxorubicin, causes oxidant stress-induced endothelial dysfunction’, *Biochim Biophys Acta Gen Subj*, 2006, doi: 10.1016/j.bbagen.2005.10.012.

[223] J. J. M. Marx and B. S. van Asbeck, ‘Use of Iron Chelators in Preventing Hydroxyl Radical Damage: Adult Respiratory Distress Syndrome as an Experimental Model for the Pathophysiology and Treatment of Oxygen-Radical-Mediated Tissue Damage’, *Acta Haematol*, 1996, doi: 10.1159/000203949.

[224] L. Xiaoping, Y. Evrovsky, D. Cole, J. Trines, L. N. Benson, and D. C. Lehotay, ‘Doxorubicin-induced acute changes in cytotoxic aldehydes, antioxidant status and cardiac function in the rat’, *Biochim Biophys Acta Mol Basis Dis*, 1997, doi: 10.1016/S0925-4439(96)00068-3.

[225] P. Angsutararux, S. Luanpitpong, and S. Issaragrisil, ‘Chemotherapy-Induced Cardiotoxicity: Overview of the Roles of Oxidative Stress’, 2015. doi: 10.1155/2015/795602.

[226] V. Milic and V. Dragojevic, ‘Doxorubicin-Induced Oxidative Injury of Cardiomyocytes - Do We Have Right Strategies for Prevention?’, in *Cardiotoxicity of Oncologic Treatments*, InTech, 2012. doi: 10.5772/34692.

[227] G. Minotti, P. Menna, E. Salvatorelli, G. Cairo, and L. Gianni, ‘Anthracyclines: Molecular advances and pharmacologie developments in antitumor activity and cardiotoxicity’, 2004. doi: 10.1124/pr.56.2.6.

[228] B. Halliwell and J. M. C. Gutteridge, *Free Radicals in Biology and Medicine*. Oxford University Press, 2015. doi: 10.1093/acprof:oso/9780198717478.001.0001.

[229] R. Hrdina, V. Gersl, I. Klimtová, T. Simůnek, J. Macháckova, and M. Adamcová, 'Anthracycline-induced cardiotoxicity', *Acta Medica (Hradec Kralove)*, vol. 43, no. 3, pp. 75–82, 2000, [Online]. Available: http://europepmc.org/abstract/MED/11089274

[230] H. G. Keizer, H. M. Pinedo, G. J. Schuurhuis, and H. Joenje, 'Doxorubicin (adriamycin): a critical review of free radical-dependent mechanisms of cytotoxicity.', *Pharmacol Ther*, vol. 47, no. 2, pp. 219–31, 1990.

[231] N. Koleini, B. E. Nickel, A. L. Edel, R. R. Fandrich, A. Ravandi, and E. Kardami, 'Oxidized phospholipids in Doxorubicin-induced cardiotoxicity', *Chem Biol Interact*, vol. 303, pp. 35–39, Apr. 2019, doi: 10.1016/J.CBI.2019.01.032.

[232] S. Kotamraju, C. R. Chitambar, S. V. Kalivendi, J. Joseph, and B. Kalyanaraman, 'Transferrin Receptor-dependent Iron Uptake Is Responsible for Doxorubicin-mediated Apoptosis in Endothelial Cells: ROLE OF OXIDANT-INDUCED IRON SIGNALING IN APOPTOSIS', *Journal of Biological Chemistry*, vol. 277, no. 19, pp. 17179–17187, May 2002, doi: 10.1074/JBC.M111604200.

[233] N. Osataphan, A. Phrommintikul, S. C. Chattipakorn, and N. Chattipakorn, 'Effects of doxorubicin-induced cardiotoxicity on cardiac mitochondrial dynamics and mitochondrial function: Insights for future interventions', *J Cell Mol Med*, vol. 24, no. 12, pp. 6534–6557, Jun. 2020, doi: 10.1111/jcmm.15305.

[234] E. Christidi and L. R. Brunham, 'Regulated cell death pathways in doxorubicin-induced cardiotoxicity', *Cell Death Dis*, vol. 12, no. 4, p. 339, Apr. 2021, doi: 10.1038/s41419-021-03614-x.

[235] O. Yokus, C. Herek, T. A. Cinli, H. Goze, and I. Serin, 'Iron overload during the treatment of acute leukemia: pretransplant transfusion experience', *Int J Hematol Oncol*, vol. 10, no. 3, Sep. 2021, doi: 10.2217/ijh-2021-0005.

[236] H. Ludwig *et al.*, 'The European Cancer Anaemia Survey (ECAS): A large, multinational, prospective survey defining the prevalence, incidence, and treatment of

anaemia in cancer patients', *Eur J Cancer*, vol. 40, no. 15, pp. 2293–2306, Oct. 2004, doi: 10.1016/j.ejca.2004.06.019.

[237] Cancer Research UK, 'Stem cell and bone marrow transplants'. Accessed: Mar. 03, 2024. [Online]. Available: https://cancerresearchuk.org/about-cancer/hodgkin-lymphoma/treatment/stem-cell-bone-marrow-transplants#:~:text=Stem%20cell%20or%20bone%20marrow,of%20cancer%2C%20including%20Hodgkin%20lymphoma

[238] Macmillan Cancer Support, 'Chemotherapy side effects'. Accessed: Mar. 03, 2024. [Online]. Available: https://www.macmillan.org.uk/cancer-information-and-support/treatment/types-of-treatment/chemotherapy/side-effects-of-chemotherapy

[239] P. K. Corey-Lisle *et al.*, 'Transfusions and patient burden in chemotherapy-induced anaemia in France', *Ther Adv Med Oncol*, vol. 6, no. 4, pp. 146–153, Jul. 2014, doi: 10.1177/1758834014534515.

[240] The American Cancer Society medical and editorial content team, 'Kinds of Blood Product Transfusions'. Accessed: Mar. 04, 2024. [Online]. Available: https://www.cancer.org/cancer/managing-cancer/treatment-types/blood-transfusion-and-donation/what-are-transfusions.html

[241] R. A. Larson, 'Receiving a Blood Transfusion During Cancer: What to Know and What to Expect', American Society of Clinical Oncology.

[242] S. Galzerano, 'Why Blood Transfusions for People with Cancer Are Necessary', Jefferson Health. Accessed: Mar. 04, 2024. [Online]. Available: https://www.jeffersonhealth.org/your-health/living-well/why-blood-transfusions-for-people-with-cancer-are-necessary

[243] P. J. Barrett-Lee, N. P. Bailey, M. E. R. O'Brien, and E. Wager, 'Large-scale UK audit of blood transfusion requirements and anaemia in patients receiving cytotoxic chemotherapy', *Br J Cancer*, vol. 82, no. 1, pp. 93–97, Jan. 2000, doi: 10.1054/bjoc.1999.0883.

[244] P. Halonen, J. Mattila, P. Suominen, T. Ruuska, M. K. Salo, and A. Mäkipernaa, 'Iron Overload in Children Who Are Treated for Acute Lymphoblastic Leukemia Estimated

by Liver Siderosis and Serum Iron Parameters', *Pediatrics*, vol. 111, no. 1, pp. 91–96, Jan. 2003, doi: 10.1542/peds.111.1.91.

[245] P. Harrison, J. R. Neilson, S. S. Marwah, L. Madden, D. Bareford, and D. W. Milligan, 'Role of non-transferrin bound iron in iron overload and liver dysfunction in long term survivors of acute leukaemia and bone marrow transplantation.', *J Clin Pathol*, vol. 49, no. 10, pp. 853–856, Oct. 1996, doi: 10.1136/jcp.49.10.853.

[246] S. M. Lichtman, L. Attivissimo, I. S. Goldman, M. W. Schuster, and A. Buchbinder, 'Secondary hemochromatosis as a long-term complication of the treatment of hematologic malignancies', *Am J Hematol*, vol. 61, no. 4, pp. 262–264, Aug. 1999, doi: 10.1002/(SICI)1096-8652(199908)61:4<262::AID-AJH7>3.0.CO;2-B.

[247] P. Arosio and S. Levi, 'Cytosolic and mitochondrial ferritins in the regulation of cellular iron homeostasis and oxidative damage', 2010. doi: 10.1016/j.bbagen.2010.02.005.

[248] E. Cocco *et al.*, 'Protective effect of mitochondrial ferritin on cytosolic iron dysregulation induced by doxorubicin in HeLa cells', *Mol Biol Rep*, 2013, doi: 10.1007/s11033-013-2792-z.

[249] P. Brissot, A. Pietrangelo, P. C. Adams, B. de Graaff, C. E. McLaren, and O. Loréal, 'Haemochromatosis', *Nat Rev Dis Primers*, vol. 4, no. 1, p. 18016, Apr. 2018, doi: 10.1038/nrdp.2018.16.

[250] K. K. Steinberg *et al.*, 'Prevalence of C282Y and H63D Mutations in the Hemochromatosis (*HFE*) Gene in the United States', *JAMA*, vol. 285, no. 17, p. 2216, May 2001, doi: 10.1001/jama.285.17.2216.

[251] J. C. Barton and C. Q. Edwards, 'HFE Hemochromatosis', *GeneReviews®*, Dec. 2018, Accessed: Mar. 04, 2024. [Online]. Available: https://www.ncbi.nlm.nih.gov/books/NBK1440/

[252] C. J. Miranda *et al.*, 'Hfe deficiency increases susceptibility to cardiotoxicity and exacerbates changes in iron metabolism induced by doxorubicin', *Blood*, 2003, doi: 10.1182/blood-2003-03-0869.

[253] The NICE Medicines and Technologies Programme, ‘Evidence review: Dexrazoxane for preventing cardiotoxicity in people aged under 25 years receiving high-dose anthracyclines or related drugs for the treatment of cancer’, Jan. 2019.

[254] S. Ali *et al.*, ‘Current status of beta-thalassemia and its treatment strategies’, *Mol Genet Genomic Med*, vol. 9, no. 12, Dec. 2021, doi: 10.1002/mgg3.1788.

[255] R. Galanello and R. Origa, ‘Beta-thalassemia’, *Orphanet J Rare Dis*, vol. 5, no. 1, p. 11, Dec. 2010, doi: 10.1186/1750-1172-5-11.

[256] U. Madan, H. Bhasin, P. Dewan, and J. Madan, ‘Improving Ineffective Erythropoiesis in Thalassemia: A Hope on the Horizon’, *Cureus*, Oct. 2021, doi: 10.7759/cureus.18502.

[257] V. Pinto and G. Forni, ‘Management of Iron Overload in Beta-Thalassemia Patients: Clinical Practice Update Based on Case Series’, *Int J Mol Sci*, vol. 21, no. 22, p. 8771, Nov. 2020, doi: 10.3390/ijms21228771.

[258] C. Borgna-Pignatti *et al.*, ‘Wintrobe’s Clinical Hematology’, 2004.

[259] S. Mavrogeni, ‘Cardiac aspects of ß-Thalassemia’, European Society of Cardiology. Accessed: Mar. 04, 2024. [Online]. Available: https://www.escardio.org/Journals/E-Journal-of-Cardiology-Practice/Volume-5/Cardiac-aspects-of-Thalassemia-Title-Cardiac-aspects-of-Thalassemia#:~:text=Prognosis,of%20symptoms%20and%20echocardiographic%20abnormalities

[260] NHS, ‘Treatment - Haemochromatosis’, NHS. Accessed: Mar. 04, 2024. [Online]. Available: https://www.nhs.uk/conditions/haemochromatosis/treatment/

[261] T. D. Coates and J. C. Wood, ‘How we manage iron overload in sickle cell patients’, *Br J Haematol*, vol. 177, no. 5, pp. 703–716, Jun. 2017, doi: 10.1111/bjh.14575.

[262] A. S. Symeonidis, ‘The role of iron and iron chelators in zygomycosis’, *Clinical Microbiology and Infection*, vol. 15, pp. 26–32, 2009, doi: 10.1111/j.1469-0691.2009.02976.x.

[263] H. C. Hatcher, R. N. Singh, F. M. Torti, and S. V Torti, ‘Synthetic and natural iron chelators: therapeutic potential and clinical use’, *Future Med Chem*, vol. 1, no. 9, pp. 1643–1670, Dec. 2009, doi: 10.4155/fmc.09.121.

[264] S. Entezari *et al.*, ‘Iron Chelators in Treatment of Iron Overload’, *J Toxicol*, vol. 2022, pp. 1–18, May 2022, doi: 10.1155/2022/4911205.

[265] A. Sigel and H. Sigel, ‘Metal Ions in Biological Systems, Volume 35: Iron Transport and Storage Microorganisms, Plants, and Animals’, *Met Based Drugs*, vol. 5, no. 5, pp. 262–262, Jan. 1998, doi: 10.1155/MBD.1998.262a.

[266] Z. D. Liu and R. C. Hider, ‘Design of iron chelators with therapeutic application’, *Coord Chem Rev*, vol. 232, no. 1–2, pp. 151–171, Oct. 2002, doi: 10.1016/S0010-8545(02)00050-4.

[267] D. G. Maxton, I. Bjarnason, A. P. Reynolds, S. D. Catt, T. J. Peters, and I. S. Menzies, ‘Lactulose 51Cr-labelled ethylenediaminetetra-acetate, <scp>l</scp> -rhamnose and polyethyleneglycol 500 as probe markers for assessment *in vivo* of human intestinal permeability’, *Clin Sci*, vol. 71, no. 1, pp. 71–80, Jul. 1986, doi: 10.1042/cs0710071.

[268] FAGERHOLM, NILSSON, KNUTSON, and LENNERNÄS, ‘Jejunal permeability in humans *in vivo* and rats *in situ* : investigation of molecular size selectivity and solvent drag’, *Acta Physiol Scand*, vol. 165, no. 3, pp. 315–324, Mar. 1999, doi: 10.1046/j.1365-201x.1999.00510.x.

[269] R. M. Santos, ‘Physicochemical Principles of Pharmacy’, *Am J Pharm Educ*, vol. 70, no. 5, Oct. 2006, Accessed: Mar. 04, 2024. [Online]. Available: /pmc/articles/PMC1637007/

[270] A. V. Hoffbrand, A. Taher, and M. D. Cappellini, ‘How I treat transfusional iron overload’, *Blood*, vol. 120, no. 18, pp. 3657–3669, Nov. 2012, doi: 10.1182/blood-2012-05-370098.

[271] J. Kwiatkowski, ‘Management of transfusional iron overload – differential properties and efficacy of iron chelating agents’, *J Blood Med*, p. 135, Sep. 2011, doi: 10.2147/JBM.S13065.

[272] G. J. Kontoghiorghes and C. N. Kontoghiorghe, ‘Efficacy and safety of iron-chelation therapy with deferoxamine, deferiprone, and deferasirox for the treatment of iron-loaded patients with non-transfusion-dependent thalassemia syndromes’, *Drug Des Devel Ther*, p. 465, Jan. 2016, doi: 10.2147/DDDT.S79458.

[273] M. R. Summers, A. Jacobs, D. Tudway, P. Perera, and C. Ricketts, ‘Studies in Desferrioxamine and Ferrioxamine Metabolism in Normal and Iron-Loaded Subjects’, *Br J Haematol*, vol. 42, no. 4, pp. 547–555, Aug. 1979, doi: 10.1111/j.1365-2141.1979.tb01167.x.

[274] GeorgeJ. Kontoghiorghes, ‘NEW ORALLY ACTIVE IRON CHELATORS’, *The Lancet*, vol. 325, no. 8432, p. 817, Apr. 1985, doi: 10.1016/S0140-6736(85)91472-2.

[275] FDA, ‘HIGHLIGHTS OF PRESCRIBING INFORMATION - FERRIPROX® (deferiprone) tablets, for oral use’, 2011.

[276] N. Mobarra *et al.*, ‘A Review on Iron Chelators in Treatment of Iron Overload Syndromes.’, *Int J Hematol Oncol Stem Cell Res*, vol. 10, no. 4, pp. 239–247, Oct. 2016.

[277] E. Poggiali, E. Cassinerio, L. Zanaboni, and M. D. Cappellini, ‘An update on iron chelation therapy.’, *Blood Transfus*, vol. 10, no. 4, pp. 411–22, Oct. 2012, doi: 10.2450/2012.0008-12.

[278] R. Galanello, ‘Deferiprone in the treatment of transfusion-dependent thalassemia: a review and perspective.’, *Ther Clin Risk Manag*, vol. 3, no. 5, pp. 795–805, Oct. 2007.

[279] C. Borgna-Pignatti, ‘Cardiac morbidity and mortality in deferoxamine- or deferiprone-treated patients with thalassemia major’, *Blood*, vol. 107, no. 9, pp. 3733–3737, May 2006, doi: 10.1182/blood-2005-07-2933.

[280] N. P. Morales, S. Rodrat, P. Piromkraipak, P. Yamanont, K. Paiboonsukwong, and S. Fucharoen, ‘Iron chelation therapy with deferiprone improves oxidative status and red blood cell quality and reduces redox-active iron in β-thalassemia/hemoglobin E patients’, *Biomedicine & Pharmacotherapy*, vol. 145, p. 112381, Jan. 2022, doi: 10.1016/j.biopha.2021.112381.

[281] A. Filosa *et al.*, 'Long-term treatment with deferiprone enhances left ventricular ejection function when compared to deferoxamine in patients with thalassemia major', *Blood Cells Mol Dis*, vol. 51, no. 2, pp. 85–88, Aug. 2013, doi: 10.1016/j.bcmd.2013.04.002.

[282] D. J. Pennell, 'Randomized controlled trial of deferiprone or deferoxamine in beta-thalassemia major patients with asymptomatic myocardial siderosis', *Blood*, vol. 107, no. 9, pp. 3738–3744, May 2006, doi: 10.1182/blood-2005-07-2948.

[283] G. C. Smith *et al.*, 'Effect of deferiprone or deferoxamine on right ventricular function in thalassemia major patients with myocardial iron overload', *Journal of Cardiovascular Magnetic Resonance*, vol. 13, no. 1, p. 34, Dec. 2011, doi: 10.1186/1532-429X-13-34.

[284] R. C. Hider and A. V. Hoffbrand, 'The Role of Deferiprone in Iron Chelation', *New England Journal of Medicine*, vol. 379, no. 22, pp. 2140–2150, Nov. 2018, doi: 10.1056/NEJMra1800219.

[285] N. Shah, 'Advances in iron chelation therapy: transitioning to a new oral formulation', *Drugs Context*, vol. 6, pp. 1–10, Jun. 2017, doi: 10.7573/dic.212502.

[286] C. Hershko, A. M. Konijn, H. P. Nick, W. Breuer, Z. I. Cabantchik, and G. Link, 'ICL670A: a new synthetic oral chelator: evaluation in hypertransfused rats with selective radioiron probes of hepatocellular and reticuloendothelial iron stores and in iron-loaded rat heart cells in culture', *Blood*, vol. 97, no. 4, pp. 1115–1122, Feb. 2001, doi: 10.1182/blood.V97.4.1115.

[287] M. Faranoush *et al.*, 'Complications in patients with transfusion dependent thalassemia: A descriptive cross-sectional study.', *Health Sci Rep*, vol. 6, no. 10, p. e1624, Oct. 2023, doi: 10.1002/hsr2.1624.

[288] E. E. Voest, S. A. B. E. van Acker, W. J. F. van der Vijgh, B. S. van Asbeck, and A. Bast, 'Comparison of Different Iron Chelators as Protective Agents Against Acute Doxorubicin-induced Cardiotoxicity', *J Mol Cell Cardiol*, vol. 26, no. 9, pp. 1179–1185, Sep. 1994, doi: 10.1006/jmcc.1994.1136.

[289] S. M. Swain and P. Vici, 'The current and future role of dexrazoxane as a cardioprotectant in anthracycline treatment: expert□panel□review', *J Cancer Res Clin Oncol*, vol. 130, no. 1, pp. 1–7, Jan. 2004, doi: 10.1007/s00432-003-0498-7.

[290] FDA, ‘HIGHLIGHTS OF PRESCRIBING INFORMATION - ZINECARD® (dexrazoxane) for injection’, 2014.

[291] A. V. S. Macedo *et al.*, ‘Efficacy of Dexrazoxane in Preventing Anthracycline Cardiotoxicity in Breast Cancer’, *JACC CardioOncol*, vol. 1, no. 1, pp. 68–79, Sep. 2019, doi: 10.1016/j.jaccao.2019.08.003.

[292] R. S. Cvetkovi and L. J. Scott, ‘Dexrazoxane’, *Drugs*, vol. 65, no. 7, pp. 1005–1024, 2005, doi: 10.2165/00003495-200565070-00008.

[293] C. K. Tebbi *et al.*, ‘Dexrazoxane-Associated Risk for Acute Myeloid Leukemia/Myelodysplastic Syndrome and Other Secondary Malignancies in Pediatric Hodgkin’s Disease’, *Journal of Clinical Oncology*, vol. 25, no. 5, pp. 493–500, Feb. 2007, doi: 10.1200/JCO.2005.02.3879.

[294] E. J. Chow *et al.*, ‘Late health outcomes after dexrazoxane treatment: A report from the Children’s Oncology Group’, *Cancer*, vol. 128, no. 4, pp. 788–796, Feb. 2022, doi: 10.1002/cncr.33974.

[295] E. C. de Baat *et al.*, ‘Dexrazoxane for preventing or reducing cardiotoxicity in adults and children with cancer receiving anthracyclines’, *Cochrane Database Systematic Reviews*, Oct. 2022, doi: 10.1002/14651858.CD014638.pub2.

[296] P. Reichardt, M.-D. Tabone, J. Mora, B. Morland, and R. L. Jones, ‘Risk–benefit of dexrazoxane for preventing anthracycline-related cardiotoxicity: re-evaluating the European labeling’, *Future Oncology*, vol. 14, no. 25, pp. 2663–2676, Oct. 2018, doi: 10.2217/fon-2018-0210.

[297] P. Menna and E. Salvatorelli, ‘Primary Prevention Strategies for Anthracycline Cardiotoxicity: A Brief Overview’, *Chemotherapy*, vol. 62, no. 3, pp. 159–168, 2017, doi: 10.1159/000455823.

[298] P. E. Schroeder and B. B. Hasinoff, ‘METABOLISM OF THE ONE-RING OPEN METABOLITES OF THE CARDIOPROTECTIVE DRUG DEXRAZOXANE TO ITS ACTIVE METAL-CHELATING FORM IN THE RAT’, *Drug Metabolism and Disposition*, vol. 33, no. 9, pp. 1367–1372, Sep. 2005, doi: 10.1124/dmd.105.005546.

[299] A. Vavrova *et al.*, ‘Catalytic Inhibitors of Topoisomerase II Differently Modulate the Toxicity of Anthracyclines in Cardiac and Cancer Cells’, *PLoS One*, vol. 8, no. 10, p. e76676, Oct. 2013, doi: 10.1371/journal.pone.0076676.

[300] D. B. Sawyer, ‘Anthracyclines and Heart Failure’, *New England Journal of Medicine*, vol. 368, no. 12, pp. 1154–1156, Mar. 2013, doi: 10.1056/NEJMcibr1214975.

[301] K. Tanabe, Y. Ikegami, R. Ishida, and T. Andoh, ‘Inhibition of Topoisomerase II by Antitumor Agents Bis(2,6-dioxopiperazine) Derivatives1’, *Cancer Res*, vol. 51, no. 18, pp. 4903–4908, Sep. 1991.

[302] E. Jirkovský *et al.*, ‘Clinically Translatable Prevention of Anthracycline Cardiotoxicity by Dexrazoxane Is Mediated by Topoisomerase II Beta and Not Metal Chelation’, *Circ Heart Fail*, vol. 14, no. 11, Nov. 2021, doi: 10.1161/CIRCHEARTFAILURE.120.008209.

[303] Y. L. Lyu *et al.*, ‘Topoisomerase IIβ–Mediated DNA Double-Strand Breaks: Implications in Doxorubicin Cardiotoxicity and Prevention by Dexrazoxane’, *Cancer Res*, vol. 67, no. 18, pp. 8839–8846, Sep. 2007, doi: 10.1158/0008-5472.CAN-07-1649.

[304] S. Deng *et al.*, ‘Dexrazoxane may prevent doxorubicin-induced DNA damage via depleting both Topoisomerase II isoforms’, *BMC Cancer*, vol. 14, no. 1, p. 842, Dec. 2014, doi: 10.1186/1471-2407-14-842.

[305] S. Zhang *et al.*, ‘Identification of the molecular basis of doxorubicin-induced cardiotoxicity’, *Nat Med*, vol. 18, no. 11, pp. 1639–1642, Nov. 2012, doi: 10.1038/nm.2919.

[306] N. Barnabé, J. A. Zastre, S. Venkataram, and B. B. Hasinoff, ‘Deferiprone protects against doxorubicin-induced myocyte cytotoxicity’, *Free Radic Biol Med*, vol. 33, no. 2, pp. 266–275, Jul. 2002, doi: 10.1016/S0891-5849(02)00873-0.

[307] E.-S. M. Ammar, S. A. Said, G. M. Suddek, and S. L. El-Damarawy, ‘Amelioration of doxorubicin-induced cardiotoxicity by deferiprone in rats’, *Can J Physiol Pharmacol*, vol. 89, no. 4, pp. 269–276, Apr. 2011, doi: 10.1139/y11-020.

[308] O. Popelová *et al.*, ‘Deferiprone Does Not Protect against Chronic Anthracycline Cardiotoxicity in Vivo’, *Journal of Pharmacology and Experimental Therapeutics*, vol. 326, no. 1, pp. 259–269, Jul. 2008, doi: 10.1124/jpet.108.137604.

[309] B. J. Cusack, S. P. Young, and R. D. Olson, ‘Daunorubicin and daunorubicinol pharmacokinetics in plasma and tissues in the rat’, *Cancer Chemother Pharmacol*, vol. 35, no. 3, pp. 213–218, 1995, doi: 10.1007/BF00686550.

[310] B. B. Hasinoff, ‘Chemistry of dexrazoxane and analogues.’, *Semin Oncol*, vol. 25, no. 4 Suppl 10, pp. 3–9, Aug. 1998.

[311] A. Piga, S. Roggero, I. Salussolia, D. Massano, M. Serra, and F. Longo, ‘Deferiprone’, *Ann N Y Acad Sci*, vol. 1202, no. 1, pp. 75–78, Aug. 2010, doi: 10.1111/j.1749-6632.2010.05586.x.

[312] D. Pennell, J. Carpenter, M. Roughton, and Z. Cabantchik, ‘On improvement in ejection fraction with iron chelation in thalassemia major and the risk of future heart failure’, *Journal of Cardiovascular Magnetic Resonance*, vol. 13, no. 1, p. 45, Dec. 2011, doi: 10.1186/1532-429X-13-45.

[313] N. K. Diop, L. K. Vitellaro, P. Arnold, M. Shang, and R. A. Marusak, ‘Iron complexes of the cardioprotective agent dexrazoxane (ICRF-187) and its desmethyl derivative, ICRF-154: solid state structure, solution thermodynamics, and DNA cleavage activity’, *J Inorg Biochem*, vol. 78, no. 3, pp. 209–216, Feb. 2000, doi: 10.1016/S0162-0134(00)00013-1.

[314] C. Thomas, G. F. Vile, and C. C. Winterbourn, ‘The hydrolysis product of ICRF-187 promotes iron-catalysed hydroxyl radical production via the Fenton reaction’, *Biochem Pharmacol*, vol. 45, no. 10, pp. 1967–1972, Apr. 1993, doi: 10.1016/0006-2952(93)90005-H.

[315] B. B. Hasinoff, ‘The use of dexrazoxane for the prevention of anthracycline extravasation injury’, *Expert Opin Investig Drugs*, vol. 17, no. 2, pp. 217–223, Feb. 2008, doi: 10.1517/13543784.17.2.217.

[316] V. Shoshan-Barmatz, V. De Pinto, M. Zweckstetter, Z. Raviv, N. Keinan, and N. Arbel, 'VDAC, a multi-functional mitochondrial protein regulating cell life and death', *Mol Aspects Med*, vol. 31, no. 3, pp. 227–285, Jun. 2010, doi: 10.1016/j.mam.2010.03.002.

[317] N. M. Mazure, 'VDAC in cancer', *Biochimica et Biophysica Acta (BBA) - Bioenergetics*, vol. 1858, no. 8, pp. 665–673, Aug. 2017, doi: 10.1016/j.bbabio.2017.03.002.

[318] Cell Signaling Technology, 'VDAC Antibody #4866', Cell Signaling Technology.

[319] Cell Signaling Technology, 'SDHA Antibody #5839', Cell Signaling Technology.

[320] Cell Signaling Technology, 'GAPDH (14C10) Rabbit mAb #2118', Cell Signaling Technology .

[321] Cell Signaling Technology, 'LAMP1 (D2D11) XP® Rabbit mAb #9091', Cell Signaling Technology.

[322] S. Wilschefski and M. Baxter, 'Inductively Coupled Plasma Mass Spectrometry: Introduction to Analytical Aspects', *Clinical Biochemist Reviews*, vol. 40, no. 3, pp. 115–133, Aug. 2019, doi: 10.33176/AACB-19-00024.

[323] L. Neufeld, 'ICP-MS Interface Cones: Maintaining the Critical Interface between the Mass Spectrometer and the Plasma Discharge to Optimize Performance and Maximize Instrument Productivity', Spectroscopy. Accessed: Mar. 05, 2024. [Online]. Available: https://www.spectroscopyonline.com/view/icp-ms-interface-cones-maintaining-critical-interface-between-mass-spectrometer-and-plasma-discharge

[324] L. Telgmann, U. Lindner, J. Lingott, and N. Jakubowski, 'Analysis and Speciation of Lanthanoides by ICP-MS', *Physical Sciences Reviews*, vol. 1, no. 11, Nov. 2016, doi: 10.1515/psr-2016-0058.

[325] Agilent, 'An Introduction to the Fundamentals of Inductively Coupled Plasma – Mass Spectrometry (ICP-MS)', Agilent. Accessed: Mar. 05, 2024. [Online]. Available: https://www.agilent.com/en/product/atomic-spectroscopy/inductively-coupled-plasma-mass-spectrometry-icp-ms/what-is-icp-ms-icp-ms-faqs

[326] D. Harvey, 'Mass Spectrometers.', LIbreTexts. Accessed: Mar. 05, 2024. [Online]. Available:

https://chem.libretexts.org/Bookshelves/Analytical_Chemistry/Instrumental_Analysis_(LibreTexts)/11%3A_Atomic_Mass_Spectrometry/11.02%3A_Mass_Spectrometers

[327] PerkinElmer, 'The 30-Minute Guide to IPC-MS', PerkinElmer.

[328] C. J. Clarke and J. N. Haselden, 'Metabolic Profiling as a Tool for Understanding Mechanisms of Toxicity', *Toxicol Pathol*, vol. 36, no. 1, pp. 140–147, Jan. 2008, doi: 10.1177/0192623307310947.

[329] Y. Chen, E.-M. Li, and L.-Y. Xu, 'Guide to Metabolomics Analysis: A Bioinformatics Workflow', *Metabolites*, vol. 12, no. 4, p. 357, Apr. 2022, doi: 10.3390/metabo12040357.

[330] M. R. Belhaj, N. G. Lawler, and N. J. Hoffman, 'Metabolomics and Lipidomics: Expanding the Molecular Landscape of Exercise Biology', *Metabolites*, vol. 11, no. 3, p. 151, Mar. 2021, doi: 10.3390/metabo11030151.

[331] G. A. Nagana Gowda and D. Raftery, 'NMR-Based Metabolomics', 2021, pp. 19–37. doi: 10.1007/978-3-030-51652-9_2.

[332] M. Mayr, 'Metabolomics', *Circ Cardiovasc Genet*, vol. 1, no. 1, pp. 58–65, Oct. 2008, doi: 10.1161/CIRCGENETICS.108.808329.

[333] I. P. GEROTHANASSIS, A. TROGANIS, V. EXARCHOU, and K. BARBAROSSOU, 'NUCLEAR MAGNETIC RESONANCE (NMR) SPECTROSCOPY: BASIC PRINCIPLES AND PHENOMENA, AND THEIR APPLICATIONS TO CHEMISTRY, BIOLOGY AND MEDICINE', *Chem. Educ. Res. Pract.*, vol. 3, no. 2, pp. 229–252, 2002, doi: 10.1039/B2RP90018A.

[334] J. B. M. E. P. R. C. D. Lambert, *Nuclear Magnetic Resonance Spectroscopy: An Introduction to Principles, Applications, and Experimental Methods*, Second Edition. WILEY, 2019.

[335] J. L. Griffin, H. Atherton, J. Shockcor, and L. Atzori, 'Metabolomics as a tool for cardiac research', *Nat Rev Cardiol*, vol. 8, no. 11, pp. 630–643, Nov. 2011, doi: 10.1038/nrcardio.2011.138.

[336] R. Salek, S. Beisken, and L. Emery, ‘Nuclear magnetic resonance (NMR)’, EMBL-EBI . Accessed: Mar. 10, 2024. [Online]. Available: https://www.ebi.ac.uk/training/online/courses/metabolomics-introduction/

[337] J. Müller *et al.*, ‘Narrative review of metabolomics in cardiovascular disease’, *J Thorac Dis*, vol. 13, no. 4, pp. 2532–2550, Apr. 2021, doi: 10.21037/jtd-21-22.

[338] N. J. Rankin *et al.*, ‘The emergence of proton nuclear magnetic resonance metabolomics in the cardiovascular arena as viewed from a clinical perspective’, *Atherosclerosis*, vol. 237, no. 1, pp. 287–300, Nov. 2014, doi: 10.1016/j.atherosclerosis.2014.09.024.

[339] J. Wallmeier *et al.*, ‘Quantification of Metabolites by NMR Spectroscopy in the Presence of Protein’, *J Proteome Res*, vol. 16, no. 4, pp. 1784–1796, Apr. 2017, doi: 10.1021/acs.jproteome.7b00057.

[340] A. A. Crook and R. Powers, ‘Quantitative NMR-Based Biomedical Metabolomics: Current Status and Applications’, *Molecules*, vol. 25, no. 21, p. 5128, Nov. 2020, doi: 10.3390/molecules25215128.

[341] O. Beckonert *et al.*, ‘Metabolic profiling, metabolomic and metabonomic procedures for NMR spectroscopy of urine, plasma, serum and tissue extracts’, *Nat Protoc*, vol. 2, no. 11, pp. 2692–2703, Nov. 2007, doi: 10.1038/nprot.2007.376.

[342] N. W. Lutz and M. Bernard, ‘Methodological Developments for Metabolic NMR Spectroscopy from Cultured Cells to Tissue Extracts: Achievements, Progress and Pitfalls’, *Molecules*, vol. 27, no. 13, p. 4214, Jun. 2022, doi: 10.3390/molecules27134214.

[343] J. R. Ussher, S. Elmariah, R. E. Gerszten, and J. R. B. Dyck, ‘The Emerging Role of Metabolomics in the Diagnosis and Prognosis of Cardiovascular Disease’, *J Am Coll Cardiol*, vol. 68, no. 25, pp. 2850–2870, Dec. 2016, doi: 10.1016/j.jacc.2016.09.972.

[344] E. Bulska and A. Ruszczyńska, ‘Analytical Techniques for Trace Element Determination’, *Physical Sciences Reviews*, vol. 2, no. 5, May 2017, doi: 10.1515/psr-2017-8002.

[345] Agilent, ‘An Introduction to the Fundamentals of Inductively Coupled Plasma – Optical Emission Spectroscopy (ICP-OES)’, Agilent. Accessed: Mar. 05, 2024. [Online]. Available: https://www.agilent.com/en/support/atomic-spectroscopy/inductively-coupled-plasma-optical-emission-spectroscopy-icp-oes/icp-oes-faq

[346] Agilent, ‘An Introduction to the Fundamentals of Atomic Absorption Spectroscopy (AAS)’, Agilent. Accessed: Mar. 06, 2024. [Online]. Available: https://www.agilent.com/en/support/atomic-spectroscopy/atomic-absorption/flame-atomic-absorption-instruments/how-does-aas-work-aas-faqs

[347] F. Raicu, C. Vlagioiu, and N. Tudor, ‘FLAME OR FURNACE AA (ATOMIC ABSORPTION)-WHICH TECHNIQUE SHOULD I USE IN MY LABORATORY? A BASIC OVERVIEW OF ELEMENTAL ANALYSIS’, *Scientific Works*, 2019.

[348] J. C. Gitz, N. Sadot, M. Zaccai, and R. Zarivach, ‘A Colorimetric Method for Measuring Iron Content in Plants’, *Journal of Visualized Experiments*, no. 139, Sep. 2018, doi: 10.3791/57408.

[349] D. Balmer, ‘COLORIMETRIC DETERMINATION OF % IRON IN UNKNOWN SAMPLE 206 ’, *university of Pennsylvania*, Jul. 2008.

[350] R. Costo *et al.*, ‘Improving the reliability of the iron concentration quantification for iron oxide nanoparticle suspensions: a two-institutions study’, *Anal Bioanal Chem*, vol. 411, no. 9, pp. 1895–1903, Mar. 2019, doi: 10.1007/s00216-018-1463-2.

[351] ThermoFisher Scientific, ‘Comparison of ICP-OES and ICP-MS for Trace Element Analysis’, ThermoFisher Scientific. Accessed: Mar. 06, 2024. [Online]. Available: https://www.thermofisher.com/uk/en/home/industrial/environmental/environmental-learning-center/contaminant-analysis-information/metal-analysis/comparison-icp-oes-icp-ms-trace-element-analysis.html#:~:text=ICP%2DMS%2C%20however%2C%20measures,parts%20per%20billion%20(ppb)

[352] M. Hedayati *et al.*, ‘An optimised spectrophotometric assay for convenient and accurate quantitation of intracellular iron from iron oxide nanoparticles’, *International Journal*

of Hyperthermia, vol. 34, no. 4, pp. 373–381, May 2018, doi: 10.1080/02656736.2017.1354403.

[353] E. Pruszkowski, 'Interferences in ICP-MS: Do we still have to worry about them?', *PerkinElmer*, 2021.

[354] D. J. Douglas and L. A. Kerr, 'Study of solids deposition on inductively coupled plasma mass spectrometry samplers and skimmers', *J Anal At Spectrom*, vol. 3, no. 6, p. 749, 1988, doi: 10.1039/ja9880300749.

[355] E. Vanclay, 'Guidelines for Troubleshooting and Maintenance of ICP-MS Systems', Mar. 2014. Accessed: Mar. 10, 2024. [Online]. Available: https://www.agilent.com/Library/eseminars/Public/updated%20ICP-MS%20Guidelines%20for%20Troubleshooting%20and%20Maintenance.pdf

[356] I. Agilent Technologies, 'Single Quadrupole ICP-MS vs Triple Quadrupole ICP-MS ', 2022.

[357] Inc. PerkinElmer, 'NexION 350 ICP-MS', 2015.

[358] Agilent, 'Controlling Cell-Formed Reaction Product Ions in ICP-QQQ', 2021.

[359] C. Jin, 'Clean Chemistry for Elemental Impurities Analysis of Pharmaceuticals in Compliance with USP 232', *AAPS PharmSciTech*, vol. 17, no. 5, pp. 1141–1149, Oct. 2016, doi: 10.1208/s12249-015-0452-4.

[360] R. S. Pappas, 'Sample Preparation Problem Solving for Inductively Coupled Plasma-Mass Spectrometry with Liquid Introduction Systems I. Solubility, Chelation, and Memory Effects.', *Spectroscopy (Springf)*, vol. 27, no. 5, pp. 20–31, May 2012.

[361] R. Chemnitzer, 'Strategies for Achieving the Lowest Possible Detection Limits in ICP-MS', *Spectroscopy*, vol. 34, no. 10, Oct. 2019.

[362] V. G. Hirsch *et al.*, 'Cardiac iron concentration in relation to systemic iron status and disease severity in non-ischaemic heart failure with reduced ejection fraction', *Eur J Heart Fail*, vol. 22, no. 11, pp. 2038–2046, Nov. 2020, doi: 10.1002/ejhf.1781.

[363] A. Paterek *et al.*, ‘Beneficial effects of intravenous iron therapy in a rat model of heart failure with preserved systemic iron status but depleted intracellular cardiac stores’, *Sci Rep*, vol. 8, no. 1, p. 15758, Oct. 2018, doi: 10.1038/s41598-018-33277-2.

[364] S. Djafarzadeh and S. M. Jakob, ‘Isolation of Intact Mitochondria from Skeletal Muscle by Differential Centrifugation for High-resolution Respirometry Measurements’, *Journal of Visualized Experiments*, no. 121, Mar. 2017, doi: 10.3791/55251.

[365] K. Neubauer, ‘Reducing the Effects of Interferences in Quadrupole ICP-MS’, *Spectroscopy -Springfield then Eugene then Duluth-*, vol. 25, 2010.

[366] T. C. Iancu, R. J. Ward, and T. J. Peters, ‘Ultrastructural observations in the carbonyl iron-fed rat, an animal model for hemochromatosis’, *Virchows Arch B Cell Pathol Incl Mol Pathol*, vol. 53, no. 1, pp. 208–217, Dec. 1987, doi: 10.1007/BF02890245.

[367] R. A. Ávila *et al.*, ‘Moderate-intensity aerobic training reduces cardiac damage attributable to experimental iron overload in rats’, *Exp Physiol*, vol. 106, no. 8, pp. 1772–1784, Aug. 2021, doi: 10.1113/EP089429.

[368] J. Khamseekaew *et al.*, ‘Effects of iron overload, an iron chelator and a T-Type calcium channel blocker on cardiac mitochondrial biogenesis and mitochondrial dynamics in thalassemic mice’, *Eur J Pharmacol*, vol. 799, pp. 118–127, Mar. 2017, doi: 10.1016/j.ejphar.2017.02.015.

[369] R. Gordan, S. Wongjaikam, J. K. Gwathmey, N. Chattipakorn, S. C. Chattipakorn, and L.-H. Xie, ‘Involvement of cytosolic and mitochondrial iron in iron overload cardiomyopathy: an update’, *Heart Fail Rev*, vol. 23, no. 5, pp. 801–816, Sep. 2018, doi: 10.1007/s10741-018-9700-5.

[370] K. Italia, R. Colah, and K. Ghosh, ‘Experimental animal model to study iron overload and iron chelation and review of other such models’, *Blood Cells Mol Dis*, vol. 55, no. 3, pp. 194–199, Oct. 2015, doi: 10.1016/j.bcmd.2015.06.003.

[371] J. Düllmann, U. Wulfhekel, P. Nielsen, and H. C. Heinrich, ‘Iron Overload of the Liver by Trimethylhexanoylferrocene in Rats’, *Cells Tissues Organs*, vol. 143, no. 2, pp. 96–108, 1992, doi: 10.1159/000147235.

[372] P. Nielsen, S. Heinelt, and J. Düllmann, ‘Chronic feeding of carbonyl-iron and TMH-ferrocene in rats. Comparison of two iron-overload models with different iron absorption’, *Comp Biochem Physiol C Pharmacol Toxicol Endocrinol*, vol. 106, no. 2, pp. 429–436, Oct. 1993, doi: 10.1016/0742-8413(93)90158-H.

[373] S. Wongjaikam, S. Kumfu, J. Khamseekaew, S. C. Chattipakorn, and N. Chattipakorn, ‘Restoring the impaired cardiac calcium homeostasis and cardiac function in iron overload rats by the combined deferiprone and N-acetyl cysteine’, *Sci Rep*, vol. 7, no. 1, p. 44460, Mar. 2017, doi: 10.1038/srep44460.

[374] G. S. Panjrath, V. Patel, C. I. Valdiviezo, N. Narula, J. Narula, and D. Jain, ‘Potentiation of Doxorubicin Cardiotoxicity by Iron Loading in a Rodent Model’, *J Am Coll Cardiol*, vol. 49, no. 25, pp. 2457–2464, Jun. 2007, doi: 10.1016/j.jacc.2007.02.060.

[375] A. Márquez-Ibarra *et al.*, ‘The Effects of Dietary Iron and Capsaicin on Hemoglobin, Blood Glucose, Insulin Tolerance, Cholesterol, and Triglycerides, in Healthy and Diabetic Wistar Rats’, *PLoS One*, vol. 11, no. 4, p. e0152625, Apr. 2016, doi: 10.1371/journal.pone.0152625.

[376] P. Nielsen and H. C. Heinrich, ‘Metabolism of iron from (3,5,5-trimethylhexanoyl) ferrocene in rats’, *Biochem Pharmacol*, vol. 45, no. 2, pp. 385–391, Jan. 1993, doi: 10.1016/0006-2952(93)90074-7.

[377] Z. Tolkien, L. Stecher, A. P. Mander, D. I. A. Pereira, and J. J. Powell, ‘Ferrous sulfate supplementation causes significant gastrointestinal side-effects in adults: a systematic review and meta-analysis.’, *PLoS One*, vol. 10, no. 2, p. e0117383, 2015, doi: 10.1371/journal.pone.0117383.

[378] I. J. Malesza *et al.*, ‘The Dark Side of Iron: The Relationship between Iron, Inflammation and Gut Microbiota in Selected Diseases Associated with Iron Deficiency Anaemia—A Narrative Review’, *Nutrients*, vol. 14, no. 17, p. 3478, Aug. 2022, doi: 10.3390/nu14173478.

[379] M. J. Cancelo-Hidalgo *et al.*, ‘Tolerability of different oral iron supplements: a systematic review’, *Curr Med Res Opin*, vol. 29, no. 4, pp. 291–303, Apr. 2013, doi: 10.1185/03007995.2012.761599.

[380] E. M. Rossi *et al.*, ‘Acute iron overload leads to hypothalamic-pituitary-gonadal axis abnormalities in female rats’, *Toxicol Lett*, vol. 240, no. 1, pp. 196–213, Jan. 2016, doi: 10.1016/j.toxlet.2015.10.027.

[381] T. D. Coates, ‘Physiology and pathophysiology of iron in hemoglobin-associated diseases’, *Free Radic Biol Med*, vol. 72, pp. 23–40, Jul. 2014, doi: 10.1016/j.freeradbiomed.2014.03.039.

[382] H.-F. Chen *et al.*, ‘A meta-analysis of association between serum iron levels and lung cancer risk’, *Cell Mol Biol*, vol. 64, no. 13, pp. 33–37, Oct. 2018, doi: 10.14715/cmb/2018.64.13.7.

[383] C. P. Wen *et al.*, ‘High Serum Iron Is Associated with Increased Cancer Risk’, *Cancer Res*, vol. 74, no. 22, pp. 6589–6597, Nov. 2014, doi: 10.1158/0008-5472.CAN-14-0360.

[384] M. E. Elsayed, M. U. Sharif, and A. G. Stack, ‘Transferrin Saturation’, 2016, pp. 71–97. doi: 10.1016/bs.acc.2016.03.002.

[385] G. Sebastiani, D. Tempesta, and A. Alberti, ‘Hepatic iron overload is common in chronic hepatitis B and is more severe in patients coinfected with hepatitis D virus’, *J Viral Hepat*, vol. 19, no. 2, Feb. 2012, doi: 10.1111/j.1365-2893.2011.01508.x.

[386] L. H. Jackson *et al.*, ‘Non-invasive MRI biomarkers for the early assessment of iron overload in a humanized mouse model of β-thalassemia’, *Sci Rep*, vol. 7, no. 1, p. 43439, Feb. 2017, doi: 10.1038/srep43439.

[387] S. N. Moon *et al.*, ‘Establishment of Secondary Iron Overloaded Mouse Model: Evaluation of Cardiac Function and Analysis According to Iron Concentration’, *Pediatr Cardiol*, vol. 32, no. 7, pp. 947–952, Oct. 2011, doi: 10.1007/s00246-011-0019-4.

[388] R. A. Rose *et al.*, ‘Iron Overload Decreases $Ca_V1.3$-Dependent L-Type Ca^{2+} Currents Leading to Bradycardia, Altered Electrical Conduction, and Atrial Fibrillation’, *Circ Arrhythm Electrophysiol*, vol. 4, no. 5, pp. 733–742, Oct. 2011, doi: 10.1161/CIRCEP.110.960401.

[389] W. J. Bartfay *et al.*, 'A Biochemical, Histochemical, and Electron Microscopic Study on the Effects of Iron-Loading on the Hearts of Mice', *Cardiovascular Pathology*, vol. 8, no. 6, pp. 305–314, Nov. 1999, doi: 10.1016/S1054-8807(99)00008-3.

[390] W. J. Bartfay and E. Bartfay, 'Iron-Overload Cardiomyopathy: Evidence for a Free Radical– Mediated Mechanism of Injury and Dysfunction in a Murine Model', *Biol Res Nurs*, vol. 2, no. 1, pp. 49–59, Jul. 2000, doi: 10.1177/109980040000200106.

[391] S. Crowe and W. J. Bartfay, 'Amlodipine Decreases Iron Uptake and Oxygen Free Radical Production in the Heart of Chronically Iron Overloaded Mice', *Biol Res Nurs*, vol. 3, no. 4, pp. 189–197, Apr. 2002, doi: 10.1177/109980040200300404.

[392] S. K. Das *et al.*, 'Iron-overload injury and cardiomyopathy in acquired and genetic models is attenuated by resveratrol therapy', *Sci Rep*, vol. 5, no. 1, p. 18132, Dec. 2015, doi: 10.1038/srep18132.

[393] S. K. Das *et al.*, 'Females Are Protected From Iron-Overload Cardiomyopathy Independent of Iron Metabolism: Key Role of Oxidative Stress', *J Am Heart Assoc*, vol. 6, no. 1, Jan. 2017, doi: 10.1161/JAHA.116.003456.

[394] N. Sumneang, N. Siri-Angkul, S. Kumfu, S. C. Chattipakorn, and N. Chattipakorn, 'The effects of iron overload on mitochondrial function, mitochondrial dynamics, and ferroptosis in cardiomyocytes', *Arch Biochem Biophys*, vol. 680, p. 108241, Feb. 2020, doi: 10.1016/j.abb.2019.108241.

[395] F. Yan, K. Li, W. Xing, M. Dong, M. Yi, and H. Zhang, 'Role of Iron-Related Oxidative Stress and Mitochondrial Dysfunction in Cardiovascular Diseases', *Oxid Med Cell Longev*, vol. 2022, pp. 1–12, Sep. 2022, doi: 10.1155/2022/5124553.

[396] N. Wilkinson and K. Pantopoulos, 'The IRP/IRE system in vivo: insights from mouse models', *Front Pharmacol*, vol. 5, Jul. 2014, doi: 10.3389/fphar.2014.00176.

[397] A. Esparza, Z. P. Gerdtzen, A. Olivera-Nappa, J. C. Salgado, and M. T. Núñez, 'Iron-induced reactive oxygen species mediate transporter DMT1 endocytosis and iron uptake in intestinal epithelial cells', *American Journal of Physiology-Cell Physiology*, vol. 309, no. 8, pp. C558–C567, Oct. 2015, doi: 10.1152/ajpcell.00412.2014.

[398] M. Al Abbas, D. Abraham, J. P. Kushner, and D. A. McClain, ‘Anti-obesity and pro-diabetic effects of hemochromatosis’, *Obesity*, vol. 22, no. 10, pp. 2120–2122, Oct. 2014, doi: 10.1002/oby.20839.

[399] D. Costamagna, P. Costelli, M. Sampaolesi, and F. Penna, ‘Role of Inflammation in Muscle Homeostasis and Myogenesis’, *Mediators Inflamm*, vol. 2015, no. 1, Jan. 2015, doi: 10.1155/2015/805172.

[400] S. Wongjaikam, S. Kumfu, J. Khamseekaew, S. C. Chattipakorn, and N. Chattipakorn, ‘Restoring the impaired cardiac calcium homeostasis and cardiac function in iron overload rats by the combined deferiprone and N-acetyl cysteine OPEN’, 2017, doi: 10.1038/srep44460.

[401] J. Govender, B. Loos, E. Marais, and A. Engelbrecht, ‘Mitochondrial catastrophe during doxorubicin-induced cardiotoxicity: a review of the protective role of melatonin’, *J Pineal Res*, vol. 57, no. 4, pp. 367–380, Nov. 2014, doi: 10.1111/jpi.12176.

[402] A. Pardo Sanz and J. L. Zamorano, ‘“Cardiotoxicity”: time to define new targets?’, *Eur Heart J*, vol. 41, no. 18, pp. 1730–1732, May 2020, doi: 10.1093/eurheartj/ehaa013.

[403] P. S. Rawat, A. Jaiswal, A. Khurana, J. S. Bhatti, and U. Navik, ‘Doxorubicin-induced cardiotoxicity: An update on the molecular mechanism and novel therapeutic strategies for effective management’, *Biomedicine & Pharmacotherapy*, vol. 139, p. 111708, Jul. 2021, doi: 10.1016/j.biopha.2021.111708.

[404] A. E. Fernández, ‘Chemotherapy-induced dysfunction’, E-Journal of Cardiology Practice.

[405] F. Pizzino *et al.*, ‘Diagnosis of Chemotherapy-Induced Cardiotoxicity’, *J Patient Cent Res Rev*, vol. 1, no. 3, pp. 121–127, Aug. 2014, doi: 10.17294/2330-0698.1025.

[406] J. L. Zamorano *et al.*, ‘2016 ESC Position Paper on cancer treatments and cardiovascular toxicity developed under the auspices of the ESC Committee for Practice Guidelines’, *Eur Heart J*, vol. 37, no. 36, pp. 2768–2801, Sep. 2016, doi: 10.1093/eurheartj/ehw211.

[407] C. Belger, C. Abrahams, A. Imamdin, and S. Lecour, ‘Doxorubicin-induced cardiotoxicity and risk factors’, *IJC Heart & Vasculature*, vol. 50, p. 101332, Feb. 2024, doi: 10.1016/j.ijcha.2023.101332.

[408] E. Braunwald, ‘Biomarkers in Heart Failure’, *New England Journal of Medicine*, vol. 358, no. 20, pp. 2148–2159, May 2008, doi: 10.1056/NEJMra0800239.

[409] M. A. Mitry and J. G. Edwards, ‘Doxorubicin induced heart failure: Phenotype and molecular mechanisms’, *IJC Heart & Vasculature*, vol. 10, pp. 17–24, Mar. 2016, doi: 10.1016/j.ijcha.2015.11.004.

[410] Hospira, ‘Temporary importation of Doxorubicin Hydrochloride 50 mg Powder for Injection (50 mg/vial) to address drug shortage issue ’, May 2016. Accessed: Mar. 10, 2024. [Online]. Available: https://www.fda.gov/media/98355/download#:~:text=Cardiac%20Toxicity%3A&text=It%20is%20recommended%20that%20the,congestive%20cardiac%20failure%20increases%20greatly

[411] A. Khanna *et al.*, ‘Increased Risk of All Cardiovascular Disease Subtypes Among Childhood Cancer Survivors’, *Circulation*, vol. 140, no. 12, pp. 1041–1043, Sep. 2019, doi: 10.1161/CIRCULATIONAHA.119.041403.

[412] E. Vandecruys, V. Mondelaers, D. De Wolf, Y. Benoit, and B. Suys, ‘Late cardiotoxicity after low dose of anthracycline therapy for acute lymphoblastic leukemia in childhood’, *Journal of Cancer Survivorship*, vol. 6, no. 1, pp. 95–101, Mar. 2012, doi: 10.1007/s11764-011-0186-6.

[413] K. Leger *et al.*, ‘Subclinical cardiotoxicity in childhood cancer survivors exposed to very low dose anthracycline therapy’, *Pediatr Blood Cancer*, vol. 62, no. 1, pp. 123–127, Jan. 2015, doi: 10.1002/pbc.25206.

[414] M. Ivanová *et al.*, ‘Chronic cardiotoxicity of doxorubicin involves activation of myocardial and circulating matrix metalloproteinases in rats’, *Acta Pharmacol Sin*, vol. 33, no. 4, pp. 459–469, Apr. 2012, doi: 10.1038/aps.2011.194.

[415] B. Bin Wu, K. T. Leung, and E. N.-Y. Poon, ‘Mitochondrial-Targeted Therapy for Doxorubicin-Induced Cardiotoxicity’, *Int J Mol Sci*, vol. 23, no. 3, p. 1912, Feb. 2022, doi: 10.3390/ijms23031912.

[416] F. Pein *et al.*, ‘Cardiac abnormalities 15 years and more after adriamycin therapy in 229 childhood survivors of a solid tumour at the Institut Gustave Roussy’, *Br J Cancer*, vol. 91, no. 1, pp. 37–44, Jul. 2004, doi: 10.1038/sj.bjc.6601904.

[417] R. Maral *et al.*, ‘[Toxicologic study and experimental antitumor activity of rubidomycin (13,057 R.P.)].’, *Pathol Biol*, vol. 15, no. 19, pp. 903–8, Oct. 1967.

[418] E. H. Herman and V. J. Ferrans, ‘Animal models of anthracycline cardiotoxicity: Basic mechanisms and cardioprotective activity’, *Prog Pediatr Cardiol*, vol. 8, no. 2, pp. 49–58, Nov. 1997, doi: 10.1016/S1058-9813(98)00002-2.

[419] E. Y. Podyacheva, E. A. Kushnareva, A. A. Karpov, and Y. G. Toropova, ‘Analysis of Models of Doxorubicin-Induced Cardiomyopathy in Rats and Mice. A Modern View From the Perspective of the Pathophysiologist and the Clinician’, *Front Pharmacol*, vol. 12, Jun. 2021, doi: 10.3389/fphar.2021.670479.

[420] F. P. Mettler, D. M. Young, and J. M. Ward, ‘Adriamycin-induced cardiotoxicity (cardiomyopathy and congestive heart failure) in rats.’, *Cancer Res*, vol. 37, no. 8 Pt 1, pp. 2705–13, Aug. 1977.

[421] R. Hayward and D. S. Hydock, ‘Doxorubicin cardiotoxicity in the rat: an in vivo characterization.’, *J Am Assoc Lab Anim Sci*, vol. 46, no. 4, pp. 20–32, Jul. 2007.

[422] NHS, ‘Doxorubicin’, Jul. 2022.

[423] Pfizer, ‘DOXORUBICIN Dosage and Administration’, 2020.

[424] M. D. Goodman, S. McPartland, D. Detelich, and M. W. Saif, ‘Chemotherapy for intraperitoneal use: a review of hyperthermic intraperitoneal chemotherapy and early post-operative intraperitoneal chemotherapy.’, *J Gastrointest Oncol*, vol. 7, no. 1, pp. 45–57, Feb. 2016, doi: 10.3978/j.issn.2078-6891.2015.111.

[425] K. N. Timm *et al.*, 'Early detection of doxorubicin-induced cardiotoxicity in rats by its cardiac metabolic signature assessed with hyperpolarized MRI', *Commun Biol*, vol. 3, no. 1, p. 692, Nov. 2020, doi: 10.1038/s42003-020-01440-z.

[426] Drugs.com, 'Doxorubicin Dosage', Drugs.com. Accessed: Mar. 08, 2024. [Online]. Available: https://www.drugs.com/dosage/doxorubicin.html

[427] NHS, 'Health Survey for England, 2021 part 1', Health Survey for England. Accessed: Mar. 08, 2024. [Online]. Available: https://digital.nhs.uk/data-and-information/publications/statistical/health-survey-for-england/2021/part-4-trends

[428] E. Lanza, A. Rozza, L. Favalli, E. Monti, P. Poggi, and F. Villani, 'The Rat Model in the Comparative Evaluation of Anthracyclines Cardiotoxicity', *Tumori Journal*, vol. 75, no. 6, pp. 533–536, Dec. 1989, doi: 10.1177/030089168907500603.

[429] F. Villani *et al.*, 'Prevention of doxorubicin-induced cardiomyopathy by reduced glutathione', *Cancer Chemother Pharmacol*, vol. 28, no. 5, pp. 365–369, 1991, doi: 10.1007/BF00685691.

[430] G. Sacco, M. Bigioni, S. Evangelista, C. Goso, S. Manzini, and C. A. Maggi, 'Cardioprotective effects of zofenopril, a new angiotensin-converting enzyme inhibitor, on doxorubicin-induced cardiotoxicity in the rat', *Eur J Pharmacol*, vol. 414, no. 1, pp. 71–78, Feb. 2001, doi: 10.1016/S0014-2999(01)00782-8.

[431] M. M. Sayed-Ahmed, M. M. Khattab, M. Z. Gad, and A.-M. M. Osman, 'Increased Plasma Endothelin-1 and Cardiac Nitric Oxide during Doxorubicin-Induced Cardiomyopathy', *Pharmacol Toxicol*, vol. 89, no. 3, pp. 140–144, Sep. 2001, doi: 10.1034/j.1600-0773.2001.d01-148.x.

[432] M. Rahimi_Balaei, M. Momeny, R. Babaeikelishomi, S. Ejtemaei Mehr, S. M. Tavangar, and A. R. Dehpour, 'The modulatory effect of lithium on doxorubicin-induced cardiotoxicity in rat', *Eur J Pharmacol*, vol. 641, no. 2–3, pp. 193–198, Sep. 2010, doi: 10.1016/j.ejphar.2010.05.046.

[433] D. S. Hydock, C.-Y. Lien, B. T. Jensen, T. L. Parry, C. M. Schneider, and R. Hayward, 'Rehabilitative exercise in a rat model of doxorubicin cardiotoxicity', *Exp Biol Med*, vol. 237, no. 12, pp. 1483–1492, Dec. 2012, doi: 10.1258/ebm.2012.012137.

[434] V. K. Todorova *et al.*, ‘Transcriptome Profiling of Peripheral Blood Cells Identifies Potential Biomarkers for Doxorubicin Cardiotoxicity in a Rat Model’, *PLoS One*, vol. 7, no. 11, p. e48398, Nov. 2012, doi: 10.1371/journal.pone.0048398.

[435] L. D. Hole, T. H. Larsen, K. O. Fossan, F. Limé, and J. Schjøtt, ‘A short-time model to study relevant indices of cardiotoxicity of doxorubicin in the rat’, *Toxicol Mech Methods*, vol. 23, no. 6, pp. 412–418, Jul. 2013, doi: 10.3109/15376516.2013.773391.

[436] N. Merlet *et al.*, ‘Increased Beta2-Adrenoceptors in Doxorubicin-Induced Cardiomyopathy in Rat’, *PLoS One*, vol. 8, no. 5, p. e64711, May 2013, doi: 10.1371/journal.pone.0064711.

[437] J. E. Toblli *et al.*, ‘Ferric Carboxymaltose-Mediated Attenuation of Doxorubicin-Induced Cardiotoxicity in an Iron Deficiency Rat Model’, *Chemother Res Pract*, vol. 2014, pp. 1–9, Apr. 2014, doi: 10.1155/2014/570241.

[438] T. Lončar-Turukalo *et al.*, ‘Heart rate dynamics in doxorubicin-induced cardiomyopathy’, *Physiol Meas*, vol. 36, no. 4, pp. 727–739, Apr. 2015, doi: 10.1088/0967-3334/36/4/727.

[439] Q.-Y. Niu, Z.-Y. Li, G.-H. Du, and X.-M. Qin, ‘1 H NMR based metabolomic profiling revealed doxorubicin-induced systematic alterations in a rat model’, *J Pharm Biomed Anal*, vol. 118, pp. 338–348, Jan. 2016, doi: 10.1016/j.jpba.2015.10.026.

[440] N. Razmaraii, H. Babaei, A. Mohajjel Nayebi, G. Asadnasab, J. Ashrafi Helan, and Y. Azarmi, ‘Cardioprotective Effect of Phenytoin on Doxorubicin-induced Cardiac Toxicity in a Rat Model’, *J Cardiovasc Pharmacol*, vol. 67, no. 3, pp. 237–245, Mar. 2016, doi: 10.1097/FJC.0000000000000339.

[441] J. L. O’Connell *et al.*, ‘Short-term and long-term models of doxorubicin-induced cardiomyopathy in rats: A comparison of functional and histopathological changes’, *Experimental and Toxicologic Pathology*, vol. 69, no. 4, pp. 213–219, Apr. 2017, doi: 10.1016/j.etp.2017.01.004.

[442] S. Ahmad, B. P. Panda, K. Kohli, M. Fahim, and K. Dubey, ‘Folic acid ameliorates celecoxib cardiotoxicity in a doxorubicin heart failure rat model’, *Pharm Biol*, vol. 55, no. 1, pp. 1295–1303, Jan. 2017, doi: 10.1080/13880209.2017.1299768.

[443] D. Cappetta *et al.*, 'Effects of ranolazine in a model of doxorubicin-induced left ventricle diastolic dysfunction', *Br J Pharmacol*, vol. 174, no. 21, pp. 3696–3712, Nov. 2017, doi: 10.1111/bph.13791.

[444] Y. Kang, W. Wang, H. Zhao, Z. Qiao, X. Shen, and B. He, 'Assessment of Subclinical Doxorubicin-induced Cardiotoxicity in a Rat Model by Speckle-Tracking Imaging', *Arq Bras Cardiol*, 2017, doi: 10.5935/abc.20170097.

[445] D. J. M. Medeiros-Lima, J. J. Carvalho, E. Tibirica, J. P. Borges, and C. Matsuura, 'Time course of cardiomyopathy induced by doxorubicin in rats', *Pharmacological Reports*, vol. 71, no. 4, pp. 583–590, Aug. 2019, doi: 10.1016/j.pharep.2019.02.013.

[446] H. Aygun and S. S. Gul, 'Cardioprotective effect of melatonin and agomelatine on doxorubicin-induced cardiotoxicity in a rat model: an electrocardiographic, scintigraphic and biochemical study', *Bratislava Medical Journal*, vol. 120, no. 04, pp. 249–255, 2019, doi: 10.4149/BLL_2019_045.

[447] V. Ö. Barış, E. Gedikli, N. Yersal, S. Müftüoğlu, and A. Erdem, 'Protective effect of taurine against doxorubicin-induced cardiotoxicity in rats: echocardiographical and histological findings', *Amino Acids*, vol. 51, no. 10–12, pp. 1649–1655, Nov. 2019, doi: 10.1007/s00726-019-02801-7.

[448] D. A. Aykan *et al.*, 'Bisoprolol and linagliptin ameliorated electrical and mechanical isometric myocardial contractions in doxorubicin-induced cardiomyopathy in rats', *Pharmacological Reports*, vol. 72, no. 4, pp. 867–876, Aug. 2020, doi: 10.1007/s43440-019-00034-9.

[449] N. Chakouri *et al.*, 'Screening for *in-vivo* regional contractile defaults to predict the delayed Doxorubicin Cardiotoxicity in Juvenile Rat', *Theranostics*, vol. 10, no. 18, pp. 8130–8142, 2020, doi: 10.7150/thno.47407.

[450] M. Ş. Adıyaman, Ö. A. Adıyaman, A. F. Dağlı, M. Z. Karahan, and M. N. Dağlı, 'Prevention of doxorubicin-induced experimental cardiotoxicity by Nigella sativa in rats', *Revista Portuguesa de Cardiologia*, vol. 41, no. 2, pp. 99–105, Feb. 2022, doi: 10.1016/j.repc.2020.12.015.

[451] M. Chen, ‘Empagliflozin attenuates doxorubicin-induced cardiotoxicity by activating AMPK/SIRT-1/PGC-1α-mediated mitochondrial biogenesis’, *Toxicol Res (Camb)*, vol. 12, no. 2, pp. 216–223, Apr. 2023, doi: 10.1093/toxres/tfad007.

[452] P. Venkatesh and A. Kasi, *Anthracyclines*. 2024.

[453] Y. Zhang *et al.*, ‘Doxorubicin Induces Sarcoplasmic Reticulum Calcium Regulation Dysfunction via the Decrease of SERCA2 and Phospholamban Expressions in Rats’, *Cell Biochem Biophys*, vol. 70, no. 3, pp. 1791–1798, Dec. 2014, doi: 10.1007/s12013-014-0130-2.

[454] J. R. Goodman, J. B. Warshaw, and P. R. Dallman, ‘Cardiac Hypertrophy in Rats with Iron and Copper Deficiency: Quantitative Contribution of Mitochondrial Enlargement’, *Pediatr Res*, vol. 4, no. 3, pp. 244–256, May 1970, doi: 10.1203/00006450-197005000-00003.

[455] V. G. Desai *et al.*, ‘Development of doxorubicin-induced chronic cardiotoxicity in the B6C3F1 mouse model’, *Toxicol Appl Pharmacol*, vol. 266, no. 1, pp. 109–121, Jan. 2013, doi: 10.1016/j.taap.2012.10.025.

[456] M. A. Fahim, ‘Ghrelin attenuates gastrointestinal epithelial damage induced by doxorubicin’, *World J Gastroenterol*, vol. 17, no. 33, p. 3836, 2011, doi: 10.3748/wjg.v17.i33.3836.

[457] K. L. Weeks and J. R. McMullen, ‘The Athlete’s Heart vs. the Failing Heart: Can Signaling Explain the Two Distinct Outcomes?’, *Physiology*, vol. 26, no. 2, pp. 97–105, Apr. 2011, doi: 10.1152/physiol.00043.2010.

[458] M. S. Willis *et al.*, ‘Doxorubicin Exposure Causes Subacute Cardiac Atrophy Dependent on the Striated Muscle–Specific Ubiquitin Ligase MuRF1’, *Circ Heart Fail*, vol. 12, no. 3, Mar. 2019, doi: 10.1161/CIRCHEARTFAILURE.118.005234.

[459] X. Fu *et al.*, ‘The Cardioprotective Mechanism of Phenylaminoethyl Selenides (PAESe) Against Doxorubicin-Induced Cardiotoxicity Involves Frataxin’, *Front Pharmacol*, vol. 11, Apr. 2021, doi: 10.3389/fphar.2020.574656.

[460] A. M. Alzahrani, P. Rajendran, V. P. Veeraraghavan, and H. Hanieh, ‘Cardiac Protective Effect of Kirenol against Doxorubicin-Induced Cardiac Hypertrophy in H9c2 Cells through Nrf2 Signaling via PI3K/AKT Pathways’, *Int J Mol Sci*, vol. 22, no. 6, p. 3269, Mar. 2021, doi: 10.3390/ijms22063269.

[461] Mayo Clinic Staff, ‘Left ventricular hypertrophy’, Mayo Clinic Press. Accessed: Mar. 09, 2024. [Online]. Available: https://www.mayoclinic.org/diseases-conditions/left-ventricular-hypertrophy/symptoms-causes/syc-20374314#:~:text=During%20left%20ventricular%20hypertrophy%2C%20the,as%20much%20force%20as%20needed

[462] M. S Oliveira, ‘Doxorubicin Cardiotoxicity and Cardiac Function Improvement After Stem Cell Therapy Diagnosed by Strain Echocardiography’, *J Cancer Sci Ther*, vol. 05, no. 02, 2013, doi: 10.4172/1948-5956.1000184.

[463] K. A. Triantafyllou, E. Karabinos, H. Kalkandi, A. I. Kranidis, and D. Babalis, ‘Clinical implications of the echocardiographic assessment of left ventricular long axis function’, *Clinical Research in Cardiology*, vol. 98, no. 9, pp. 521–532, Sep. 2009, doi: 10.1007/s00392-009-0046-9.

[464] L. Gianni, E. H. Herman, S. E. Lipshultz, G. Minotti, N. Sarvazyan, and D. B. Sawyer, ‘Anthracycline Cardiotoxicity: From Bench to Bedside’, *Journal of Clinical Oncology*, vol. 26, no. 22, pp. 3777–3784, Aug. 2008, doi: 10.1200/JCO.2007.14.9401.

[465] J. Butany, E. Ahn, and A. Luk, ‘Drug-related cardiac pathology’, *J Clin Pathol*, vol. 62, no. 12, pp. 1074–1084, Dec. 2009, doi: 10.1136/jcp.2008.058255.

[466] M. M. Hudson *et al.*, ‘Noninvasive Evaluation of Late Anthracycline Cardiac Toxicity in Childhood Cancer Survivors’, *Journal of Clinical Oncology*, vol. 25, no. 24, pp. 3635–3643, Aug. 2007, doi: 10.1200/JCO.2006.09.7451.

[467] R. Q. Migrino, D. Aggarwal, E. Konorev, T. Brahmbhatt, M. Bright, and B. Kalyanaraman, ‘Early Detection of Doxorubicin Cardiomyopathy Using Two-Dimensional Strain Echocardiography’, *Ultrasound Med Biol*, vol. 34, no. 2, pp. 208–214, Feb. 2008, doi: 10.1016/j.ultrasmedbio.2007.07.018.

[468] É. de Madron, ‘Global Left Ventricular Systolic Function Assessment’, in *Clinical Echocardiography of the Dog and Cat*, Elsevier, 2015, pp. 111–125. doi: 10.1016/B978-0-323-31650-7.00007-7.

[469] M. S. Hazari, N. Haykal-Coates, D. W. Winsett, D. L. Costa, and A. K. Farraj, ‘Continuous Electrocardiogram Reveals Differences in the Short-Term Cardiotoxic Response of Wistar-Kyoto and Spontaneously Hypertensive Rats to Doxorubicin’, *Toxicological Sciences*, vol. 110, no. 1, pp. 224–234, Jul. 2009, doi: 10.1093/toxsci/kfp092.

[470] A. Warhol, S. A. George, S. N. Obaid, T. Efimova, and I. R. Efimov, ‘Differential cardiotoxic electrocardiographic response to doxorubicin treatment in conscious versus anesthetized mice’, *Physiol Rep*, vol. 9, no. 15, Aug. 2021, doi: 10.14814/phy2.14987.

[471] M. Saddik and G. D. Lopaschuk, ‘Myocardial triglyceride turnover and contribution to energy substrate utilization in isolated working rat hearts.’, *J Biol Chem*, vol. 266, no. 13, pp. 8162–70, May 1991.

[472] G. D. Lopaschuk, Q. G. Karwi, R. Tian, A. R. Wende, and E. D. Abel, ‘Cardiac Energy Metabolism in Heart Failure’, *Circ Res*, vol. 128, no. 10, pp. 1487–1513, May 2021, doi: 10.1161/CIRCRESAHA.121.318241.

[473] W. C. Stanley, F. A. Recchia, and G. D. Lopaschuk, ‘Myocardial Substrate Metabolism in the Normal and Failing Heart’, *Physiol Rev*, vol. 85, no. 3, pp. 1093–1129, Jul. 2005, doi: 10.1152/physrev.00006.2004.

[474] D. Montaigne *et al.*, ‘Doxorubicin induces mitochondrial permeability transition and contractile dysfunction in the human myocardium’, *Mitochondrion*, vol. 11, no. 1, pp. 22–26, Jan. 2011, doi: 10.1016/j.mito.2010.06.001.

[475] Q. Guo *et al.*, ‘Cyclovirobuxine D Attenuates Doxorubicin-Induced Cardiomyopathy by Suppression of Oxidative Damage and Mitochondrial Biogenesis Impairment’, *Oxid Med Cell Longev*, vol. 2015, pp. 1–11, 2015, doi: 10.1155/2015/151972.

[476] J. Guo *et al.*, ‘Cardioprotection against doxorubicin by metallothionein Is associated with preservation of mitochondrial biogenesis involving PGC-1α pathway’, *Eur J Pharmacol*, vol. 737, pp. 117–124, Aug. 2014, doi: 10.1016/j.ejphar.2014.05.017.

[477] E. A. Melkonian and M. P. Schury, *Biochemistry, Anaerobic Glycolysis*. 2024.

[478] C. Granchi, S. Bertini, M. Macchia, and F. Minutolo, 'Inhibitors of Lactate Dehydrogenase Isoforms and their Therapeutic Potentials', *Curr Med Chem*, vol. 17, no. 7, pp. 672–697, Mar. 2010, doi: 10.2174/092986710790416263.

[479] X. Li *et al.*, 'Lactate metabolism in human health and disease', *Signal Transduct Target Ther*, vol. 7, no. 1, p. 305, Sep. 2022, doi: 10.1038/s41392-022-01151-3.

[480] X. Zheng *et al.*, 'Bnip3 mediates doxorubicin-induced cardiomyocyte pyroptosis via caspase-3/GSDME', *Life Sci*, vol. 242, p. 117186, Feb. 2020, doi: 10.1016/j.lfs.2019.117186.

[481] Y. Xia *et al.*, 'LCZ696 improves cardiac function via alleviating Drp1-mediated mitochondrial dysfunction in mice with doxorubicin-induced dilated cardiomyopathy', *J Mol Cell Cardiol*, vol. 108, pp. 138–148, Jul. 2017, doi: 10.1016/j.yjmcc.2017.06.003.

[482] O. A. Alshabanah *et al.*, 'Doxorubicin Toxicity can be Ameliorated during Antioxidant L-Carnitine Supplementation', *Oxid Med Cell Longev*, vol. 3, no. 6, pp. 428–433, 2010, doi: 10.4161/oxim.3.6.14416.

[483] P. A. Watkins, 'Fatty Acyl-CoA Synthetases', in *Encyclopedia of Biological Chemistry*, Elsevier, 2013, pp. 290–295. doi: 10.1016/B978-0-12-378630-2.00100-6.

[484] J. Bryant, J. Picot, G. Levitt, I. Sullivan, L. Baxter, and A. Clegg, 'Cardioprotection against the toxic effects of anthracyclines given to children with cancer: a systematic review', *Health Technol Assess (Rockv)*, vol. 11, no. 27, Jul. 2007, doi: 10.3310/hta11270.

[485] A. Khositseth, S. Jirasakpisarn, S. Pakakasama, L. Choubtuym, and D. Wattanasirichaigoon, 'Carnitine levels and cardiac functions in children with solid malignancies receiving doxorubicin therapy', *Indian Journal of Medical and Paediatric Oncology*, vol. 32, no. 01, pp. 38–42, Jan. 2011, doi: 10.4103/0971-5851.81889.

[486] M. SAYED-AHMED, 'PROPIONYL-? -CARNITINE AS POTENTIAL PROTECTIVE AGENT AGAINST ADRIAMYCIN-INDUCED IMPAIRMENT OF

FATTY ACID BETA-OXIDATION IN ISOLATED HEART MITOCHONDRIA', *Pharmacol Res*, vol. 41, no. 2, pp. 143–150, Feb. 2000, doi: 10.1006/phrs.1999.0583.

[487] M. M. SAYED-AHMED, S. SHAARAWY, S. A. SHOUMAN, and A.-M. M. OSMAN, 'REVERSAL OF DOXORUBICIN-INDUCED CARDIAC METABOLIC DAMAGE BYL-CARNITINE', *Pharmacol Res*, vol. 39, no. 4, pp. 289–295, Apr. 1999, doi: 10.1006/phrs.1998.0438.

[488] M. M. Sayed-Ahmed, 'Role of carnitine in cancer chemotherapy-induced multiple organ toxicity', *Saudi Pharmaceutical Journal*, vol. 18, no. 4, pp. 195–206, Oct. 2010, doi: 10.1016/j.jsps.2010.07.008.

[489] StayWell Company, 'Carnitine Deficiency', Cedars-Sinai. Accessed: Mar. 10, 2024. [Online]. Available: https://www.cedars-sinai.org/health-library/diseases-and-conditions/c/what-is-carnitine-deficiency.html

[490] S. Zervou, H. J. Whittington, A. J. Russell, and C. A. Lygate, 'Augmentation of Creatine in the Heart', *Mini-Reviews in Medicinal Chemistry*, vol. 16, no. 1, pp. 19–28, Oct. 2015, doi: 10.2174/1389557515666150722102151.

[491] N. Psychogios *et al.*, 'The human serum metabolome.', *PLoS One*, vol. 6, no. 2, p. e16957, Feb. 2011, doi: 10.1371/journal.pone.0016957.

[492] N. Pappan and A. Rehman, *Dyslipidemia*. 2024.

[493] N. Nikolac, 'Lipemia: causes, interference mechanisms, detection and management', *Biochem Med (Zagreb)*, pp. 57–67, 2014, doi: 10.11613/BM.2014.008.

[494] G. R. Thompson, 'Management of dyslipidaemia', *Heart*, vol. 90, no. 8, pp. 949–955, Aug. 2004, doi: 10.1136/hrt.2003.021287.

[495] M. de Oliveira, M. Antunes, and M. Amil, 'Plasma lipemia: When the blood donor becomes a patient', *Transfusion and Apheresis Science*, vol. 61, no. 1, p. 103294, Feb. 2022, doi: 10.1016/j.transci.2021.103294.

[496] A. Mika *et al.*, 'Potential Application of 1H NMR for Routine Serum Lipidome Analysis –Evaluation of Effects of Bariatric Surgery', *Sci Rep*, vol. 7, no. 1, p. 15530, Nov. 2017, doi: 10.1038/s41598-017-15346-0.

[497] M. D. McNeely and C. G. Massion, ‘The measurement of total fatty acid in serum.’, *Ann Clin Lab Sci*, vol. 2, no. 5, pp. 376–82, 1972.

[498] A. Avilés, J. Herrera, E. Ramos, R. Ambriz, J. Aguirre, and J. Pizzuto, ‘Hepatic injury during doxorubicin therapy.’, *Arch Pathol Lab Med*, vol. 108, no. 11, pp. 912–3, Nov. 1984.

[499] K. N. Timm *et al.*, ‘Metabolic Effects of Doxorubicin on the Rat Liver Assessed With Hyperpolarized MRI and Metabolomics’, *Front Physiol*, vol. 12, Jan. 2022, doi: 10.3389/fphys.2021.782745.

[500] O. S. Bains, T. A. Grigliatti, R. E. Reid, and K. W. Riggs, ‘Naturally Occurring Variants of Human Aldo-Keto Reductases with Reduced In Vitro Metabolism of Daunorubicin and Doxorubicin’, *Journal of Pharmacology and Experimental Therapeutics*, vol. 335, no. 3, pp. 533–545, Dec. 2010, doi: 10.1124/jpet.110.173179.

[501] N. Kassner *et al.*, ‘**Carbonyl Reductase 1 Is a Predominant Doxorubicin Reductase in the Human Liver**’, *Drug Metabolism and Disposition*, vol. 36, no. 10, pp. 2113–2120, Oct. 2008, doi: 10.1124/dmd.108.022251.

[502] P. L. Prasanna, K. Renu, and A. Valsala Gopalakrishnan, ‘New molecular and biochemical insights of doxorubicin-induced hepatotoxicity’, *Life Sci*, vol. 250, p. 117599, Jun. 2020, doi: 10.1016/j.lfs.2020.117599.

[503] A. Arvind, S. A. Osganian, D. E. Cohen, and K. E. Corey, *Lipid and Lipoprotein Metabolism in Liver Disease*. 2000.

[504] M. Alves-Bezerra and D. E. Cohen, ‘Triglyceride Metabolism in the Liver’, in *Comprehensive Physiology*, Wiley, 2017, pp. 1–22. doi: 10.1002/cphy.c170012.

[505] S. Arunachalam, P. B. Tirupathi Pichiah, and S. Achiraman, ‘Doxorubicin treatment inhibits PPARγ and may induce lipotoxicity by mimicking a type 2 diabetes-like condition in rodent models’, *FEBS Lett*, vol. 587, no. 2, pp. 105–110, Jan. 2013, doi: 10.1016/j.febslet.2012.11.019.

[506] M. O. Ifeanacho, J. C. Ikewuchi, C. C. Ikewuchi, P. C. Nweke, R. Okere, and T. L. B. Nwate, ‘Prevention of doxorubicin-induced dyslipidaemia, plasma oxidative stress and

electrolytes imbalance in Wistar rats by aqueous leaf-extracts of Chromolaena odorata and Tridax procumbens', *Sci Afr*, vol. 11, p. e00636, Mar. 2021, doi: 10.1016/j.sciaf.2020.e00636.

[507] E. Alexandri *et al.*, 'NMR and computational studies reveal novel aspects in molecular recognition of unsaturated fatty acids with non-labelled serum albumin', *FEBS J*, vol. 289, no. 18, pp. 5617–5636, Sep. 2022, doi: 10.1111/febs.16453.

[508] G. Marín-Royo *et al.*, 'The Impact of Cardiac Lipotoxicity on Cardiac Function and Mirnas Signature in Obese and Non-Obese Rats with Myocardial Infarction', *Sci Rep*, vol. 9, no. 1, p. 444, Jan. 2019, doi: 10.1038/s41598-018-36914-y.

[509] Division for Heart Disease and Stroke Prevention, 'The Scoop on Statins: What Do You Need to Know?', Million Hearts.

[510] NHS, 'Statins', NHS. Accessed: Mar. 10, 2024. [Online]. Available: https://www.nhs.uk/conditions/statins/

[511] H. Abdel-Qadir *et al.*, 'Statin Exposure and Risk of Heart Failure After Anthracycline- or Trastuzumab-Based Chemotherapy for Early Breast Cancer: A Propensity Score–Matched Cohort Study', *J Am Heart Assoc*, vol. 10, no. 2, Jan. 2021, doi: 10.1161/JAHA.119.018393.

[512] M. Obasi *et al.*, 'Statins to mitigate cardiotoxicity in cancer patients treated with anthracyclines and/or trastuzumab: a systematic review and meta-analysis', *Cancer Causes & Control*, vol. 32, no. 12, pp. 1395–1405, Dec. 2021, doi: 10.1007/s10552-021-01487-1.

[513] S. Aldobeaban, B. Mzahim, and A. A. Alshehri, 'Recurrent hypoglycemia secondary to metformin toxicity in the absence of co-ingestions: a case report', *J Med Case Rep*, vol. 12, no. 1, p. 223, Dec. 2018, doi: 10.1186/s13256-018-1758-0.

[514] J. Ritterhoff and R. Tian, 'Metabolic mechanisms in physiological and pathological cardiac hypertrophy: new paradigms and challenges', *Nat Rev Cardiol*, vol. 20, no. 12, pp. 812–829, Dec. 2023, doi: 10.1038/s41569-023-00887-x.

[515] J. Du, B. A. Wagner, G. R. Buettner, and J. J. Cullen, ‘Role of labile iron in the toxicity of pharmacological ascorbate’, *Free Radic Biol Med*, vol. 84, pp. 289–295, Jul. 2015, doi: 10.1016/j.freeradbiomed.2015.03.033.

[516] O. Kakhlon and Z. I. Cabantchik, ‘The labile iron pool: characterization, measurement, and participation in cellular processes1 1This article is part of a series of reviews on “Iron and Cellular Redox Status.” The full list of papers may be found on the homepage of the journal.’, *Free Radic Biol Med*, vol. 33, no. 8, pp. 1037–1046, Oct. 2002, doi: 10.1016/S0891-5849(02)01006-7.

[517] American Heart Association editorial staff, ‘Types of Heart Failure’, American Heart Association . Accessed: Mar. 10, 2024. [Online]. Available: https://www.heart.org/en/health-topics/heart-failure/what-is-heart-failure/types-of-heart-failure

[518] S. Failla and M. Parmar, *Iron Dextran*. 2024.

[519] Cleveland Clinic medical professional, ‘Iron Infusion’, Cleveland Clinic. Accessed: Mar. 10, 2024. [Online]. Available: https://my.clevelandclinic.org/health/treatments/14571-intravenous-iron-supplementation

[520] A. Sukumaran, J. Chang, M. Han, S. Mintri, B.-A. Khaw, and J. Kim, ‘Iron overload exacerbates age-associated cardiac hypertrophy in a mouse model of hemochromatosis’, *Sci Rep*, vol. 7, no. 1, p. 5756, Jul. 2017, doi: 10.1038/s41598-017-05810-2.

[521] Q. Lu *et al.*, ‘Effects of Chemotherapy on Serum Lipids in Chinese Postoperative Breast Cancer Patients’, *Cancer Manag Res*, vol. Volume 12, pp. 8397–8408, Sep. 2020, doi: 10.2147/CMAR.S253397.

[522] T. He *et al.*, ‘Adjuvant chemotherapy-associated lipid changes in breast cancer patients’, *Medicine*, vol. 99, no. 33, p. e21498, Aug. 2020, doi: 10.1097/MD.0000000000021498.

[523] G. Arpino *et al.*, ‘Metabolic and anthropometric changes in early breast cancer patients receiving adjuvant therapy’, *Breast Cancer Res Treat*, vol. 154, no. 1, pp. 127–132, Nov. 2015, doi: 10.1007/s10549-015-3586-x.

[524] K. R. Feingold, *Cholesterol Lowering Drugs*. 2000.

[525] D. J. Kumbhani and A. Saha, ‘Statins to Prevent the Cardiotoxicity of Anthracyclines - STOP-CA’, American College of Cardiology Foundation. Accessed: Mar. 10, 2024. [Online]. Available: https://www.acc.org/Latest-in-Cardiology/Clinical-Trials/2023/08/08/16/06/stop-ca

[526] Wake Forest University Health Sciences, ‘Preventing Anthracycline Cardiovascular Toxicity With Statins (PREVENT)’, National Library of Medicine. Accessed: Mar. 10, 2024. [Online]. Available: https://clinicaltrials.gov/study/NCT01988571

[527] Y. M. Hong, H. S. Kim, and H.-R. Yoon, ‘Serum Lipid and Fatty Acid Profiles in Adriamycin-Treated Rats after Administration of L-Carnitine’, *Pediatr Res*, vol. 51, no. 2, pp. 249–255, Feb. 2002, doi: 10.1203/00006450-200202000-00020.

[528] C. Abrahams, N. J. Woudberg, and S. Lecour, ‘Anthracycline-induced cardiotoxicity: targeting high-density lipoproteins to limit the damage?’, *Lipids Health Dis*, vol. 21, no. 1, p. 85, Sep. 2022, doi: 10.1186/s12944-022-01694-y.

[529] K. Renu *et al.*, ‘Exploring the Pattern of Metabolic Alterations Causing Energy Imbalance via PPARα Dysregulation in Cardiac Muscle During Doxorubicin Treatment’, *Cardiovasc Toxicol*, vol. 22, no. 5, pp. 436–461, May 2022, doi: 10.1007/s12012-022-09725-x.

[530] A. R. Wende and E. D. Abel, ‘Lipotoxicity in the heart’, *Biochimica et Biophysica Acta (BBA) - Molecular and Cell Biology of Lipids*, vol. 1801, no. 3, pp. 311–319, Mar. 2010, doi: 10.1016/j.bbalip.2009.09.023.

[531] A. Willebrands, H. F. ter Welle, and S. J. Tasseron, ‘The effect of a high molar FFA/albumin ratio in the perfusion medium on rhythm and contractility of the isolated rat heart’, *J Mol Cell Cardiol*, vol. 5, no. 3, pp. 259–273, Jun. 1973, doi: 10.1016/0022-2828(73)90066-7.

[532] A. Pugazhendhi, T. N. J. I. Edison, B. K. Velmurugan, J. A. Jacob, and I. Karuppusamy, ‘Toxicity of Doxorubicin (Dox) to different experimental organ systems’, *Life Sci*, vol. 200, pp. 26–30, May 2018, doi: 10.1016/j.lfs.2018.03.023.

[533] F. P. Boeno, J. Patel, R. N. Montalvo, S. S. Lapierre-Nguyen, C. M. Schreiber, and A. J. Smuder, ‘Effects of Exercise Preconditioning on Doxorubicin-Induced Liver and Kidney Toxicity in Male and Female Rats’, *Int J Mol Sci*, vol. 24, no. 12, p. 10222, Jun. 2023, doi: 10.3390/ijms241210222.

[534] Bethesda, *Doxorubicin*. 2012.

[535] J. N. van der Veen, J. P. Kennelly, S. Wan, J. E. Vance, D. E. Vance, and R. L. Jacobs, ‘The critical role of phosphatidylcholine and phosphatidylethanolamine metabolism in health and disease’, *Biochimica et Biophysica Acta (BBA) - Biomembranes*, vol. 1859, no. 9, pp. 1558–1572, Sep. 2017, doi: 10.1016/j.bbamem.2017.04.006.

[536] J. Ling, T. Chaba, L.-F. Zhu, R. L. Jacobs, and D. E. Vance, ‘Hepatic ratio of phosphatidylcholine to phosphatidylethanolamine predicts survival after partial hepatectomy in mice’, *Hepatology*, vol. 55, no. 4, pp. 1094–1102, Apr. 2012, doi: 10.1002/hep.24782.

[537] C. J. Walkey, L. Yu, L. B. Agellon, and D. E. Vance, ‘Biochemical and Evolutionary Significance of Phospholipid Methylation’, *Journal of Biological Chemistry*, vol. 273, no. 42, pp. 27043–27046, Oct. 1998, doi: 10.1074/jbc.273.42.27043.

[538] Z. Li *et al.*, ‘The ratio of phosphatidylcholine to phosphatidylethanolamine influences membrane integrity and steatohepatitis’, *Cell Metab*, vol. 3, no. 5, pp. 321–331, May 2006, doi: 10.1016/j.cmet.2006.03.007.

[539] S. Shama *et al.*, ‘Phosphatidylethanolamines Are Associated with Nonalcoholic Fatty Liver Disease (NAFLD) in Obese Adults and Induce Liver Cell Metabolic Perturbations and Hepatic Stellate Cell Activation’, *Int J Mol Sci*, vol. 24, no. 2, p. 1034, Jan. 2023, doi: 10.3390/ijms24021034.

[540] H. Yoon, J. L. Shaw, M. C. Haigis, and A. Greka, ‘Lipid metabolism in sickness and in health: Emerging regulators of lipotoxicity’, *Mol Cell*, vol. 81, no. 18, pp. 3708–3730, Sep. 2021, doi: 10.1016/j.molcel.2021.08.027.

[541] M. Hedayatnia *et al.*, ‘Dyslipidemia and cardiovascular disease risk among the MASHAD study population’, *Lipids Health Dis*, vol. 19, no. 1, p. 42, Dec. 2020, doi: 10.1186/s12944-020-01204-y.

[542] S. Tanzey, X. Shao, A. Brooks, and P. Scott, ‘Synthesis of [11C]deferiprone and inhibition of radiolysis’, *Journal of Nuclear Medicine*, vol. 61, no. supplement 1, p. 1119, May 2020, [Online]. Available: http://jnm.snmjournals.org/content/61/supplement_1/1119.abstract

[543] M. Lewandowski and K. Gwozdzinski, ‘Nitroxides as Antioxidants and Anticancer Drugs’, *Int J Mol Sci*, vol. 18, no. 11, p. 2490, Nov. 2017, doi: 10.3390/ijms18112490.

[544] J. Wolfram and M. Ferrari, ‘Clinical cancer nanomedicine’, *Nano Today*, vol. 25, pp. 85–98, Apr. 2019, doi: 10.1016/j.nantod.2019.02.005.

[545] L. A. Smith *et al.*, ‘Cardiotoxicity of anthracycline agents for the treatment of cancer: Systematic review and meta-analysis of randomised controlled trials’, *BMC Cancer*, vol. 10, no. 1, p. 337, Dec. 2010, doi: 10.1186/1471-2407-10-337.

[546] H. Maeda, ‘Toward a full understanding of the EPR effect in primary and metastatic tumors as well as issues related to its heterogeneity’, *Adv Drug Deliv Rev*, vol. 91, pp. 3–6, Aug. 2015, doi: 10.1016/j.addr.2015.01.002.

[547] M. Gyöngyösi *et al.*, ‘Liposomal doxorubicin attenuates cardiotoxicity via induction of interferon-related DNA damage resistance’, *Cardiovasc Res*, Jul. 2019, doi: 10.1093/cvr/cvz192.

[548] X.-R. Li, X.-H. Cheng, G.-N. Zhang, X.-X. Wang, and J.-M. Huang, ‘Cardiac safety analysis of first-line chemotherapy drug pegylated liposomal doxorubicin in ovarian cancer’, *J Ovarian Res*, vol. 15, no. 1, p. 96, Aug. 2022, doi: 10.1186/s13048-022-01029-6.

[549] H. Wang *et al.*, ‘Uptake and release profiles of PEGylated liposomal doxorubicin nanoparticles: A comprehensive picture based on separate determination of encapsulated and total drug concentrations in tissues of tumor-bearing mice’, *Talanta*, vol. 208, p. 120358, Feb. 2020, doi: 10.1016/j.talanta.2019.120358.

[550] S.-Q. Shi, F.-F. Jiang, T. Hong, Y. Zhuang, L. Chen, and X.-L. Huang, ‘Comparison of pegylated liposomal doxorubicin and paclitaxel plus carboplatin-based chemotherapy as first line treatment for patients with ovarian cancer: a systematic review and meta-

analysis of randomized controlled trials.', *Eur Rev Med Pharmacol Sci*, vol. 24, no. 6, pp. 2911–2927, Mar. 2020, doi: 10.26355/eurrev_202003_20655.

[551] E. Tahover, Y. P. Patil, and A. A. Gabizon, 'Emerging delivery systems to reduce doxorubicin cardiotoxicity and improve therapeutic index', *Anticancer Drugs*, vol. 26, no. 3, pp. 241–258, Mar. 2015, doi: 10.1097/CAD.0000000000000182.

[552] X.-R. Li, X.-H. Cheng, G.-N. Zhang, X.-X. Wang, and J.-M. Huang, 'Cardiac safety analysis of first-line chemotherapy drug pegylated liposomal doxorubicin in ovarian cancer', *J Ovarian Res*, vol. 15, no. 1, p. 96, Aug. 2022, doi: 10.1186/s13048-022-01029-6.

[553] D. H. Tran and Z. V. Wang, 'Glucose Metabolism in Cardiac Hypertrophy and Heart Failure', *J Am Heart Assoc*, vol. 8, no. 12, Jun. 2019, doi: 10.1161/JAHA.119.012673.

[554] E. C. Laiakis *et al.*, 'Effects of Low Dose Space Radiation Exposures on the Splenic Metabolome', *Int J Mol Sci*, vol. 22, no. 6, p. 3070, Mar. 2021, doi: 10.3390/ijms22063070.

[555] C. Gopalan and E. Kirk, *Biology of Cardiovascular and Metabolic Diseases*. Elsevier, 2022. doi: 10.1016/C2019-0-04900-X.

[556] A. C. Alves *et al.*, 'Influence of doxorubicin on model cell membrane properties: insights from in vitro and in silico studies', *Sci Rep*, vol. 7, no. 1, p. 6343, Jul. 2017, doi: 10.1038/s41598-017-06445-z.

[557] W. Chen *et al.*, 'CN128: A New Orally Active Hydroxypyridinone Iron Chelator', *J Med Chem*, vol. 63, no. 8, pp. 4215–4226, Apr. 2020, doi: 10.1021/acs.jmedchem.0c00137.